N72 30895

NASA CONTRACTOR
REPORT

CASE FILE
COPY

NASA CR-61390

SATURN BASE HEATING HANDBOOK

By C. R. Mullen, R. L. Bender, R. L. Bevill,
J. Reardon, and L. Hartley

The Boeing Company
Huntsville, Alabama

May 1, 1972

Final Report

Prepared for

NASA-GEORGE C. MARSHALL SPACE FLIGHT CENTER
Marshall Space Flight Center, Alabama 35812

TECHNICAL REPORT STANDARD TITLE PAGE

1. REPORT NO.	2. GOVERNMENT ACCESSION NO.	3. RECIPIENT'S CATALOG NO.
NASA CR-61390		

TITLE AND SUBTITLE	5. REPORT DATE
Saturn Base Heating Handbook , Final Report	May 1, 1972
	6. PERFORMING ORGANIZATION CODE
AUTHOR(S) C. R. Mullen; R. L. Bender; R. L. Bevill; J. J. Reardon; L. Hartley	8. PERFORMING ORGANIZATION REPORT # TD-050
PERFORMING ORGANIZATION NAME AND ADDRESS The Boeing Company Huntsville, Alabama	10. WORK UNIT NO.
	11. CONTRACT OR GRANT NO. Contract NAS8-5608
	13. TYPE OF REPORT & PERIOD COVERED NASA Contractor Report
SPONSORING AGENCY NAME AND ADDRESS National Aeronautics and Space Administration Washington, D. C. 20546	14. SPONSORING AGENCY CODE

SUPPLEMENTARY NOTES

ABSTRACT

Over the last ten years, a significant amount of model and flight test base heating data have been generated on the Saturn I, IB and Saturn V launch vehicle development programs to assure an adequate base area thermal design. This handbook contains a summary of model and flight test base heating data from the S-I, S-IB, S-IV, S-IC, and S-II stages and a review of available analytical prediction methods. Sufficient experimental data are provided to make the handbook a good single source of Saturn base heating data which can be used for preliminary base heating design predictions of future launch vehicles.

KEY WORDS
Base heating, rocket plumes, thermal environment

18. DISTRIBUTION STATEMENT

Unclassified - Unlimited

Terry F. Greenwood
Aero-Astrodynamics Laboratory

SECURITY CLASSIF. (of this report)	20. SECURITY CLASSIF. (of this page)	21. NO. OF PAGES	22. PRICE
Unclassified	Unclassified	505	$6.00

C - Form 3292 (May 1969)

ACKNOWLEDGEMENTS

This handbook was prepared by The Boeing Company Aerophysics Group at the request of Dr. T. F. Greenwood and Mr. D. C. Seymour of the Marshall Space Flight Center Aero-Astrodynamics Laboratory.

Mr. C. R. Mullen of The Boeing Company was responsible for overall direction of the handbook compilation, technical editing, prepared the Introduction and provided contributions to the General Base Heating Problem Description and Prediction Philosophy (Section 2.0). Mr. L. Hartley of the Chrysler Corporation Space Division provided the S-I and S-IB data (Section 3.0). Messrs. R. L. Bender and R. L. Bevill of The Boeing Company prepared the S-IC and S-IV data (Sections 4.0 and 5.0), respectively. Mr. J. Reardon of REMTECH provided the data for the S-II stage (Section 6.0). Mr. Bender also contributed significantly to the text and arrangement of each individual section to maximize continuity and clarity throughout the report.

Mr. B. Laten prepared the figures for the Boeing sections of the report as well as formatting the data from the other prime contributors. All typed material is the work of Miss Diana Bogart.

Data from the Cornell Aeronautical Laboratories, Arnold Engineering Development Center (AEDC), Chrysler and Boeing documents have been used extensively throughout the report.

CONTENTS

SATURN BASE HEATING HANDBOOK

1.0	INTRODUCTION	1-1
2.0	GENERAL BASE HEATING PROBLEM DESCRIPTION AND PREDICTION PHILOSOPHY	2-2
3.0	SATURN S-I STAGE	3-2
4.0	SATURN S-IC STAGE	4-2
5.0	SATURN S-IV STAGE	5-2
6.0	SATURN S-II STAGE	6-2
7.0	OTHER DATA	7-2

1.0 INTRODUCTION

Base heating for over a decade has been a major consideration in the design of booster systems, especially for multiple-engine configurations. Early failures in the Polaris, Jupiter and Atlas flight test programs and similar failures of the Thor during high altitude nuclear tests spotlighted the importance of proper base heating design considerations. Every major booster development program since these early failures have included extensive model testing, analytical studies and highly instrumented flight vehicles to properly assess the adequacy of the base design.

The prediction of base heating is very complex because of the large number of variables upon which it depends. There are currently no satisfactory methods for defining the base flow field and the methods of calculating convective or radiative heating from hot recirculating gases are crude at best. Experimental model and flight test data are therefore used extensively in base heating predictions although computational methods for determining radiative heat transfer from exhaust plumes have advanced rapidly in the last few years and are considered adequate for base heating predictions. Caution must be exercised in the use of experimental data in predicting base heating environments. Model scaling effects and lack of simulation complicate the use of model data and both model and flight instrumentation accuracy produce wide bands of uncertainty.

The Saturn launch vehicle development programs in the last ten years have produced a significant amount of model and flight test base heating data for a number of different configurations. The initial design of the Saturn I Block I vehicle was conceived in 1958, and the first flight in the Saturn I program was the SA-1 flight on October 27, 1961. Since that time there have been 25 additional flights with the Saturn vehicles; the most recent being the Apollo 16 flight utilizing the AS-511 Saturn V launch vehicle on April 16, 1972. The Saturn/Apollo launch vehicle configurations can be seen in Figure 1-1. The S-I and S-IB vehicles consist of two stages each and the Saturn V consists of three stages. These stage configurations have produced data for four different engine arrangements and two types of propellant. Minor configurational changes have produced parametric data useful in preliminary design work.

The MSFC Aero-Astrodynamics Laboratory felt the need for a single source of Saturn base heating data which would aid future base heating predictions on advanced booster concepts such as the Space Shuttle. Therefore, the following sections contain data from the Saturn I and IB (Section 3.0), S-IC (Section 4.0), S-IV (Section 5.0), and S-II (Section 6.0) development programs. The S-IVB stage of the Saturn V vehicle is a single engine stage producing a very low radiation heating environment. Base heating has not been an important S-IVB design consideration and has therefore not been included in this handbook.

1.0 (Continued)

The base heating handbook includes a description of the general base heating problem and prediction philosophy (Section 2.0), vehicle configuration descriptions, model and flight test data and references. Because of the volume of base heating data available, the handbook summarizes the most important data and refers the reader to more detailed data contained in the references. There is, however, enough data provided to make the handbook a good single source of Saturn base heating data which can be used for preliminary design base heating predictions.

Data contained herein have been taken from a large number of reports with differing formats and units and no attempt has been made to make the units or formats consistent. The table below is provided so that conversions from one set of units to another can be made.

Multiply	By	To Obtain
Watts/cm^2	0.88	Btu/ft^2sec
Kilocalorie/m^2sec	0.370	Btu/ft^2sec
°K	1.8	°R
Meters	3.281	Feet
N/cm^2	1.45	PSI

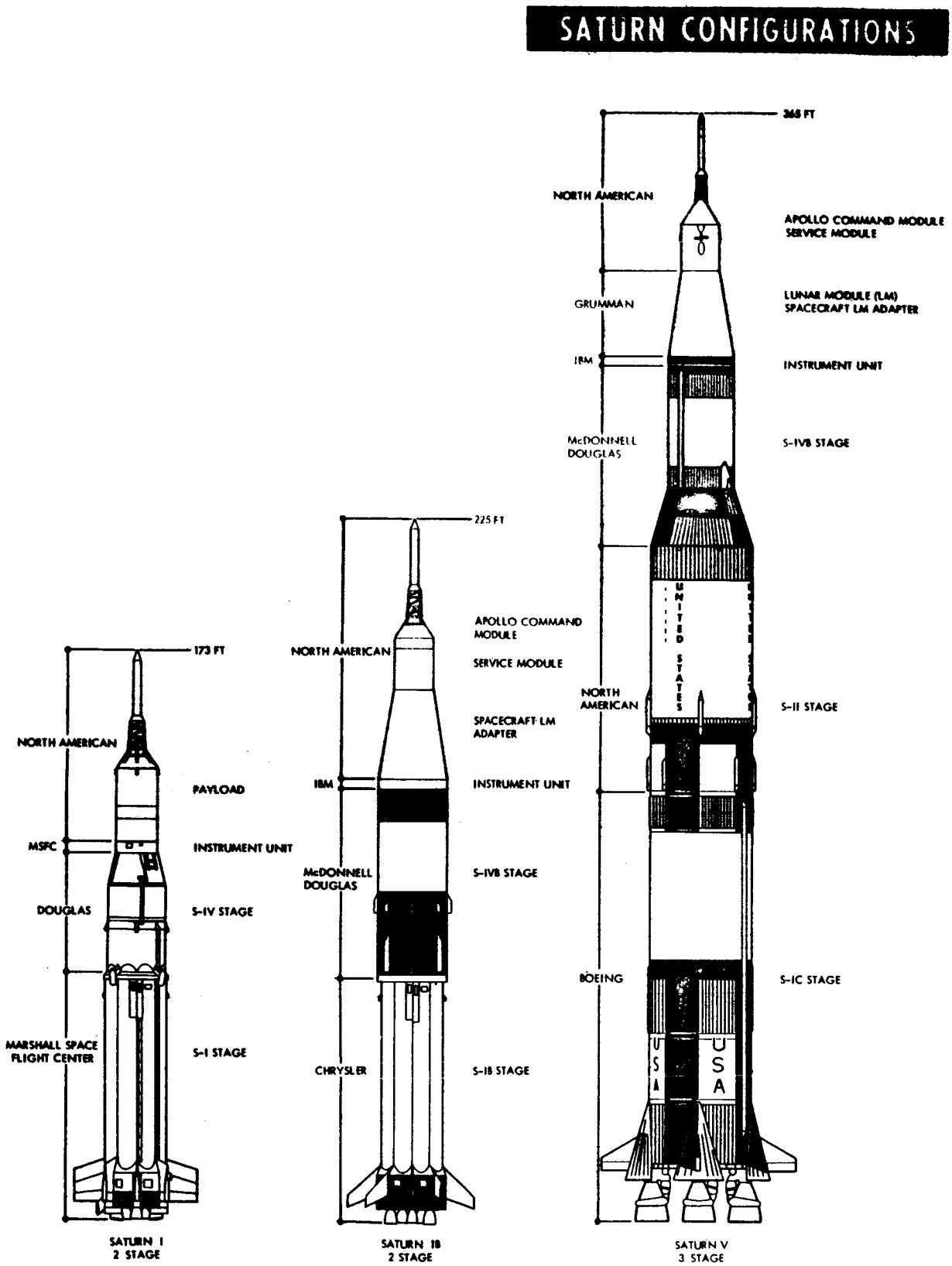

FIGURE 1-1. SATURN/APOLLO LAUNCH VEHICLE CONFIGURATIONS

THIS PAGE LEFT BLANK INTENTIONALLY

CONTENTS

SECTION 2.0 GENERAL BASE HEATING PROBLEM DESCRIPTION AND PREDICTION PHILOSOPHY

2.1 PREDICTION PHILOSOPHY 2-4

2.2 SUMMARY OF SATURN EXPERIMENTAL DATA 2-6

2.3 SUMMARY OF ANALYTICAL METHODS 2-9

2.4 PARAMETERS INFLUENCING BASE HEATING 2-15

2.5 REFERENCES 2-16

2.0 GENERAL BASE HEATING PROBLEM DESCRIPTION AND PREDICTION PHILOSOPHY

Heating in the base region of the Saturn class booster vehicles has been one of the primary areas of concern and investigation by NASA/MSFC and its contractors throughout the last decade. Although the base heating problem differs from stage to stage and with different propellants, certain basic aspects of base heating are the same on all multi-engine boosters. Base heating is caused by radiation from the exhaust plumes and radiation and convective heating caused by hot gases which are recirculated into the base region. Both radiation and convective heating are increased when secondary combustion of fuel-rich exhaust gases occurs along the plume boundary or in the reversed flow field.

Typical multi-engine base flow fields are shown in Figure 2.1-1 for low altitude, medium altitude and high altitude conditions. Radiation and convection can be significant at lift-off with splashing from the launch pad. At low altitude, the predominant heating mode is radiation from the plumes. Due to the ejector action of the plumes, convective cooling results from the aspirated flow of ambient air across the base. As the exhaust plumes expand with increasing altitude they impinge upon one another creating high pressure areas which cause a reversal or recirculation of some of the lower energy exhaust flow. These recirculated gases create a convective heating environment, and, depending on the gas constituents, can also be a source of significant hot gas radiation. At higher altitudes, if the flow does not choke, the density of the gas in the base is reduced which reduces the heating environment. If choking occurs, the pressure and heating become constant and independent of altitude and free stream flow.

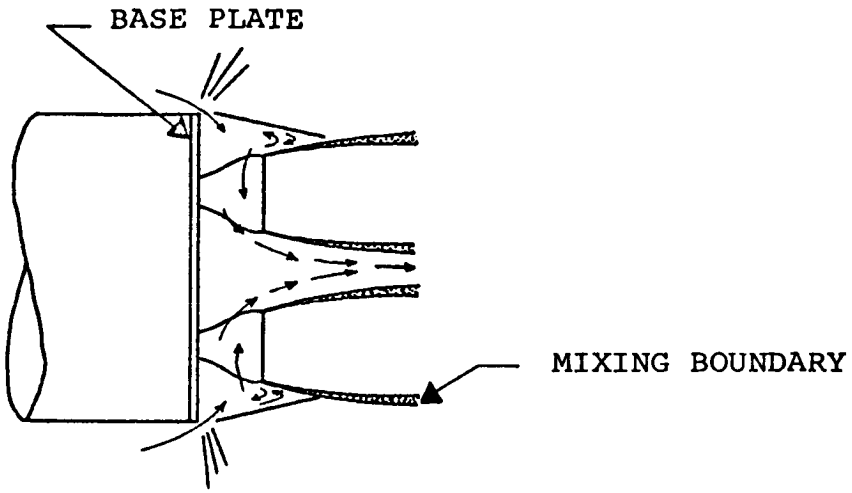

ASPIRATION FLOW (LOW ALTITUDE)

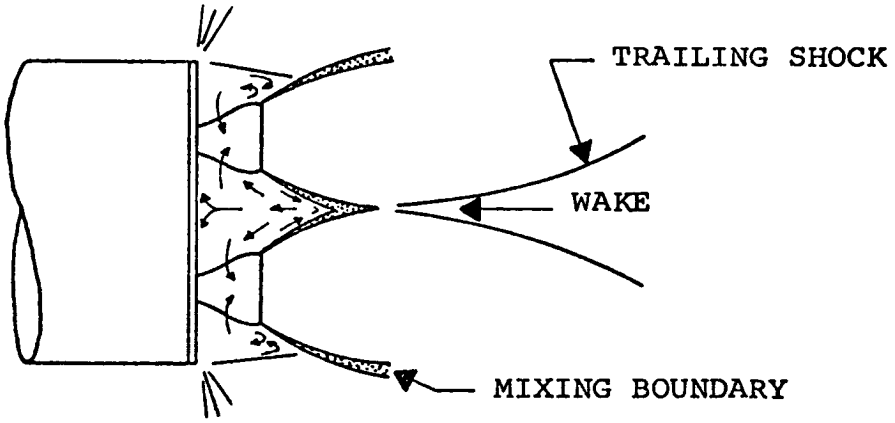

TRANSITIONAL FLOW

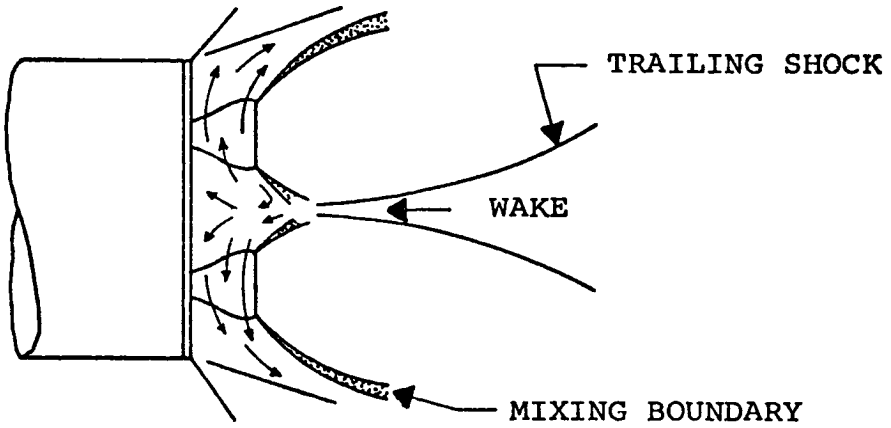

CHOKED REVERSE FLOW (HIGH ALTITUDE)

FIGURE 2.1-1. QUALITATIVE DESCRIPTION OF FLOW FIELDS FOR A CLUSTERED ROCKET CONFIGURATION

2.1 PREDICTION PHILOSOPHY

Base region design prediction philosophy for the Saturn vehicles have varied slightly from contractor to contractor, and depended somewhat upon the sequence of vehicles under development (the Saturn V stages benefited from previous Saturn I predictions and flight data). However, in general, the following prediction philosophy has been followed on all Saturn stages:

1. Analytical and empirical techniques have been used for radiation predictions.

2. Flight data from comparable vehicles have been used to define magnitudes of gas temperature and convective heating. The effect of altitude on main plume radiation, and the radiation potential of recirculated gases can also be predicted from flight data.

3. Model test data of the specific configuration have been used to predict when hot gases would be expected in the base region, to indicate magnitudes of base pressure and base gas temperature, and to determine relative heating effects with changes in configuration.

Table 2.1-1 illustrates the prediction philosophy in block diagram form. Preliminary design predictions on the base heating environment are obtained from a combination of analytical calculations and previous launch vehicle model and flight data having similar configurations. Analytical adjustments are made for differences in parameters which affect base heating. Thermal environments for detailed design are based on preliminary predictions which are adjusted using model test data of the configuration of interest, full scale static engine test exhaust plume radiation measurements (LOX/RP-1) and analytical radiation calculations (LOX/H_2). Care must be taken in the model test simulation to provide the best possible data. The model data must be carefully scaled for application to the prototype. The best currently available scaling procedures still result in rather large uncertainties for full-scale heat fluxes. It is therefore good practice to overdesign the heat shield of early vehicles and to remove any excessive shielding from subsequent vehicles as flight test data become available. Early flights should be well instrumented to define the base thermal environment to determine the adequacy of the base area thermal design.

The prediction methods used by each stage contractor are described in more detail in each stage section. Model test data and flight test data peculiar to each stage are also included in those sections. A summary of model and flight test data has been prepared and is described in Section 2.2. A cursory review of analytical methods, with emphasis on the chronological development of these methods, is contained in Section 2.3.

TABLE 2.1-1.

PREDICTION METHODS

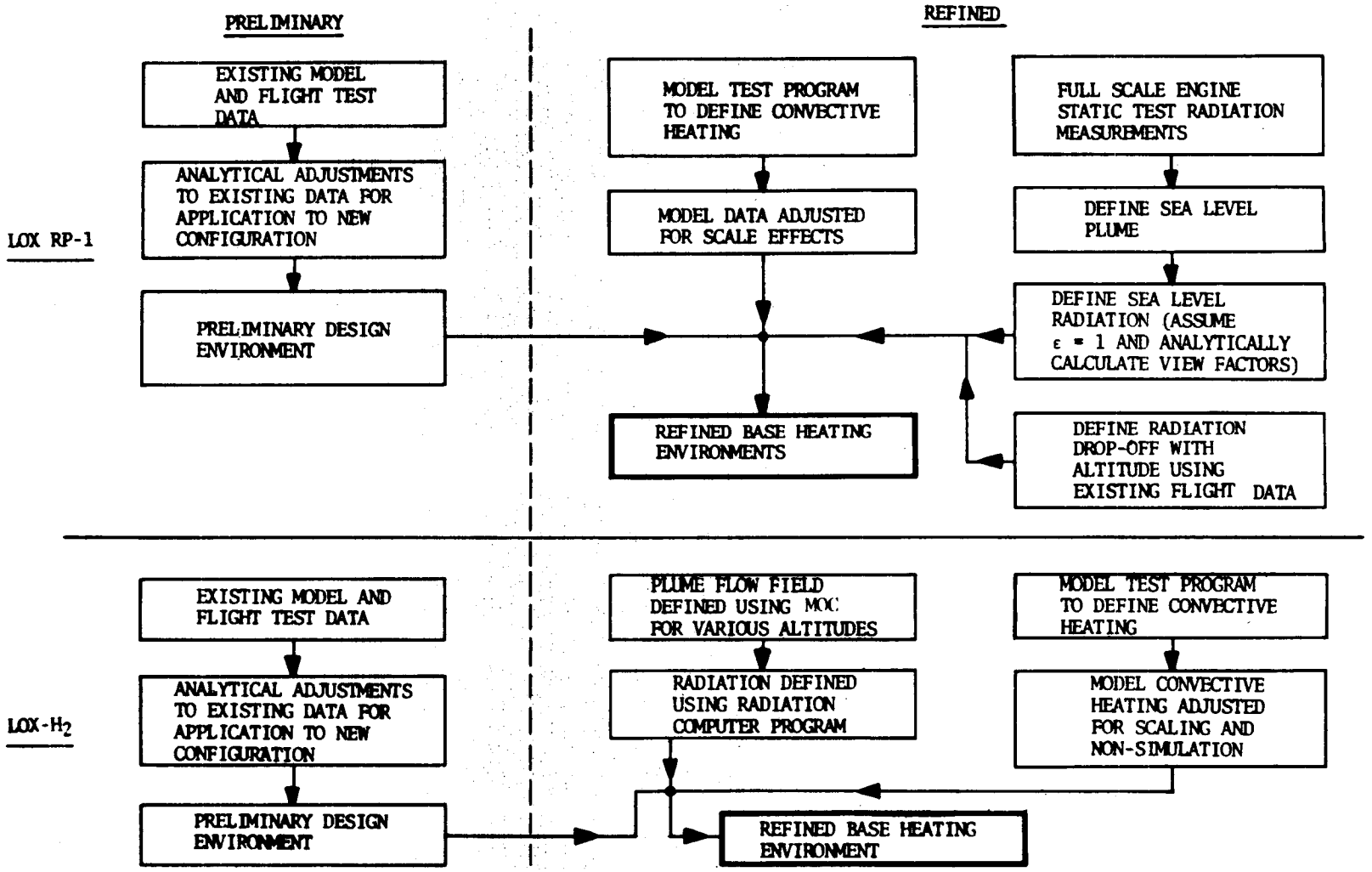

2.2 SUMMARY OF SATURN EXPERIMENTAL DATA

In the time span from October 27, 1961, to present, there have been 25 flights with Saturn vehicles. These flights are summarized below:

VEHICLE	NUMBER OF FLIGHTS
Saturn I Block I	4 flights (SA-1 through SA-4)
Saturn I Block II	6 flights (SA-5 through SA-10)
Saturn IB	5 flights (SA-201 through SA-205)
Saturn V	11 flights (AS-501 through AS-511)

The base regions of the Saturn I, Block I and II vehicles were heavily instrumented with thermocouples, calorimeters, and pressure measurements. The first four Saturn IB flights and the first five Saturn V flights were also heavily instrumented. These instruments have produced a considerable quantity of useful base heating and pressure data. A summary of the Saturn Flight Base Heating Data is included in Table 2.2-1. Detailed discussions of the flight tests and parametric data are included in each stage section.

Throughout the Saturn program, model tests were conducted to assist the base heating design predictions and to gain insight into the effect of parametric variables and configuration changes. Early model tests for the S-I and S-IV stages of the Saturn I vehicle were hot flow, long duration tests performed mainly at AEDC Propulsion Wind Tunnel and Rocket Test Facility. Later tests with the S-IB, S-II and S-IC stages were conducted using the short-duration experimental techniques. These tests were conducted principally at CAL and Lewis Research Center. A summary of Saturn Model Base Heating Tests is presented in Table 2.2-2. Detailed discussions of the individual test programs are included in each stage section.

TABLE 2.2-1. SUMMARY OF SATURN FLIGHT BASE HEATING

VEHICLE	STAGE	BASE CONFIGURATION	ENGINE	TYPE PROPELLANT	NOMINAL OPERATING CHARACTERISTICS		ALTITUDE RANGE (KM)	TYPICAL HEATING ENVIRONMENT ($WATTS/CM^2$)	
					P_c (PSIA)	O/F		RADIATION	CONVECTION
SATURN I (BLOCK I & II)	S-I		H-1	LOX/RP-1	600	2.25	0-60	37.0	7.0
	S-IV		RL-10	LOX/LH_2	300	5.0	60-225	*	1.3*
SATURN IB	S-IB		H-1	LOX/RP-1	600	2.3	0-60	41.0	4.5
	S-IVB		J-2	LOX/LH_2	715	5.5	60-185	0.3	0
SATURN V	S-IC		F-1	LOX/RP-1	1000	2.28	0-60	19.0	4.0
	S-II		J-2	LOX/LH_2	715	5.5	60-190	1.5	2.0
	S-IVB		J-2	LOX/LH_2	715	5.5	190	0.3	0

* Total heating rate measured on SA-6 is assumed to be convective heating.

TABLE 2.2-2. SUMMARY OF SATURN MODEL BASE HEATING

VEHICLE	STAGE	BASE CONFIGURATION	SCALE	TEST FACILITY	TYPE TEST	TEST CONDITIONS		MODEL PROPELLANTS	MODEL TURBINE EXHAUST SIMULATION
						MACH RANGE	ALTITUDE RANGE (FEET)		
SATURN I (BLOCK I & II)	S-I		5.47% 5.47% 5.47%	AEDC-PWT 16 FOOT TRANSONIC AEDC-RTF AEDC-RTF	LONG DURATION-HOT FLOW LONG DURATION-HOT FLOW LONG DURATION-HOT FLOW	0.6 - 1.5 0.8, 1.5 1.63 3.07	10,000-42,000 16,000; 27,500 33,000-45,000 70,000-80,000	LOX/RP-1 LOX/RP-1 LOX/RP-1	GH_2 GH_2 GH_2
	S-IV	4 ENGINE 6 ENGINE	1/10 1/27.75 1/10 1/10	AEDC-RTF/T-3 (4 ENGINE) AEDC-RTF (4 ENGINE) CAL ALTITUDE CHAMBER (4 ENGINE) CAL ALTITUDE CHAMBER (6 ENGINE)	LONG DURATION-HOT FLOW LONG DURATION-COLD FLOW SHORT DURATION-HOT FLOW SHORT DURATION-HOT FLOW	NO EXTERNAL FLOW NO EXTERNAL FLOW NO EXTERNAL FLOW NO EXTERNAL FLOW	118,500-152,500 150,000 140,000-200,000 120,000-220,000	GOX/GH_2 AIR H_2O_9/H_2 GOX/GH_2	HELIUM HEATER SIMULATION AMBIENT H_2 PREDICTED H_2-N_2 MIXTURE
SATURN IB	S-IB		5.47%	AEDC-RTF/T-1	SHORT DURATION-HOT FLOW	1.18 1.63	30,000 40,000	GOX/ETHYLENE	COLD H_2
	S-IVB		NO TESTING						
SATURN V	S-IC		1/45 1/45 1/45 1/45	CAL 8x8 TRANSONIC LeRC 8x6 TRANSONIC LeRC 10x10 SUPERSONIC CAL HIGH ALTITUDE CHAMBER	SHORT DURATION-HOT FLOW SHORT DURATION-HOT FLOW SHORT DURATION-HOT FLOW SHORT DURATION-HOT FLOW	0.6 - 1.2 0.2 - 1.65 2.0 - 3.5 NO EXTERNAL FLOW	13,000-34,000 8,000-50,000 51,000-96,000 125,000-205,000	GOX/ETHYLENE GOX/ETHYLENE GOX/ETHYLENE GOX/ETHYLENE	GH_2 GH_2 GH_2 GH_2
	S-II		1/25 1/25	CAL HIGH ALTITUDE CHAMBER MSFC IMPULSE BASE FLOW FACILITY	SHORT DURATION-HOT FLOW SHORT DURATION-HOT FLOW	NO EXTERNAL FLOW NO EXTERNAL FLOW	150,000-265,000 150,000-265,000	GOX/GH_2 GOX/GH_2	GH_2 GH_2
	S-IVB		NO TESTING						

2.3 SUMMARY OF ANALYTICAL METHODS

The following subsections contain a description of the analytical tools available for predicting radiation and convective base heating. Extensive analytical investigations have been made over the past fifteen years to gain a better understanding of the physical phenomena associated with the base environment so that accurate mathematical models of the flow field and heat transfer mechanisms could be constructed. Programs are available to calculate the radiative heat flux from the exhaust products of solid or liquid propulsion systems. The definition of the flow field and thermodynamic properties pose the major problem to the calculation of radiation.

The convective aspect of the base heating problem is less understood. There are differing opinions among investigators about the physical flow model as well as the governing equations to be used to define the heating mechanism. The many variables and complex flow fields associated with base recirculation have made it difficult to develop accurate analytical procedures for predicting the convective environment on arbitrary configurations. Because of these limitations and basic disagreements about the physical model, the summary of convective analytical models will be limited to a listing of pertinent references. No attempt will be made to compare the various approaches or assess the applicability of individual methods.

2.3.1 Analytical Methods for Predicting Radiation from Rocket Exhausts

The significance of exhaust plume radiation in the thermal environment of rocket vehicles, and the problems involved in the accurate prediction of this radiation vary with each application. Although the most important factors in these variations are the propellants used and the altitude range to be considered, other factors, such as engine arrangement, engine chamber pressure, nozzle area ratio, and the method of exhausting fuel rich turbo-pump exhaust gases, can also have a significant influence on the problem, Reference 2-1.

The propellants define the radiating constituents which must be considered. In the first stage of both the Saturn I and the Saturn V vehicles, kerosene/oxygen propellants are used. In these cases, the dominant radiating species is carbon particles, although significant concentrations of water vapor, carbon dioxide and carbon monoxide are also present. Since the upper stages of the Saturn vehicles use hydrogen/oxygen propellants, the only significant radiative constituent for these stages is water vapor.

The primary radiation source at low altitudes (below 10 km) is the mixing layer where air combines with the fuel-rich exhaust plume to produce a high temperature afterburning mantle. As altitude increases, the reduction in atmospheric pressure eliminates the combustion on the exterior of the plume. With the elimination of plume afterburning, the most significant radiation sources become the high temperature regions formed by the shock waves surrounding the impingement planes between the plumes of clustered engines.

2.3.1 (Continued)

Two characteristics of the radiation from exhaust plumes of first-stage vehicles were used in the development of the preliminary prediction techniques. The first important characteristic is that the afterburning around the exhaust plume is most intense at low altitudes, and the second characteristic is the effect of the carbon particles in the exhaust gas. The carbon particles provide continuum radiation and greatly increase the optical thickness of the gases, so that radiation can be approximated by assuming a continuum radiation emanating from the outer layers of gases. This approximation, combined with empirical measurements of the equivalent black-body temperature of the exhaust plume, provides a flame model consisting of cylindrical sections with a temperature assigned to each section. The shape and temperatures of the cylindrical model have been determined on the Saturn I and Saturn V H-1 and F-1 engines respectively, using optical and radiometer data from full scale engine static tests. This model can be used with appropriate form factors to predict the radiation environment in the base region for sea level conditions. The decrease in radiant heating with increasing altitudes, which is estimated from previous flight data, is applied to the predicted sea level heating rates to estimate the variation in radiant heat load throughout the flight. A typical flame model and altitude decay curve are shown in Figure 2.3-1.

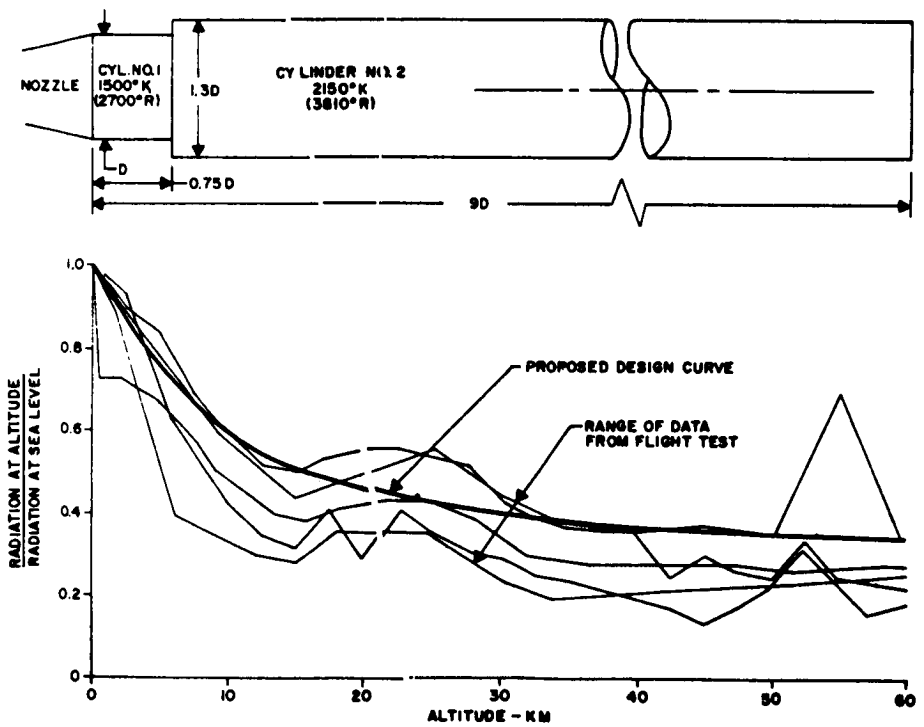

FIGURE 2.3-1. TYPICAL FLAME PATTERN AND ALTITUDE DECAY DATA

2.3.1 (Continued)

This method predicts sea level heating environment extremely well but the altitude decay can be complicated by hot gas radiation from the recirculated exhaust gases. Currently experimental data must be used to predict the radiation from hot recirculating gases.

Since the initial methods depend upon a prior knowledge of certain empirical data, a more fundamental approach was sought. The ensuing research programs led to the development of a calculation method using band models with a modified Curtis-Godson approximation to account for inhomogeneous gas properties. These new methods have been found effective in predicting radiative heat transfer from LOX-H_2 using flow properties from a method of characteristics program and adjustments for interaction regions. However, LOX/RP-1 exhaust flow mixing layers and afterburning cannot be predicted reliably and therefore empirical data must still be obtained.

A digital computer program (Reference 2-2) has been written to calculate radiation using the band models for axisymmetric and three-dimensional exhaust plumes with water vapor, carbon dioxide, carbon monoxide and carbon particles. Reference 2-3 describes the program and some of the results compared with experimental data.

Preliminary base heating radiation predictions should be based on simplified cylinder models and existing flight data. The radiation program is used to verify and refine preliminary predictions.

2.3.2 Analytical Methods for Predicting Base Convective Heating

It is difficult to present an overall analytical model of the base flow field which can be used to determine absolute values of recovery temperature or heat transfer rate. The usual procedure is to divide the reverse flow field into fundamental components which are then analyzed individually. The flow field is generally divided into the following components:

1. Internal nozzle flow including the boundary layer
2. Plume expansion
3. Turbulent mixing region
4. Interaction/recompression region
5. Reverse flow model
6. Vented mass flow
7. Plume induced flow separation

The final solution of base pressure, recovery temperature and heat transfer rate requires properties which are determined by the reverse flow and vented mass flow analyses; and inherently contains all errors and assumptions present in each component analysis.

2.3.2 (Continued)

Many investigators have constructed elaborate analytical models of individual flow components. Most of this work has been directed at the turbulent mixing region, using the original theory of Korst and interpretation of Goethert. Only a few investigators have tried to describe the complete flow field; but, in recent years, several reviews of the "state-of-the-art" have tied together the various individual flow field contributions to construct an overall flow field model. From these reviews, a list of the most significant investigators has been prepared in chronological order of their major publication.

Goethert	-	1961
Marion, etc.	-	1962
Page and Dixon	-	1963, 1966
Taylor and Tou	-	1967
Brewer and Craven	-	1969
Lamb, etc.	-	1969-1970

Table 2.3-1 summarizes the individual flow component and environment component methods used by these investigators. To illustrate the extent of publication directed at individual flow components, Table 2.3-2 has been prepared referencing approximately 130 reports. This list is only a partial compilation of the applicable literature.

Even though a significant number of analytical studies have been made to define a better method of calculating convective heating, design predictions still depend heavily upon experimental model and flight test data.

TABLE 2.3-1. COMPONENTS OF CONVECTIVE BASE HEATING METHODS

COMPONENT / AUTHOR	INTERNAL NOZZLE FLOW		PLUME EXPANSION	TURBULENT MIXING	INTERACTION/RECOMPRESSION		RECIRCULATING FLOW				
	ISENTROPIC CORE	BOUNDARY LAYER			PLUME INTERACTION	ESCAPE CRITERION	REVERSED FLOW MODEL	VENTED MASS FLOW RATE	RECOVERY BASE TEMPERATURE	BASE HEAT TRANSFER	BASE PRESSURE
GOETHERT (1961)	---	ESTIMATED	LATVALA APPROXIMATE METHOD	2-D KORST & CHOW (1959) & EMPIRICAL ORIGIN SHIFT	MAXIMUM IMPINGEMENT ANGLE	MODIFIED KORST MODEL	CHOKED FLOW AT TOTAL VENT AREA	$\dot{M}_V = F_1 (P_b, A_V, C_f)$	$T_{ob} = T_o$ PLUME BOUNDARY	$Q \sim P_b^{0.8}$	$\dot{M}_V = \int_{y_j}^{y_d} \rho_m U_m \, dy$ $\dot{M}_R = \dot{M}_V$
MARION, etc. (1962)	---	ESTIMATED	METHOD OF CHARACTER-ISTICS	GOETHERT METHOD	GOETHERT METHOD	GOETHERT METHOD	CHOKING BETWEEN PLUMES	GOETHERT FORMULA	$T_{ob} = T_o$ PLUME BOUNDARY	---	$\dot{M}_R = \dot{M}_V$
PAGE & DIXON (1963, 1966)	---	NEGLECTED	PRANDTL-MEYER EXPANSION	KORST MODEL (1954)	ISENTROPIC COMPRESSION	GOETHERT METHOD	CHOKED FLOW AT MINIMUM AREA	$\dot{M}_V = F_2 (P_b, T_o, A_{min})$	$T_{ob} = T_o$ PLUME BOUNDARY	MODIFIED SIBULKIN STAGNATION POINT HEAT TRANSFER FORMULA	$\dot{M}_R = \dot{M}_V$
TAYLOR & TOU (1967)	METHOD OF CHARACTER-ISTICS	MODIFIED METHOD OF ELLIOTT	PRANDTL-MEYER EXPANSION	ZUMWALT & TANG (1964) (AXI-SYM. KORST MODEL) GOETHERT EMPIRICAL ORIGIN SHIFT	AXISYMMETRICAL JET IMPINGEMENT ON A FLAT PLATE	GOETHERT METHOD	FICTITIOUS FULLY DEVELOPED TURBULENT JET	$\dot{M}_V = F_3 \left[C_f, A_V, (P_b - P_\infty), \rho_b \right]$	$T_{ob} = \dfrac{\int_o^{y_d} \rho_e \, U_e \, T_{o_e} \, dy}{\int_o^{y_d} \rho_e \, J_e \, d_y}$	MODIFIED GARDON-AKFIRAT CORRELATION	$\dot{M}_R = \dot{M}_V$
BREWER & CRAVEN (1969)	---	---	---	NOT APPLICABLE	INVISCID PLUME-PLUME IMPINGEMENT	NON-VISCOUS DETACHED SHOCK-LATERAL FLOW PATTERN	SUPERSONIC AXISYMMETRIC TURBULENT JET	---	---	---	---
LAMB, etc. (1970)	---	NEGLECTED	LOVE CIRCULAR ARC APPROXI-MATION	KORST MODEL	LOVE CIRCULAR ARC APPROXIMATION	LAMB & HOOD TURBULENT REATTACHMENT MODEL	ANALYTICALLY DETERMINED REVERSE JET	NOT REQUIRED	NOT INVESTIGATED	NOT INVESTIGATED	REVERSED JET IMPINGEMENT ON BASE WALL

TABLE 2.3-2. CONVECTIVE HEATING - SURVEY OF ANALYTICAL METHODS

FLOW MODEL COMPONENT	REFERENCES
• INTERNAL NOZZLE FLOW	
(1) ISENTROPIC CORE	2-5, 2-6, 2-41
(2) BOUNDARY LAYER	2-4, 2-6, 2-7, 2-23, 2-34, 2-5, 2-60, 2-61, 2-68, 2-69, 2-77
• PLUME EXPANSION	2-7, 2-22, 2-29, 2-45, 2-62, 2-82, 2-83, 2-16, 2-84, 2-85, 2-36, 2-90, 2-111, 2-112
• TURBULENT MIXING	2-8, 2-9, 2-10, 2-26, 2-37, 2-47, 2-49, 2-35, 2-53, 2-56, 2-57, 2-58, 2-59, 2-66, 2-70, 2-71, 2-74, 2-85, 2-36, 2-39, 2-41, 2-40, 2-96, 2-98, 2-100
• INTERACTION/RECOMPRESSION	
(1) PLUME INTERACTION	2-11, 2-12, 2-13, 2-25, 2-27, 2-28, 2-16, 2-30, 2-31, 2-46, 2-47, 2-49, 2-35, 2-52, 2-64, 2-65, 2-66, 2-79, 2-93
(2) ESCAPE CRITERION	2-13, 2-14, 2-17, 2-25, 2-27, 2-28, 2-31, 2-32, 2-49, 2-35, 2-52
• REVERSED FLOW MODEL	2-17, 2-18, 2-19, 2-16, 2-25, 2-31, 2-36, 2-37, 2-46, 2-47, 2-49, 2-35, 2-52, 2-53, 2-65, 2-66, 2-67, 2-70, 2-84, 2-41, 2-40, 2-90, 2-91, 2-92, 2-95
• VENTED MASS FLOW RATE	2-21, 2-18, 2-31, 2-16
• PLUME INDUCED FLOW SEPARATION	2-23, 2-24, 2-34, 2-101, 2-102, 2-103, 2-104, 2-105, 2-106, 2-107, 2-108, 2-109
BASE ENVIRONMENT COMPONENT	
• RECOVERY TEMPERATURE	2-18, 2-15, 2-33, 2-35, 2-40, 2-42, 2-43, 2-44, 2-89
• CONVECTIVE HEAT TRANSFER	2-15, 2-20, 2-21, 2-18, 2-31, 2-33, 2-37, 2-40, 2-42, 2-43, 2-44, 2-49, 2-47, 2-48, 2-50, 2-17, 2-54, 2-55, 2-63, 2-72, 2-73, 2-75, 2-76, 2-77, 2-78, 2-86, 2-80, 2-89, 2-92, 2-94, 2-95
• BASE PRESSURE	2-11, 2-17, 2-40, 2-46, 2-35, 2-53, 2-84, 2-79, 2-80, 2-92, 2-97, 2-110

2.4 PARAMETERS INFLUENCING BASE HEATING

Previous investigators have studied the effect of various parameters on base flow and associated heating phenomena. From these investigations and others, three general groupings of variables influencing base heating have emerged. These groups are (1) vehicle trajectory variables, e.g., vehicle altitude and Mach number; (2) propellant variables such as type of propellant, O/F ratio, combustion chamber pressure and temperature, thermodynamic and transport properties which influence the velocity and exhaust gas radiation characteristics; and (3) geometrical variables such as nozzle area ratio, nozzle exit angle, base vent area, engine spacing, distance from base to nozzle exit plane, method of turbine exhaust injection, engine shroud length, base flow deflectors, engine gimbaling, engine out and method of nozzle cooling.

A table has been prepared (Table 2.4-1 from Ref. 2-81) which summarizes the qualitative effect of some of the more important variables on such phenomena as full base recirculation altitude, base pressure, base convective heating, and gaseous radiation. These general trends are based on experimental model and flight test experience and under certain circumstances could have an opposite trend.

TABLE 2.4-1. EFFECT OF MAJOR PARAMETERS ON BASE PHENOMENA (REF. 2-81)

MAJOR VARIABLES INCREASING / PHENOMENA	NOZZLE AREA RATIO	NOZZLE HALF ANGLE	BASE TO NOZZLE EXIT DISTANCE	ROCKET SPACING	EFFECTIVE SPECIFIC HEAT RATIO	ROCKET CHAMBER PRESSURE	BASE VENT FACTOR	FREE STREAM MACH NO.
FULL BASE RECIRCULATION ALTITUDE	⇧	⇩	⇧	⇧	⇧	⇩	⇧	⇧
BASE PRESSURE	⇩	⇧	⇩	⇩	⇩	⇧	⇩	⇩
BASE CONVECTIVE HEATING	⇩	⇧	⇩	⇩	⇩	⇧	⇩	⇧
GASEOUS RADIATION TO BASE	⇩	⇧	⇩	⇩	⇧	⇩	⇩	⇩

⇧ Increasing ⇩ Decreasing

It should be pointed out that this table represents the qualitative effect on the simple, uncomplicated flow field, It does not deal with such problems as engine gimbaling, engine-out operation, fuel-rich base injectants, combustion at the base, external fins and protuberances on the base, all of which tend to greatly complicate the problem of determining the base flow characteristics and thermal environment of a launch vehicle.

2.5 REFERENCES

2-1. Rochelle, W. C., "Review of Thermal Radiation from Liquid and Solid Propellant Rocket Exhausts," NASA TM X-53579, February 1967.

2-2. Reardon, J. E. and Huffaker, R. M., "Radiative Heat Transfer Calculations for Saturn Exhaust Plumes."

2-3. Reardon, J. E., "Prediction of Radiation from Rocket Exhaust Gases," AIAA Paper No. 70-841, July 1970.

2-4. Elliott, D. G., Bartz, D. R., and Silver, S., "Calculation of Turbulent Boundary Growth and Heat Transfer in Axisymmetric Nozzles," Jet Propulsion Laboratory TR 32-387, February 1963.

2-5. Shapiro, A. H., "The Dynamics and Thermodynamics of Compressible Fluid Flow," Volume II, New York, The Ronald Press Company, 1954.

2-6. Farmer, R. C.; Prozan, R. J.; McGimsey, L. R.; and Ratliff, A. W., "Verification of a Mathematical Model which Represents Large, Liquid Rocket-Engine Exhaust Plumes," AIAA Paper No. 66-650 presented at AIAA Second Propulsion Joint Specialist Conference, June 13-17, 1966.

2-7. Weinbaum, S., "Rapid Expansion of a Supersonic Boundary Layer and Its Application to the Near Wake," AIAA Journal, Volume 4, No. 2, February 1962.

2-8. Kessler, T. J., "A Theory for Two-Dimensional Supersonic Turbulent Base Flows," AIAA Paper No. 69-68, 1969.

2-9. Peters, C. E., Peters, T., and Billings, R. E., "Mixing and Burning of Bounded Coaxial Streams," AEDC-TR-65-4, Arnold Engineering Development Center, March 1965.

2-10. Ferri, A., Moretti, G., and Slutsky, S., "Mixing Processes in Supersonic Combustion," Journal Society Induct. Applied Mathematics, Volume 13, No. 1, March 1965.

2-11. Lamb, J. P., Abbud, K. A., and Lenzo, C. S., "A Theory for Base Pressures in Multi-Nozzle Rocket Configurations," Journal of Spacecraft and Rockets, April 1970.

2-12. Marion, E. D., Daniels, D. J., Herstine, G. L., and Burge, G. W., "Exhaust Reversal from Cluster Nozzles - A New Flow Model," ARS Paper No. 62-2706, 1962.

2-13. Page, R. H., Kessler, T. J., and Hill, Jr. W. G., "Reattachment of Two-Dimensional Supersonic Turbulent Flows," ASME Paper No. 67-FE-20, 1967.

2.5 (Continued)

2-14. Page, R. H., and Dixon, R. J., "Base Heating on a Multiple Propulsion Nozzle Missile," AIAA Paper No. 63-179, 1963. Also Dixon, R. J. and Page, R. H., "Theoretical Analysis of Launch Vehicle Base Flow," AGARD Conference Proceedings No. 4, Separated Flows, Part II, 1966.

2-15. Taylor, R. A. and Tou, P. P., "Convective Heat Transfer in the Base Region of Large Space Boosters with Clustered Engines," Procedure Heat Transfer Fluid Mechanics Institute, Stanford University Press, 1967.

2-16. Lamb, J. P. and Hood, C. G., "An Integral Analysis of Turbulent Reattachment Applied to Plane Supersonic Base Flows," Transaction ASME, Series C. Volume 90, No. 3, November 1968.

2-17. Goethert, B. H., "Base Flow Characteristics of Missiles with Cluster-Rocket Exhausts," Aerospace Engineering, March 1961.

2-18. Brewer, E. B., and Craven, C. E., "Experimental Investigation of Base Flow Field at High Altitude for a Four-Engine Clustered Nozzle Configuration," NASA TN D-5164, May 1969.

2-19. Hendershot, K. C., "Some Observations on Exhaust Recirculation from Clustered Rocket Nozzles," AIAA Paper No. 66-681 presented at AIAA Second Propulsion Joint Specialist Conference, June 13-17, 1966.

2-20. Gardon, R., and Akfirat, J. C., "Heat Transfer Characteristics of Impinging Two-Dimensional Air Jet," Journal of Heat Transfer, Transaction of the ASME, Volume 88, Series C, 1966.

2-21. Lamb, J. P., Hood, C. G., and Johnson, M. G., "A Convective Transport Model for Turbulent Supersonic Planar Base Flows," ASME Paper No. 70HT/SpT-35, June 1970.

2-22. Omar, M. E., "Two-Dimensional and Axisymmetric Real or Ideal Gas Flows by Method of Characteristics," Boeing Computer Program No. AS-1096, March 1965, The Boeing Company.

2-23. Lin, C. C., Editor, "Turbulent Flows and Heat Transfer," Volume V, High Speed Aerodynamics and Jet Propulsion, Princeton University Press, 1959.

2-24. Shaffer, W. L., and Wilkinson, C. L., "Analysis of Exhaust Plume Induced Turbulent Boundary Layer Separation on an Axisymmetric Launch Vehicle," Boeing Document No. D5-14242, March 1971.

2-25. Lykondis, P., "A Review of Hypersonic Wake Studies," AIAA Journal, April 1966.

2.5 (Continued)

2-26. Crocco, L., and Lees, L., "A Mixing Theory for the Interaction Between Dissipative Flows and Nearly Isentropic Streams," Journal of the Aerospace Science, October 1962.

2-27. Chapman, D. R., "An Analysis of Base Pressure at Supersonic Velocities and Comparison with Experiments," NACA TN-2137, 1951.

2-28. Korst, H. H., "A Theory for Base Pressures in Transonic and Supersonic Flow," Transactions of the ASME: Journal of Applied Mechanics, Volume 23, 1956.

2-29. Chu, C. W., Niemann, A. F., and Powers, S. A., "An Inviscid Analysis of the Plume Created by Multiple Rocket Engines and a Comparison with Available Schlieren Data. Part I: Calculation of Multiple Rocket Engine Exhaust Plumes by the Method of Characteristics," AIAA Paper No. 66-651, June 1966.

2-30. Chapman, D. R., "A Theoretical Analysis of Heat Transfer in Regions of Separated Flow," NACA TN 3792, 1956.

2-31. Larson, H. K., "Heat Transfer in Separated Flows," Journal of Aero/Space Sciences, Volume 26, 1959, pp. 731-737.

2-32. Korst, H. H., "Dynamics and Thermodynamics of Separated Flows," Proceedings of Sumposium on Single and Multi-Component Flow Processes, Rutgers Engineering Research Publication No. 45, 1965; also AGARD Conference Proceedings No. 4, "Separated Flows," 1966.

2-33. Page, R. H., and Dixon, R. J., "Base Heat Transfer in a Turbulent Separated Flow," Fifth International Sumposium of Space Technology, Tokyo, 1963.

2-34. Schlichting, H., "Boundary Layer Theory," McGraw-Hill, Sixth Edition, 1968.

2-35. Korst, H. H., Chow, W. L., and Zumwalt, G. W., "Research on Transonic and Supersonic Flow of a Real Fluid at Abrupt Increases in Cross Section," University of Illinois, ME TN 392-5, 1959.

2-36. Donaldson, C. du P., and Gray, K. E., "Theoretical and Experimental Investigation of the Compressible Free Mixing of Two Dissimilar Gases," AIAA Journal, Volume 4, 1966, pp. 2017-2025

2-37. Larson, R. E., et al, "Heat Transfer Below Reattaching Turbulent Flows," AIAA Paper 65-825, 1965.

2.5 (Continued)

2-38. Hill, J. A. F., and Nicholson, J. E., "Compressibility Effects on Fluid Entrainment by Turbulent Mixing Layers," NASA CR-131, 1964.

2-39. Chow, W. L., and Korst, H. H., "On the Flow Structure Within a Constant Pressure Compressible Turbulent Jet Mixing Region," NASA TN D-1894, 1963.

2-40. Lamb, J. P., and Bass, R. L., "Some Correlations of Theory and Experiment for Developing Turbulent Free Shear Layers," Journal of Basic Engineering, Transactions of the ASME, Volume 90, Series D, 1968, pp. 572-580.

2-41. Mueller, T. J., "Determination of the Turbulent Base Pressure in Supersonic Axisymmetric Flow," Journal of Spacecraft, Vol. 5, 1968, pp. 101-104.

2-42. Economos, C., "Experimental Determination of Heat Transfer Due to Hydrogen Combustion in a Base Flow Region," AIAA Paper 66-108, 1966.

2-43. Bloom, M. H., and Pallone, A., "Shroud Tests of Pressure and Heat Transfer over Short Afterbodies with Separated Wakes," WADC TN 58-185, 1958.

2-44. Fletcher, L. S., "Experimental Investigation of Blunt Base Heat Transfer in an Axisymmetric Turbulent Supersonic Separated Flow," AFOSR 69-2149 TR, July 1969, Mechanical and Aerospace Engineering Department, Rutgers University.

2-45. Pindzola, M. and Hensel, R. W., "High Altitude Jet Spreading and Some Associated Interference Problems on Space Vehicles," Proceedings of the Fluid Dynamic Aspects of Space Flight, AGARD Fluid Dynamics Panel, Marseille, France, April 1964.

2-46. Musial, N. T. and Ward, J. J., "Base Flow Characteristics for Several Four-Clustered Rocket Configurations at Mach Numbers from 2.0 to 3.5," NASA TN D-1093, December 1961.

2-47. Charczenko, N. and Hayes, C., "Jet Effects at Supersonic Speeds on Base and Afterbody Pressures of a Missile Model Having Single and Multiple Jets," NASA TN D-2046, November 1963.

2-48. Beheim, M. A. and Obery, L. J., "Wind Tunnel Studies of Booster Base Heating," IAS Paper 62-166, Presented at IAS National Summer Meeting, June 19-22, 1962.

2-49. Sergeant, R. J., "Base Heating Scaling Criteria for a Four-Engine Rocket Cluster Operating at High Altitude," AIAA Paper 65-826, Presented at AIAA Aerothermochemistry of Turbulent Flows Conference, December 13-15, 1965.

2.5 (Continued)

2-50. Hendershot, K. C., "The Application of Short-Duration Techniques to the Experimental Study of Base Heating - Summary Report," CAL Report HM-1510-Y-18, April 1965.

2-51. Latvala, E., "Spreading of Rocket Exhaust Jets at High Altitude," AEDC TR-59-11, June 1959.

2-52. Nash, J. F., "An Analysis of Two-Dimensional Turbulent Flow Including the Effect of the Approaching Boundary Layer," National Physical Laboratory Aero Report 1036, July 1962.

2-53. Zumwalt, G. W. and H. H. Tang, "Transient Base Pressure Study of an Axisymmetric Supersonic Missile Flying Head-On Through a Blast Wave," Sandia Corporation Research Report SBW-6, Feb. 1964.

2-54. Goethert, B. H., "Base Heating Problems of Missiles and Space Vehicles," ARA Paper 1666-61, March 1961.

2-55. Wilson, H. B., Jr., "A Short-Duration Technique for Simulated Rocket Exhaust and Wind Tunnel Flow and Its Application to the Study of Scalar Effect of Recirculating Flow Fields," Chapter 15 in Proceedings of the 1966 Heat Transfer and Fluid Mechanics Institute, Stanford University Press, 1966.

2-56. Korst, H. H., R. H. Page and M. E. Childs, "Compressible Two-Dimensional Jet Mixing at Constant Pressure," University of Illinois ME Technical Note 392-1, April 1954.

2-57. Chapman, D. R., "Laminar Mixing of a Compressible Fluid," NACA Report 958, 1950.

2-58. Pai, S. I., "Axially Symmetric Jet Mixing of a Compressible Fluid," Journal of the Aero. Science, 1952, 10 (2), 141-148.

2-59. Bauer, R. C., "An Analysis of Two-Dimensional Laminar and Turbulent Compressible Mixing," AIAA Journal, 1966, 4 (3), 392-395.

2-60. Persh, J., "A Theoretical Investigation of Turbulent Boundary Layer Flow with Heat Transfer at Supersonic and Hypersonic Speeds," NAVORD Report 3854, May 1955.

2-61. Hoenig, R. J., "Compressible Turbulent Boundary Layer Growth on Cooled Rocket Nozzle Walls," Lockheed Missiles and Space Co./ HREC TN 54/20-16, December 1964.

2-62. Steiger, M. H., W. Hinz, P. M. Sforza and N. Trentacoste, "Studies in Three-Dimensional Free-Mixing: I. Finite Difference Solutions and II. Experimental Results," AIAA Paper No. 65-49, Jan. 1965.

2.5 (Continued)

2-63. Sergeant, R. J., "The Application of Short-Duration Techniques to the Experimental Study of Base Heating, Part II: A Study of Reynolds Number and Temperature Effects on Base Heating for a Four-Engine Hot Rocket Configuration Operation at High Altitude," Cornell Aeronautical Laboratory Report No. HM-1510-Y-1(II), April 1965.

2-64. Love, E. S., "The Base Pressure at Supersonic Speeds of Two-Dimensional Airfoils and Bodies of Revolution (With and Without Fins) Having Turbulent Boundary Layers," NACA RML-53002, 1953.

2-65. Cortright, E. M., and Kochendorfer, F. D., "Jet Effects on Flow Over Afterbodies in Supersonic Streams," NACA RME-53H25, 1953.

2-66. Korst, H. H., Page, R. H. and Childs, M. E., "A Theory for Base Pressures in Transonic and Supersonic Flow," Tech Report 392-2, Eng. Exp. Station, University of Illinois, March 1965.

2-67. Goethert, B. H., and Barnes, L. T., "Some Studies of the Flow Pattern at the Base of Missiles with Rocket Exhaust Jets," AEDC TR-58-12 (originally published in October 1958; reissued as unclassified and nonproprietary).

2-68. Burke, A. F., "Turbulent Boundary Layers on Highly Cooled Surfaces at High Mach Numbers," CAL Report 118, November 1961.

2-69. Donaldson, C. duP, "Heat Transfer and Skin Friction for Turbulent Boundary Layers on Heated or Cooled Surfaces," NACA RM L 52H04, October 1952.

2-70. Carlson, D. R., "An Analytical Study and Discussion of a Typical Four-Unit Clustered-Rocket-Nozzle Configuration at High Altitude, Including Calculations for Jet Interaction at 160,000 Feet," CAL Memo dated September 26, 1962.

2-71. Korst, H. H. and Chow, W. L., "Compressible Non-Isoenergetic Two-Dimensional Turbulent Jet Mixing at Constant Pressure," University of Illinois Eng. EXP STA. ME-TN-392-4, January 1959.

2-72. Bird, K. D., Matthis, C. L. and Reece, J. W., "The Application of Short-Duration Techniques to the Experimental Study of Base Heating, Part I: High-Altitude Testing Techniques and Experimental Results for a 4-Engine Rocket Configuration," CAL Report HM-1510-Y-1(I), April 1962.

2-73. Hubbartt, J. E., "Analysis of the Saturn S-II Base Heating Model," Informal Report Georgia Institute of Technology, 1965.

2-74. Keston, J., et al, "The Influence of Turbulence on the Transfer of Heat to Cylinders Near the Stagnation Point."

2.5 (Continued)

2-75. Krause, F., et al, "Heat Transfer Below Reattaching Turbulent Flows," AIAA 65-825 Presented at AIAA Conference on Aerothermochemistry of Turbulent Flows, December 13-15, 1965.

2-76. Rubesin, M. W., "The Effect of an Arbitrary Surface-Temperature Variation Along a Flat Plate on the Convective Heat Transfer in an Incompressible Turbulent Boundary Layer," NACA TN-2345, April 1951.

2-77. Lighthill, M. J., "Contributions to the Theory of Heat Transfer Through a Laminar Boundary Layer," Proceedings of the Royal Society of London, Series A, Vol. 202, No. 1070, August 7, 1950, pp. 359-377.

2-78. Wehofer, S., "Rocket Exhaust Contaminants and Base Heating Tests," AEDC-TR-65-191, October 1965.

2-79. Goethert, B. H., and Matz, R. J., "Experimental Investigation of Base Flow Characteristics of Four-Nozzle Cluster-Rocket Models," AGARDograph No. 87, Vol. 2, The Fluid Dynamic Aspects of Space Flight, 1965.

2-80. Wasko, R. A., and Cover, T. L., "Experimental Investigation of Base Flow Fields at High Altitudes for Configurations of Four and Five Clustered Nozzles," NASA TM X-1371, 1967.

2-81. Etemad, G. A., and Korkan, K. D., "Base Flow Characteristics and Thermal Environment of Launch Vehicles with Strap-on Solid Rocket Motors," Journal of Astronautical Sciences, Volume 15, No. 1, 1968, pp. 5-13.

2-82. Love, E. S., et al, "Experimental and Theoretical Studies of Axisymmetric Free Jets," NASA TR R6, 1959.

2-83. Lord, W. T., "On Axisymmetrical Gas Jets, With Application to Rocket Jet Flow at High Altitudes," Royal Aircraft Estab. Report No. Aero. 2626, 1959.

2-84. Bauer, R. C., "Theoretical Base Pressure Analysis of Axisymmetric Ejectors without Induced Flow," AEDC TDR 64-3, 1964.

2-85. Rom, J., "Study of Similarity of High Temperature, Turbulent Jets," AIAA Journal, Volume 6, No. 7, 1968, pp. 1368-1370.

2-86. Dahm, W. K., "Present Techniques and Problems in the Determination of the Base Heating Environment of Propelled Booster and Space Vehicles," Paper presented at the Fifth International Symposium on Space Technology and Science in Tokyo, Japan, September 2-7, 1963.

2.5 (Continued)

2-87. Wilson, H. B., "A New Technique for Simulating Rocket Engine Flow for Study of Base Heating Problems," Paper presented at the AIAA Aerodynamic Testing Conference in Los Angeles, California, Paper No. 66-760, September 21-23, 1966.

2-88. Sola, J. M., and Nelium, M. A., "Base-Flow-Field Investigation of a Four-Engine Saturn S-IV (3.6-Percent Scale) Cold-Flow Model at Simulated Altitudes up to 194,000 Feet," AEDC-TDR-62-76, May 1962 (Confidential).

2-89. Dewey, C. F., "A Correlation of Convective Heat Transfer and Recovery Temperature Data for Cylinders in Compressible Flow," International Journal of Heat and Mass Transfer, Volume 8, 1965.

2-90. Chu, C. W., "Conditions for Non-Reversing of Exhaust Gas in a Multijet Plume," Northrop NORAIR Monthly Progress Report No. 5, Contract NAS8-11260, December 1964.

2-91. Cubbage, J. M., "Investigation of Exhaust Backflow from a Simulated Cluster of Three Wide Space Rocket Nozzles in a Near-Space Environment," NASA TN D-3016, September 1965.

2-92. Weidner, J. P., and J. M. Cubbage, "Base Pressures and Convective Heat Transfer Coefficients for Clustered Sonic Nozzles with Emphasis on Choked Exhaust Backflow," NASA TN D-2929, September 1965.

2-93. Craven, C. E., "Optical Measurement of Multiplume Interaction, Interim Report," LMSC/HREC D148854 TM 54/20-236, Lockheed Missiles and Space Company, August 1969.

2-94. Llinas, J. and W. C. Rustay, "Temperature and Density Measurements in the Base Region of a Clustered Rocket Model Using an Electron Beam Technique," Cornell Aeronautical Laboratory Report HM-2107-Y-2, July 1966.

2-95. Abbud, K. A., "A Three-Dimensional Theoretical Model for Base Flow in Multinozzle Rockets," University of Texas, 1968.

2-96. DuP. C. Donaldson, "On the Form of the Turbulent Skin-Friction Law and Its Extension to Compressible Flows," NACA TN-2692, 1952.

2-97. Redeker, E., "Summary of References Containing Base Drag Data on Single Nozzle Missile Configurations," The Boeing Company Document No. D2-125621-1, 1968.

2-98. Dixon, R. J., J. M. Richardson, and R. H. Page, "Turbulent Base Flow on an Axisymmetric Body with a Single Exhaust Jet," AIAA Paper 69-650, June 1969.

2.5 (Continued)

2-99. Addy, A. L., "Analysis of the Axisymmetric Base-Pressure and Base-Temperature Problem with Supersonic Interacting Freestream Nozzle Flows Based on the Flow Model of Korst, et al," USAMC RD-TR-69-12, U. S. Army Missile Command, Redstone Arsenal, Alabama, July 1969.

2-100. Tang, H. H., C. P. Gardiner, and J. W. Barnes, "Jet Mixing Theory, Extensions and Applications in Separated Flow Problems," DAC Report 59181, Douglas Aircraft Company, February 1967.

2-101. Fong, M. C., and C. F. Ehrlich, "Propulsion Effects on Aerodynamic Characteristics of Lifting Reentry Vehicles," AFFDL-TR-70-12, Air Force Dynamics Laboratory, March 1970.

2-102. McGhee, R. J., "Jet Plume-Induced Flow Separation on a Lifting Entry Body at Mach Numbers from 4 to 6," NASA TM X-1997, April 1970.

2-103. Carriere, P., and M. Seriex: Effects Aerodynamiques de L'Eclatement d'un Jet de Fusee. Jahrbuch 1961, Der Wissenschaftlichen Gesellschaft Fin Luftfahrt E.V.

2-104. Clayton, F. L. and J. E. Wuerer, "Flow Separation in High Speed Flight, A Review of the State of the Art," DAC Report SM-46429, Douglas Aircraft Company, April 1965.

2-105. Gadd, G. E., "A Theoretical Investigation of Laminar Separation in Supersonic Flow," Journal of the Aeronautical Sciences, October 1957, pp. 759-771.

2-106. Chapman, D. R., D. M. Kuehn, and H. K. Larson, "Investigation of Separated Flows in Supersonic and Subsonic Streams with Emphasis on the Effect of Transition," NACA Report 1356, 1958.

2-107. Erdos, J. and A. Pallone, "Shock/Boundary Layer Interaction and Flow Separation," AVCO Corporation Report RAD-TR-61-23 (Contract AF04(647)-685)), August 1961.

2-108. Alpineri, L. J., and R. H. Adams, "Flow Separation Due to Jet Pluming," AIAA Journal, Volume 4, No. 10, October 1966.

2-109. Falanga, R. A., W. F. Hinson, and D. H. Crawford, "Exploratory Tests of the Effects of Jet Plumes on the Flow over Cone/Cylinder/Flare Bodies," NASA TN D-1000, 1962.

2-110. Krieger, R. J., "Simplified Base Pressure Prediction Techniques," Memo E241-160, McDonnell Astronautics Company, Eastern Division, August 26, 1970.

2.5 (Continued)

2-111. D'Attoree, L., G. Nowak, and H. V. Thommen, "An Inviscid Analysis of the Plume Created by Multiple Rocket Engines and a Comparison with Available Schlieren Data. Part II: A Finite Difference Method," Space Science Laboratory, General Dynamics/Convair, AIAA Paper 66-651, 1966, and GD/C-DBE-66-014.

2-112. Chu, C. W., A. F. Niemann, and S. A. Powers, "Calculation of Multiple Rocket Engine Exhaust Plumes by the Method of Characteristics, Part I," AIAA Paper 66-651, 1966.

2-113. Smith, H. E., "The Flowfield and Heat Transfer Downstream of a Rearward-Facing Step in Supersonic Flow, ARL 67-0056, Aerospace Research Laboratories, March 1967.

2-114. Scherberg, M. G., "Wake Recirculations Generated by Flows Over Rearward-Facing Steps," ARL 69-0103, Aerospace Research Laboratories, July 1969.

2-115. Culotta, A. J., "A Critical Survey of the State of the Art for Solution of the Supersonic Base Flow Problem," OR 10135, Martin Marietta Corporation, Orlando, Florida, June 1969.

2-116. Hama, F. R., "Experimental Studies on the Lip Shock," AIAA Journal, Vol. 6, No. 2, February 1968.

2-117. Donaldson, I. S., "On the Separation of a Supersonic Flow at a Sharp Corner," AIAA Journal, Vol. 5, No. 6, June 1967.

2-118. Roshko, A., and G. J. Thomke, "Effect of a Shoulder Modification on Turbulent Supersonic Base Flow," AIAA Journal, Vol. 5, No. 4, April 1967.

2-119. Weiss, R. F., and S. Weinbaum, "Hypersonic Boundary Layer Separation and the Base Flow Problem," AIAA Journal, Vol. 4, No. 8, August 1966.

2-120. Weinbaum, S., "Rapid Expansion of a Supersonic Boundary Layer and Its Application to the Near Wake," AIAA Journal, Vol. 4, No. 2, February 1966.

2-121. Nash, J.F., "A Review of Research on Two-Dimensional Base Flow," R&M 3323, Aero Research Council, 1963.

2-122. Gardon, R., and J. C. Akfirat, "Heat Transfer Characteristics of Impinging Two-Dimensional Air Jets," Journal of Heat Transfer, February 1966, pp. 101-108.

2.5 (Continued)

2-123. Snedeker, R. S., and C. D. Donaldson, "Experiments on Free and Impinging Underexpanding Jets from a Convergent Nozzle," ARPA Report No. 63, Aeronautical Research Associates of Princeton, Inc., September 1964.

2-124. Donaldson, C. D., R. S. Snedker, and D. P. Margolis, "A Study of the Mean and Turbulent Structure of a Free Jet and Jet Impingement Heat Transfer," ARAP Report No. 96, Aeronautical Research Associates of Princeton, Inc., December 1966.

2-125. Rosenbaum, H., and C. D. Donaldson, "An Analysis of Jet Impingement Heat Transfer," ARAP Report No. 101, Aeronautical Research Associates of Princeton, Inc., March 1967.

2-126. Trentacoste, N., and P. M. Sforza, "An Experimental Investigation of Three-Dimensional Free Mixing in Incompressible, Turbulent Free Jets," AFOSR 66-0657, PIBAL, Report No. 871, Polytechnic Institute of Brooklyn, March 1966.

2-127. Waldrop, W. R., "Base Recirculation Flow Prediction Using a Time-Dependent Finite Difference Technique," LMSC/HREC D 162322, Lockheed Missiles and Space Company, Huntsville Research and Engineering Center, May 1970.

2-128. Erdos, J., and V. Zakkay, "Numerical Solution of Several Steady Wake Flows of the Mixed Supersonic/Subsonic Type by a Time-Dependent Method and Comparison with Experimental Data," AIAA Paper No. 69-649, June 1969.

CONTENTS

3.0 SATURN S-I AND S-IB STAGES

3.1	S-I AND S-IB CONFIGURATIONS	3-3
3.2	H-1 ENGINE CHARACTERISTICS	3-18
3.3	PREDICTION METHODS	3-25
3.4	MODEL TESTS AND PARAMETRIC DATA	3-30
3.5	FLIGHT TESTS AND PARAMETRIC DATA	3-64
3.5.1	FLAME SHIELD	3-65
3.5.2	HEAT SHIELD	3-65
3.5.3	FIN TRAILING EDGE	3-66
3.5.4	ENGINES	3-67
3.5.5	INBOARD ENGINE OUT EFFECTS	3-67
3.5.6	INFRARED SPECTRA	3-68
3.6	MODEL-FLIGHT DATA COMPARISON	3-88
3.7	REFERENCES	3-97

3.0 SATURN S-I AND S-IB STAGES

Base heating on the S-I and S-IB stages was a result of radiative and convective environments produced by eight (8) H-1 engine exhausts. The engine cluster cross-type arrangement was the same on all S-I and S-IB stages. There were, however, variations in the base region configuration and in the routing of the inboard engine turbine exhausts. The following paragraphs describe the S-I and S-IB configurations, trajectories, H-1 engine characteristics, base heating prediction methods, model and flight test data and references.

3.1 S-I and S-IB CONFIGURATIONS

In 1958 when the design of the Saturn engine cluster was conceived, the designers foresaw a circular engine arrangement. Analysis indicated, however, that the thermal environment on the inside of this engine circle would necessitate a large and massive thermal protection system. Therefore, to reduce the magnitude of the thermal protection requirements the cross-type engine arrangement shown in Figure 3.1-1 was chosen. The four inner engines were fixed and placed as closely together as possible at the center of the arrangement. The area remaining between the four inner engine nozzles was sealed near the exit plane with a flame shield. This was to prevent the hot gases reversed by the intersection of the inboard engine exhausts from circulating into the remainder of the base region. The hot recirculating gas and intense radiation expected between the inner region engines were thus confined in a small, easily protected area. The four movable outer engines were grouped about the four central engines at a distance which minimized, within design limitation, the potential jet interference and flow reversal. The centerline of each fixed inboard engine nozzle was canted out at 3 degrees. Outboard engine nozzles had a 6-degree cant in their null position and could gimbal an additional 6 degrees in any direction.

To protect the engine compartment against the recirculating high temperature gases at the higher altitudes and the radiation emitted by the H-1 engine exhausts, a base heat shield was placed forward of the flame shield. This base heat shield was positioned approximately at the throat plane of the eight H-1 engine nozzles. This effectively minimized the thermal environment to the base heat shield since it was as far removed as possible from the nozzle exit plane. The area between the movable outboard engines and the heat shield was enclosed with high temperature resistant flexible cloth curtains.

The H-1 engine gas turbine discharges a fuel-rich exhaust (O/F $\approx$ 0.33). Afterburning of similar turbine exhaust gases caused high heating rates on the Jupiter missile when they were discharged into the base region, so initial efforts were directed toward dumping the turbine exhaust overboard. However, since the gas generator and turbine are attached to the H-1 engine, discharge of turbine exhaust from the outboard (movable) engines into the ambient flow was mechanically difficult. Hence, the outboard engine turbine exhaust gases are discharged with an exhausterator or aspirator located circumferentially around the exit of each outboard engine nozzle. Discharge of the inboard engine turbine exhaust was initially overboard through ducts that protruded from the side wall of the engine compartment. However, later in the Saturn program the inboard engine turbine exhaust ducts were rerouted and the gases were dumped through the flame shield.

In an attempt to reduce the severity of the base region thermal environment air scoops and flow deflectors were mounted around the periphery of the base. Their purpose was to catch and divert the cool ambient air over the heat shield. However, the thickness of the boundary layer along the tail barrel and the presence of shocks at the higher velocities make the scoops and deflectors ineffective.

3.1 (Continued)

With the exception of the inboard engine turbine exhaust reroute, all the foregoing configurational discussion pertains equally to all Saturn S-I and S-IB stages. The following discussion attempts to identify the base region configuration changes that evolved throughout the Saturn flight test program.

The S-I stage of the first four Saturn I vehicles (SA-1 through SA-4) employed the Block I configuration. A base view schematic of this configuration is shown in Figure 3.1-2. As noted in this figure each of the movable outboard engines were protected by a shroud that extended beyond the heat shield. Their purpose was to prevent aerodynamic loads on the outer engines. The overall geometric configuration of the Block I base was scalloped with a minimum of protrusions from the tail barrel. The primary mission of the Block I flights was to check out the S-I stage with its eight 165,000 pound thrust engines.

The S-I stage of the Block II vehicles (SA-5 through SA-10) had the base configuration shown in Figure 3.1-3. Thrust for each of the H-1 engines on these vehicles was uprated to 188,000 pounds. As noted in the figure, fins were added for stability, fairings were placed around the inboard engine turbine exhaust ducts and the Block II base had a circular geometry. The outboard engine shrouds, which on the Block I configuration were an extension of the tail barrel, were attached to the Block II torque ring at the aft end of the tail unit assembly.

A profile view of the two S-I stage configurations is shown in Figure 3.1-4. Note that the Block II fins are perpendicular to the centerline of the vehicle. Also, since the upper stages of the Block I configuration were dummy and carried water ballast, there were no hydrogen vent lines required.

Generally speaking the S-IB stage external configuration was very similar to the S-I, Block II configuration. The primary exception being that the fins were redesigned with a sweep to both the leading and trailing edges. One other design change for the first five S-IB stages was the uprating of the H-1 engine sea level thrust to 200,000 pounds. The remaining S-IB stages are equipped with eight 205,000 pounds thrust H-1 engines.

Base and profile views of the S-IB-1 are shown in Figures 3.1-5 and 3.1-6, respectively. Similar views of S-IB-2 are shown in Figures 3.1-7 and 3.1-8 while S-IB-3 and subsequent S-IB stages are shown in Figures 3.1-9 and 3.1-10. Several minor configurational changes in the S-IB stage base region marked the progression from S-IB-1 to S-IB-3. The S-IB-1 base was equipped with engine shrouds mounted as shown in Figures 3.1-5 and 3.1-6. These were similar to the engine shrouds on the Saturn I, Block II configurations. These shrouds were removed from subsequent S-IB stages. S-IB-1 and S-IB-2 had flame shields that were identical to those employed on the Saturn I, Block II series. A new flame shield was designed for S-IB-3 and succeeding stages to permit dumping of turbine exhaust gases directly into the base. This eliminated the pumping required by the earlier system. Schematics of

3.1 (Continued)

the two flame shield designs are shown in Figure 3.1-11. The redesigned flame shield was moved to the H-1 engine nozzle exit plane and the turbine exhaust duct outlets were placed along the inward facing wall of the inboard nozzles. The surface area of the new flame shield was 652.5 square inches. This is approximately one-half of the area of the previously employed flame shields.

The flight trajectories for the S-I Block I and Block II and the S-IB vehicles are shown in Figure 3.1-12.

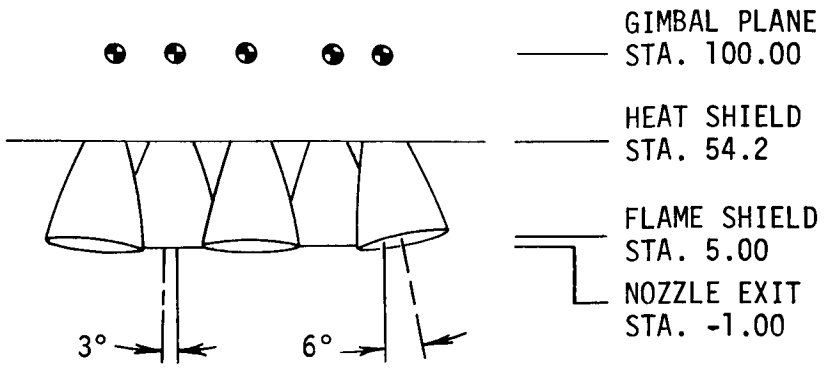

NOZZLE EXIT DIAMETER = 46"

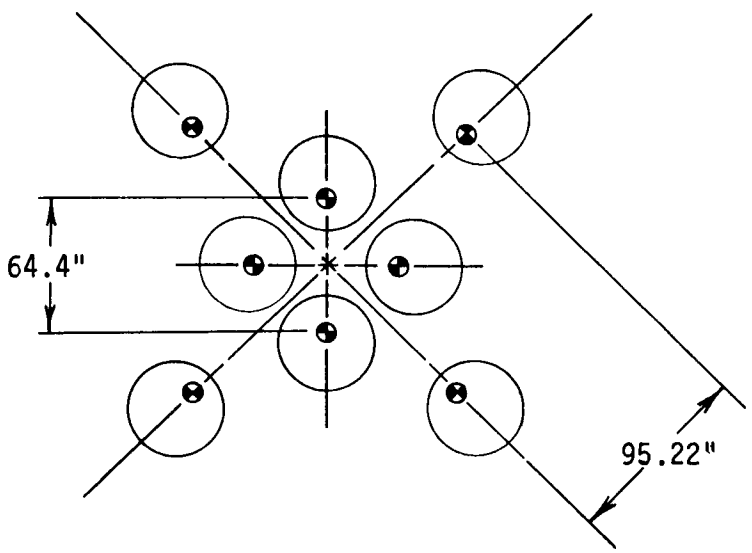

FIGURE 3.1-1. 'SATURN S-I AND S-IB CROSS-TYPE ENGINE ARRANGEMENT

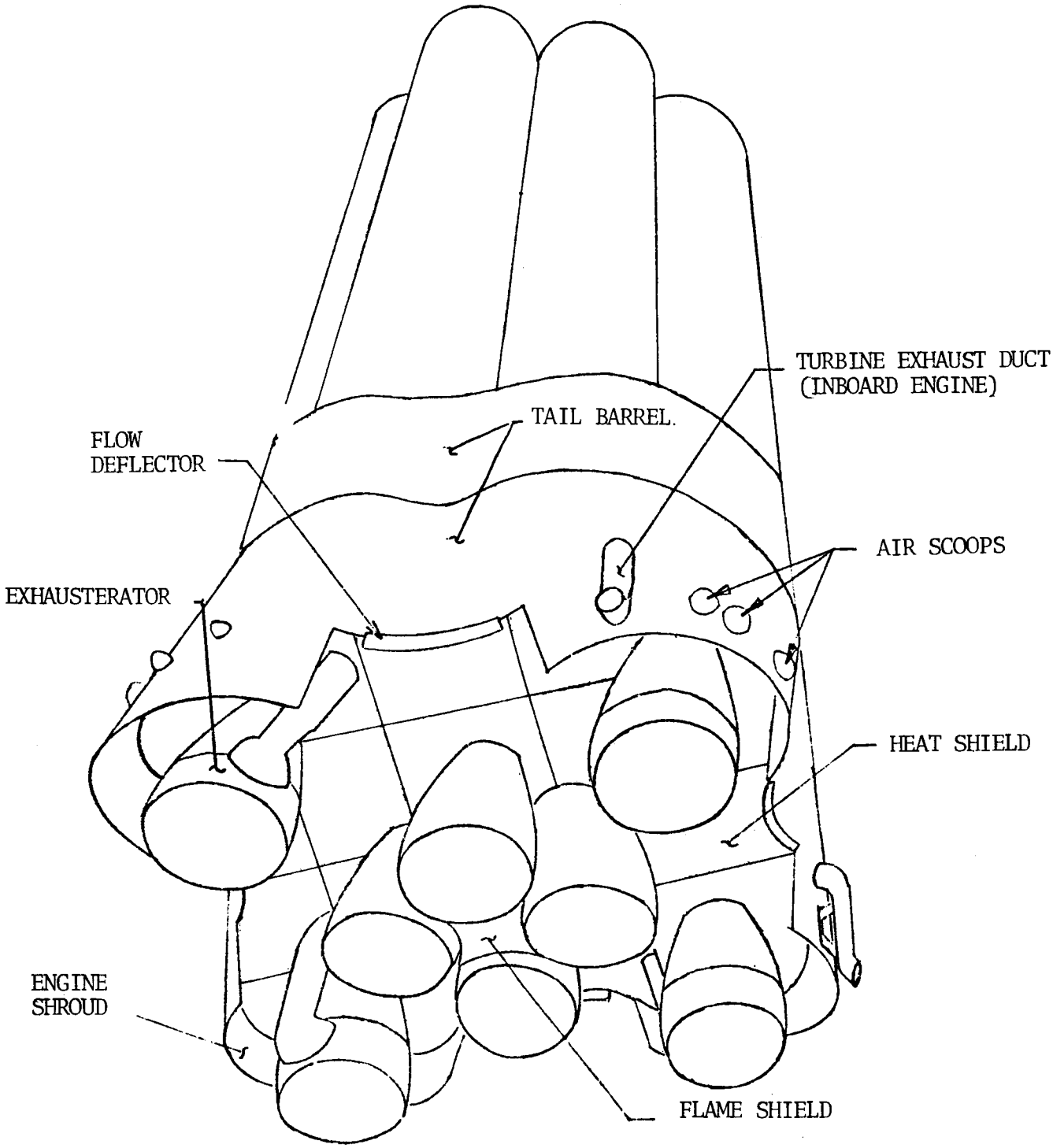

FIGURE 3.1-2. BASE VIEW OF SATURN S-I, BLOCK I, STAGE

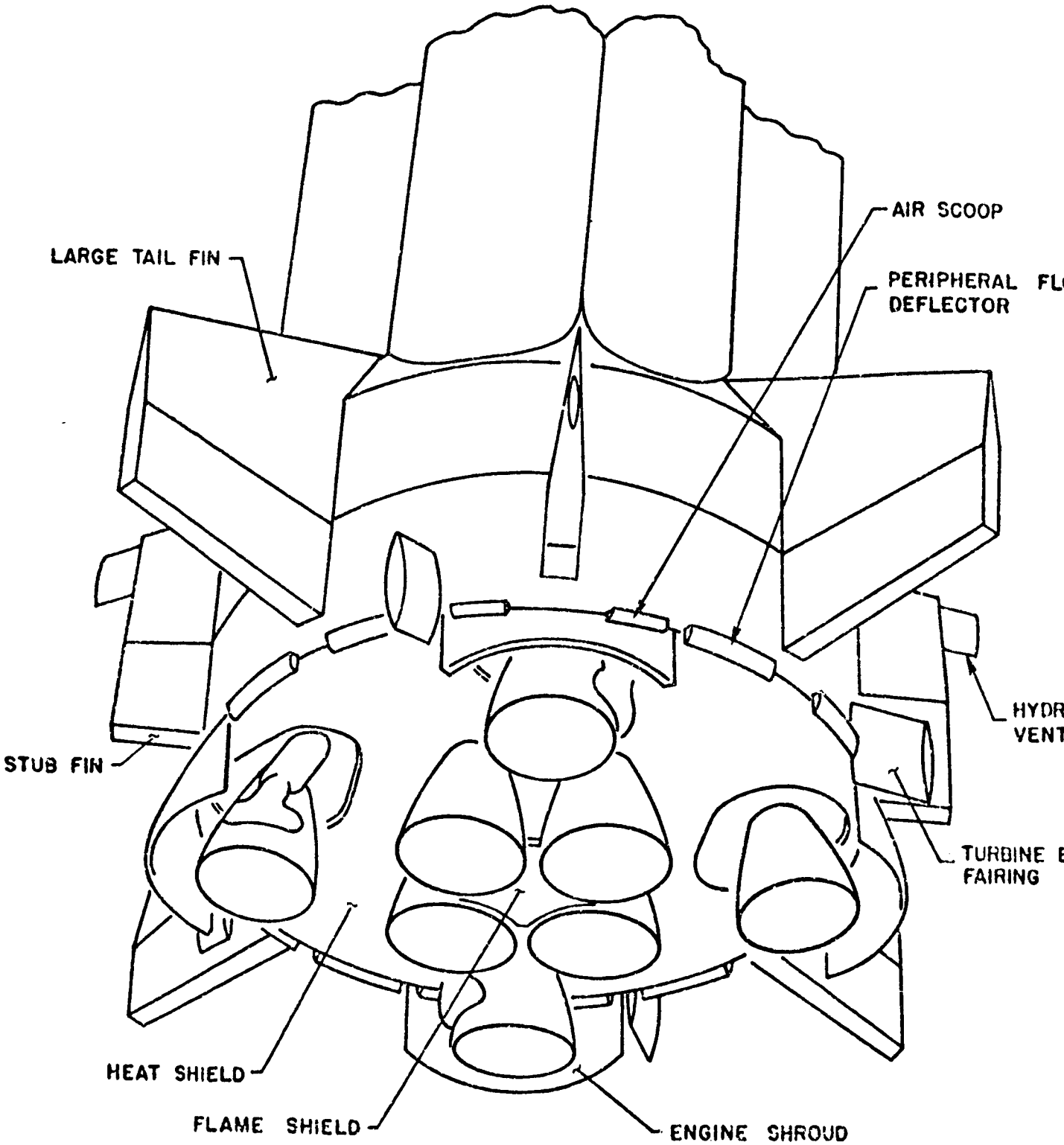

FIGURE 3.1-3. BASE VIEW OF SATURN S-I, BLOCK II, STAGE

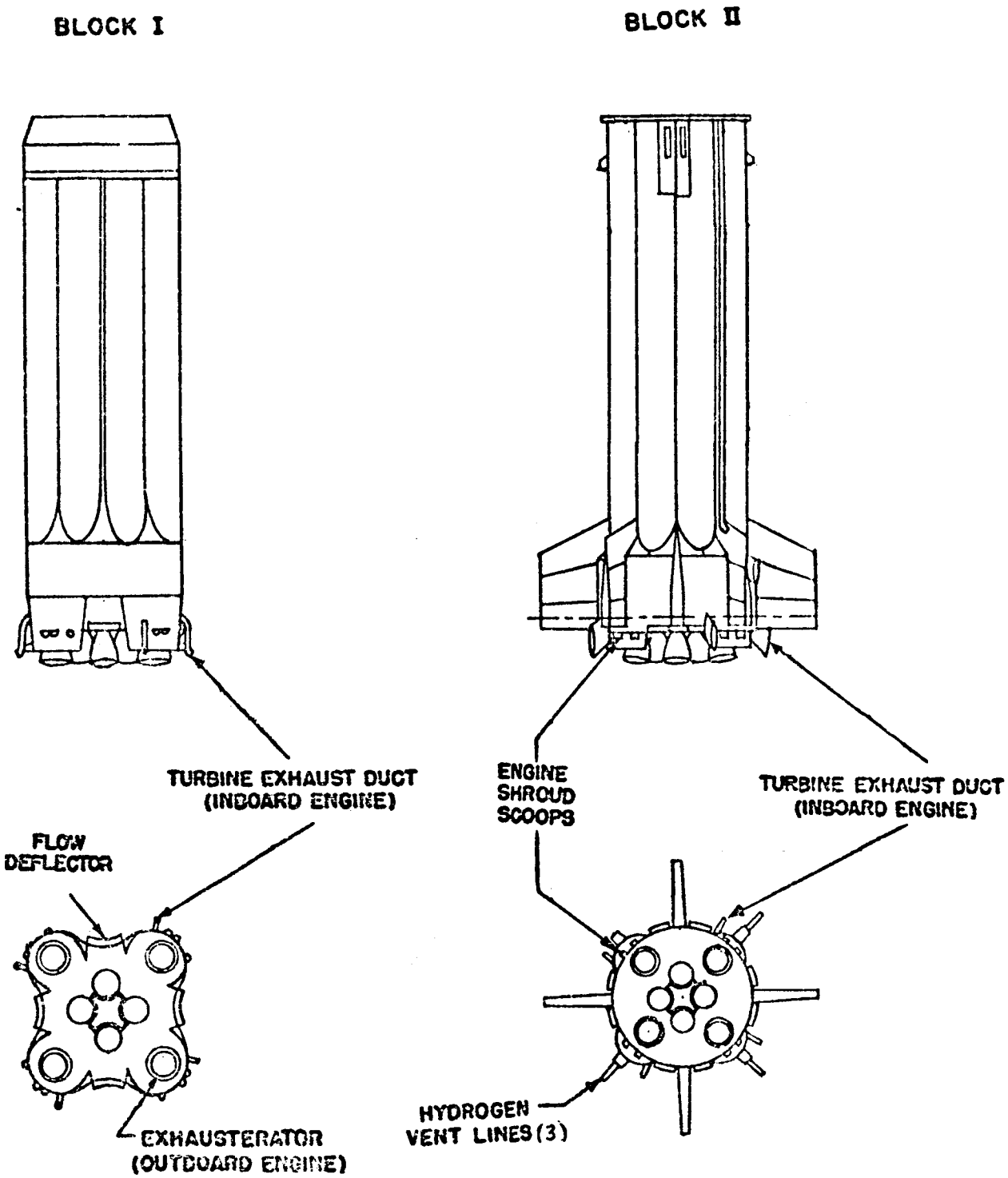

FIGURE 3.1-4. SATURN S-I STAGE

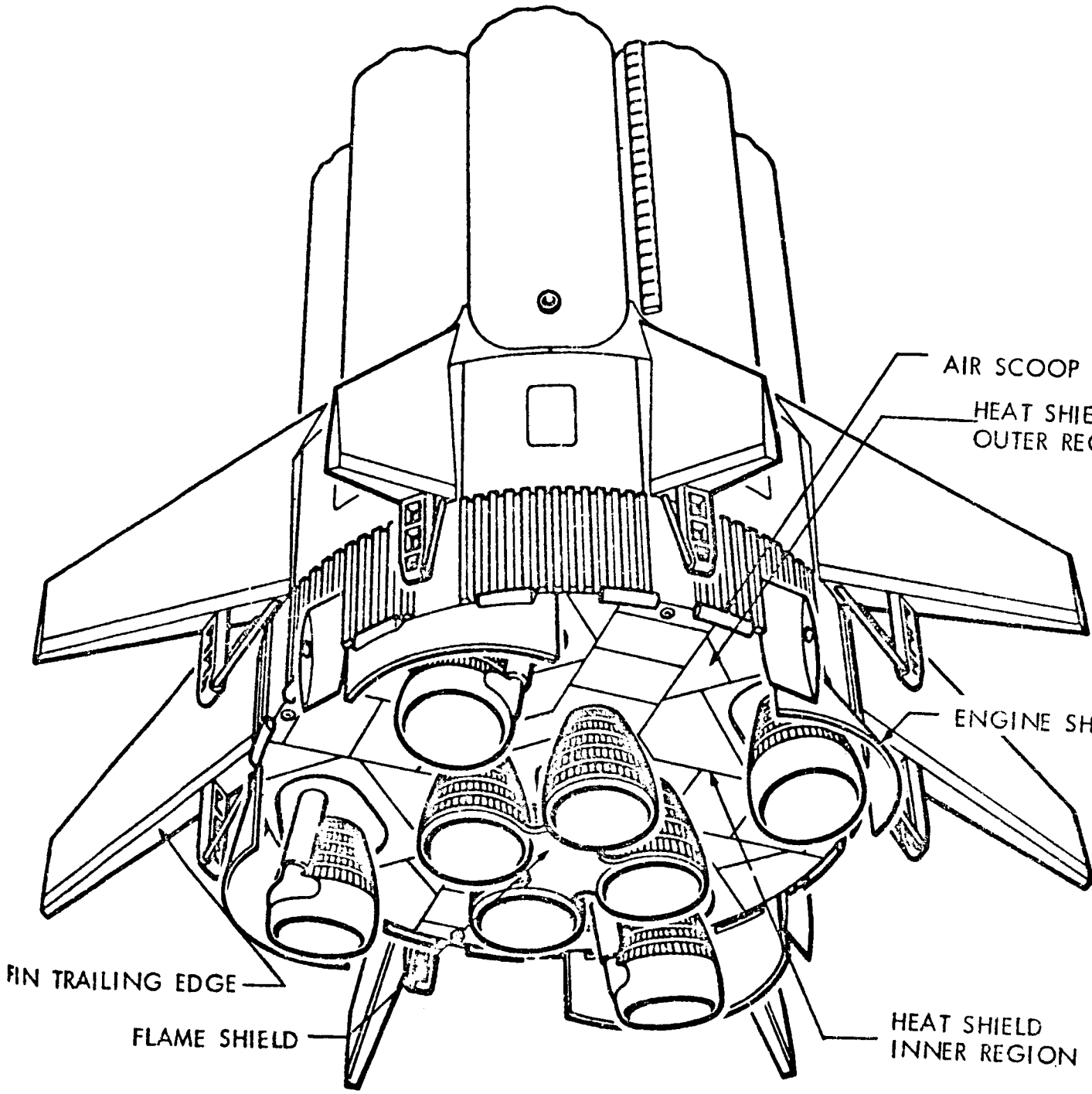

FIGURE 3.1-5. , SA-201 BASE CONFIGURATION

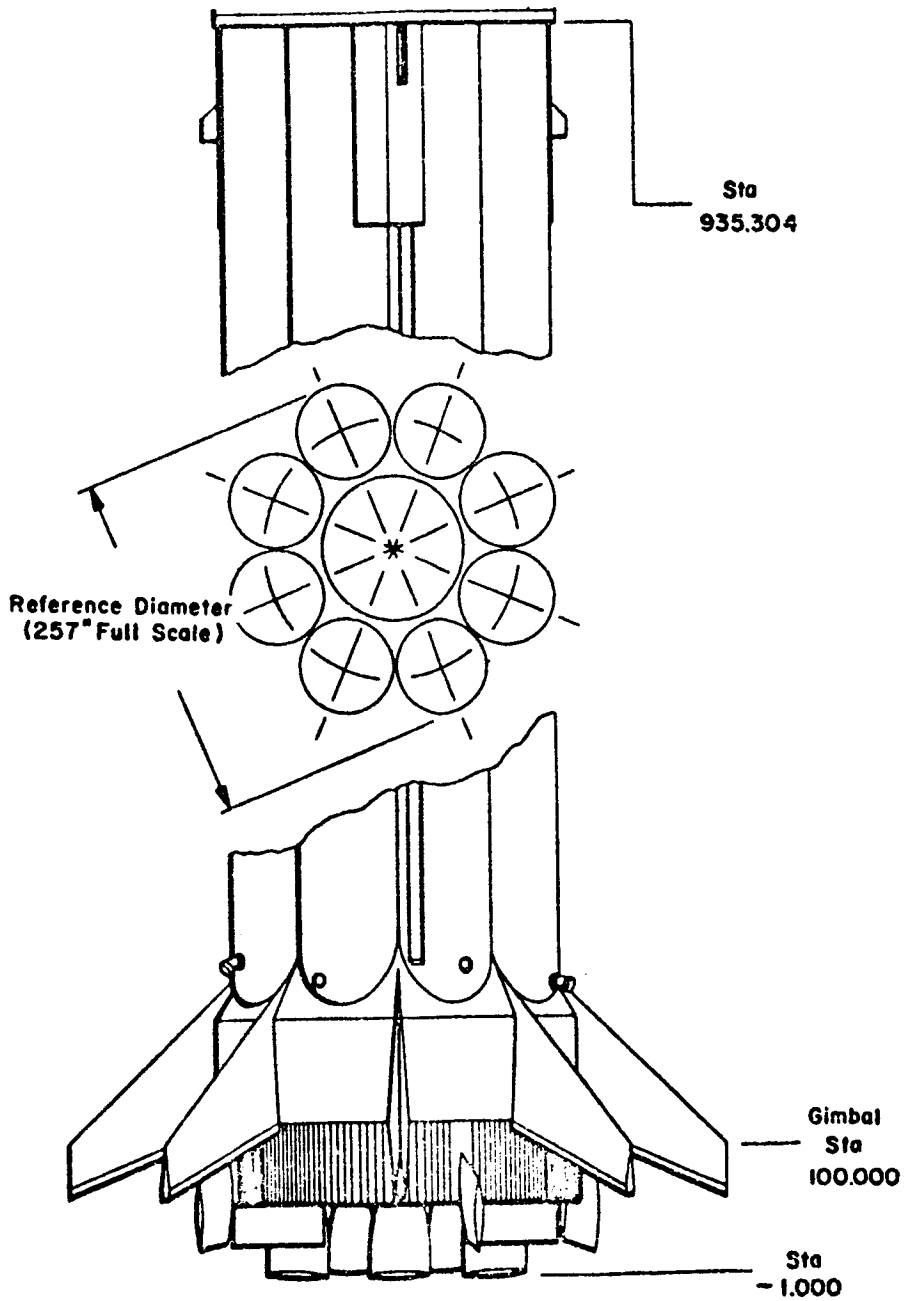

FIGURE 3.1-6. S-IB-1 EIGHT (8) 200K THRUST - H-1 ENGINES

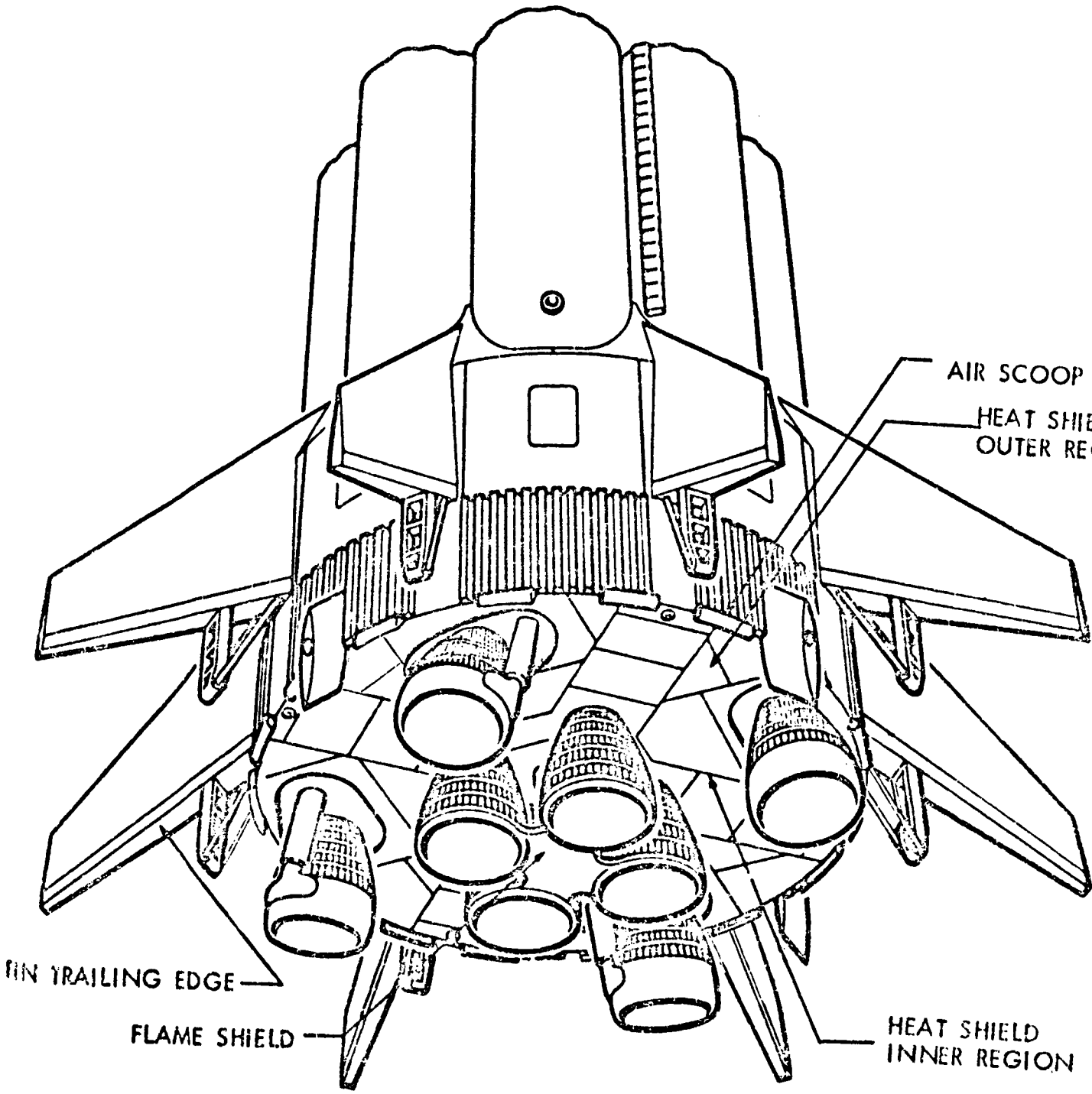

FIGURE 3.1-7. SA-201 BASE CONFIGURATION

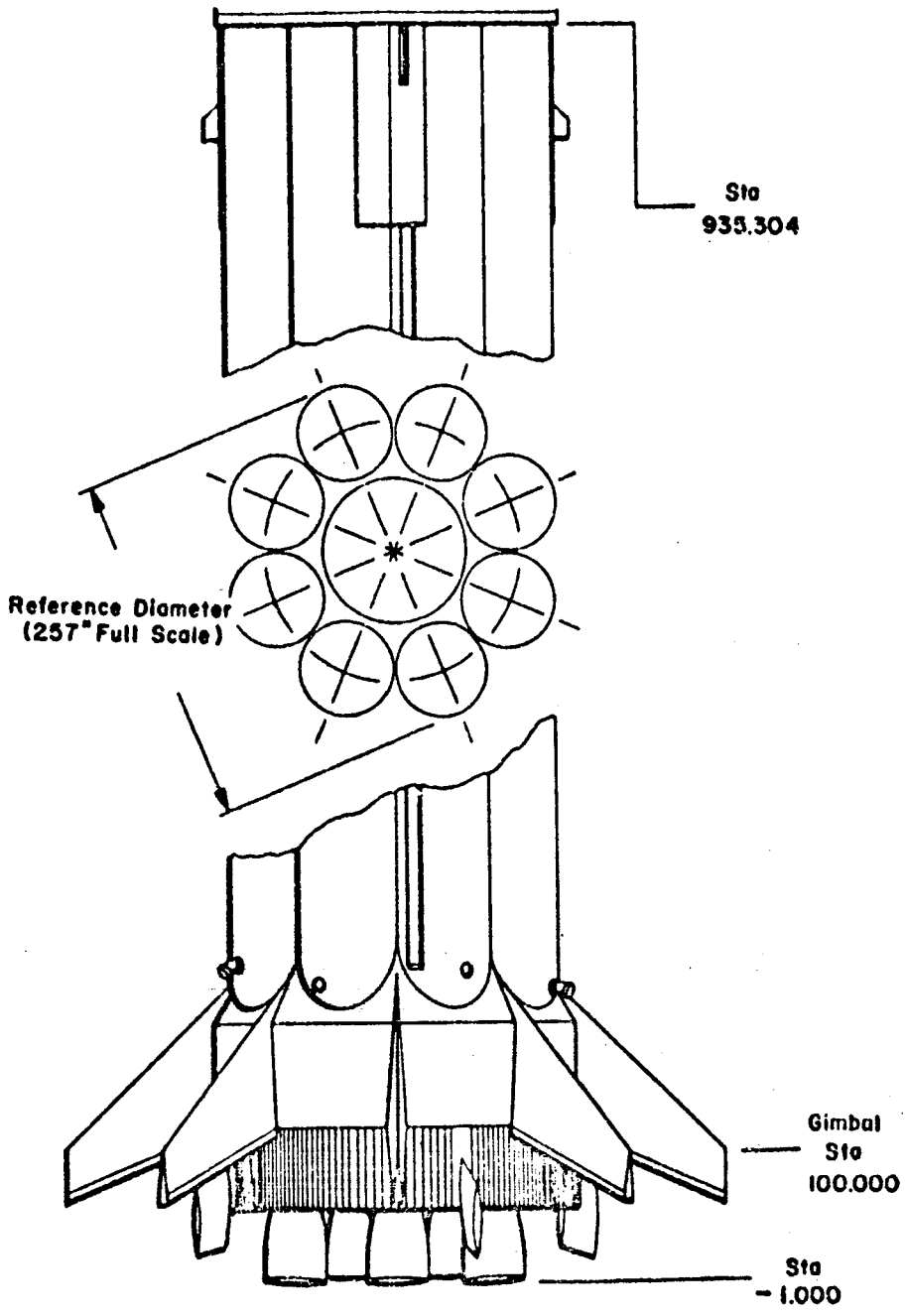

FIGURE 3.1-8. S-IB-2 EIGHT (8) 200K THRUST - H-1 ENGINES

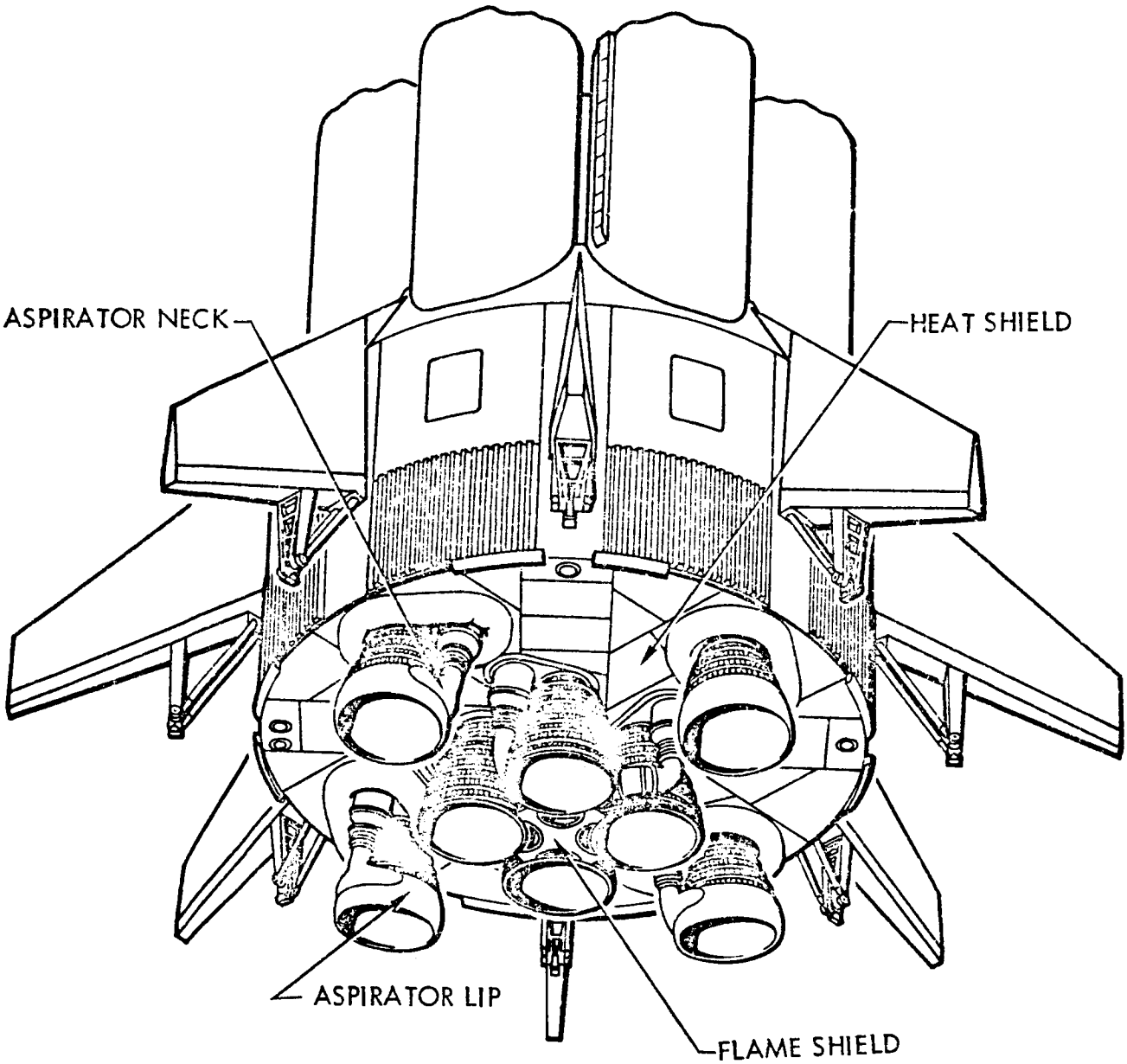

FIGURE 3.1-9. BASE VIEW OF SA-203 AND SUBSEQUENT LAUNCH VEHICLE

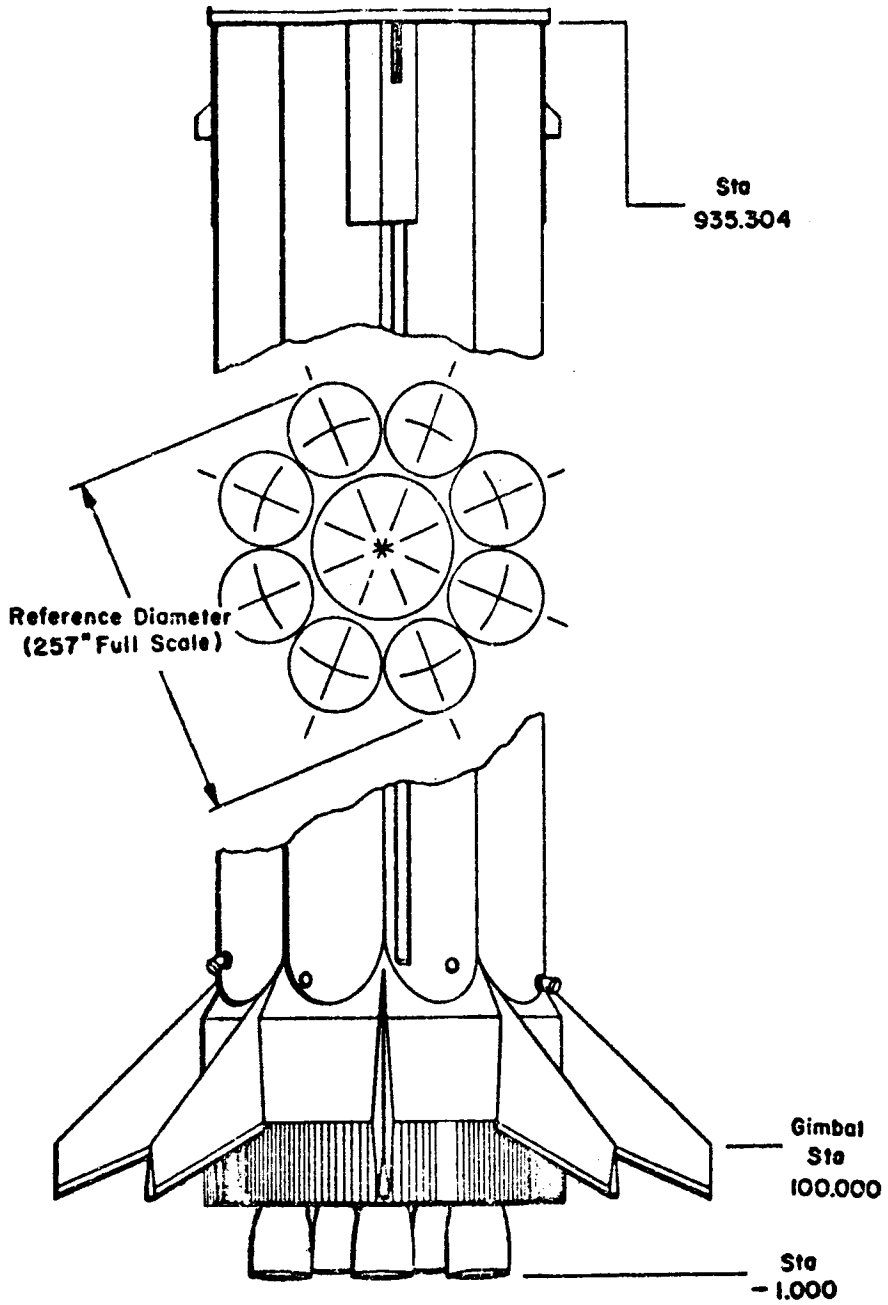

FIGURE 3.1-10. S-IB-3 THROUGH S-IB-5 EIGHT (8) 200K LB. THRUST - H-1 ENGINES

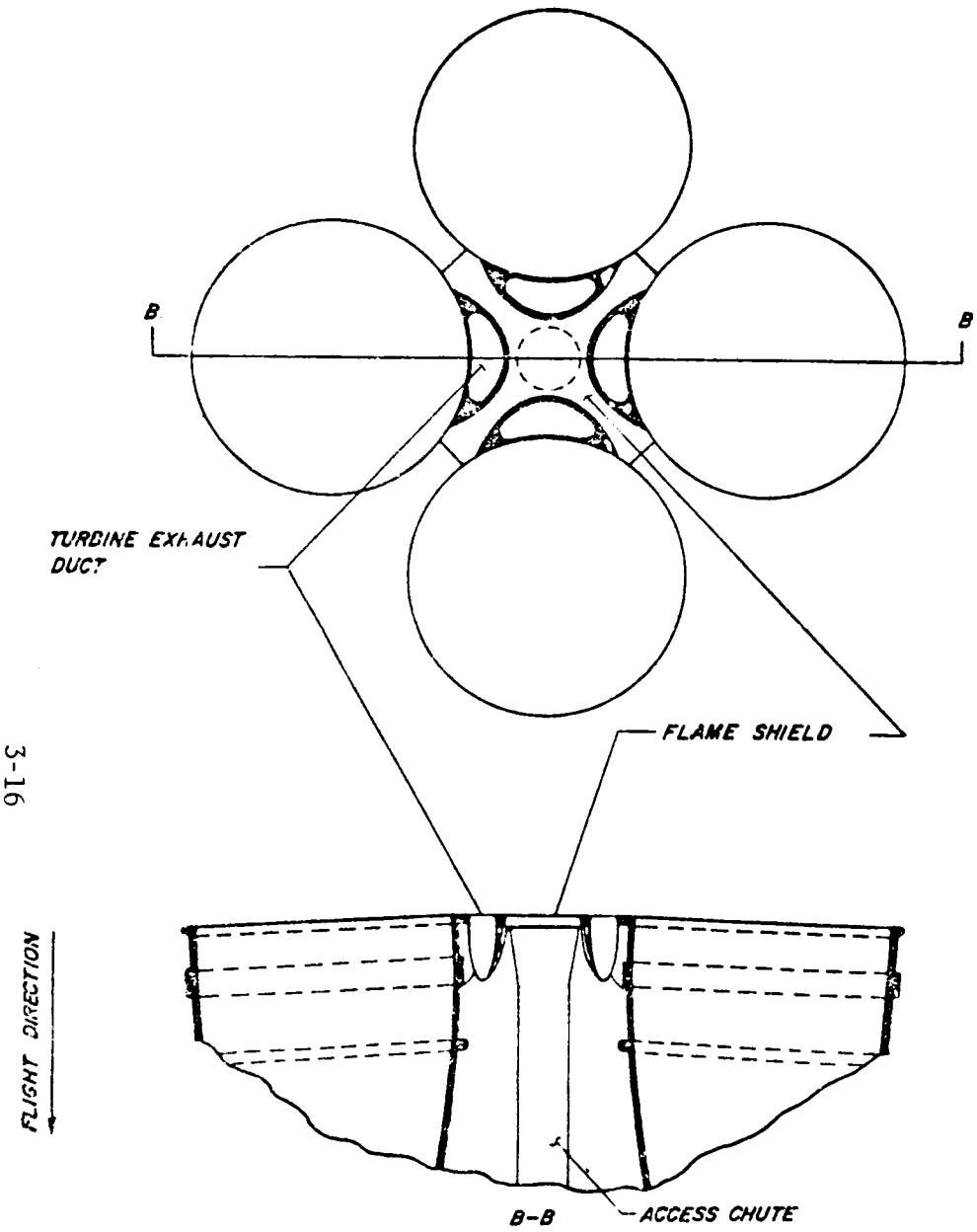

Location of Flame Shield for Saturn IB Vehicles Starting with SA 203

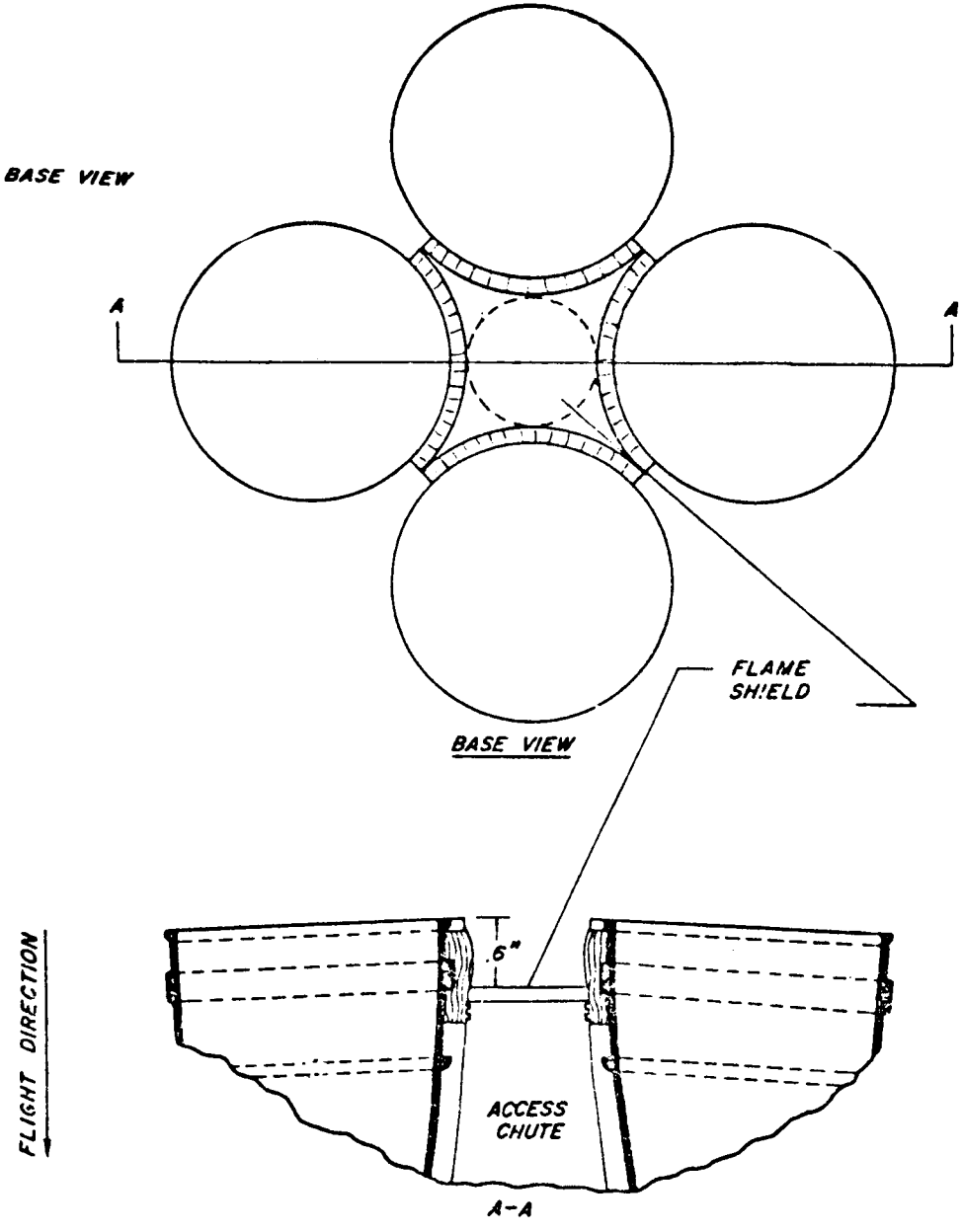

Location of Flame Shield for Saturn I and IB Vehicles Through SA-202

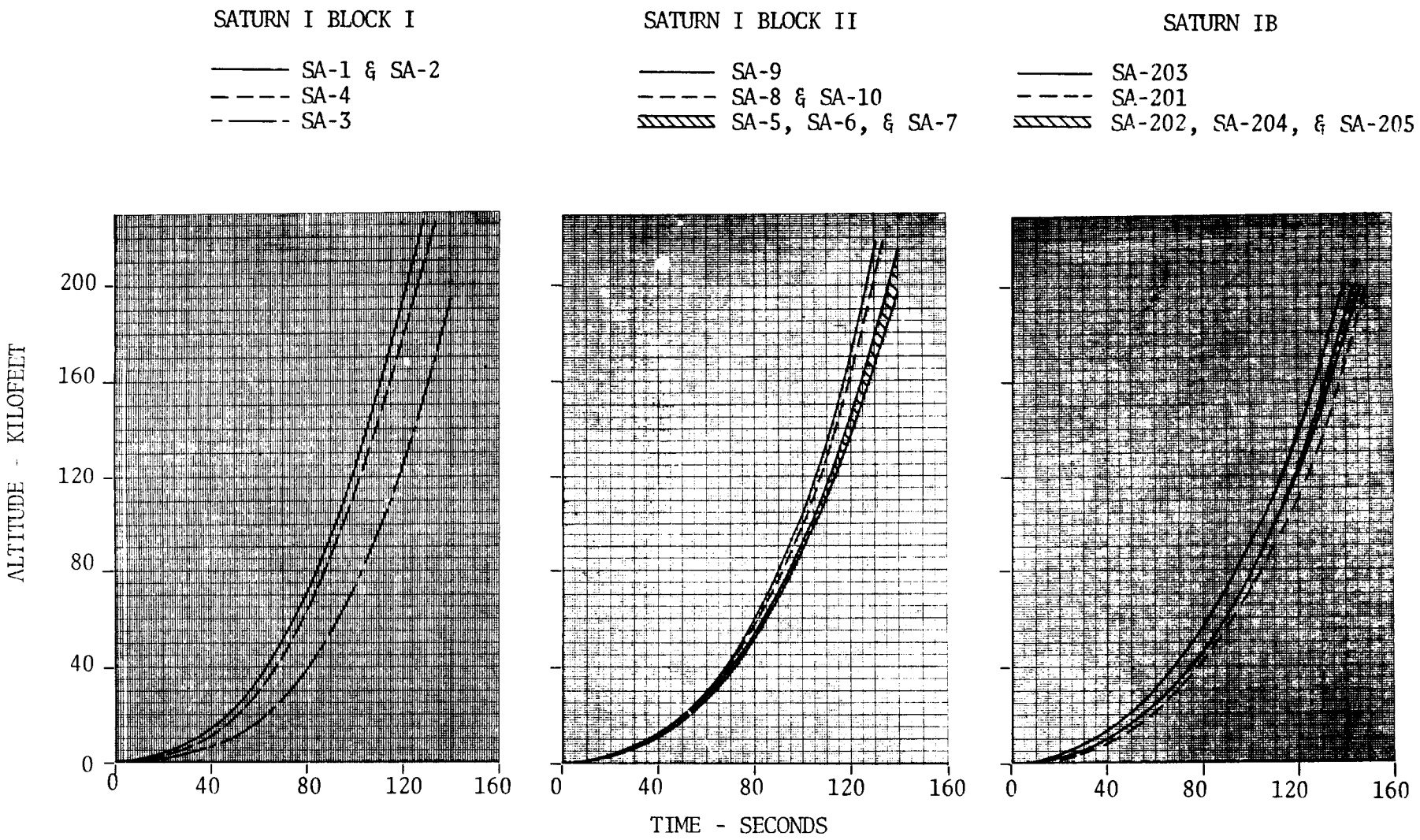

FIGURE 3.1-12. SATURN I AND SATURN IB TRAJECTORIES

3.2 H-1 ENGINE CHARACTERISTICS

The Rocketdyne H-1 engine is a fixed thrust, bi-propellant, single start rocket engine. Basically, the physical characteristics of the inboard engines and the outboard engines in the eight-engine cluster are identical. The major difference is in the turbine exhaust system. The present inboard engines (Figure 3.2-1) have a curved exhaust duct while the outboard engines utilize an aspirator.

On the S-I and S-IB stages, the H-1 engines are started in pairs 100 milliseconds apart beginning with the inboard engines. First stage powered flight lasts approximately 140 seconds, after which the inboard engines are shut down simultaneously. Approximately 4 seconds later the outboard engines are simultaneously shut down.

H-1 engine and thrust chamber operational and physical characteristics are presented in Table 3.2-1. Characteristics are given for the 165K, 188K and 200K thrust versions of the H-1. Launch vehicle effectivity are also given for each of the different engines. On the SA-206 flight, and subsequent, a 205K version of the engine will be used.

The H-1 engine nozzle is shown in Figure 3.2-2. The fuel tubes noted in this figure are brazed together and supported by ten circumferential stiffener bands. During engine operation, fuel (RP-1) is pumped through these tubes and has an estimated average temperature of 120°F.

Typical H-1 engine inviscid plume boundaries are shown in Figure 3.2-3 for five (5) altitudes. Detailed plumes at 20 and 59 KM are shown in Figures 3.2-4 and 3.2-5, respectively. Plots of this type were used in obtaining configuration factors to various base region locations in connection with radiant environment predictions. Actual plume shapes are significantly affected by variations in chamber pressure, nozzle configuration, base pressure and external flow properties. Additionally, plume shapes are affected by exhaust plume chemical reactions and afterburning which have not been considered in the inviscid plume boundary of Figures 3.2-3 through 3.2-5.

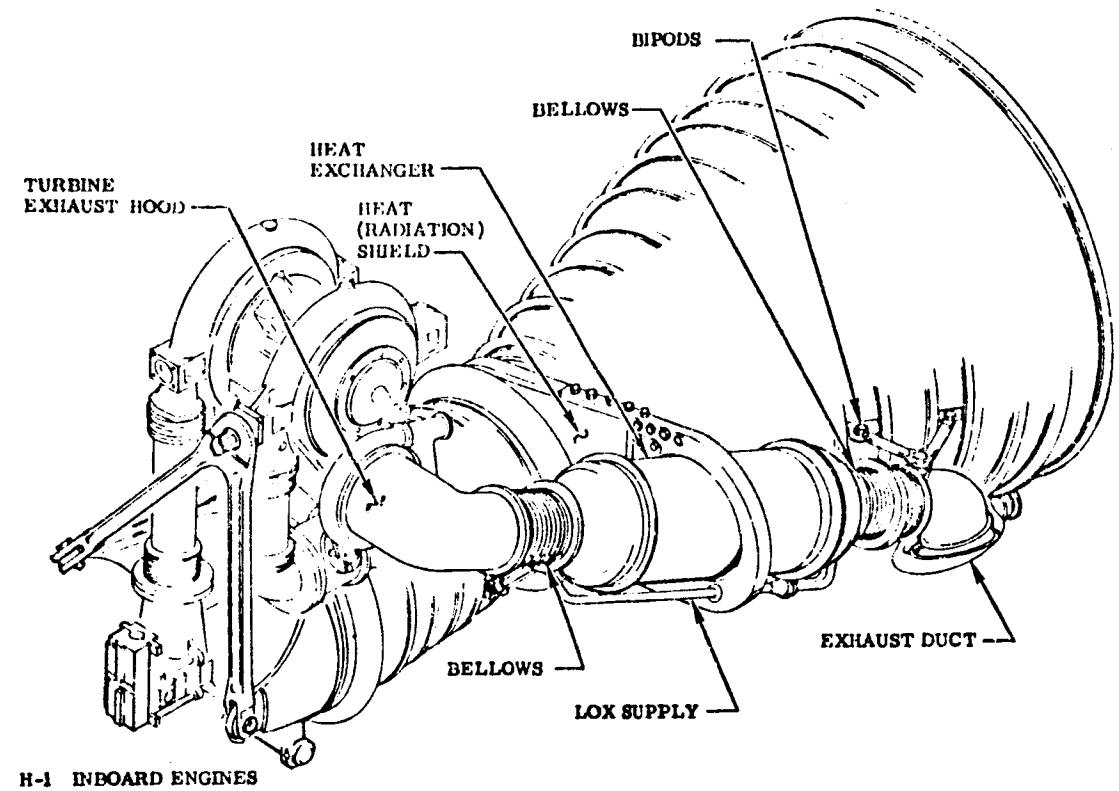

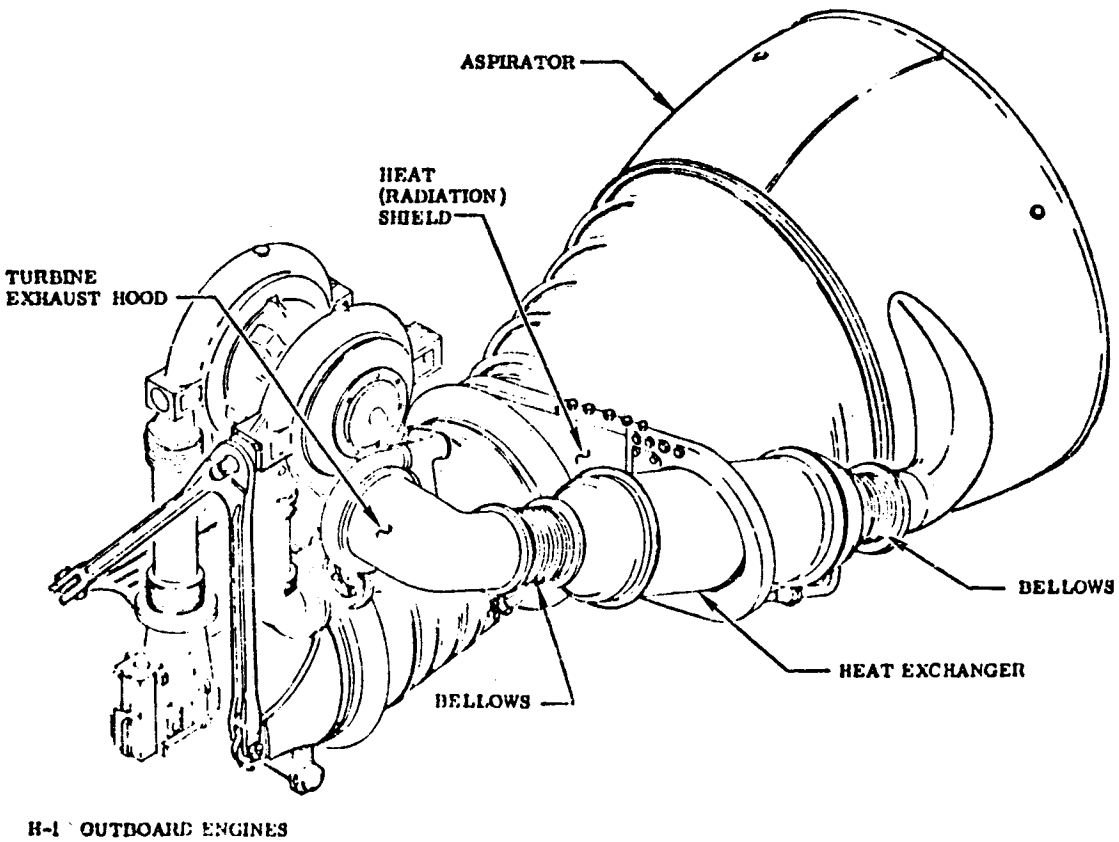

FIGURE 3.2-1. H-1 ENGINE TURBINE EXHAUST SYSTEM

TABLE 3.2-1. H-1 ENGINE OPERATIONAL AND PHYSICAL PARAMETERS

ENGINE PARAMETERS	UNIT OF MEASUREMENT	LAUNCH VEHICLE EFFECTIVITY		
		SA-1 - SA-4	SA-5 - SA-10	S-IB-1 - S-IB-5
● Operational Parameters (a)				
Engine				
Thrust	lb	165,000	188,000	200,000
Mixture Ratio, O/F	-	2.275	2.272	2.23
Specific Impulse	sec	248.0	257.0	262.8
LOX Weight Flow	lb/sec	455.0	509.0	525.5
Fuel Weight Flow	lb/sec	200.0	224.0	235.6
Thrust Chamber				
Thrust	lb	-	-	199,300
Mixture Ratio, O/F	-	2.40	2.382	2.338
Specific Impulse	sec	257.0	262.0	267.9
Chamber Pressure, Injector End	PSIA	578.0	650.0	689.3
C-Star, Injector End	ft/sec	5960	5980	6093
C_F, Injector End	-	1.39	1.41	1.415
LOX Weight Flow	lb/sec	(451.0)	505.0	521.0
Fuel Weight Flow	lb/sec	(188.0)	212.0	222.8
● Physical Parameters				
Throat Diameter	in.	16.2	16.2	16.2
Exit Diameter	in.	46	46	46
Combustion Chamber Diameter, Injector End	in.	20.56	20.56	20.56
Nozzle Expansion Area Ratio, A_e/A_t	-	8:1	8:1	8:1
Characteristic Length $L^*=V_c/A_t$	in.	-	-	39.10
Overall Length	in.	-	-	86.15

(a) Sea Level Values
No. in ( ) are determined from other parameters

FIGURE 3.2-2. H-1 ENGINE THRUST CHAMBER

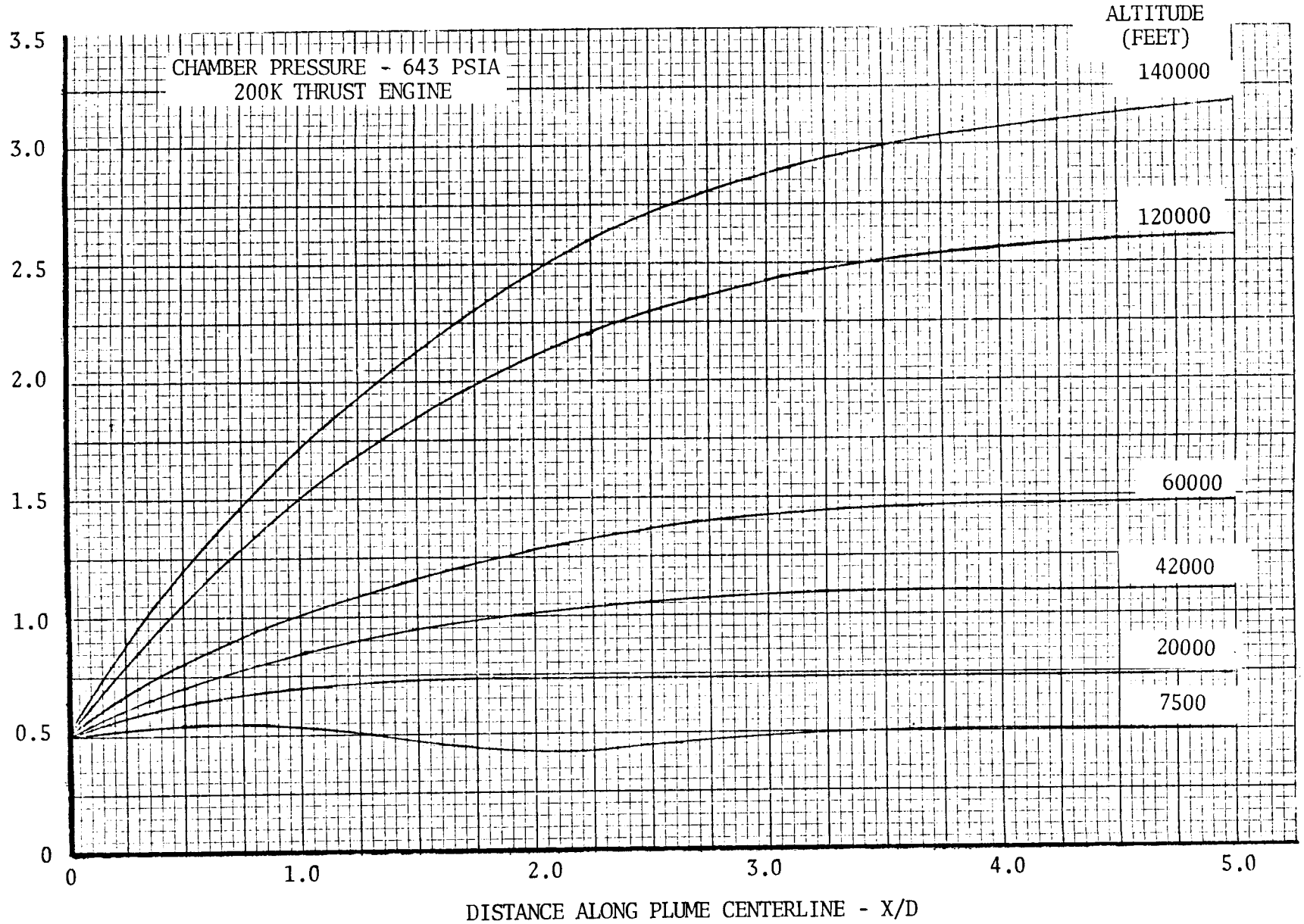

FIGURE 3.2-3. TYPICAL H-1 ENGINE PLUME SHAPE

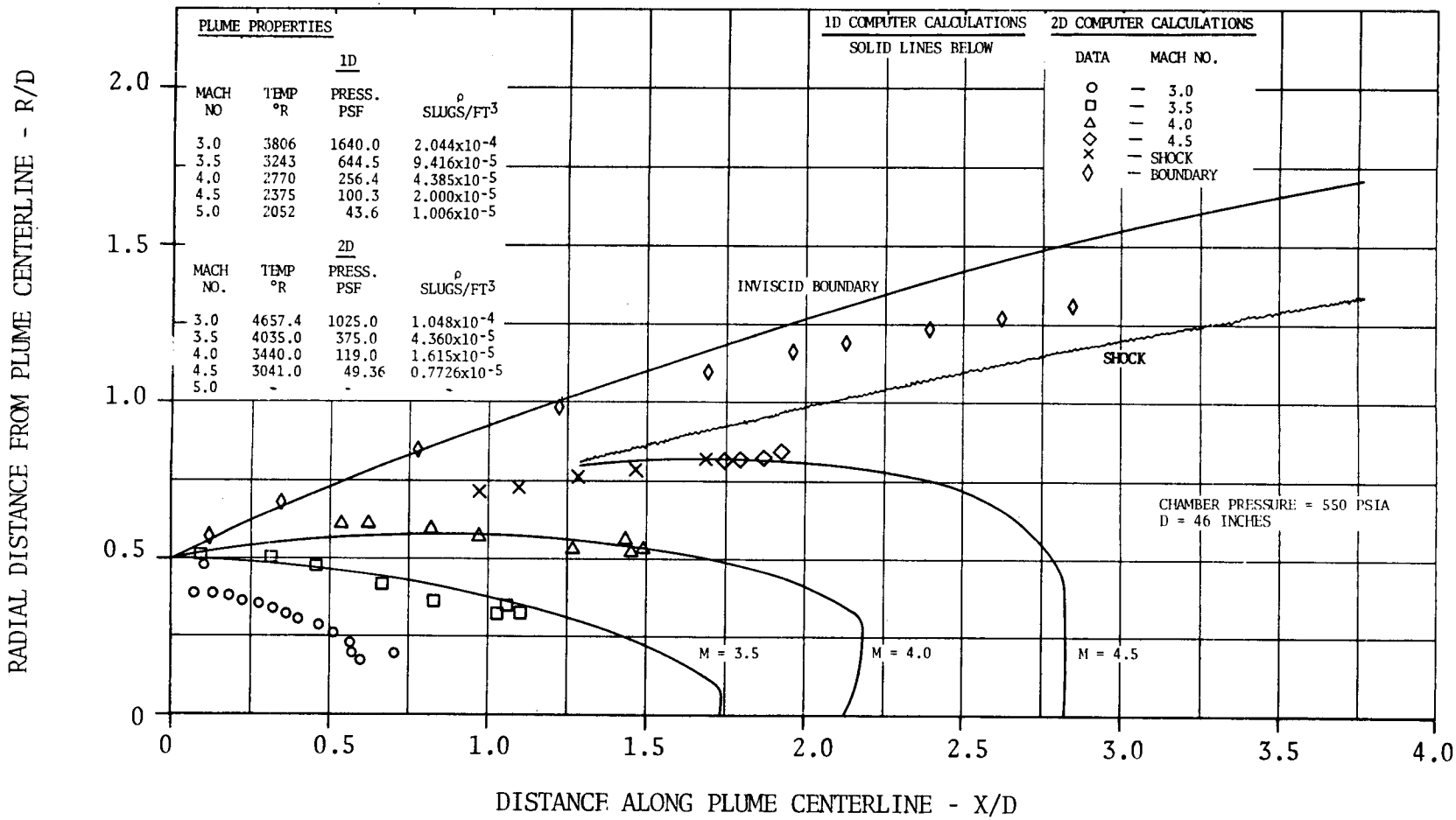

FIGURE 3.2-4. H-1 ENGINE PLUME AT 20.24 KM ALTITUDE

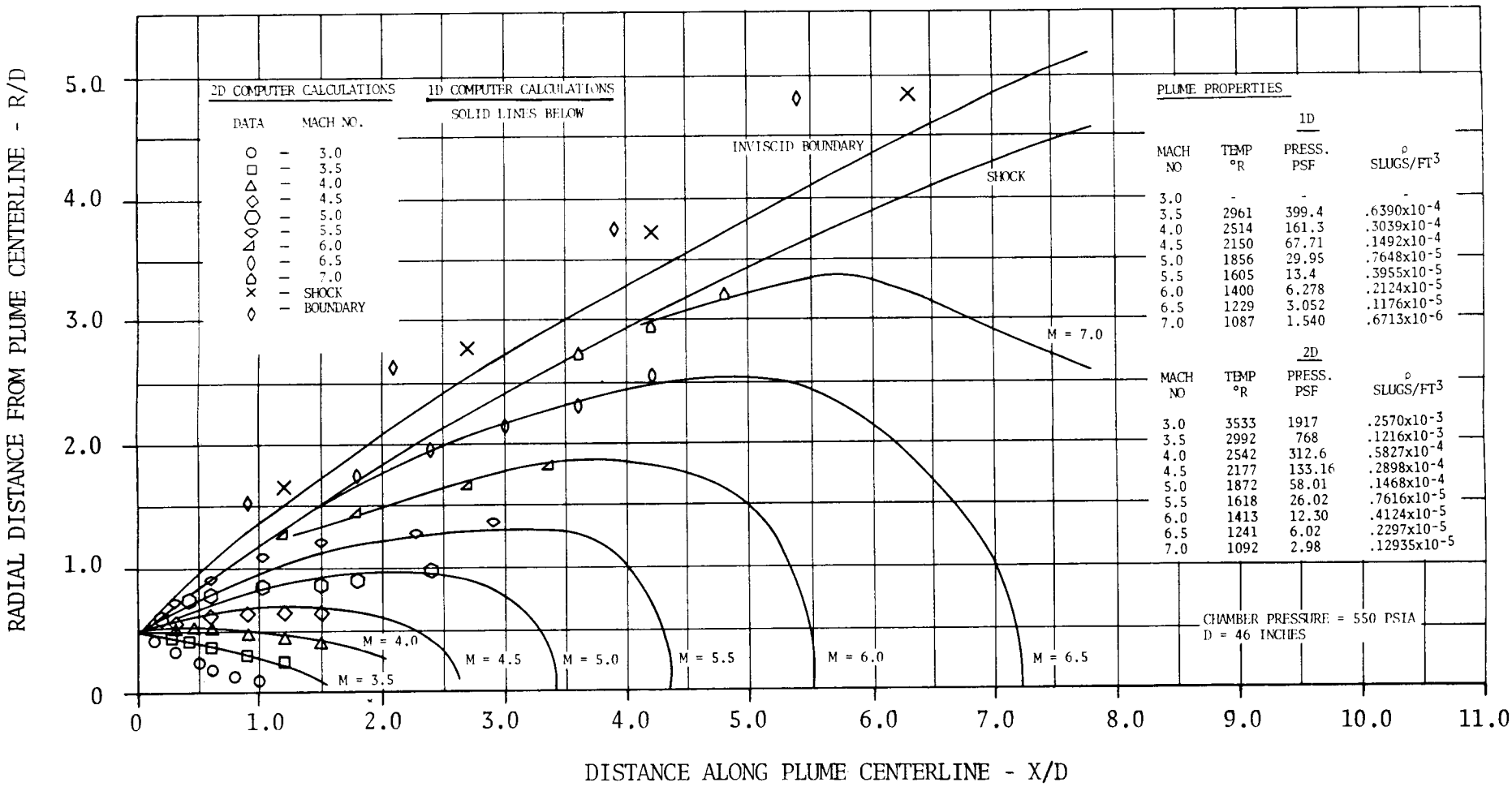

FIGURE 3.2-5. H-1 ENGINE PLUME AT 59.22 KM ALTITUDE

3.3 PREDICTION METHODS

During the boost phase of flight for both the S-I and S-IB stage, the eight H-1 engine cluster produces a complex interplay of radiative and convective heating. Each of these environmental components vary with altitude and base region location. The total heating environment to any location in the base region is the sum of the radiative and convective fluxes. This subsection discusses the analytical and empirical methods which were employed to formulate S-I and S-IB stage base region thermal environment and pressure predictions.

Radiation

The tools and formulations required for reliable analytical predictions of base region radiation have only recently been developed, and were in their infancy at the time of the original S-I and S-IB design. Hence for S-I and S-IB design applications, it was necessary to rely heavily on data from full scale static tests and from previously acquired flight and model data.

Primitive analytical predictions did aid in establishing base region radiation intensities for the initial S-I design. Configuration factors to cylindrical sea level plumes (Figure 3.3-1) were calculated, an optically thick plume radiating with an emissivity of 1.0 was assumed, and plume emission temperatures were based on radiance data from H-1 engine static firings. As the Saturn flight test program progressed, vast quantities of radiant heating data were acquired from strategically located calorimeters in the base region. On the basis of these data, the base region radiant environment was continually updated.

Convection

During the design phase of the S-I and S-IB stages there were no analytical convective heating analyses that could be performed. The tools required to probe the complexities of the base flow produced by the H-1 engine cluster arrangement were not available. Initial base flow models and convective heating predictions were made on the basis of wind tunnel scale model test data. These data indicated the convective heating trends that would occur at the various altitudes, i.e., during the various phases of the base flow phenomena, and at various base region radial locations.

Flight convective heating data from the base of the Saturn I vehicles were used to update the convective heating predictions. These data were also useful in evaluating the various analytical approaches for predicting the convective base heating environment which were under development at the time of the first flights. CCSD's analytical prediction approach was formulated by noting the similarity between the reversed flow caused by two adjacent plumes and the flow issuing from a fully developed turbulent jet positioned at the point of plume interaction. Preliminary analytical predictions for heat shield convective heat transfer coefficients resulting from the use of this prediction approach are presented in Figure 3.3-2. The average heat transfer coefficient derived from S-I, Block II flight data correlations is also shown in Figure 3.3-2 to compare with the analytical prediction.

3.3 (Continued)

Base region recovery temperatures used in S-I Block II and S-IB design analyses were deduced from measured gas temperature data. A band of S-I stage heat shield gas temperature data is shown in Figure 3.3-3 as a function of vehicle altitude. Superimposed on this data band is a plot of recovery temperature (T_R) that is consistent with measured total calorimeter wall temperatures and convective heating rates. The difference between the T_R curve and the average measured gas temperature is equal to the measured temperature rise produced by catalytic reaction (ΔT_C) and/or localized burning in the base region.

Pressure

Base pressure predictions for the early Saturn I vehicles were made on the basis of empirical formulations resulting from Jupiter flight data and Saturn I model test data. As the flight test program progressed, the basis for predictions was gradually updated as more flight data became available. On the basis of these data it was found that, for any given base region location, pressure coefficients could be consistently correlated with Mach number. Other trajectory variations were found to have only second order effects on the base pressure coefficients.

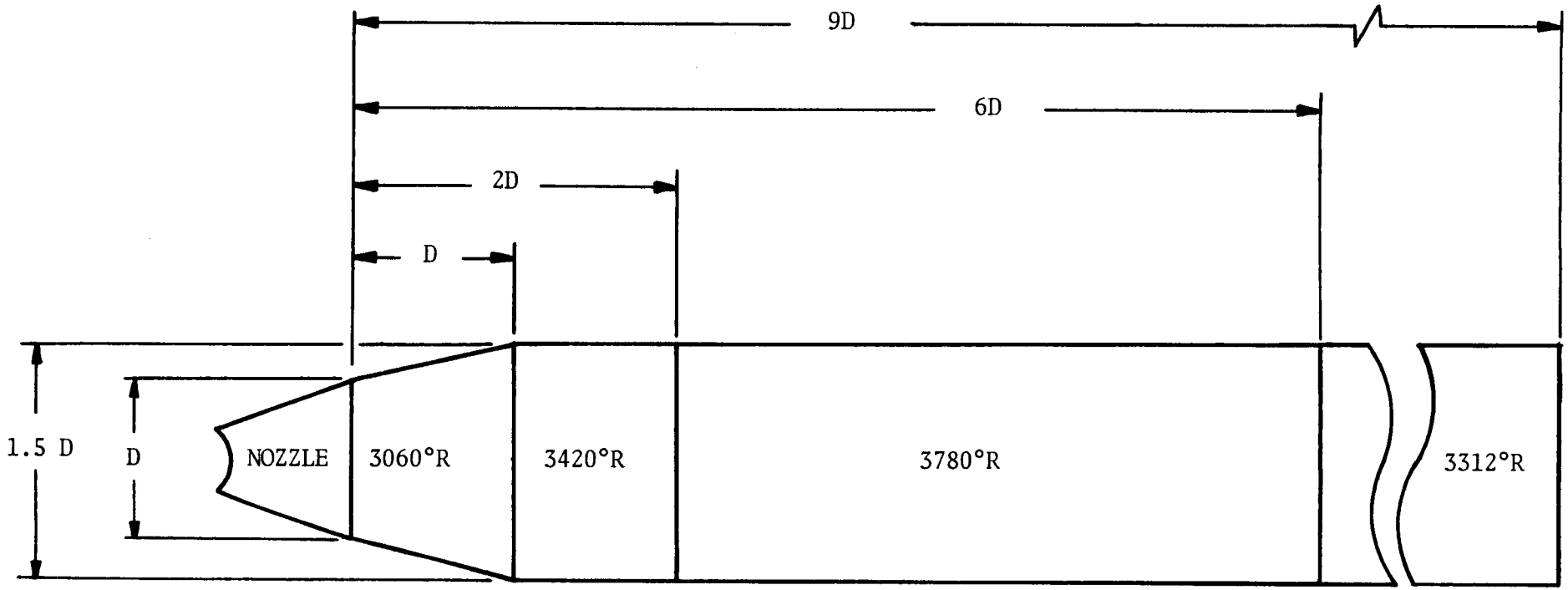

NOTE: 1. NOT TO SCALE
2. D=45.59 INCHES
3. EMISSIVITY=1.0

FIGURE 3.3-1. H-1 ENGINE SEA LEVEL PLUME MODEL

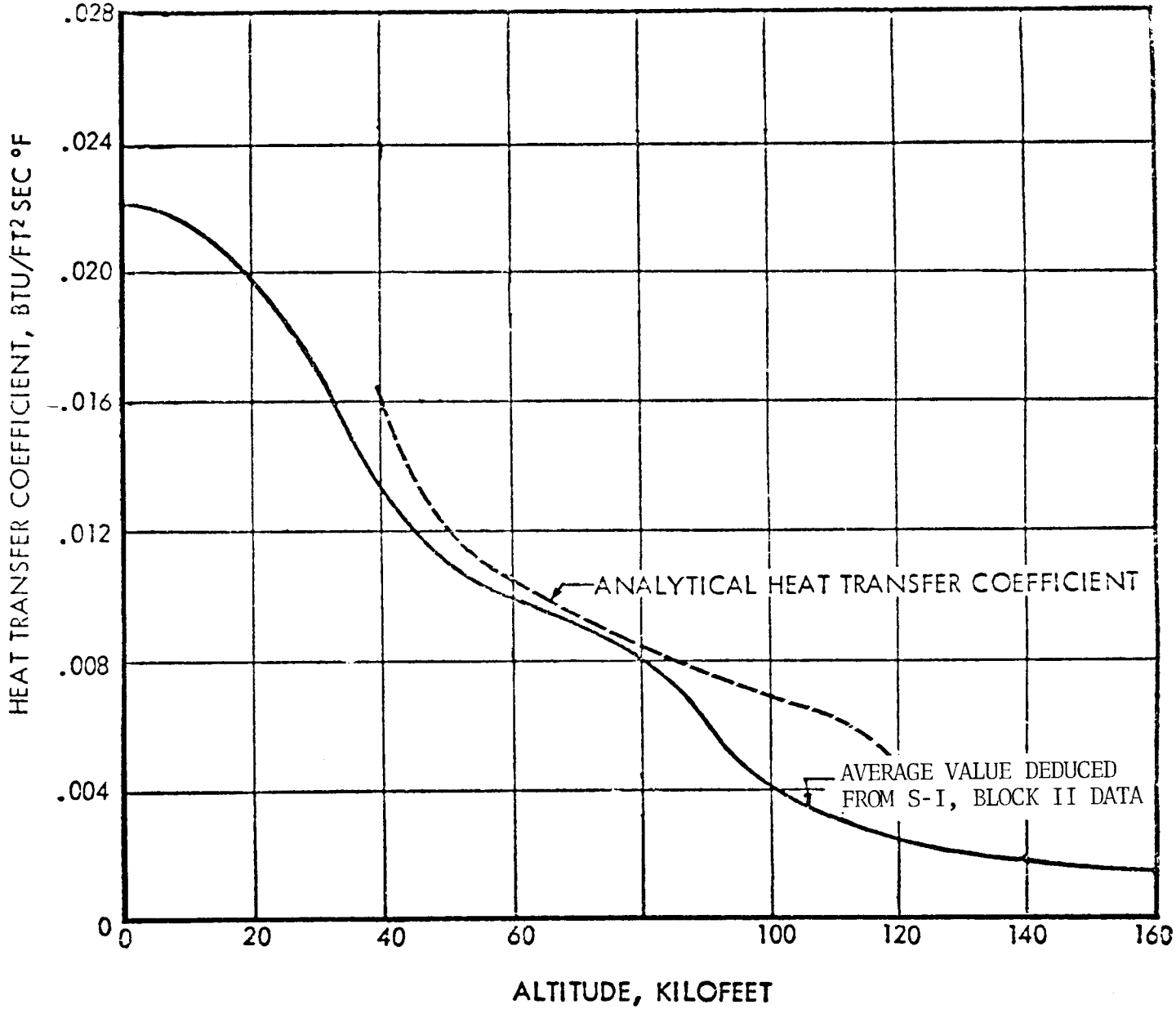

FIGURE 3.3-2. COMPARISON OF ANALYTICAL AND EMPIRICAL HEAT TRANSFER COEFFICIENT PREDICTIONS

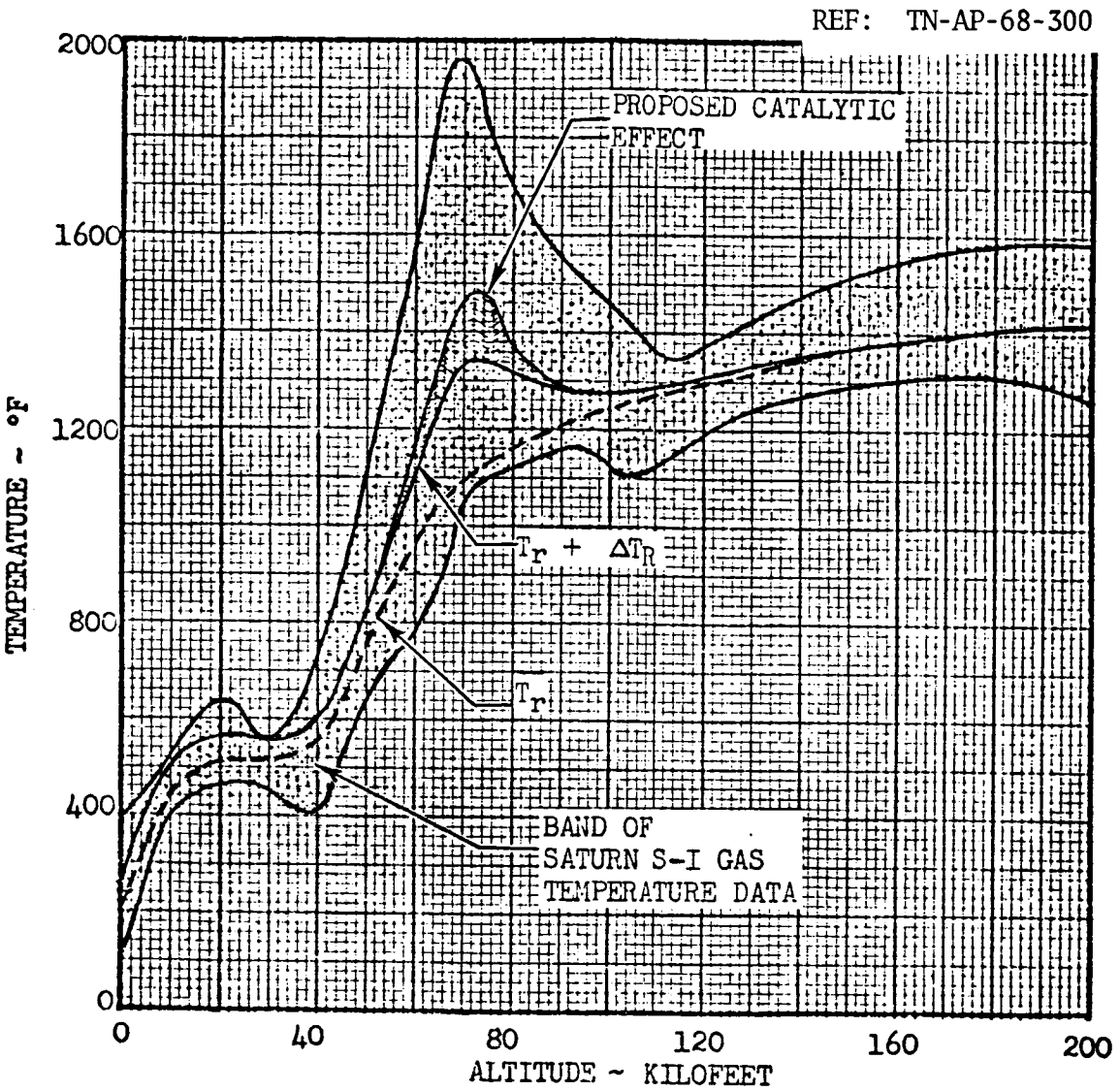

FIGURE 3.3-3. CORRELATION OF SATURN BASE REGION RECOVERY TEMPERATURE ΔT_R AND ΔT_C WITH MEASURED GAS TEMPERATURES

3.4 MODEL TESTS AND PARAMETRIC DATA

Early in the Saturn program, a considerable effort was expended on model tests to determine the base heating characteristics of the Saturn design. These data were useful in determining the required heat protection for the base area of the first Saturn I vehicles.

Numerous model test programs were conducted in facilities at the Lewis Research Center, Arnold Engineering Development Center, and the Cornell Aeronautical Laboratory. It is beyond the scope of this document to discuss and present all model tests and data available; however, representative tests and data are presented.

The following paragraphs give a brief discussion of three of the early model tests. A fourth test using short-duration experimental techniques on a Saturn S-IB booster model is also discussed.

Saturn S-I Booster Model at Transonic Mach Numbers (AEDC-PWT)

These tests were conducted in the 16-Foot Transonic Tunnel of the Propulsion Wind Tunnel (PWT) Facility, Arnold Engineering Development Center (AEDC), Air Force Systems Command (AFSC), in May 1961. Results from these tests are presented in Reference 3-1. These tests were conducted to determine base heating on a 5.47-percent scale model of the Saturn S-I Booster.

Various turbine exhaust stack configurations were tested over a Mach number range of 0.6 to 1.5, an altitude range of 10,000 feet to 42,000 feet, and a missile angle-of-attack range of 0 to -7 1/2 degrees. Rocket engines using liquid oxygen and RP-1 were used to simulate the full-scale engine exhaust, and hydrogen was used to simulate the turbo-pump exhaust.

Tests were conducted both with and without simulated turbine exhaust. Various compromises were required in the scale model for these tests. The data should, therefore, be used with caution to obtain full-scale values. The data were, however, considered useful in obtaining trends and for configurational comparisons. Compromises in the model included differences in inner engine cant-angle and clearance at the exits, engine-exit to free-stream static pressure ratio, engine O/F ratio, engine combustion efficiency, and turbine exhaust aerodynamic characteristics. The effect of these compromises are discussed in Reference 3-1.

The turbine exhaust configurations tested are shown in Figure 3.4-1 and representative data from these tests are shown in Figures 3.4-2 through 3.4-10. Flame shield or star shield heating was essentially unaffected by the various exhaust configurations tested. There was, however, a noticeable difference in data obtained with turbine-exhaust-off and turbine-exhaust-on operation. This turbine exhaust on/off effect on star shield heating rates is shown in Figure 3.4-2 for various Mach numbers and altitudes. The equilibrium wall temperature determined by extrapolating the data to a heating rate of zero is shown in Figure 3.4-3.

3.4 (Continued)

Gas temperature thermocouples, projecting through the primary heat shield, had a very rapid response and measured essentially constant temperatures during each of the phases of operation (turbine-exhaust-off and turbine-exhaust-on). A qualitative comparison of the base burning for the turbine exhaust stack configurations was, therefore, readily obtained from these temperature data (shown in Figure 3.4-4). The data indicate no burning with turbine exhaust configuration 3; and configuration 2, compared to 1-A, showed increased burning at $M_\infty = 1.2$ and reduced burning at $M_\infty = 0.8$. No burning was observed below 500 psfa free-stream static pressure for any of the model test configurations.

The ratio of primary heat shield base pressure to free-stream static pressure is shown in Figure 3.4-5 for trajectory conditions. At $M_\infty = 1.2$ a significant increase in base pressure was observed when the simulated turbine exhaust was used. The effect was the same for all turbine exhaust configurations. The increase in base pressure was not influenced by the exhaust stack configuration and was believed to be attributable to the change in the jet wake caused by the exhausterators.

The ratio of base pressure on the star shield to free-stream static pressure is shown in Figure 3.4-6. Comparison of the star shield base pressure ratios with the primary shield base pressure ratios indicates high aspiration at the low Mach numbers. The equalized pressures at $M_\infty = 1.4$ and 1.5 indicate the transition to backflow or flow reversal. This was also shown by the star shield heating (Figure 3.4-3).

The effect of higher trajectory altitudes at $M_\infty = 1.2$ is shown in Figure 3.4-7. The base pressure ratios for turbine-exhaust-off operation were found to be a linear function of the free-stream static pressure and increased as the free-stream static pressure was reduced. At the higher altitudes (lower pressures) the change in base pressure produced by the turbine exhaust was negligible. The effect of the engine exhaust on the base pressure was small at the higher pressures and very large at the lower pressure. The higher Mach number data at comparable free-stream static pressures indicate that the power-on base pressure is also dependent upon Mach number as well as free-stream static pressure.

Conclusions drawn from these test results, and published in Reference 3-1 are as follows:

1. Simulated turbine exhaust flow caused increased star shield equilibrium wall temperatures and lower film coefficients for all exhaust stack configurations at the lower Mach number and altitude trajectory conditions.

2. Negligible effects of the turbine-exhaust on star shield heating at the maximum test Mach number indicated the transition from inner engine base aspiration to backflow occurred at this condition. Equalization of the primary heat shield and star shield pressures at these test conditions also showed this base flow transition.

3.4 (Continued)

3. Burning of the simulated turbine exhaust gases in the missile base did occur at some of the test conditions when the other exhaust stack configurations were used.

4. The base burning phenomenon was found to be influenced by trajectory altitude at M_∞ = 1.2 with near zero increases in heating rates due to the turbine exhaust at higher altitudes.

5. Increased base heating due to increasing the angle of attack was not significant below approximately 4 degrees. At 7 1/2 degrees, large increases in base heating were produced.

Saturn SA-1 Booster Model at M = 0.8 and 1.15 (AEDC-RTF)

These tests were conducted in the Rocket Test Facility (RTF), Arnold Engineering Development Center (AEDC), Air Force Systems Command (AFSC), during the period February through June 1961. Results from these tests are presented in Reference 3-2. The purpose of these tests was to determine the base recirculation characteristics of the simulated propellant pump turbine exhaust gases of a 5.47 percent scale model of the SA-1 Saturn afterbody.

Base heating and pressure data were obtained at simulated flight trajectory conditions of Mach number 0.8 (16,000 feet altitude) and Mach number 1.5 (27,500 feet altitude) using several turbine exhaust duct configurations. The effect on base heating of one engine inoperative, of variation in turbine exhaust gas momentum, of finned-model operation, of variation in engine O/F ratio, and of variation in altitude were also investigated. Gaseous hydrogen was used to simulate the combustible turbine exhaust gas of the full-scale missile. Liquid oxygen, RP-1 fueled rocket engines, each developing about 500 pounds thrust, were used to simulate the prototype engines. Representative data from these tests are presented in Figures 3.4-8 through 3.4-10.

For the prototype booster the turbine exhaust gases are relatively cool in comparison with the temperature of the engine exhaust jets. Therefore, little increase in base heating should occur, even if these gases do recirculate into the base; unless the gases when combined with atmospheric air ignite and burn in or very near the base. Because the gases are fuel-rich, the possibility of ignition does exist, provided the proper conditions of mixture ratio and stay time are present. The most obvious solution to this aspect of the base heating problem is to minimize the amount of recirculated turbine exhaust gases because it is not possible to control either mixture ratio or stay time.

The three overboard turbine exhaust duct configurations tested are essentially the same as were shown in Figure 3.4-1. Heating results from the Mach 0.8 and Mach 1.15 tests are presented in Figure 3.4-8 as a comparison of the maximum total heating rates obtained. The cross-hatched section of each bar represents the average heating rates recorded with turbine-exhaust-off. The solid section represents heating rates caused by hydrogen burning with turbine-exhaust-on.

3.4 (Continued)

Of the three test configurations, the streamlined turbine exhaust duct, configuration 3, resulted in the lowest total peak heating rates at both Mach 0.8 and 1.15. At Mach 0.8, with configuration 3, no increase in heat flux from hydrogen burning occurred at either the heat or flame shields. It was not determined whether this was due to the lack of hydrogen recirculation into the base or due to recirculation without ignition. At Mach 1.15 the hydrogen definitely recirculated and burned near the heat shield, as shown by the 8 Btu/ft^2sec increase in heat shield heating rate; burning did not occur at the flame shield.

The other duct configurations, with their larger frontal area, produced a larger and more turbulent wake than the airfoil-shaped streamlined ducts. Consequently, they entrained a greater quantity of the discharged hydrogen, which was subsequently drawn into the model base to form a combustible hydrogen-air mixture.

When one of the inboard engines was inoperative, the most noticeable change was produced in the flame shield or center region. For this condition the flame shield is no longer enclosed and much of the aspirating effect is lost. Additionally, the radiation heat source is reduced by 25-percent and the back flow from the exhaust jets into the center region is decreased. Flame shield heating rates for seven-engine and eight-engine operation are compared in Figure 3.4-9. Turbine exhaust duct configuration 1-A was used for the engine-out tests.

The addition of four stabilizing fins to the model afterbody altered the external flow field locally and created a large turbulent wake upstream of the model skirt trailing edge. At Mach 0.8 the results was a 17-percent decrease in base pressure from that obtained without the fins installed. Heating results, summarized in Figure 3.4-10, show that the addition of the fins caused a 40-percent increase in the average heat shield values. The lower base pressure for the finned configuration either caused a larger quantity of hydrogen to be drawn into the base region or altered the hydrogen-air ratio in the base region or both. Either could cause more severe base burning.

Investigations of O/F ratio on base heating showed decreased total heating when O/F ratio was increased from 1.7 to 2.2. The lower heating rates at the higher O/F ratio were assumed to be the result of a lower heat release from hydrogen burning in the base region. No significant difference in base heating rates was observed for turbine-exhaust-off operation at the higher O/F ratio.

A complete summary of the results obtained during this investigation, as published in Reference 3-2, is as follows:

3.4 (Continued)

1. Based on peak total base heat transfer rates, the most effective configuration for the overboard discharge of simulated turbine exhaust gases (hydrogen) was the streamlined turbine exhaust duct configuration. Peak total base heating rates were 10.0 and 15.0 Btu/ft^{2}sec at Mach 0.8 and 1.15, respectively.

   Hydrogen discharge from the long turbine exhaust ducts resulted in peak total base heating rates of 26.5 and 33.8 Btu/ft^{2}sec at Mach 0.8 and 1.15, respectively. Modification of the attachment brackets for the long ducts reduced the peak to 22.0 Btu/ft^{2}sec at Mach 1.15.

   Hydrogen discharge from the short turbine exhaust ducts resulted in the most severe base heating at both Mach numbers; peaks were 52.5 and 36.0 Btu/ft^{2}sec at Mach 0.8 and 1.15, respectively.

2. The region on the model base which indicated the highest heat transfer rate usually was located between the inboard and outboard engines.

3. During firings with one engine intentionally inoperative, the flame shield and base heat transfer rates were reduced; however, base burning appeared to be marginal for this configuration because one firing at Mach 0.8 resulted in base heating rates slightly greater than those obtained during operation with all eight engines.

4. Operation with the stabilizing fins installed on the model afterbody resulted in a 40-percent increase in average base heating rates above that of the non-finned configurations.

5. The major effect on base and flame shield heating of an increase in the nominal O/F ratio from 1.7 to 2.2 was to decrease hydrogen burning in the case of the long and short duct configurations. However, the streamlined ducts did not follow this trend and indicated increased burning at both the base and flame shield.

6. Flame shield heat transfer rates increased rapidly when altitude was increased from 15,000 to 40,000 feet. Between 40,000 and 85,000 feet altitude (without external airflow) the heating rate was essentially constant.

7. Increasing the turbine exhaust gas momentum per unit area from 36 to 120 percent of the full-scale value resulted in decreasing base burning during the discharge of pure hydrogen and a hydrogen-nitrogen mixture. Base burning did not occur when the percentage of full-scale momentum per unit area was greater than 180 percent.

8. When hydrogen was discharged from the exhausterators only, there was no measurable increase in base heating above that obtained from operation without hydrogen flow.

3.4 (Continued)

9. With no base burning, base pressure ratio decreased approximately 13 percent as Mach number was increased from 0.8 to 1.5 because of the increase in base pumping action created by the high velocity external airstream. When base burning did occur, base pressure ratio increased about 1 percent over the same Mach number range.

10. Flame shield pressure coefficient increased from -0.58 at Mach 0.8 to -0.23 at Mach 1.15. No influence of degree of base burning or of overboard duct configuration on flame shield pressures could be detected.

Saturn SA-1 Booster Model at M = 1.63 and 3.07 (AEDC-RTF)

These tests were conducted in the Rocket Test Facility (RTF), Arnold Engineering Development Center (AEDC), Air Force Systems Command (AFSC), during the period July through September 1961. Results from these tests are presented in Reference 3-3. The purpose of these tests was to continue the investigation of base recirculation characteristics of several different turbine exhaust ducts on a 5.47-percent scale model of the Saturn SA-1 booster afterbody.

Base heating and pressure data were obtained with external airflow at Mach numbers 1.63 (33,000 to 45,000-foot altitude) and 3.07 (70,000 to 80,000-foot altitude) using the three turbine exhaust duct configurations shown in Figure 3.4-1. The effect on base heating and base pressure of one inboard engine inoperative and of altitude variation was also investigated. Gaseous hydrogen was again used to simulate the combustible products of the turbine exhaust. Representative data from these tests are presented in Figures 3.4-11 through 3.4-13.

For these tests no burning occurred in the base region regardless of the turbine exhaust duct configuration, free-stream Mach number, or the altitude at which testing was accomplished. Although no base burning occurred some base heating was present which was attributed to recirculation of hot rocket exhaust gases.

Flame shield calorimeter data, shown in Figure 3.4-11, indicate a maximum heat transfer rate at the center of the flame shield. This was true for both test Mach numbers with the heat transfer rate generally decreasing with increased distance from the center. With one inboard engine inoperative, the heat transfer to the flame shield was substantially reduced. This decrease in heat transfer was as predicted since, (1) the radiation heat source is reduced by 25-percent, (2) the reversed flow from the intersecting jets is substantially reduced, and (3) the exit area for the flow that is reversed is greatly enlarged.

3.4 (Continued)

Variations of base heat shield to free-stream pressure ratio with altitude are shown in Figure 3.4-12. Several "off-trajectory" runs were made at both Mach numbers to establish a trend. Because of pressure ratio limitations the trajectory altitude for Mach = 3.07 could not be obtained. The trend of the data indicates an increase in base pressure ratio as altitude increases.

There were also small but distinct differences between various duct configurations. This was attributed to differences in aerodynamic characteristics and not to differences in amount of recirculated hydrogen.

The base pressure was affected very little when an inboard engine was inoperative. It was noted, however, that the pressures were measured on the side of the base opposite the inoperative inboard engine.

Flame shield pressure data are presented in Figure 3.4-13. These data are presented as a ratio of flame shield pressure to base pressure. This ratio was used because the gases from the flame shield region exhaust into the base region and therefore, are influenced more by base pressure than by ambient pressure. A critical pressure ratio of 1.79 (P_{FS}/P_B) was computed for the gases in the flame shield region. As shown in Figure 3.4-13, data were greater than 1.79 for all Mach 3.07 tests. An extrapolation of these data to a pressure ratio of 1.79 indicates that the flame shield to base pressure ratio would become critical at about 63,000-foot altitude.

Several tests were made at both M_∞ = 1.63 and M_∞ = 3.07 with one inboard engine inoperative. The flame shield pressure in both cases (Figure 3.4-13) showed a marked decrease when compared with that taken with all eight engines operating. This is attributed to the fact that the area available for the rejected gas to escape was greatly increased while the amount of rejected gases was decreased. The flame shield pressure was approximately equal to the base pressure at Mach number 1.63 and was only slightly higher than the base pressure at Mach number 3.07.

A summary of the results obtained during this investigation and published in Reference 3-3 is as follows:

1. No burning of the hydrogen, which simulated the turbine exhaust products, occurred in the base at either Mach number 1.63 or 3.07.

2. Maximum heat transfer was approximately 4.0 Btu/ft^{2}sec with minimum values of 2.5 Btu/ft^{2}sec in the region between the rocket nozzles and skirt extensions.

3. The heat transfer rate to the flame shield at Mach number 1.63 was 113 Btu/ft^{2}sec at the center. At Mach number 3.07, the heat flux was 72 Btu/ft^{2}sec at the center. At both test Mach numbers, flame shield heating rates decreased with increased distance from the center of the flame shield.

3.4 (Continued)

4. A profile of calculated values of film heat transfer coefficient for the flame shield indicated the maximum at the center and the minimum at the greatest distance from the center. At Mach number 1.63, data indicated the average maximum value was 0.227 Btu/ft^{2}sec-°F, and the average minimum value was 0.066 Btu/ft^{2}sec-°F, whereas at Mach number 3.07 the average maximum value was 0.143 Btu/ft^{2}sec-°F, and the average minimum value was 0.059 Btu/ft^{2}sec-°F.

5. Base pressure data indicated a slight increase, when hydrogen flow was initiated, with all duct configurations evaluated.

6. There was little effect on base pressure during operation with an inoperative inboard engine.

7. Flame shield pressure measured near the center of the shield was constant at approximately 2.87 psia for all testing with eight engines operating.

8. An extrapolation of the Mach number 3.07 data to a pressure ratio of 1.79 indicates that the flame shield to base pressure ratio would become critical at about 63,000 feet.

9. The flame shield pressure with one inboard engine inoperative was equal to the base pressure at Mach number 1.63 and was 15 percent higher than base pressure at Mach number 3.07.

Later in the Saturn flight test program consideration was given to removing the engine shrouds (effective on SA-202) and rerouting the inboard engine turbine exhaust (effective on SA-203). The following discussion involves an experimental investigation, using short-duration techniques, that was to examine the effects of these design modifications.

Uprated Saturn S-IB Booster Model at M = 1.18 and 1.63 Using Short-Duration Techniques

These tests were conducted in the AEDC/RTF/T-1 cell with a 5.47-percent scale model of the Saturn S-IB and S-I/Block II stages during the period June through November 1965. The purpose of these tests was to examine the effects of various turbine exhaust configurations, removal of engine shrouds and flow deflectors, one outboard engine inoperative, and altitude variations on the base heating rates and pressures.

Tests were conducted at simulated trajectory conditions of M = 1.18/altitude = 30,000 feet and M = 1.63/altitude = 40,000 feet. Two basic Saturn S-IB turbine exhaust configurations were tested: (1) full exhausterators on the outboard engines and over stacks (OB) for the inboard engines (Configuration 3, Figure 3.4-1); and (2) full exhausterators on the outboard engines and partial exhausterators (PDI) on the inboard engines (see Figure 3.4-14). Gaseous oxygen (O_2) and ethylene (C_2H_4) were used to simulate the LOX/RP-1 propellant employed on the full scale S-I and S-IB. Cold hydrogen gas was used for simulation of the fuel-rich turbine exhaust gases.

3.4 (Continued)

Initial test results were reported in Reference 3-4. However, the figures presented herein, and the accompanying discussions were taken from Reference 3-5. These figures present a brief summary of the significant test results. For a more detailed analysis of these or any of the experimental results, the reader is referred to the original or initial test data report.

The average base (heat shield) heating rates for all S-IB configurations tested are summarized in bar chart form in Figure 3.4-15. Radiation heating was virtually independent of model configuration and ambient conditions. Total heating without turbine exhaust simulation was also effectively independent of configuration or test conditions.

Significant increases in total heating rate were experienced in all cases with hydrogen turbine exhaust flow, indicating the presence of base burning. At both Mach numbers investigated, the average base heating rate with the basic S-IB configuration was significantly less with the OB turbine exhaust configuration than for the PDI configuration. Removal of the flow deflectors and engine shrouds generally tended to increase the base heating rates with either turbine exhaust configuration. This effect was more pronounced (particularly in the base of the OB turbine exhaust) when the No. 1 outboard engine was inoperative.

Average base pressure ratios (i.e., $\bar{P}_B/P_\infty$) for the various S-IB configurations and test conditions investigated are summarized in Figure 3.4-16. At Mach 1.18, base pressures were essentially unchanged between "engine-off" and "engine-on" conditions. At Mach 1.63 (and the higher altitude), base pressure increased substantially over the engine-off levels during engine firing. In all cases, the addition of H_2 turbine exhaust resulted in higher base pressures, indicative of base burning. In general, base pressure levels were similar for both the OB and PDI turbine exhaust configurations. Removal of the engine shrouds and flow deflectors resulted in significantly higher base pressures as might be intuitively expected. With No. 1 engine inoperative, the average base pressures were generally lower than the equivalent configuration with all engines operating.

For the Mach 1.18/30,000-foot trajectory condition shown in Figure 3.4-17, neither removal of the engine shrouds nor an inoperative No. 1 engine produced a noticeable effect on the flame shield heating rates. For the PDI configuration, flame shield heating rates decreased markedly (from a maximum of nearly 120 Btu/ft^{2}sec to $\approx$2 Btu/ft^{2}sec) with simulated turbine exhaust injection. This is not particularly surprising since the turbine exhaust flow would tend to provide a naturally cool barrier between the flame shield and recirculating hot rocket exhaust gases. Somewhat unexpected, however, was the indicated slight decrease in heating rate near the center of the flame shield with turbine exhaust flow from the OB ducts. It is not presently clear why a reduction in flame shield heating rates should occur when the turbine exhaust is dumped overboard into the free stream.

3.4 (Continued)

Flame shield heating rate distributions for the Mach 1.63/40,000-foot trajectory condition are shown in Figure 3.4-18. Considering first the OB turbine exhaust configuration, it was noted that the peak heating rate of 120-130 Btu/ft^{2}sec is consistent with that obtained at the lower altitude M = 1.18 trajectory condition. Further, as was also observed at M = 1.18, an inoperative No. 1 engine had little effect on flame shield heating rate, either with or without turbine exhaust simulation. With all engines operating and shrouds on (Figure 3.4-18a), a comparatively large decrease in heating rate was observed with hydrogen turbine exhaust flow, in agreement with a similar observation at M = 1.18 and just as baffling. It is noted, however, that this effect was completely cancelled when the engine shrouds were removed (i.e., heat shield heating rates were the same with or without turbine exhaust flow).

Heating rates with the PDI turbine exhaust configuration appear to be independent of model geometry or number of engines firing and show a large decrease in heating rate with turbine exhaust flow similar to that observed at the M = 1.18 test condition.

Flame shield pressures are summarized in non-dimensional form in Figure 3.4-19 for the various geometries and flight conditions investigated. For the Mach 1.18/30,000-foot altitude condition, the flame shield-to-ambient pressure ratio was essentially independent of all test variables, maintaining a value of ≈0.70. For the Mach 1.63/40,000-foot condition, no valid flame shield pressure data were obtained with the OB configuration due to a faulty pressure transducer installation. With the PDI configuration, flame shield pressure was consistently slightly below free stream pressure with no turbine exhaust flow (i.e., $P_{FS}/P_\infty \approx 0.9$), and a little higher than free-stream pressure with turbine exhaust flow (i.e., $P_{FS}/P_\infty \approx 1.10$). No appreciable change in flame shield pressure accompanied removal of the shrouds and deflectors or an inoperative No. 1 engine.

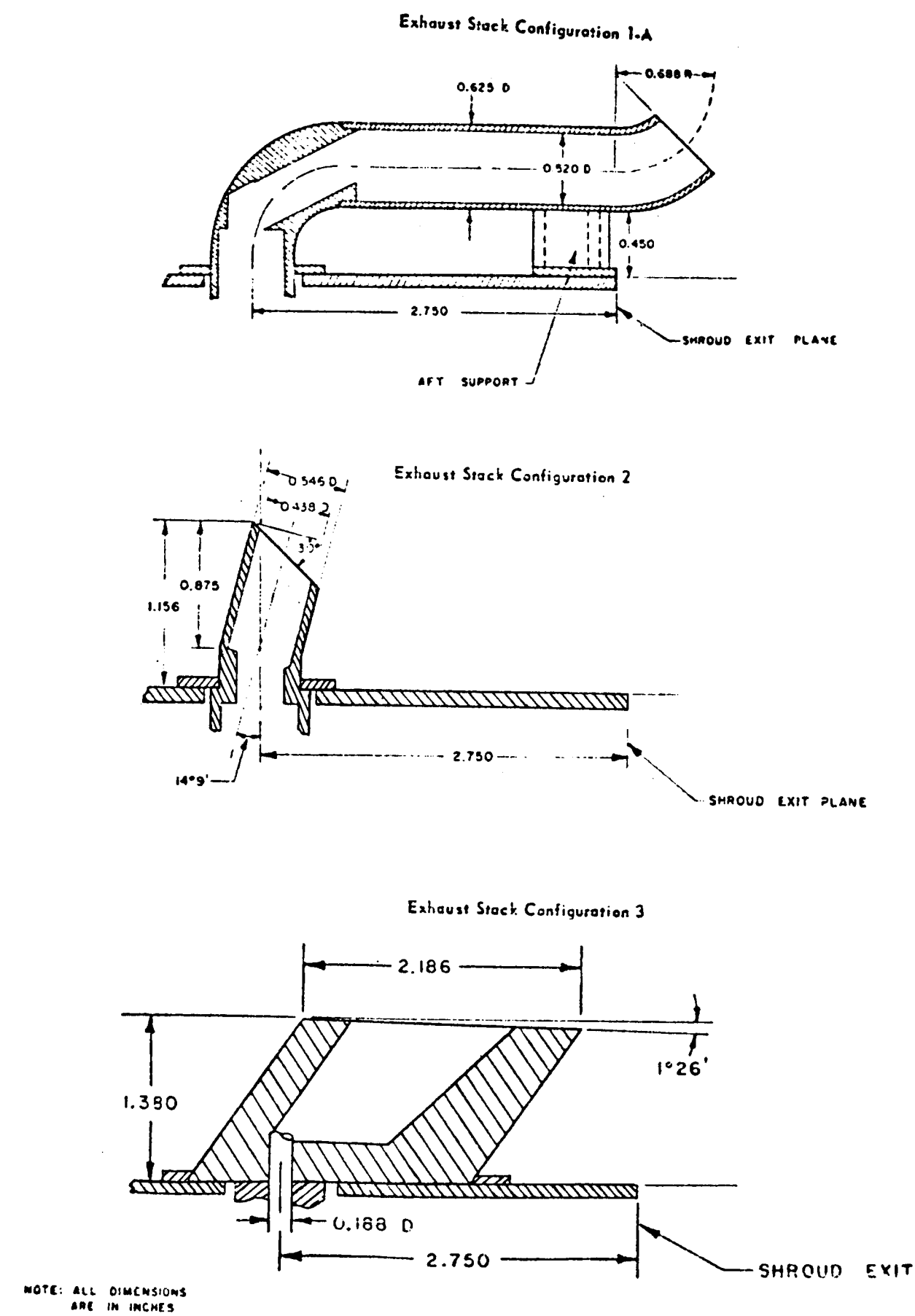

FIGURE 3.4-1. TURBINE EXHAUST CONFIGURATIONS

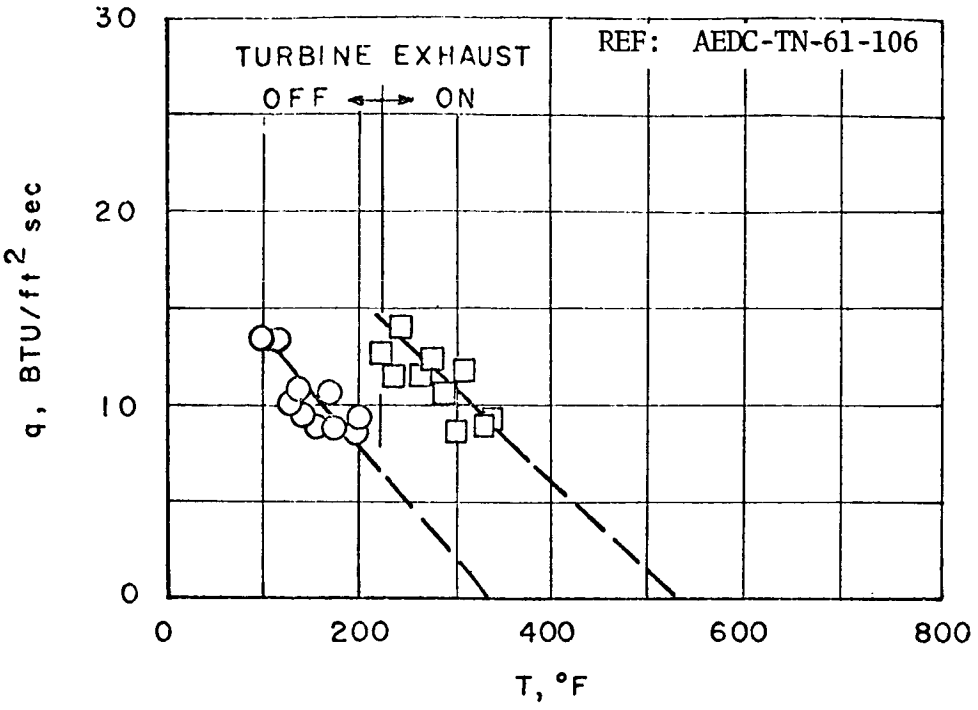

a. M_∞ = 0.6, Altitude 10,000 ft

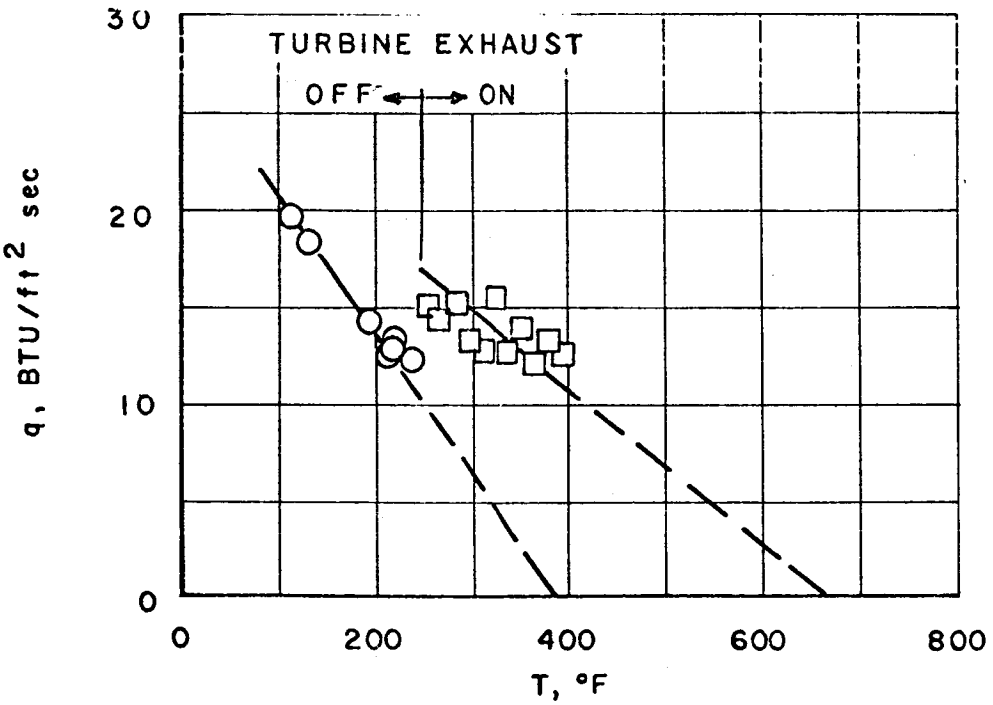

b. M_∞ = 0.8, Altitude 16,000 ft

FIGURE 3.4-2. STAR SHIELD HEATING RATES AS A FUNCTION OF CALORIMETER TEMPERATURE FOR CONFIGURATION 1-A

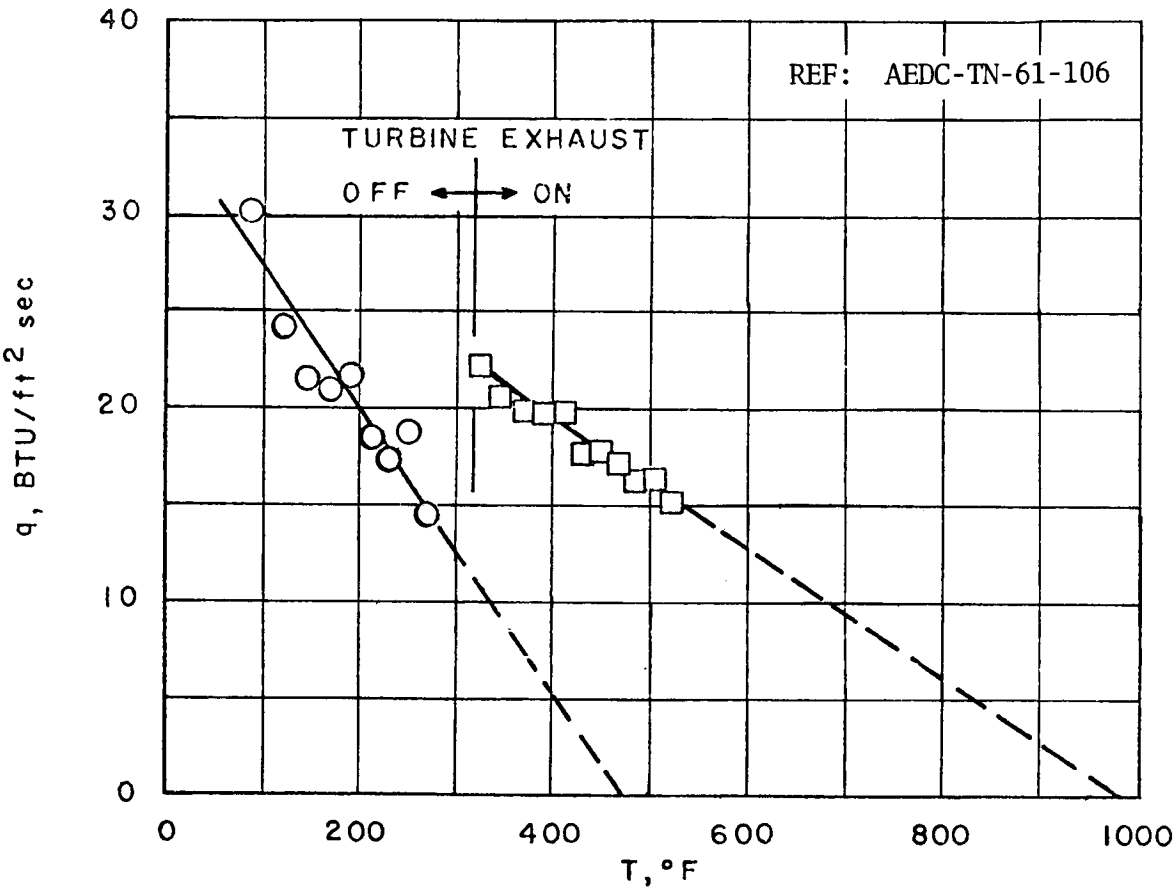

c. M_∞ = 1.0, Altitude 22,000 ft

FIGURE 3,4-2. STAR SHIELD HEATING RATES AS A FUNCTION OF CALORIMETER TEMPERATURE FOR CONFIGURATION 1-A (CONTINUED)

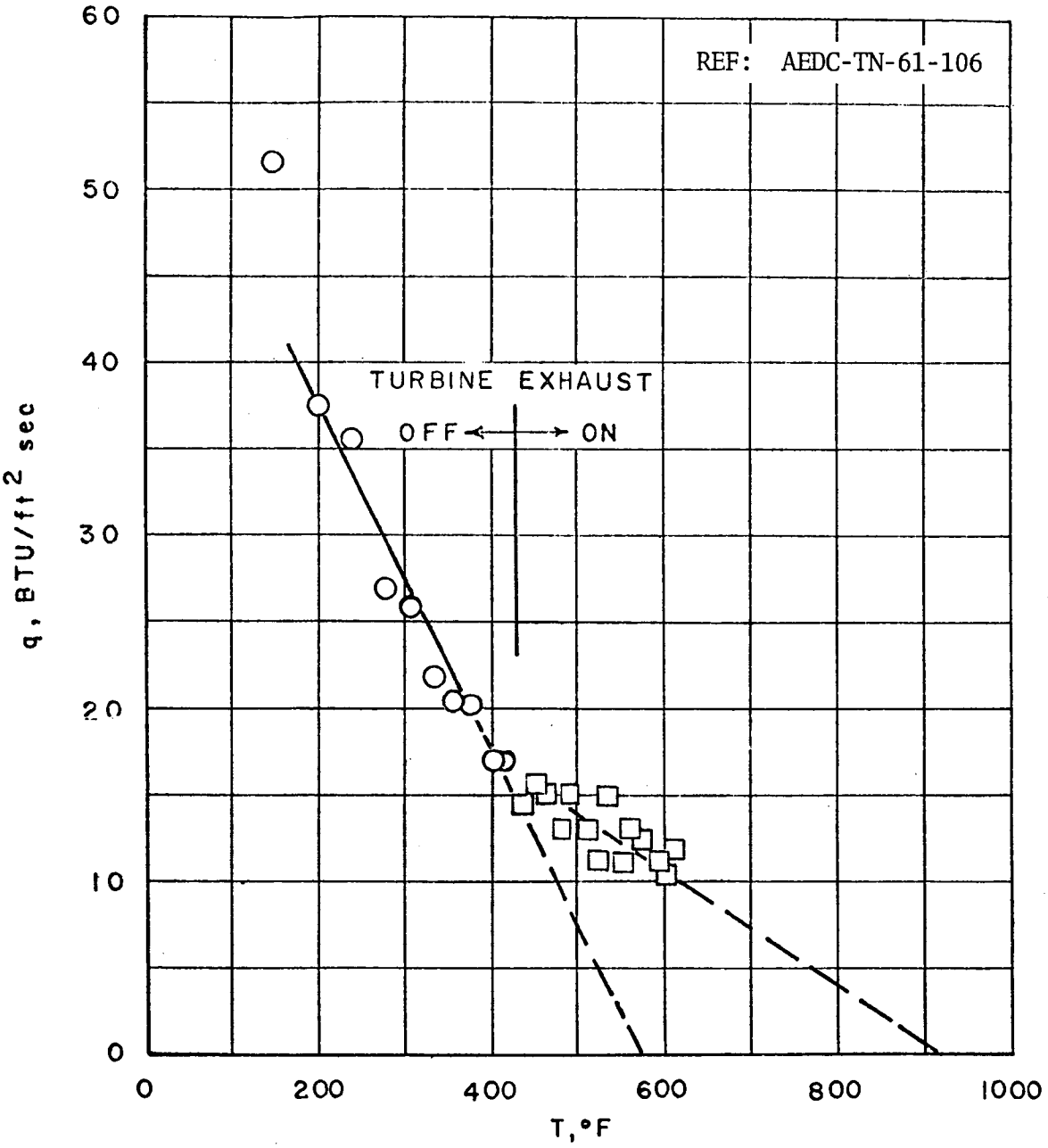

d. $M_\infty = 1.2$, Altitude 29,000 ft

FIGURE 3.4-2. STAR SHIELD HEATING RATES AS A FUNCTION OF CALORIMETER TEMPERATURE FOR CONFIGURATION 1-A (CONTINUED)

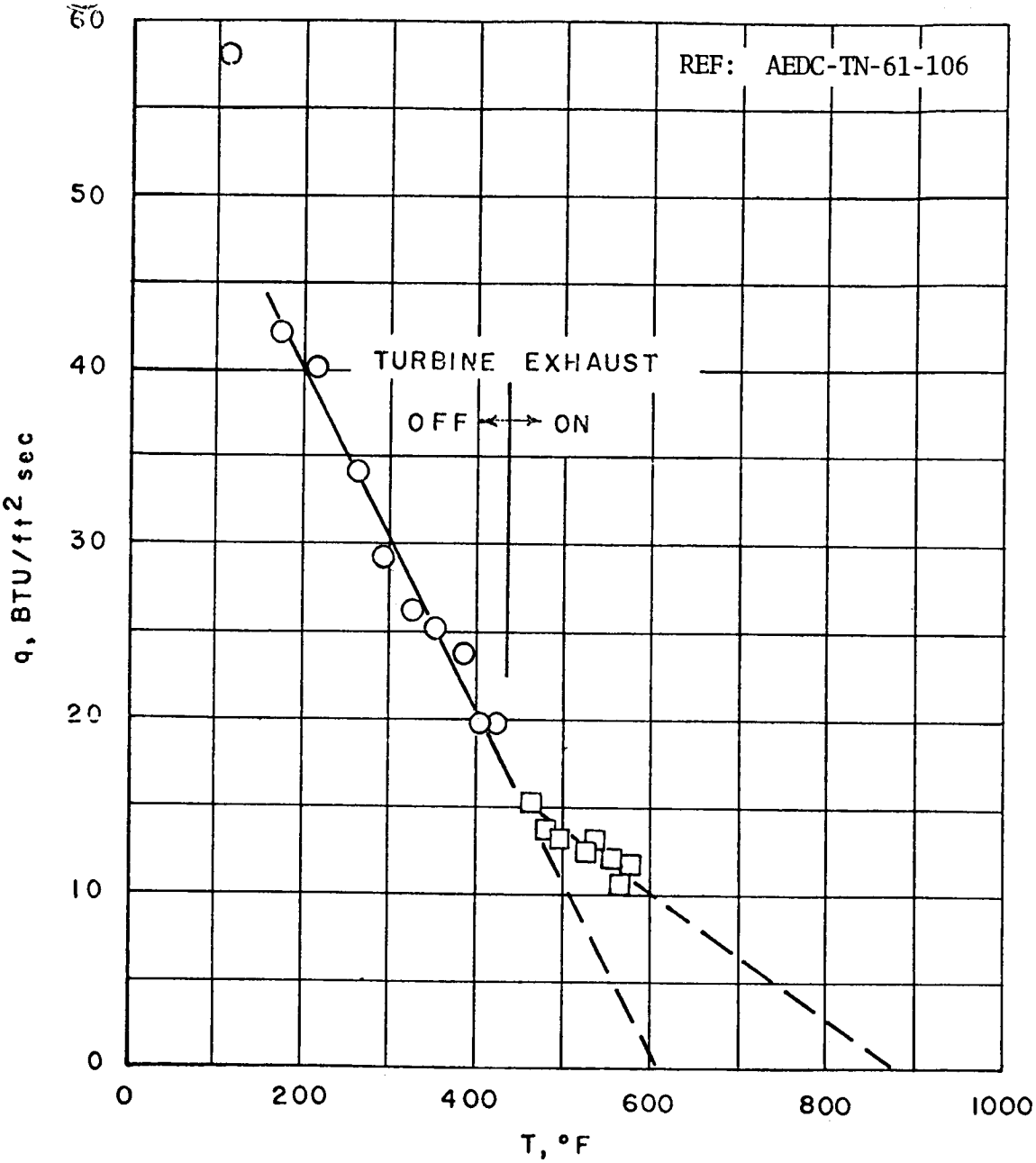

e. $M_\infty = 1.2$, Altitude 35,000 ft

FIGURE 3.4-2. STAR SHIELD HEATING RATES AS A FUNCTION OF CALORIMETER TEMPERATURE FOR CONFIGURATION 1-A (CONTINUED)

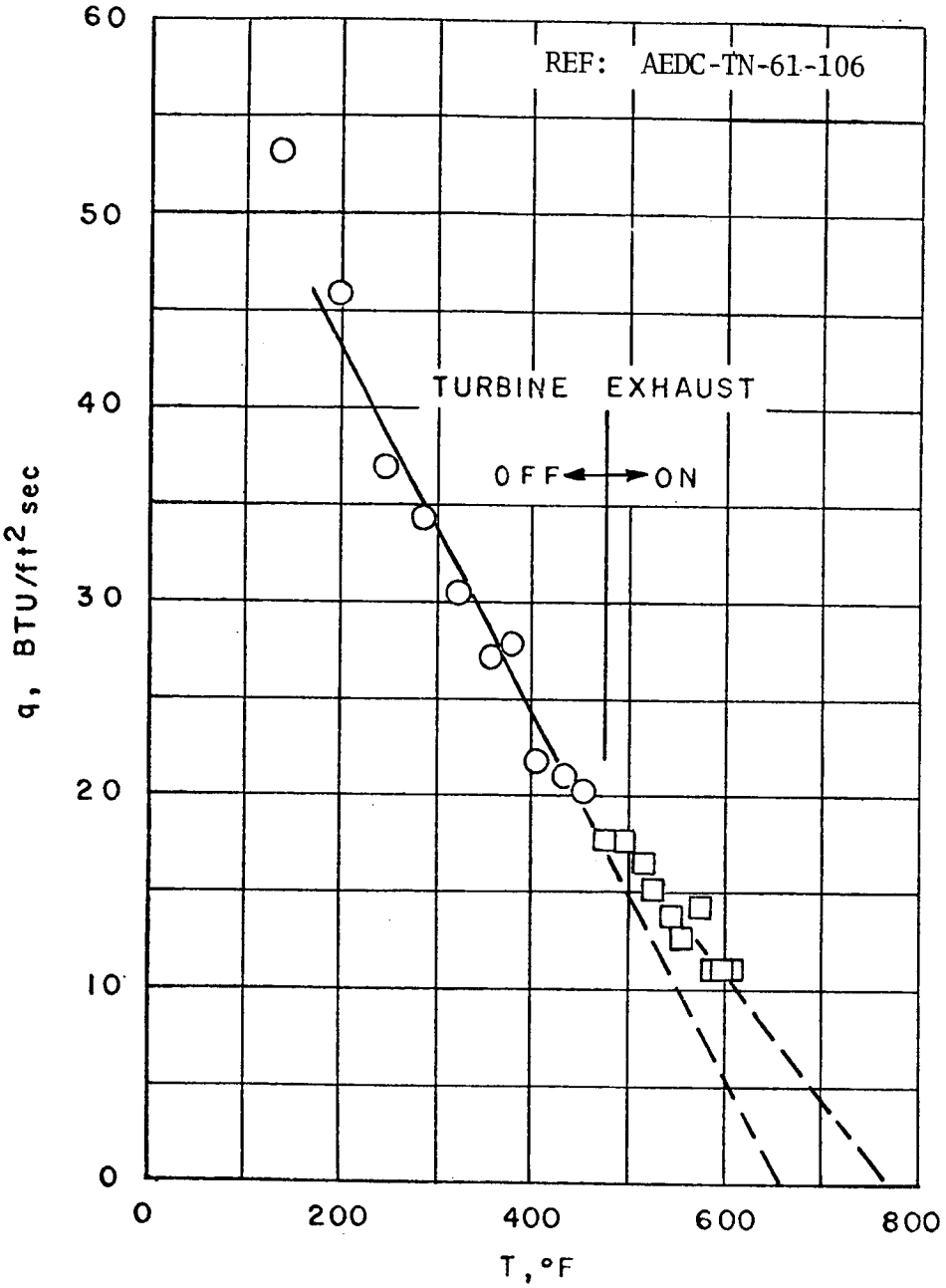

f. $M_\infty = 1.2$, Altitude 42,000 ft

FIGURE 3.4-2. STAR SHIELD HEATING RATES AS A FUNCTION OF CALORIMETER TEMPERATURE FOR CONFIGURATION 1-A (CONTINUED)

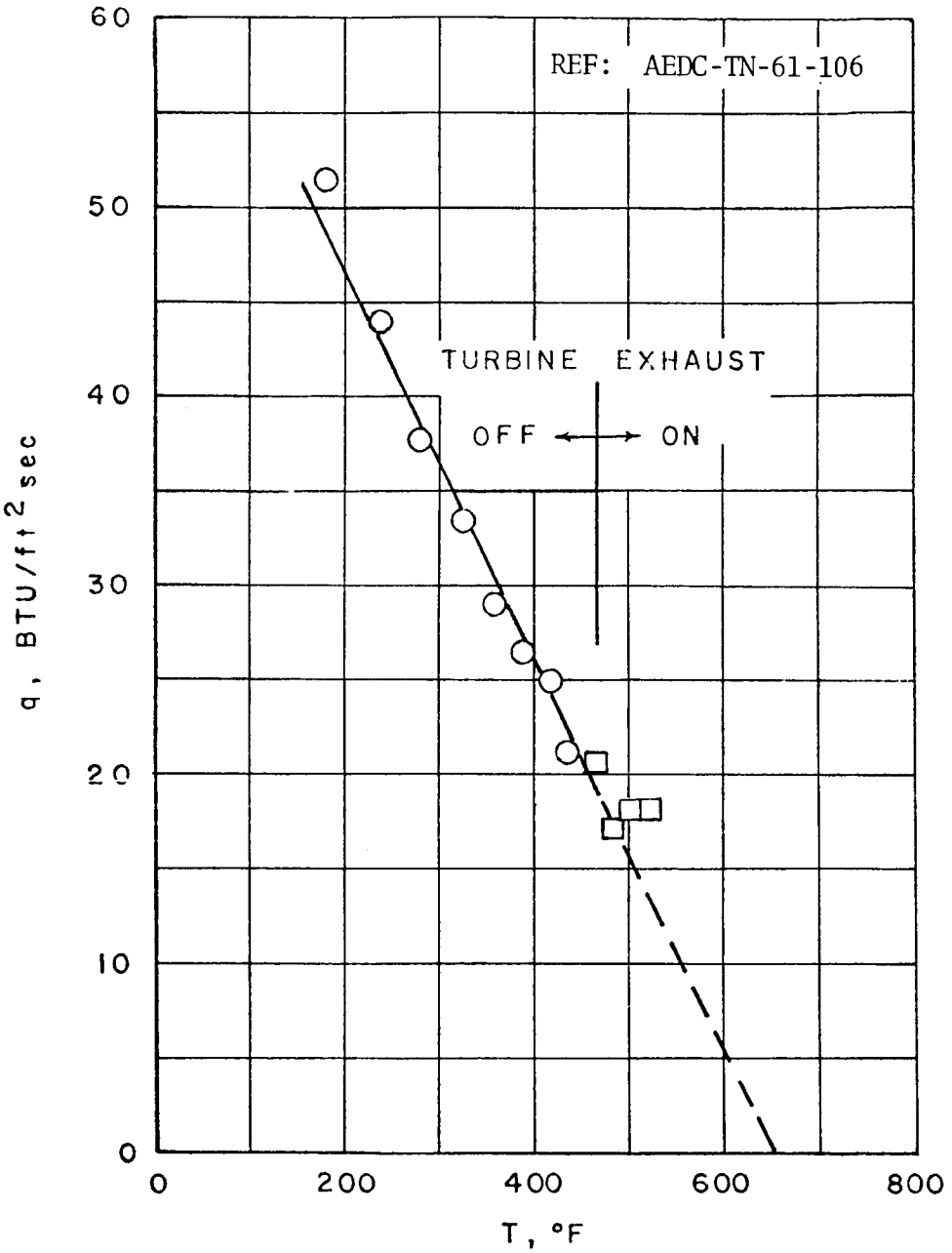

g. M_∞ = 1.4, Altitude 35,000 ft

FIGURE 3.4-2. STAR SHIELD HEATING RATES AS A FUNCTION OF CALORIMETER TEMPERATURE FOR CONFIGURATION 1-A (CONCLUDED)

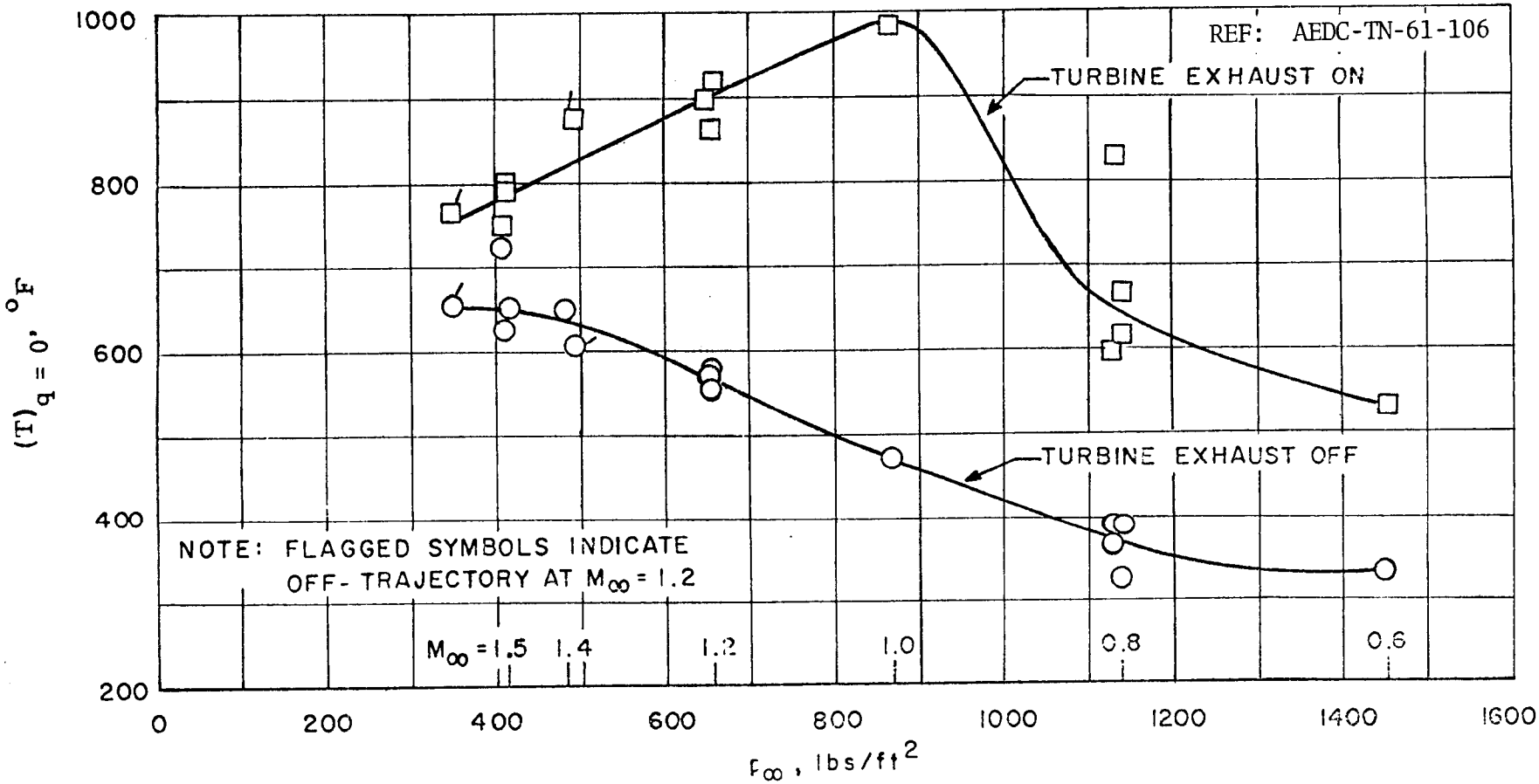

FIGURE 3.4-3. STAR SHIELD EQUILIBRIUM TEMPERATURE

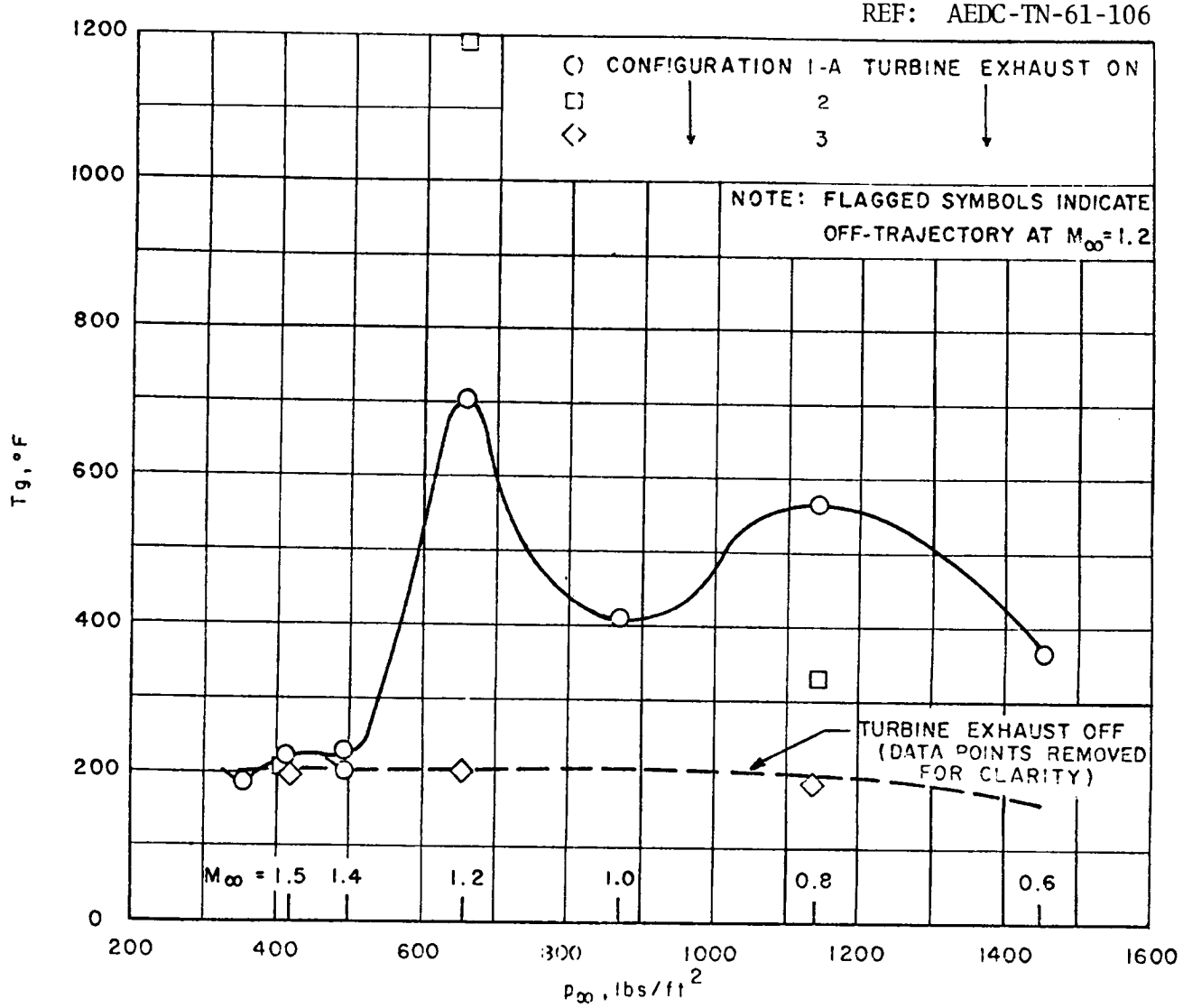

FIGURE 3.4-4. GAS TEMPERATURES CLOSE TO PRIMARY HEAT SHIELD FOR TRAJECTORY CONDITIONS

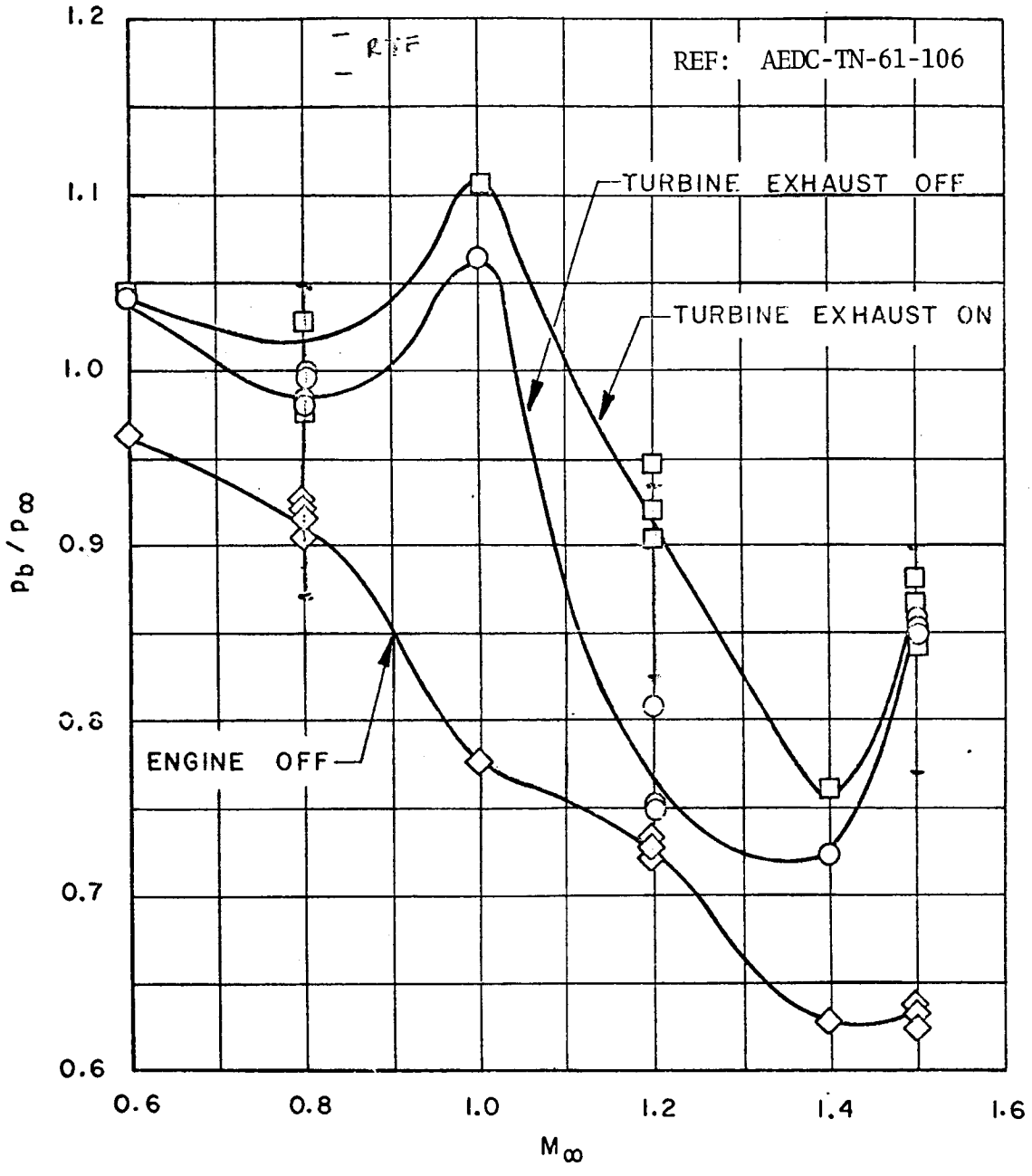

FIGURE 3.4-5. BASE PRESSURE RATIO FOR TRAJECTORY CONDITIONS ON THE PRIMARY HEAT SHIELD

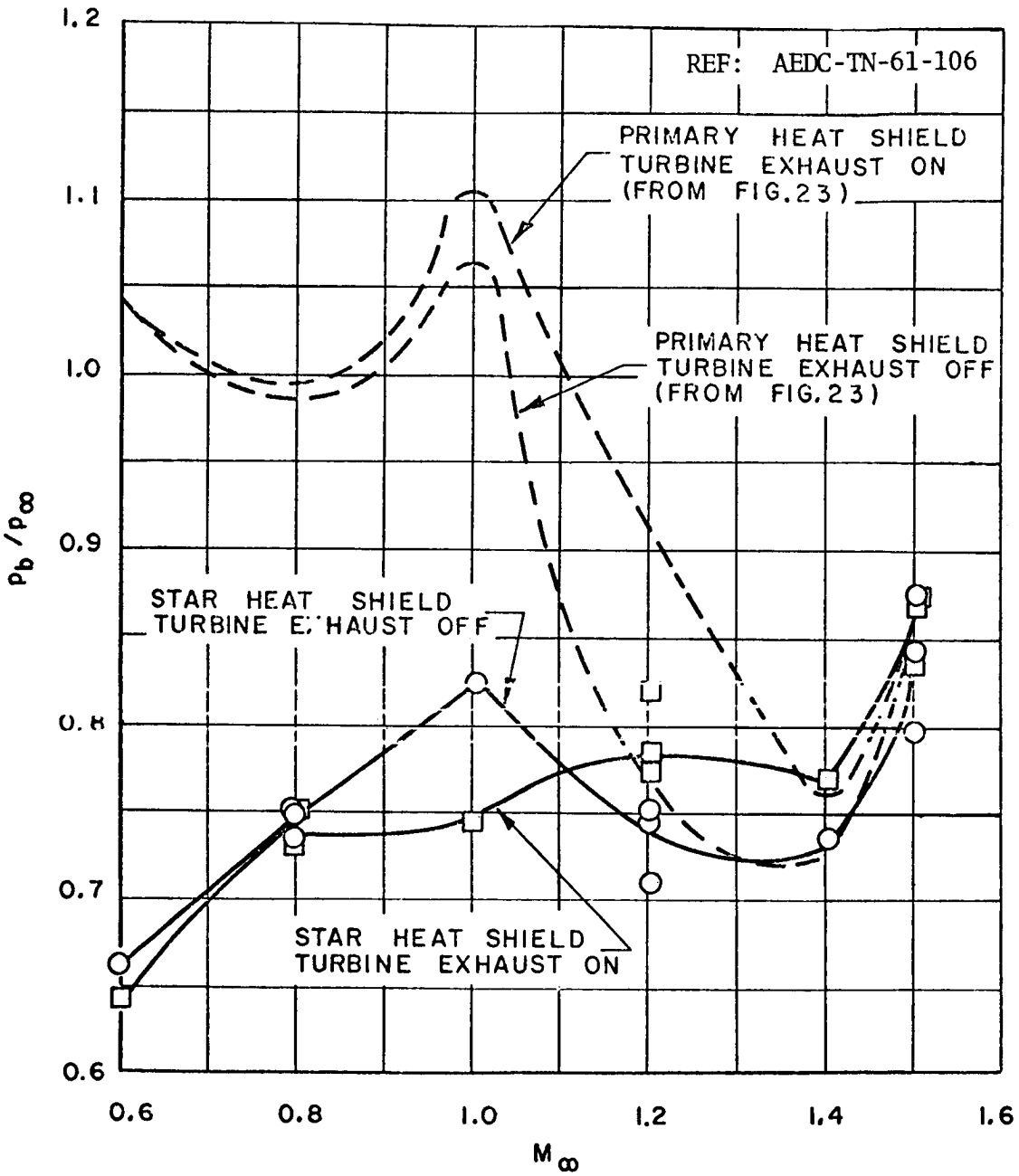

FIGURE 3.4-6. BASE PRESSURE RATIO AT TRAJECTORY CONDITIONS ON THE STAR HEAT SHIELD

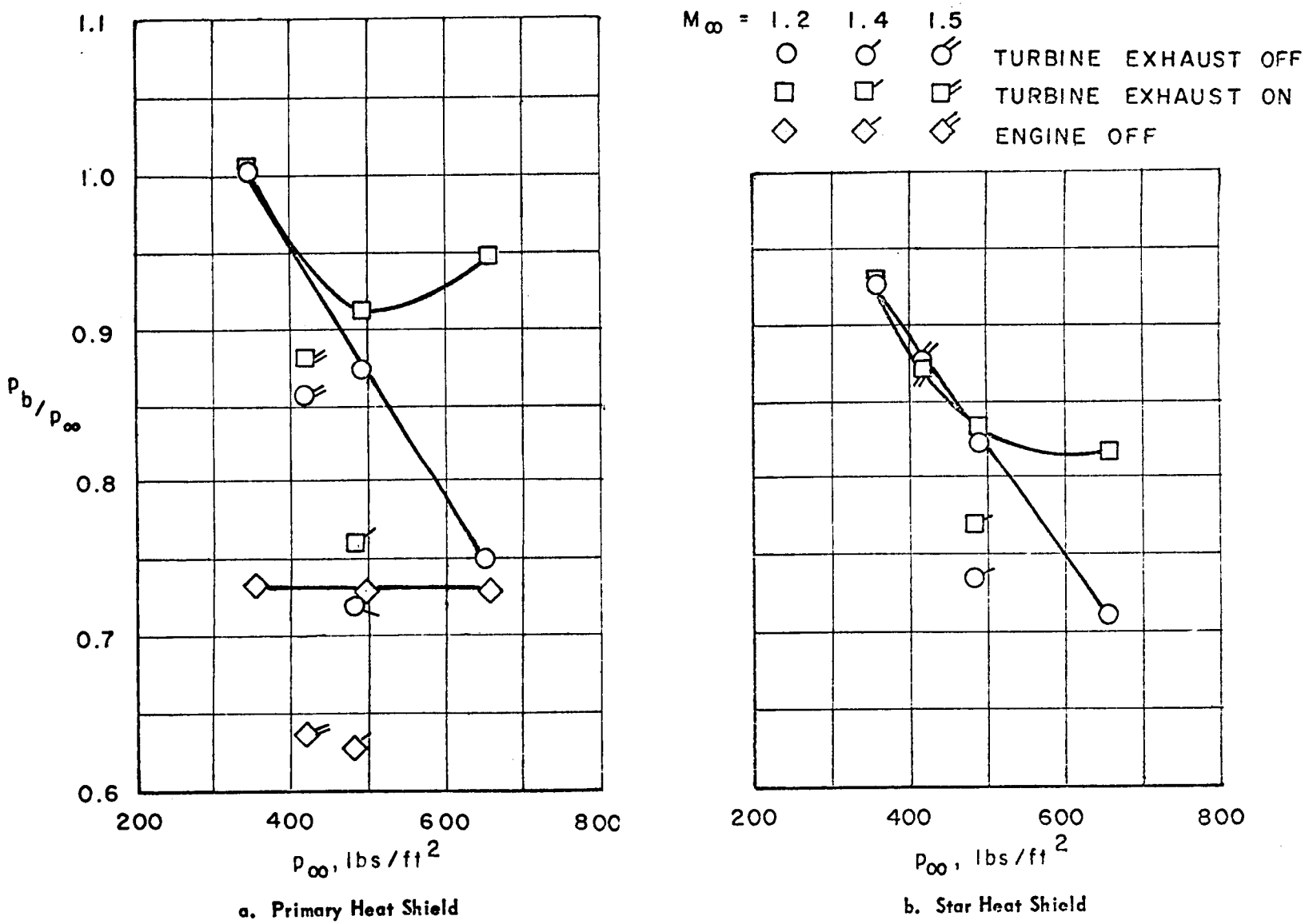

FIGURE 3.4-7. BASE PRESSURE RATIO AS A FUNCTION OF FREE-STREAM STATIC PRESSURE, CONFIGURATION 1-A

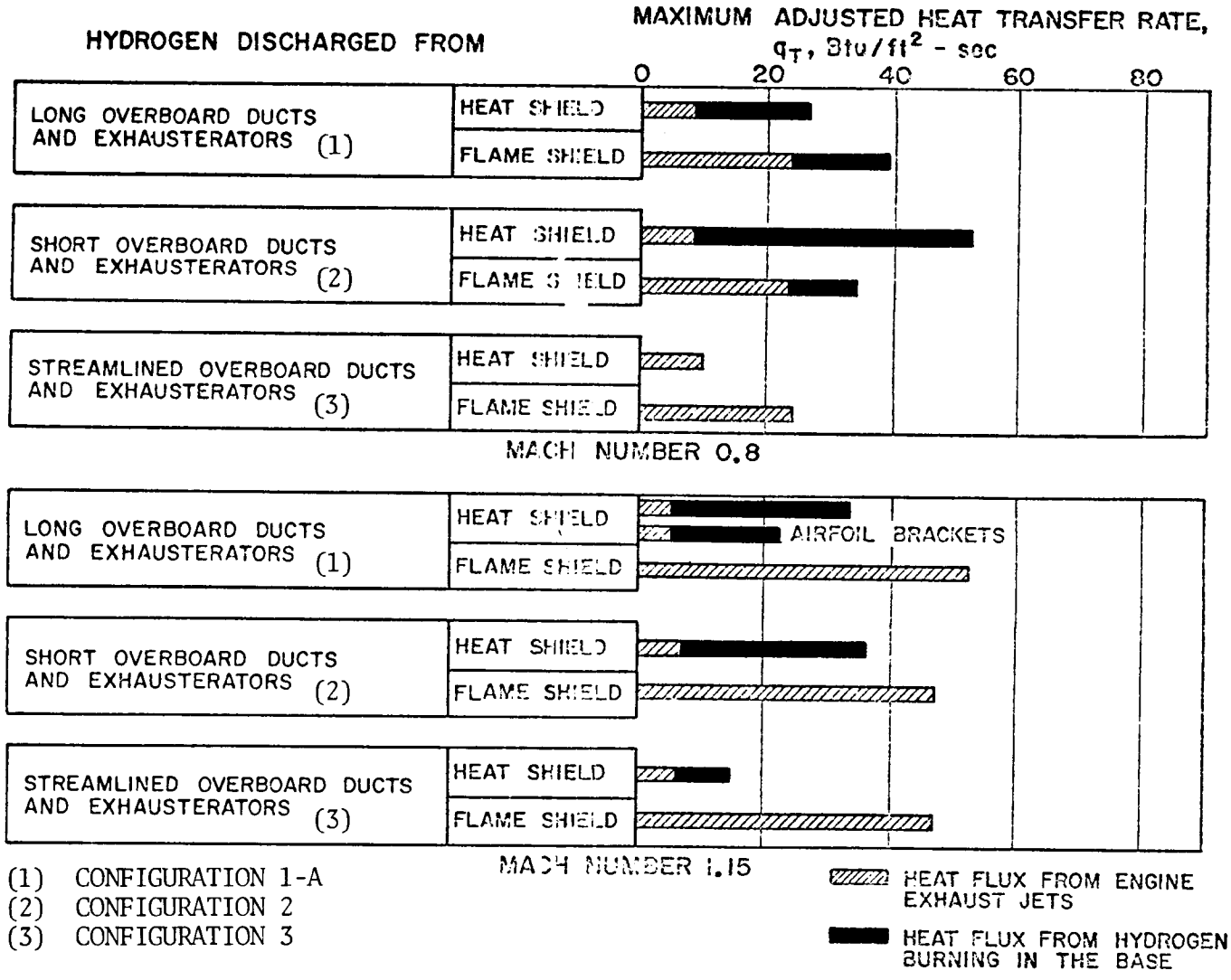

FIGURE 3.4-8. COMPARISON OF MAXIMUM TOTAL HEAT TRANSFER RATES FOR THREE OVERBOARD TURBINE EXHAUST DUCT CONFIGURATIONS AT MACH NUMBERS 0.8 AND 1.15

REF: AEDC-TN-61-134

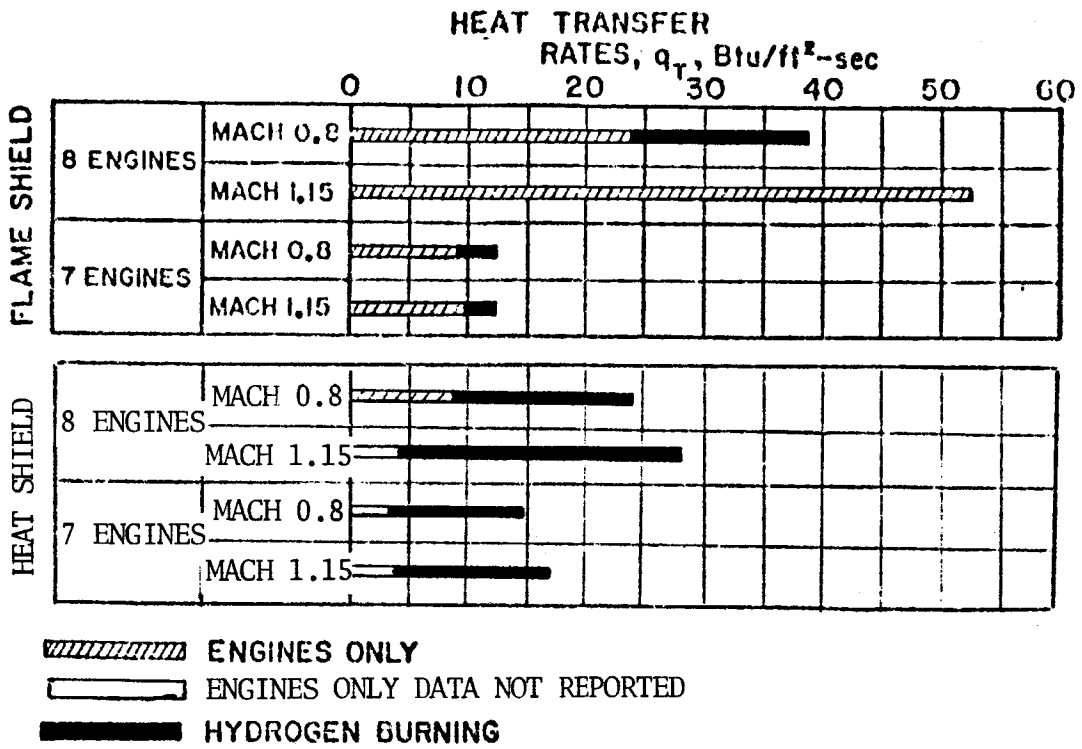

FIGURE 3.4-9. COMPARISON OF AVERAGE TOTAL HEAT TRANSFER RATES FOR SEVEN AND EIGHT ENGINE OPERATION

REF: AEDC-TN-61-134

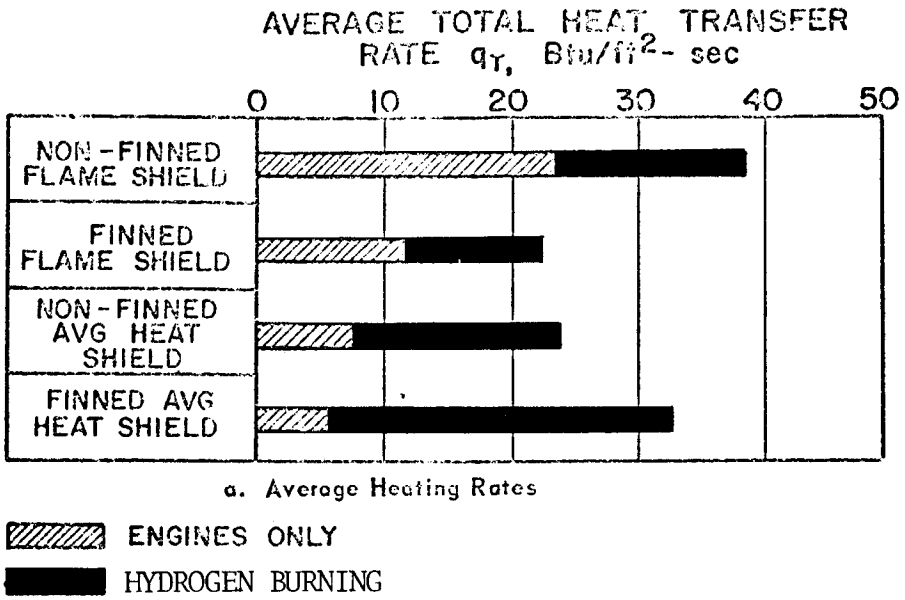

FIGURE 3.4-10. COMPARISON OF TOTAL HEAT TRANSFER RATES WITH AND WITHOUT STABILIZING FINS

REF: AEDC-TDR-62-9

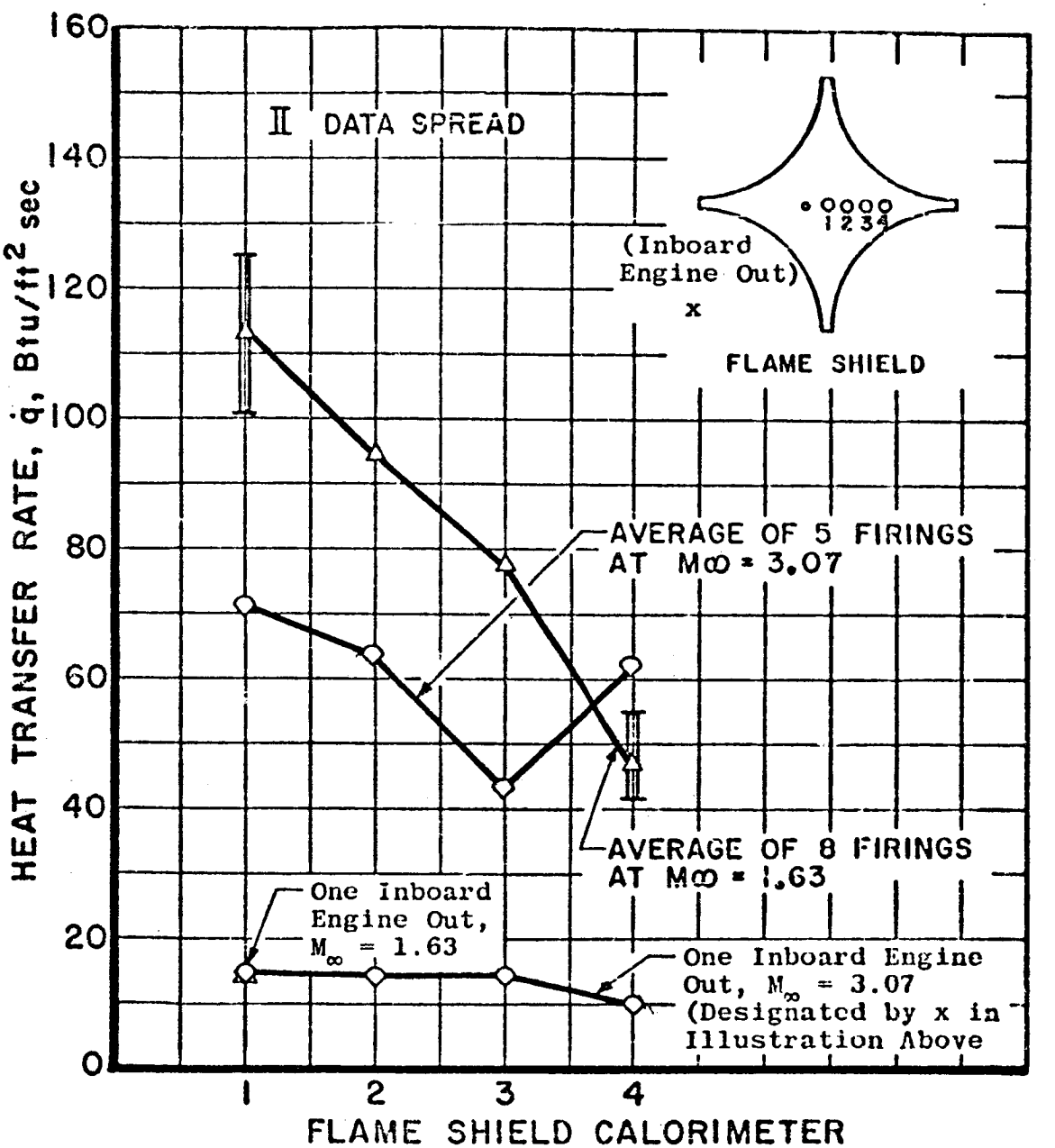

FIGURE 3.4-11. HEAT TRANSFER VARIATIONS WITH FLAME SHIELD CALORIMETER LOCATION

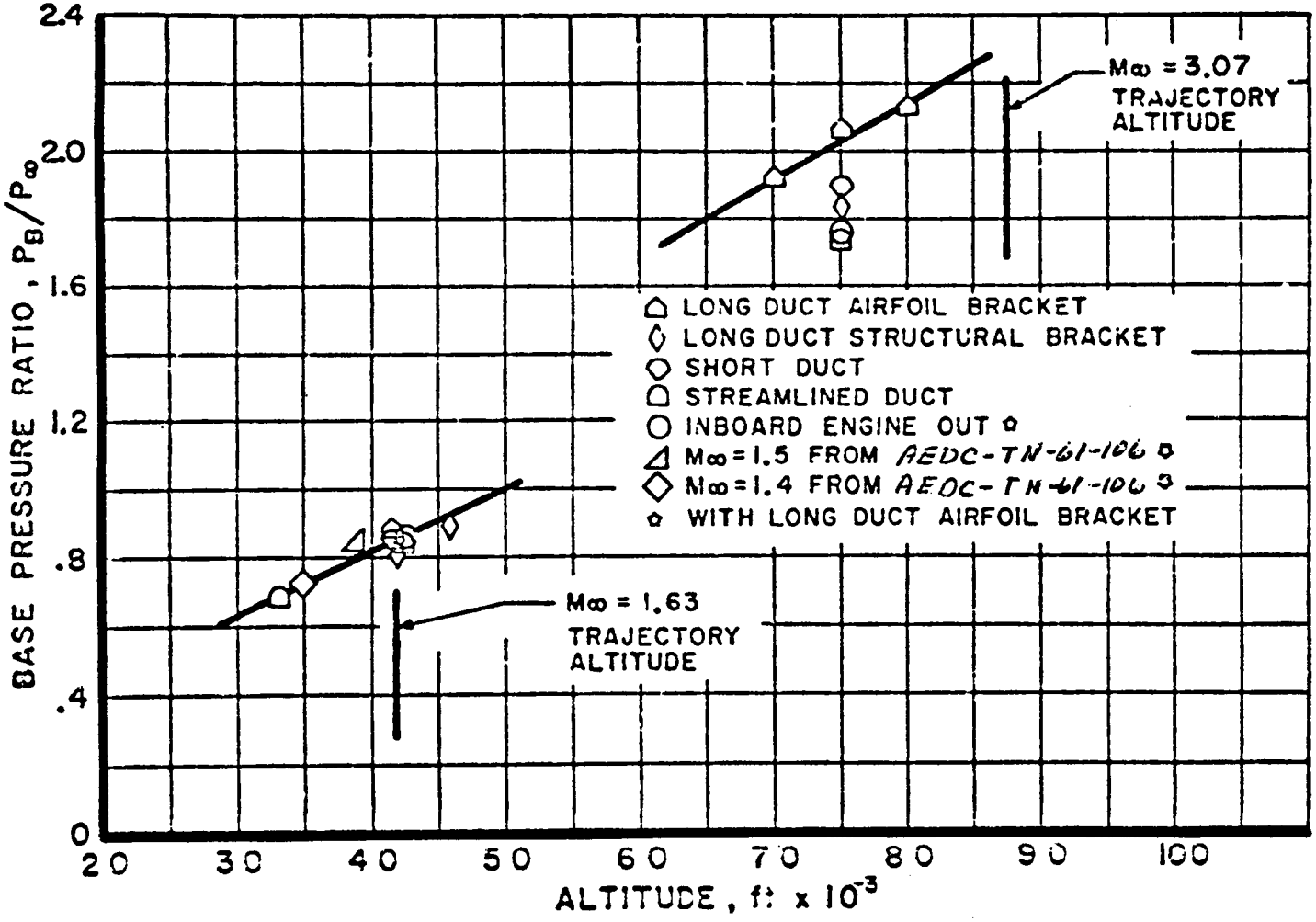

FIGURE 3.4-12. VARIATION OF BASE PRESSURE RATIO WITH ALTITUDE

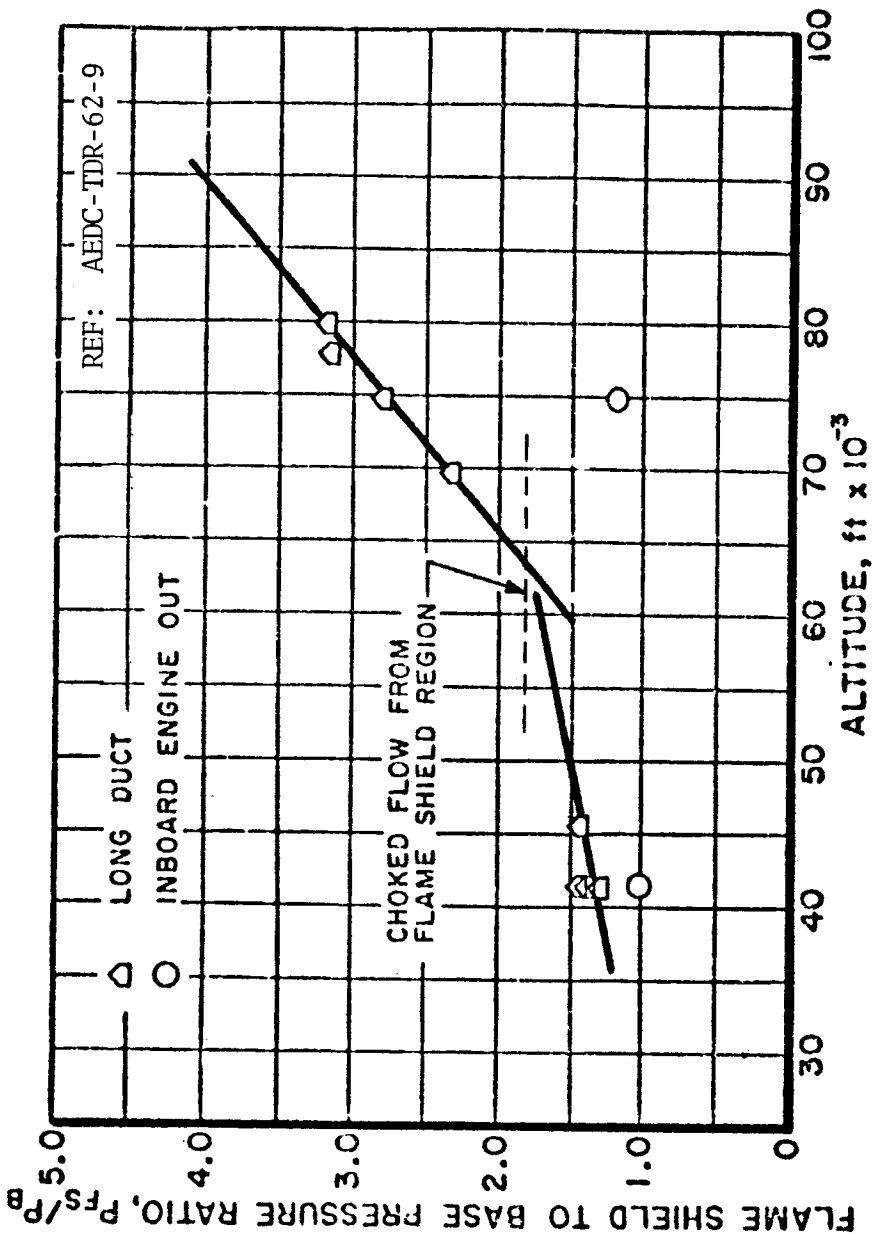

FIGURE 3.4-13. VARIATION OF FLAME SHIELD PRESSURE RATIO WITH ALTITUDE

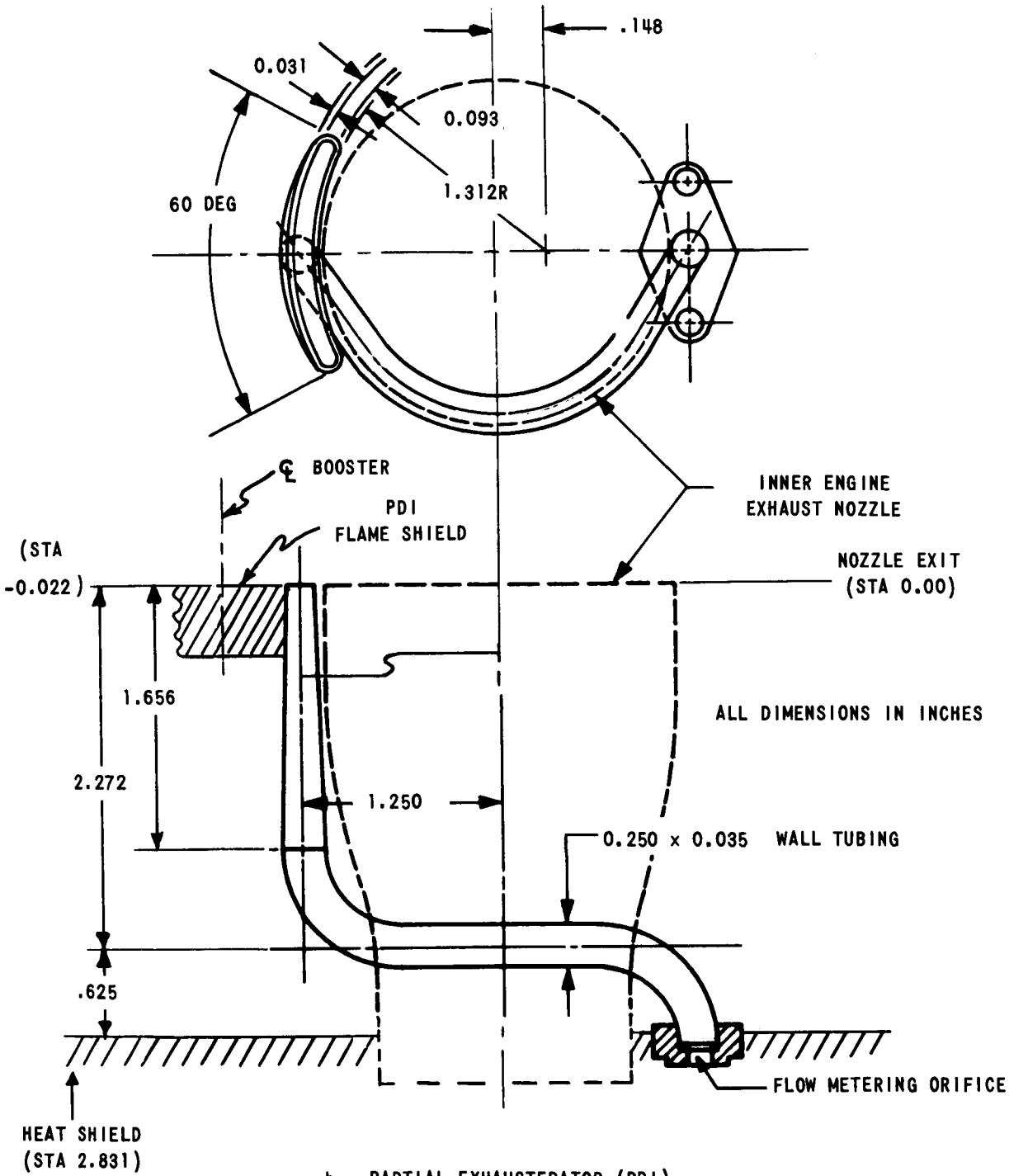

b. PARTIAL EXHAUSTERATOR (PDI)

FIGURE 3.4-14. INNER ENGINE TURBINE EXHAUST DUCT DETAILS, PARTIAL EXHAUSTERATOR (PSI)

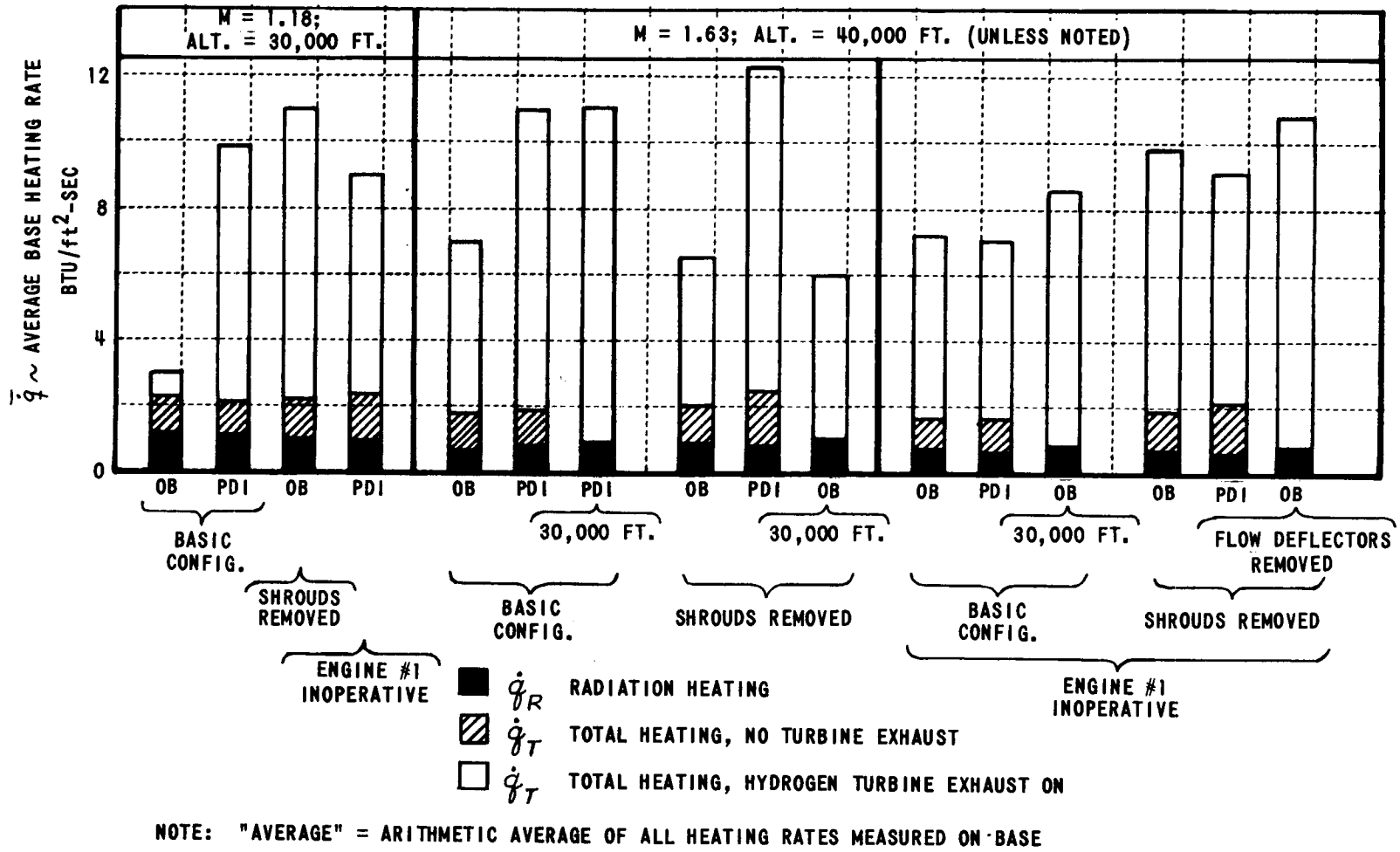

FIGURE 3.4-15. S-IB AVERAGE BASE (HEAT SHIELD) HEATING RATES

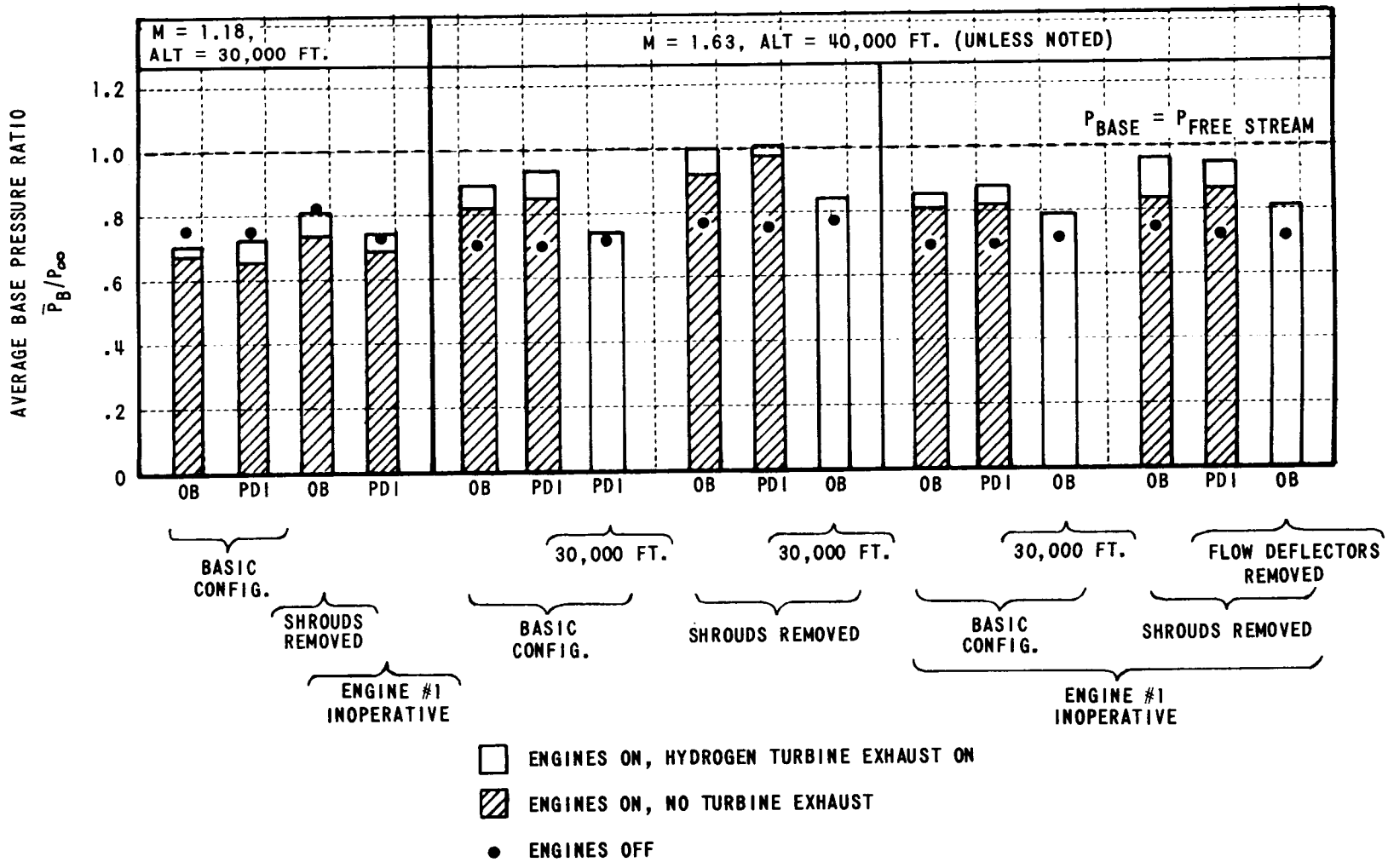

FIGURE 3.4-16. S-IB AVERAGE BASE (HEAT SHIELD) PRESSURE RATIOS

REF: CAL NO. HM-2045-Y-4

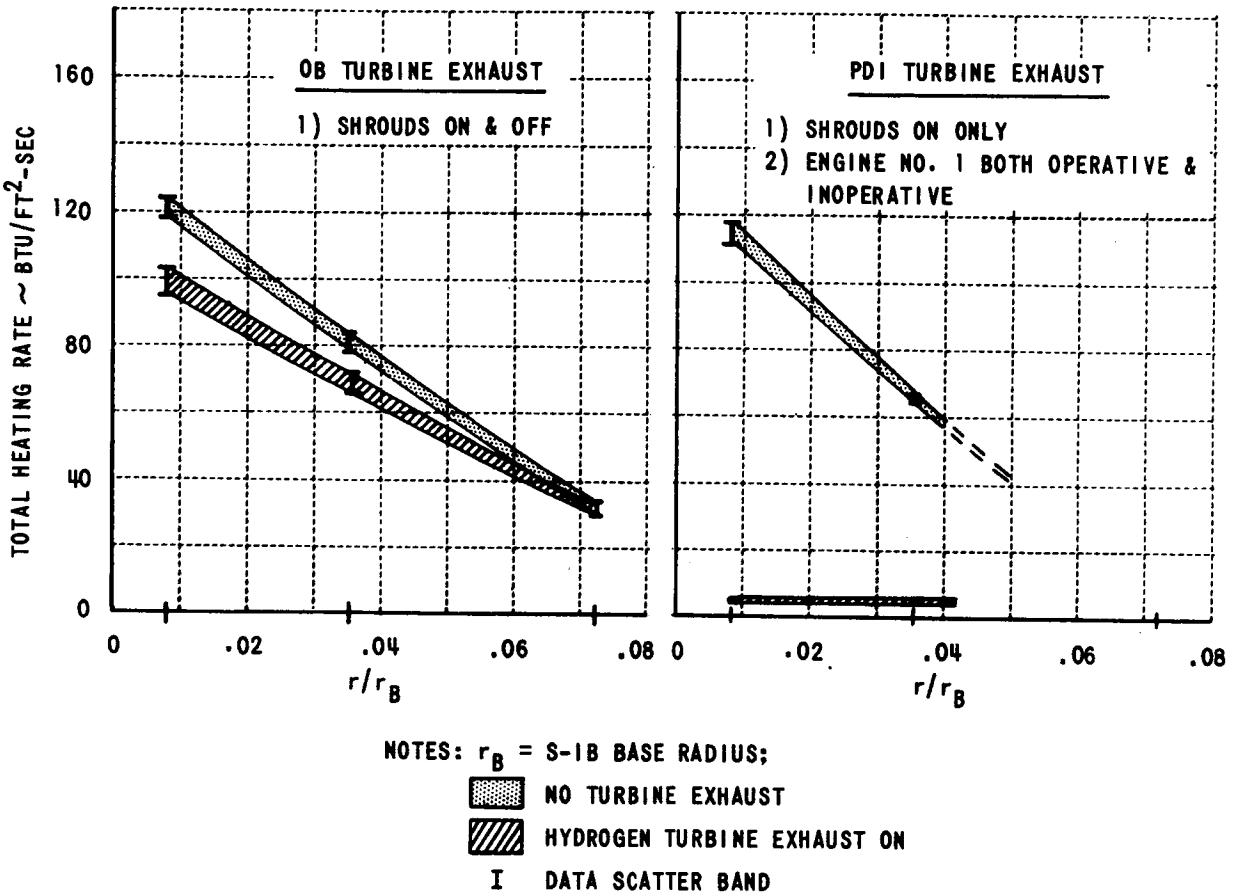

FIGURE 3.4-17. S-IB FLAME SHIELD HEATING RATE DISTRIBUTION AT M = 1.18, ALTITUDE = 30,000 FEET

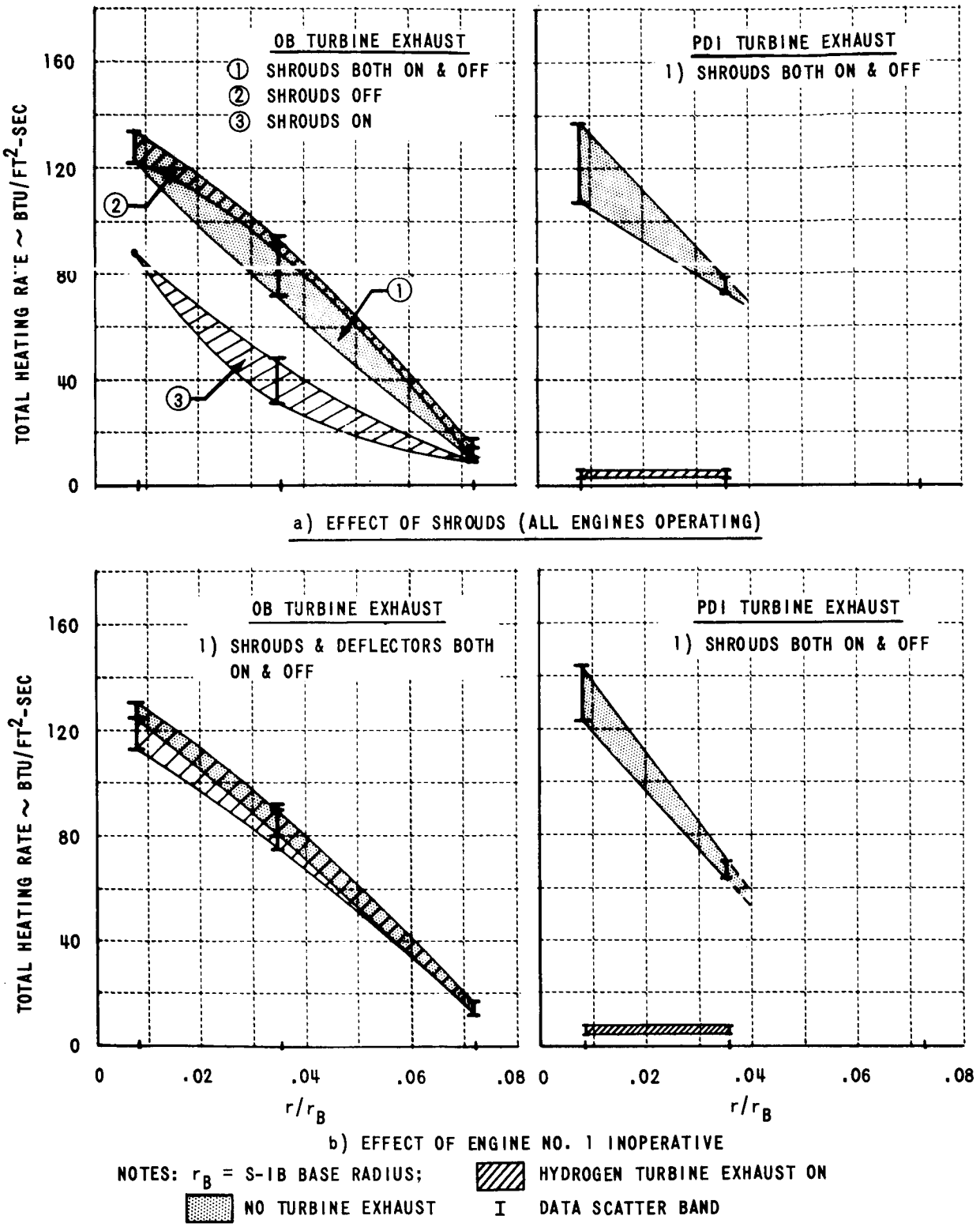

FIGURE 3.4-18. S-IB FLAME SHIELD HEATING RATE DISTRIBUTIONS AT M = 1.63, ALTITUDE = 40,000 FEET

REF: CAL NO. HM-2045-Y-4

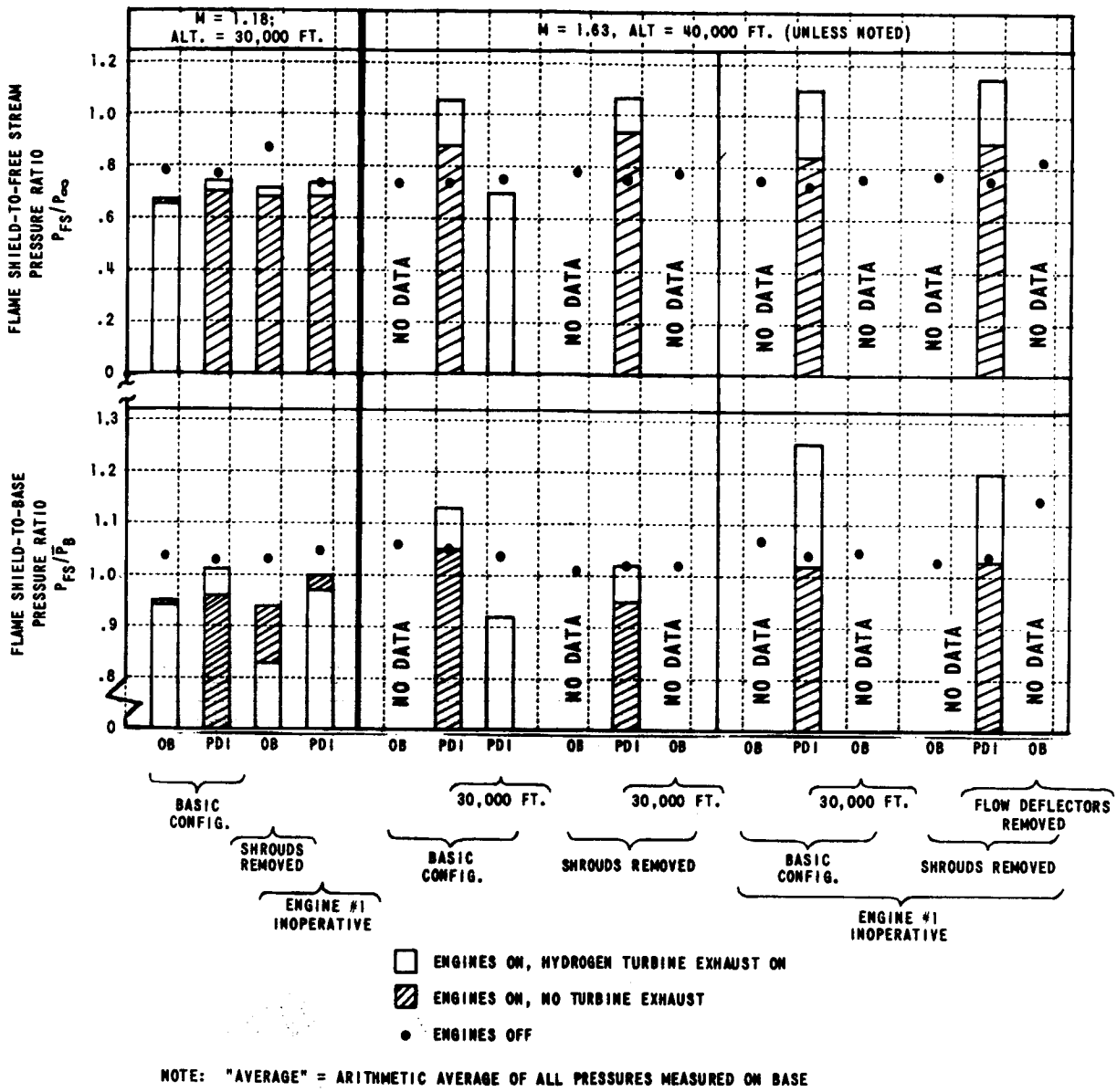

NOTE: "AVERAGE" = ARITHMETIC AVERAGE OF ALL PRESSURES MEASURED ON BASE

FIGURE 3.4-19. S-IB FLAME SHIELD PRESSURE RATIOS

3.5 FLIGHT TESTS AND PARAMETRIC DATA

During the time span between October 27, 1961, and January 22, 1968, a considerable quantity of useful base heating and base pressure data were obtained from the Saturn I and IB vehicles. This time span encompasses the Saturn I, Block I flights, the Saturn I, Block II flights and the first four flights of the Saturn IB. The base region of these fourteen (14) vehicles was heavily instrumented with thermocouples, calorimeters and pressure measurements. The instrumentation plan for SA-205 and subsequent vehicles was considerably reduced.

A summary of the flight data from the S-I Block I and Block II and the S-IB flights is contained in this paragraph and the data were taken from References 3-6, 3-7, 3-8 and 3-9. For a more detailed presentation of these flight data the above referenced summary reports and/or the individual flight evaluation reports should be consulted. Instrumentation used to measure the base environment on the Block I vehicles was not considered representative of the "state-of-the-art" at that time. Simple evolutionary changes were made from flight to flight to improve the situation, however certain inherent losses in the instrumentation and calibration techniques precluded in the Block I data any attainment of a great degree of accuracy in the measurement of the thermal environment. More sophisticated instruments were developed and installed on the Block II and IB vehicles which eliminated some of the sources of error.

Early in the Saturn flight test program it was found that the best correlation of base region data was obtained when plotted versus altitude. For similar configurations and base region locations the environment is influenced most by the exhaust plumes, which are influenced most by pressures, which are dependent on altitude. The figures discussed in the remainder of this subsection contain curves that are representative of measured pressures, heating rates and gas temperatures. These curves were obtained by averaging all data traces recorded under normal operating conditions from a given location or region. The areas of the base region for which data are presented include two regions of the heat shield. These two heat shield regions, shown in Figure 3.5-1, were defined by data as areas of uniform heating.

In presenting the average data traces for the various locations a designation has been made between the basic vehicle configurations. There were generally four distinguishable data bands for a given location. The average of each data band is presented herein and labeled as either: S-I, Block I; S-I, Block II; S-IB, 201/202; or, S-IB, 203/204. The S-IB, 201/202 label refers to data obtained from the SA-201 and SA-202 flight vehicle. Variations in data between SA-201 and SA-202 that could be attributed to engine shroud removal were nil. Hence, the two data groups were combined. Alterations in the base region environment produced by the inboard engine turbine exhaust reports on S-IB-3 and subsequent S-IB stages are shown by the curves labeled S-IB, 203/204. In all instances it should be noted that on an altitude plot, the initial phase of the flight is very distorted. The first kilometer of altitude covers a time span of approximately 25 seconds. Hence many of the data variations that occur during the early stages of launch are not accurately portrayed.

3.5.1 Flame Shield

The most severe environment measured in the base region was on the flame shield. Averages of the data from this region shown in Figure 3.5-2 reflect the nearness of the flame shield to the inboard engine exhaust. The peak or hump that occurs prior to 10 kilometers of altitude is due to the strong flow reversal produced by the intersecting inboard engine exhausts. Above an altitude of 15 kilometers the data are nearly steady and "choked" conditions exist in the flame shield region. Note that for SA-203 and -204 the reversal and "choked" condition occurred at lower altitudes and the environment was less severe. Both conditions are directly attributable to the turbine exhaust dump, at approximately 750°K, into the flame shield region. Since flame shield radiation calorimeters were not flown on the S-I, Block I configuration nor on the SA-201/202 vehicles, their relatively low total heat flux data cannot be explained.

Average flame shield pressure data are represented in Figure 3.5-3 as the difference in flame shield pressure and ambient pressure. The data comparison in Figure 3.5-3 supports the thermal data by showing that flow reversal and "choked" flow condition in the flame shield region occurred at a lower altitude on SA-203 and -204 than on the previous flight vehicles. Data also show that under "choked" conditions the flame shield pressures were approximately 50 percent higher for the SA-203/204 configuration.

3.5.2 Heat Shield

Average heat shield thermal data for the four basic configurations are compared in Figures 3.5-4 and 3.5-5 for the inner and outer regions, respectively. With the heat shield located approximately 54 inches forward of the nozzle exit plane the thermal environment is less severe than on the flame shield. Additionally the spacing of the nozzles around the heat shield is effectively farther apart than for the flame shield. Therefore, reversal of the exhaust gases onto the heat shield does not begin until an altitude of approximately 10 kilometers. The effects of this reversal was shown by data to be more pronounced in the outer region of the heat shield. Also, incident radiation in the outer region was more significant at all altitudes. The reasoning here is that a significant portion of the view from the inner region is of the relatively cool engine nozzles.

For the inner region there were no radiation calorimeters flown on SA-201 or SA-202. Hence, there was one less curve to add to the already wide range of average inner region heat flux data. The only agreement between the average data for the four configurations was with the general trend of the data.

In the outer region the data spread was a little tighter and the trends were repeated on practically all configurations. The average S-IB total heat flux data for the 201/202 configuration and the 203/204 configuration were very close to being the same. Hence the average S-IB total heat flux data are presented as one curve.

3.5.2 (Continued)

Heat shield pressure data for the S-I, Block II and S-IB vehicles are presented in Figure 3.5-6. For pressures, there was no distinction made between the inner and outer region. Also, the spread of pressure data for the S-IB configurations was small. Hence, only one S-IB heat shield average data trace is presented. The larger pressure difference for the flame shield area (Figure 3.5-3) than for the heat shield reflects the effects of nozzle spacing and extension length. At the low altitudes the closer spacing of the nozzles allows the exhaust to create a lower pressure in the star region. In the heat shield area the aspirating effect is reduced by the greater distance between nozzle exhausts and the distance aft of the heat shield where the pumping action occurs. Following flow reversal, there is sufficient area in the heat shield to vent the reversed gases from the area. However, in the flame shield area the gases are trapped because of the small spacing between nozzles.

3.5.3 Fin Trailing Edge

A direct comparison of the S-I, Block II and S-IB fin trailing edge thermal environment cannot be made without a brief explanation. The trailing edge of the S-I, Block II and S-IB fins are depicted in Figure 3.5-7. The trailing edge of the Block II fins were perpendicular to the vehicle axis and joined the tail barrel approximately 17 inches forward of the heat shield. For the S-IB, the fin trailing edge is swept aft at a 25-degree angle and joins the tail barrel approximately 60 inches forward of the heat shield. Due to the change in configuration, the form factors from the S-IB fin trailing edge near the tail barrel to the exhaust plumes is lower than it was on the S-I, Block II. This is shown in Figure 3.5-8 by the S-IB/Block II fin trailing edge form factor ratios at location R_1. For locations away from the tail barrel (locations R_2 and R_3), the blockage afforded by the tail barrel decreases and the S-IB fin trailing edge form factors exceed those computed for comparable radial locations on the Block II fins. These form factors as well as the data presented in Figure 3.5-9 are for fins located between outboard engines. For these fins the influence of the Block II and SA-201 engine shrouds on thermal environment was negligible.

On the Block II vehicles the fin trailing edge gas temperature probe and the total calorimeter were mounted relatively close to the tail barrel at approximately the position designated as R_1 in Figure 3.5-7. Radiation calorimeters were mounted at both R_1 and R_3 and their data traces on each of the Block II flights were very similar. Hence, for presentation herein (Figure 3.5-9), there is no distinction made between inboard and outboard position for the Block II data. For the SA-201 and -202 vehicles there were instruments of all three kinds at both the inboard (R_1) position and the outboard (R_3) position. Furthermore, data traces from these two fin trailing edge positions were very distinct for all three sets of data. There is no apparent S-IB/Block II form factor correlation with measured data. However, there is a very definite form factor correlation with S-IB data at inboard and outboard positions.

3.5.4 Engines

Fifteen slope-type total calorimeters were flown on the bell and aspirator surface of the engines on the last two Block II vehicles. These instruments were exposed to the external, base region, environment through cut-outs in the asbestos insulation which covered the exterior of the engine nozzles. Unfortunately, either due to unfavorable installations and/or instrument malfunctions, a complete and accurate evaluation of the Block II engine thermal environments could not be made.

On SA-201 through -204, eighteen engine measurements were flown, seventeen membrane type total calorimeters and one gas temperature thermocouple. Data from these measurements were of better quality than received from the Block II flights. Average total heat flux data traces shown in Figure 3.5-10 were recorded near the exit plane on the outboard facing side of the inboard engine nozzle. The original thinking was that the inboard engine turbine exhaust reroute would have little or no effect on the thermal environment at this location. However, data for the 203/204 configuration are noticeably higher during the middle altitude range. Average total heat flux data for the aspirator neck, which is labeled in Figure 3.1-9, are presented in Figure 3.5-11. These data were notably higher than the inboard engine data at the low altitudes. This correlation is in agreement with radiation form factors at the two locations.

The most severe thermal environment on the engines occurs near the exit on the inboard facing side of the outboard engine. Total heat flux data measured at this location were very erratic, but indications were that heating at this location is more severe than at any other instrumented location in the S-IB base region. Near sea level, data ranged between 45 and 74 watts/cm^2. Following the typical dip in heating at around 10 kilometers of altitude (with data between 28 and 36 watts/cm^2) the data increased to heating levels of between 55 and 72 watts/cm^2 at altitudes above 45 kilometers. Gas temperatures at this location, which were measured on SA-204, were generally 100 to 300°K above the average S-IB, 203/204 heat shield data. Above 25 kilometers of altitude these gas temperature data were steady at 1250°K.

3.5.5 Inboard Engine Out Effects

Data from two Saturn I flights have shown that the thermal effects of a premature shutdown of an inboard engine are most pronounced in the flame shield area. Effects in other areas of the base were within the bounds established by data from other flights. For the heat shield area adjacent to the inoperative engine there was a slight reduction in heating. This was attributed to a reduction in radiation form factor for this area.

On the second S-I, Block II flight (SA-6) one of the inboard engines shut down after approximately 117 seconds of a scheduled 140 second burn. On S-I, Block I flight (SA-4) a scheduled premature inboard engine shutdown occurred at 100 seconds of a 113 second normal burn. Flame shield flight data for the last 50 to 60 seconds of the SA-6 flight are shown in Figure 3.5-12. The dashed vertical line indicates the approximate time of Engine No. 8 cutoff (E8CO).

3.5.5 (Continued)

Since heating rates on SA-6 were recorded by slug-type calorimeters the heat flux data response at 117 seconds was not instantaneous. However, the data did show a definite increase in total heating rate and a decrease in radiant heating rate. Gas temperature and pressure data both dropped sharply at 117 seconds. These changes in environment on SA-6 were caused by the premature shutdown of an inboard engine. Similar trends were observed on SA-4 when an engine shut down early.

3.5.6 Infrared Spectra

The infrared radiant spectra of the S-IB rocket engine exhaust plumes were measured on the SA-203 vehicle. An analysis and evaluation of these flight spectra data was documented in Reference 3-10. Basically the data showed that the infrared spectrum from the plumes was a continuum and that its intensity level decreased with altitude. Below an altitude of thirty-thousand feet, there was evidence of strong H_2O, CO_2, and CH molecule absorption. These absorption bands are shown by the spectral data shown in Figure 3.5-13. The black body curves at 5000°R through 2500°R are shown in this figure for intensity level reference.

The following conclusions, originally reported in Reference 3-10 were reached after careful evaluation of all the SA-203 spectral data:

1. The fact that the radiation levels early in flight were of the same order or perhaps slightly greater than for a black body at the temperature of the rocket engine exhaust (about 4200°R) implied that the plume emissivity in the longer wavelength region was approximately unity. Temperatures in the plume that are slightly greater than the engine exhaust value do exist due to the phenomenon of afterburning at low altitudes.

2. The presence of a large amount of carbon indicated by the near-continuum radiation in the plumes was expected because the Saturn IB H-1 engines burn a mixture of RP-1 (similar to kerosene) and liquid oxygen, which can produce large amounts of soot. Turbine exhaust gases dumped at the nozzle exit also contribute to the high carbon concentration.

3. The absorption by H_2O and CO_2 were caused by relatively cool gases in the base region along the line of sight of the spectrometer.

4. The presence of CH absorption was probably caused by raw fuel injected into the base region by the engine turbine exhaust.

5. The decrease in the intensity level at elevated altitudes was caused by plume expansion to the lower pressures and cessation of afterburning due to lack of oxygen in the ambient atmosphere.

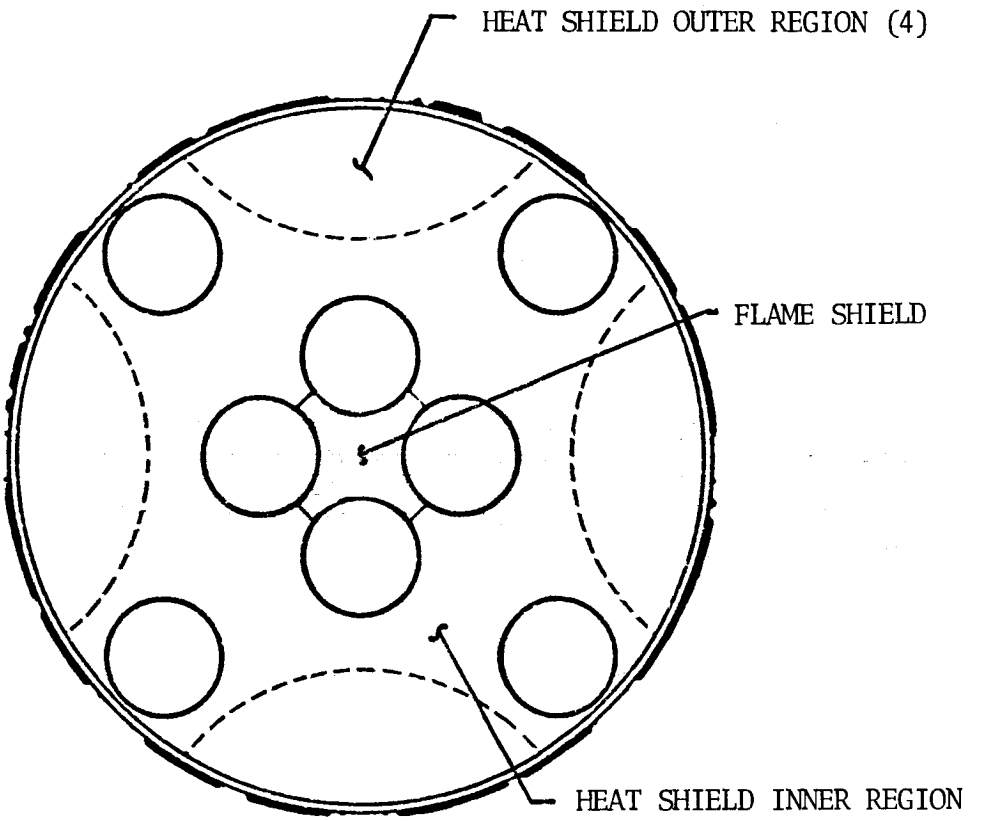

FIGURE 3.5-1. AREAS OF UNIFORM HEATING ON S-I AND S-IB STAGE BASE HEAT SHIELD

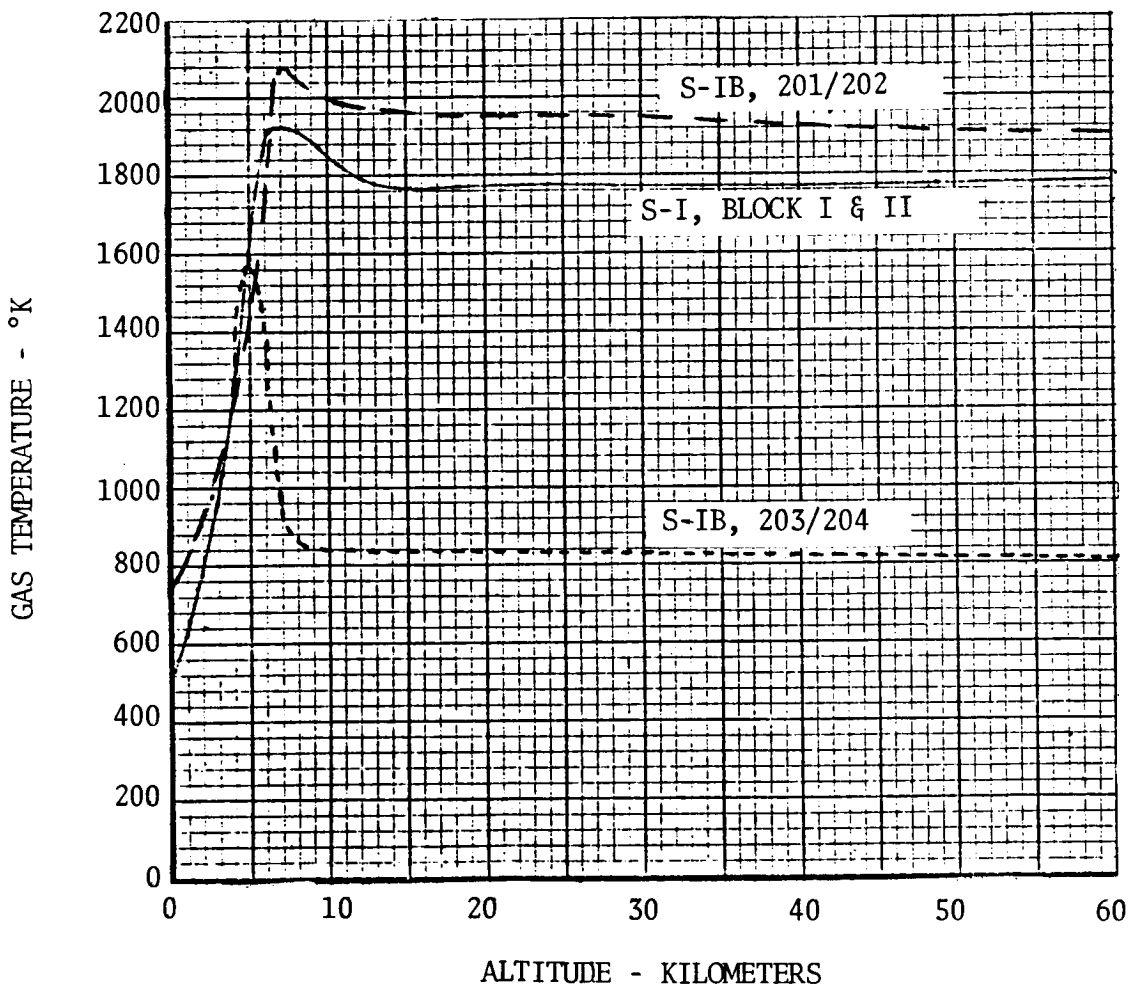

FIGURE 3.5-2. AVERAGE OF S-I AND S-IB FLAME SHIELD THERMAL DATA (CONTINUED)

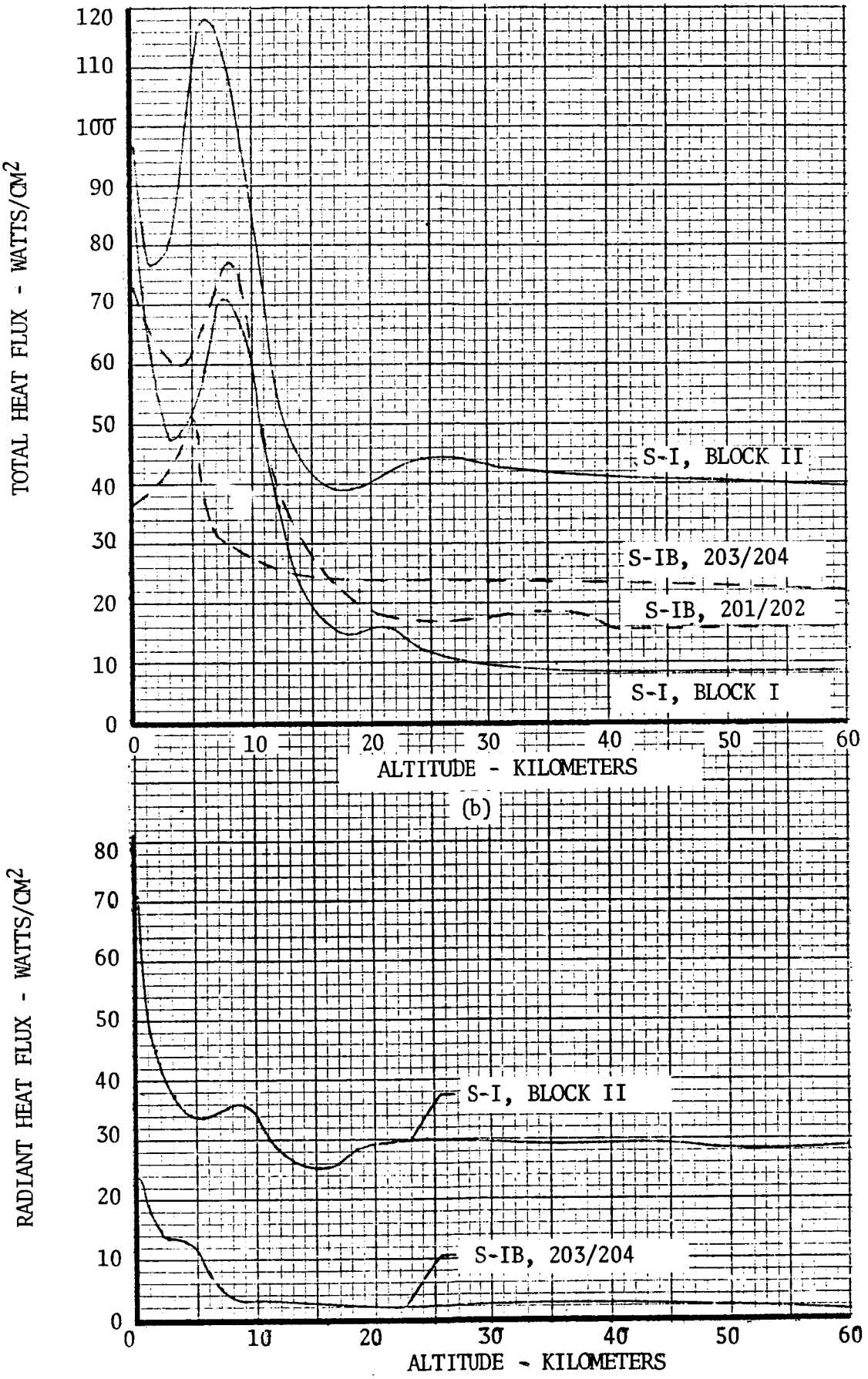

FIGURE 3.5-2. AVERAGE OF S-I AND S-IB FLAME SHIELD THERMAL DATA (CONCLUDED)

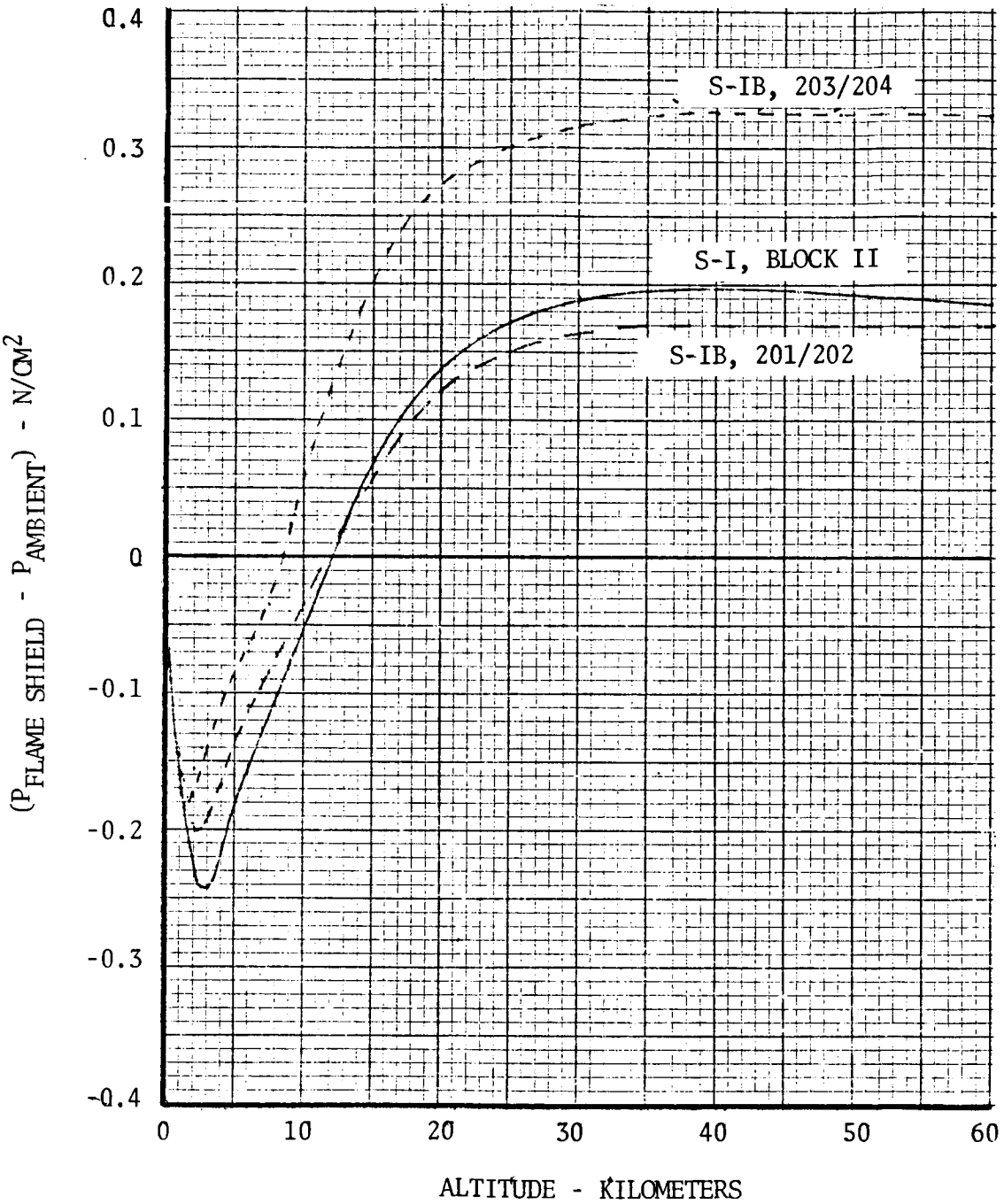

FIGURE 3.5-3. AVERAGE S-I AND S-IB FLAME SHIELD PRESSURES

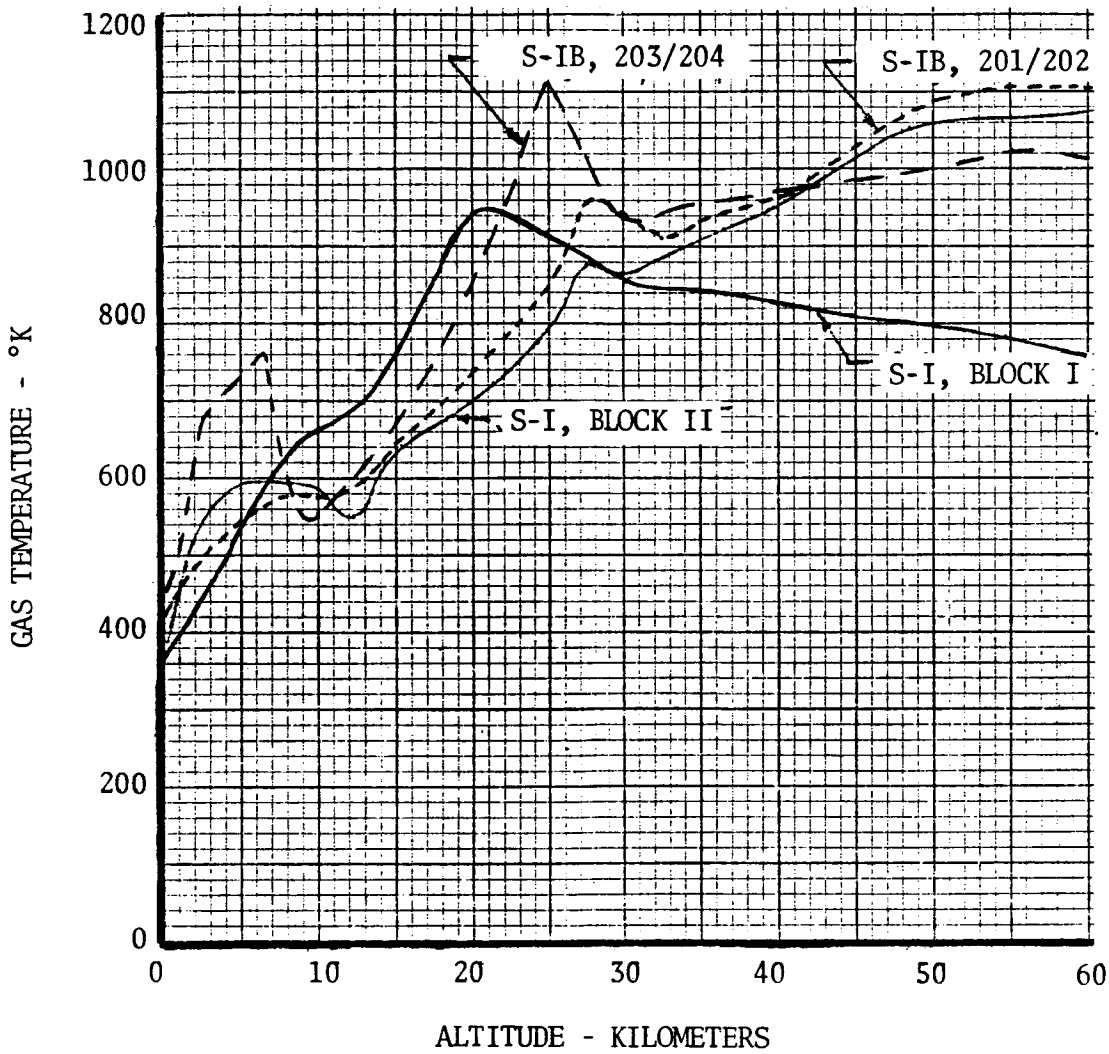

FIGURE 3.5-4. AVERAGE OF S-I AND S-IB HEAT SHIELD INNER REGION THERMAL DATA (CONTINUED)

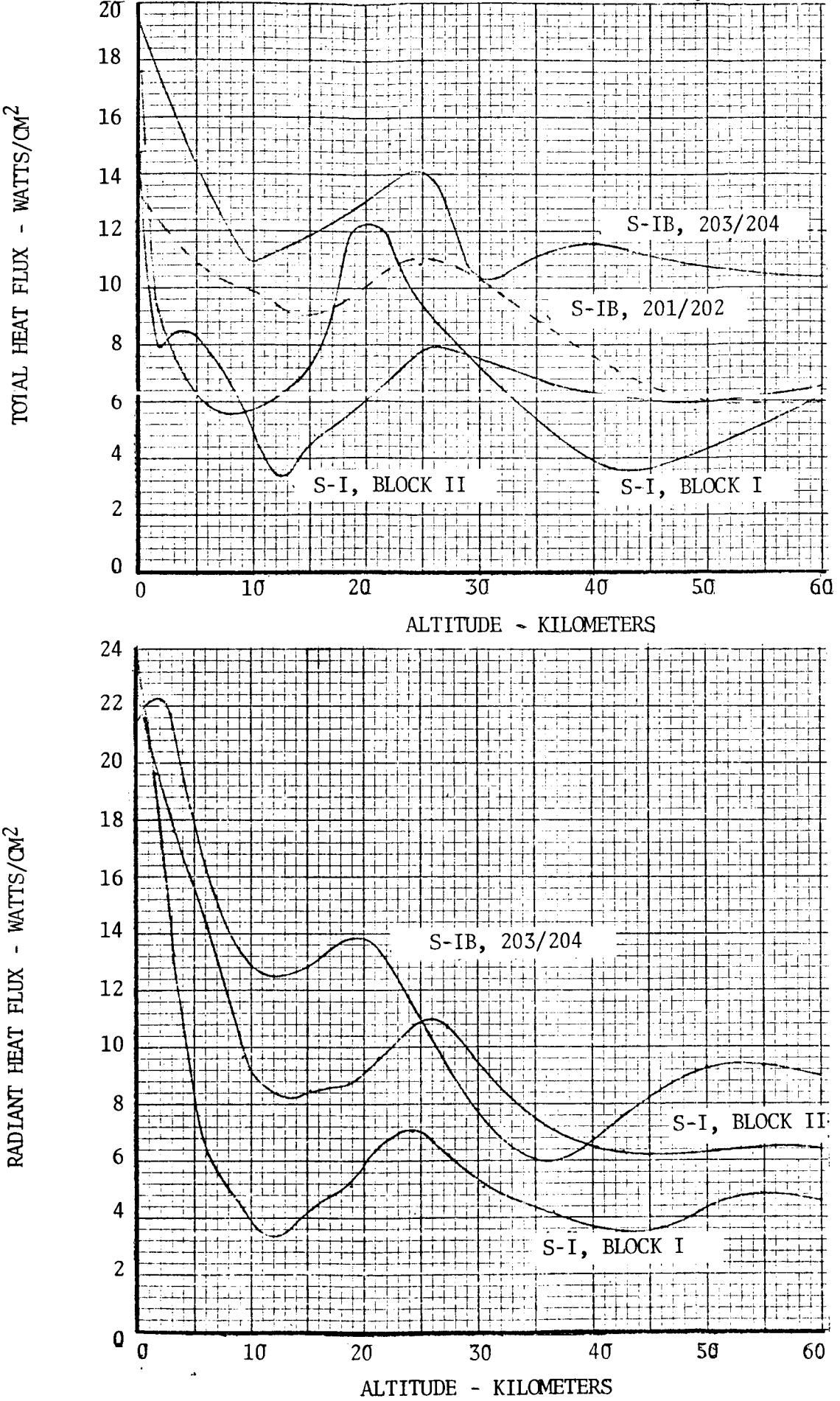

FIGURE 3.5-4. AVERAGE OF S-I AND S-IB HEAT SHIELD INNER REGION THERMAL DATA (CONCLUDED)

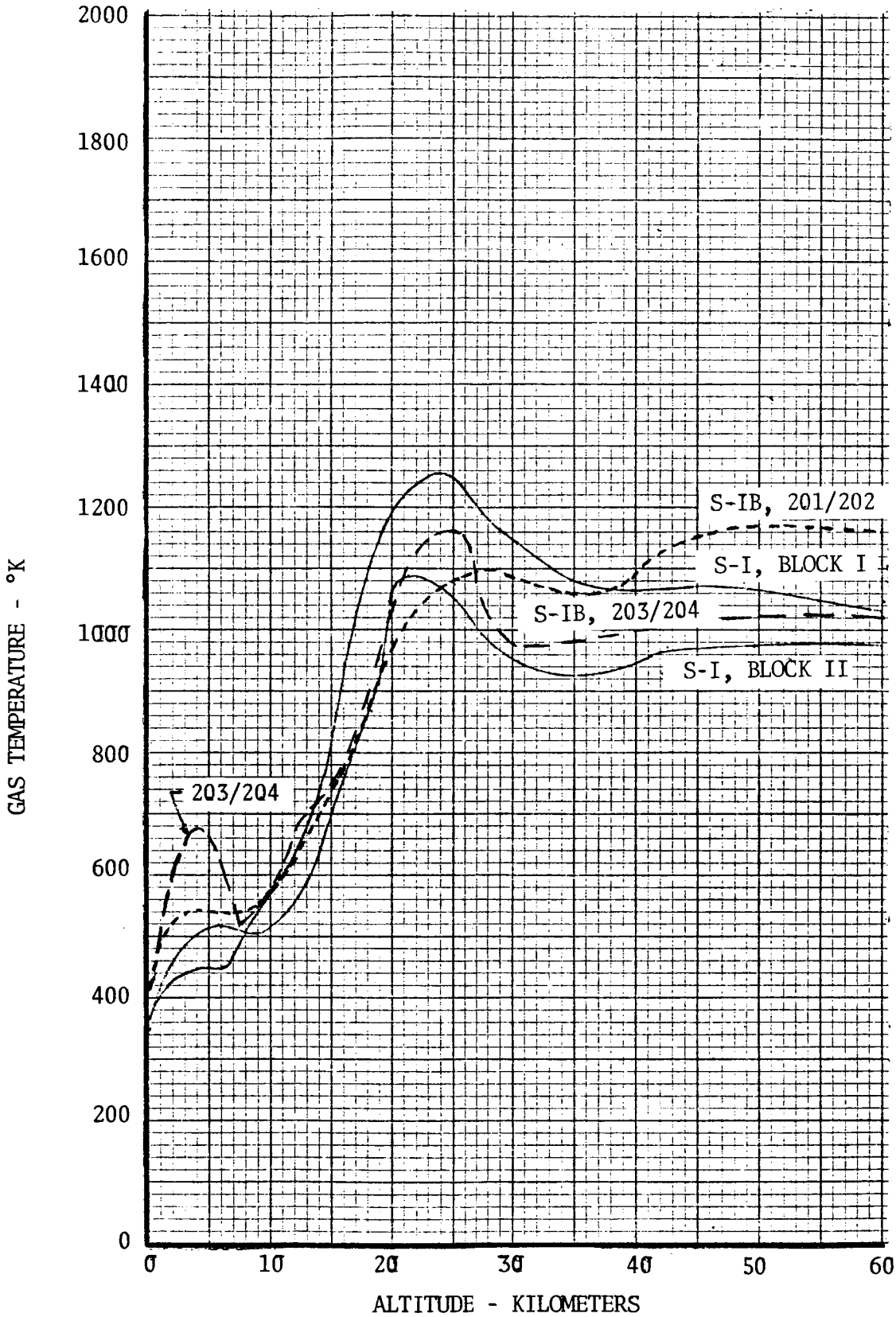

FIGURE 3.5-5. AVERAGE OF S-I AND S-IB HEAT SHIELD OUTER REGION THERMAL DATA (CONTINUED)

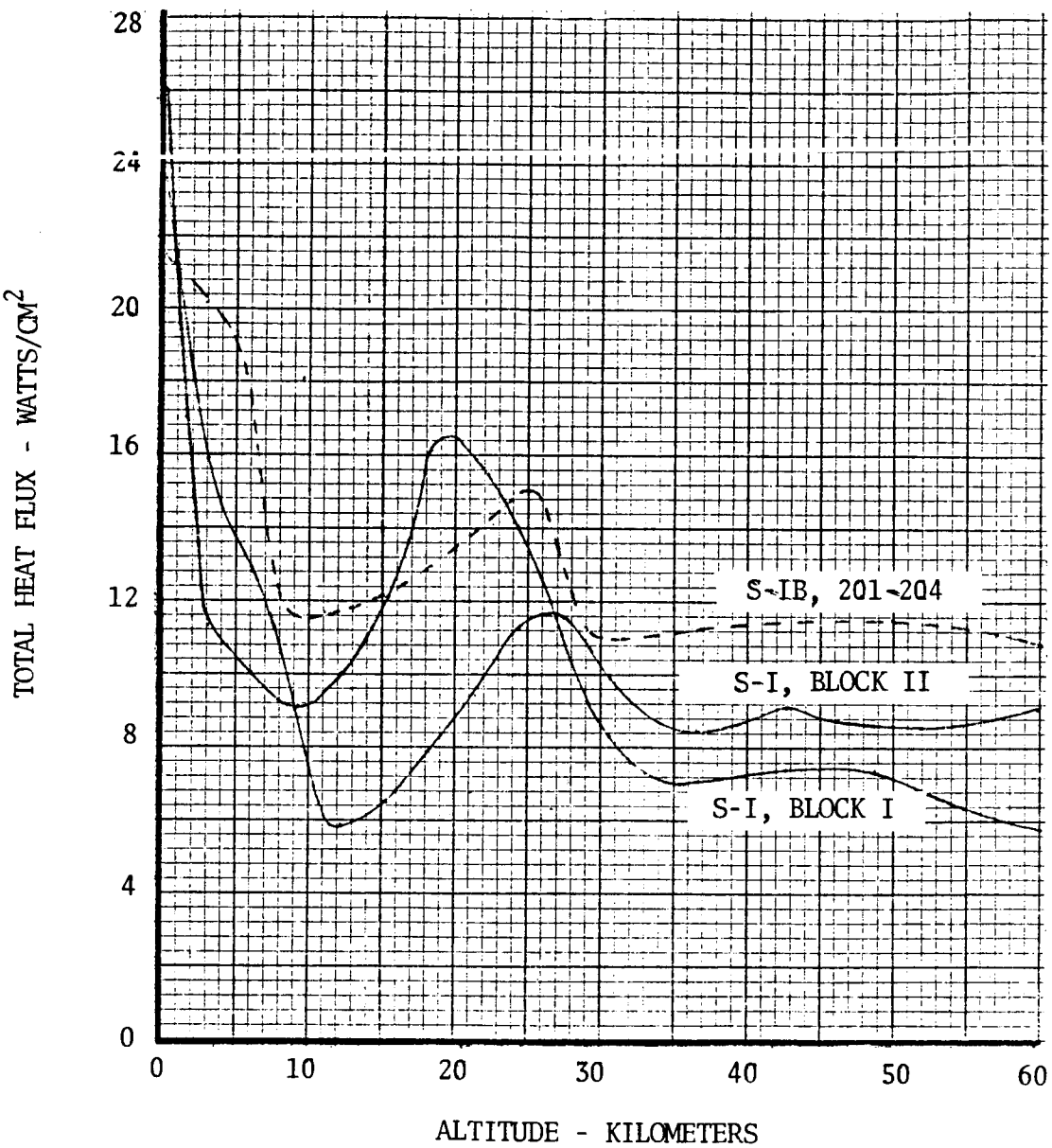

FIGURE 3.5-5. AVERAGE OF S-I AND S-IB HEAT SHIELD OUTER REGION THERMAL DATA (CONTINUED)

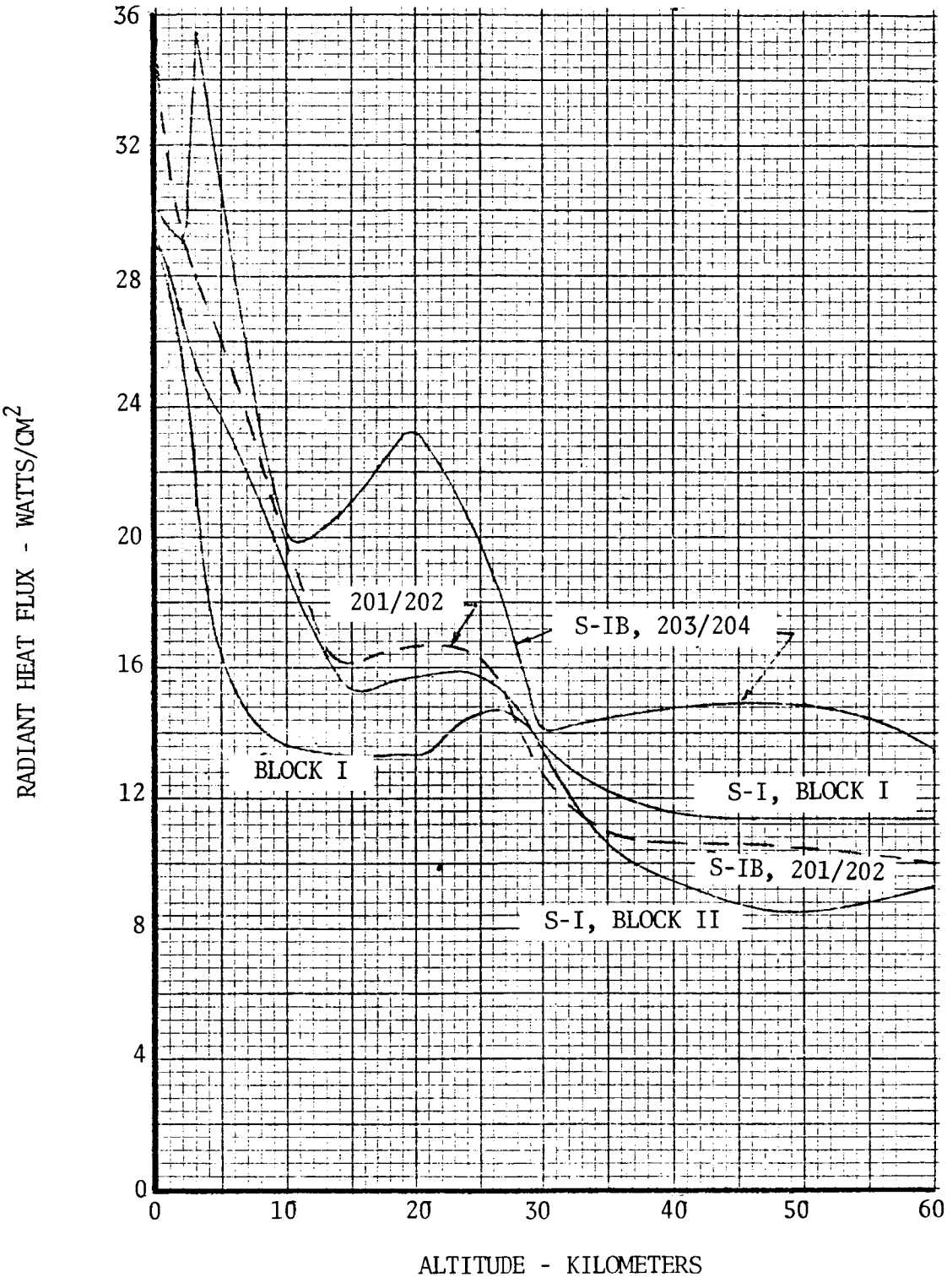

FIGURE 3.5-5. AVERAGE OF S-I AND S-IB HEAT SHIELD OUTER REGION THERMAL DATA (CONCLUDED)

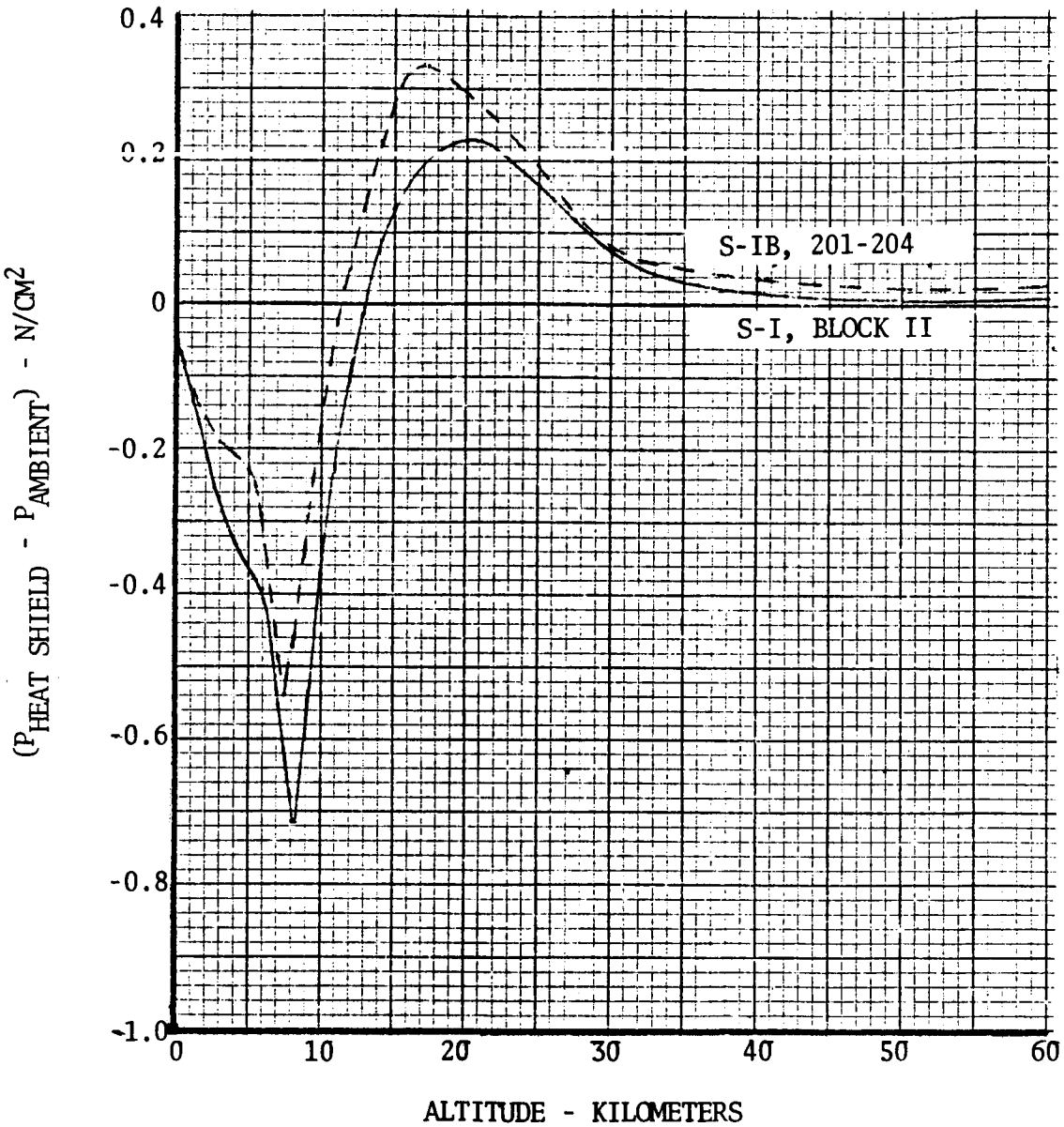

FIGURE 3.5-6. AVERAGE S-I AND S-IB HEAT SHIELD PRESSURES

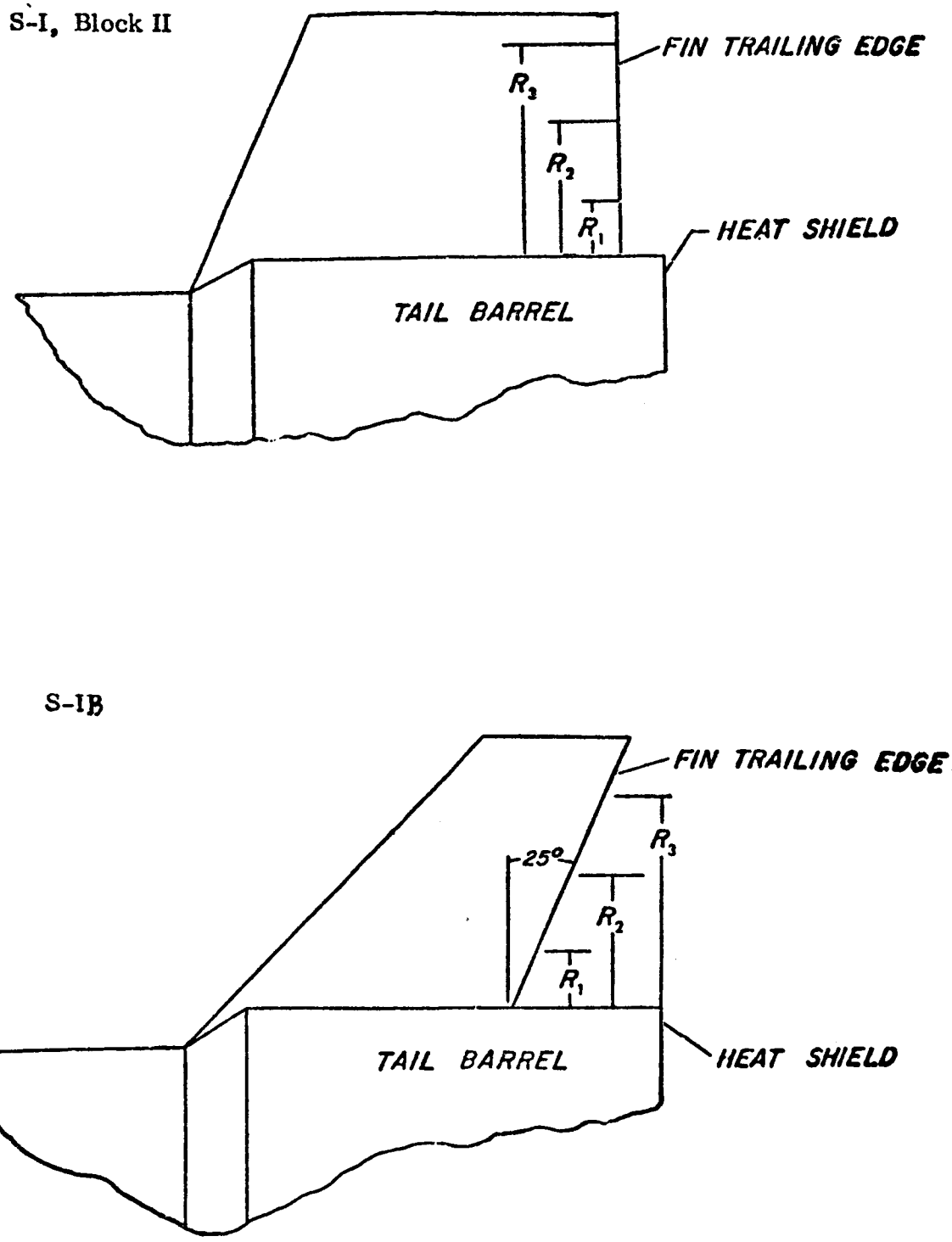

FIGURE 3.5-7. FIN CONFIGURATIONS

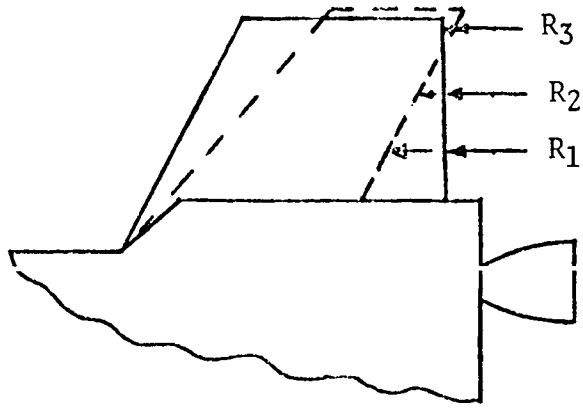

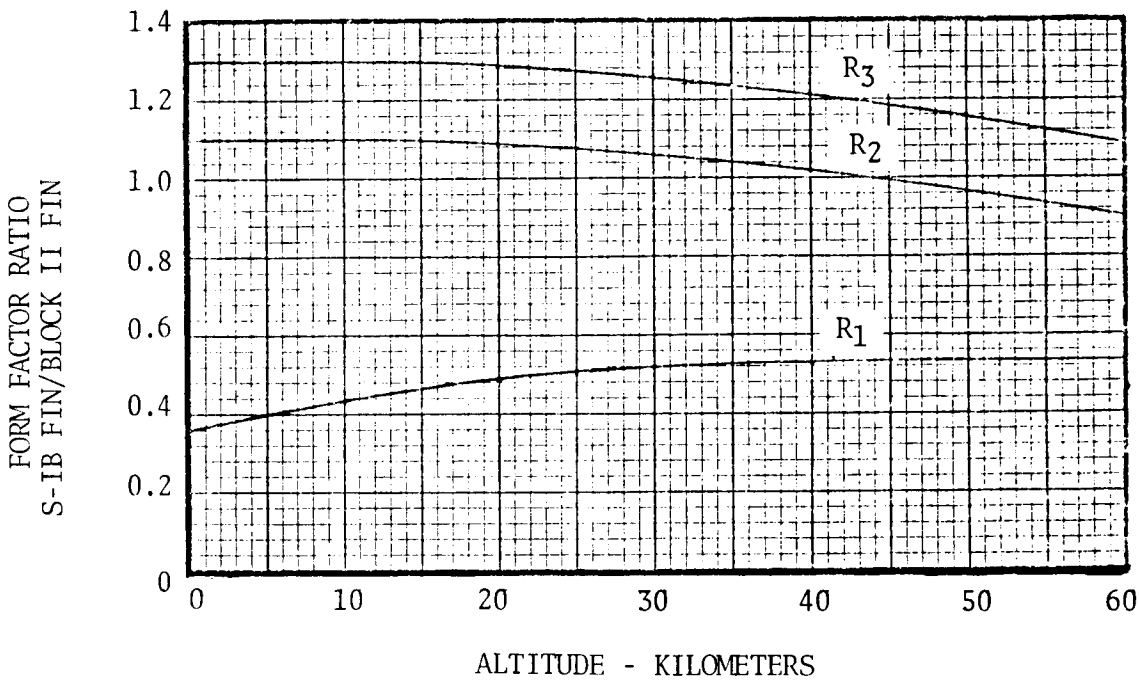

FIGURE 3.5-8 S-IB/BLOCK II FORM FACTORS: FIN TRAILING EDGE TO EXHAUST PLUMES

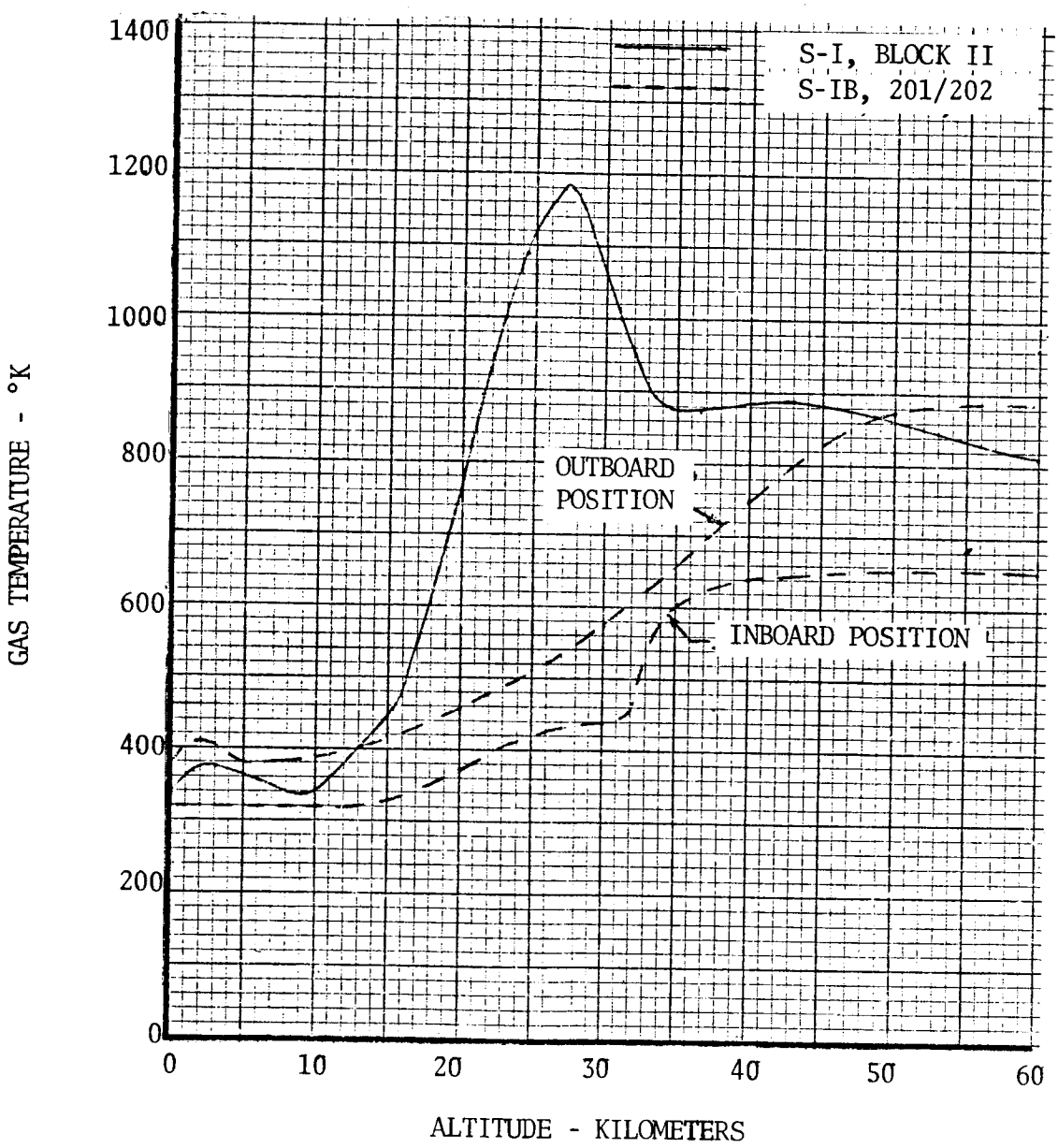

FIGURE 3.5-9. AVERAGE OF S-I AND S-IB FIN TRAILING EDGE THERMAL DATA (CONTINUED)

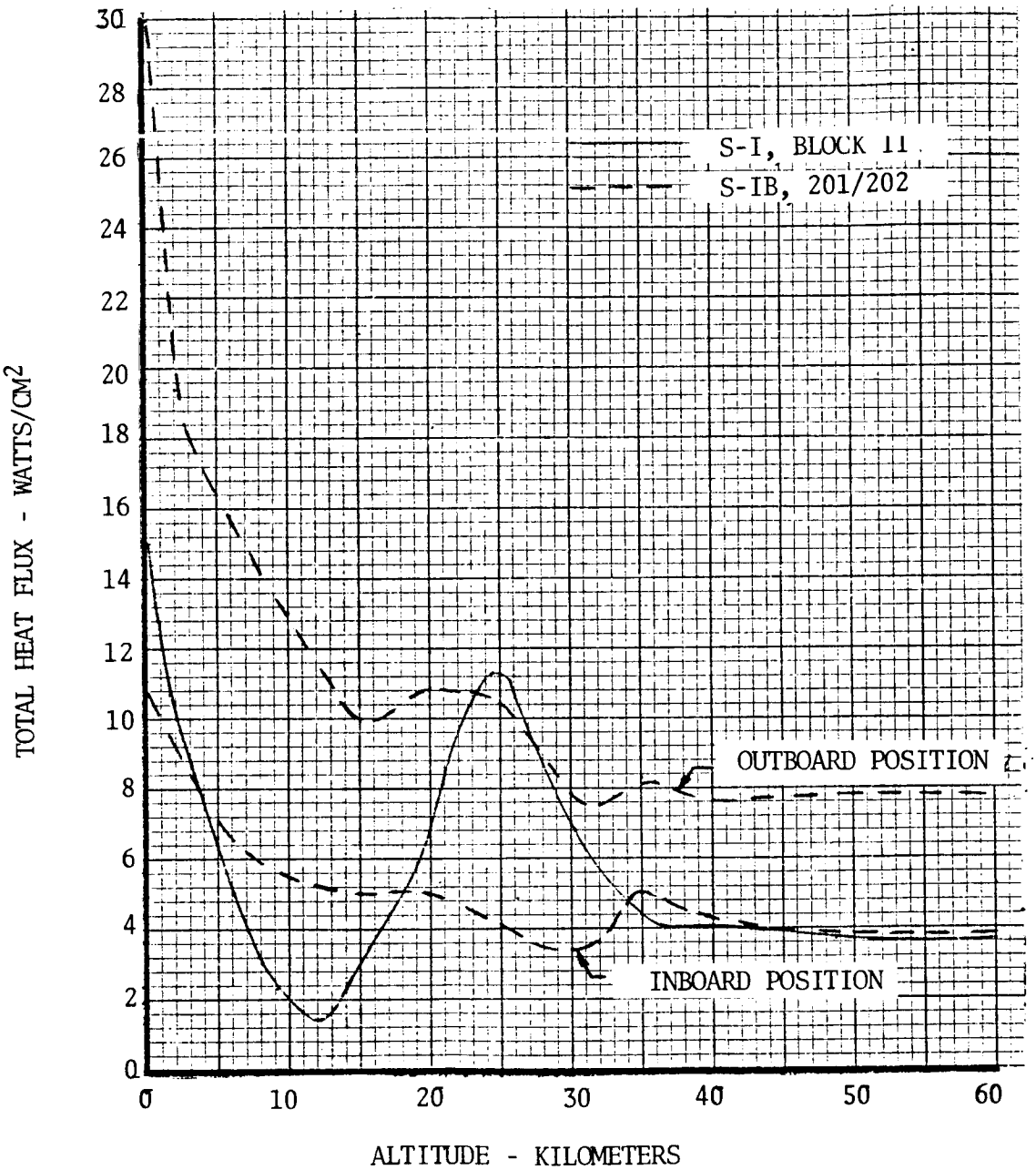

FIGURE 3.5-9. AVERAGE OF S-I AND S-IB FIN TRAILING EDGE THERMAL DATA (CONTINUED)

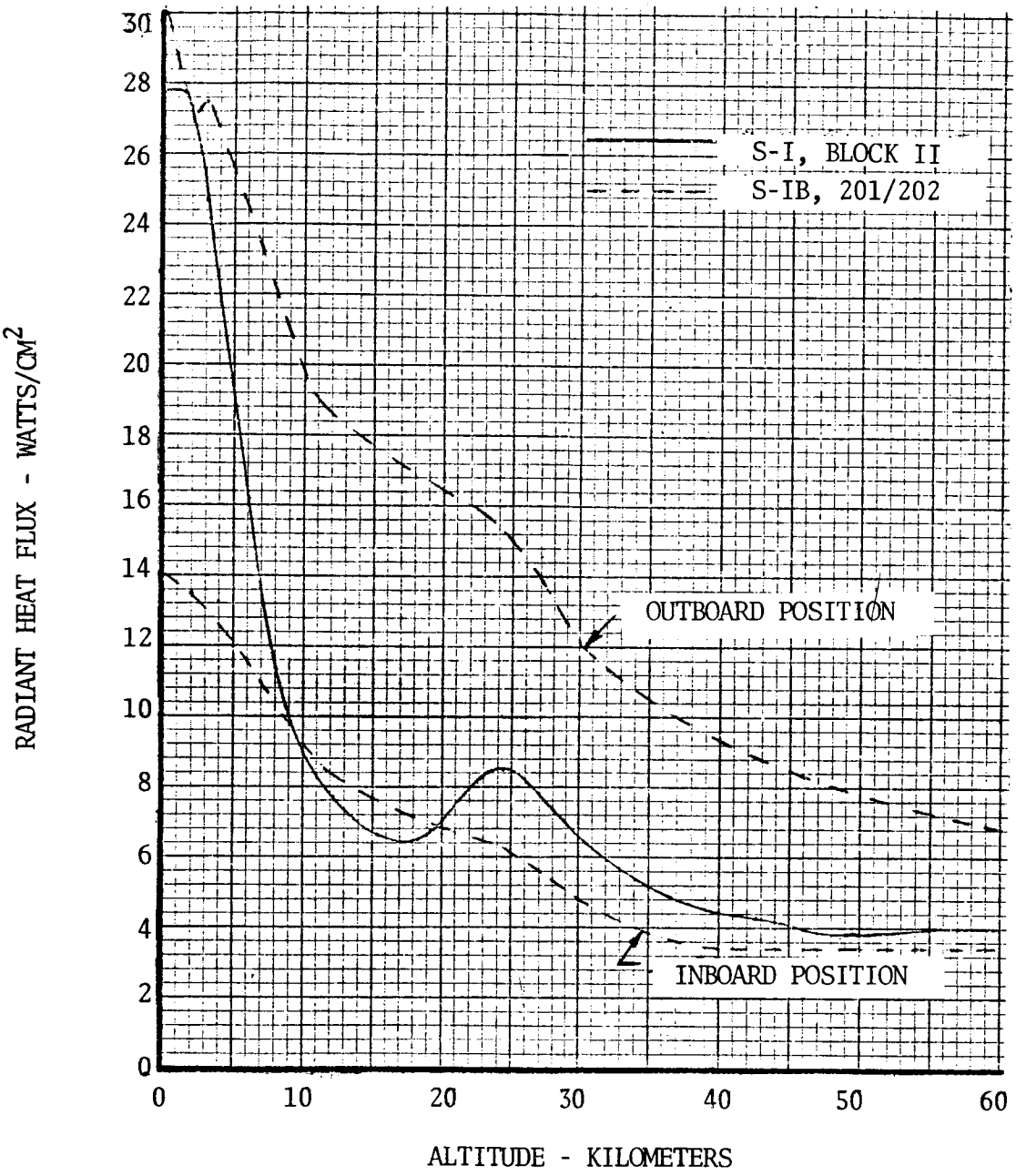

FIGURE 3.5-9. AVERAGE OF S-I AND S-IB FIN TRAILING EDGE THERMAL DATA (CONCLUDED)

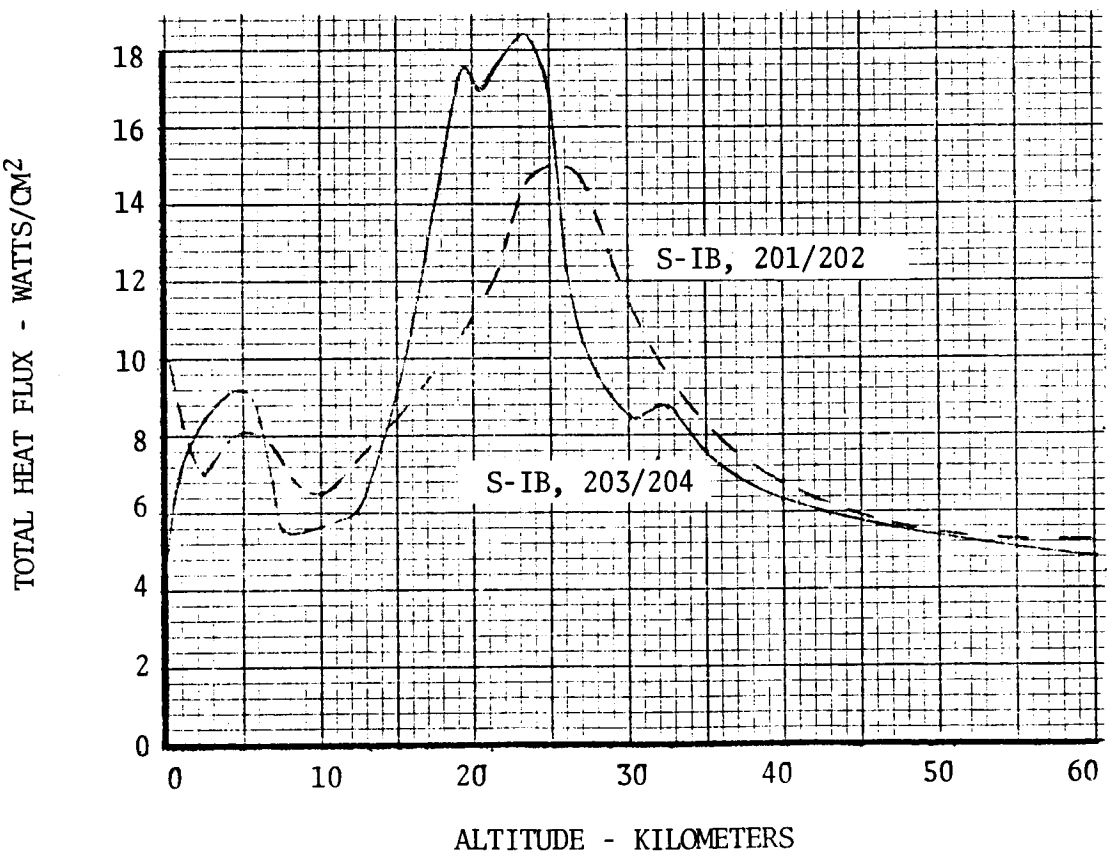

FIGURE 3.5-10. AVERAGE INBOARD ENGINE NOZZLE THERMAL ENVIRONMENT

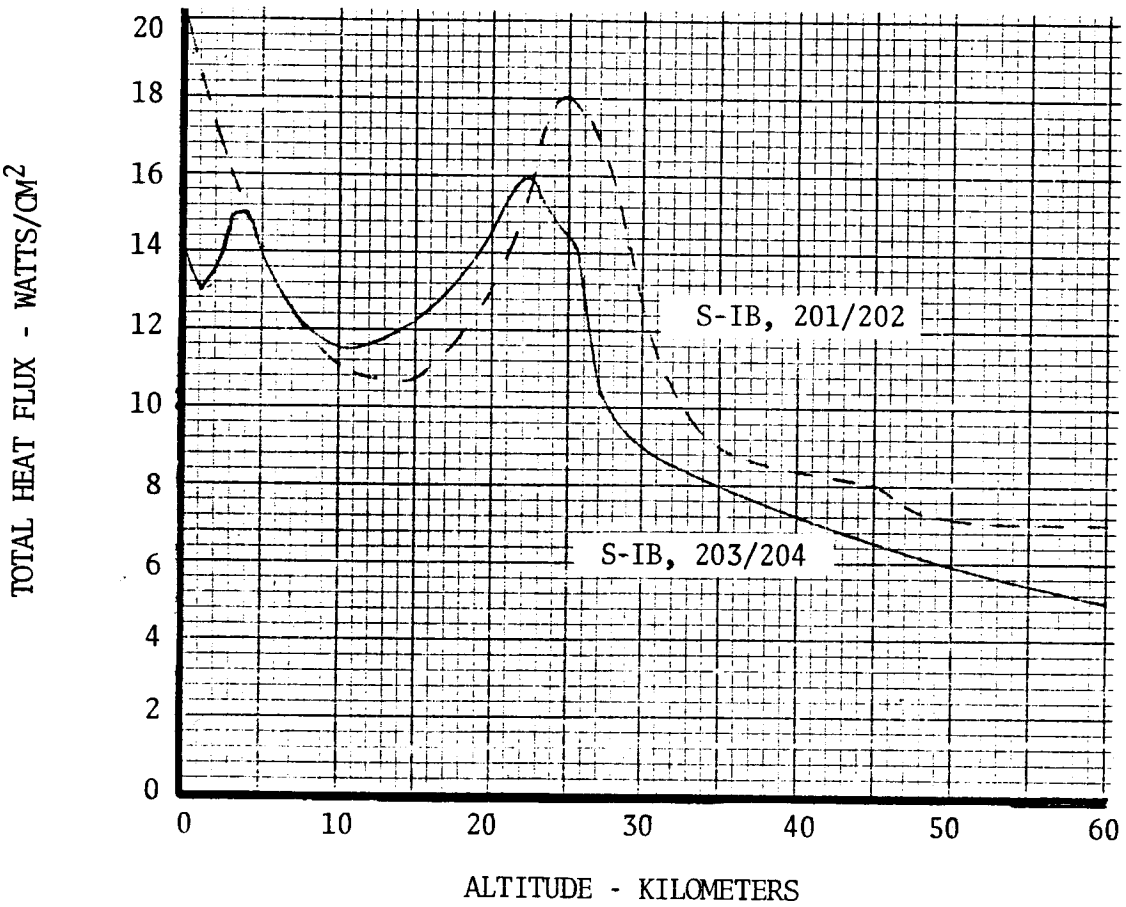

FIGURE 3.5-11. AVERAGE OUTBOARD ENGINE ASPIRATOR NECK THERMAL ENVIRONMENT

* CORRECTED FOR COATING DETERIORATION - $\alpha = 0.2$

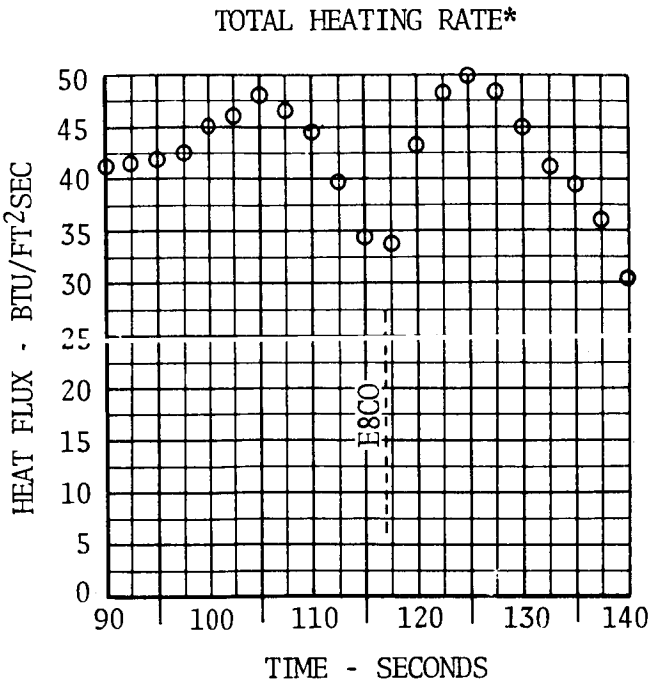

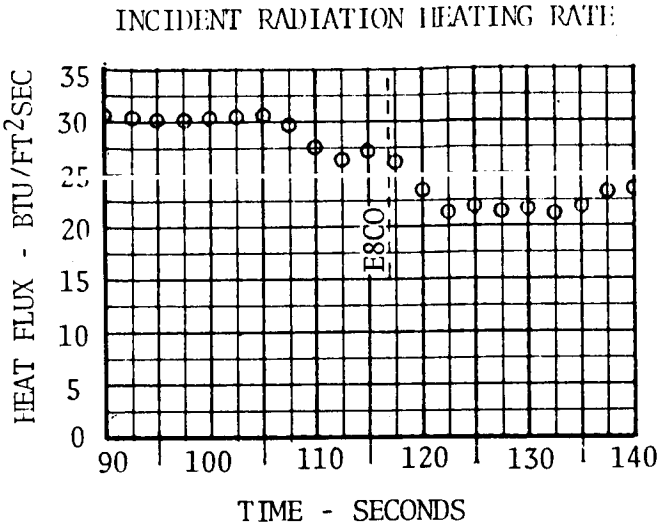

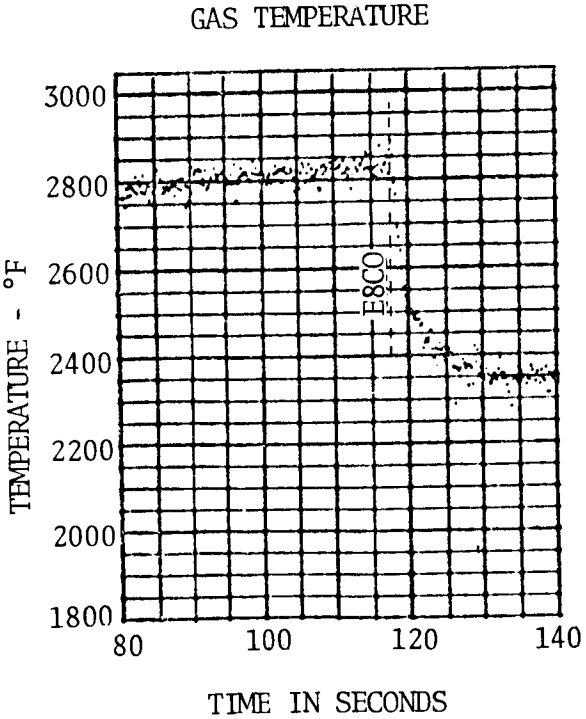

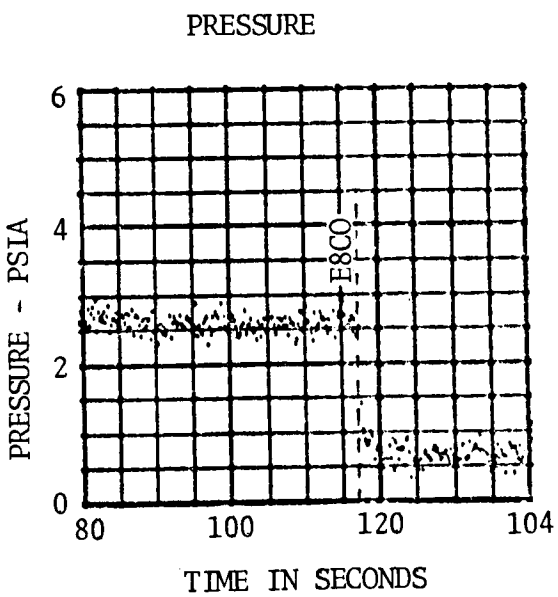

FIGURE 3.5-12. SA-6 FLAME SHIELD FLIGHT DATA COVERING TIME OF PREMATURE ENGINE NO. 8 CUTOFF

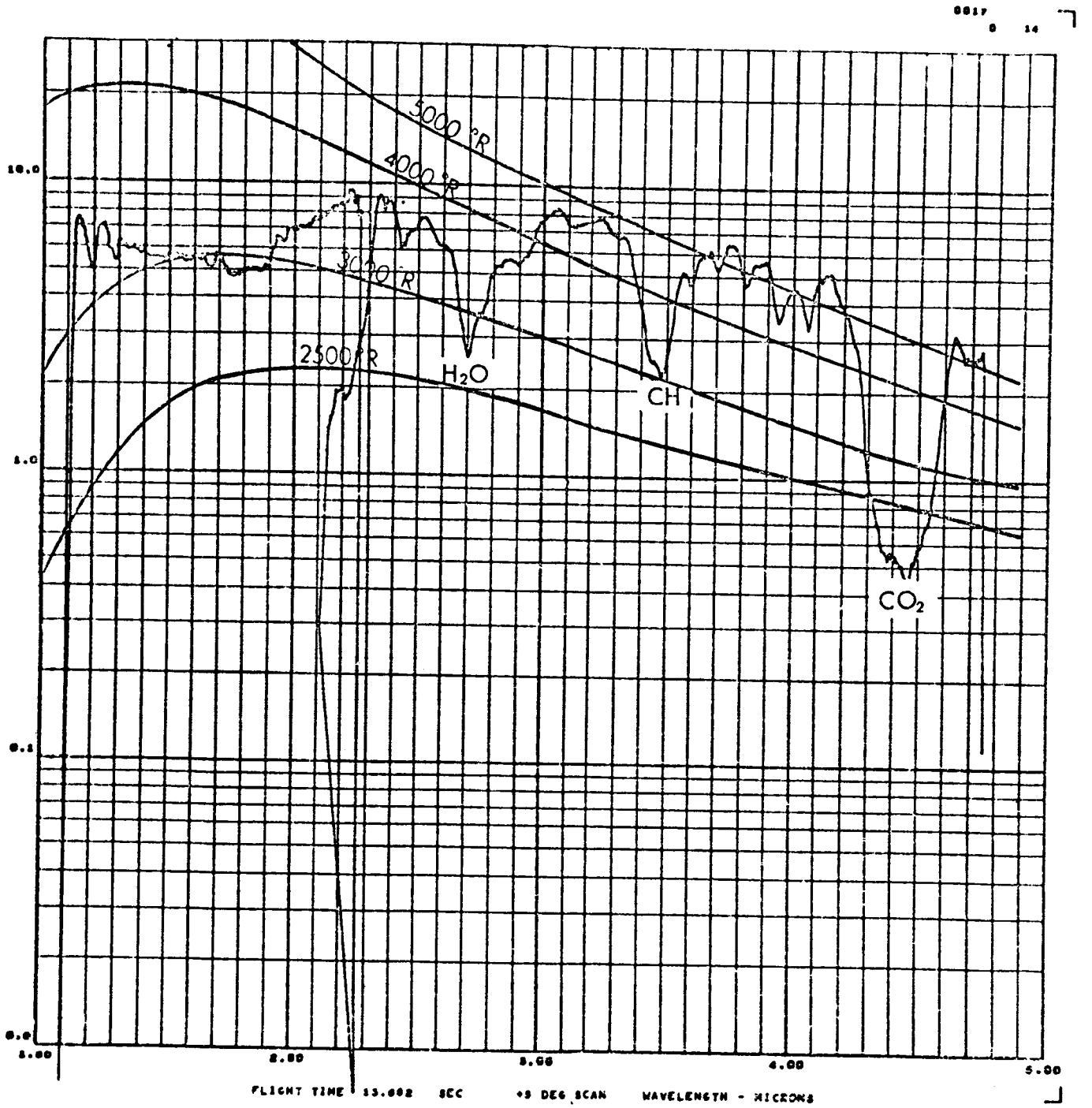

FIGURE 3.5-13. SPECTRUM FROM OUTBOARD ENGINE PLUME AT 1,400 FEET

3.6 MODEL-FLIGHT DATA COMPARISONS

Saturn S-I data comparisons presented herein were originally presented in Reference 3-6. Representative comparisons of total heating rates, radiation heating rates, base gas temperatures and base pressures are presented.

Data shown in Figure 3.6-1 compares radiation heating rates taken from AEDC and Cornell tests on an S-I booster 5.47-percent scale model with Block I flight data at approximately the same location on the base. Both the flight and AEDC measurements were made with similar slug type calorimeters. The Cornell data were obtained by a totally different procedure using thin-film resistance gages on a short duration test technique model. The model heating rates shown are all for a sensor temperature of 38°C. From a radiation standpoint, the model turbine exhaust flow simulation was poor since hydrogen gas was used for all the model tests. During flight the engine turbine exhausts a kerosene fuel-rich mixture (O/F ≈ .33) which has significantly different radiation characteristics from the model simulation. Basic gas laws indicate that similarity between the model and full scale exists only when the exhaust plumes are optically thin and when the products of a linear dimension and density are identical for both. The Saturn plume is far from optically thin, and at altitudes up to about 10 kilometers the radiation is predominantly due to secondary combustion of the fuel-rich engine exhaust with air. This process is influenced by scale, and the plume geometry of the model deviates significantly from the flight plume. It is indeed remarkable, considering all the negative factors involved, that the model and flight data shown in Figure 3.6-1 compare so well.

Model and flight total heating rates are compared in Figure 3.6-2. The convective component of these data require an additional correction for scale effects before a valid comparison is possible. The proper scaling procedure for this type of base flow has been very difficult to determine, and additional effort in this area is needed. The present data were corrected and correlated for heat transfer on the rear of bodies in separated flow. On this basis the Nusselt number is proportional to the Reynolds number to the two-thirds power. The scaling method used is discussed in Appendix C of Reference 3-6. The equation used for correlating the convective heating rates is

$$\dot{q}_{c_{flt}} = \left[\left(\frac{D_{mod}}{D}\right)^{1/3} \frac{(T_R - T_w)_{flt}}{(T_R - T_w)_{mod}}\right] \dot{q}_{c_{mod}}$$

where: $\dot{q}_{c_{flt}}$ = convective component of the flight measured heating rate data

D_{mod} = diameter of the model base

D_{flt} = diameter of the flight vehicle base

3.6 (Continued)

$(T_R - T_w)_{mod}$ = recovery temperature minus calorimeter temperature for the model

$(T_R - T_w)_{flt}$ = recovery temperature minus calorimeter temperature for the flight vehicle, $T_R = T_{gas}$ for the flight data

$\dot{q}_{c_{mod}}$ = model convective heating rate data

After the scaling, this equation was applied to the convective component of the model data, the radiation was then added, and the total value plotted (Figure 3.6-2). Although comparison with the range of the Block I data is good, the spread of the data in both cases is rather large.

Flight and model base gas temperatures are compared at approximately the same location in Figure 3.6-3. The model data required no correction and follow well the Block I measurement of C65-3 up to the altitude where reverse flow becomes a factor. Beyond this altitude the model gas temperature decreases; this indicates that there is less burning of the simulated turbine exhaust flow in the base or that less of the hydrogen turbine exhaust gas reaches the base of the model. It is believed that, from this critical altitude on up, scale effects prohibit burning of the turbine exhaust in the base area of the models, while it may continue on the flight vehicle.

Pressures were measured at various locations on the base of all model tests; average base pressure ratios were obtained and compared with the flight results in Figures 3.6-4, 3.6-5 and 3.6-6. The model data for the base-to-ambient pressure ratio in Figure 3.6-4 indicate generally lower pressure for the three model tests up to the point of the inboard flow reversal. Above this altitude the model data indicate a higher pressure than the flight data. According to Reference 3-6 the differences below 12 kilometers of altitude can be attributed to the mismatch of the flow boundary conditions upstream of the model base and the improper scaling of the flow deflectors and air scoops to the model boundary layer conditions (they were scaled geometrically from the flight dimensions).

The flame shield to ambient pressure ratio model data are compared to flight in Figure 3.6-5. The comparison of the data in this region is very good over the whole model test range. This is due in part to the small influence of the external flow conditions on this region and to the similarity of the model engine and flight plume shapes. The flame shield to the base pressure ratio data shown in Figure 3.6-6 also compared well with the model data.

These curves, in Figure 3.6-6, are equivalent to the pressure ratio across a supersonic nozzle with the space between the inboard engines taken as the nozzle throat, the flame shield pressure as the reservoir, and the base pressure as the downstream conditions. The critical pressure ratio, or the condition where Mach one is reached in the areas between adjacent inboard

3.6 (Continued)

engines, is found at some point along the curve. This defines the altitude at which the inboard engine reverse flow becomes fully choked and at which the maximum possible mass of hot gas is introduced into the heat shield area. The critical pressure ratio is defined as

$$\left(\frac{P_o}{P_1}\right)_{crit} = \left(\frac{\gamma + 1}{2}\right)^{\frac{\gamma}{\gamma - 1}} = \left(\frac{P_F}{\bar{P_B}}\right)_{crit}$$

where: P_o = reservoir pressure

P_1 = downstream pressure

γ = specific heat ratio for the hot exhaust gases

P_F = flame shield pressure

$\bar{P_B}$ = average base pressure

The critical pressure ratio, assuming γ to be 1.23, is equal to 1.79.

Data shown for SA-1, SA-2, and SA-4 in Figure 3.6-6 for this ratio would indicate that the flow chokes between 16.9 and 19.2 km. Confirmation of this range is derived from the observation of the absolute flame shield pressure, temperature, and the total heating rate. All these data indicate that choking occurred between 15 and 20 km altitude. The choking altitude derived from model data was reported in Reference 306 to be 18.74 km. This was for a critical pressure ratio of 1.72.

REF: NASA TM X-53326

COMPARISON OF RADIATIVE HEATING RATES ON MODEL AND FLIGHT TESTS ON SATURN I VEHICLES

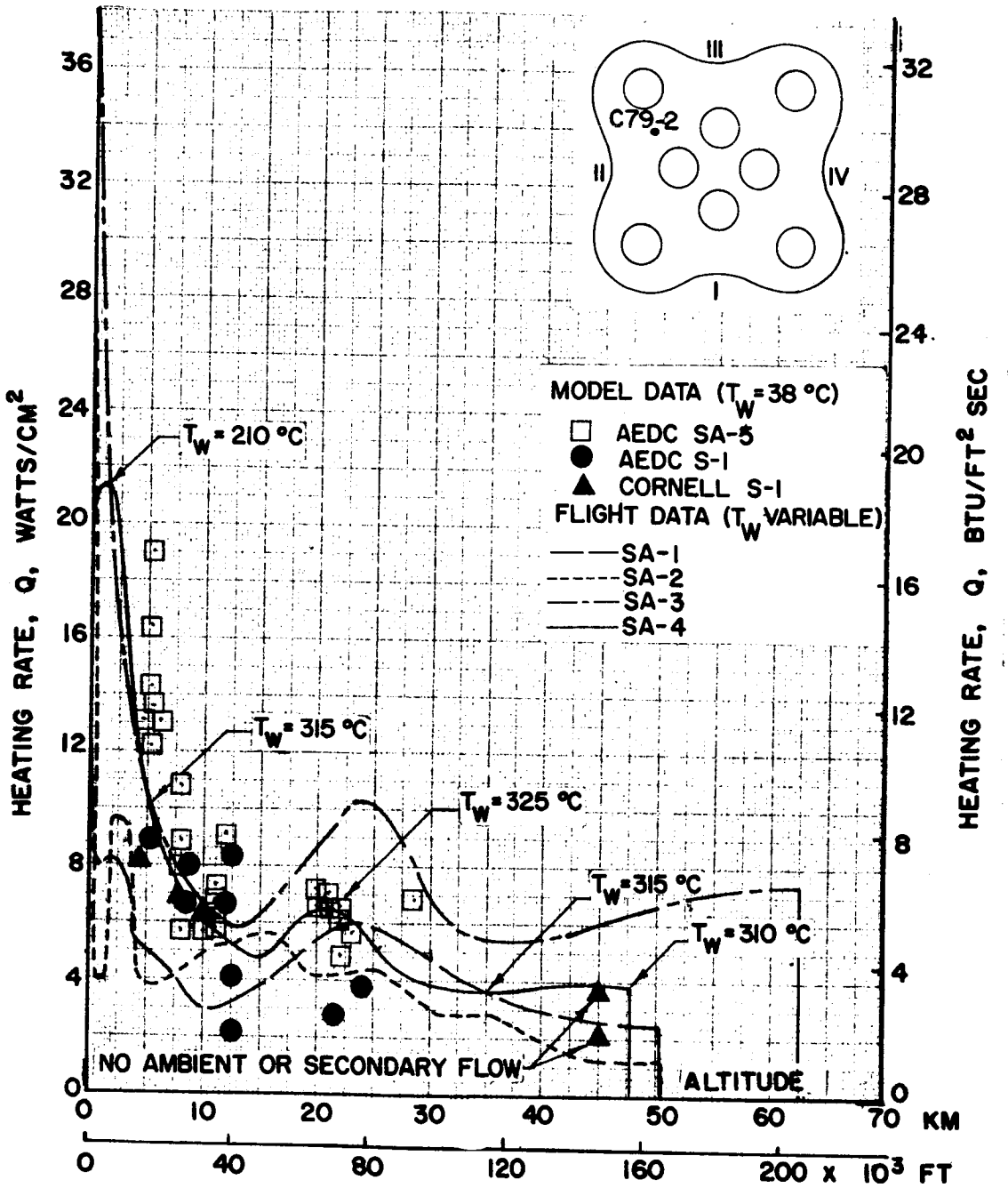

FIGURE 3.6-1. COMPARISON OF RADIATIVE HEATING RATES ON MODEL AND FLIGHT TESTS ON SATURN I VEHICLES

REF: NASA TM X-53326

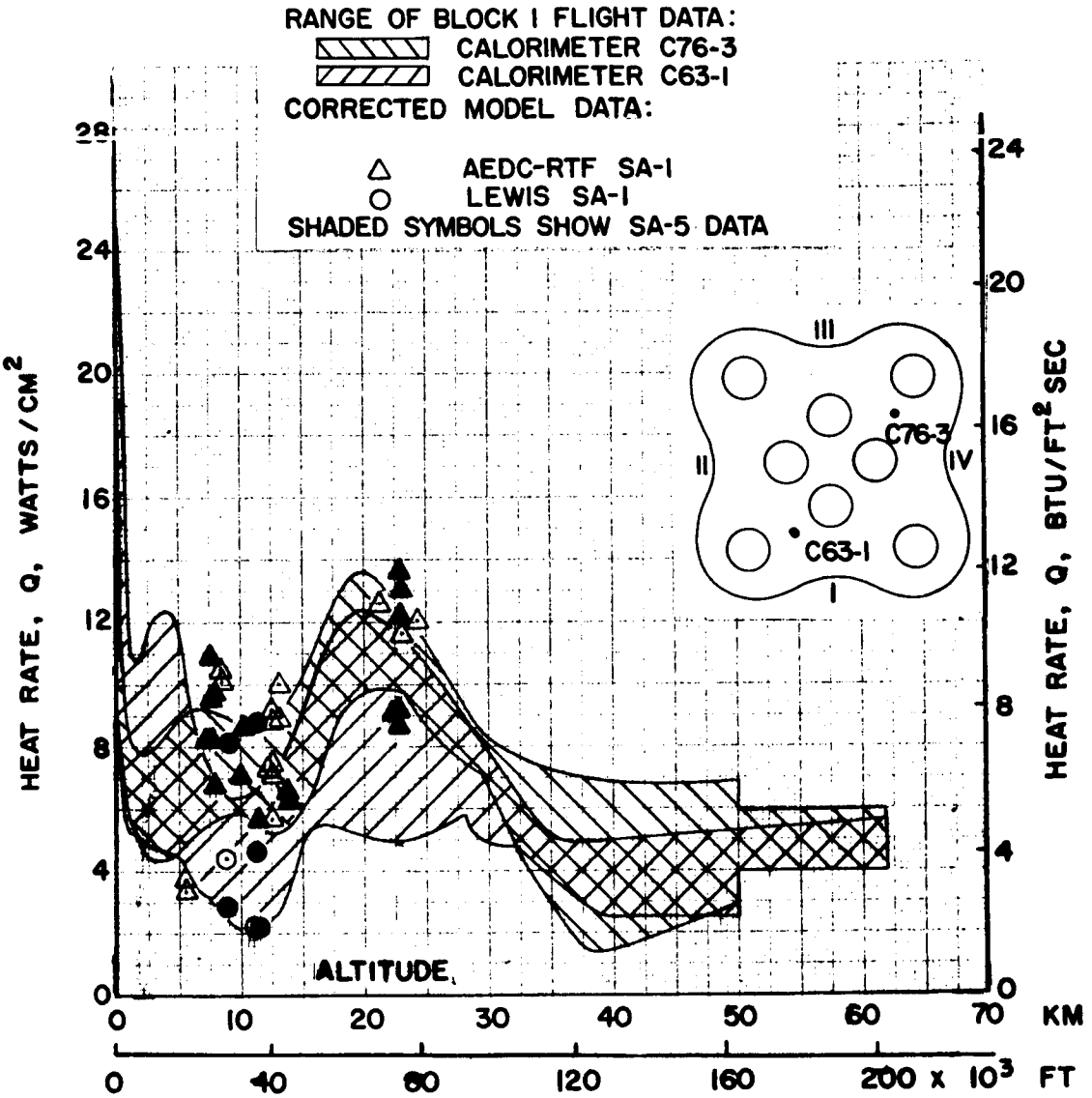

FIGURE 3.6-2. COMPARISON OF HEATING RATES FROM SATURN I BLOCK I FLIGHT DATA WITH MODEL DATA

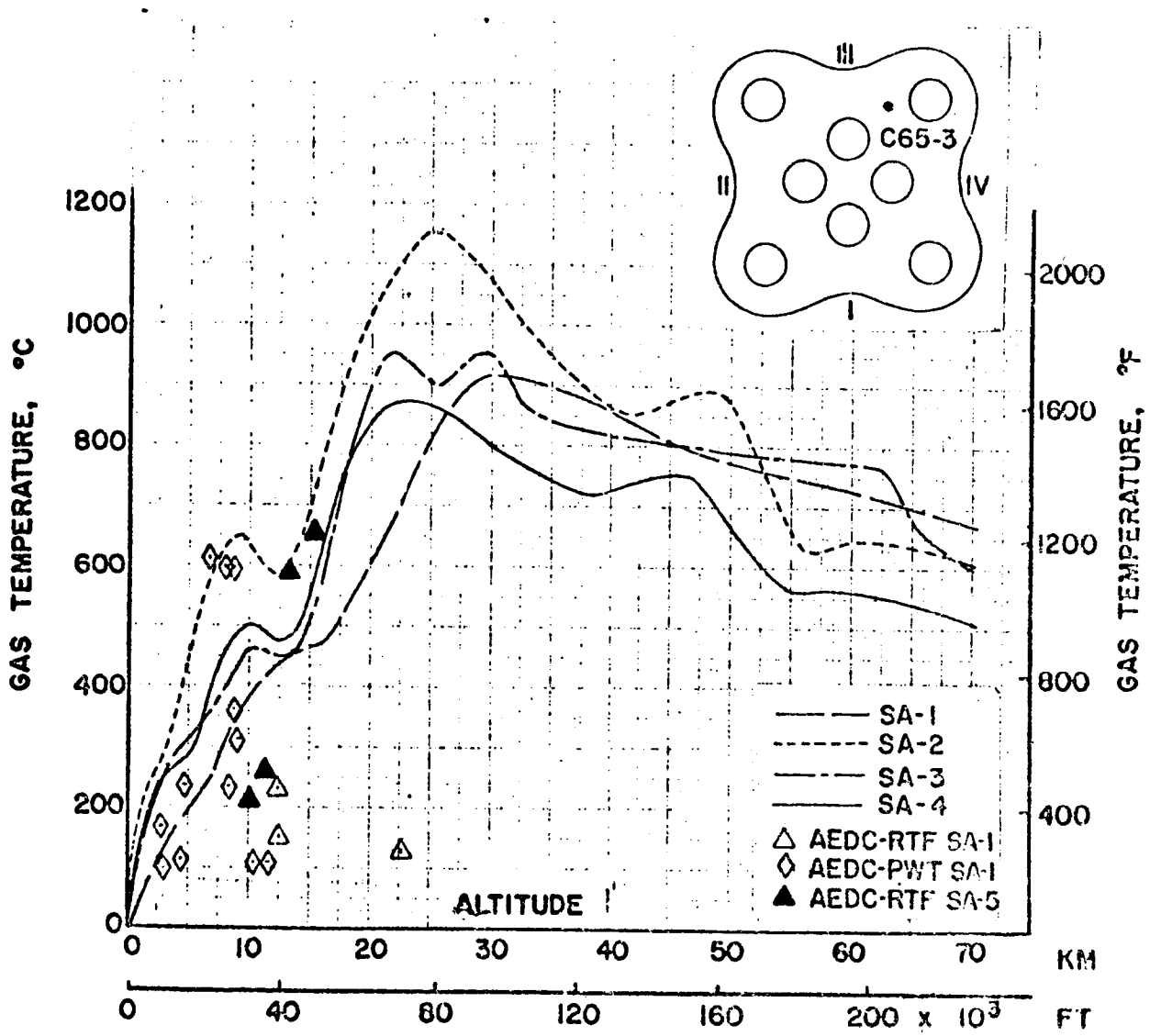

FIGURE 3.6-3. GAS TEMPERATURES FROM SATURN I BLOCK I FLIGHT DATA COMPARED WITH MODEL DATA

REF: NASA TM X-53326

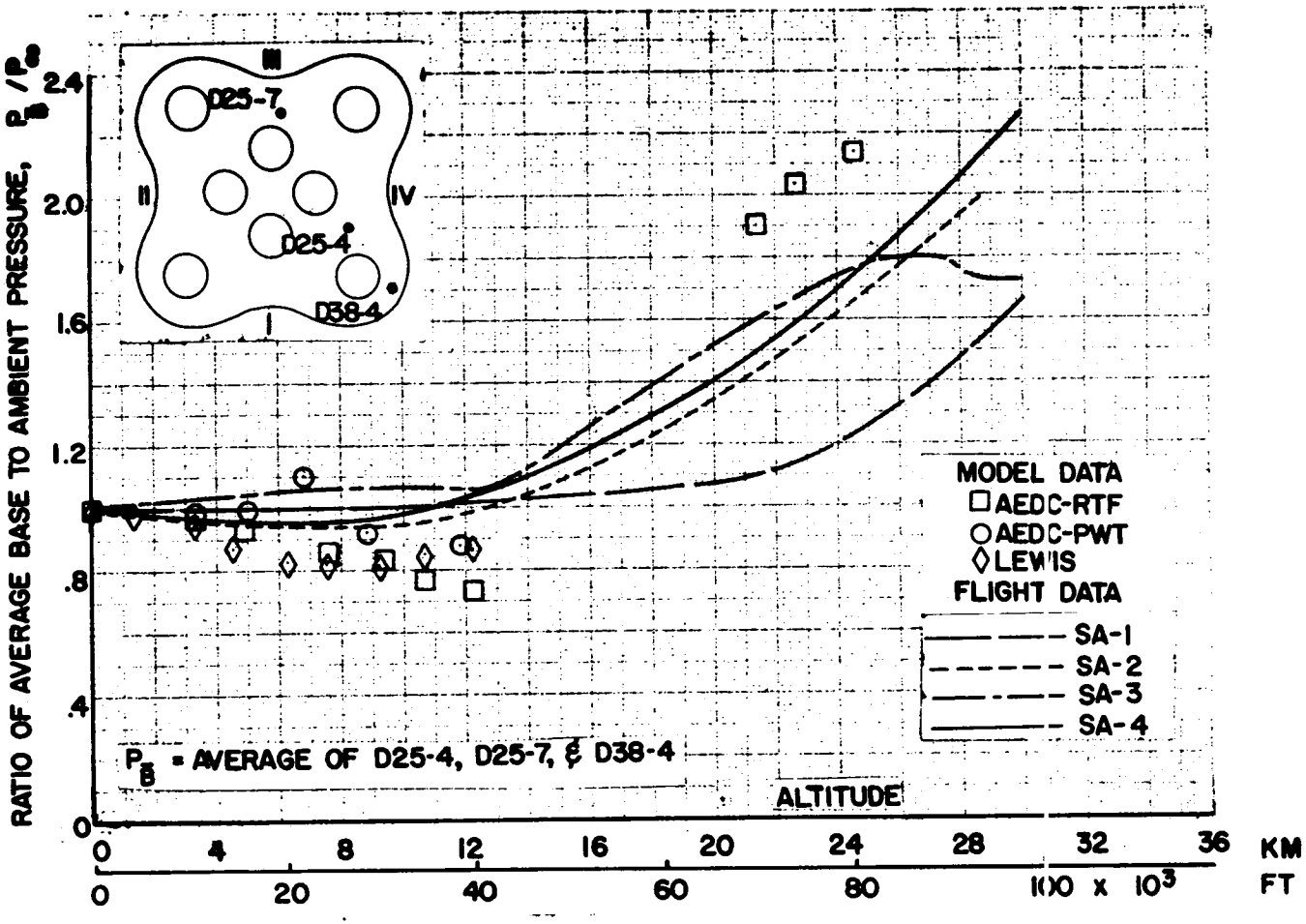

FIGURE 3.6-4. COMPARISON OF RATIO OF AVERAGE BASE PRESSURE TO AMBIENT PRESSURE ON SATURN I BLOCK I VEHICLES

REF: NASA TM X-53326

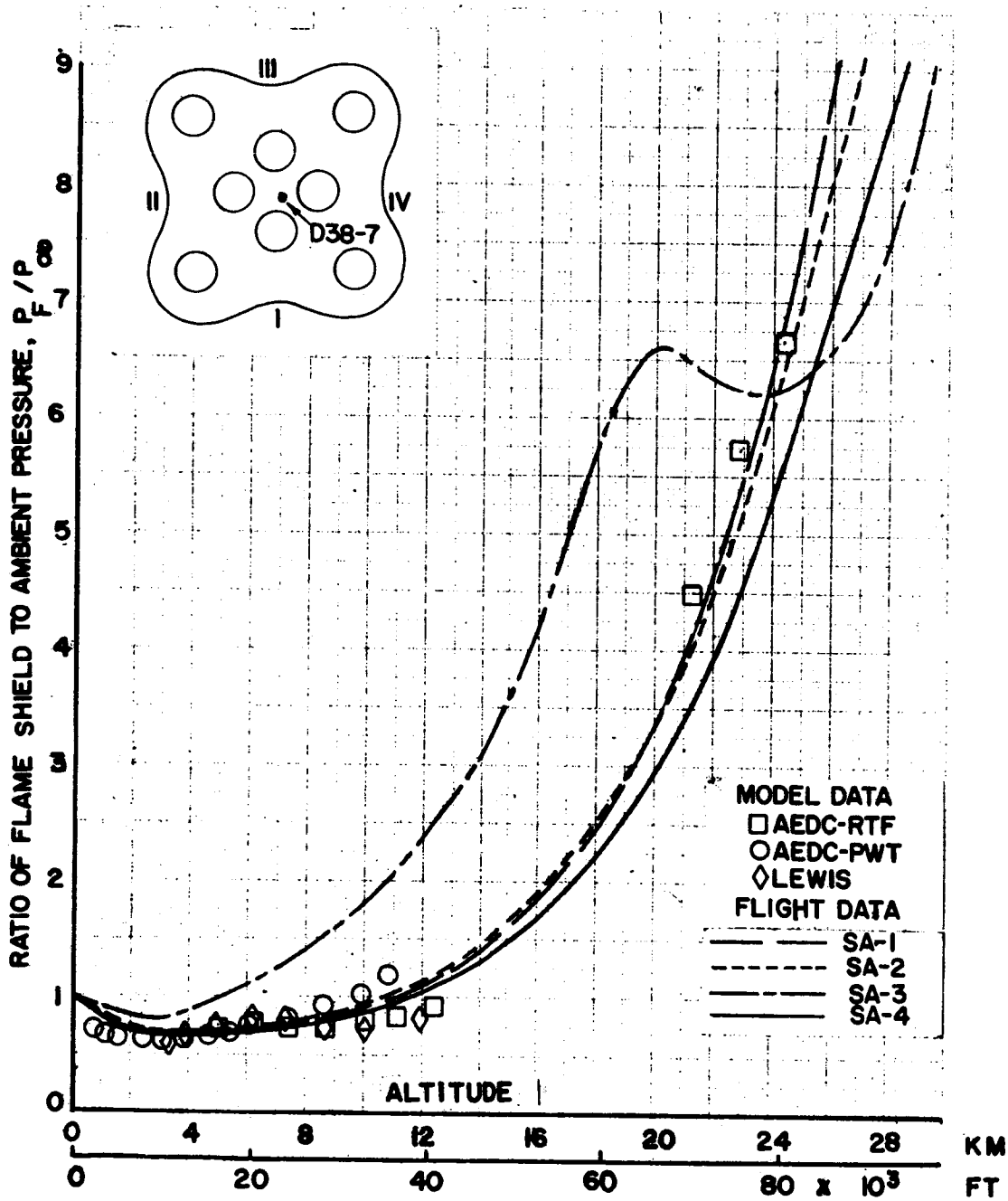

FIGURE 3.6-5. COMPARISON OF RATIO OF FLAME SHIELD TO AMBIENT PRESSURE FOR SATURN I BLOCK I VEHICLES

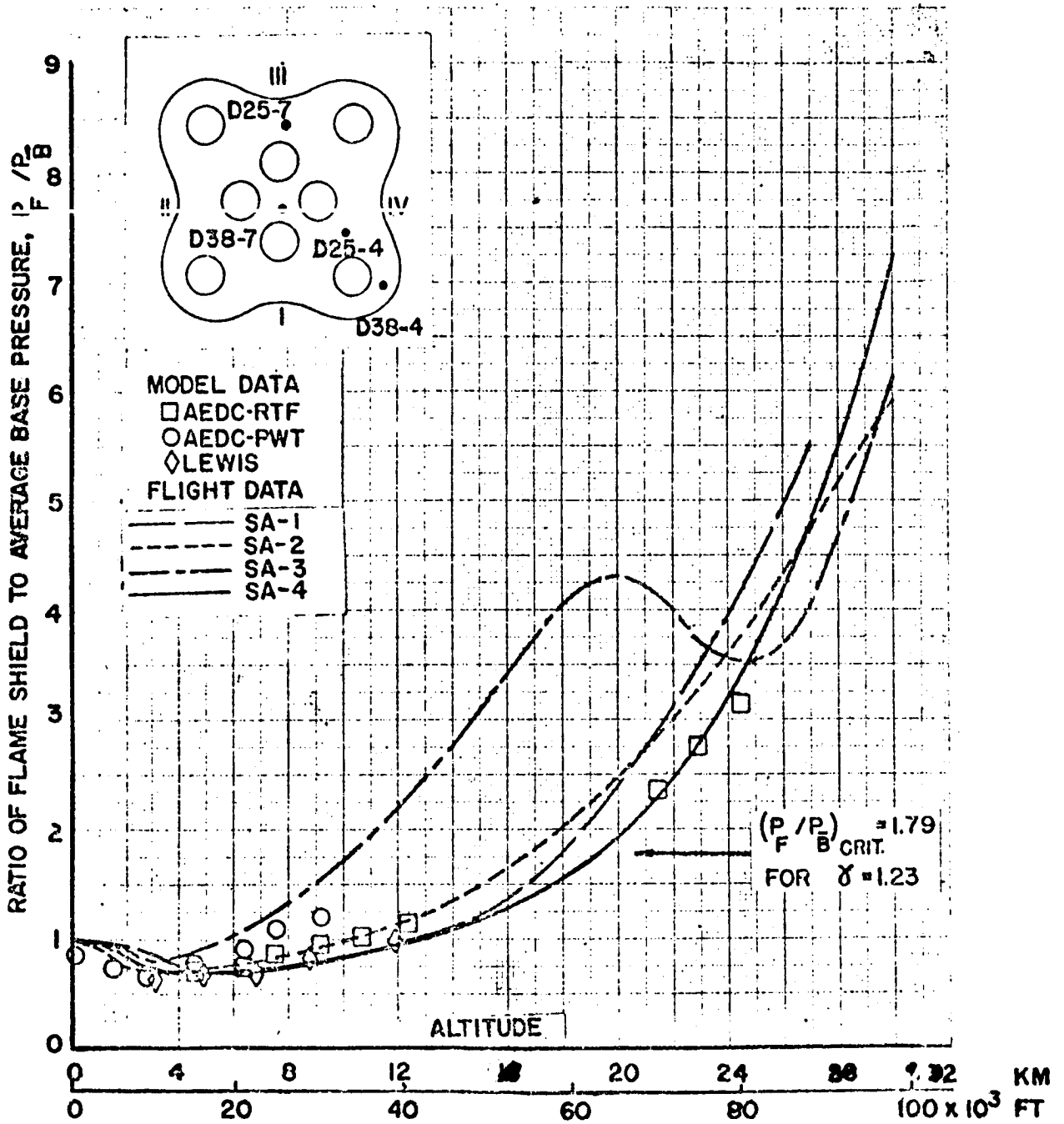

FIGURE 3.6-6. COMPARISON OF RATIO OF FLAME SHIELD TO AVERAGE PRESSURE FOR SATURN I BLOCK I VEHICLES

3.7 REFERENCES

3-1. AEDC-TN-61-106, "An Investigation of Base Heating on a 5.47-Percent Scale Model of the Saturn S-I Booster at Transonic Mach Numbers," Arnold Engineering Development Center, August 1961.

3-2. AEDC-TN-61-134, "An Investigation of Base Heating with a 5.47-Percent Saturn SA-I Booster Model at Mach Numbers 0.8 and 1.15," Arnold Engineering Development Center, November 1961.

3-3. AEDC-TDR-62-9, "An Investigation of Base Heating on a 5.47-Percent Scale Model Saturn SA-I Booster Afterbody at Mach Numbers 1.63 and 3.07," Arnold Engineering Development Center, January 1962.

3-4. AEDC-TR-66-46, "Base Heating on a 5.47-Percent Scale Model Saturn IB Booster Afterbody at Mach Numbers of 1.18 and 1.63 at Trajectory Attitudes," March 1966.

3-5. CAL No. HM-2045-Y-4, "An Investigation of the Base Environment of the Uprated Saturn S-IB Booster at Mach Numbers 1.18 and 1.63 Using Short-Duration Experimental Techniques," Cornell Aeronautical Laboratory, March 1969.

3-6. NASA TM X-53326, "Summary of Base Thermal Environment Measurements on the Saturn I Block I Flight Vehicles," National Aeronautics and Space Administration, September 3, 1965.

3-7. CCSD TN-AE-65-115, "Summary of Saturn I, S-I Stage, Base and Aerodynamic Heating Data," Chrysler Corporation Space Division, November 1, 1965.

3-8. CCSD TN-AE-66-140, "Summary of Aerodynamic Data Obtained from the Saturn I, Block II Flight Test Program," Chrysler Corporation Space Division, 1966.

3-9. CCSD TN-AP-68-333, "S-IB Stage Environment Summary Flight Evaluation Report, S-IB-1 through S-IB-4," Chrysler Corporation Space Division, July 20, 1968.

3-10. CCSD TN-AP-67-161, "Infrared Spectra of the Saturn IB Rocket Exhaust Plumes Measured During Flight," Chrysler Corporation Space Division, February 1967.

THIS PAGE LEFT BLANK INTENTIONALLY

CONTENTS

4.0 SATURN S-IC BASE ENVIRONMENT

4.1	S-IC CONFIGURATION	4-2
4.2	F-1 ENGINE CHARACTERISTICS	4-7
4.3	PREDICTION METHODS	4-18
4.4	MODEL TEST AND PARAMETRIC DATA	4-22
4.5	FLIGHT TEST AND PARAMETRIC DATA	4-84
4.6	COMPARISON OF MODEL AND FLIGHT TEST RESULTS	4-129
4.7	REFERENCES	4-137

4.0 SATURN S-IC STAGE

4.1 S-IC CONFIGURATION

The S-IC stage provides first stage boost of the Saturn V launch vehicle to an altitude of about 200,000 feet (approximately 38 miles), and provides acceleration to increase the vehicle velocity to 7,700 feet per second (approximately 4,560 knots). It then separated from the S-II stage and falls to earth about 360 nautical miles downrange.

The S-IC stage (Figure 4.1-1) is a cylindrical booster, 138 feet long and 33 feet in diameter, powered by five liquid propellant F-1 rocket engines. These engines develop a nominal sea level thrust of 7,650,000 pounds total. and have a burn time of 150.7 seconds. The stage dry weight is approximately 305,100 pounds and total weight at ground ignition is approximately 4,792,200 pounds.

The Saturn V/S-IC stage base configuration consists of five F-1 engines mounted in a cross-engine arrangement of four maneuverable engines around a fixed center engine (Figure 4.1-2). A heat shield is located 19 feet forward of the engine exit and base flow deflectors were located on the AS-501 around the periphery of the base to flush combustible gas mixtures from the base area. These flow deflectors were removed on AS-502. The heat shield panels are constructed of 15-7-MO stainless steel honeycomb, 1.00 inch thick, brazed to 0.01 inch steel face sheets. A 0.25 inch thick honeycomb sheet is crushed to 0.14 inch thick and brazed to the hot side facing sheet. M-31, which is a ceramic composed of an inorganic binder with asbestos and potassium titanate fibers, is troweled into the crushed core and is approximately 0.3 inch thick.

Each outboard F-1 engine is protected from aerodynamic loading by a conically shaped engine fairing (Figure 4.1-1). The fairings also house the retro-rockets and the engine actuator supports. The fairing components are primarily titanium alloy below Station 115.5 and aluminum alloy above this station. Four fixed, titanium covered, stabilizing fins augment the stability of the Saturn V vehicle.

Each F-1 engine is enclosed in a "cocoon" which consists of fibrous silica insulation enclosed in inconel foil, except for the nozzle extension where wire reinforced asbestos is used as shown in Figure 4.1-3.

AS-501 flight trajectory data are tabulated in Table 4.1-1. All Saturn V flight trajectories were similar.

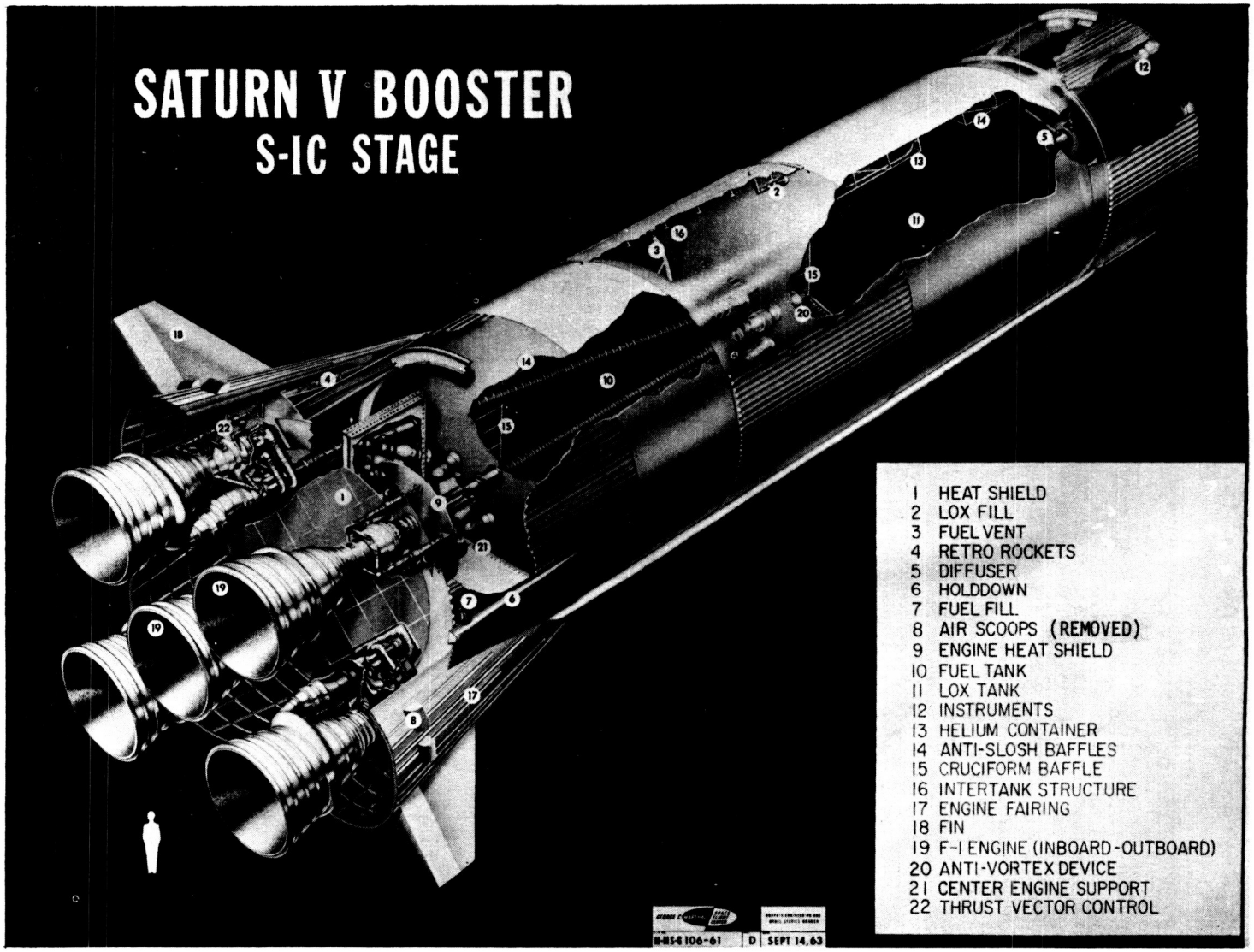

FIGURE 4.1-1 S-IC STAGE BASE REGION

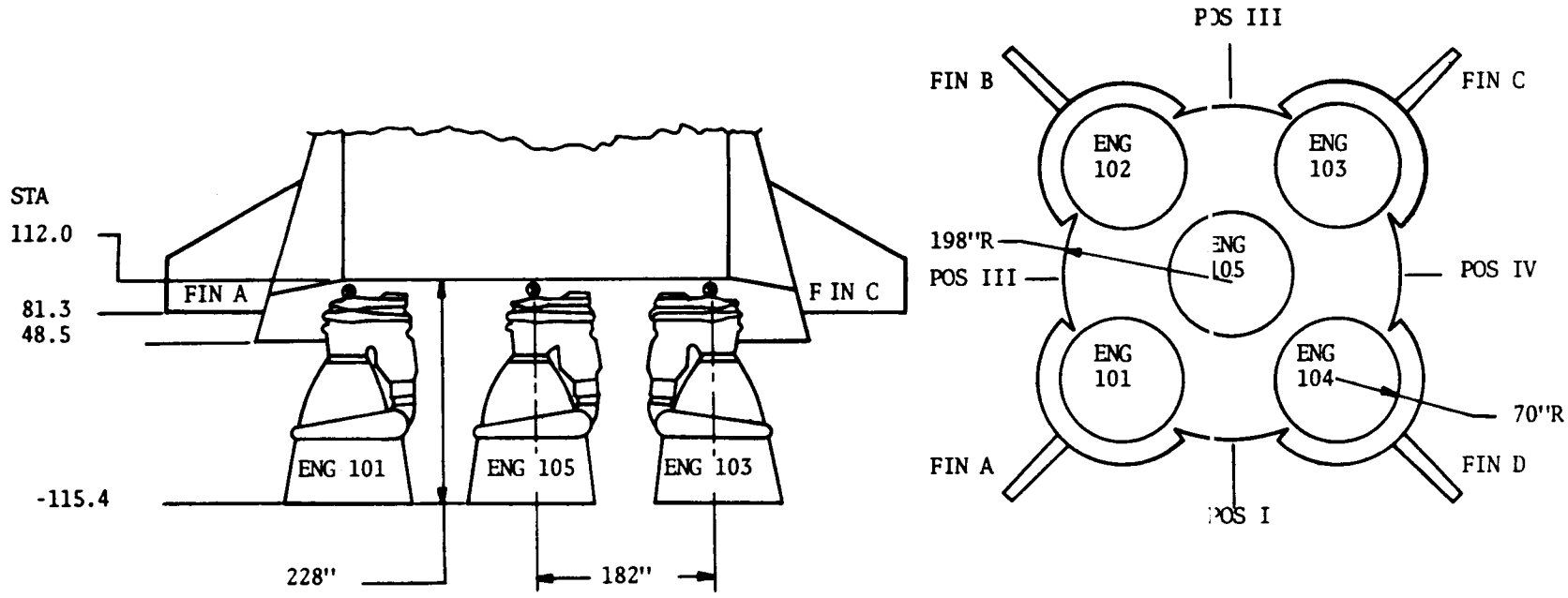

FIGURE 4.1-2. S-IC STAGE BASE CONFIGURATION

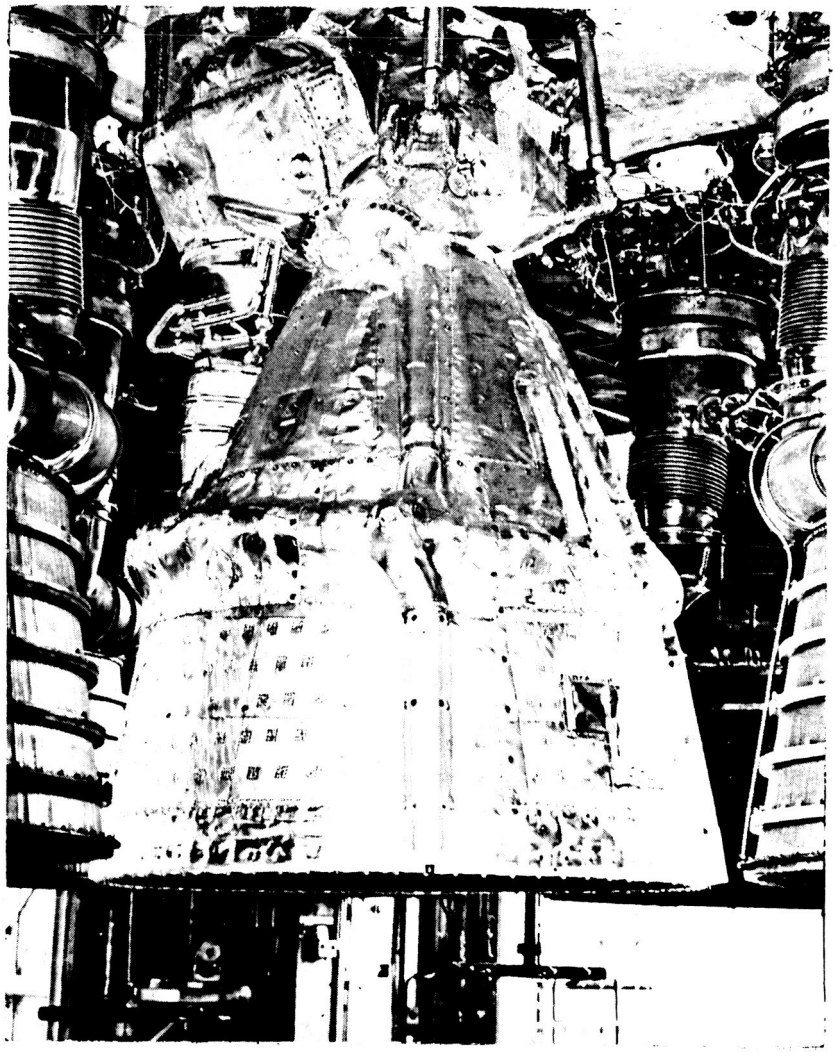

FIGURE 4.1-3. S-IC STAGE CENTER F-1 ENGINE WITH INSULATION COCOON

4.1 (Continued)

TABLE 4.1-1. AS-501 FLIGHT TRAJECTORY DATA

FLIGHT TIME (SECONDS)	ALTITUDE (FEET)	PRESSURE (PSF)	TEMPERATURE (°R)	MACH NUMBER
60.0	23,200	878.0	447.4	0.96
75.0	39,000	427.5	395.6	1.53
84.0	51,400	240.0	359.5	2.05
90.0	61,000	140.5	362.3	2.40
95.0	69,400	91.6	381.3	2.66
101.0	80,500	55.0	398.0	3.05
106.0	90,800	35.0	403.0	3.38
110.0	99,000	23.2	405.0	3.60
115.0	111,000	14.0	404.0	4.06
119.0	120,000	10.0	435.0	4.25
123.5	130,000	6.4	355.0	4.55
127.4	140,000	4.4	471.0	4.85
131.1	150,000	3.0	481.0	5.16

4.2 F-1 ENGINE CHARACTERISTICS

The F-1 engine (Figure 4.2-1) is a single start, 1,530,000 pound fixed thrust, calibrated, bi-propellant engine which uses liquid oxygen as the oxidizer and RP-1 as the fuel at a mixture ratio of 2.26:1. Engine features include a bell-shaped thrust chamber with a 10:1 expansion ratio and detachable, conical nozzle extension which increases the thrust chamber expansion ratio to 16:1. The thrust chamber is cooled regeneratively by fuel, and the nozzle extension is cooled by gas generator exhaust gases injected (parallel to the main nozzle flow) inside the F-1 nozzle from a shingle-type construction from the 10:1 to 16:1 area ratio. This produced a fuel-rich gas mixture surrounding each of the engine exhaust flows. Liquid oxygen and RP-1 fuel are supplied to the thrust chamber by a single turbopump powered by a gas generator which uses the same propellant combination. RP-1 fuel is also used as the turbopump lubricant and as the working fluid for the engine fluid power system. The four outboard engines are capable of gimbaling and have provisions for supply and return of RP-1 fuel as the working fluid for the thrust vector control system. External thermal insulation provides an allowable engine environment during flight operation.

One-dimensional nozzle exit plane properties and nominal propellant flow rates are tabulated in Table 4.2-1 and 4.2-2, respectively.

TABLE 4.2-1. F-1 ENGINE PROPERTIES

Exit Pressure	890.94 psf
Exit Temperature	2599.3°R
Exit Mach Number	3.68
Gamma	1.222
Gas Constant	64.1 $ft.lb_F/lb_m$ °R
Chamber Pressure	139,000 psf
Chamber Temperature	6510°R
Exit Divergence Angle	11°
Nozzle Exit Diameter	140 inches

TABLE 4.2-2. NOMINAL F-1 ENGINE PROPELLANT FLOW RATES

	COMBUSTION CHAMBER	TURBINE EXHAUST	OVERALL ENGINE
Oxidizer Flow (lb_m/sec)	3931.0	50.2	3981.2
Fuel Flow (lb_m/sec)	1633.4	120.3	1753.7
Total Flow (lb_m/sec)	5564.4	170.5	5734.9
Mixture Ratio (O/F)	2.405	0.42	2.2702

Single F-1 engine plumes were generated for several altitudes for the AS-501 flight by using the LMSC/HREC Method of Characteristics Computer Program (Reference 4-1). These plumes were calculated using two-dimensional exit conditions.

The NASA/Lewis Thermochemical Program was used to perform the real gas calculations, and it was found that frozen flow conditions exist in the plume flow fields for all flight times investigated.

Table 4.2-3 presents the frozen-flow gas species concentrations, and the Mach number profiles are given in Figures 4.2-2 through 4.2-11. The pressure and temperature profiles for the plumes are given in Figures 4.2-12 and 4.2-13, respectively.

TABLE 4.2-3. PLUME FROZEN FLOW SPECIES CONCENTRATIONS

SPECIES	SPECIES MASS FRACTIONS
CO	0.3398
CO_2	0.1620
H	0.0004
H_2	0.1642
H_2O	0.3337
OH	0.0001

F-1 engine dimensions

NOZZLE AREA RATIO ϵ = 16:1

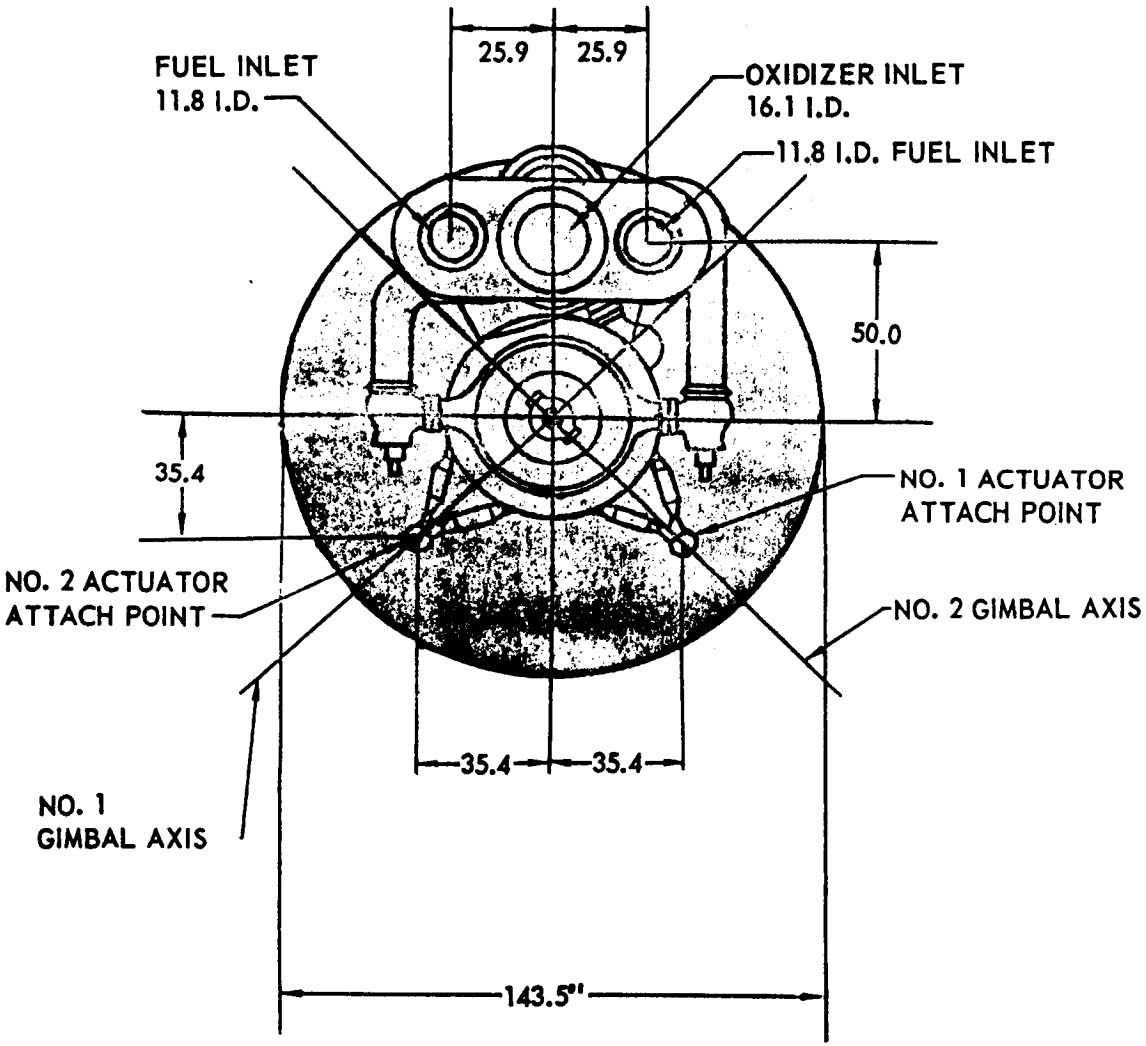

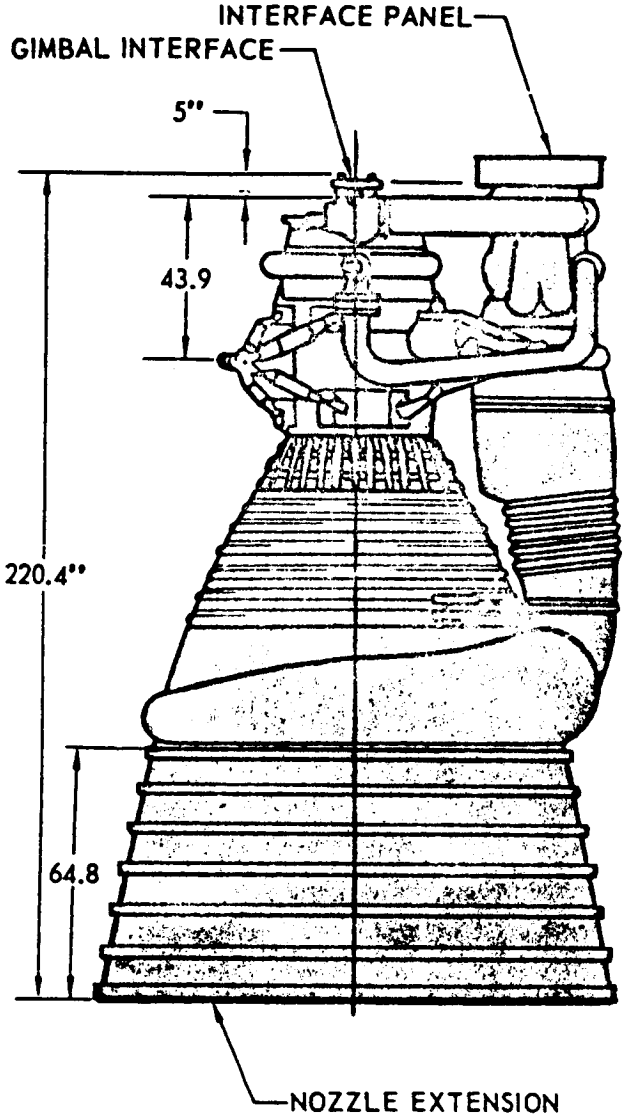

FIGURE 4.2-1. F-1 ENGINE

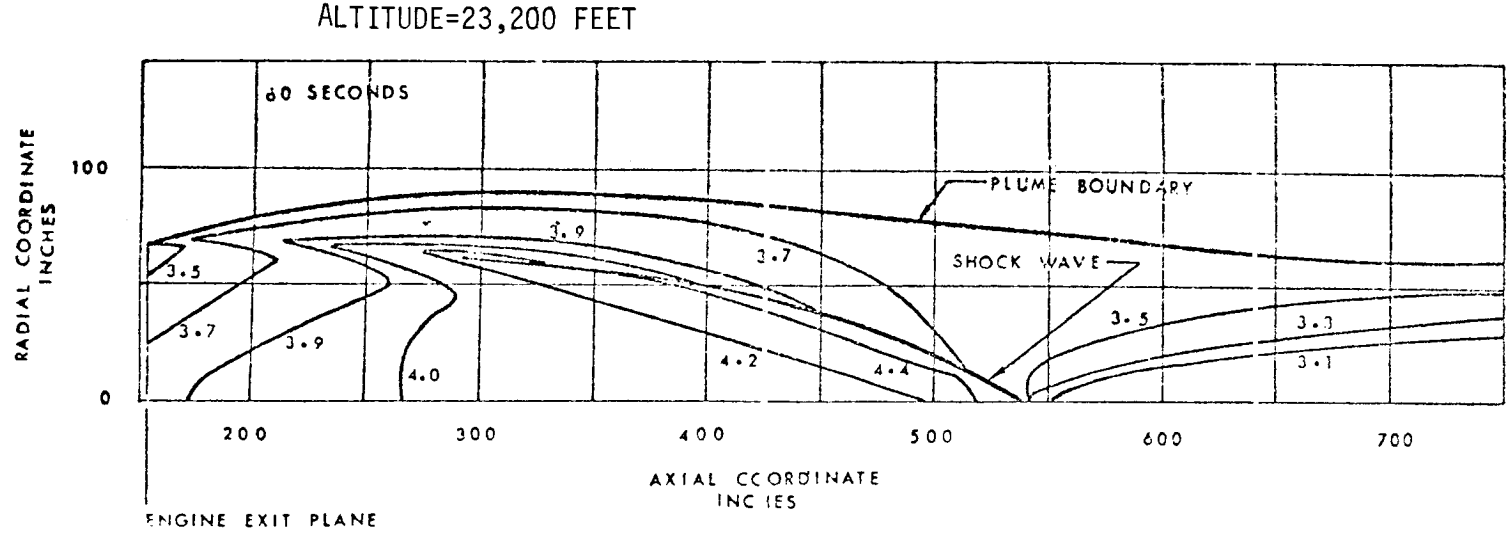

FIGURE 4.2-2 F-1 ENGINE PLUME MACH NUMBER CONTOURS

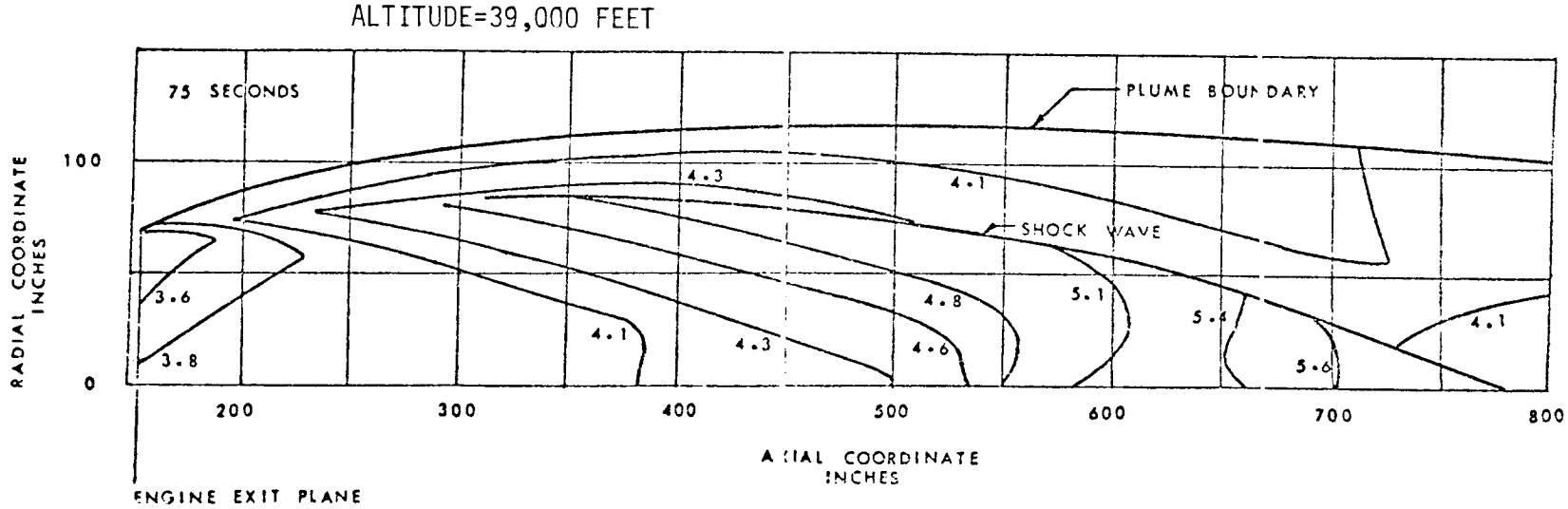

FIGURE 4.2-3 F-1 ENGINE PLUME MACH NUMBER CONTOURS

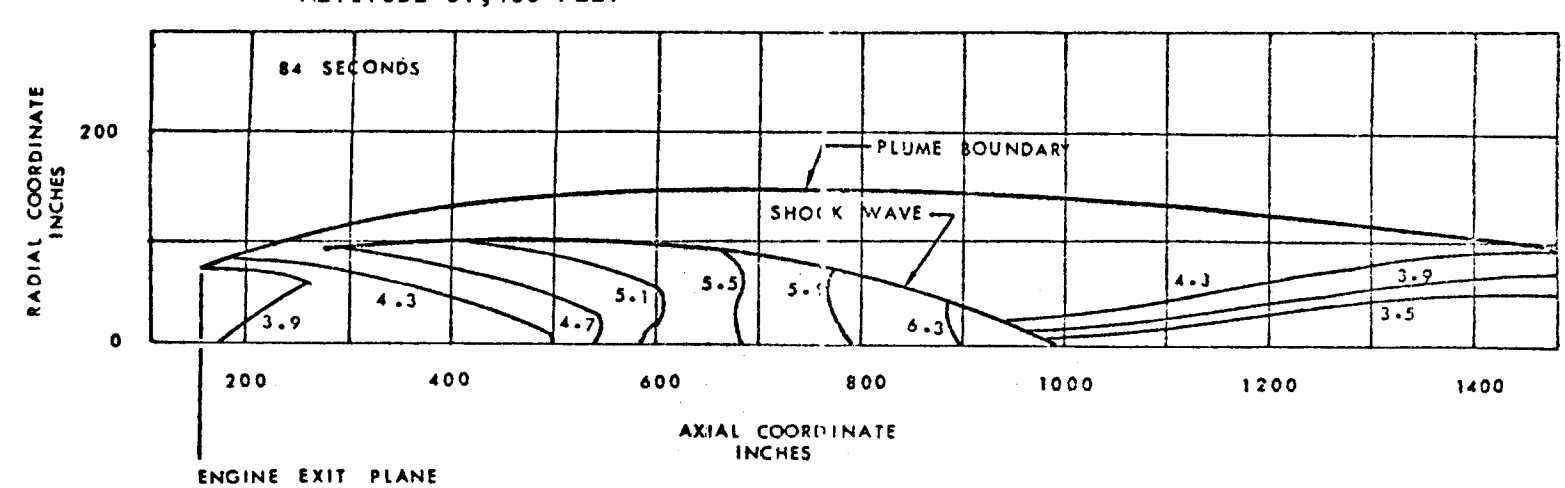

FIGURE 4.2-4 F-1 ENGINE PLUME MACH NUMBER CONTOURS

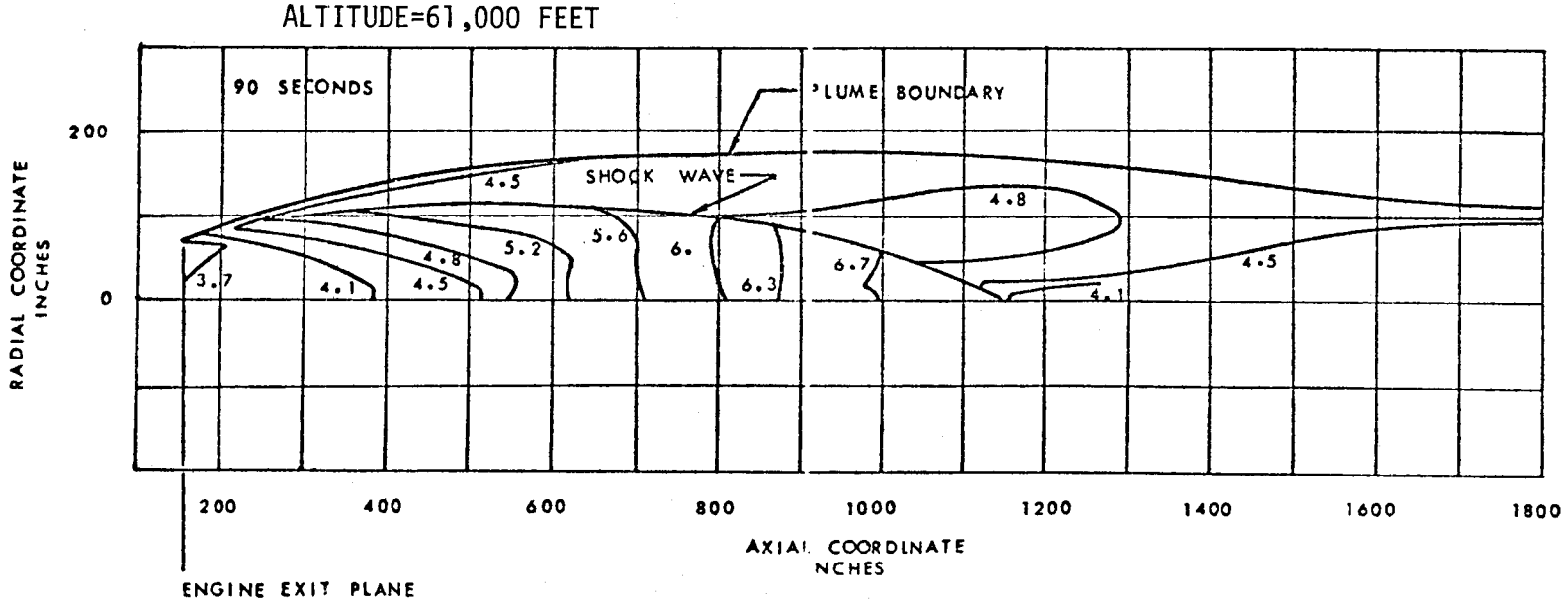

FIGURE 4.2-5 F-1 ENGINE PLUME MACH NUMBER CONTOURS

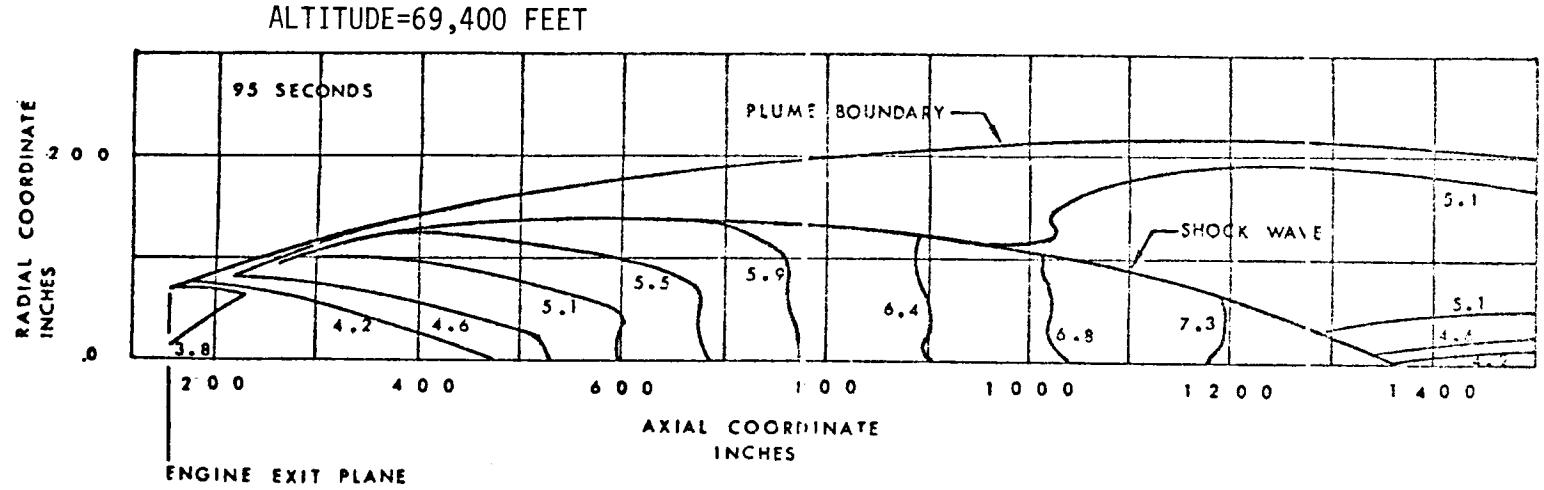

FIGURE 4.2-6 F-1 ENGINE PLUME MACH NUMBER CONTOURS

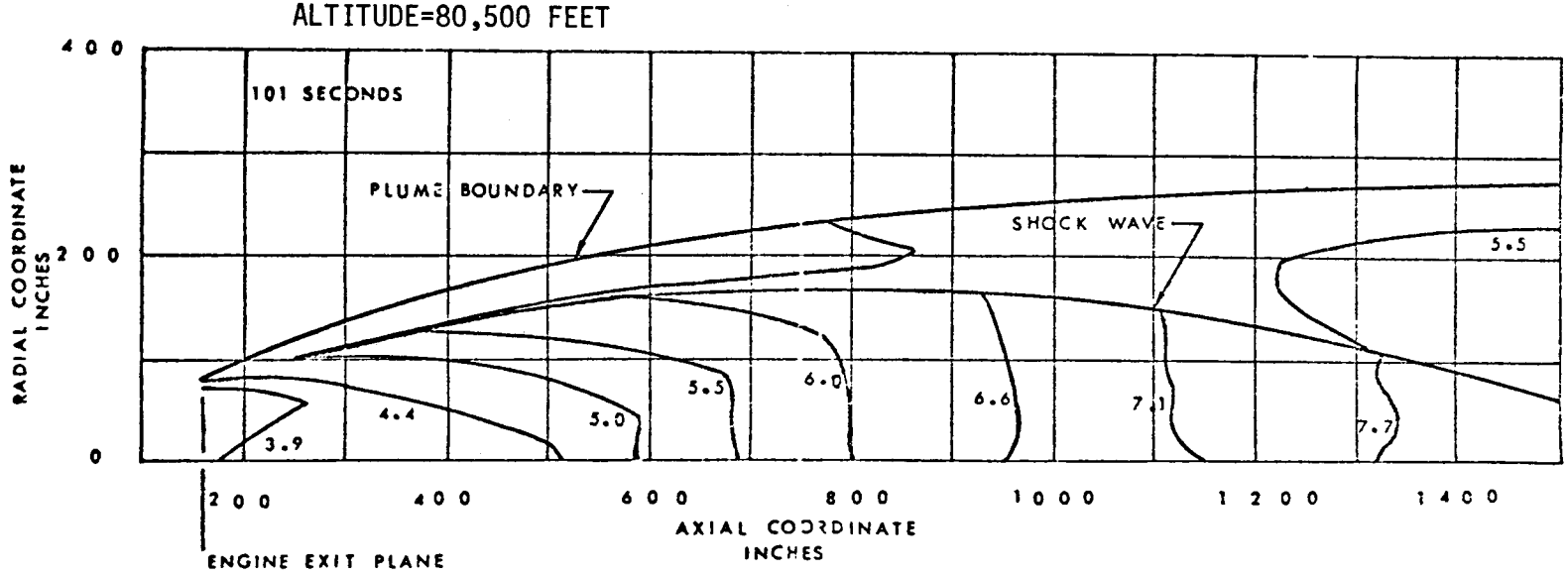

FIGURE 4.2-7 F-1 ENGINE PLUME MACH NUMBER CONTOURS

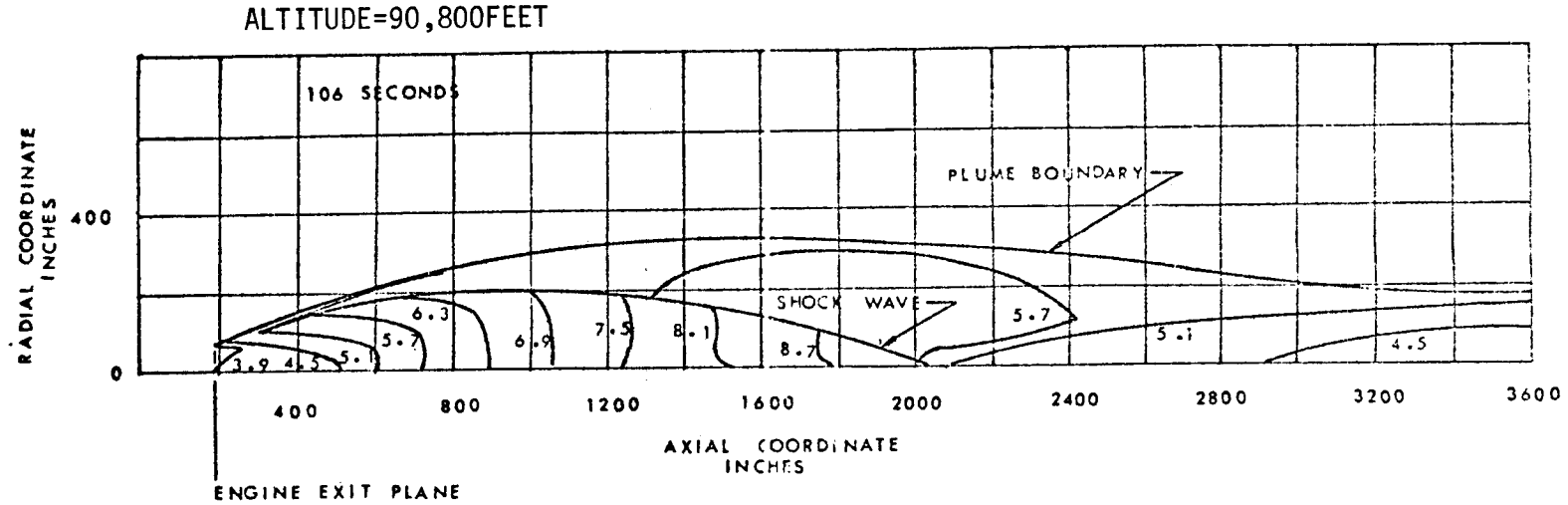

FIGURE 4.2-8 F-1 ENGINE PLUME MACH NUMBER CONTOURS

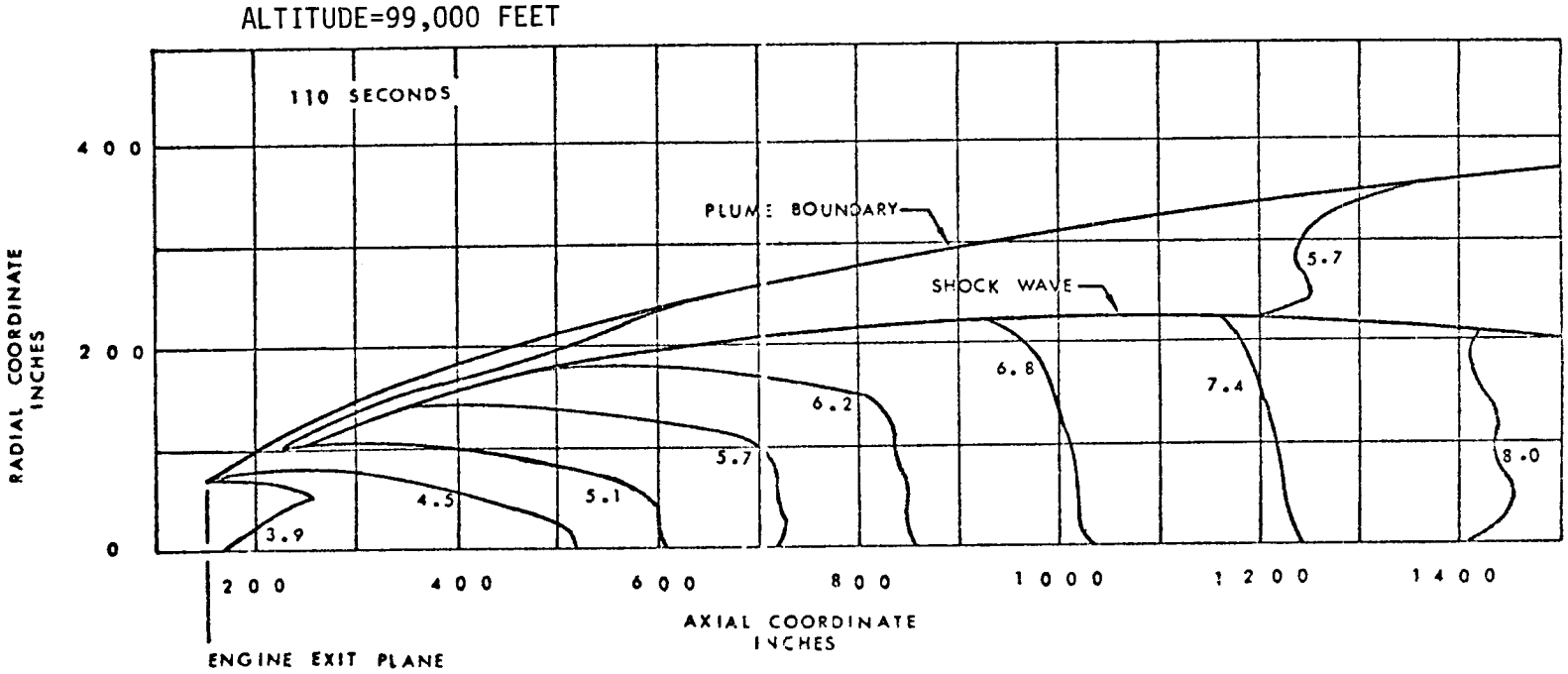

FIGURE 4.2-9 F-1 ENGINE PLUME MACH NUMBER CONTOURS

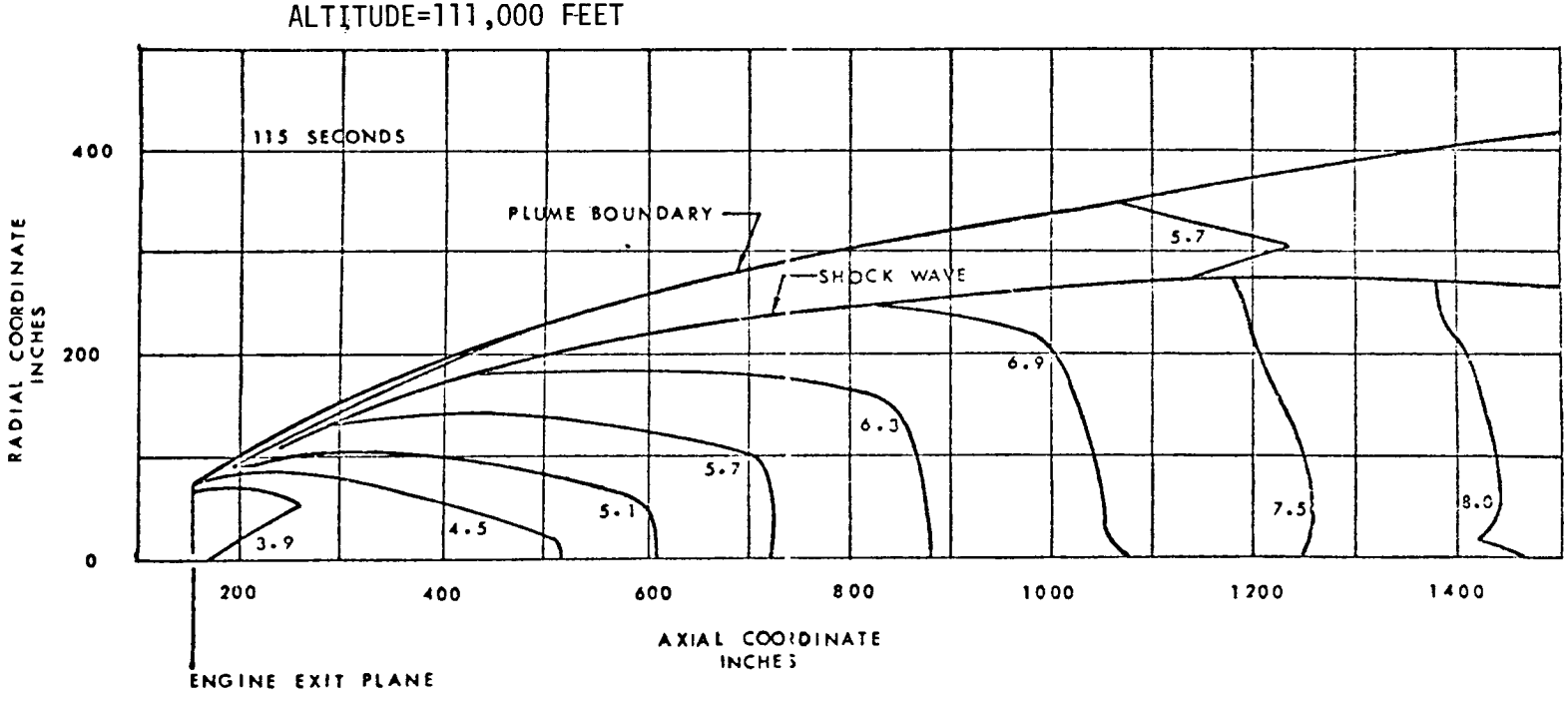

FIGURE 4.2-10 F-1 ENGINE PLUME MACH NUMBER CONTOURS

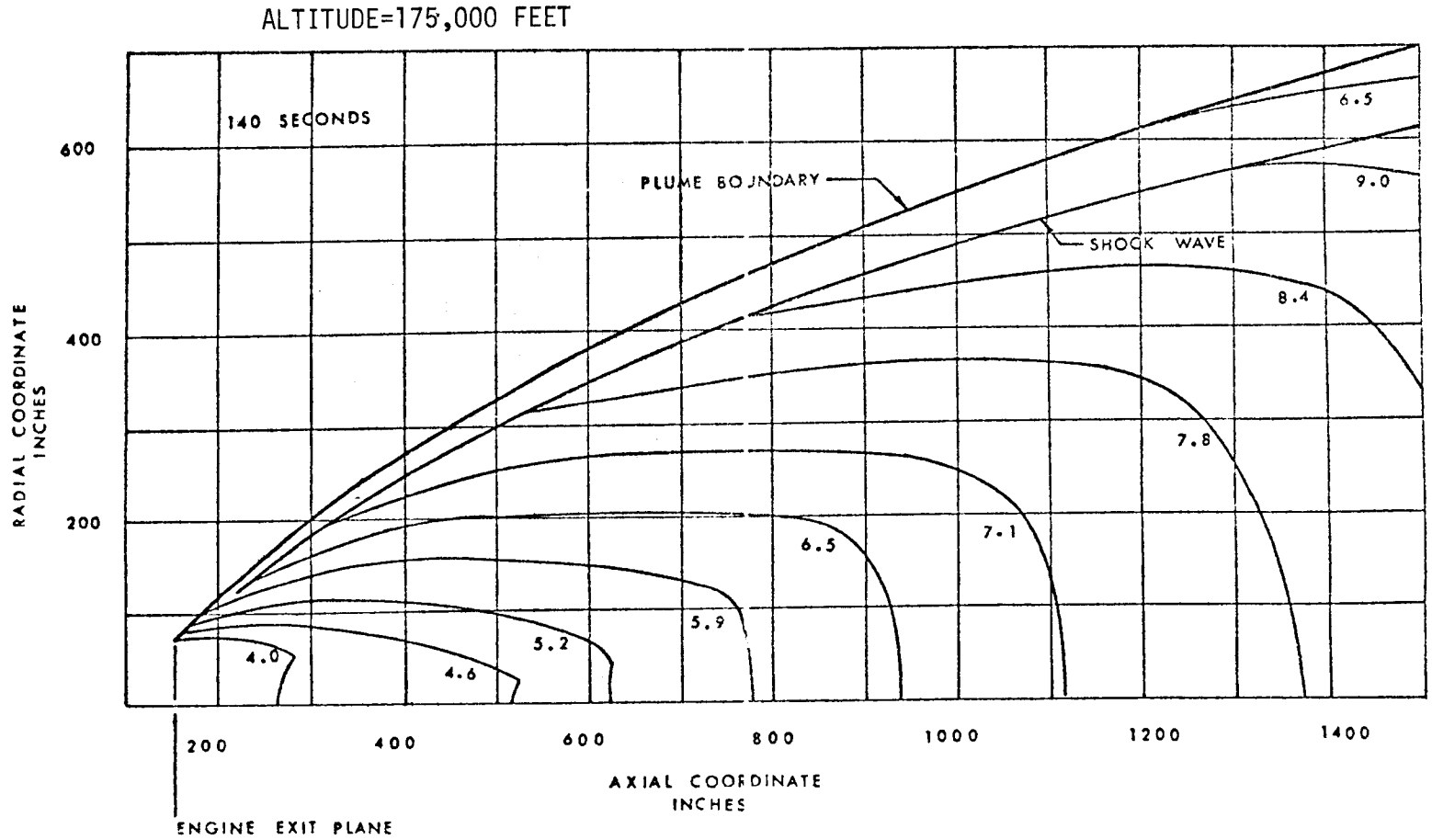

FIGURE 4.2-11 F-1 ENGINE PLUME MACH NUMBER CONTOURS

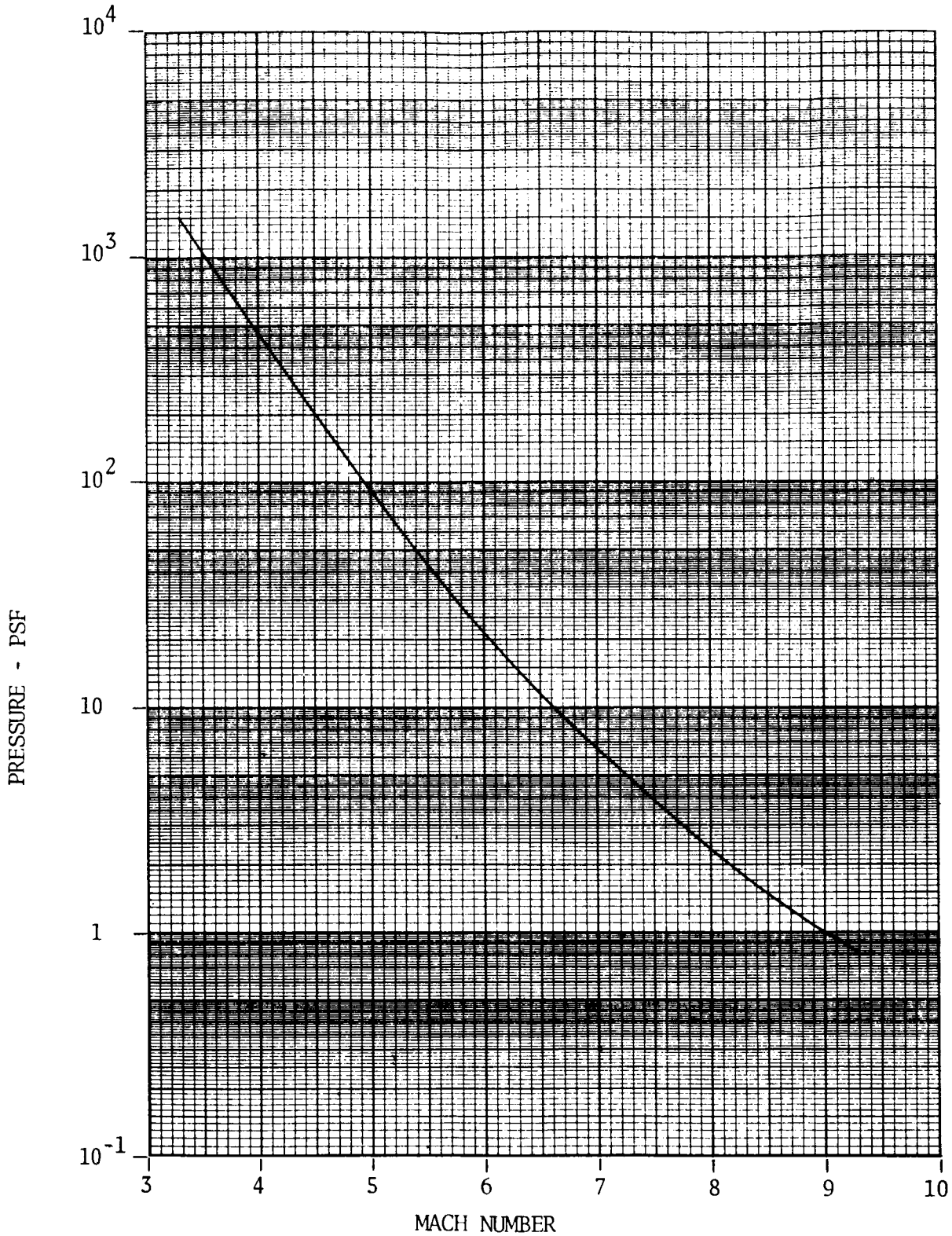

FIGURE 4.2-12. VARIATION OF PRESSURE FOR THE F-1 ENGINE PLUME MACH NUMBER CONTOURS

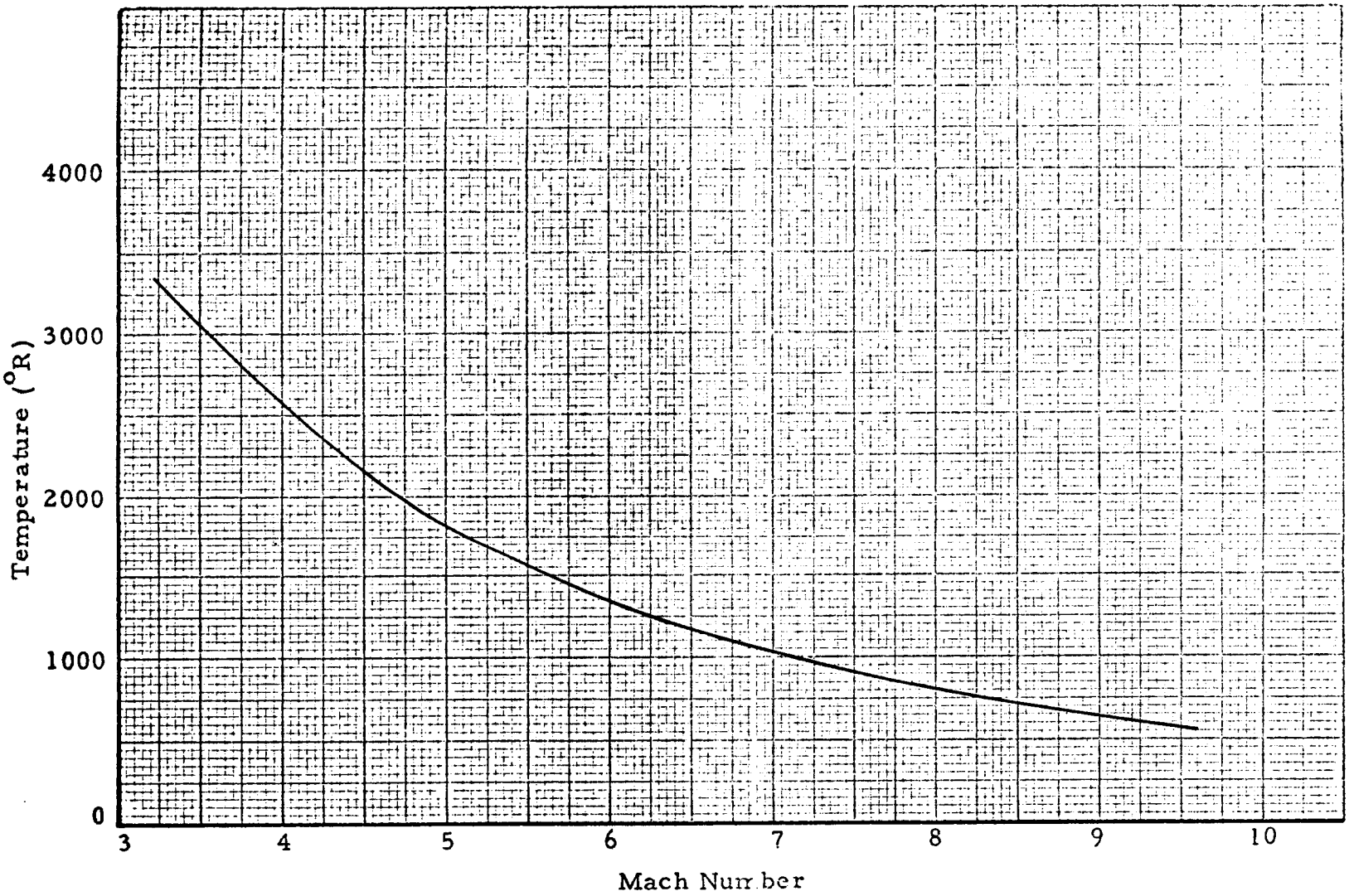

FIGURE 4.2-13 - Variation of Temperature for the F-1 Engine Plume Mach Number Contours

4.3 PREDICTION METHODS

S-IC stage base heating predictions have been based primarily upon model and flight test data for convection, and analytical and experimental methods for radiation.

Radiation

Prior to the first flight, the maximum value of radiation was believed to occur at sea level. The prediction method at that time consisted of a sea level prediction using a shell model (Figure 4.3-1) based on F-1 engine radiance measurements (Figure 4.3-2) from engine development tests and analytical methods to define form factors. The decrease in radiation with altitude was based upon Saturn I and IB flight data. S-IC short duration model data could not be used to substantiate the prediction because of poor turbine exhaust simulation and incorrect plume emissivity with the model.

After the first flights, it was determined that maximum values of radiation do not occur at sea level, but instead result from recirculated gases present in the base region at higher altitudes. Radiation at altitudes above sea level after the start of recirculation are currently defined using flight test data. Based upon flight data, it is evident that the earlier the gases are present in the base, the higher will be the temperature and, consequently, higher radiation will result. The ability to predict the radiation hump analytically is seriously limited and requires additional development of analytical tools.

Convection

Convective heating environment predictions were based originally on model and flight data from the Saturn I and model data from the S-IC. Analytical calculations were not adequate to predict convective heating because of the complexity of the flow field. The convective heating rates from the model tests were conservative and were tempered by the S-I flight data to originally define the prototype S-IC convective heating as shown in Figure 4.3-3. Model data were used to predict initial flow reversal into the base, base pressure, base gas temperature, and relative heating effects with changes in configuration.

Pressure

Base pressure predictions included an average base pressure for design criteria as well as base pressure distributions at five heat shield locations. The average analytical estimate was made using S-I Block I flight data and Korst's two-dimensional mixing theory. The base pressure distributions were based on S-I Block II flight data and S-I and S-IC model data.

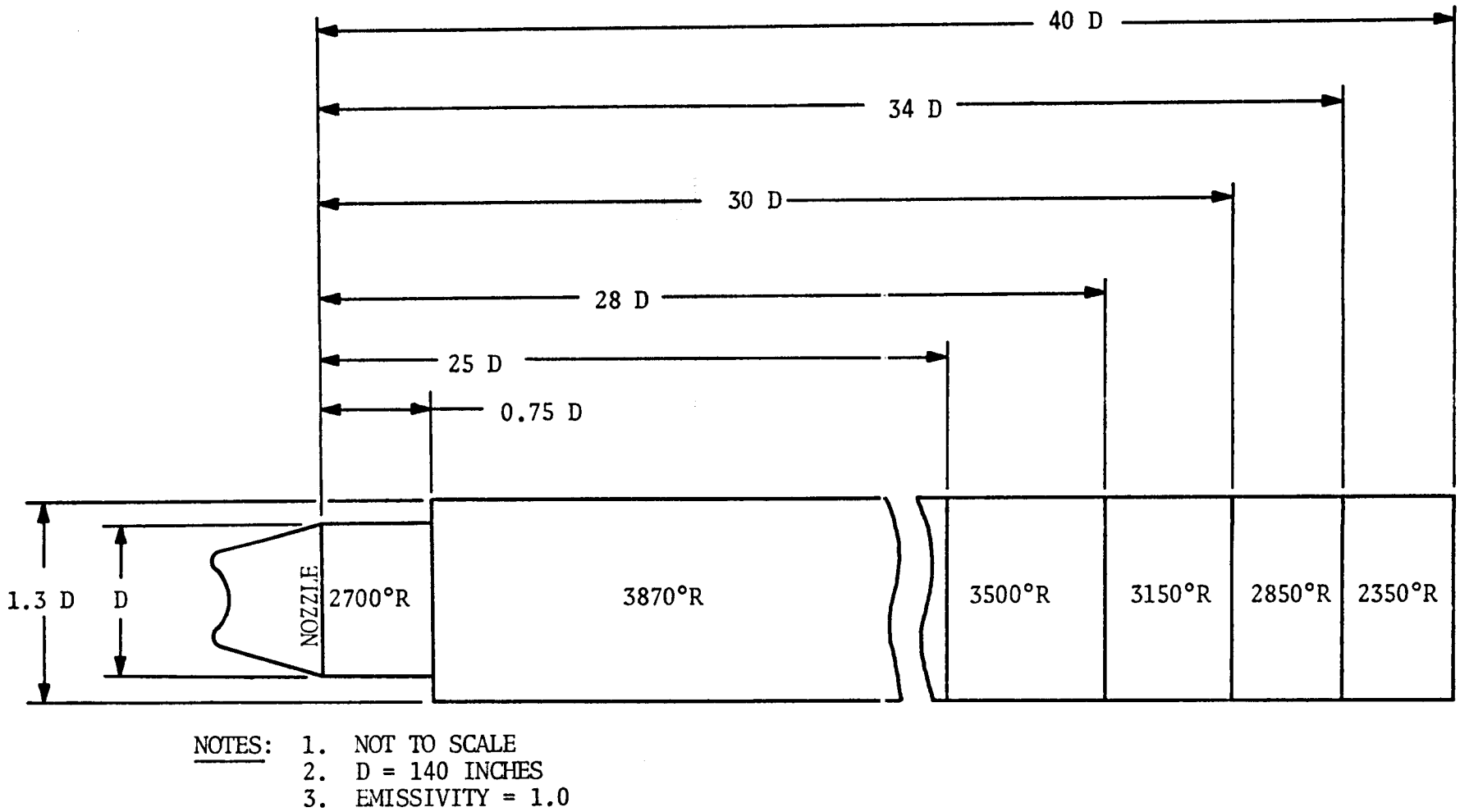

NOTES:
1. NOT TO SCALE
2. D = 140 INCHES
3. EMISSIVITY = 1.0

FIGURE 4.3-1. F-1 ENGINE SEA LEVEL PLUME MODEL

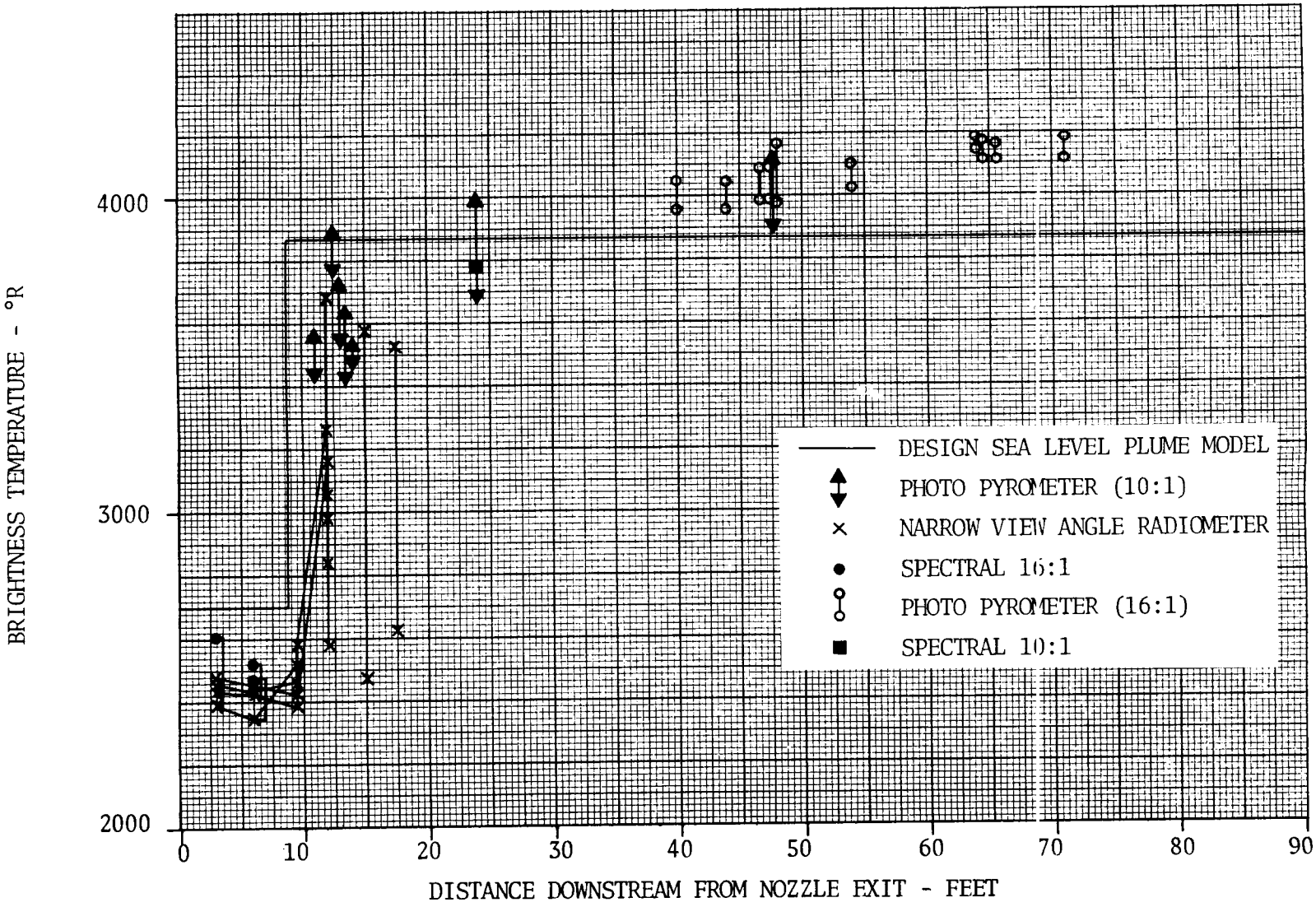

FIGURE 4.3-2. F-1 ENGINE PLUME PHOTOGRAPHIC PYROMETER DATA

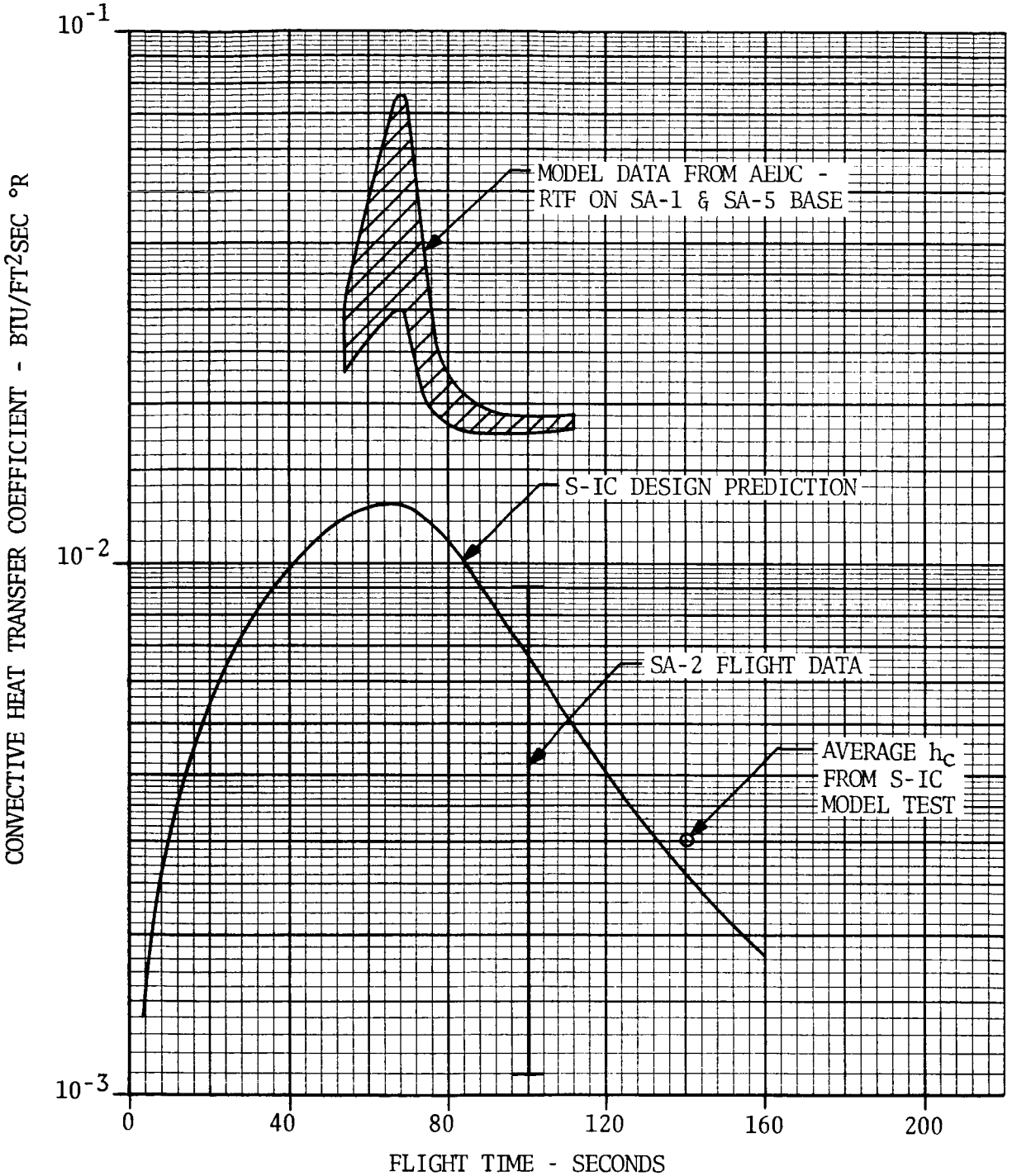

FIGURE 4.3-3. COMPARISON OF THEORETICAL AND EXPERIMENTALLY DERIVED HEAT TRANSFER COEFFICIENT

4.4 MODEL TESTS AND PARAMETRIC DATA

All Saturn V/S-IC stage model base heating tests were performed with a 1/45th scale test model utilizing the short-duration test technique. Tests were conducted at four separate test facilities, in the time period from February 1963 through August 1965. The test results provide S-IC stage base heating and pressure wind tunnel data through the first 100,000 feet of flight and trajectory altitude chamber data from 125,000 through 205,000 feet. The complete analysis of all tests was reported in a single two-volume document, Reference 4-5.

A general description of the model, instrumentation, test facilities, and test conditions is contained in the following paragraphs. Representative data are presented for all base locations with the basic configuration model (nearest simulation to the actual S-IC flown on the Saturn V). Data are also shown to illustrate the effects of parametric variations in base geometry and operating characteristics.

Model Description

The same general model was used throughout the test program with major modifications on the combustor from one test sequence to the next. The 2.22 percent scale test model of the Saturn S-IC stage, Figure 4.4-1, was designed by Cornell Aeronautical Laboratory (CAL) and fabricated by Marshall Space Flight Center, NASA. Detailed descriptions of the model, including the engines, engine fairings, scoops and flow deflector configurations, and base plate are included in Reference 4-5, and are shown in Figures 4.4-2 through 4.4-4.

Model Operation

A schematic of the model propulsion system is shown in Figure 4.4-1. The system employed the standard short-duration techniques for metering the gases, mixing, ignition, and discharging the gases. These techniques have been described in detail in CAL documentation and will not be discussed in this section. The S-IC model had approximately 20 to 30 milliseconds of steady state operation.

Two methods of turbine exhaust simulation were used with the S-IC model. Ethylene was originally used for a few low altitude runs because it more nearly simulates the actual gas conditions of the flight vehicle. It did burn in the base but it coated the heating gages so badly with soot that it was impractical to use. Hydrogen gas was used for the remaining tests since it had a wide flammability limit but did not impose a sooting problem. The hydrogen was injected at a rate that simulated the caloric content of the unburned fuel in the prototype turbine exhaust.

TABLE 4.4-1. COMBUSTION PARAMETERS

PARAMETER	GOX-ETHYLENE	LOX RP-1
O/F	2.20 - 2.30	2.25
T_C	6830 - 6870°R	6400°R
P_C	1030 - 1100 psia	1050 psia
γ	1.22 - 1.206	1.223
R	73.6 - 72.5	70

Test Conditions and Facilities

Table 4.4-2 lists the test conditions for the four facilities used in the test program. Test and trajectory total temperature and altitude comparisons are shown in Figure 4.4-5. The dates of the tests are shown in parentheses.

Each model configuration is described by groups of letters and numbers using the following format:

a)	Forebody	B
b)	Engine Fairing Length	FS
c)	Deflector Size	D
d)	Engine Fairing Scoop Size	SC
e)	Engines	N
f)	Base Plate	PL

Subscript numbers indicate the configuration variations and are defined in Figures 4.4-1, 4.4-3 and 4.4-4. Table 4.4-3 is a compilation of the various configurations tested in each of the facilities.

Instrumentation

The short-duration instrumentation, provided by CAL, consisted of: 1) thin-film heat transfer gages for the measurement of short duration heating, (2) CAL developed piezo-electric pressure transducers to measure short duration surface pressures, (3) a pressure rake to measure boundary layer total pressure distribution, and (4) Kistler piezo-electric crystal transducers and chromel-alumel thermocouples to measure model performance. Detailed descriptions of the short duration instrumentation can be obtained from References 4-6 through 4-8. Calibration procedures for the S-IC short duration tests are contained in Reference 4-9.

TABLE 4.4-2. FACILITY TEST CONDITIONS

FACILITY	MACH	TEST ALTITUDE (FEET)	TRAJECTORY (FEET)
Lewis 8 by 6 (May - August 1965)	0.55	1,600	12,000
	0.80	7,400	18,000
	1.00	13,400	26,000
	1.35	22,600	35,000
	1.66	29,400	43,000
	1.95	35,200	50,000
Lewis 10 by 10 (October 1963)	2.00	51,000	51,000
	2.50	66,000	66,000
	3.00	81,000	81,000
	3.50	96,000	96,000
	3.50	150,000	96,000
CAL 8 by 8 (February 1963)	0.60	13,000	13,000
	0.80	18,000	18,000
	1.00	26,000	26,000
	1.20	34,000	34,000
CAL Altitude Chamber (June 1963)	No External Flow	125,000	125,000
		135,000	135,000
		145,000	145,000
		155,000	155,000
		165,000	165,000
		175,000	175,000
		185,000	185,000
		195,000	195,000
		205,000	205,000

TABLE 4.4-3. CONFIGURATIONS TESTED

FACILITY	CAL 8 x 8	LeRC 8 x 6	LeRC 10 x 10	CAL Altitude
FOREBODY	B_1	B_4	B_3	B_1
CONFIGURATION				
FS_1N_1-5	PL_1	PL_1, PL_3	PL_1	PL_1, PL_3
FS_4N_1-5		PL_1	PL_1	
$FS_1D_2N_1$-5		PL_1, PL_2		
$FS_4D_2N_1$-5		PL_1		
$FS_4SC_1N_1$-5				PL_1
$FS_1D_1SC_1N_1$-5	PL_1		PL_1	
$FS_1D_1SC_2N_1$-5		PL_1, PL_2		
$FS_2SC_1N_1$-5	PL_1			
$FS_4D_1SC_1N_1$-5	PL_1			
$FS_1D_3SC_1N_1$-5	PL_1			
$FS_1D_3SC_2N_1$-5			PL_1	
FS_1N_7			PL_1	PL_1
$FS_1D_1N_7$		PL_1		
$FS_1D_2N_7$		PL_1		
$FS_1N_{G_3}N_{G_4}$			PL_1	PL_1
$FS_1N_{G_5}N_{G_6}$			PL_1	PL_1
$FS_1D_2N_{G_7}N_{G_8}$		PL_1, PL_2		
$FS_1D_1SC_2N_{G_7}N_{G_8}$		PL_1		
$FS_1D_2N_{G_{10}}N_{G_{11}}N_{G_{12}}$		PL_1, PL_2		

NOTES:
1. PL_1 - base plate instrumented with both heating and pressure
   PL_2 - base plate is instrumented only for pressure
   PL_3 - Hot base plate
2. Base plate shown in table indicates configurations tested and facilities used.

Polaroid pictures record the oscilloscope traces of the instrumentation outputs. Data were measured directly from the pictures.

Base instrumentation consisted of total heating, radiation heating, and static pressure gages on the three base plates. The instrumentation locations on each base plate are shown in Figure 4.4-6. Figures 4.4-7 and 4.4-8 show the external and internal nozzle instrumentation. The base of the fin and the engine fairing are instrumented as shown in Figure 4.4-9.

Model Development

Considerable development of the short-duration technique occurred during the test program. Non-symmetrical exhaust was noted in the first tests in the Cornell Transonic Tunnel. CAL revised the mixer plate and testing was resumed in the CAL high-altitude facility. Flow symmetry nozzles continued unsatisfactory, and the means for measuring the oxygen-to-fuel (O/F) ratio was believed to be unreliable.

Prior to tests in the Lewis Research Laboratory 10-by-10-foot supersonic tunnel, the combustor was redesigned and a splash plate was introduced. Results from this series of tests indicate that radiation and convection was considerably lower than estimated. Data repeatability was poor and motion pictures indicated continued combustion instability.

Before testing in the Lewis transonic tunnel extensive tests were run at CAL and some combustor redesign was accomplished. The instabilities of the previous test were traced to liquefaction of the ethylene. Preheating the ethylene eliminated the problem.

Configuration changes also occurred during the two years in which tests were conducted. Consequently, the configurations tested in one facility may be inconsistent with those of another facility. For example, during two tests (CAL Altitude Chamber and LRC 10-by-10), two gimbal patterns were run. These represented extreme cases; outboard engines gimbaled as far as they physically could toward each other and toward the center engine. Before the LRC 8-by-6 test was conducted a nominal prototype gimbal pattern was established. Because of time limitations, this was the only gimbal pattern tested in the LRC 8-by-6 tunnel. Therefore, the plots in this section showing the effects of gimbaling do not have the same gimbal pattern for the entire altitude range.

Test Results

Detailed data presentations including most of the pertinent model test results are shown in Volumes 1 and 2 of Reference 4-5. The format in the Reference was to show composite data in Volume 1 and specific results from each test facility in Volume 2. The procedure followed in this section of the handbook is to elaborate on the composite data with specific emphasis on the parametric comparisons. In general, data from all four test

4.4 (Continued)

facilities will be combined and plotted versus altitude. The figures and the purpose of each figure comparison are summarized in the table below.

FIGURE NUMBER	PURPOSE OF PRESENTATION
Figures 4.4-1 through 4.4-9	Model Description and Instrumentation
Figures 4.4-10 through 4.4-13	Nominal Environments
Figures 4.4-14 through 4.4-16	Turbine Exhaust Effect
Figures 4.4-17 through 4.4-19	Engine Fairing Length Effect
Figures 4.4-20 through 4.4-22	Scoops and Flow Deflector Effect
Figures 4.4-23 through 4.4-25	Gimbaling Effect
Figures 4.4-26 through 4.4-28	Center Engine Out Effect
Figure 4.4-29	Engine On - Engine Off Base Pressure
Figures 4.4-30 through 4.4-36	Internal Engine Environment
Figures 4.4-37 and 4.4-38	Wall Temperature Effect
Figure 4.4-39	Model Boundary Layer Thickness
Figures 4.4-40 through 4.4-52	Environment Distributions over Heat Shield

Brief descriptions of the model test data comparisons are included in the following paragraphs. The discussion will be limited to data comparison only. Comparisons of the model data with theoretical predictions and with Saturn V/S-IC stage flight data are included in Section 4.6. Detailed discussions of the data repeatability, exhaust flow composition, and flow establishment are in included in Reference 4-5 and are not presented in the handbook.

Nominal Environments

Average radiation and convective heating rate data and base pressure data are shown in Figures 4.4-10 and 4.4-11 for the nominal configuration heat shield and center engine, respectively. The nominal configuration, designated $FS_1N_{1-5}PL_1$, has nominal length engine fairings, no scoops and flow deflectors, and the engines in the null positions. All data shown were taken from runs without turbine exhaust simulation.

Radiation heating rates at various base locations are shown in Figure 4.4-12, including data measured on the heat shield, engine, engine fairing and trailing edge of the fin. A similar comparison with measured convective heating rates is presented in Figure 4.4-13.

4.4 (Continued)

Turbine Exhaust Effect

The effect of turbine exhaust simulation on the heat shield environments can be seen in the comparisons of Figures 4.4-14, 4.4-15 and 4.4-16. All data shown for the configuration with turbine exhaust utilized hydrogen simulation. In general, the effect of turbine exhaust injection on base region radiation is negligible, i.e., within the scatter and accuracy of the data. A noticeable increase of approximately 300 percent in convective heating occurred with turbine exhaust in the CAL 8-by-8 test which encompassed the transonic range from M = 0.6 to 1.2. Convective heating measured at the other test facilities was unaffected by the addition of turbine exhaust.

Engine Fairing Length Effect

Data from a short fairing length configuration is compared with the nominal configuration data in Figures 4.4-17 through 4.4-19. At the lower altitudes reducing the fairing length reduced the heat shield radiation and slightly increased the heat shield convection. No effect on either environment component was experienced at the higher altitudes (above 40,000 feet).

Scoops and Flow Deflector Effect

The addition of nominal scoops and flow deflectors to the basic configuration produced the effect on the environments shown in Figure 4.4-20 through 4.4-22. A very slight increase in radiation was noticed at the lower altitudes. A significant reduction in convective heating occurred on the heat shield (Figure 4.4-22) at lower altitudes up to 100,000 feet, indicating that during aspiration the scoops and deflectors aid in scavenging the base region of recirculated gases. The engine fairings and engines show some reduction in convective heating also.

Gimbaling Effect

The most pronounced effect of gimbaling was the increased convective heating which occurred at the higher altitudes as seen in Figures 4.4-23 through 4.4-25. Radiation heating was not greatly affected, although some reduction in average heat shield radiation was noted in the sea level to 40,000-foot range.

Center Engine Out

The effect of an inoperative center engine on the base region radiation and convective heating environments can be seen in Figures 4.4-26 through 4.4-28. As seen in Figure 4.4-26, average radiation to the heat shield is reduced with the center engine out at the lower altitudes. Convective heating is also reduced throughout the entire range of altitudes tested.

4.4 (Continued)

Engine-On - Engine-Off Base Pressure

Static pressures were measured on the heat shield prior to engine firing and during engine firing with the PL_1 base plates. Pressures from the CAL 8-by-8 test and Lewis 10-by-10 test, which were on trajectory, are compared in Figure 4.4-29. The upper curve compares engine-on and engine-off base pressure for the baseline configuration without scoops and deflectors. A similar comparison for the nominal scoop and deflector configuration is compared in the lower curve. In both curves, it is noted that when the engines are operating, there is a distinct base pressure increase. It is also evident that the no-engine-flow base pressure is higher with scoops on as would be expected.

Internal Engine Environment

Radiation heating to the internal surfaces of the non-operating center engine is shown in Figures 4.4-30 through 4.4-33. A limited amount of data is also shown on Figures 4.4-30 and 4.4-31 for an outboard engine out. As seen in these figures, the internal engine radiation is slightly higher than the base heat shield radiation levels and exhibits a similar drop-off with altitude. Due to the low magnitudes of the measured radiation and scatter in the data, there is no significant difference noted in the data measured near the nozzle lip and that measured internally near the throat.

Internal engine convective heating is shown in Figures 4.4-34 through 4.4-36. Convective heating inside the center engine is severe especially at the higher altitudes as seen in Figure 4.4-36. A significant decrease is also noted between the lip and internally near the throat.

Wall Temperature Effect

A special base plate was fabricated with internal electrical coils so that convective heating rates could be obtained at various wall temperatures. The equation and sketch below illustrate the procedure used to calculate recovery temperature and heat transfer coefficients:

$$q = h_c \, (T_r - T_w)$$

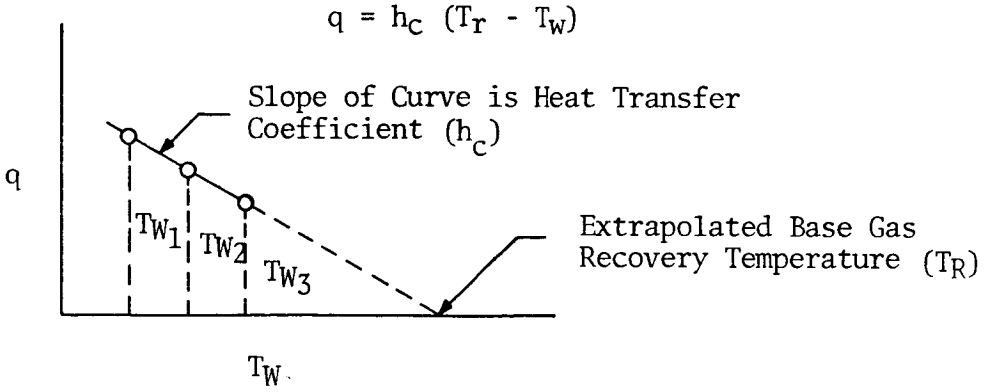

Heating rate data were obtained at three wall temperatures; 350°F, 200°F, and the cold base temperature of 130°F. The heating rates are plotted as a function of wall temperature and the line through the data is then extrapolated to the zero heating rate point which is the adiabatic wall temperature or assumed base gas recovery temperature. The slope of the curve corresponds to the heat transfer coefficient as is evident from the equation.

Typical test results in the transonic range are shown in Figure 4.4-37. The base recovery temperature ranged from 400°F to 600°F for all configurations tested. The heat transfer coefficients were in the range of 0.008 to 0.016 Btu/ft^{2}sec-°R. Data from this portion of the test are of low quality, containing a large amount of scatter. Some of the data even indicated a physical impossibility, an increase in heating rate with increase in wall temperature. However, the results are generally substantiated by the convection heating rate data.

Typical test results at high altitude (165,000 feet) are shown in Figure 4.4-38. Convective heating rates were measured at wall temperatures of 80°F, 400°F, 700°F and 900°F. The average recovery gas temperature obtained at this altitude was 1500°F. Problems were encountered which made the data interpretation difficult. The total heating rates with the hot base at ambient conditions do not compare well with those obtained using the non-heated (cold) base. Radiation heating rates are considerably higher on the hot base plate. It was expected that the radiation heating would be lower. For these reasons, the recovery gas temperature obtained is questionable.

Model Boundary Layer Thickness

Boundary layer measurements were made in the three wind tunnels by a total pressure rake. Actual total pressure in the boundary layer is determined by correcting the probe readings for the normal shock that stands in front of the rake. The boundary layer edge is defined as the point at which 0.998 of the free-stream velocity is reached. In all three tunnels, the measured boundary layer thickness coincides with the turbulent flow estimate as seen in Figure 4.4-39.

Environment Distributions Over Heat Shield

Radiation heating rate distributions across the heat shield are shown in Figures 4.4-40 through 4.4-43. At the lower altitudes, the maximum radiation rate is recorded at a radial position of r/R = 0.75 between outboard engines. At higher altitudes, the magnitudes are quite low and there is no significant variation with radial position.

4.4 (Continued)

Convective heating distributions across the heat shield are shown in Figures 4.4-44 through 4.4-49. At lower altitudes, a consistent trend was not noted in the location of the maximum value. However, at the higher altitudes, convective heating increases in the outboard direction with maximum values occurring at approximately r/R = 0.775.

Base pressure distributions are shown in Figures 4.4-49 through 4.4-52. In general, minimum base pressure (static) occurred near r/R = 0.65 indicating maximum velocity over the heat shield at this location. The radial position r/R = 0.65 is located approximately at the minimum vent area between outboard engines. Base static pressure on either side of the minimum vent area (outboard or inboard) has approximately the same magnitude.

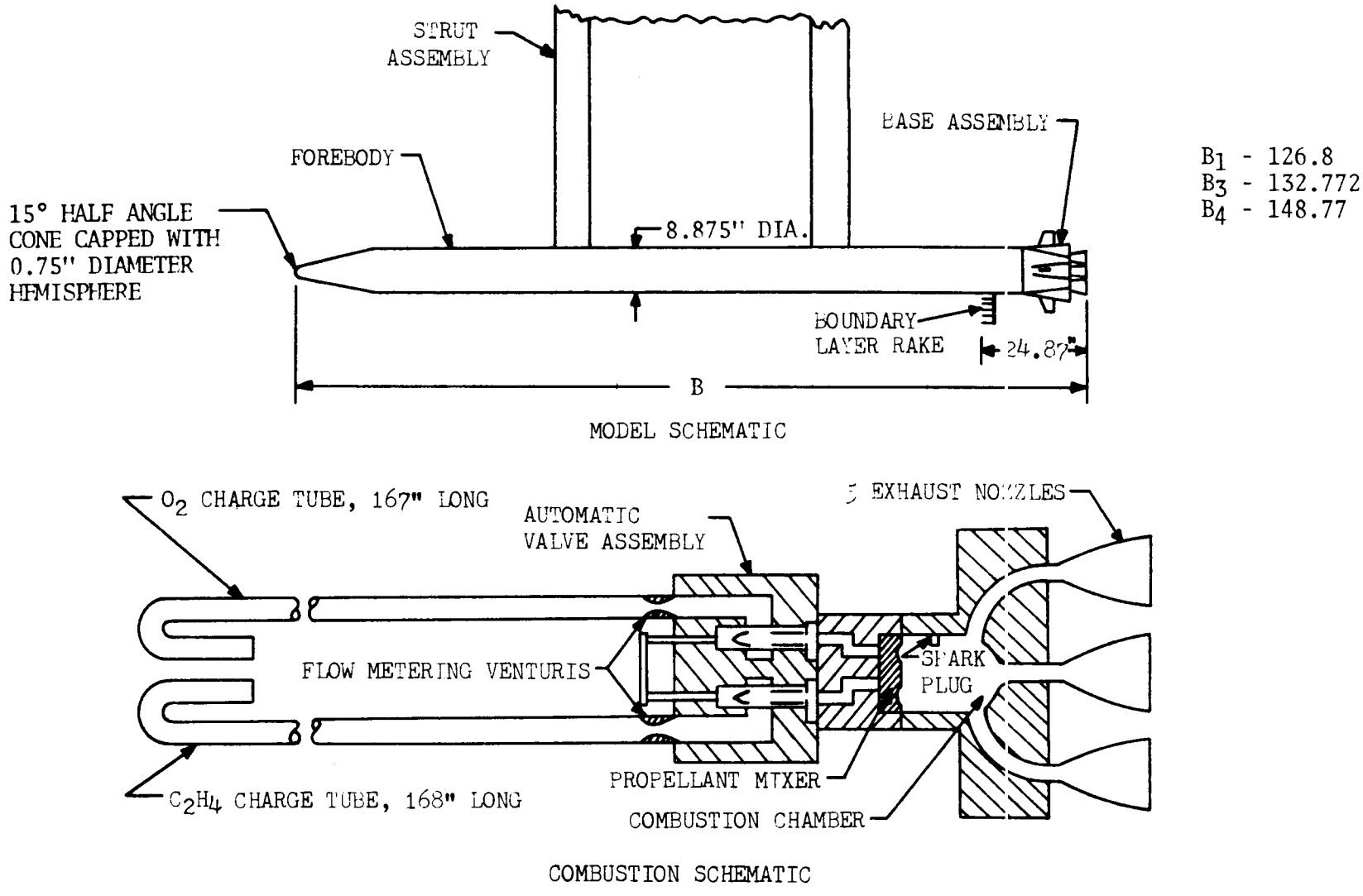

FIGURE 4.4-1. MODEL COMBUSTION SYSTEM

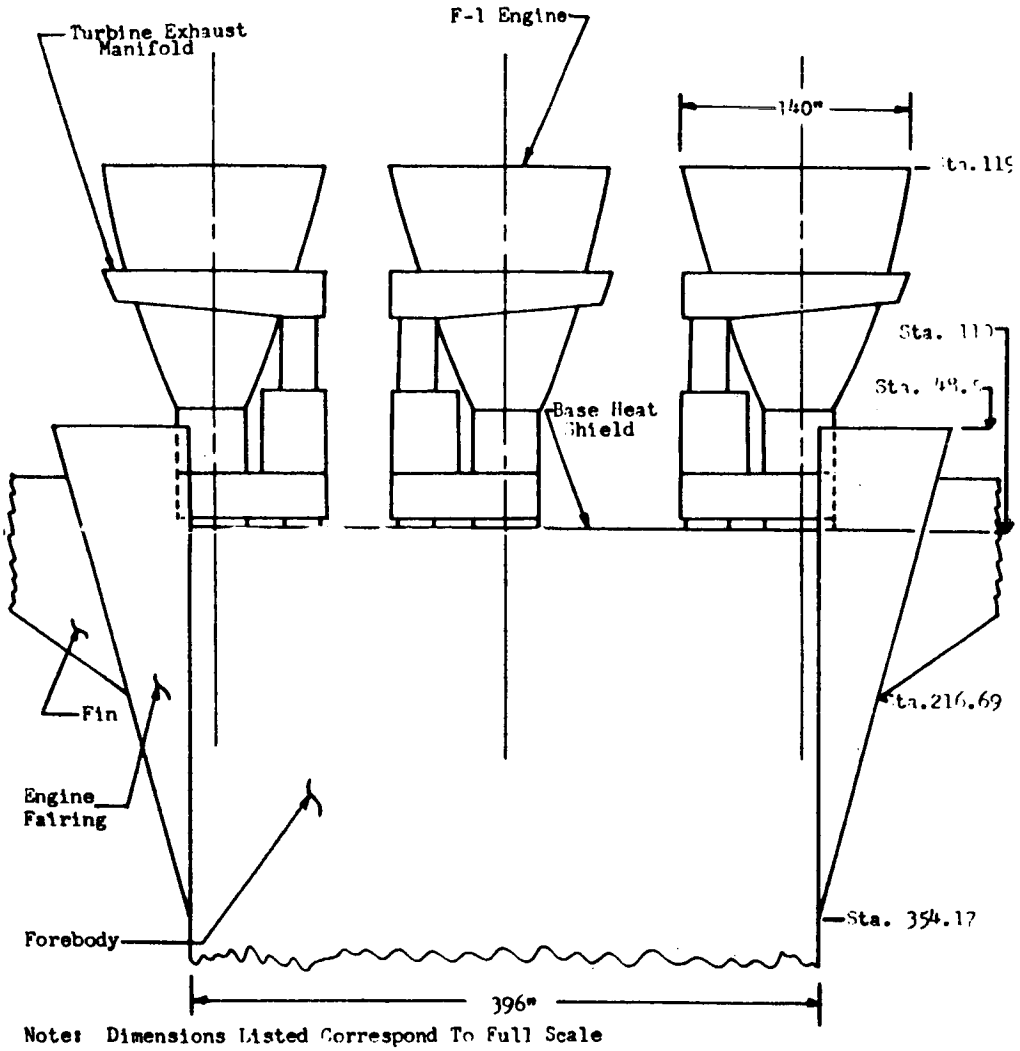

NOTE: Turbine exhaust injected normal to nozzle internal surface at 10:1 area ratio by two rows of 52, 0.0595-inch diameter holes spaced on 0.0714-inch staggered centers.

FIGURE 4.4-2. MODEL BASE GEOMETRY

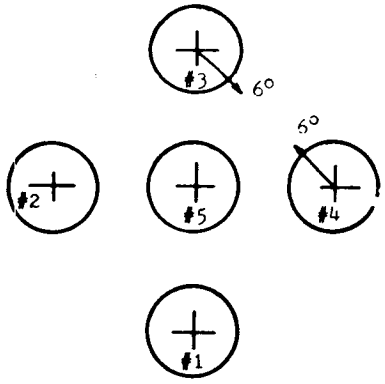

GIMBAL PATTERN #1 ($N_{G_3}N_{G_4}$)

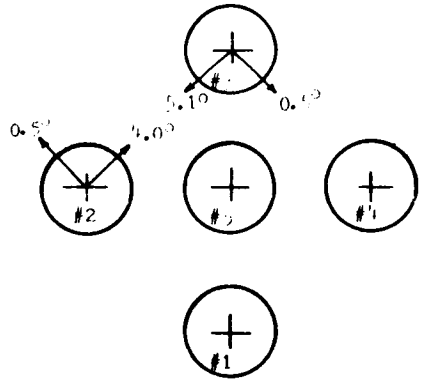

GIMBAL PATTERN #4 ($N_{G_9}N_{G_{10}}$)

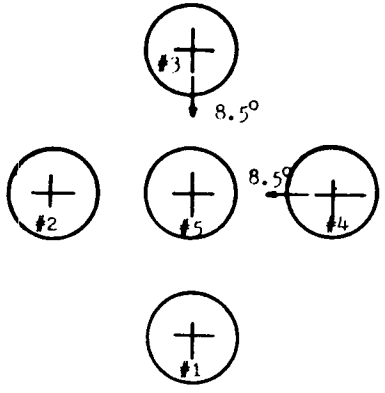

GIMBAL PATTERN #2 ($N_{G_5}N_{G_6}$)

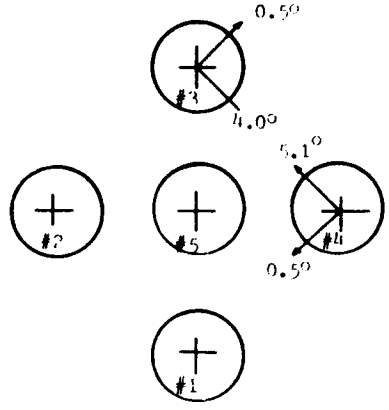

GIMBAL PATTERN #3 ($N_{G_7}N_{G_8}$)

NOTE: N_7 AND N_{10} INDICATE PLUGGED AND INSTRUMENTED ENGINE LOCATED AT ENGINE POSITIONS 5 AND 2 RESPECTIVELY (SEE NOMENCLATURE)

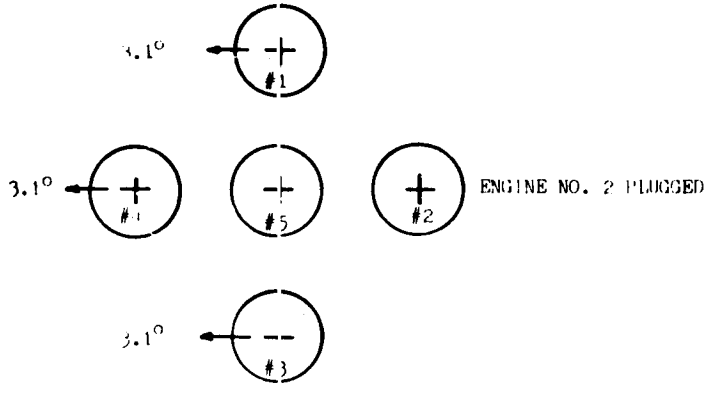

NOTE: ARROWS INDICATE DIRECTION OF ENGINE GIMBAL

GIMBAL PATTERN #5 ($N_{G_{11}}N_{G_{12}}N_{G_{13}}$)

FIGURE 4.4-3. GIMBAL PATTERNS

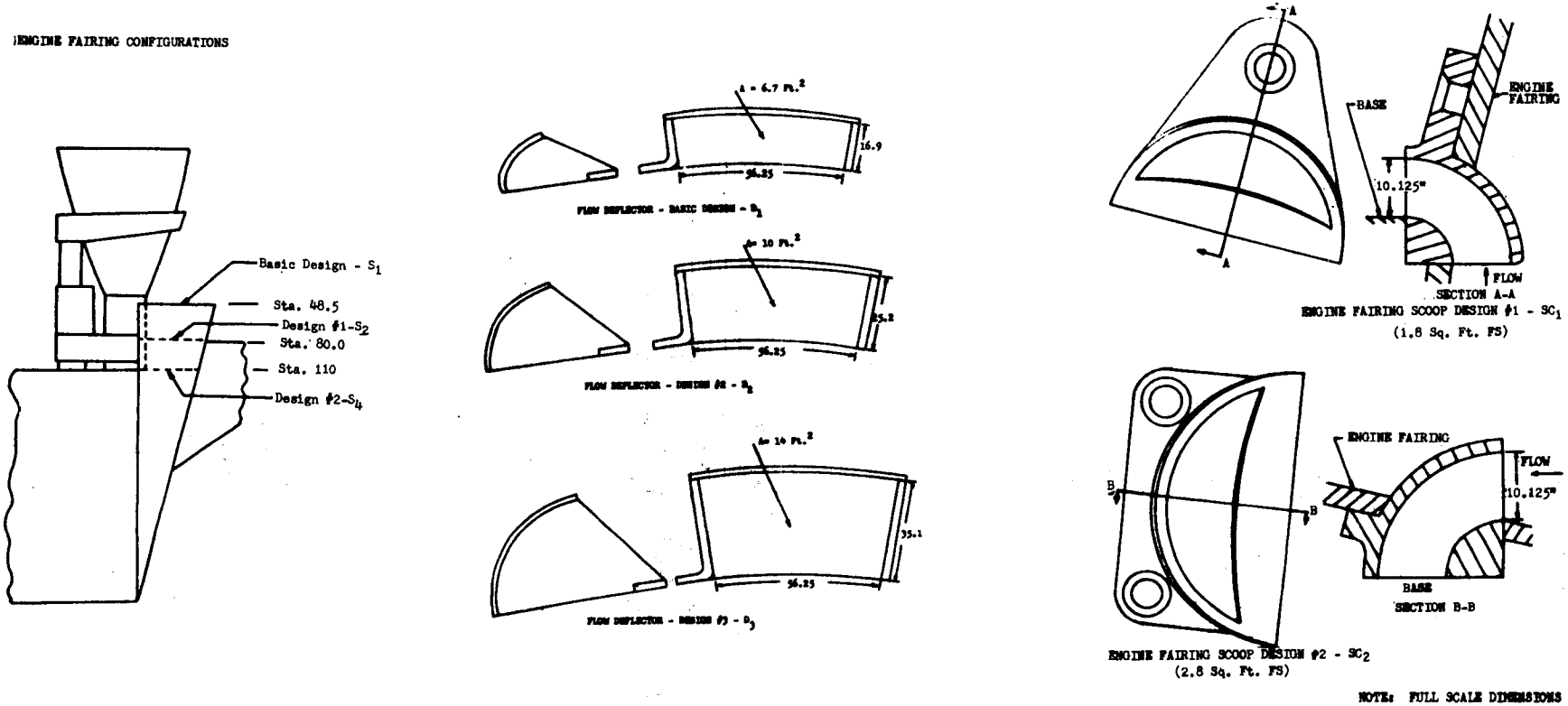

FIGURE 4.4-4. ENGINE FAIRING, SCOOP AND FLOW DEFLECTOR CONFIGURATIONS

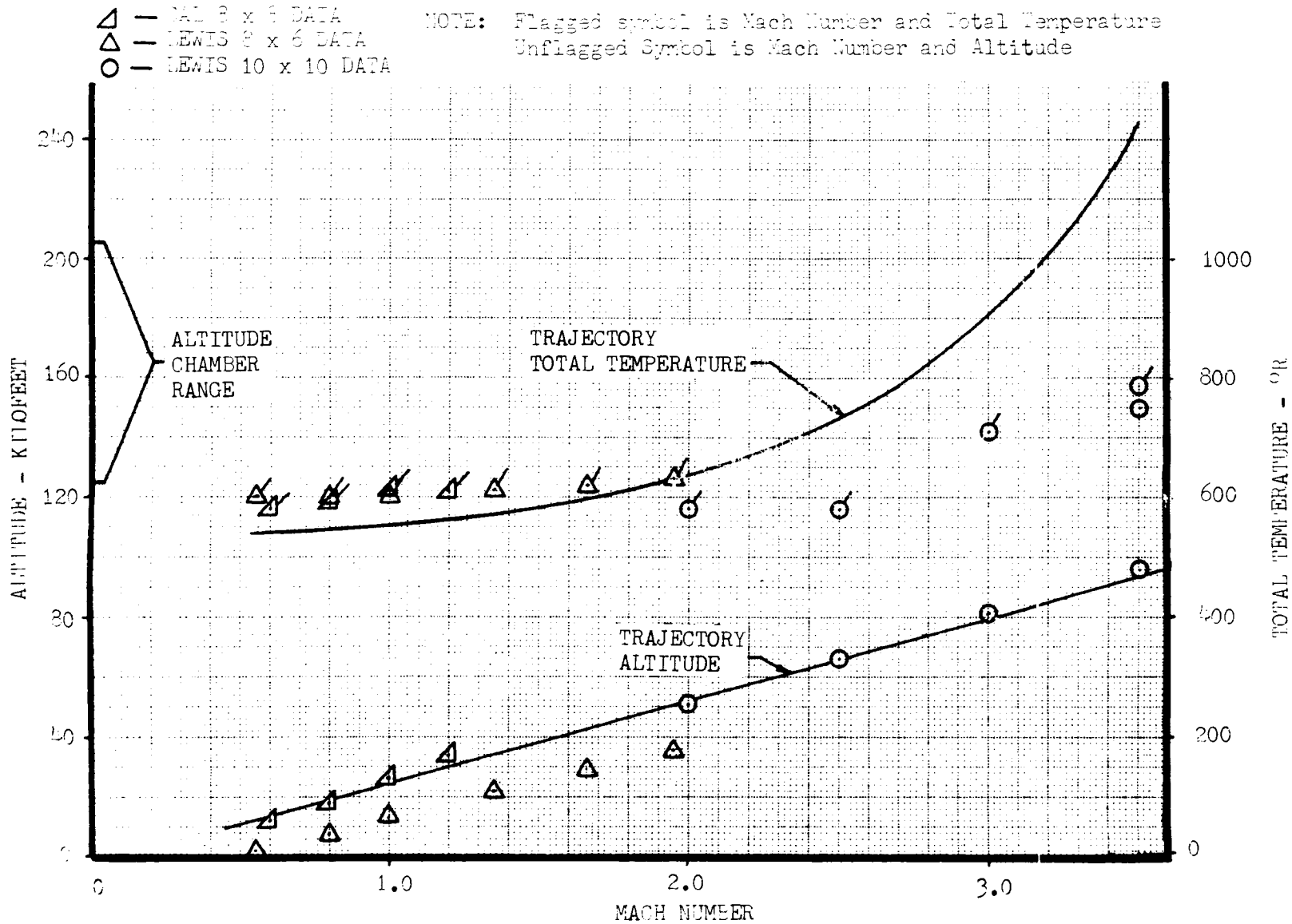

FIGURE 4.4-5. FACILITY TEST CONDITIONS

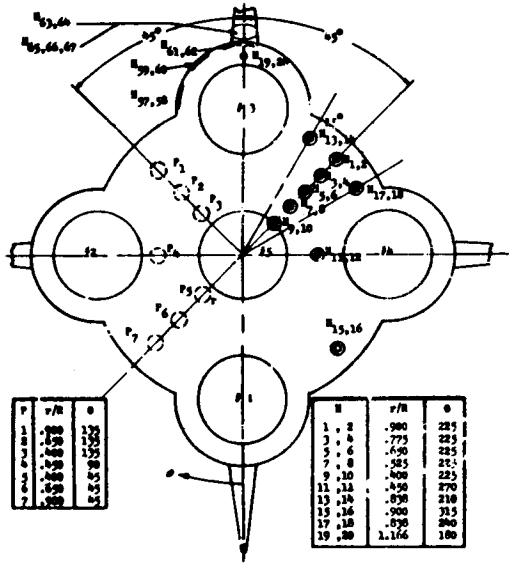

P	r/R	θ
1	.588	135°
2	.588	135°
3	.588	135°
4	.588	90°
5	.588	45°
6	.588	45°
7	.588	45°

H	r/R	θ
1 , 2	.900	225°
3 , 4	.775	225°
5 , 6	.650	225°
7 , 8	.525	225°
9 ,10	.400	225°
11 ,11	.450	270°
12 ,14	.838	210°
13 ,16	.900	315°
17 ,18	.838	240°
19 ,20	1.166	180°

PRESSURE AND HEAT TRANSFER BASE PLATE - PL_1

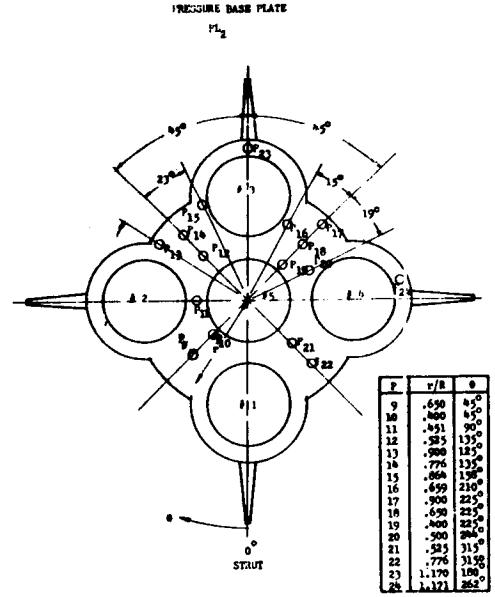

P	r/R	θ
9	.650	45°
10	.800	45°
11	.451	90°
12	.525	135°
13	.900	135°
14	.776	135°
15	.864	150°
16	.659	210°
17	.900	225°
18	.650	225°
19	.800	225°
20	.500	270°
21	.525	315°
22	.776	315°
23	1.170	180°
24	1.171	262°

PRESSURE BASE PLATE

PL_2

STRUT

HOT BASE INSTRUMENTATION PLATE - PL_3

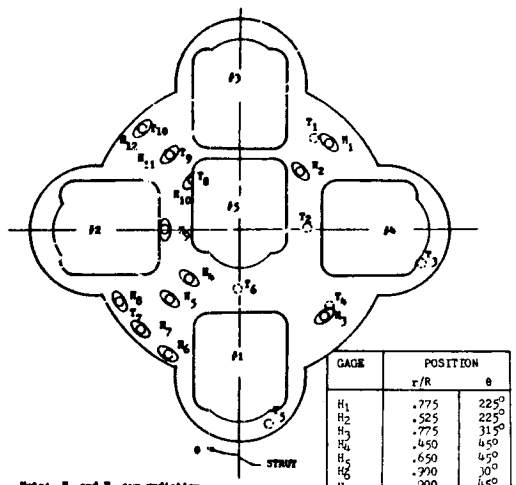

GAGE	POSITION r/R	POSITION θ
H_1	.775	225°
H_2	.525	225°
H_3	.775	315°
H_4	.450	45°
H_5	.650	45°
H_6	.900	30°
H_7	.900	45°
H_8	.900	60°
H_9	.450	90°
H_{10}	.450	135°
H_{11}	.650	135°
H_{12}	.900	135°

STRUT

Note: H_1 and H_2 are radiation gages. All others measure total heating.

T - THERMOCOUPLE
H - HEAT TRANSFER GAGE
STRUT LOCATION = 0.0°

FIGURE 4.4-6. BASE PLATE INSTRUMENTATION

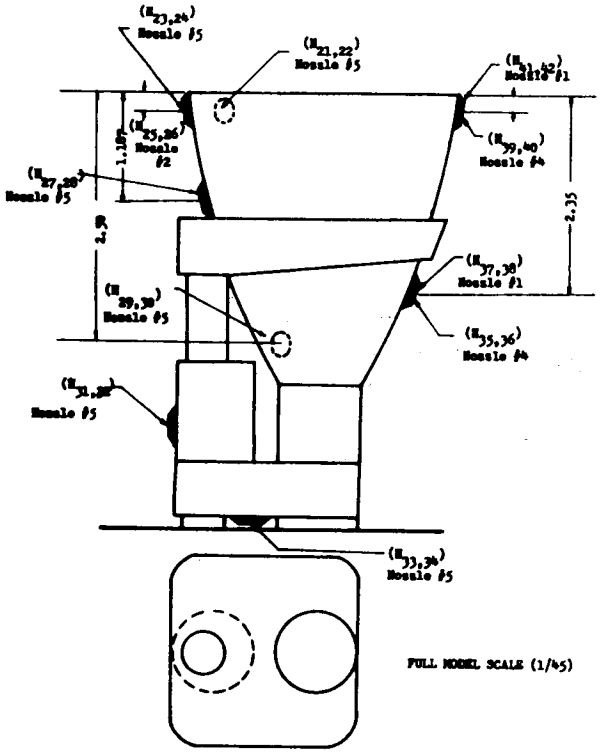

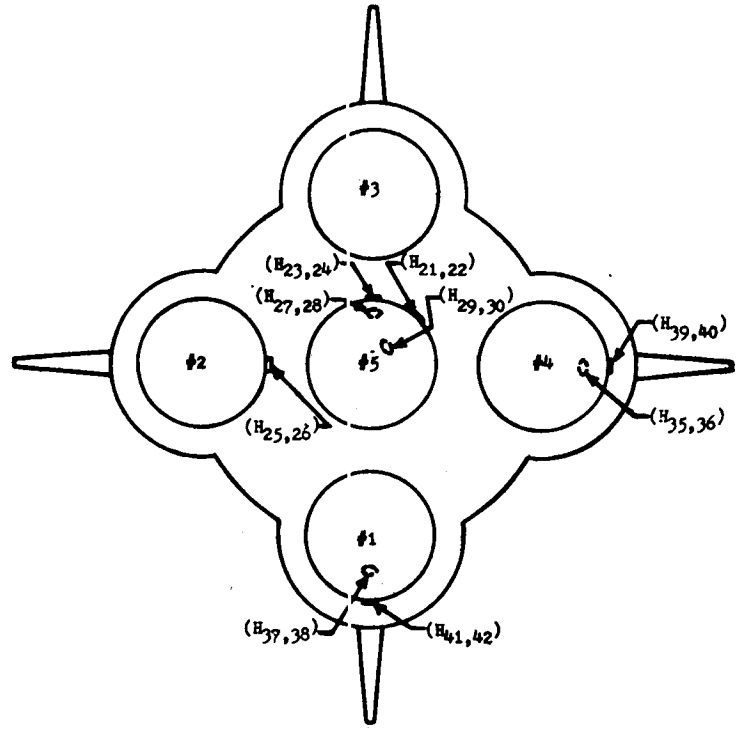

FIGURE 4.4-7. ENGINE INSTRUMENTATION (INTERNAL AND EXTERNAL)

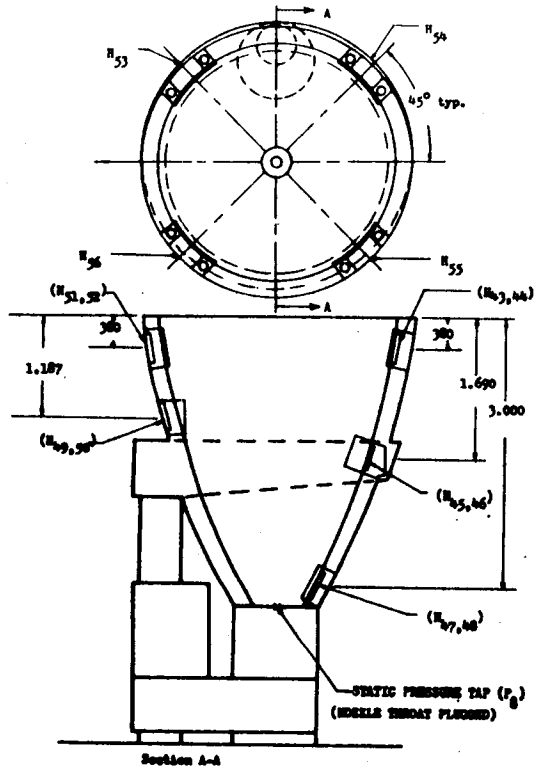

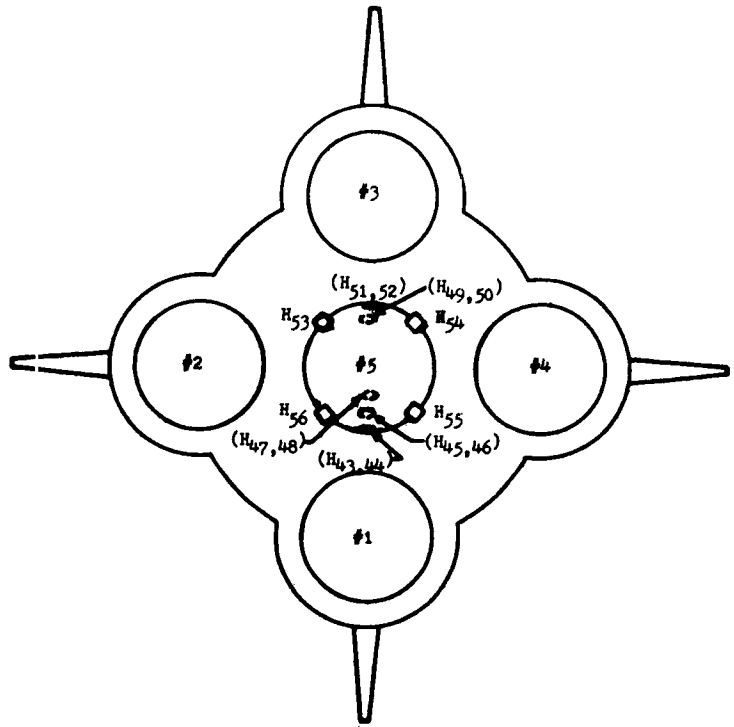

FIGURE 4.4-8. ENGINE INSTRUMENTATION (EXTERNAL)

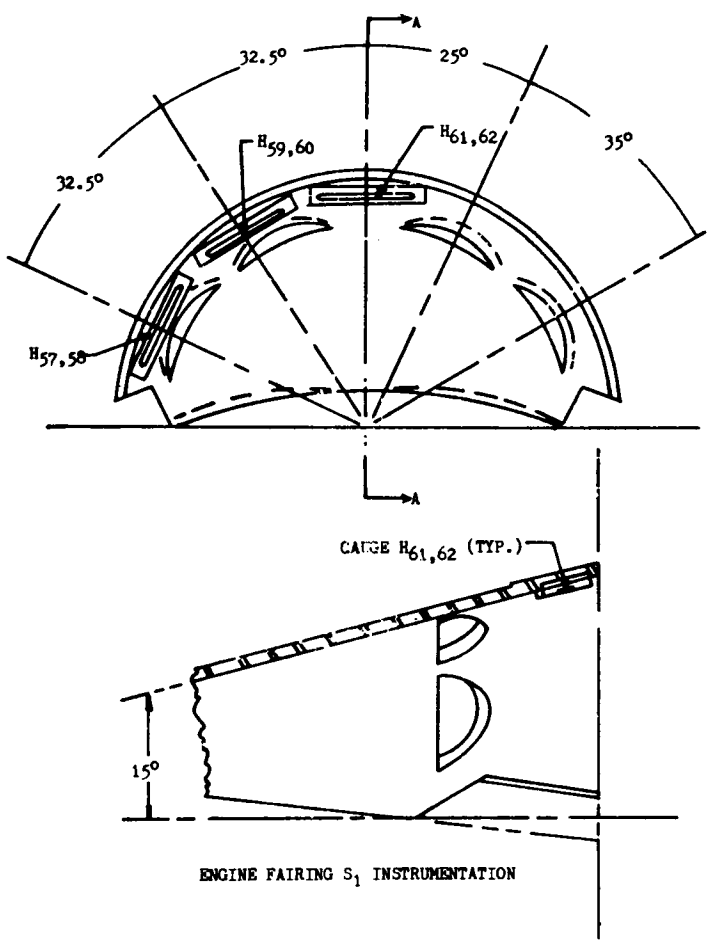

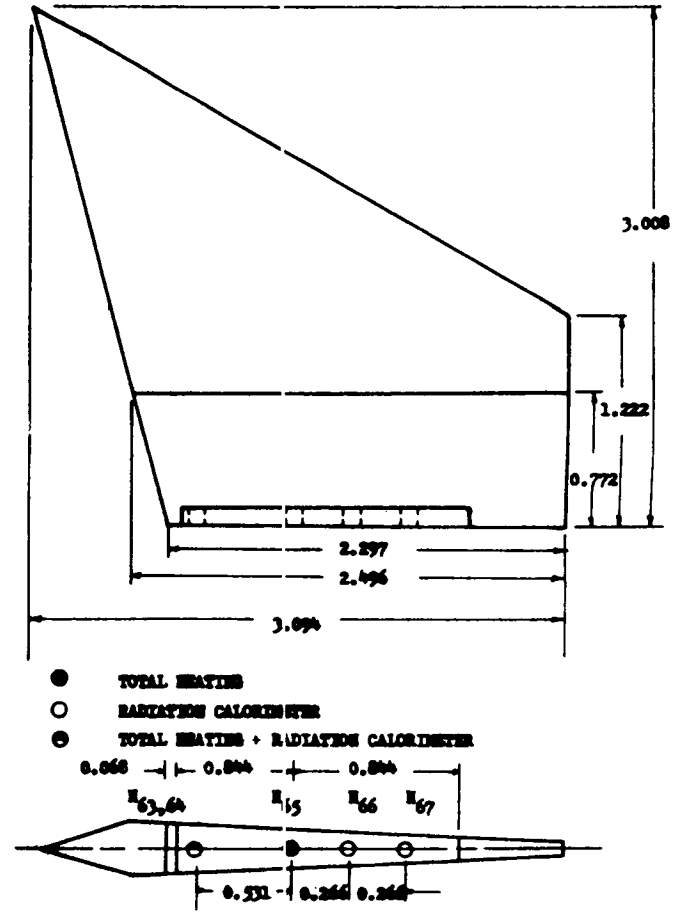

FIGURE 4.4-9. FIN AND ENGINE FAIRING INSTRUMENTATION

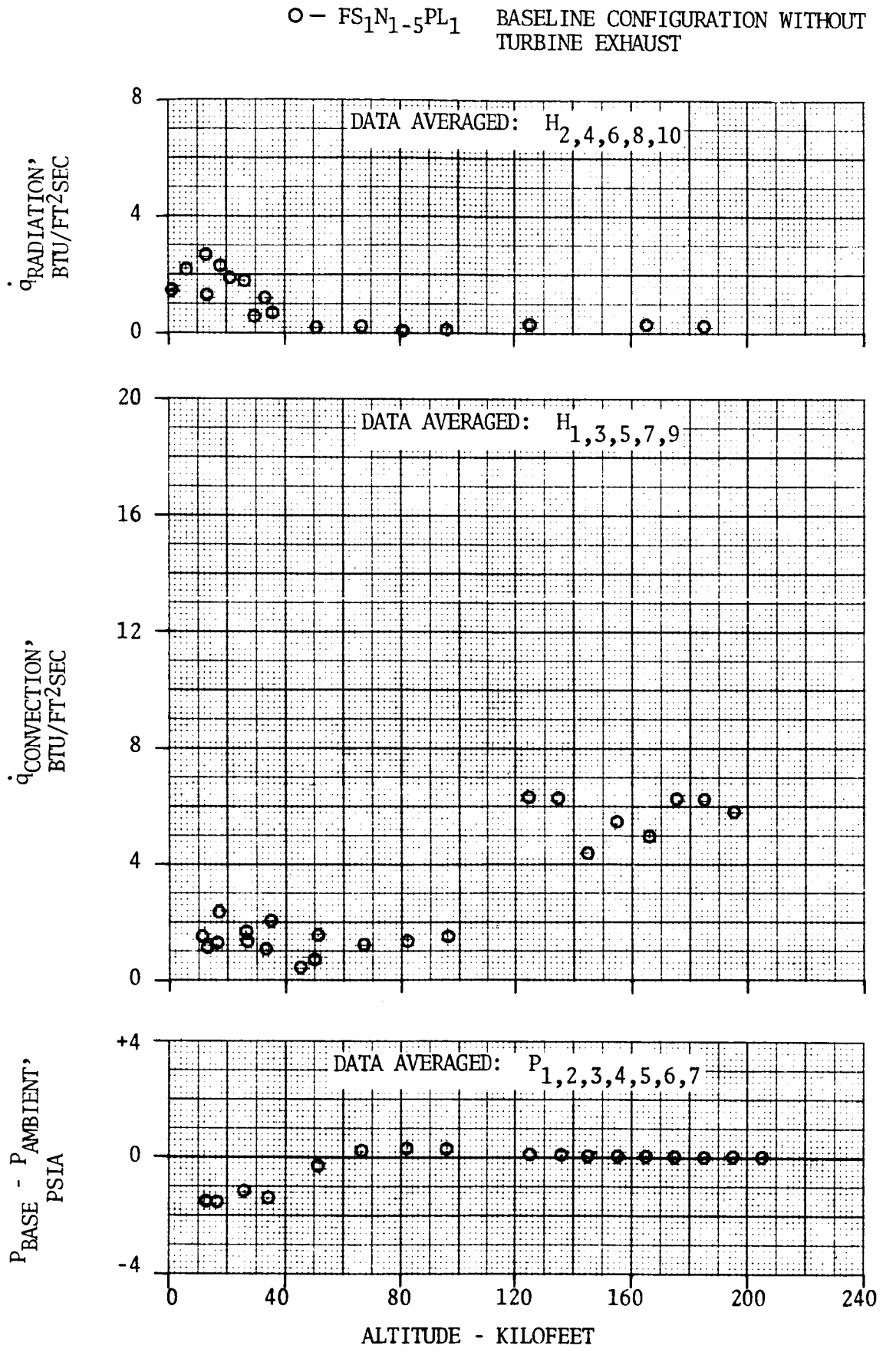

FIGURE 4.4-10 NOMINAL CONFIGURATION HEAT SHIELD ENVIRONMENTS

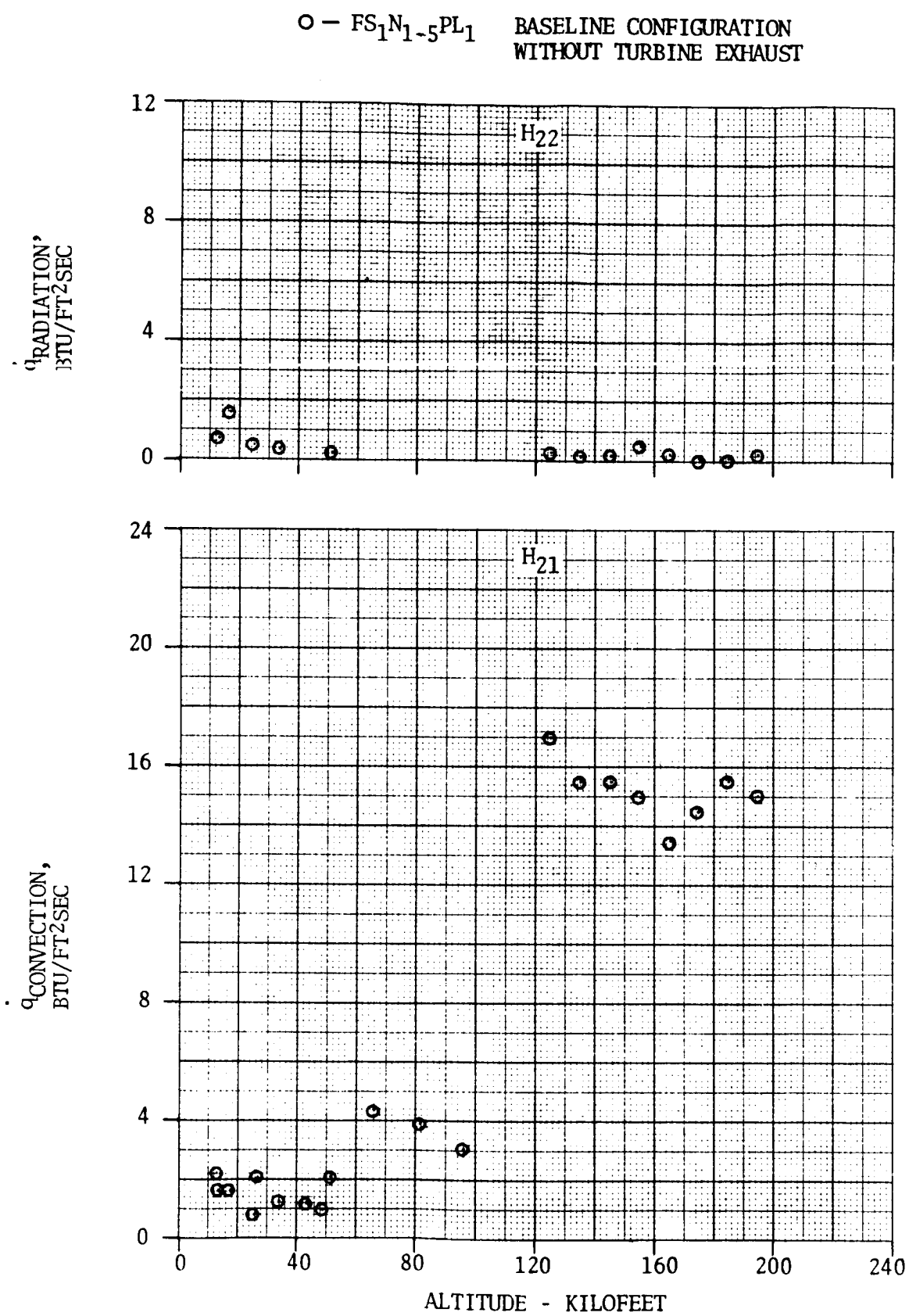

FIGURE 4.4-11 NOMINAL CONFIGURATION ENGINE ENVIRONMENTS

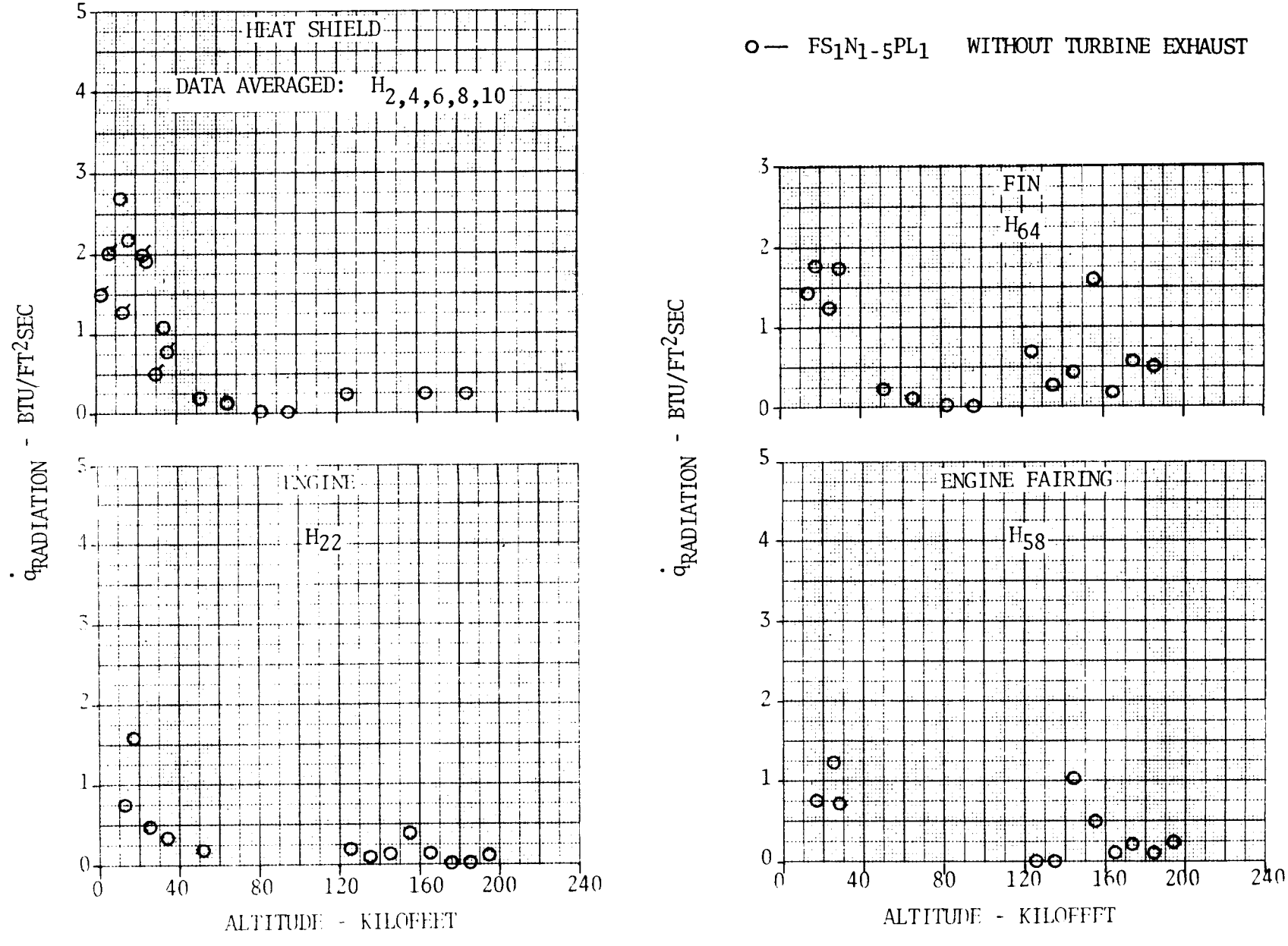

FIGURE 4.4-12 NOMINAL CONFIGURATION BASE REGION RADIATION

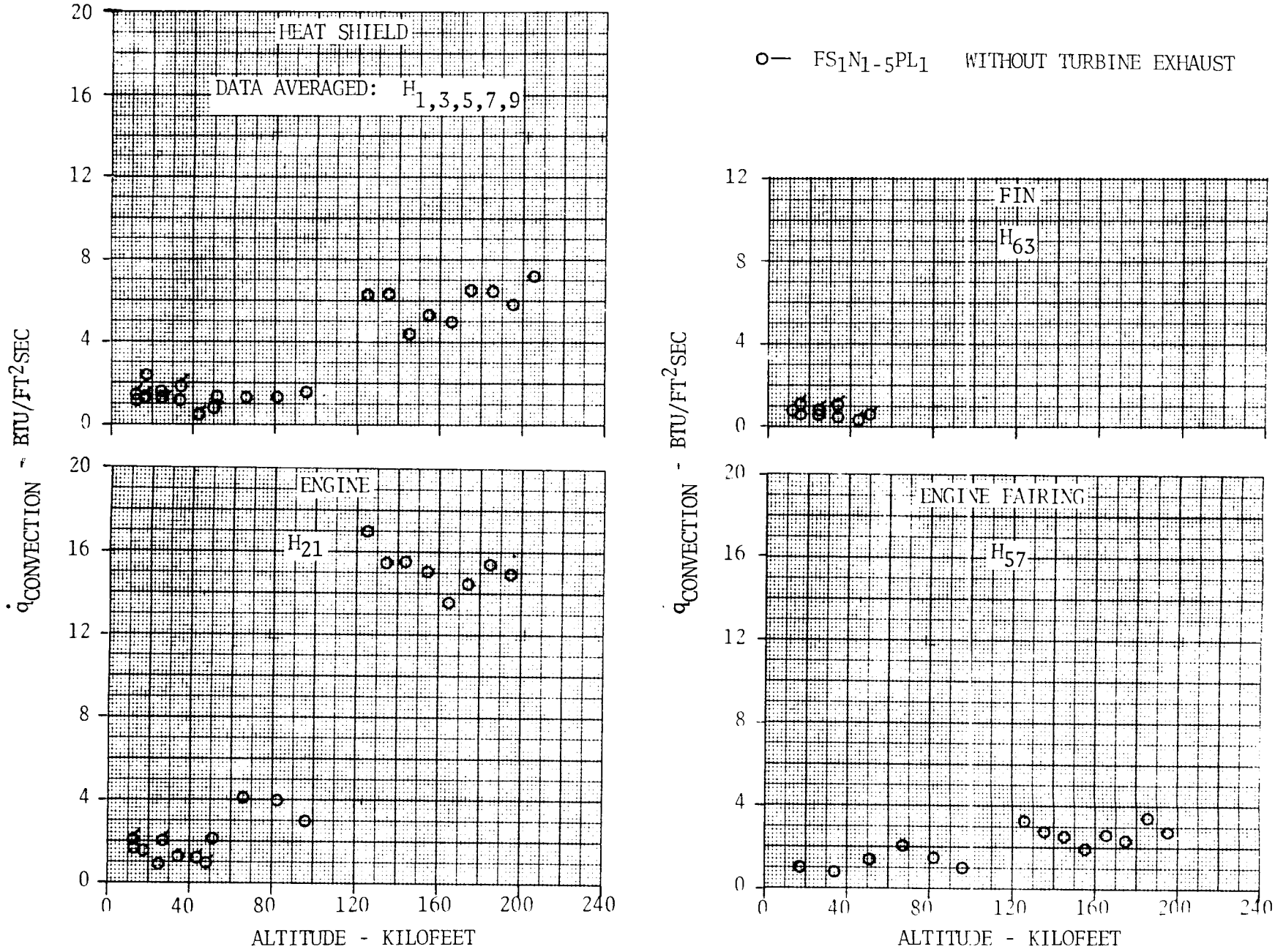

FIGURE 4.4-13 NOMINAL CONFIGURATION BASE REGION CONVECTION

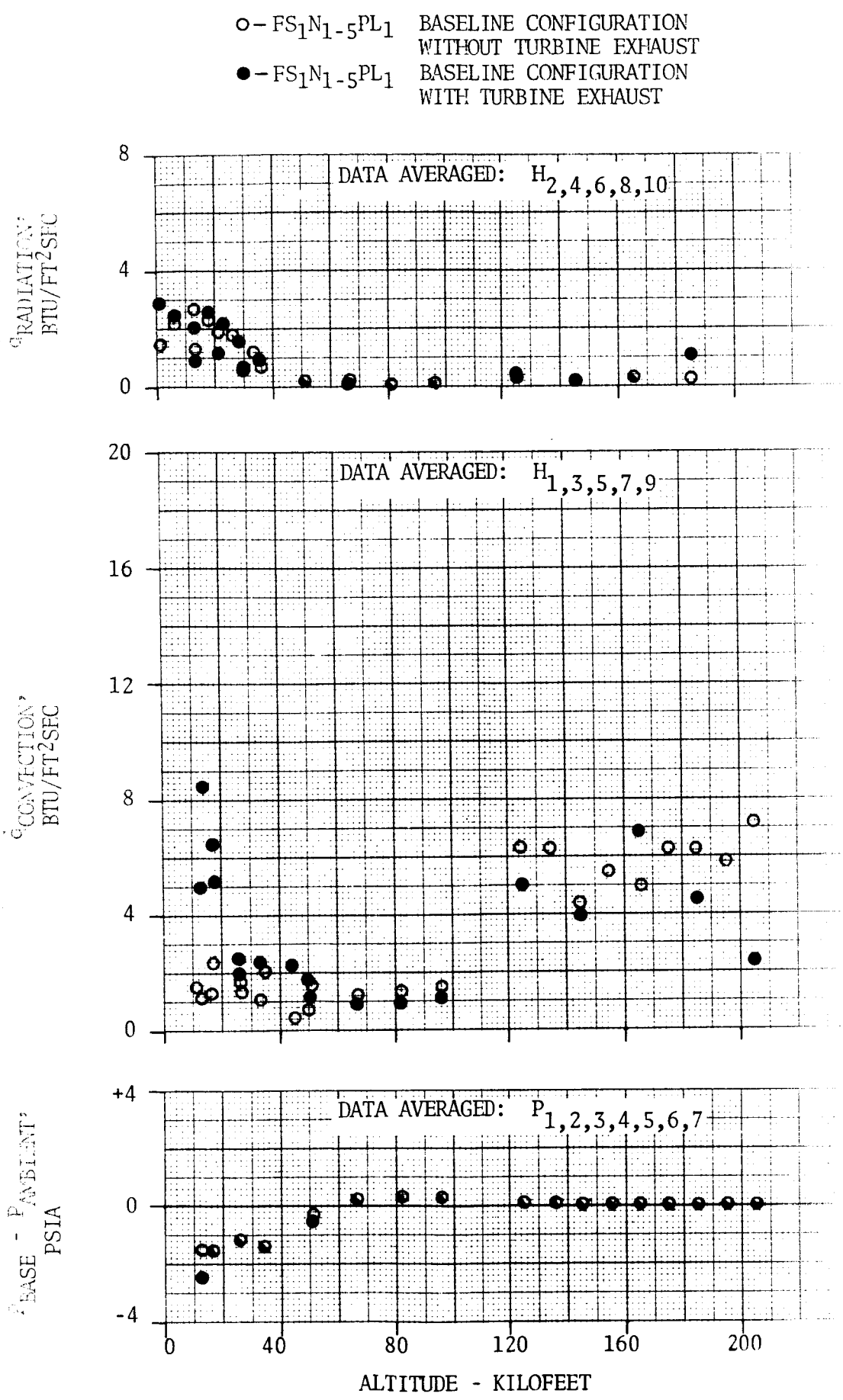

FIGURE 4.4-14 EFFECT OF TURBINE EXHAUST ON HEAT SHIELD ENVIRONMENT

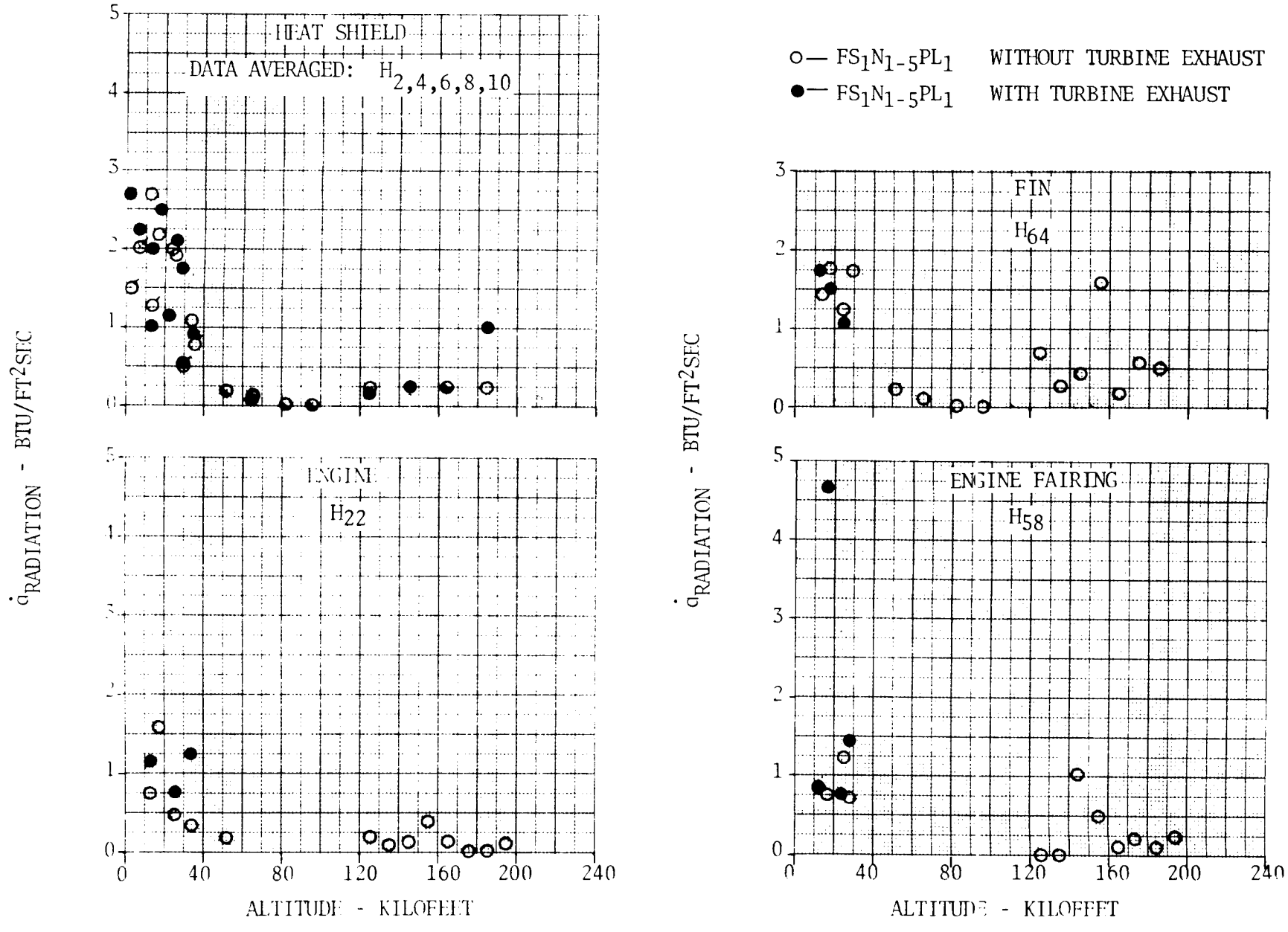

FIGURE 4.4-15 EFFECT OF TURBINE EXHAUST ON BASE REGION RADIATION

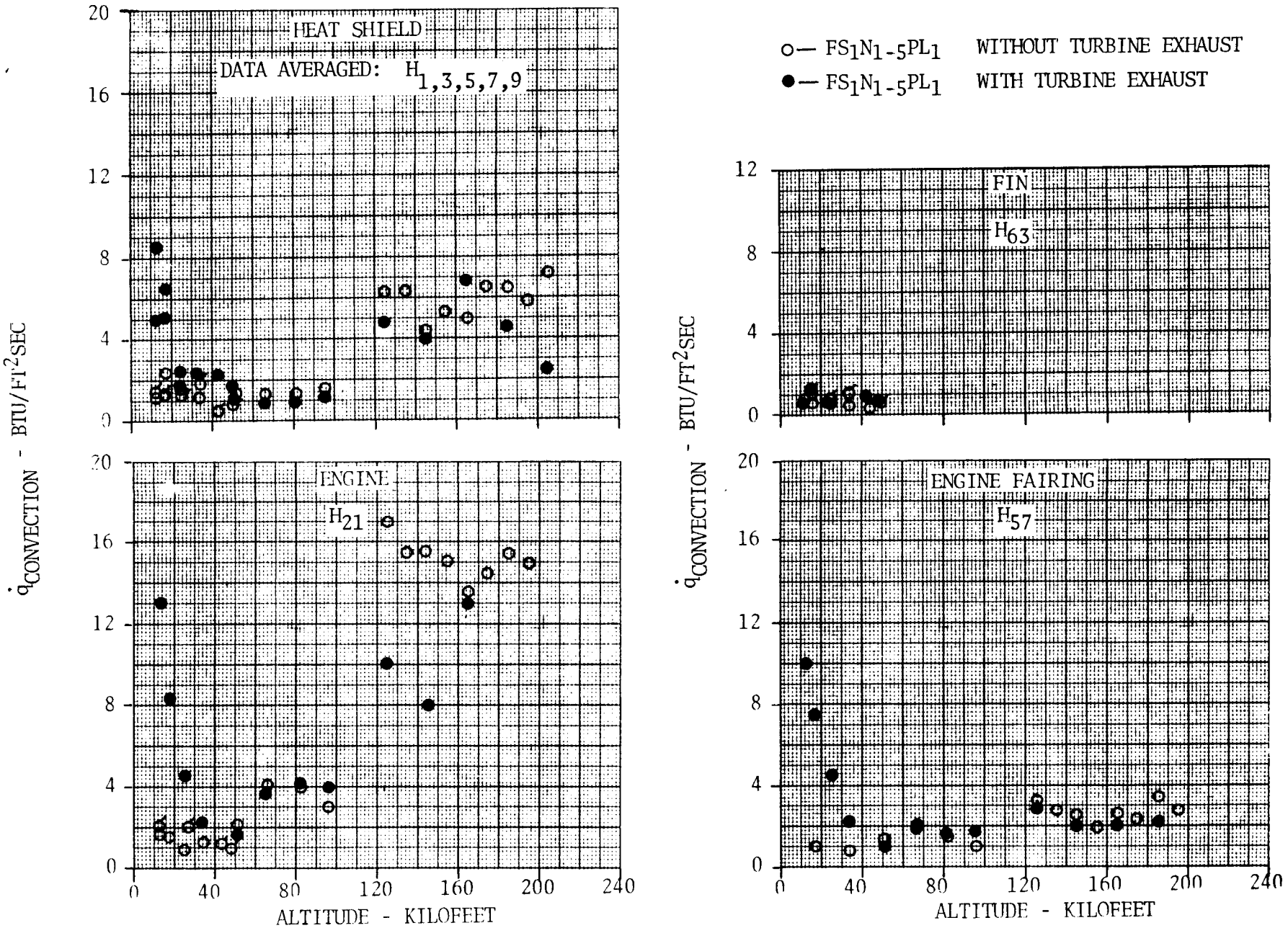

FIGURE 4.4-16 EFFECT OF TURBINE EXHAUST ON BASE REGION CONVECTION

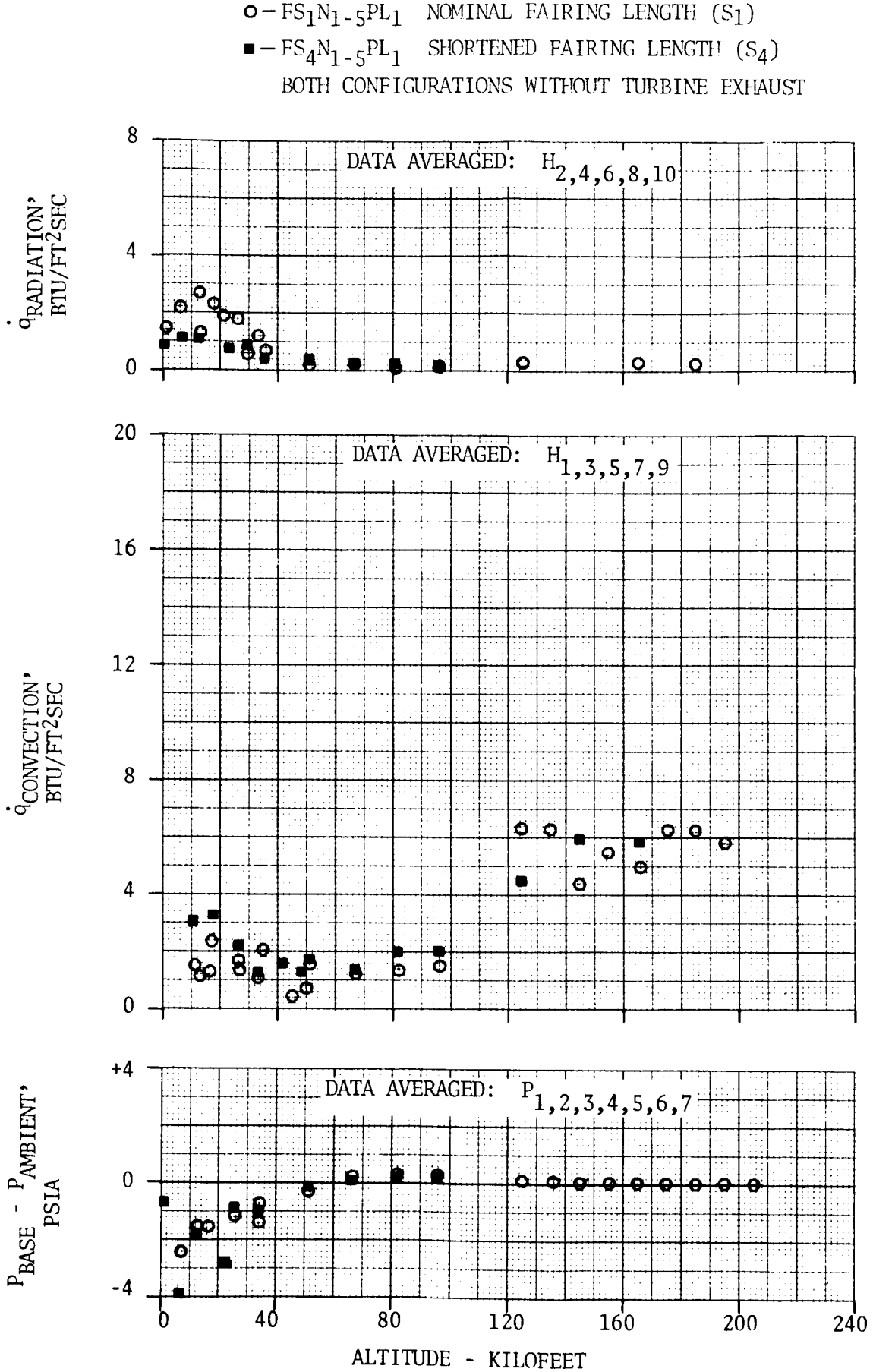

FIGURE 4.4-17 EFFECT OF ENGINE FAIRING LENGTH ON HEAT SHIELD ENVIRONMENTS

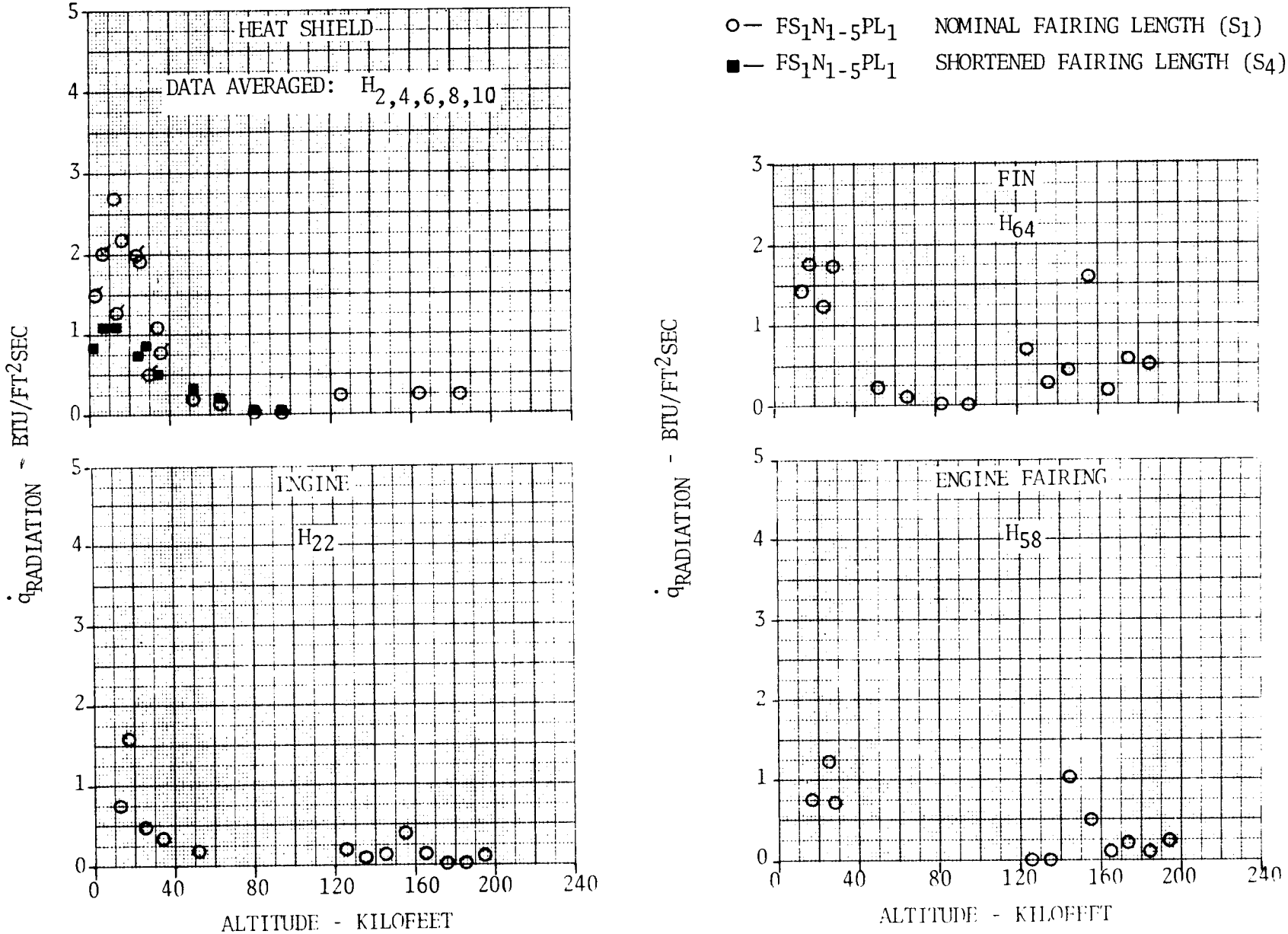

FIGURE 4.4-18 EFFECE OF ENGINE FAIRING LENGTH ON BASE REGION RADIATION

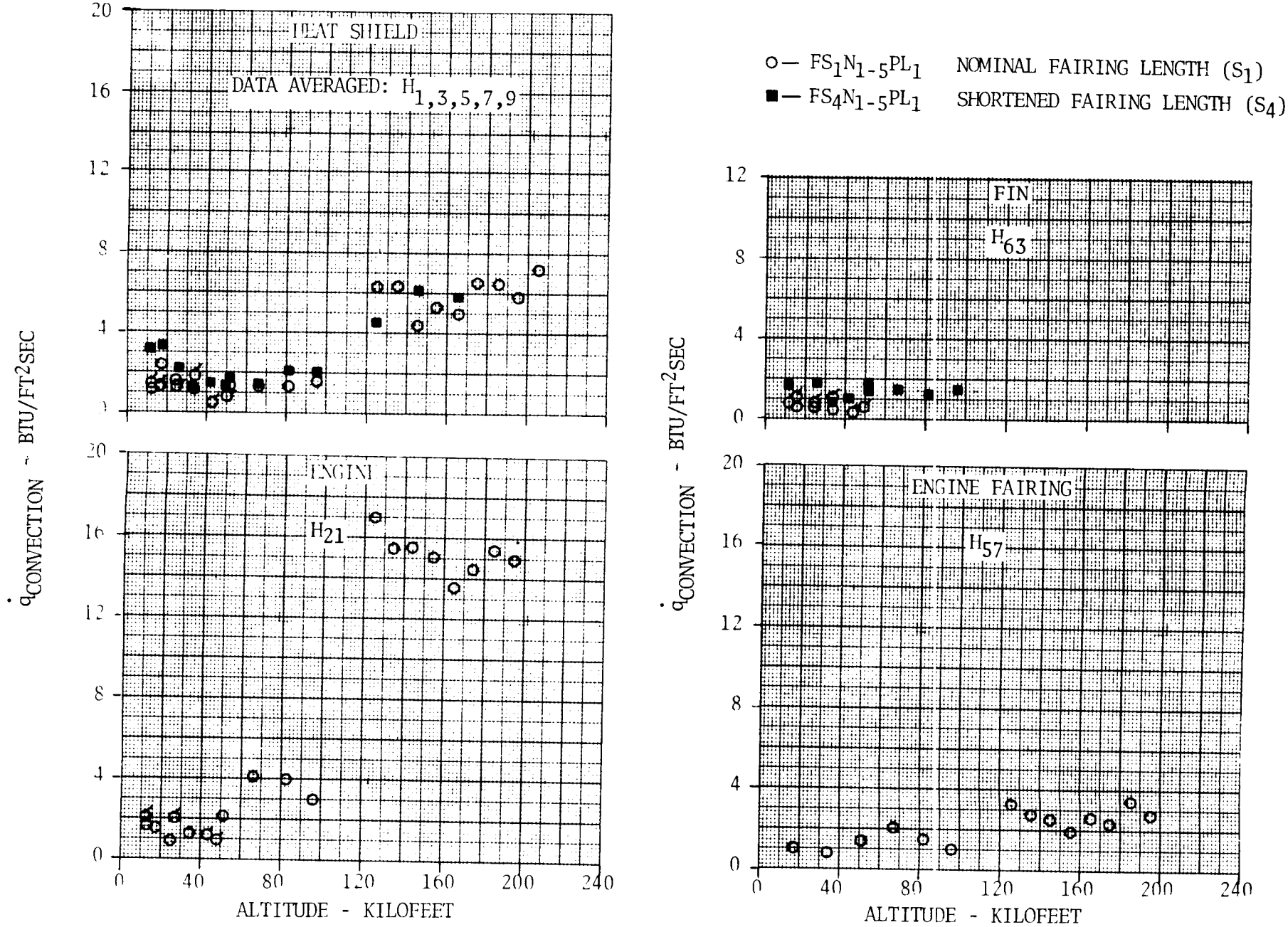

FIGURE 4.4-19 EFFECT OF ENGINE FAIRING LENGTH ON BASE REGION CONVECTION

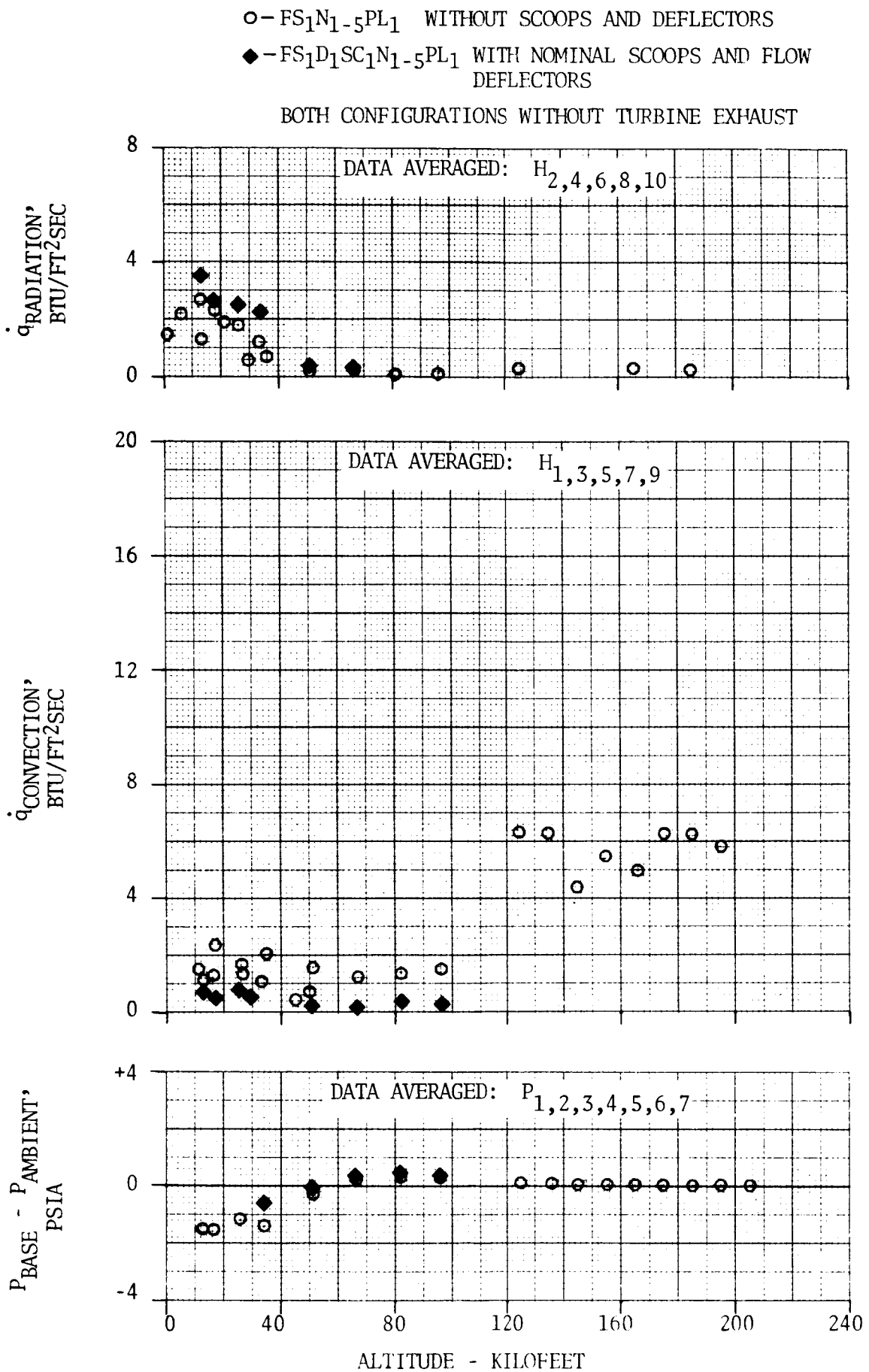

FIGURE 4.4-20 EFFECT OF SCOOPS AND FLOW DEFLECTORS ON HEAT SHIELD ENVIRONMENTS

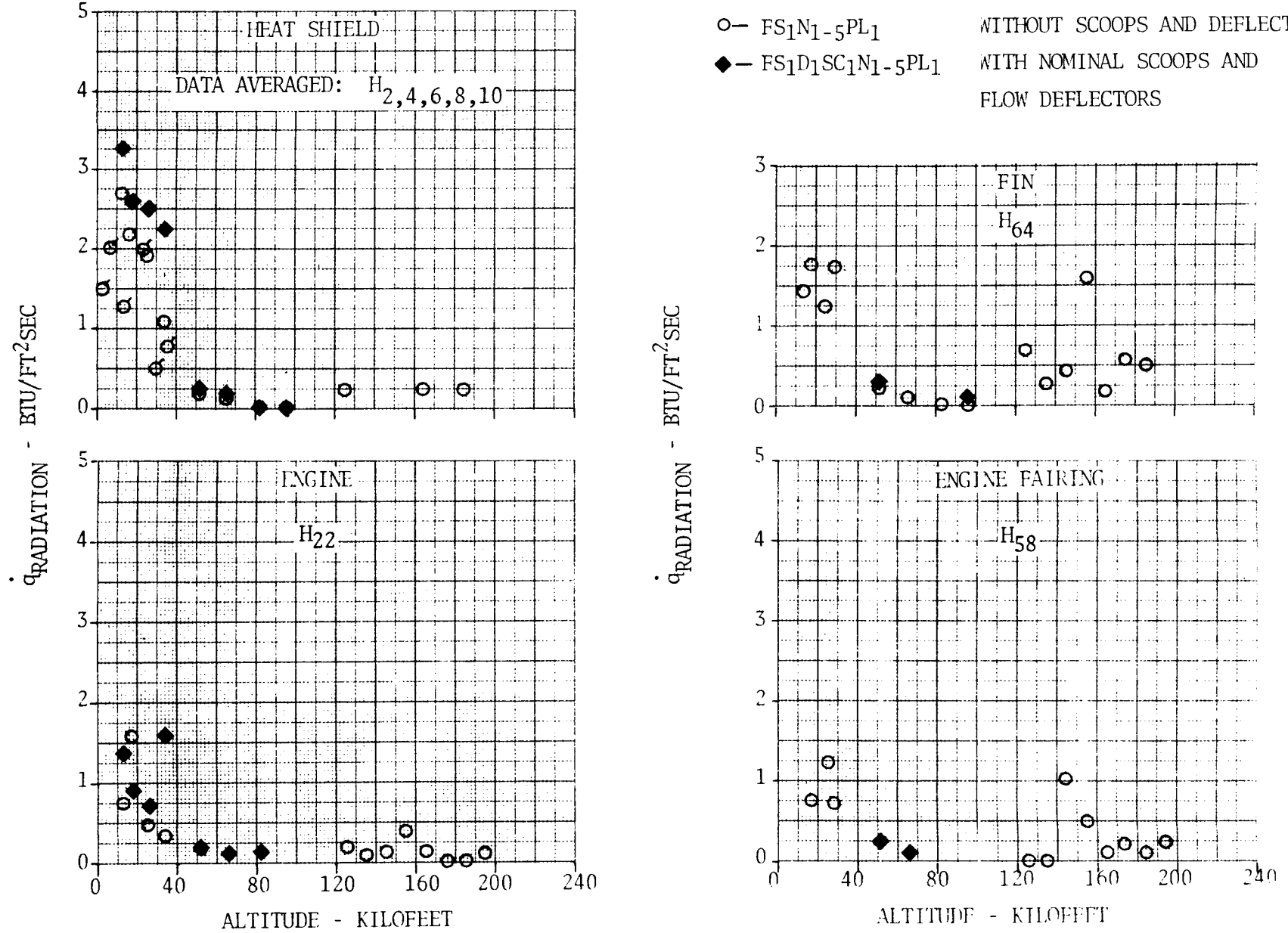

FIGURE 4.4-21 EFFECT OF SCOOPS AND FLOW DEFLECTORS ON BASE REGION RADIATION

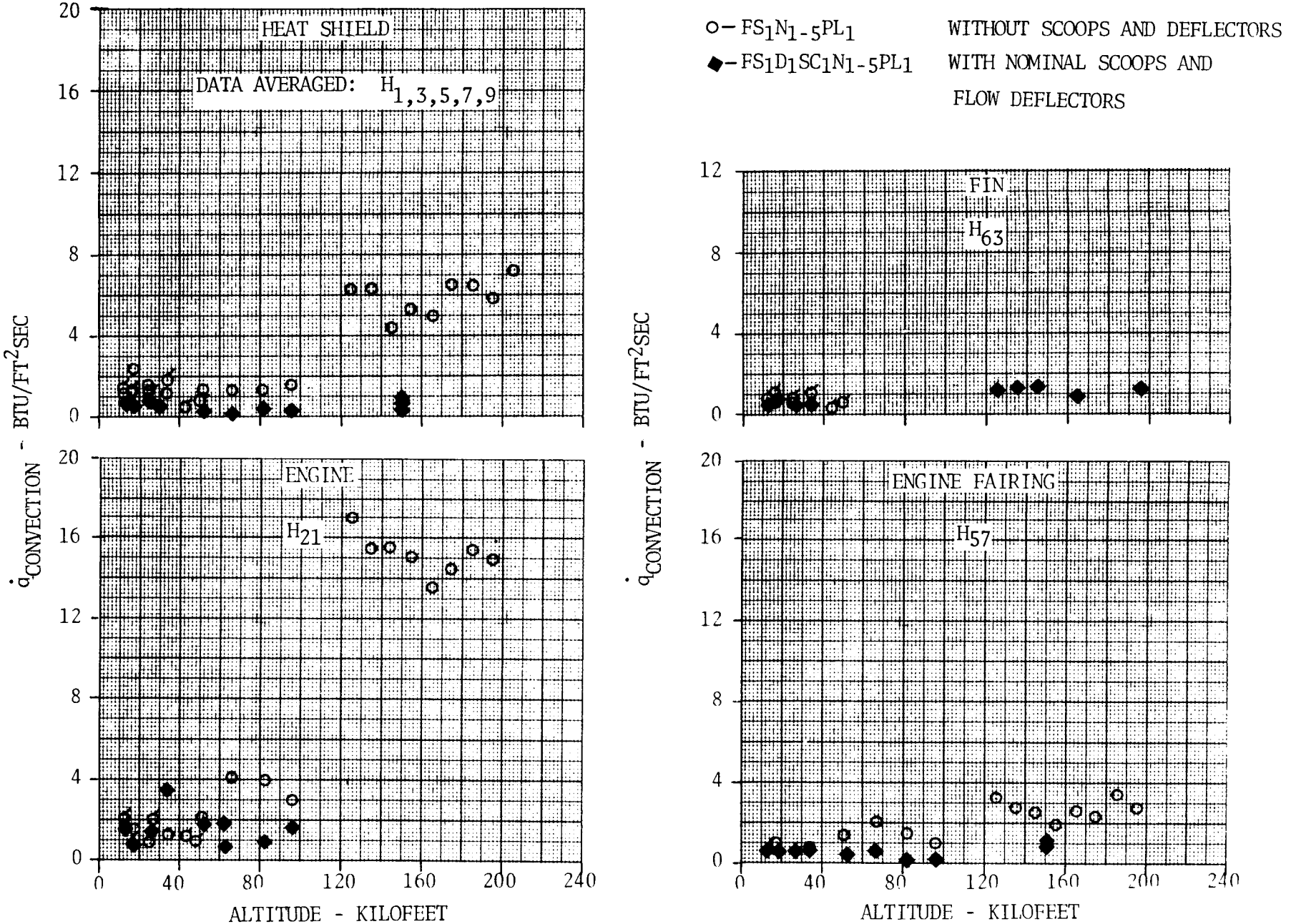

FIGURE 4.4-22 EFFECT OF SCOOPS AND FLOW DEFLECTORS ON BASE REGION CONVECTION

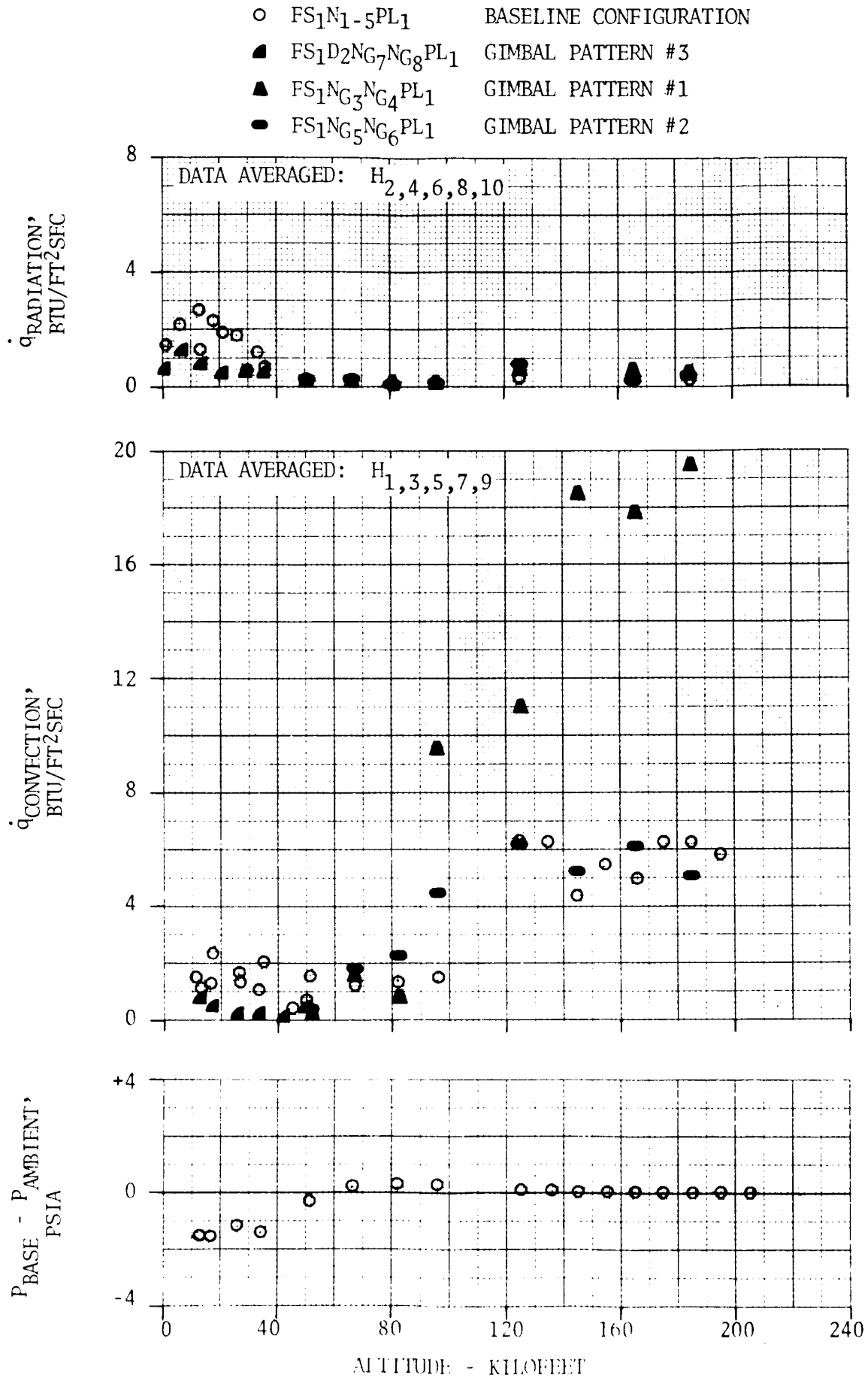

FIGURE 4.4-23 EFFECT OF GIMBALING ON HEAT SHIELD ENVIRONMENTS

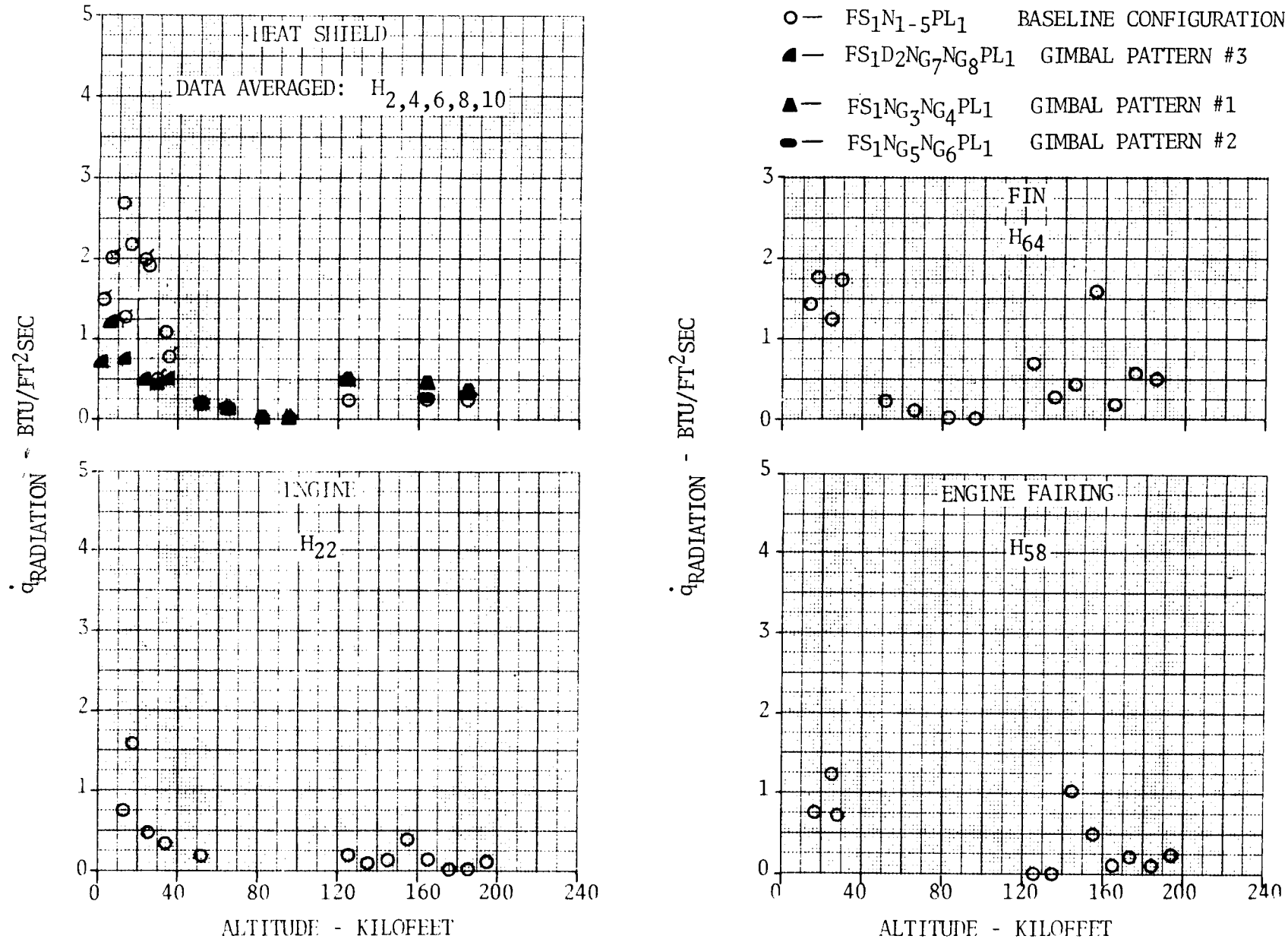

FIGURE 4.4-24 EFFECT OF GIMBALING ON BASE REGION RADIATION

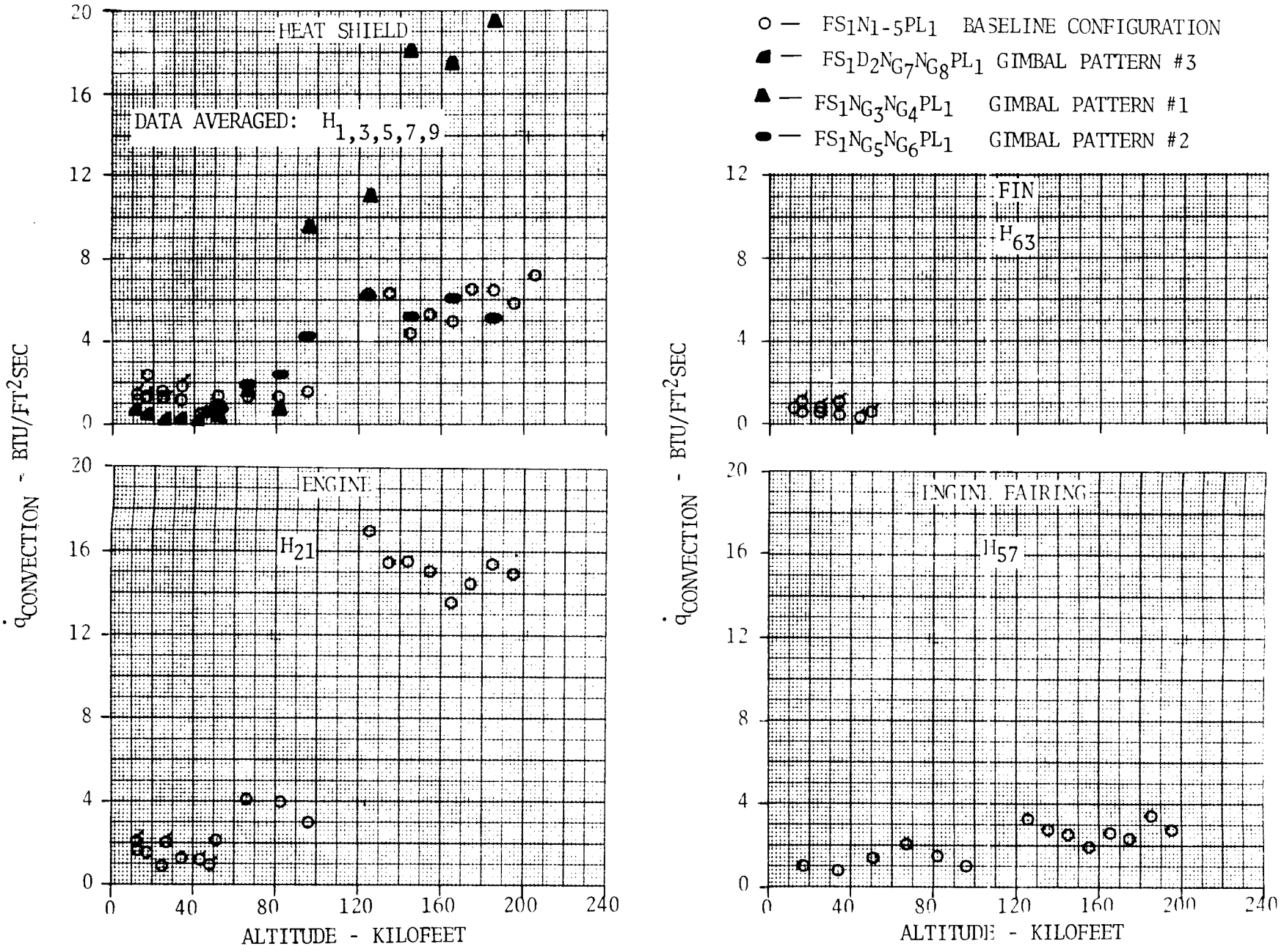

FIGURE 4.4-25 EFFECT OF GIMBALING ON BASE REGION CONVECTION

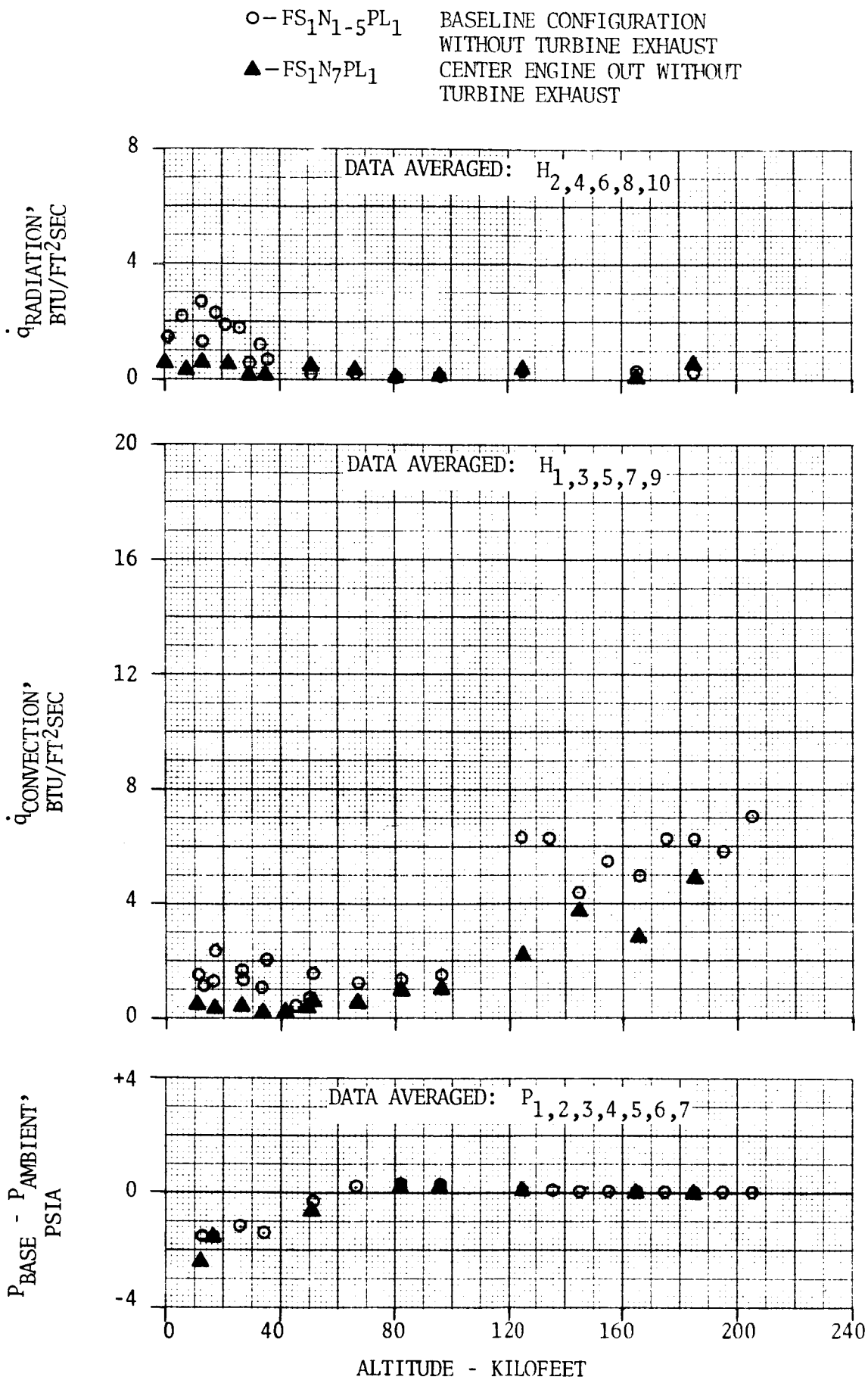

FIGURE 4.4-26 EFFECT OF CENTER ENGINE OUT ON HEAT SHIELD ENVIRONMENTS

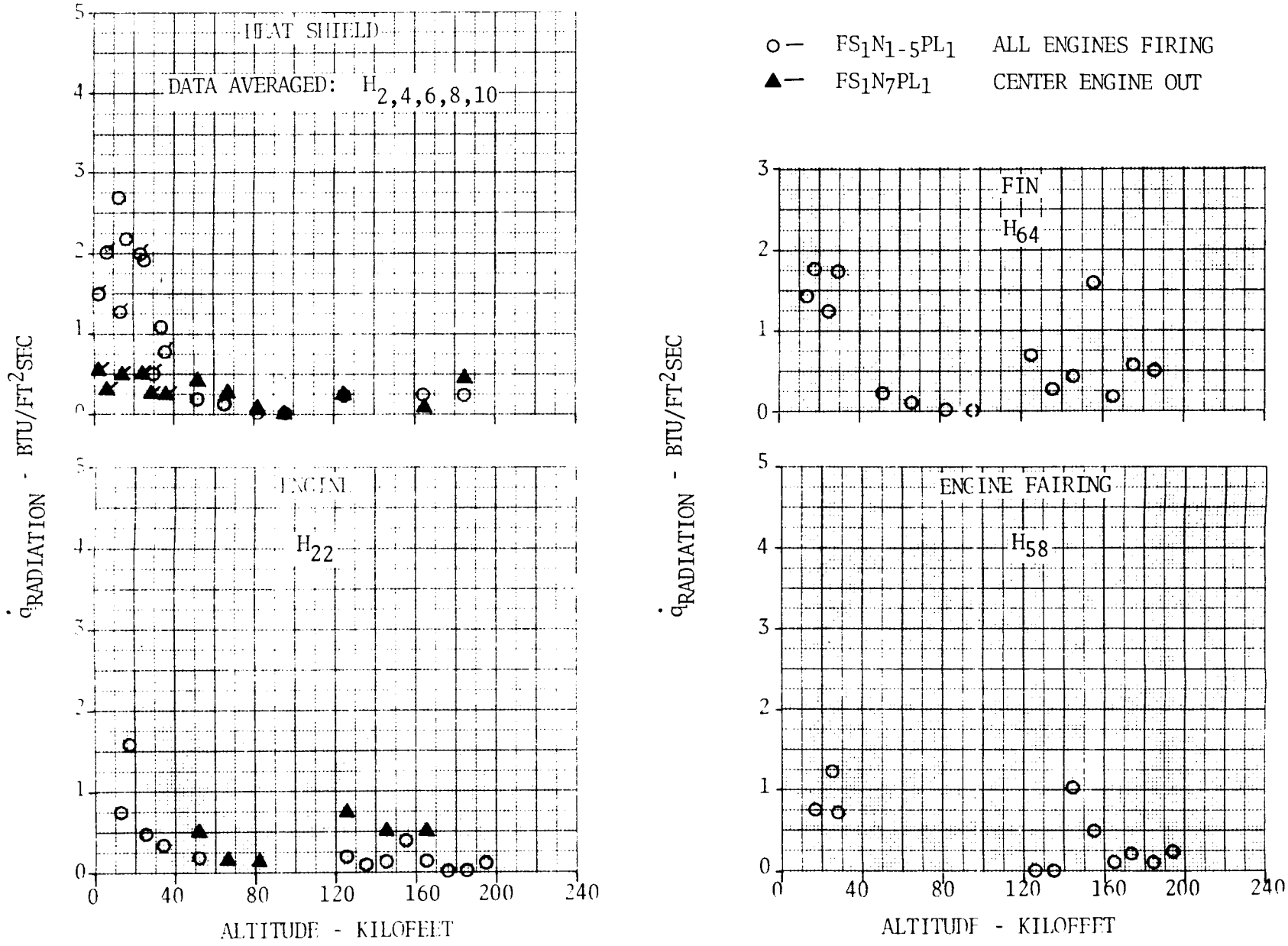

FIGURE 4.4-27 EFFECT OF CENTER ENGINE OUT ON BASE REGION RADIATION

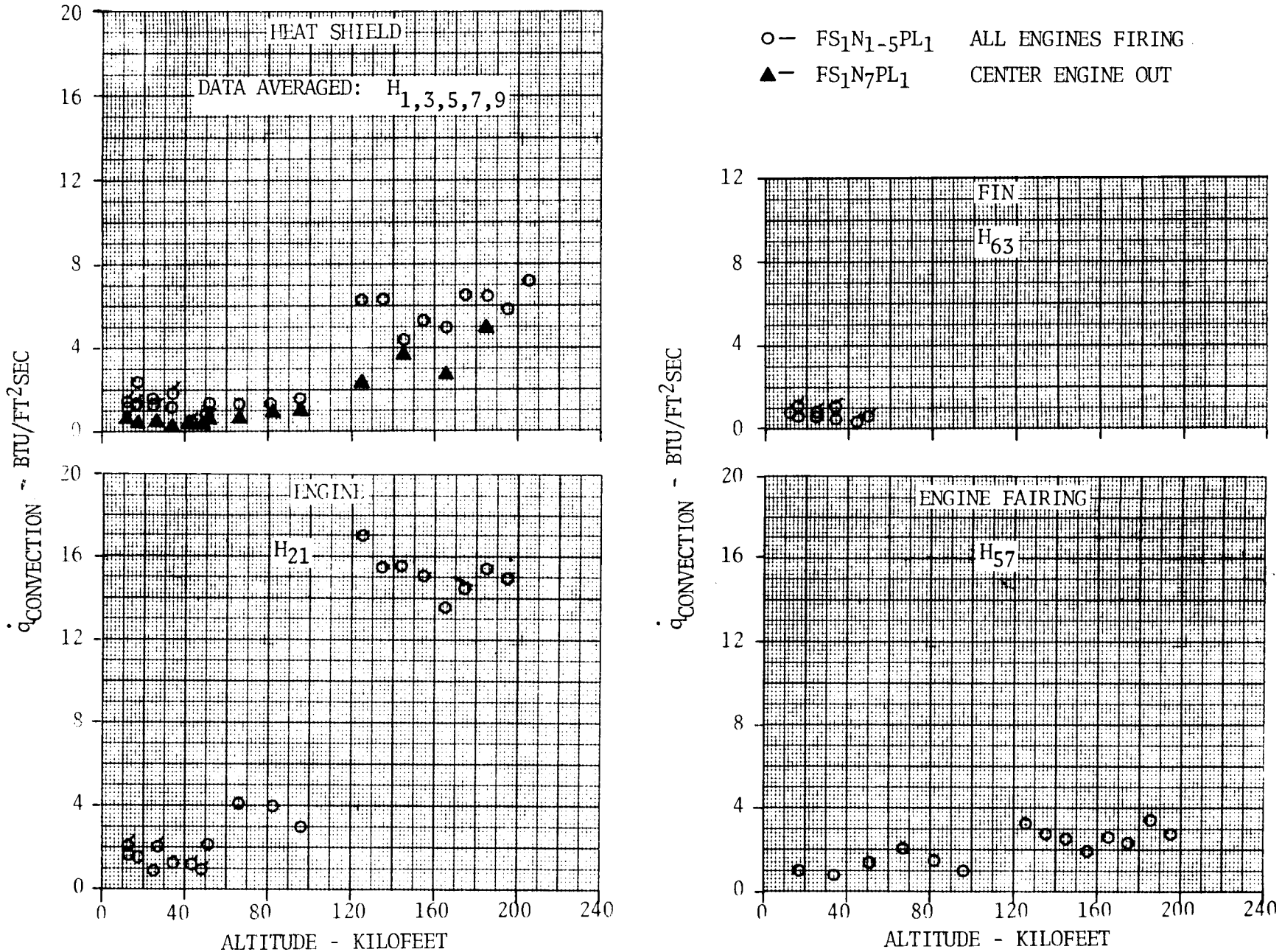

FIGURE 4.4-28 EFFECT OF CENTER ENGINE OUT ON BASE REGION CONVECTION

O – $FS_1N_{1-5}PL_1$ ENGINES ON

DATA AVERAGED: $P_{1,2,3,4,5,6,7}$

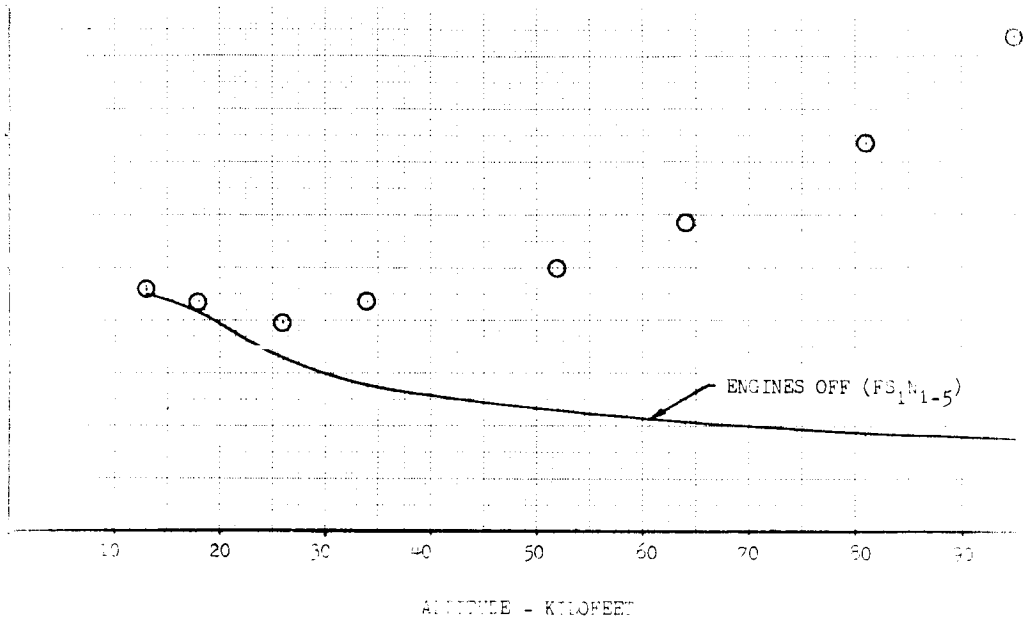

Δ – $FS_1D_1SC_1N_{1-5}$ ENGINES ON

DATA AVERAGED: $P_{1,2,3,4,5,6,7}$

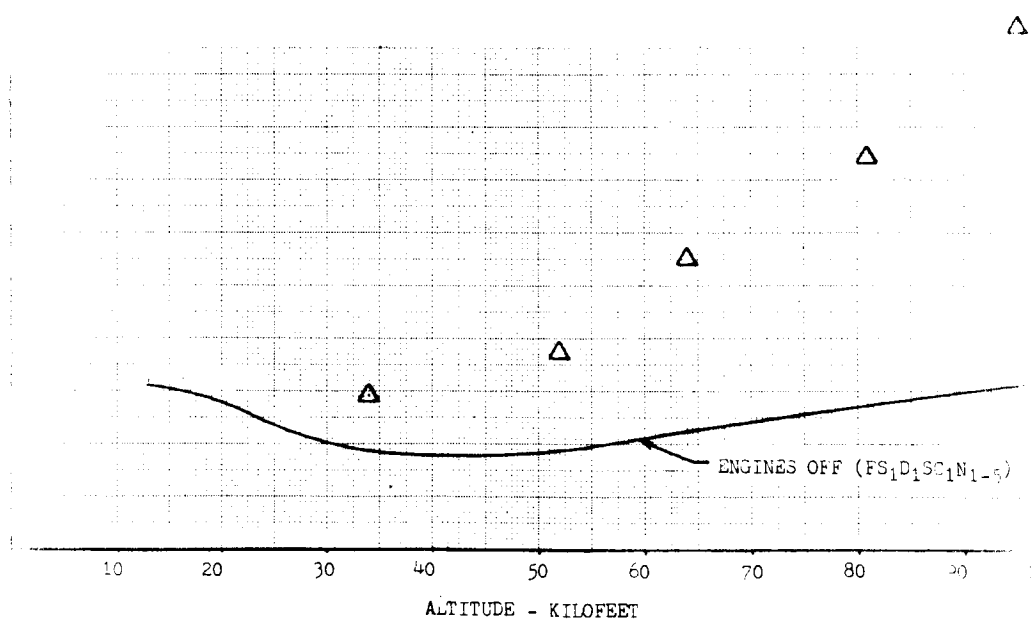

NOTE: MODEL DATA FROM CAL 8x8 AND LeRC 10x10 TUNNELS

4.4-29 COMPARISON OF ENGINE OFF AND ENGINE ON BASE PRESSURE

TUNNEL LEWIS 8 BY 6

SYM.	INST.	CONFIG.
◇	$H_{54,56}$	$B_4FS_1D_2N_7PL_1$

SYM.	INST.	CONFIG.
◇	$H_{54,56}$	$B_4FS_1D_2N_{10}N_{G_{11}}N_{G_{12}}N_{G_{13}}PL_2$

NOTE: 1. Flag denotes gauge H_{56}

2. Solid symbol denotes turbine exhaust

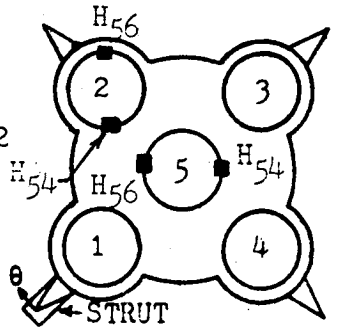

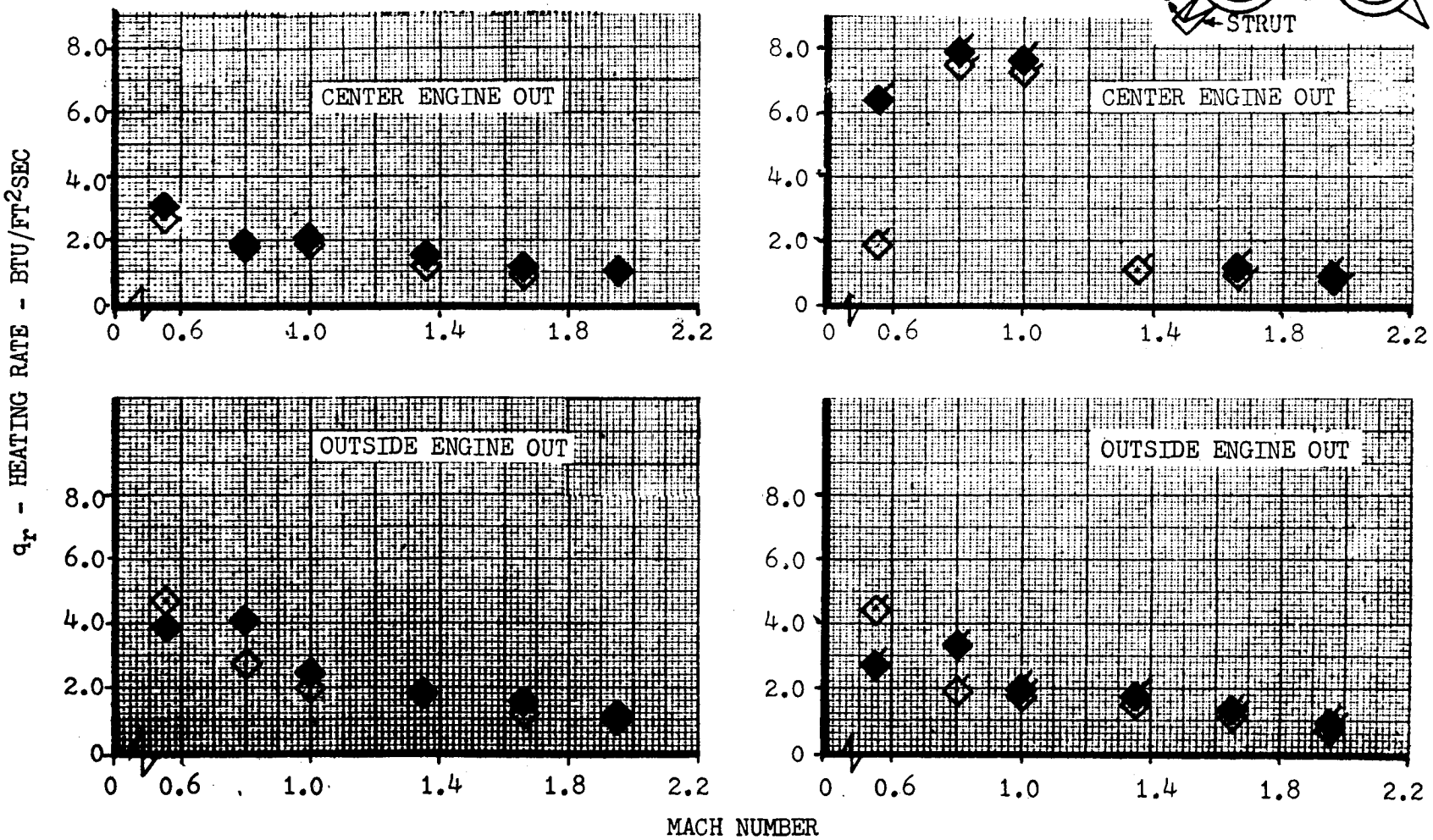

FIGURE 4.4-30 INTERNAL ENGINE RADIATION FROM M = 0.55 TO M = 1.96

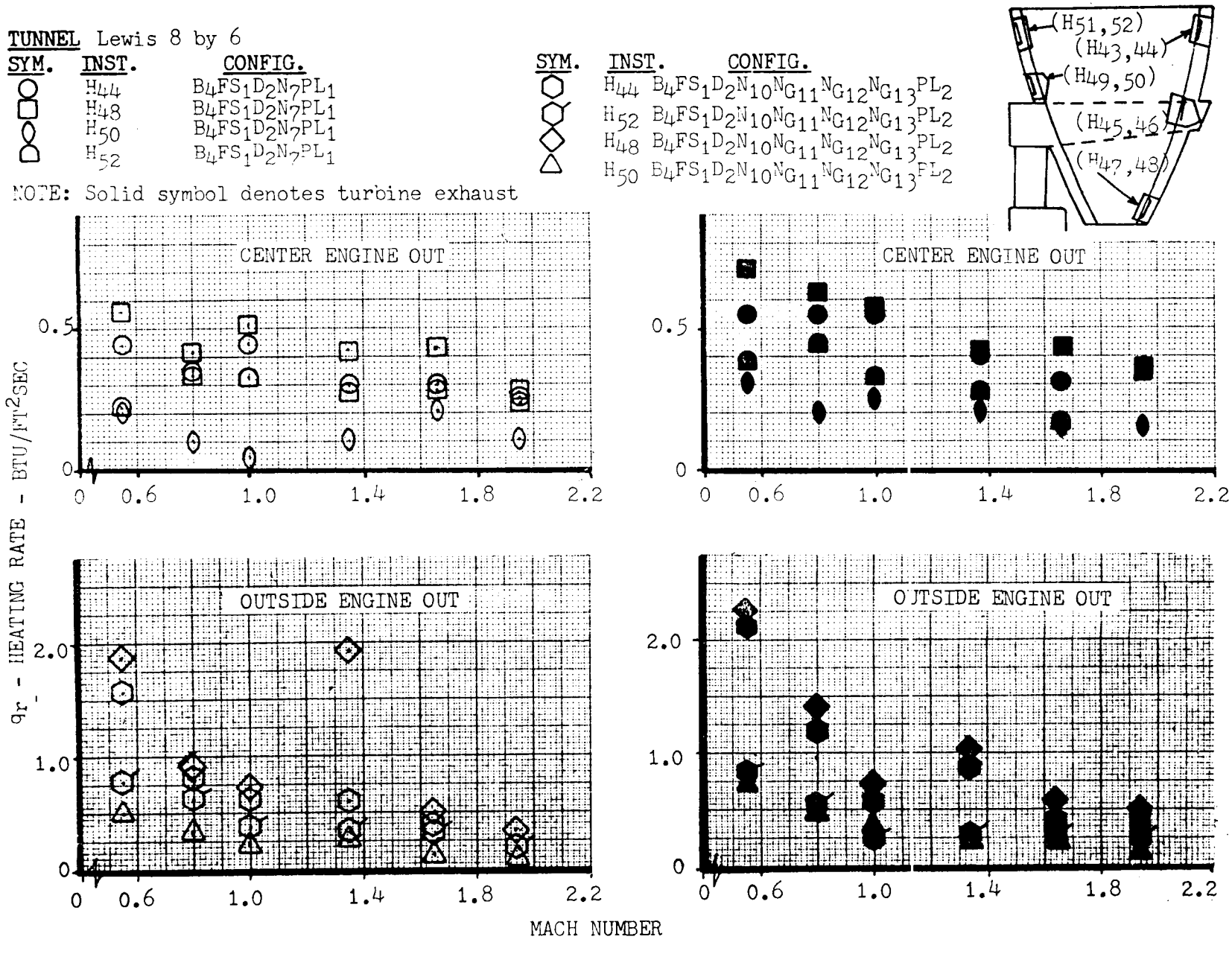

FIGURE 4.4-31 INTERNAL ENGINE RADIATION FROM M = 0.55 TO M = 1.96

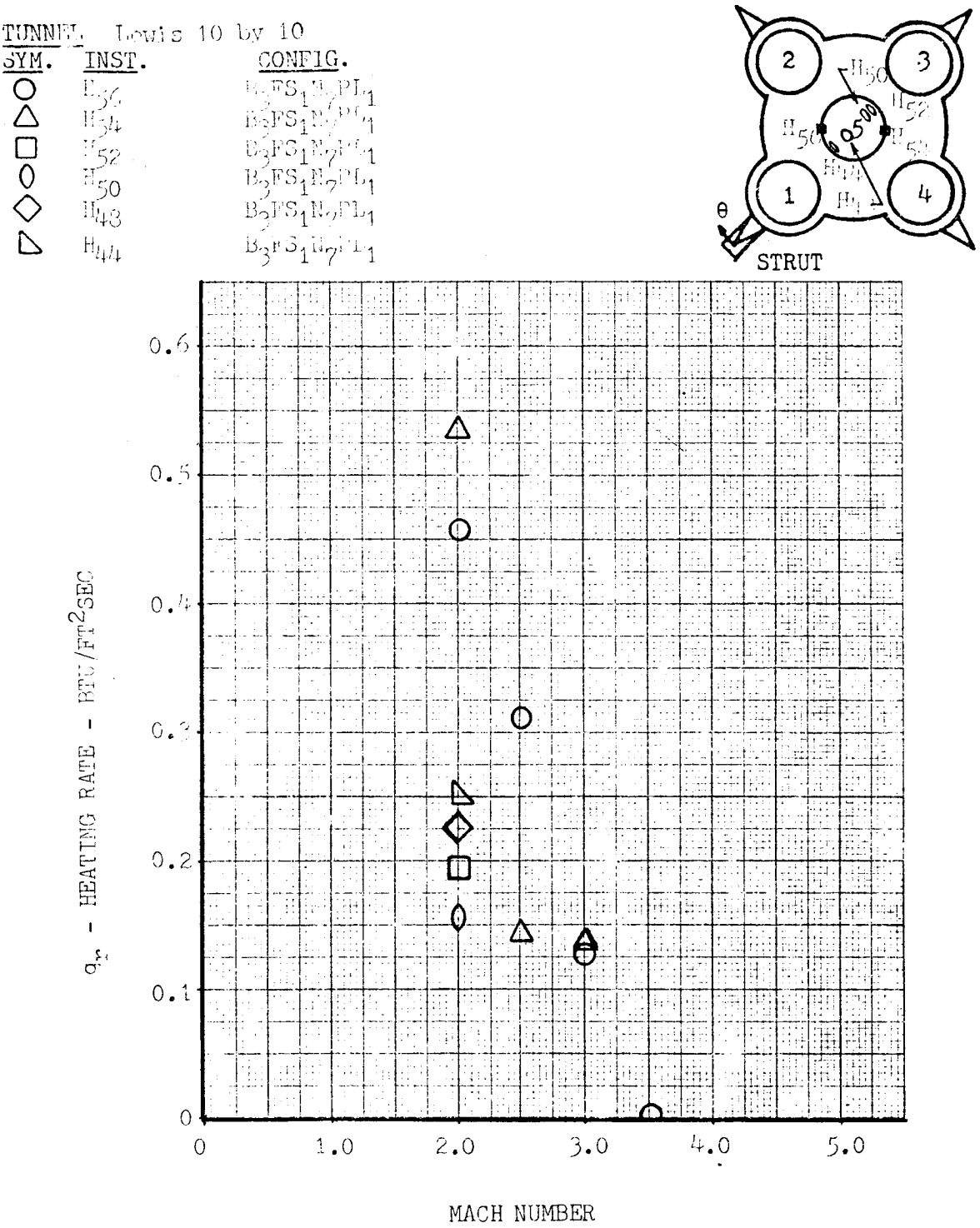

FIGURE 4.4-32 INTERNAL ENGINE RADIATION FROM M = 2.0 TO 3.5

TUNNEL Cornell Altitude Chamber

SYM.	INST.	CONFIG.
□	H_{22}	$B_1FS_1N_{1-5}PL_1$
◇	H_{44}	$B_1FS_1N_7PL_1$
◇	H_{48}	$B_1FS_1N_7PL_1$
○	H_{54}	$B_1FS_1N_7PL_1$

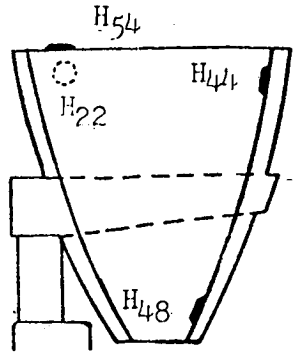

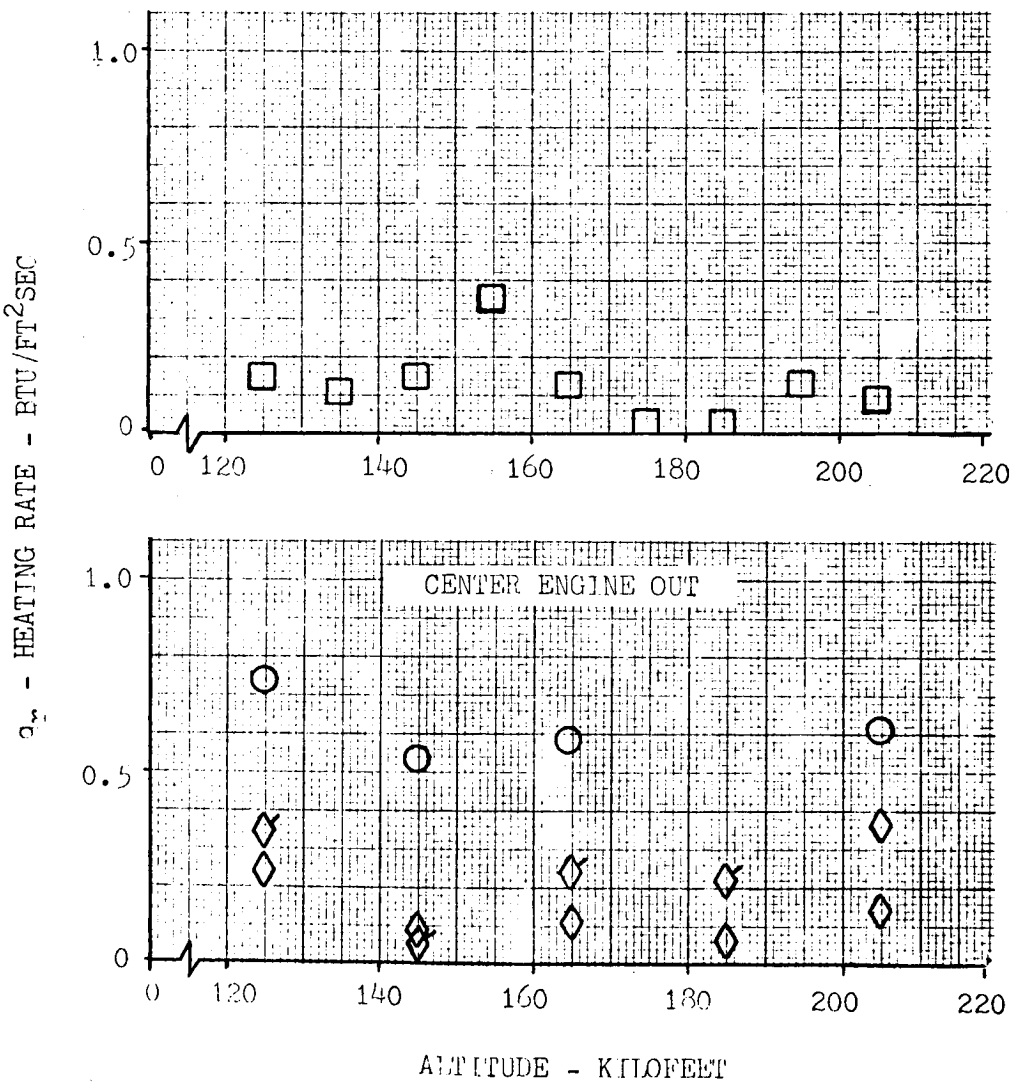

FIGURE 4.4-33 INTERNAL ENGINE RADIATION FROM 125,000 TO 205,000 FEET

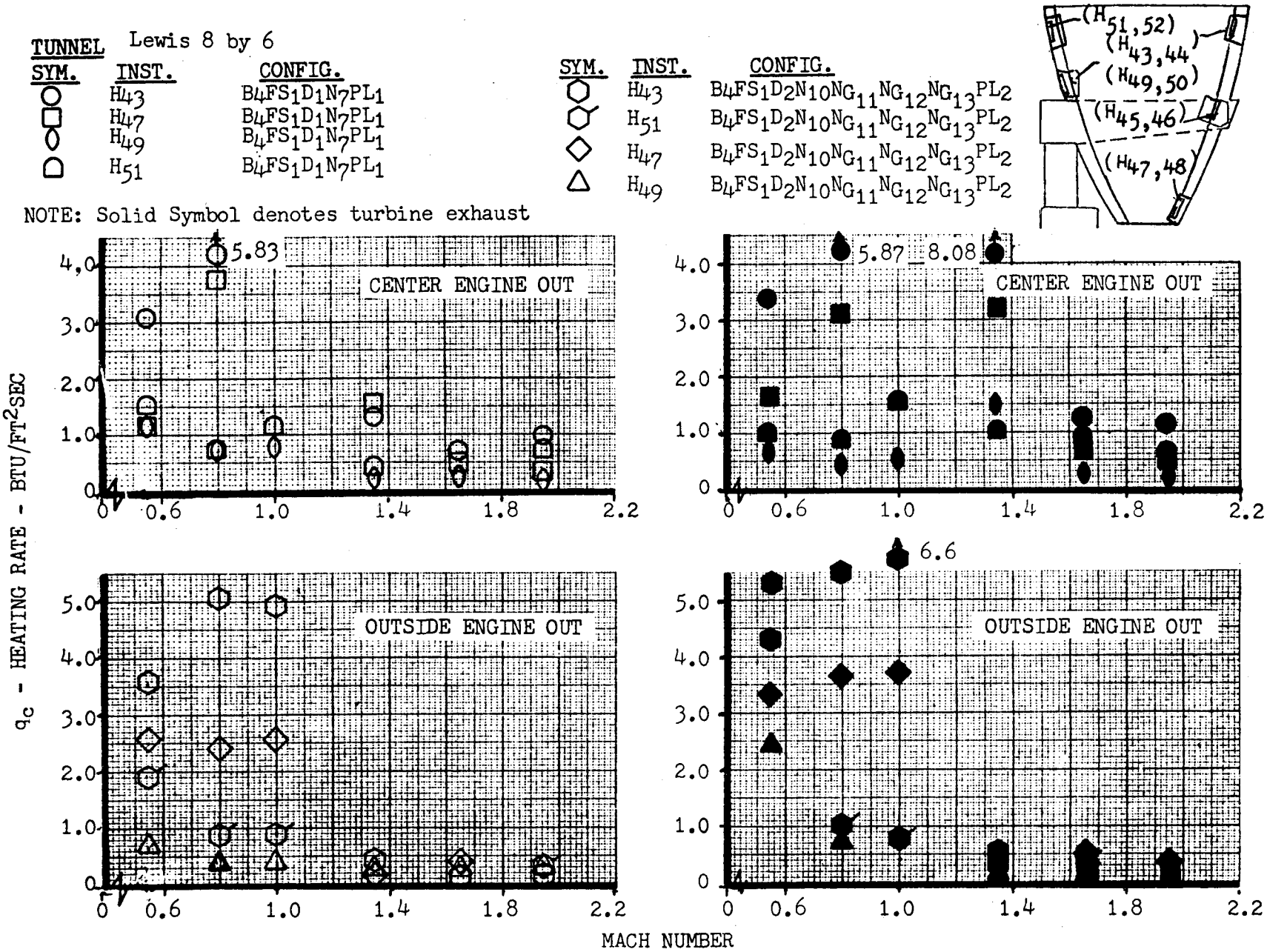

FIGURE 4.4-34 INTERNAL ENGINE CONVECTION FROM M = 0.55 TO 1.96

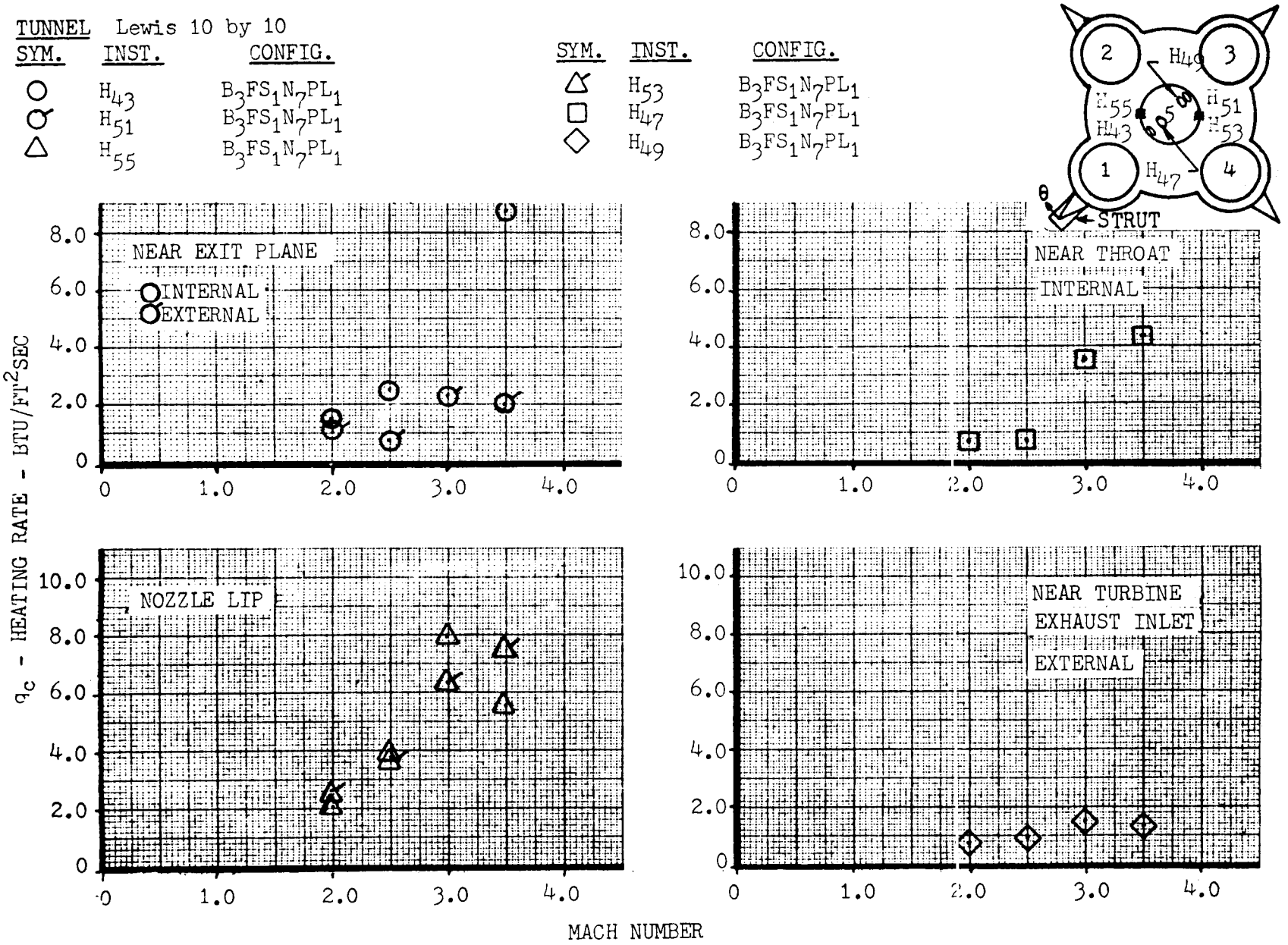

FIGURE 4.4-35 INTERNAL ENGINE CONVECTION FROM M = 2.0 TO 3.5

TUNNEL Cornell Altitude Chamber

SYM.	INST.	CONFIG.
◇	H_{53}	$B_1FS_1N_7PL_1$
◇	H_{55}	$B_1FS_1N_7PL_1$
◇	H_{43}	$B_1FS_1N_7PL_1$
◇	H_{51}	$B_1FS_1N_7PL_1$
◇	H_{47}	$B_1FS_1N_7PL_1$

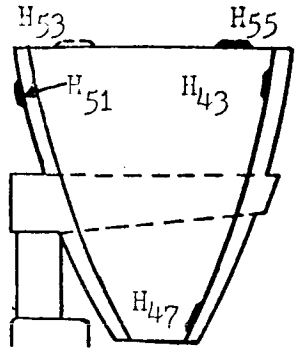

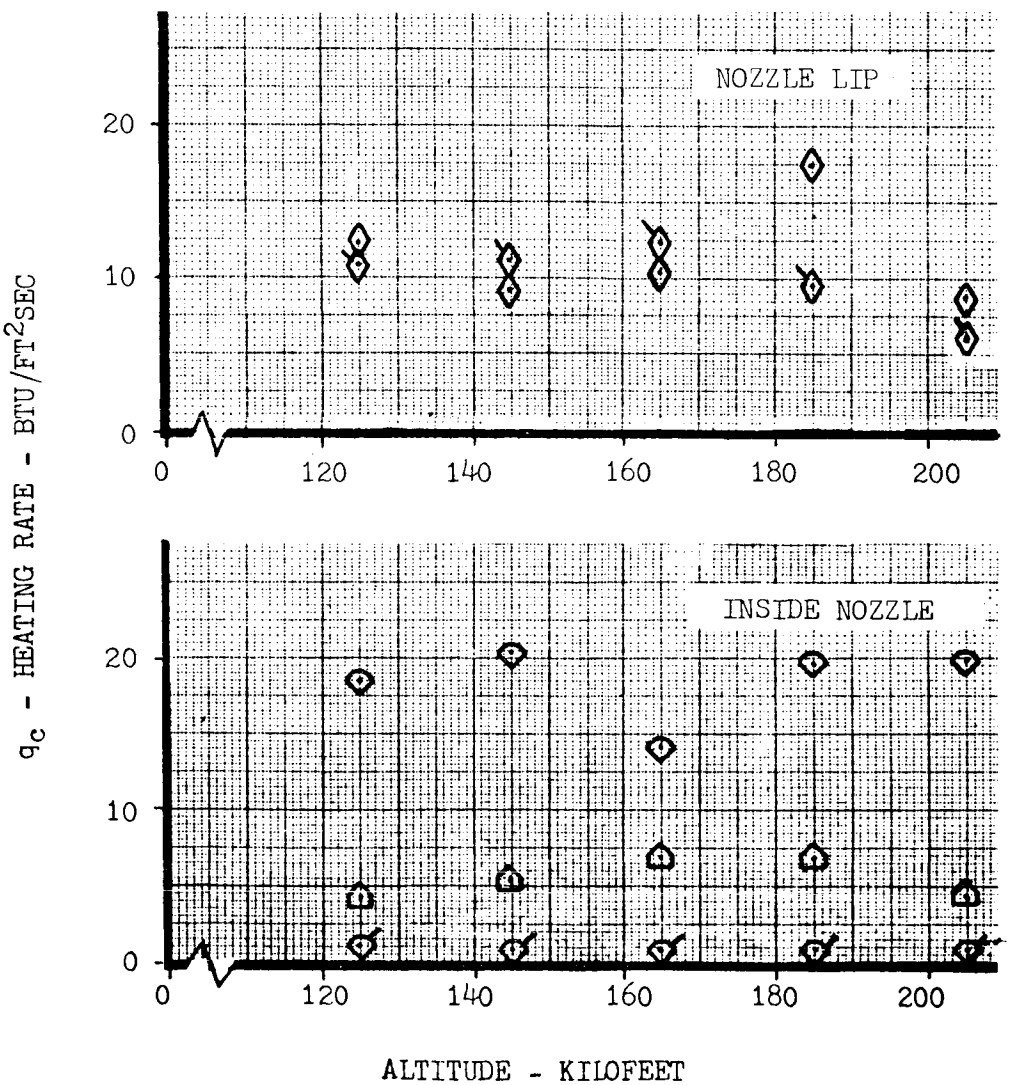

FIGURE 4.4-36 INTERNAL ENGINE CONVECTION FROM 125,000 TO 205,000 FEET

△ H_7 $B_4FS_1N_{1-5}PL_3$

▲ H_{12} $B_4FS_1N_{1-5}PL_3$

□ H_5 $B_4FS_1N_{1-5}PL_3$

◇ H_{10} $B_4FS_1N_{1-5}PL_3$

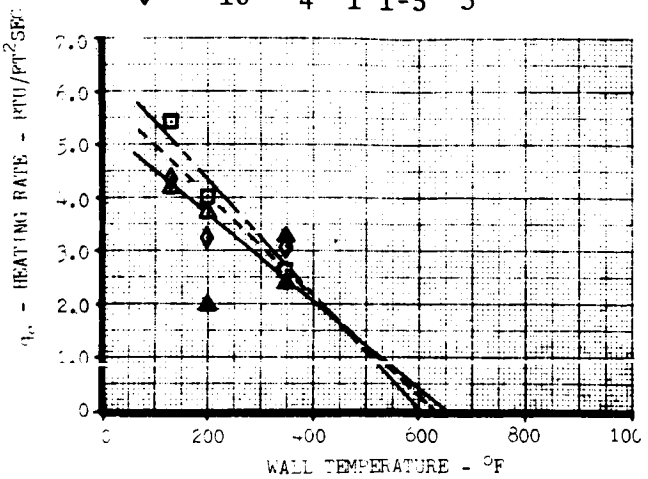

MACH 0.55
WITH TURBINE EXHAUST

GAUGE	h_c
$H_{7,12}$	.0061
H_5	.0108
H_{10}	.0094

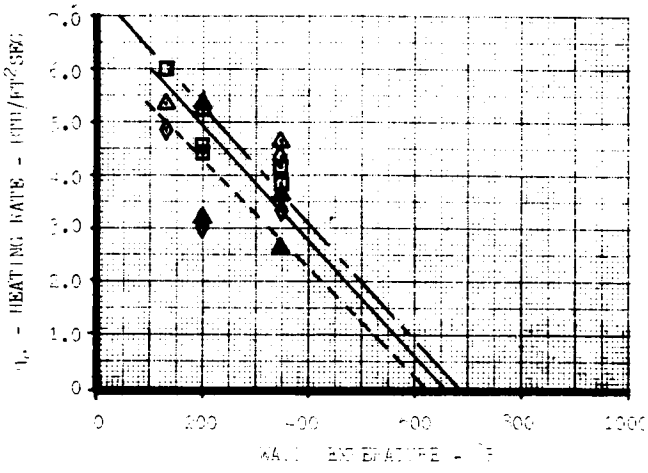

MACH 0.80
WITH TURBINE EXHAUST

GAUGE	h_c
$H_{7,12}$	.0109
H_5	.0110
H_{10}	.0105

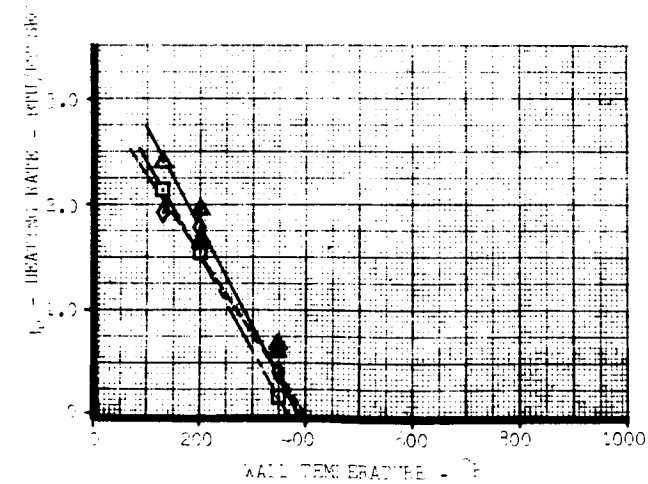

MACH 1.20
WITH TURBINE EXHAUST

GAUGE	h_c
$H_{7,12}$	.0092
H_5	.0078
H_{10}	.0094

FIGURE 4.4-37 EFFECT OF WALL TEMPERATURE ON BASE CONVECTIVE HEATING

□	H_{10}	$B_1FS_1N_1\text{-}5PL_1$
□	H_{11}	$B_1FS_1N_1\text{-}5PL_1$
□	H_{12}	$B_1FS_1N_1\text{-}5PL_1$
◇	H_5	$B_1FS_1N_1\text{-}5PL_1$
◇	H_6	$B_1FS_1N_1\text{-}5PL_1$
◇	H_7	$B_1FS_1N_1\text{-}5PL_1$

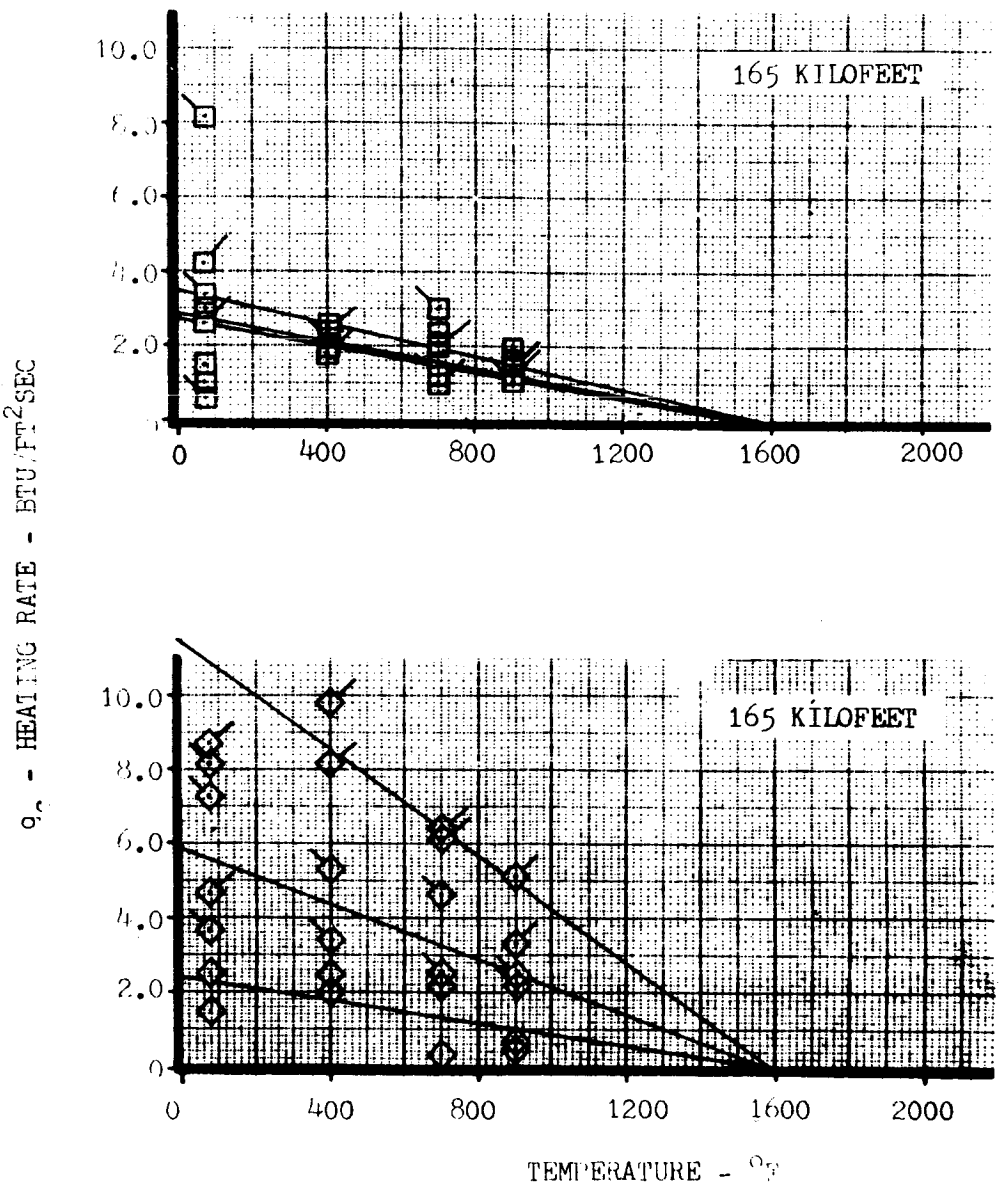

FIGURE 4.4-38 EFFECT OF WALL TEMPERATURE ON BASE CONVECTIVE HEATING

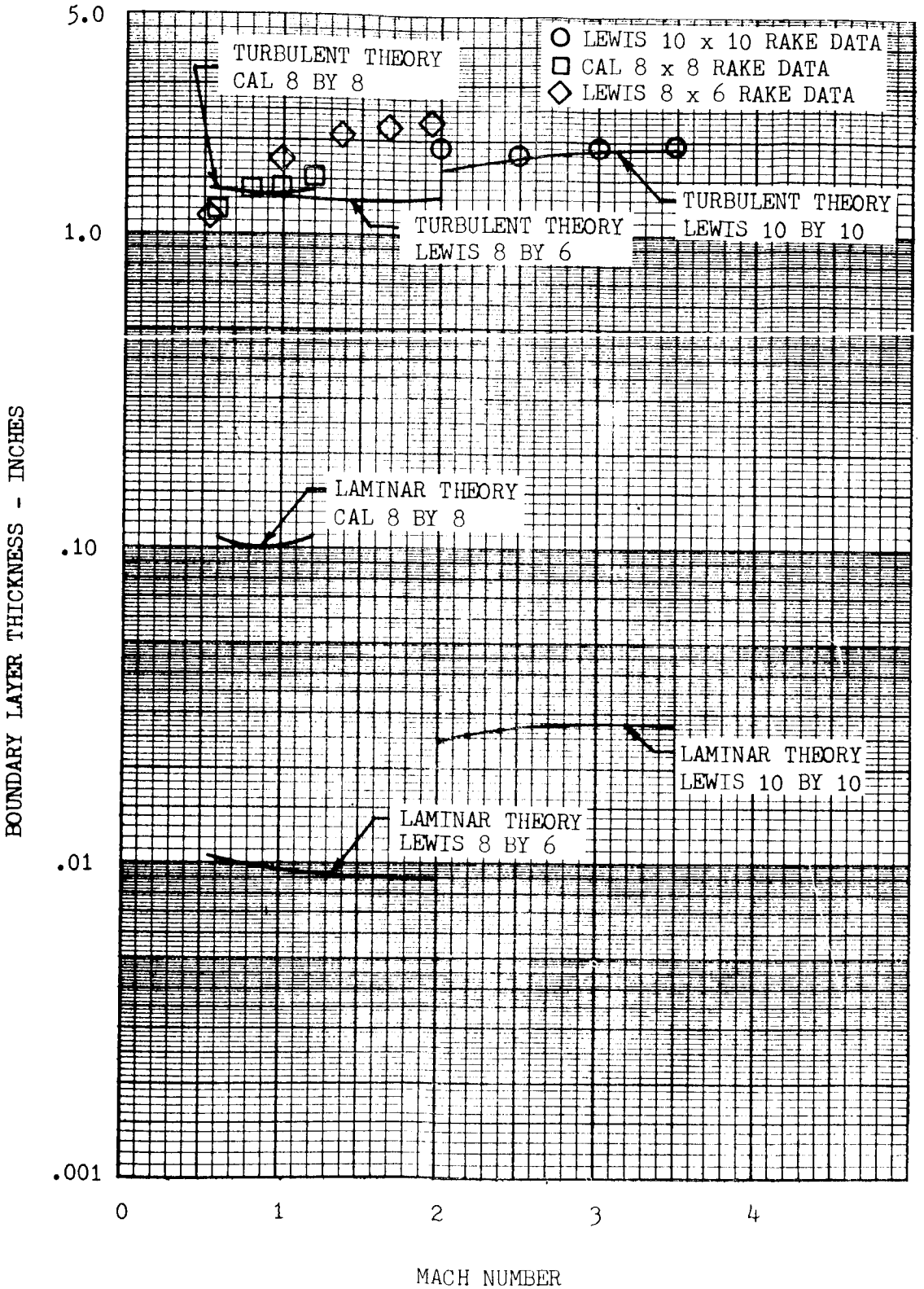

FIGURE 4.4-39 MODEL BOUNDARY LAYER THICKNESS VERSUS THEORY

TUNNEL Lewis 8 by 6

SYM.	INST.	CONFIG.	SYM.	INST.	CONFIG.
○	$H_{10,8,6,4,2}$	$B_4FS_1N_{1-5}PL_1$			

NOTE: 1. Solid symbol denotes H_2 turbine exhaust
2. Half solid symbol denotes C_2H_4 turbine exhaust

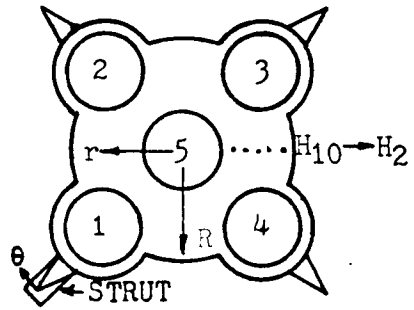

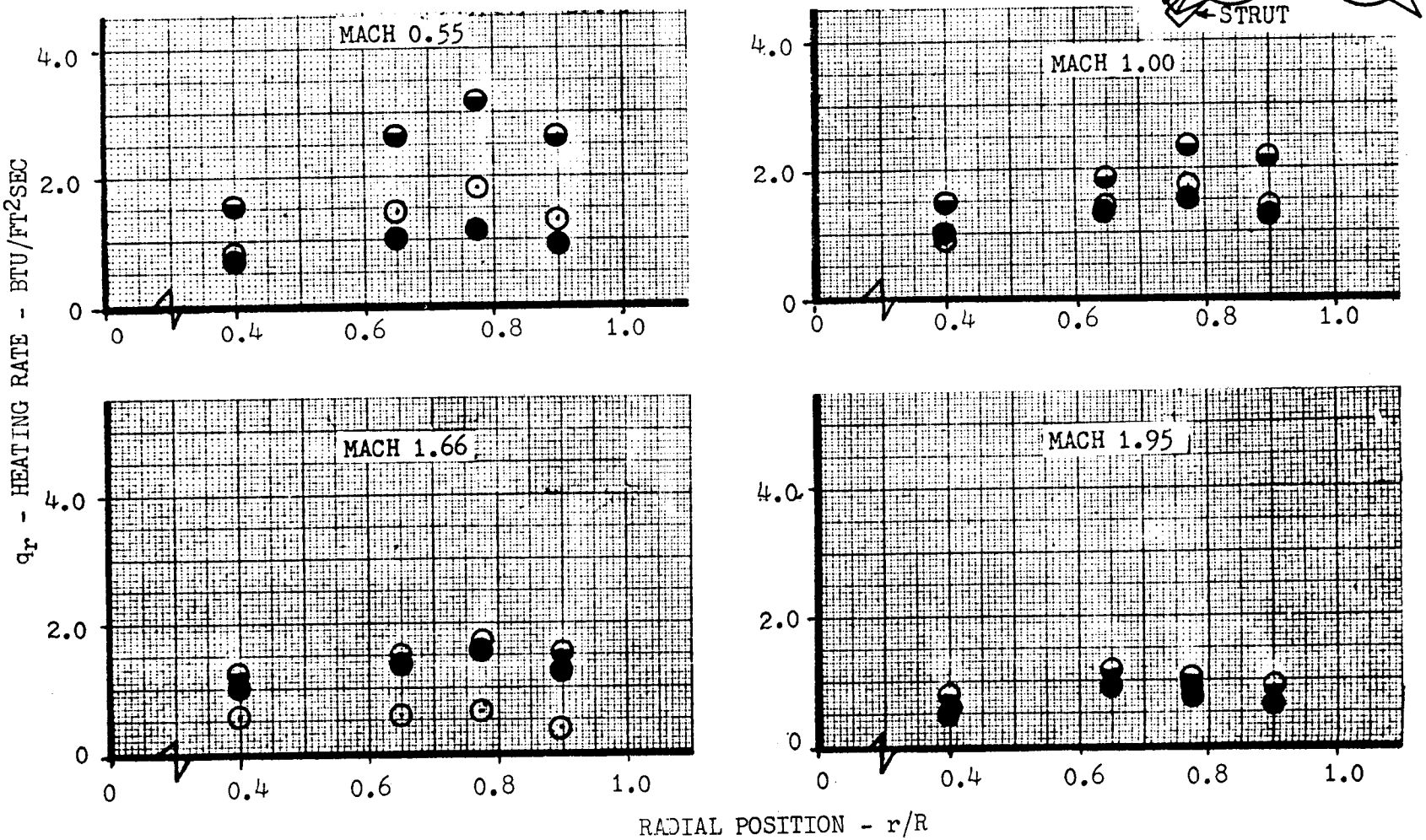

FIGURE 4.4-40 RADIATION HEATING DISTRIBUTION FROM M = 0.55 TO 1.95

TUNNEL CAL 8 BY 8

SYM.	INST.	CONFIG.	SYM.	INST.	CONFIG.
□		$B_1FS_1N_{1-5}PL_1$	□		$B_1FS_1N_{1-5}PL_1$
□		$B_1FS_1N_{1-5}PL$	□		$B_1FS_1N_{1-5}PL_1$

NOTE: Solid symbol denotes turbine exhaust

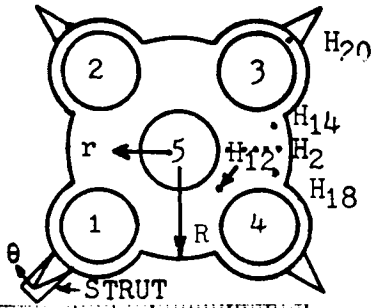

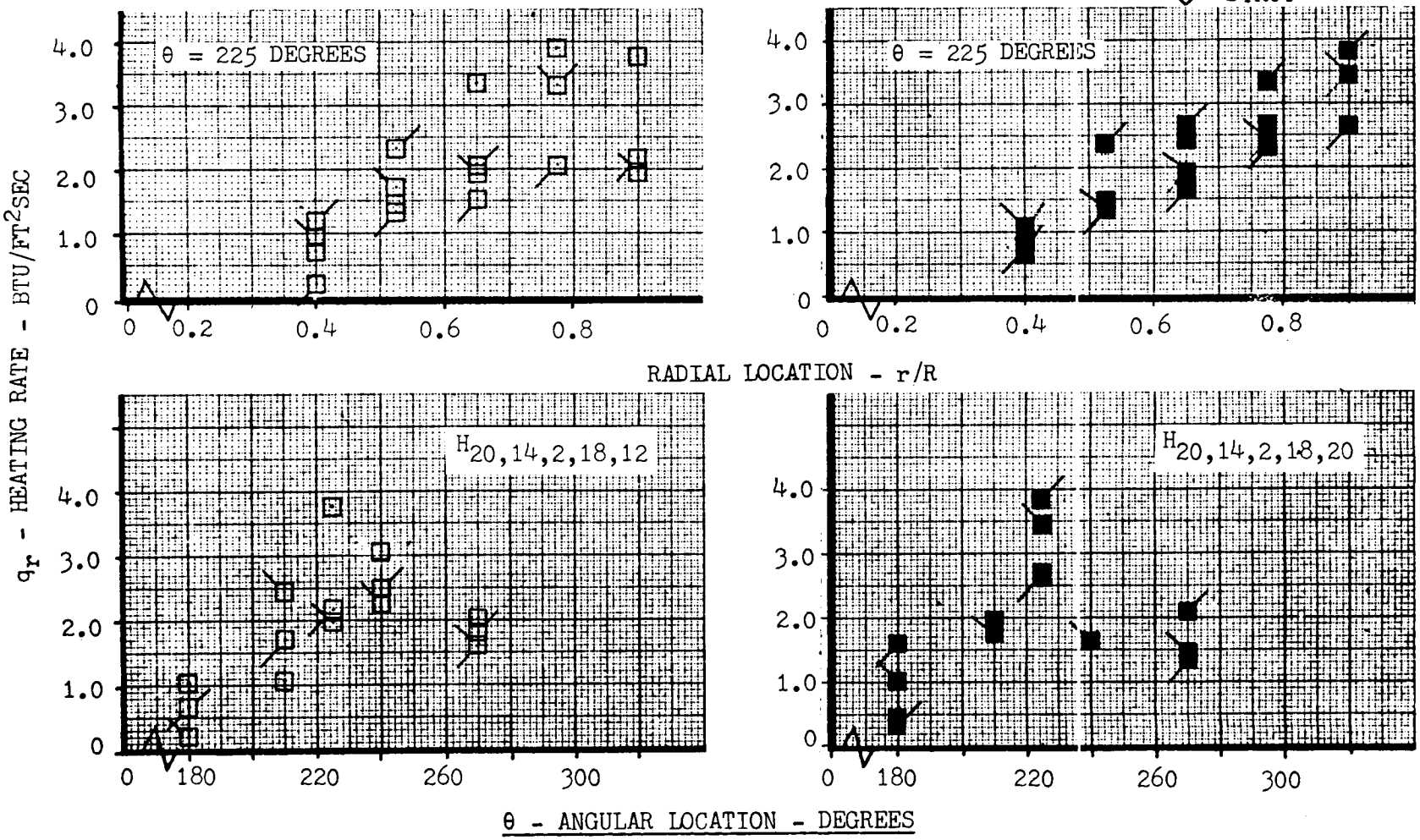

FIGURE 4.4-41 RADIATION HEATING DISTRIBUTION AT M = 1.2

TUNNEL Lewis 10 by 10

SYM.	INST.	CONFIG.
○	$H_{2,4,6,8,10}$	$B_3FS_1SC_1D_1N_{1-5}PL_1$

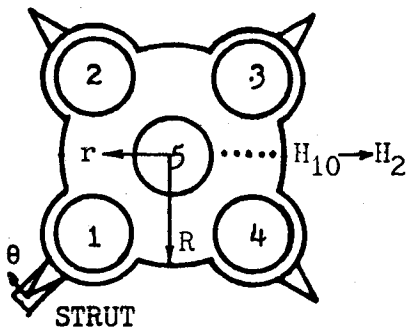

NOTE: 1. Solid symbol denotes turbine exhaust
2. Flag right denotes Mach 2.0 data
3. Flag left denotes Mach 3.5 data

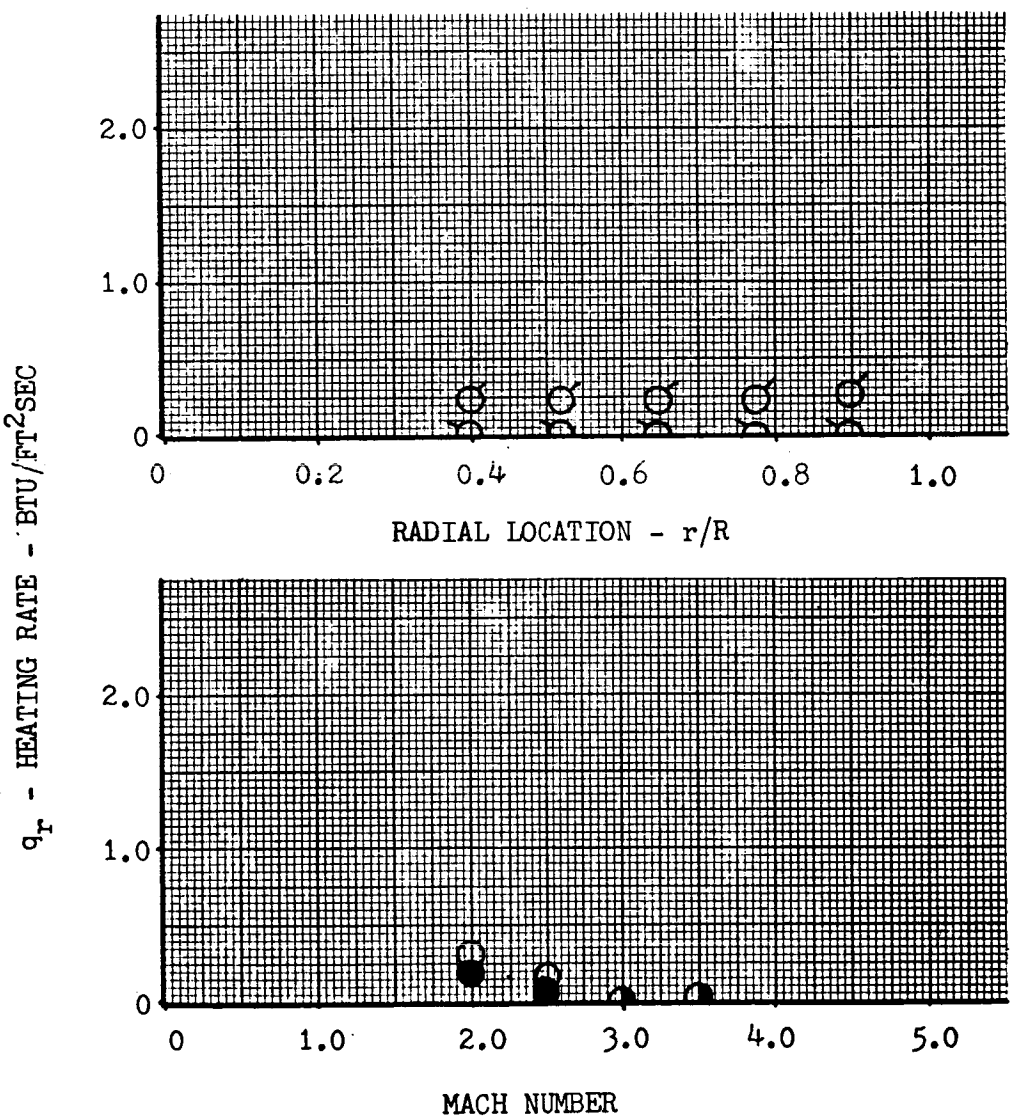

FIGURE 4.4-42 RADIATION HEATING DISTRIBUTION FROM M = 2.0 TO 3.5

TUNNEL Cornell Altitude Chamber

SYM.	INST.	CONFIG.
□	$H_{2,4,6,8,10}$	$B_1FS_1N_{1-5}PL_1$
△	$H_{2,4,6,8,10}$	$B_1FS_1N_{G_3}N_{G_4}PL_1$
◺	$H_{2,4,6,8,10}$	$B_1FS_1N_{G_5}N_{G_6}PL_1$
◇	$H_{2,4,6,8,10}$	$B_1FS_1N_7PL_1$

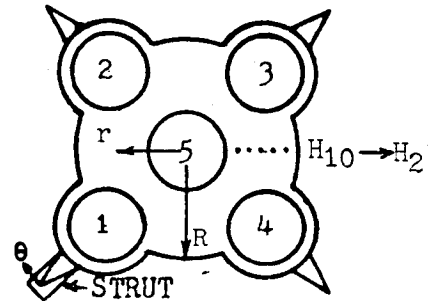

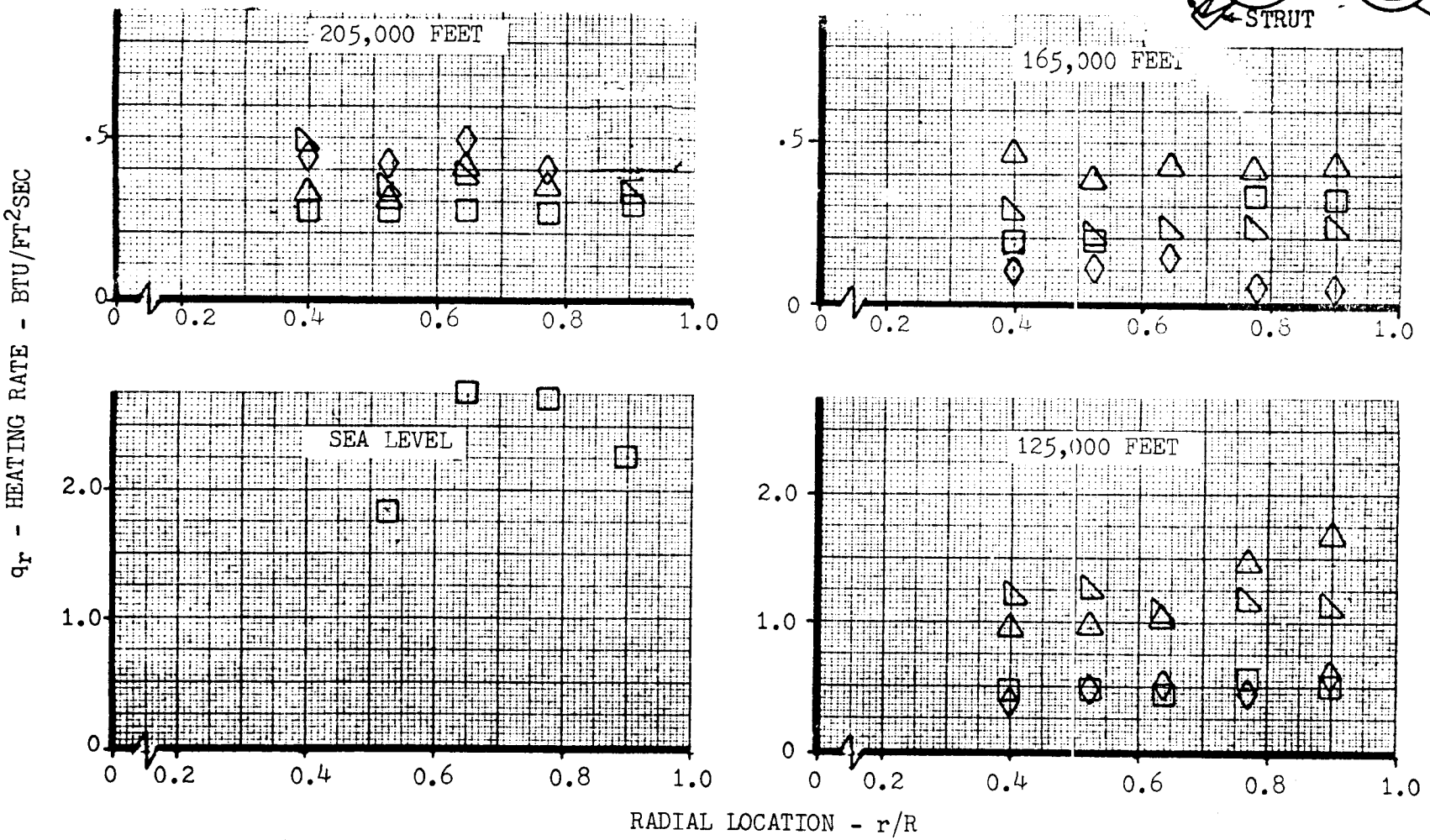

FIGURE 4.4-43 RADIATION HEATING DISTRIBUTION FROM 125,000 TO 205,000 FEET

TUNNEL CAL 8 BY 8

SYM.	MACH NO.	CONFIG.
□	0.6	$B_1FS_1N_{1-5}PL_1$
◪	0.8	$B_1FS_1N_{1-5}PL_1$

SYM.	MACH NO.	CONFIG.
◪	1.0	$B_1FS_1N_{1-5}PL_1$
◪	1.2	$B_1FS_1N_{1-5}PL_1$

NOTE: Solid symbol denotes turbine exhaust

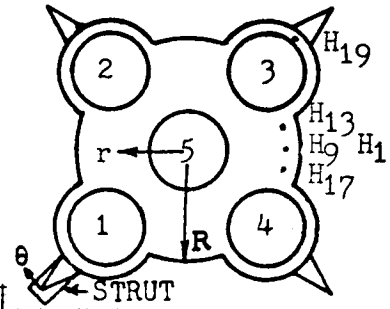

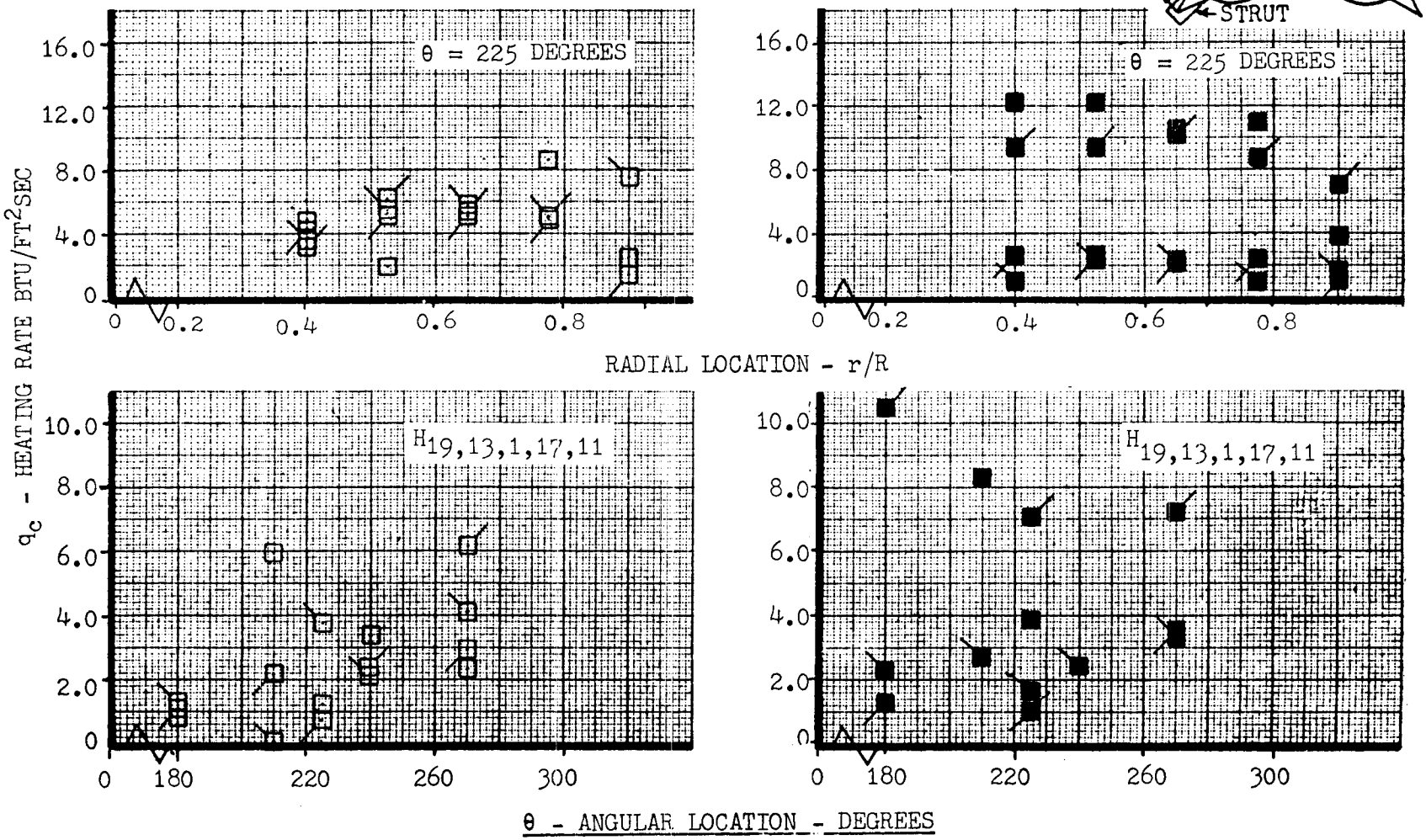

FIGURE 4.4-44 CONVECTIVE HEATING DISTRIBUTION FROM M = 0.6 TO 1.2

TUNNEL	LEWIS 8 BY 6	
SYM.	INST.	CONFIG.
○	$H_{1,3,5,9}$	$B_4FS_1N_{1-5}$

NOTE: 1. Solid symbol denotes H_2 turbine exhaust
2. Half solid symbol denotes C_2H_4 turbine exhaust

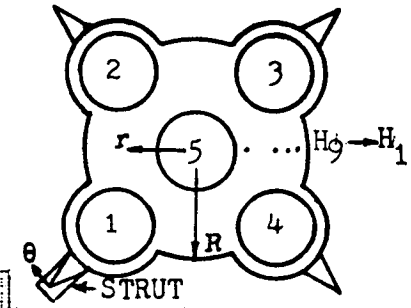

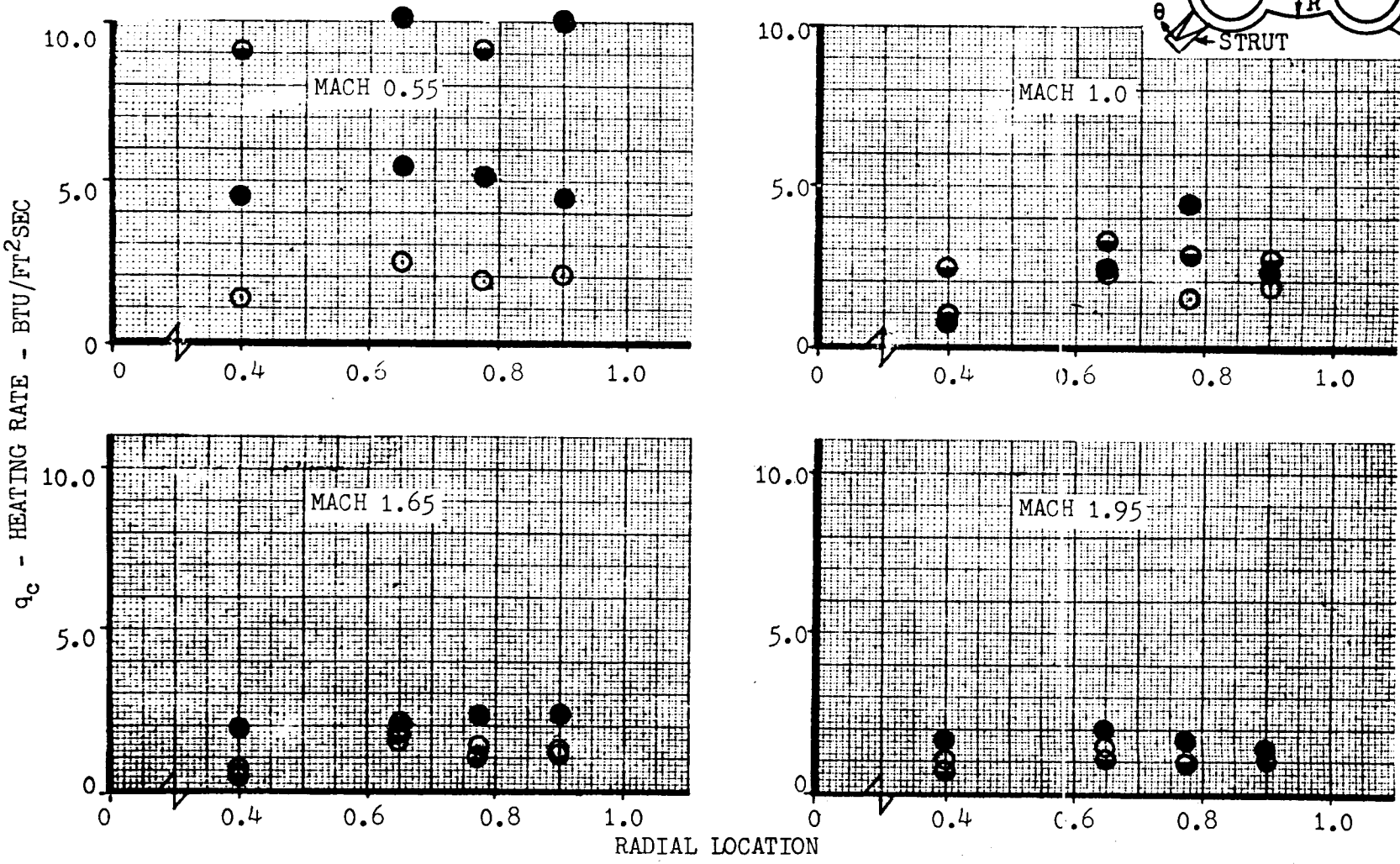

FIGURE 4.4-45 CONVECTIVE HEATING DISTRIBUTION FROM M = 0.55 TO 1.95

TUNNEL Lewis 10 by 10

SYM.	INST.	CONFIG.
□	$H_{1,3,5,7,9}$	$B_3FS_1N_{1-5}PL_1$
○	$H_{1,3,5,7,9}$	$B_3FS_1SC_1D_1N_{1-5}PL_1$
△	$H_{1,3,5,7,9}$	$B_3FS_1SC_2D_3N_{1-5}PL_1$

SYM.	INST.	CONFIG.
◇	$H_{1,3,5,7,9}$	$B_3FS_4N_{1-5}PL_1$
◇	$H_{1,3,5,7,9}$	$B_3FS_1NG_3NG_4PL_1$
◺	$H_{1,3,5,7,9}$	$B_3FS_1NG_5NG_6PL_1$
⬠	$H_{1,3,5,7,9}$	$B_3FS_1N_7PL_1$

NOTE: Data are at Mach 3.5

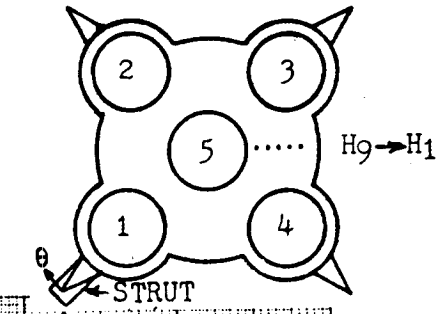

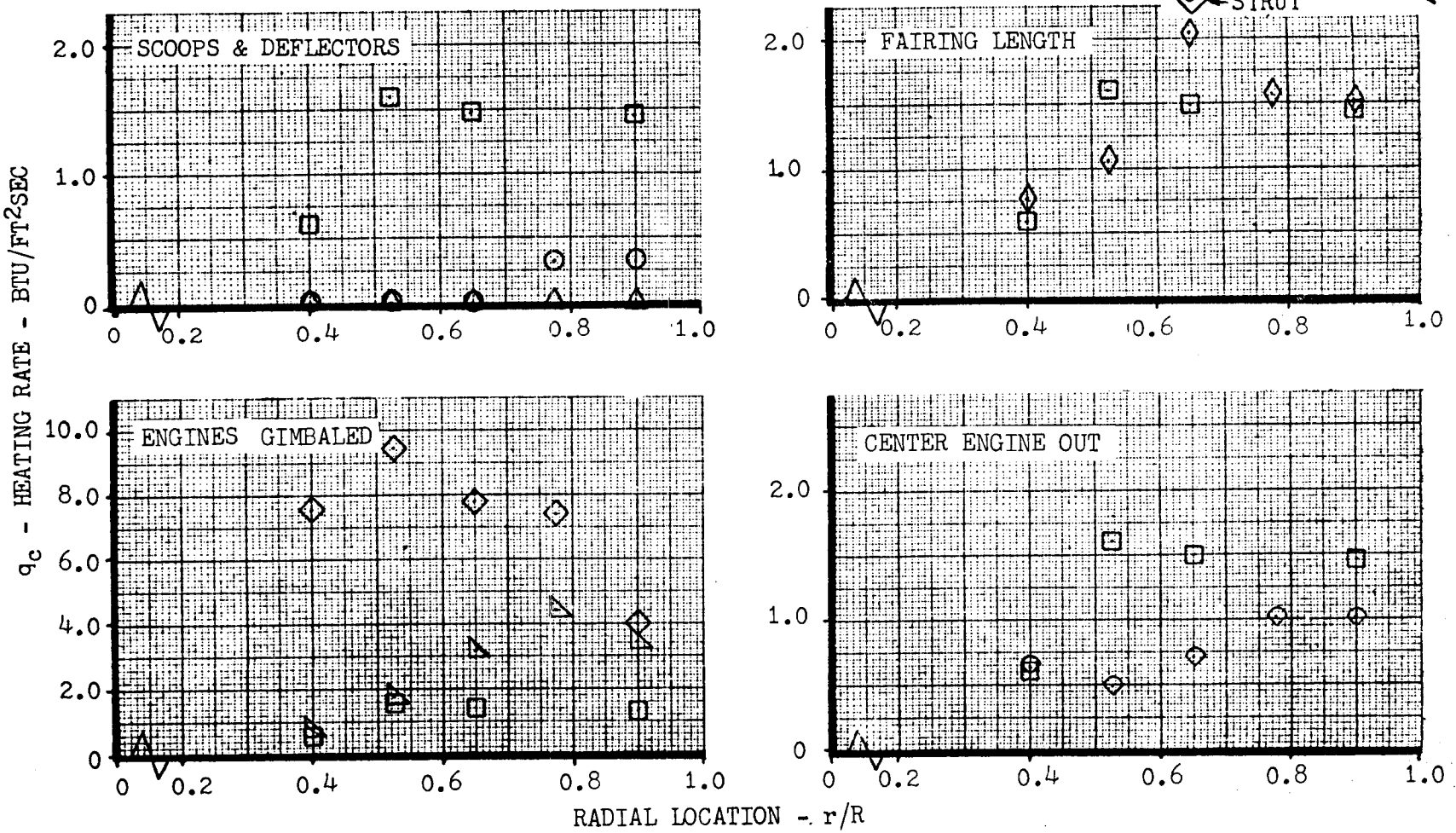

FIGURE 4.4-46 CONVECTIVE HEATING DISTRIBUTION AT M = 3.5

TUNNEL Cornell Altitude Chamber

SYM.	INST.	CONFIG.
□	$H_{1,3,5,7,9}$	$B_1FS_1N_{1-5}PL_1$
○	$H_{1,3,5,7,9}$	$B_1FS_4SC_1N_{1-5}PL_1$
△	$H_{1,3,5,7,9}$	$B_1FS_1N_{G_3}N_{G_4}PL_1$
◺	$H_{1,3,5,7,9}$	$B_1FS_1N_{G_5}N_{G_6}PL_1$
◇	$H_{1,3,5,7,9}$	$B_1FS_1N_7PL_1$

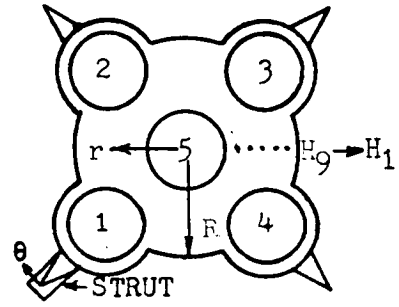

NOTE: Solid symbol denotes turbine exhaust.

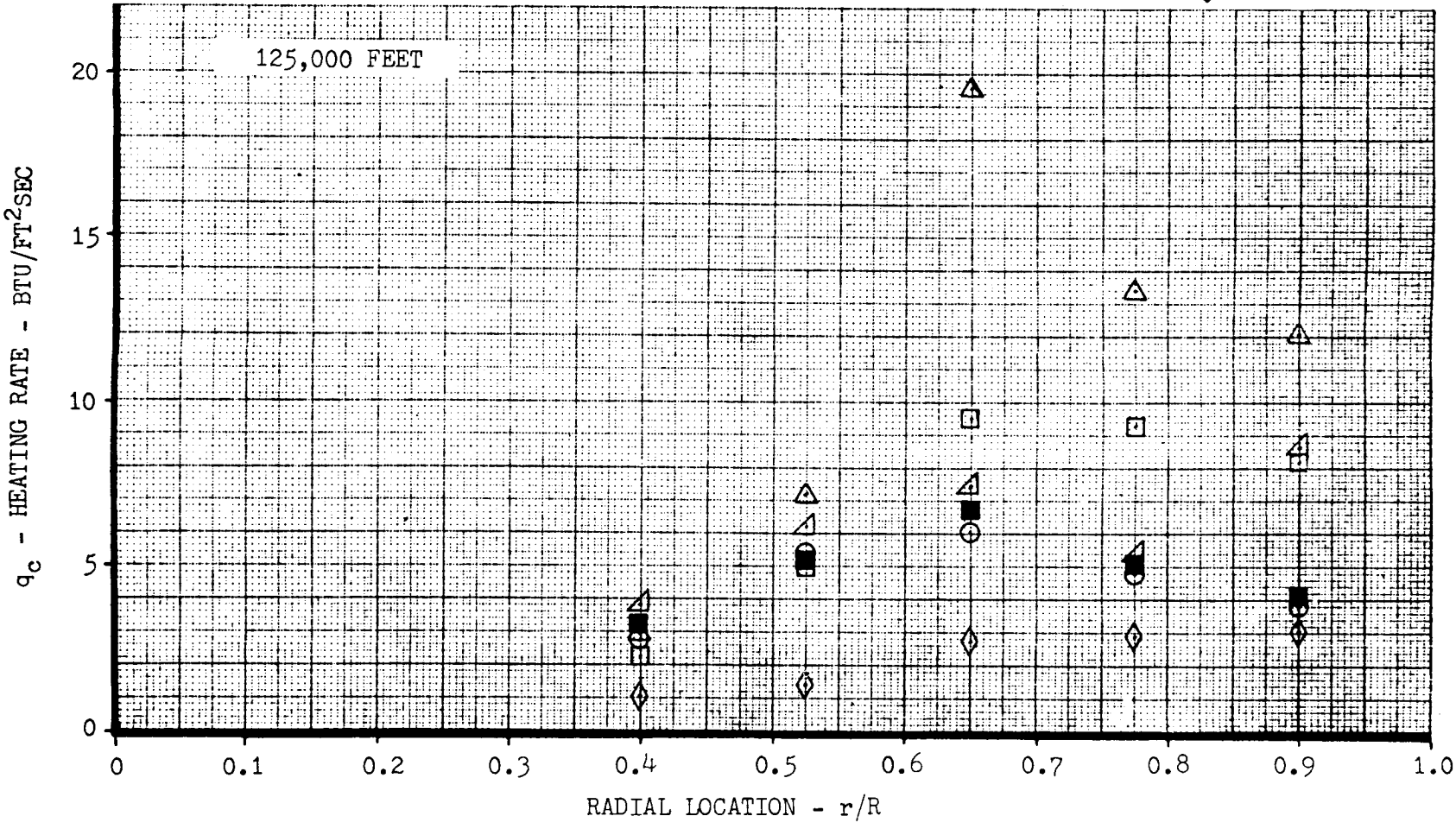

FIGURE 4.4-47 CONVECTION HEATING DISTRIBUTION AT 125,000 FEET

TUNNEL Cornell Altitude Chamber

SYM.	INST.	CONFIG.
□	$H_{1,3,5,7,9}$	$B_1FS_1N_{1-5}PL_1$
○	$H_{1,3,5,7,9}$	$B_1FS_4SC_1N_{1-5}PL_1$

SYM.	INST.	CONFIG.
△	$H_{1,3,5,7,9}$	$B_1FS_1N_{G_3}N_{G_4}PL_1$
◺	$H_{1,3,5,7,9}$	$B_1FS_1N_{G_5}N_{G_6}PL_1$
◇	$H_{1,3,5,7,9}$	$B_1FS_1N_7PL_1$

NOTE: Solid symbol denotes turbine exhaust

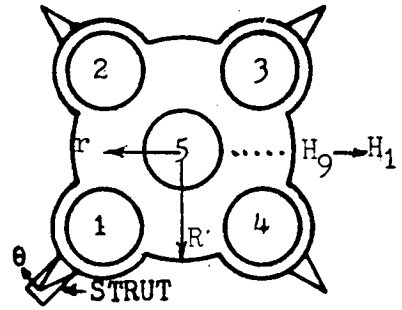

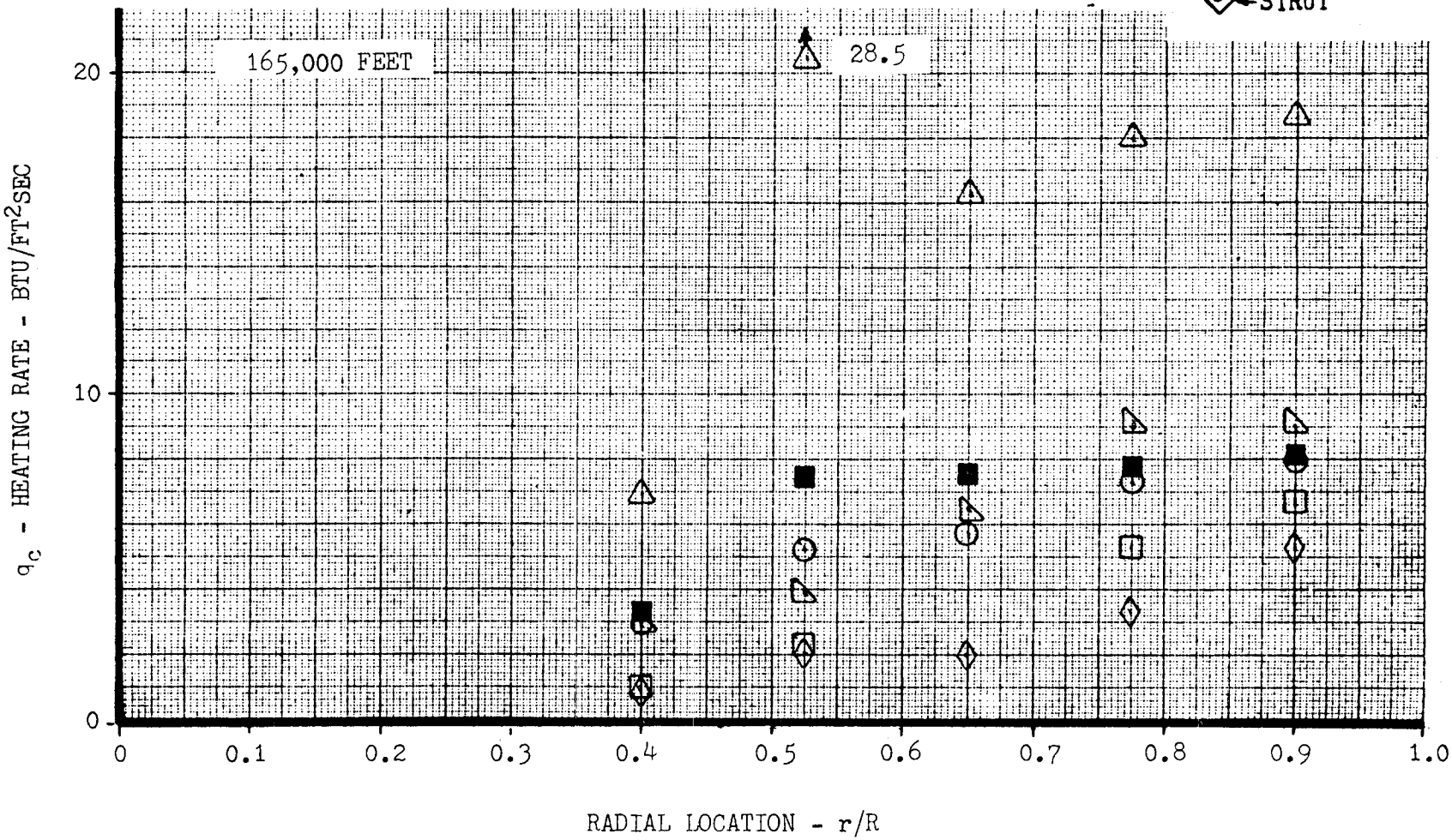

FIGURE 4.4-48 CONVECTIVE HEATING DISTRIBUTION AT 165,000 FEET

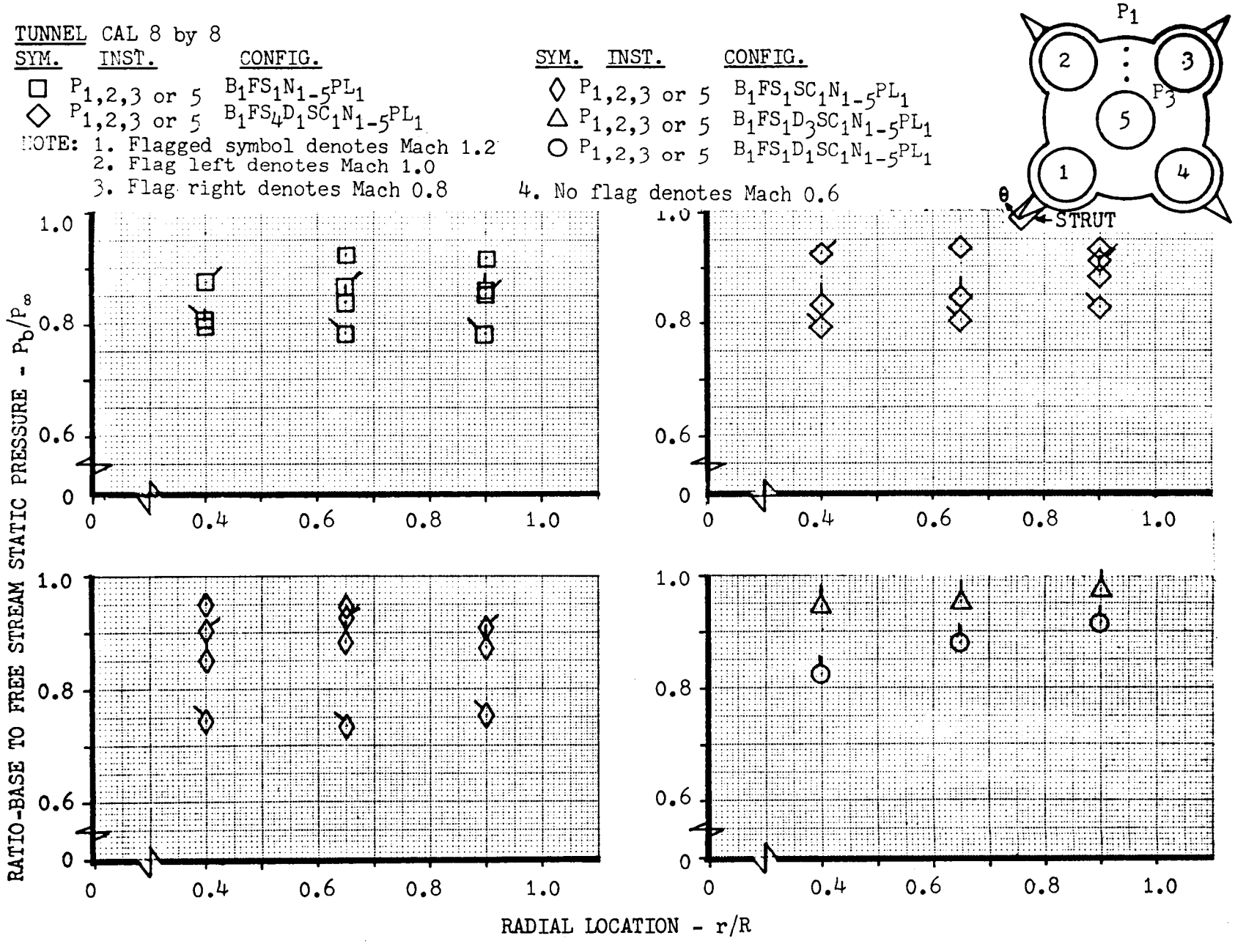

FIGURE 4.4-49 BASE PRESSURE DISTRIBUTION FROM M = 0.6 TO 1.2

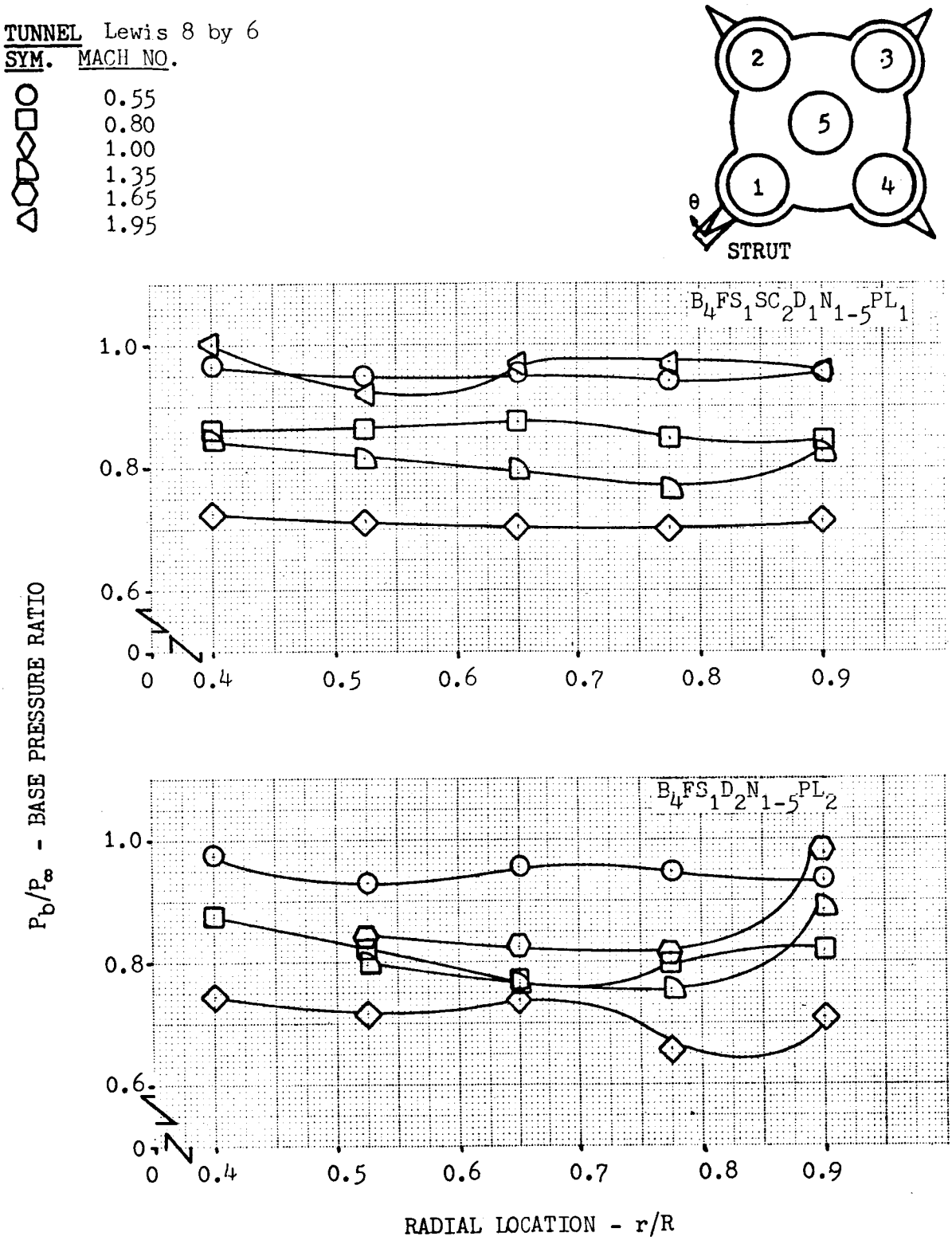

FIGURE 4.4-50 BASE PRESSURE DISTRIBUTION FROM M = 0.55 TO 1.95

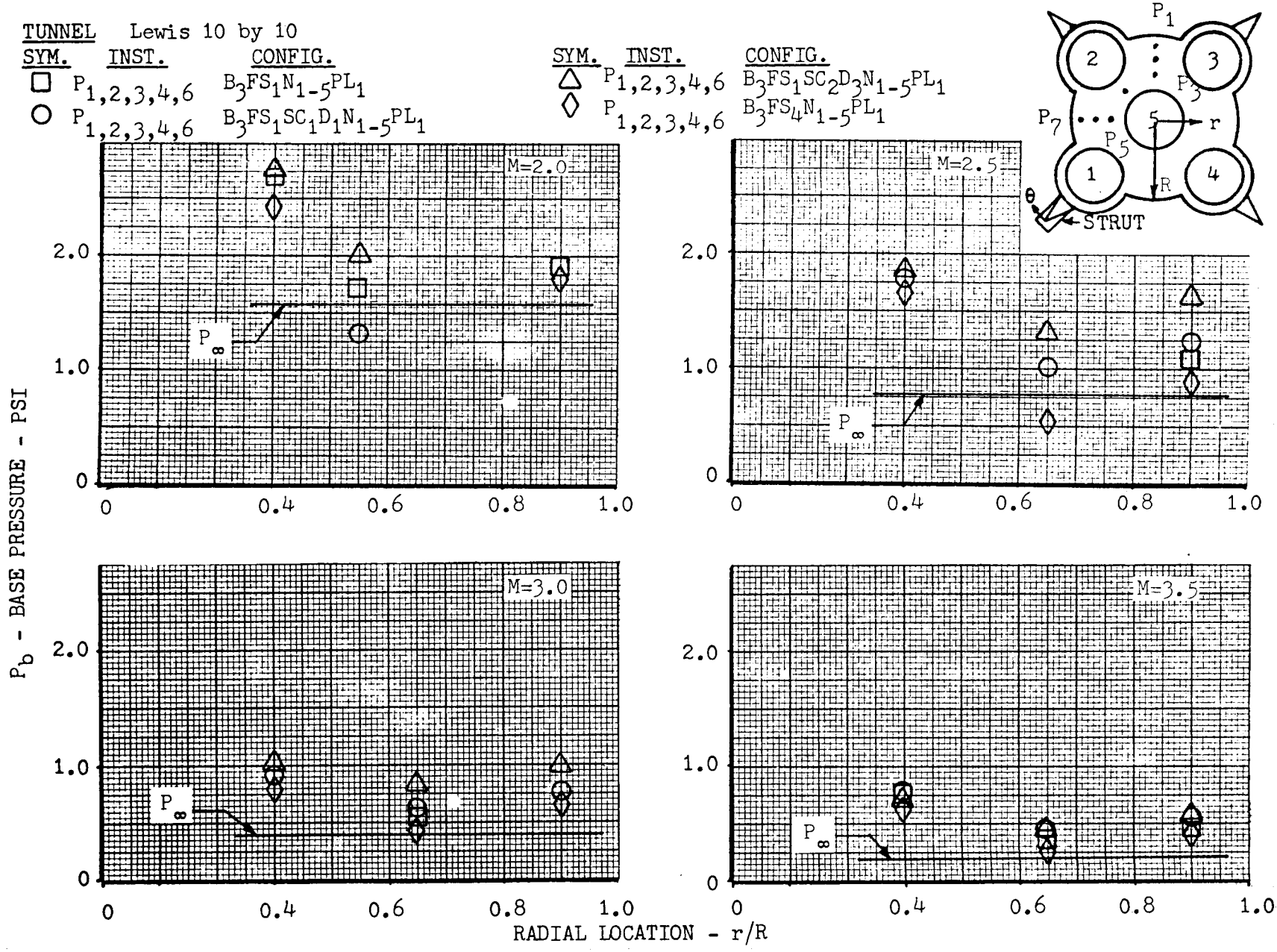

FIGURE 4.4-51 BASE PRESSURE DISTRIBUTION FROM M = 2.0 TO 3.5

TUNNEL Cornell Altitude Chamber

SYM.	INST.	CONFIG.
□	$P_{2,6}$	$B_1FS_1N_{1-5}PL_1$
◇	$P_{1,7}$	$B_1FS_1N_{1-5}PL_1$

NOTE: Flagged symbol denotes $P_{6,7}$

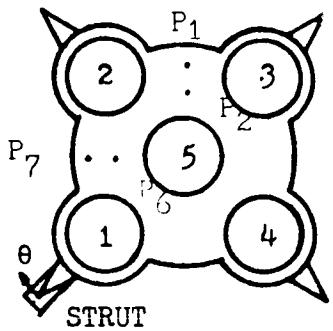

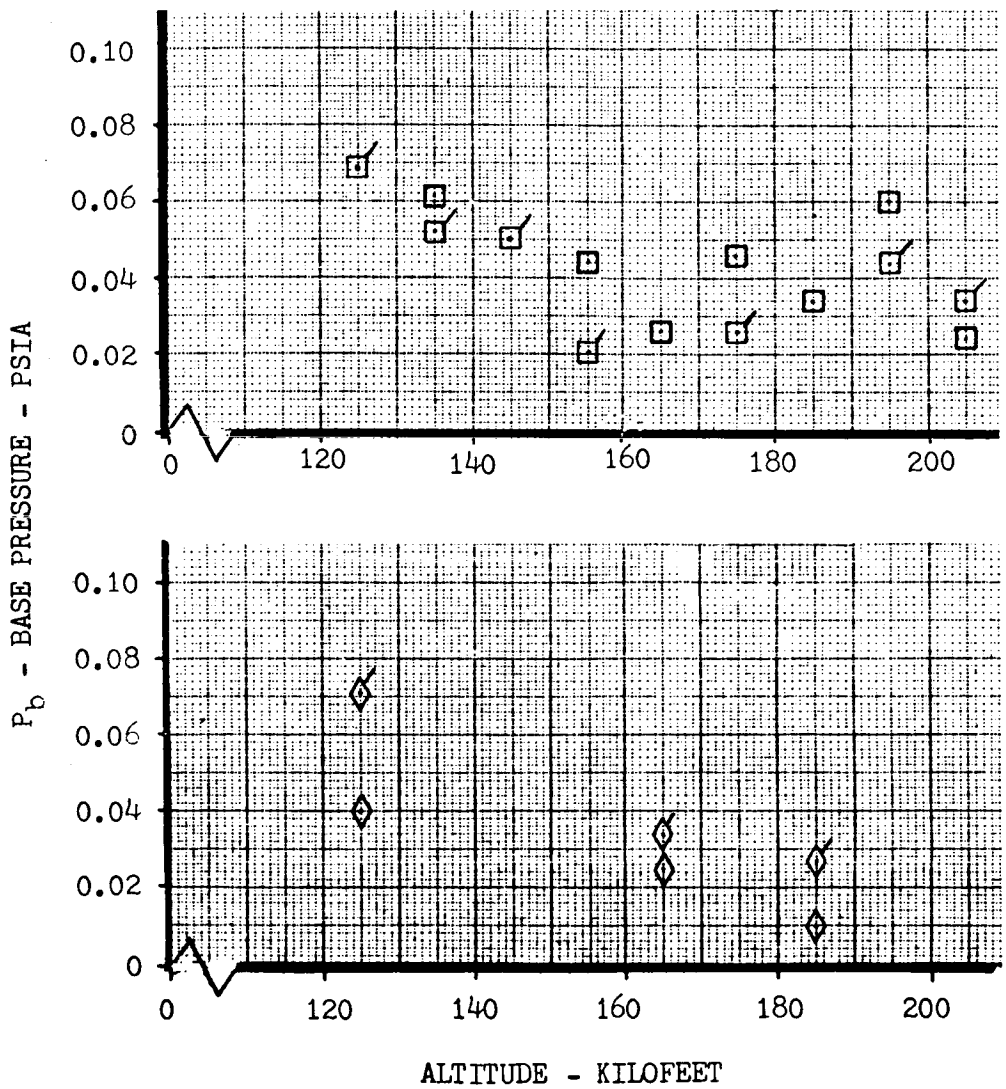

FIGURE 4.4-52 BASE PRESSURE DISTRIBUTION FROM 125,000 TO 205,000 FEET

4.5 FLIGHT TEST AND PARAMETRIC DATA

Apollo 4, 6, 8, 9 and 10 (AS-501 through AS-505) were launched successfully November 9, 1967; April 4, 1968; December 21, 1968; March 3, 1969; and May 18, 1969, respectively, from Cape Kennedy Florida. These missions were the first five flights of the Saturn V launch vehicle and the primary objectives were qualification of the vehicle and spacecraft for the lunar landing mission. Apollo 8 was the first manned Saturn V Apollo flight.

This section contains the S-IC base region flight heating and pressure data for vehicles AS-501 through AS-505. For convenience of analysis, the AS-501, AS-502 and AS-503 data are plotted and compared on one set of graphs and the AS-504 and AS-505 are plotted and compared on another. Figures 4.5-8 through 4.5-34 contain nearly all of the base heating data measured during these flights; and, since much of the flight instrumentation on the S-IC stage was removed on AS-506 and subsequent vehicles, these data constitute the majority of the S-IC base heating data existing. The data were taken from References 4-10 and 4-11.

Configurational changes on the S-IC stage included removal of the base region flow deflectors after the flight of AS-501, 2-degree outboard cant on the F-1 control engines of AS-503 and subsequent vehicles and early AS-503 inboard engine cutoff. No significant vehicle configuration or flight operating procedure changes were made which affected the base heating environments on vehicles AS-504 and AS-505.

The following paragraphs describe briefly the flight instrumentation, base flow field, thermal environments and flight parametric effects. Flight data will be compared to illustrate the parametric effects of flow deflectors, engine out, nozzle gimbaling and engine pre-cant.

Instrumentation

Thermal environment measurements were made in the S-IC stage base region by instruments located on the base heat shield, engines and fin trailing edge.

The S-IC base heat shield thermal instrumentation consisted of radiation calorimeters, total calorimeters, and gas temperature probes. The instruments were located on the heat shield as shown in Figure 4.5-1. These instruments are described and summarized in Table 4.5-1. Base heat shield pressure instrumentation consisted of static pressure taps and pitot-static pressure probes. The pitot-static and static pressure probe locations are shown in Figure 4.5-2 and are described and summarized in Table 4.5-2.

The F-1 engine instrumentation consisted of radiation calorimeters, total calorimeters, gas temperature probes, static pressure taps and pitot-static pressure probes. The instruments were located on the engines as shown in Figures 4.5-3 through 4.5-5 and are described and summarized in Table 4.5-3.

4.5 (Continued)

The total and radiation calorimeter sensing surfaces were 0.17 inches and 0.55 inches in diameter, respectively. They were mounted such that the sensing surfaces of the total calorimeter and the sapphire windows of the radiation calorimeters were flush with the heat shield surface. The radiation calorimeter window surfaces were nitrogen purged to eliminate carbon particle contamination. The calorimeters were asymptotic instruments which maintain a low wall temperature (610°R "effective"). These calorimeters are discussed in more detail in References 4-12 and 4-13. The instrument temperatures were monitored at the sensing surface edge during flight. An "effective" sensing surface temperature, which is used with the indicated heating rate, was determined by techniques discussed in Reference 4-14.

The heat shield gas temperature probes consisted of a platinum-platinum rhodium thermocouple with a 0.25 inch diameter molybdenum single shield. Gases were admitted to the sensing surface through four equally spaced openings facing parallel to the heat shield. Gas temperature probe installations were used with the sensing surface mounted at distances aft of the heat shield surface of 0.25, 0.50, 1.00 and 2.50 inches.

Base Flow Fields

During liftoff, the flow fields near the base region were erratic due to the disrupting influence of the launch complex. The Saturn V AS-501 sea level flow field is shown in Figure 4.5-6. The reflected flame resulting from the F-1 engine exhaust being turned by the trench flame deflector and the steam resulting from the flame and LUT water quench influenced the base and engine environment until the vehicle cleared the launch complex.

Afterburning of exhaust gases was clearly evident in flight tracking films at the lower altitudes for all three vehicles. Dark fuel-rich exhaust gases were noted at the F-1 nozzle exit plane followed by a flame front approximately three-fourths of a nozzle diameter downstream. Radiation from these high temperature exhaust plumes was the major contributor to the thermal environment during the early part of flight. Exhaust gas recirculation was noted on the engine nozzle extensions.

As altitude increases, the exhaust plumes expanded until they interacted with each other. The exhaust plume interactions created high pressure regions in the exhaust flow field, forcing low energy exhaust gases forward into the base region. It was noted in the review of flight film that the plumes remain highly luminous until 25 to 28 KM of altitude. A gradual graying of the plumes was then observed from 28 to 40 KM of altitude, and the plumes were totally gray and virtually indistinguishable from 40 KM to the end of S-IC stage boost.

4.5 (Continued)

Exhaust flow reversal was not clearly indicated by pressure probes located in the S-IC base region of AS-501, AS-502, or AS-503. Neither the pitot pressure probes located on the three vehicles nor the pitot-static pressure probes located on AS-503 indicates significant changes in flow directions or velocities. Refer to Tables 4.5-1, 4.5-2, and 4.5-3 for a description of the location of these instruments.

Television cameras were mounted on the S-IC heat shield of AS-502 and AS-503 vehicles. The flow field visualization provided by the TV cameras was extremely important because of the correlations which were possible with flight data from the heat shield and engine instrumentation. A comparison of AS-503 heat shield radiation heating rates and events observed by the base region TV cameras is presented in Figure 4.5-7. The TV camera data showed recirculated gases were first present in the base region near the heat shield at 12.2 kilometers for AS-502 and at 12.7 kilometers for AS-503. The recirculated exhaust flow appeared fully established at 18.5 and 20.1 kilometers for AS-502 and AS-503, respectively. The arrival of recirculated gases in the base area was accompanied by radiation increases on all base and engine calorimeters.

The flight data and TV data also showed that flow field changes occurred at at center engine cutoff. Center engine cutoff was characterized by a momentary brightening of the base area. The effects of center engine cutoff on base heating levels are described in the following paragraphs.

S-IC Heat Shield Thermal Environment

The S-IC heat shield heating and pressure environments which have been measured on the AS-501 through AS-505 launch vehicles are shown in Figures 4.5-8 through 4.5-16.

The radiation at sea level agrees well with analytical calculations. The radiation was expected to decrease with increasing altitude but a sharp rise in radiation is noted which peaks between 18 and 30 KM. This hump corresponds to the TV camera data which indicated hot exhaust gases reaching the base about the time of radiation increase. It has been concluded that the radiation hump which was measured is caused by hot recirculating gases in the base region. A similar hump was noted on the Saturn I and IB flights but because of the significantly higher sea level radiation on the Saturn I and IB, the hump was not as prominent.

The AS-501 base environments were not as severe as the data from AS-502 through AS-505 because of the removal of the flow deflectors after the AS-501 flight. Flow deflector effects will be discussed in a subsequent paragraph.

4.5 (Continued)

The total heating environments to the heat shield are also shown in Figures 4.5-8 through 4.5-16. The principal component of total heating was radiation and the shapes and trends of the total calorimeter data are similar to those previously discussed for radiation. The total calorimeters did indicate rundown periods of data loss or drop-out which are unexplained.

Maximum total and radiation heating rates measured on the base heat shield are 22 and 20 Btu/ft^{2}sec, respectively, occurring at approximately 20 KM. The differences between total and radiation calorimeter measurements on the heat shield indicate that a convective cooling rate was experienced by the calorimeters to approximately 9 KM. Small convective heating rates occurred from 9 KM through the remainder of first stage boost. Total and radiation heating was approximately the same at all heat shield locations along a radial line between engines. Comparisons of gas temperature measurements on the heat shield surface are shown in Figure 4.5-12. It is evident that a significant gas temperature gradient exists near the heat shield.

Total heating and gas temperature data on the heat shield between an outboard engine and engine fairing are shown in Figure 4.5-13. The heating environments are significantly reduced in these areas.

The base pressures measured on the AS-501, AS-502 and AS-503 vehicle are shown in Figures 4.5-14 through 4.5-16. The base pressure exceeds the ambient pressure at approximately 10 KM.

Total heating and gas temperature data from AS-501, AS-502 and AS-503 for the engine fairing and base of the fin are shown in Figure 4.5-17. It is evident that fin total heating measurements for all three flights are approximately the same. The initial rise in heating occurs at 15 KM which correlates with the recirculated exhaust gases reaching the heat shield as observed by TV cameras. The second rise in the total heating environment occurs shortly after flow separation is first observed.

S-IC Engine Thermal Environment

The S-IC stage heating and pressure measurements on the F-1 engines during the AS-501 through AS-505 flights are shown in Figures 4.5-18 through 4.5-34.

In general, the F-1 engine thermal environment flight data exhibited similar trends throughout flight as the S-IC heat shield data. The heating to the engines is significantly higher than to the heat shield. The characteristic "radiation hump" starts at 10 KM (about 2 KM earlier than the heat shield) and peaks at approximately 20 KM. The gas temperature on the engines are generally higher than the heat shield and correlate with the rise in engine radiation. Total heating rates and radiation rates are similar at low altitude. The forward part of the engine experiences a convective cooling early in flight with a small amount of convective heating at the higher altitudes (similar to the heat shield). Near the nozzle exit the total heating rate is generally higher than the radiation heating. Maximum total and radiation heating rates to the engines are 32 and 27 Btu/ft^{2}sec, respectively, occurring at approximately 16 KM.

4.5 (Continued)

Total heating rates measured at similar locations on three different engines are shown in Figure 4.5-30 and indicate the flow in the base is reasonably symmetrical. F-1 engine pressure data are shown in Figures 4.5-31 through 4.5-34. The exit plane pressures begin to exceed ambient pressures at 8 to 10 kilometers.

Base Flow Deflector Effects

The flow deflectors which were on the AS-501 flight vehicle to remove combustible hot gas mixtures from the base area were removed on the AS-502 vehicle, since the measured base environment on the AS-501 was well below design limits. The comparison of AS-501 and AS-502 flight data on the heat shield (Figure 4.5-9) show that significant differences do exist with radiation and total heating peaking higher and earlier for the AS-502 than for the AS-501. It was expected that flow deflectors would only affect the convective heating; but because of the unexpected radiation from the recirculated exhaust gases in the base region, radiation was the heating mechanism most affected.

Engine areas near the exit plane were not as significantly affected by the flow deflectors as the heat shield (Figure 4.5-20). Outboard locations, such as the outboard surfaces of the outboard engine and the base of the fins, were not expected to experience significant flowfield or heating changes when the deflectors were removed. The comparison of flight data to the base of the fin in Figure 4.5-17 shows similar environments for both flights. The AS-501 base pressures on the heat shield shown in Figure 4.5-14 were higher in the 3 to 12 km altitude regime than on AS-502 which is attributed to the flow deflector removal on AS-502. Flow deflectors, however, did not affect the engine external surface pressures.

It was concluded that the differences between the AS-501 and AS-502 flight data were almost entirely due to flow deflector effects. Subsequent flight data have also confirmed this conclusion.

Center Engine Out Effects

The center engine on the S-IC stage is shut down prior to outboard engine shutdown to limit the g loading on the upper stages. This provides base heating data for an engine out configuration. At engine shutdown a spike in the calorimeter and gas temperature data is evident and is coincident with a momentary brightening in the base region observed by the TV camera coverage. This brightening is probably caused by the high concentration of residual exhaust products and carbon particles from the center engine residual fuel which could raise the emissivity of the base gases and therefore the radiation. As the residual exhaust products are depleted, a reduction in emissivity and radiation would occur. The level of heating following the IECO spike is for a center engine out configuration. IECO occurred at 135.5 seconds (49.64 kilometers), 144.72 seconds (56.07 kilometers), and 125.88 seconds (41.5 kilometers) on flights AS-501, AS-502, and AS-503,

respectively. S-IC heat shield and engine environments during IECO are shown in Figures 4.5-35 and 4.5-36. These figures show the most pronounced effects of center engine out. Most of the flight data after the spike returned to the levels and trends which were evident before center engine out.

Gimbaling Effects

F-1 engine gimbal angles have not exceeded 1° during Saturn V flights through AS-509. No specific effect due to this small gimbal angle has been discernible from the flight data. Gimbal effects are within the accuracy of the instrument readings for these small angles.

Engine Outboard Pre-Cant

Gas temperatures measured on the S-IC heat shield are shown in Figures 4.5-8, 4.5-9 and 4.5-11. The delay in the initial rise in radiation and the slightly lower peak values recorded on AS-503, when compared with AS-502, is also evident in the heat shield gas temperature data in the inboard locations. This effect is attributed to the outboard engine cant on AS-503, which delayed the altitude of initial plume impingement and allowed cooler gases to be recirculated around the center engine. Gas temperatures near the periphery of the base heat shield were not greatly affected by the 2 degree cant and were in close agreement with AS-502 flight data.

TABLE 4.5-1. S-IC BASE HEAT SHIELD THERMAL ENVIRONMENT INSTRUMENTATION

MEASUREMENT NUMBER	INSTRUMENT TYPE	RANGE °K	LOCATION		REMARKS
			STATION	RADIAL	
C60-106	Cal., Rad.	0-22.72*	112.0	r/R = 0.84, Pos. II	Facing Aft
C61-106	Cal., Rad.	0-22.72*	112.0	r/R = 0.61, Pos. II	Facing Aft
C151-106	Cal., Rad.	0-22.72*	112.0	r/R = 0.60, Fin A	Facing Aft
C49-106	Gas Temp.▲	273-2023	112.0	r/R = 0.84, Pos. II	Mounted 0.25" Off Surface
C50-106	Gas Temp.▲	273-2023	112.0	r/R = 0.61, Pos. II	Mounted 0.25" Off Surface
C51-106	Gas Temp.▲	273-2023	112.0	r/R = 0.61, Pos. II	Mounted 1.0" Off Surface
C52-106	Gas Temp.▲	273-2023	112.0	r/R = 0.61, Pos. II	Mounted 2.5" Off Surface
C53-110	Gas Temp.▲	273-2023	97.0	r/R = 1.11 ②	Mounted 1.0" Off Surface
C54-106	Gas Temp.▲	273-2023	112.0	r/R = 1.28, Fin D	Mounted 0.50" Off Surface
C55-106	Gas Temp.▲	273-2023	112.0	r/R = 0.46, Fin A	Mounted 1.0" Off Surface
C25-106	Cal., Total	0-45.44■	112.0	r/R = 0.84, Pos. II	Facing Aft
C26-106	Cal., Total	0-45.44	112.0	r/R = 0.61, Pos. II	Facing Aft
C27-106	Cal., Total	0-45.44	112.0	r/R = 0.60, Fin A	Facing Aft
C28-114	Cal., Total	0-45.44	81.0	r/R = 1.51, ①	Facing Aft
C144-106	Cal., Total	0-56.80	112.0	r/R = 0.46, Pos. II	Facing Aft
C148-110	Cal., Total	0-45.44	97.0	r/R = 1.11, Fin C Side of Engine Fairing, Fin D ②	Facing Engine No. 104
* D36-106	Pitot Pressure	0-13.79	112.0	r/R = 0.61, Pos. II	Facing Aft
* D39-106	Pitot Pressure	0-13.79	112.0	r/R = 0.61, Pos. II	Facing Inboard
* D40-106	Pitot Pressure	0-13.79	112.0	r/R = 0.61, Pos. II	Facing Outboard
** D168-106	Pitot-Static Pressure	0-3.45††	112.0	r/R = 0.61, Pos. II	Facing Inboard
** D169-106	Pitot-Static Pressure	0-3.45††	112.0	r/R = 0.61, Pos. II	Facing Outboard

†† N/cm^2
① Trailing Edge of Fin D
② Internal Engine Fairing Fin D
■ watts/cm^2
▲ Platinum - Platinum + 10% Rhodium Thermocouple Probe
* AS-501 and AS-502
** AS-503

TABLE 4.5-2. S-IC STAGE F-1 ENGINE THERMAL ENVIRONMENT INSTRUMENTATION

MEASUREMENT NUMBER	INSTRUMENT TYPE	RANGE °K	LOCATION		REMARKS
			STATION	RADIAL	
C57-101	Cal., Rad.	0-113.65■	-116.0	Facing Engine No. 105	Engine No. 101
C58-105	Cal., Rad.	0-68.16■	-116.0	Facing Pos. II	Engine No. 105
C150-101	Cal., Rad.	0-68.16■	48.0	Facing Engine No. 105	Engine No. 101
C43-101	Gas Temp.▲	273-2023	-116.0	Facing Engine No. 102	Engine No. 101
C44-101	Gas Temp.▲	273-2023	-116.0	Facing Engine No. 105	Engine No. 101
C45-101	Gas Temp.▲	273-2023	- 48.0	Facing Outboard	Engine No. 101
C46-101	Gas Temp.▲	273-2023	70.0	Facing Engine No. 103	Engine No. 101
C47-101	Gas Temp.▲	273-2023	59.0	Facing Engine No. 105	Engine No. 101
C48-101	Gas Temp.▲	273-2023	56.0	Facing Outboard	Engine No. 101
C56-105	Gas Temp.▲	278-2073	- 92.0	Facing Engine No. 101	Engine No. 105
C14-101	Cal., Total	0-113.65■	-116.0	Facing Engine No. 105	Engine No. 101
C15-101	Cal., Total	0-68.16■	-116.0	Facing Engine No. 102	Engine No. 101
C16-105	Cal., Total	0-68.16■	-116.0	Facing Pos. II	Engine No. 105
C17-101	Cal., Total	0-68.16■	- 48.0	Facing Engine No. 105 and Down	Engine No. 101
C18-101	Cal., Total	0-45.44	- 48.0	Facing Outboard and Down	Engine No. 101
C19-101	Cal., Total	0-45.44	0.0	Facing Engine No. 105	Engine No. 101
C20-105	Cal., Total	0-45.44	45.0	Facing Engine No. 104	Engine No. 105
C21-101	Cal., Total	0-45.44	70.0	Facing Engine No. 105	Engine No. 101
C22-101	Cal., Total	0-45.44	59.0	Facing Engine No. 105	Engine No. 101
C23-101	Cal., Total	0-22.72	56.0	Facing Engine Fairing Fin A	Engine No. 101
C123-103	Cal., Total	0-68.16	- 48.0	Facing Engine No. 105 and Down	Engine No. 103
C142-105	Cal., Total	0-56.80	- 48.0	Facing Engine No. 101	Engine No. 105
D23-101	Static Pressure	0-13.79††	-110.0	Facing Engine No. 102	Engine No. 101
D24-101	Static Pressure	0-13.79††	-110.0	45° From Fin A Toward Position II	Engine No. 101
D25-101	Static Pressure	0-13.79††	-110.0	Facing Outboard	Engine No. 101
D26-101	Static Pressure	0-13.79††	- 70.0	Facing Outboard	Engine No. 101
D27-101	Static Pressure	0-13.79	- 15.0	Facing Outboard	Engine No. 101
D28-101	Static Pressure	0-13.79	-110.0	Facing Engine No. 105	Engine No. 101
D29-101	Static Pressure	0-13.79	- 70.0	Facing Engine No. 105	Engine No. 101
D30-101	Static Pressure	0-13.79	- 15.0	Facing Engine No. 105	Engine No. 101
*D31-105	Pitot Pressure	0-13.79	- 92.0	Facing Forward	①
*D32-105	Pitot Pressure	0-13.79	- 92.0	Facing Aft	①
*D33-105	Static Pressure	0-13.79	- 92.0	Facing Engine No. 101	①
*D34-105	Static Pressure	0-13.79	- 92.0	Facing Position II	Engine No. 105
**D166-105	Pitot-Static Pressure	0-3.45	- 92.0	Facing Forward	①
**D167-105	Pitot-Static Pressure	0-3.45	- 92.0	Facing Aft	①

†† N/cm^2

① Six (6) Inches from Engine No. 105 Toward Engine No. 101

■ watts/cm^2

▲ Platinum - Platinum + 10% Rhodium Thermocouple Probe

* AS-501 and AS-502

** AS-503

TABLE 4.5-3. S-IC BASE HEAT SHIELD PRESSURE INSTRUMENTATION

MEASUREMENT NUMBER	INSTRUMENT TYPE	RANGE N/cm^2	LOCATION
D0035-106	Static Pressure	0-13.79	Station 112, 166 Inch Radius, Position II
D0036-106*	Static Pressure	0-13.79	Station 112, 120 Inch Radius, Position II
D0037-106	Static Pressure	0-13.79	Station 112, 91 Inch Radius, Fin C Centerline
D0038-106	Static Pressure	0-13.79	Station 112, 220 Inch Radius, 80 Inches from Fin B Centerline toward Position II
D0042-106	Static Pressure	0-13.79	Station 112, 260 Inch Radius, 40° from Position II toward Fin B Centerline
D0043-106	Static Pressure	0-13.79	Station 112, 80 Inch Radius, Position II
D0044-106	Static Pressure	0-13.79	Station 112, 150 Inch Radius, 25° from Fin A Centerline toward Position II
D0045-106	Static Pressure	0-13.79	Station 112, 80 Inch Radius, 25° from Fin A Centerline toward Position II
D0046-106	Differential Pressure	± 2.07	Station 112, 120 Inch Radius, Position IV
D0047-106	Differential Pressure	± 2.07	Station 112, 91 Inch Radius, Fin D Centerline

* Instrument not on AS-503

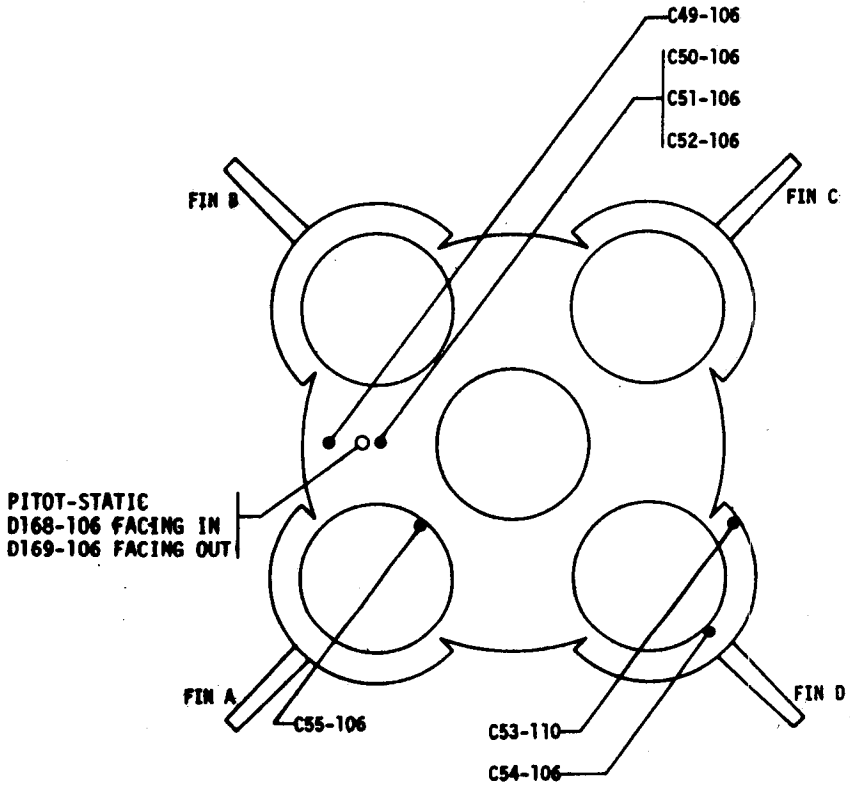

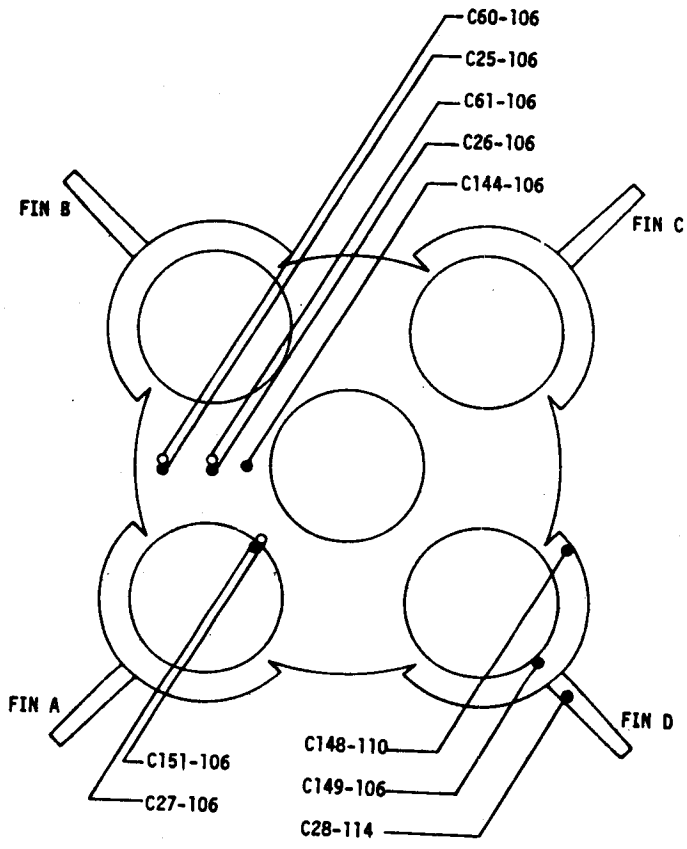

FIGURE 4.5-1. S-IC BASE HEAT SHIELD THERMAL INSTRUMENTATION

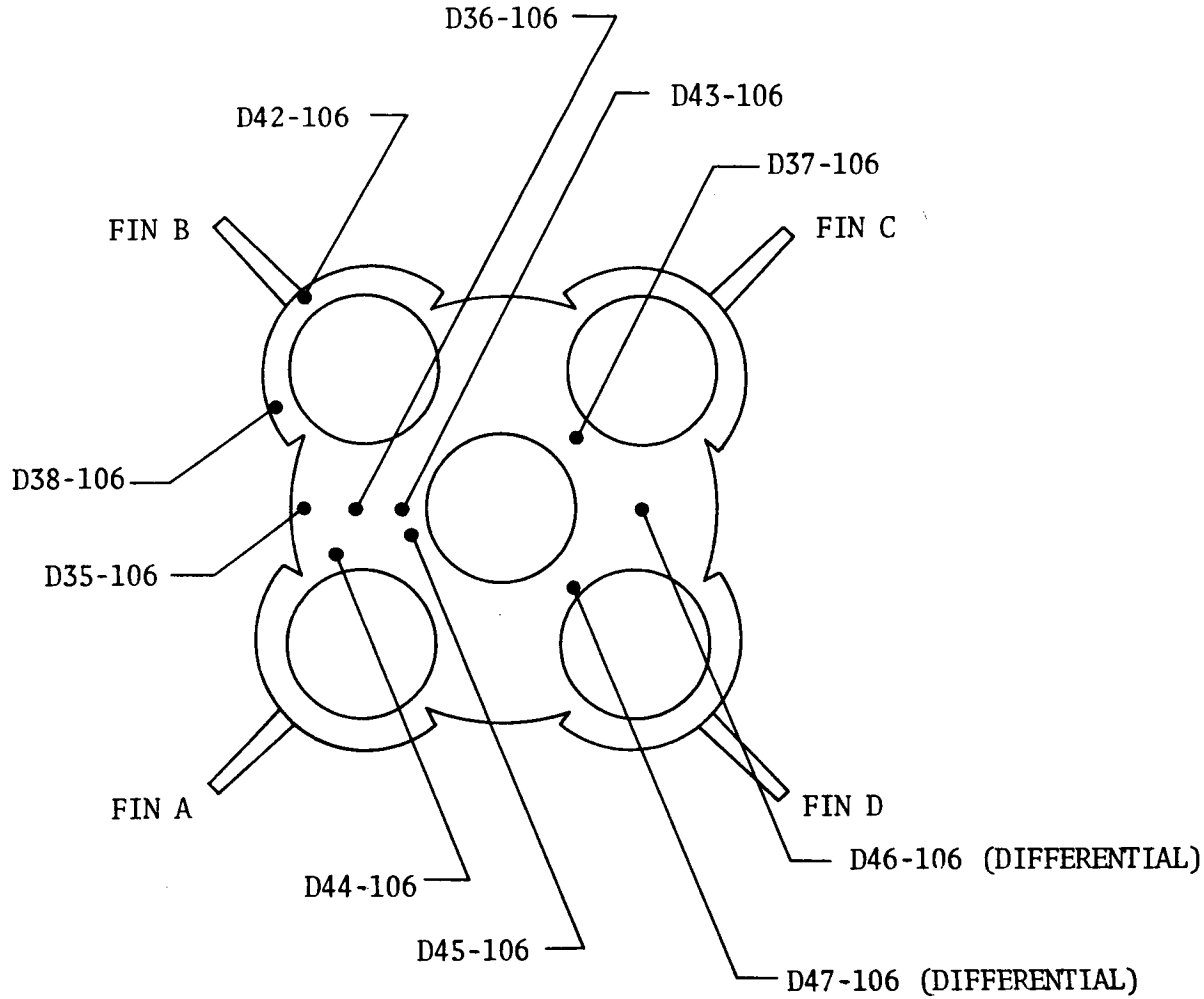

FIGURE 4.5-2. S-IC BASE HEAT SHIELD PRESSURE INSTRUMENTATION

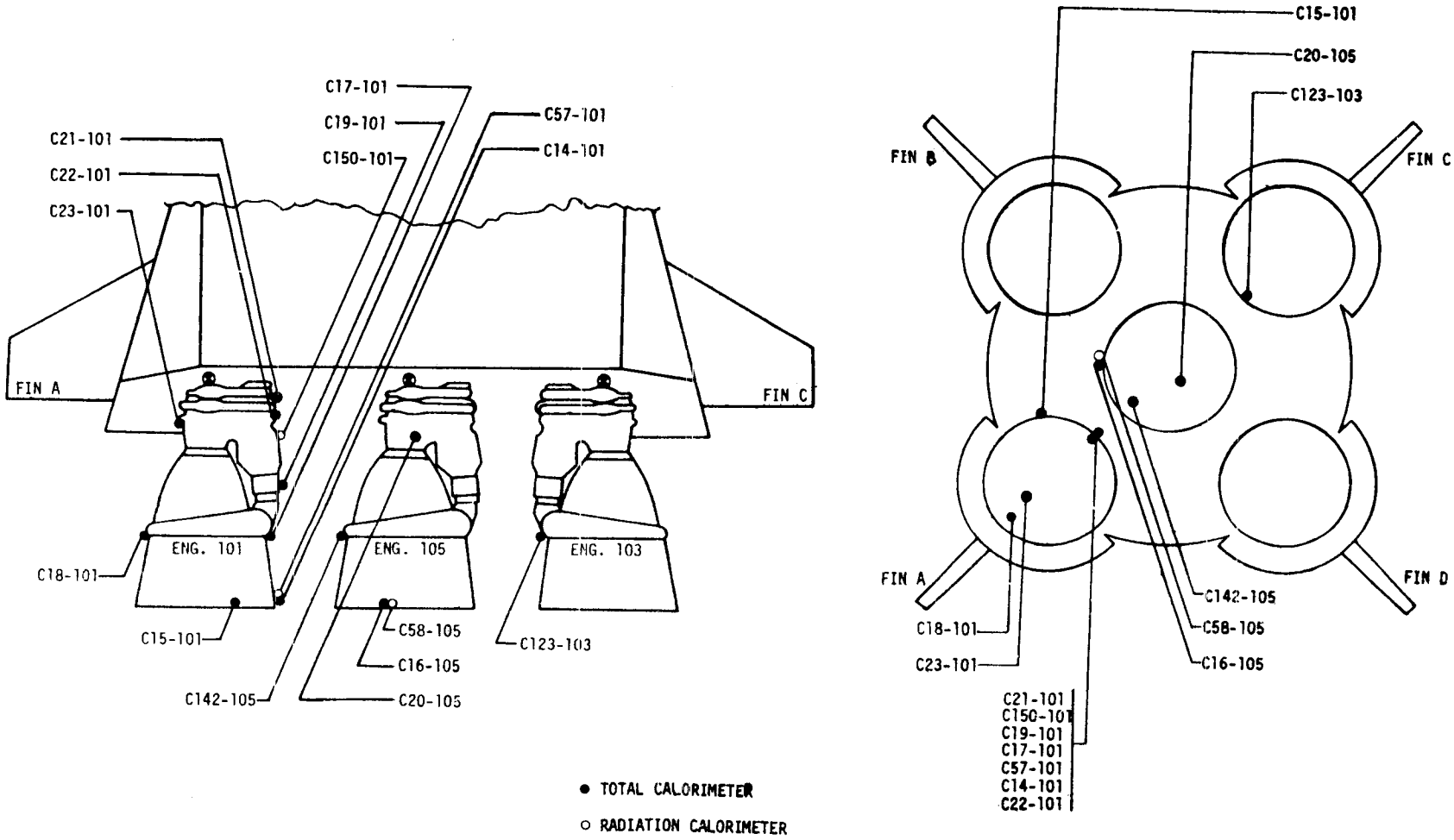

FIGURE 4.5-3 F-1 ENGINE HEATING RATE INSTRUMENTATION

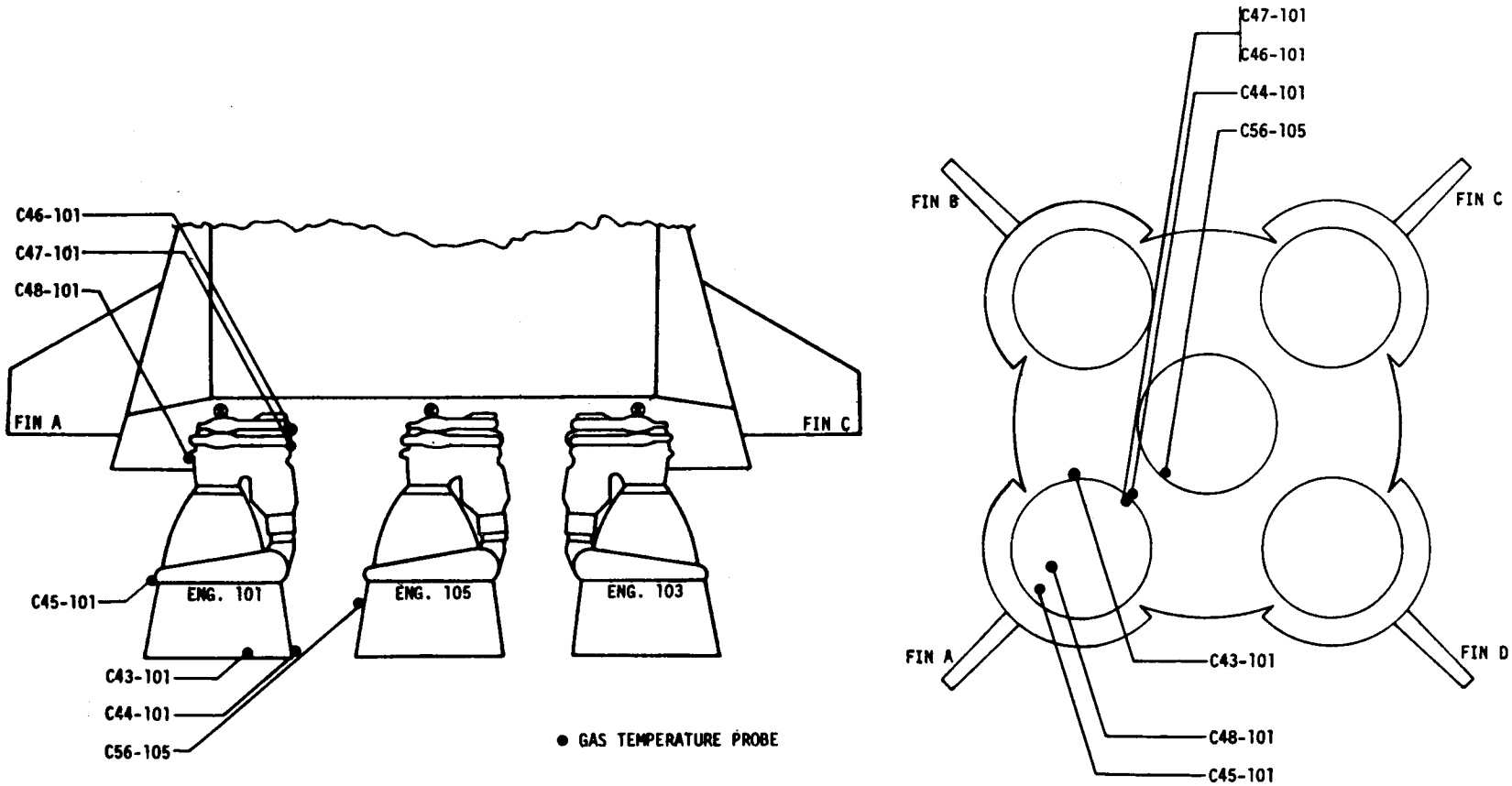

FIGURE 4.5-4 F-1 ENGINE GAS TEMPERATURE INSTRUMENTATION

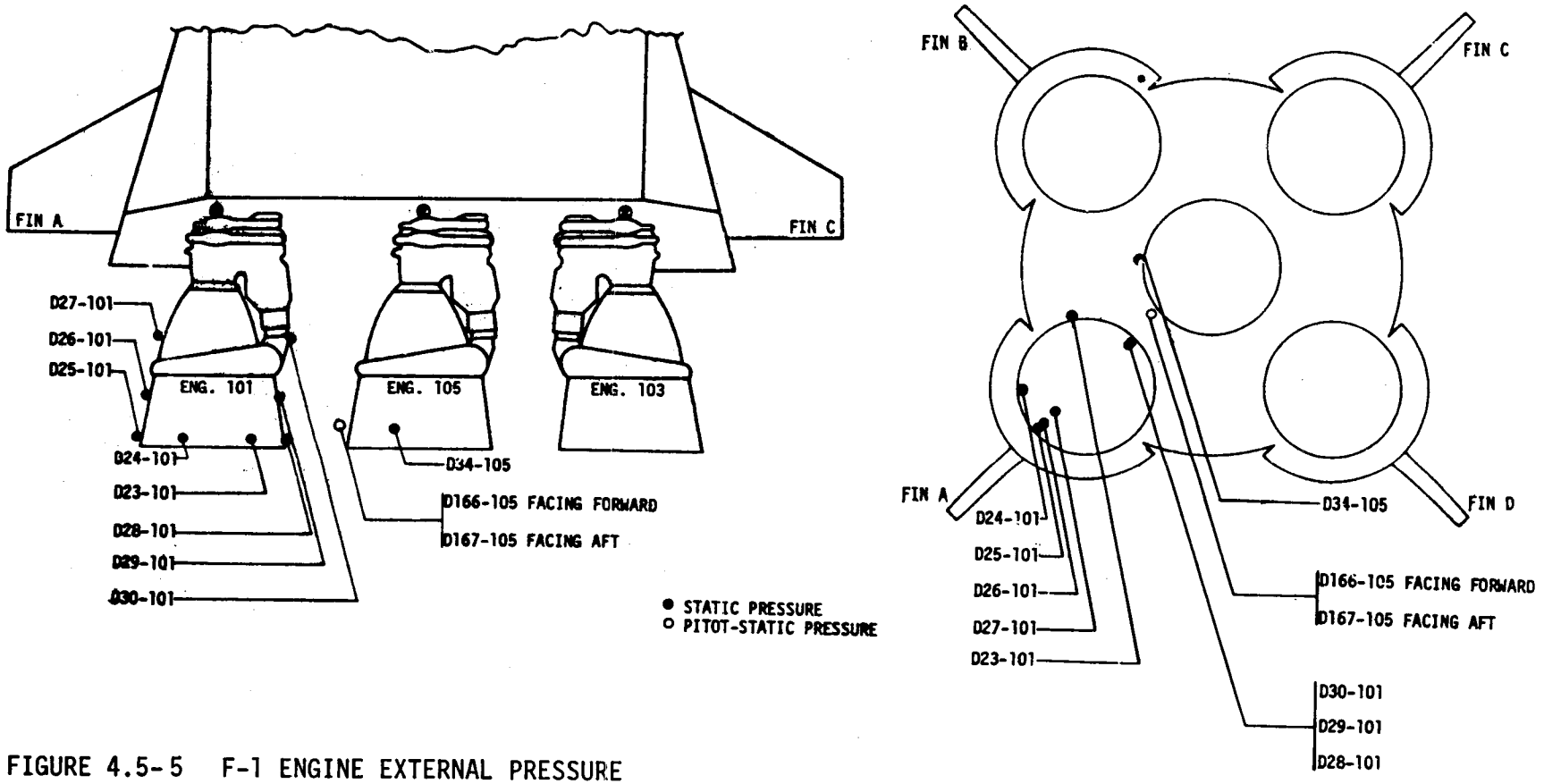

FIGURE 4.5-5 F-1 ENGINE EXTERNAL PRESSURE

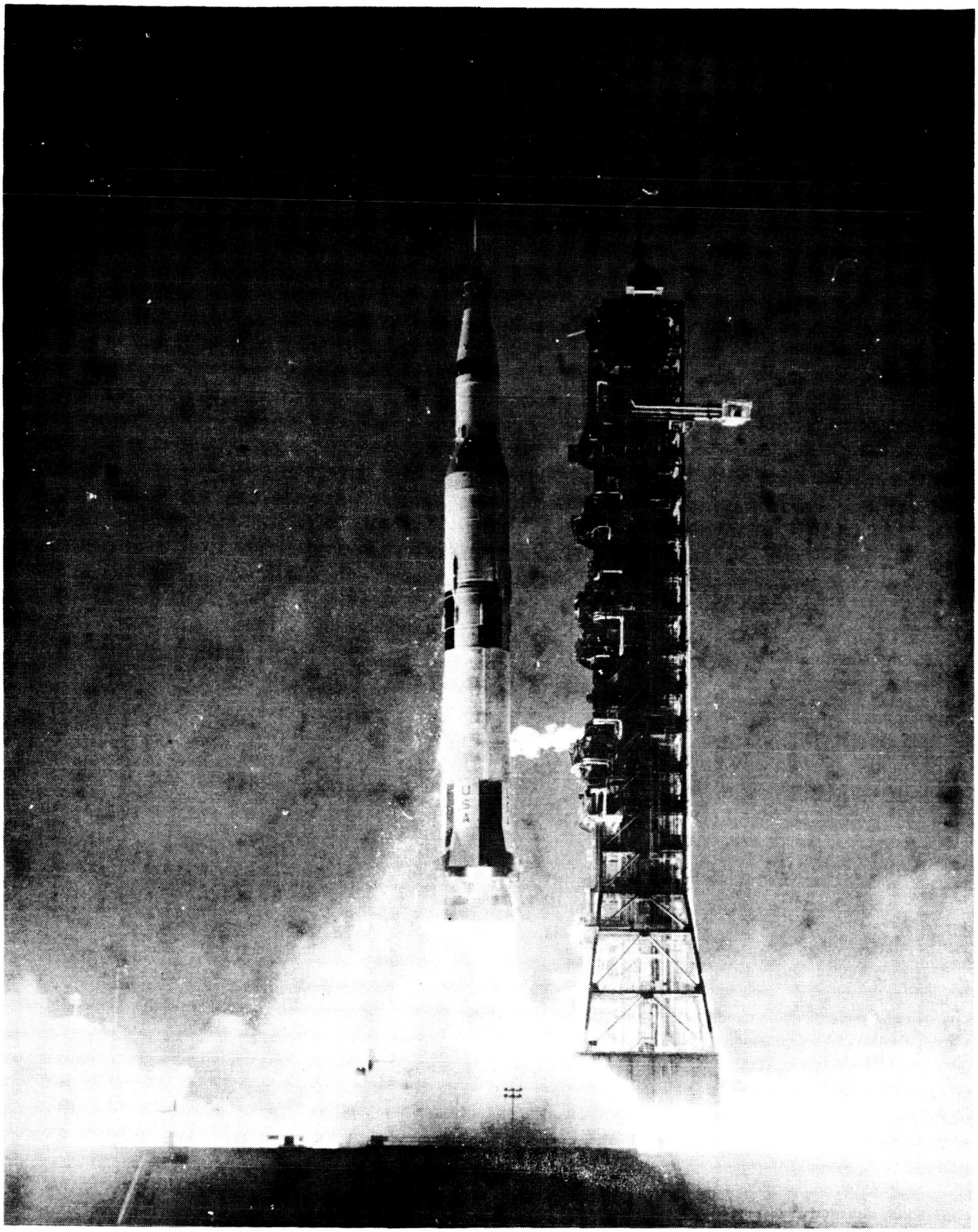

FIGURE 4.5-6 AS-501 LIFTOFF

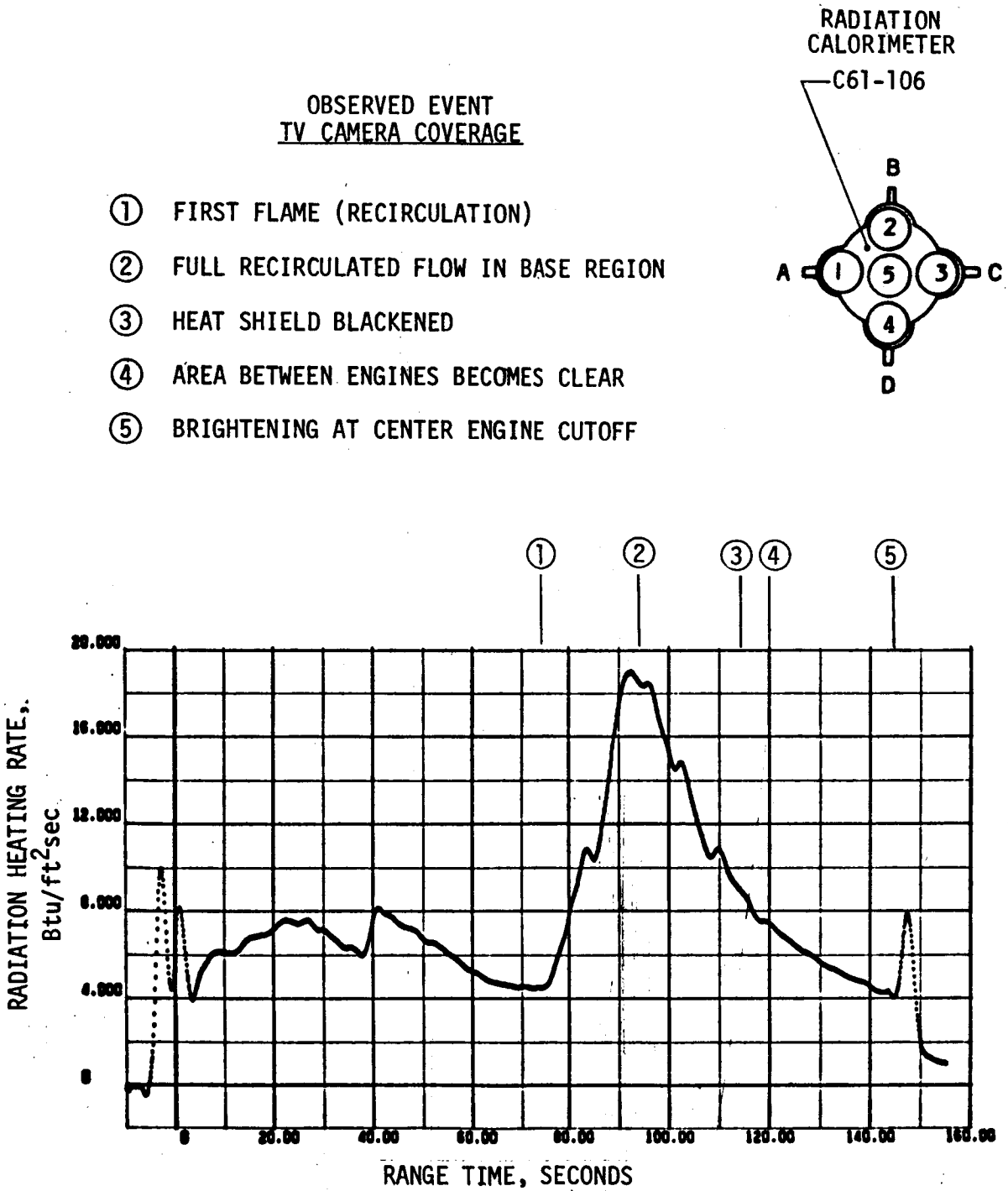

FIGURE 4.5-7. COMPARISON OF FLIGHT DATA AND TV CAMERA COVERAGE, AS-502 FLIGHT DATA

AS-501, 502, 503

AS-504, AS-505

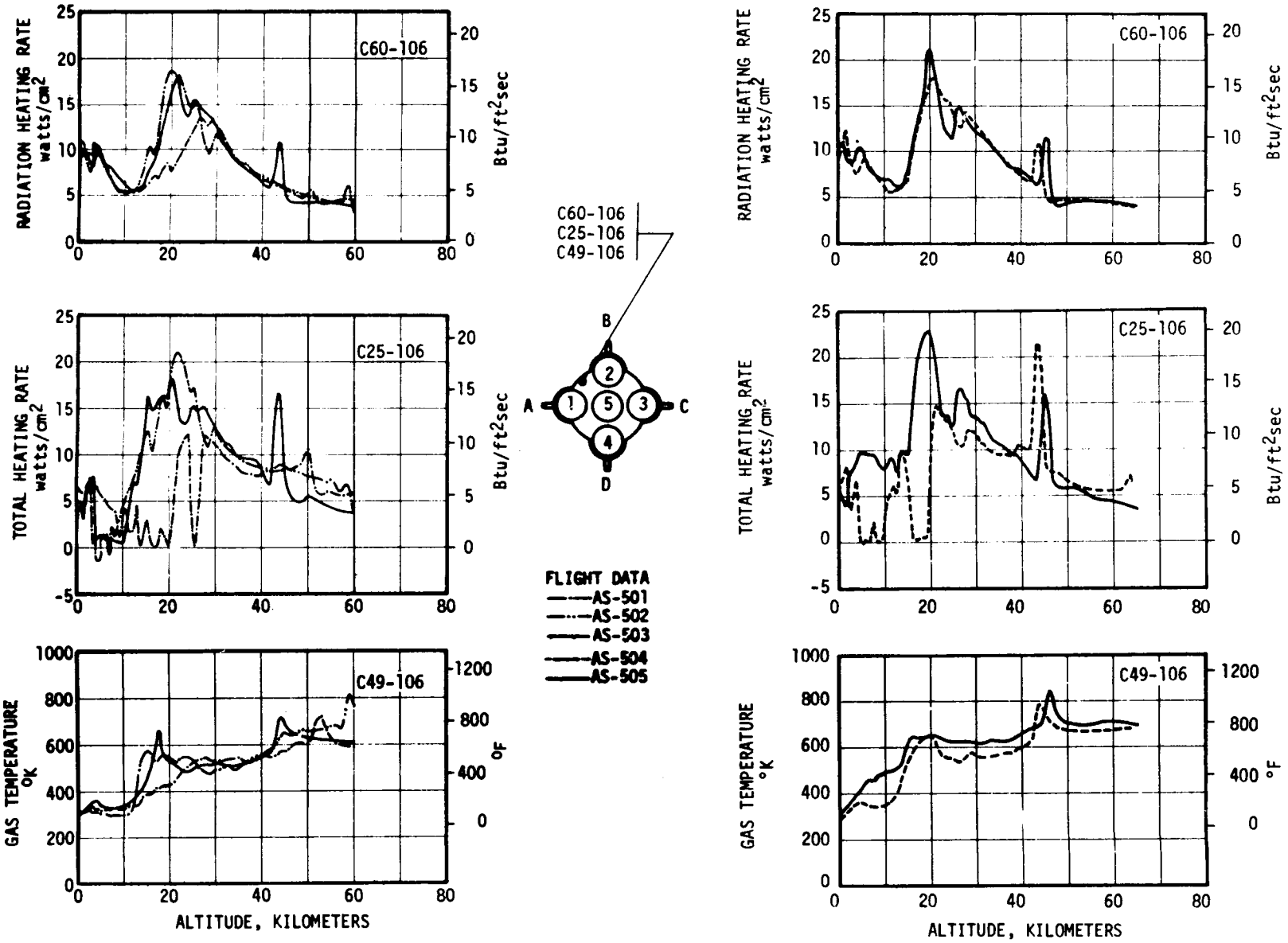

FIGURE 4.5-8 S-IC HEAT SHIELD ENVIRONMENT - r/R = 0.84 BETWEEN OUTBOARD ENGINES - AS-501 THROUGH AS-505

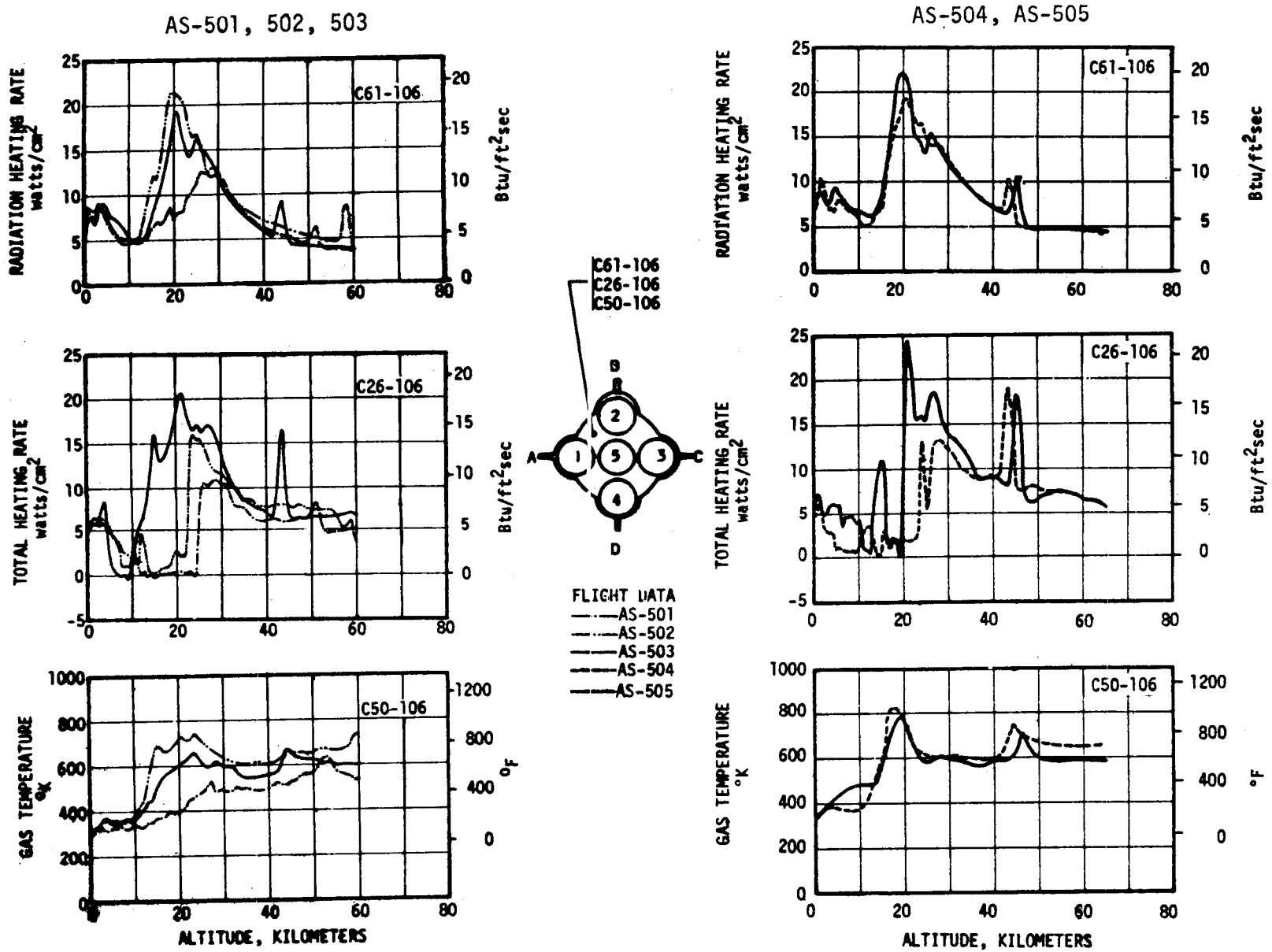

FIGURE 4.5-9 S-IC HEAT SHIELD ENVIRONMENT - r/R = 0.61 BETWEEN OUTBOARD ENGINES - AS-501 THROUGH AS-505

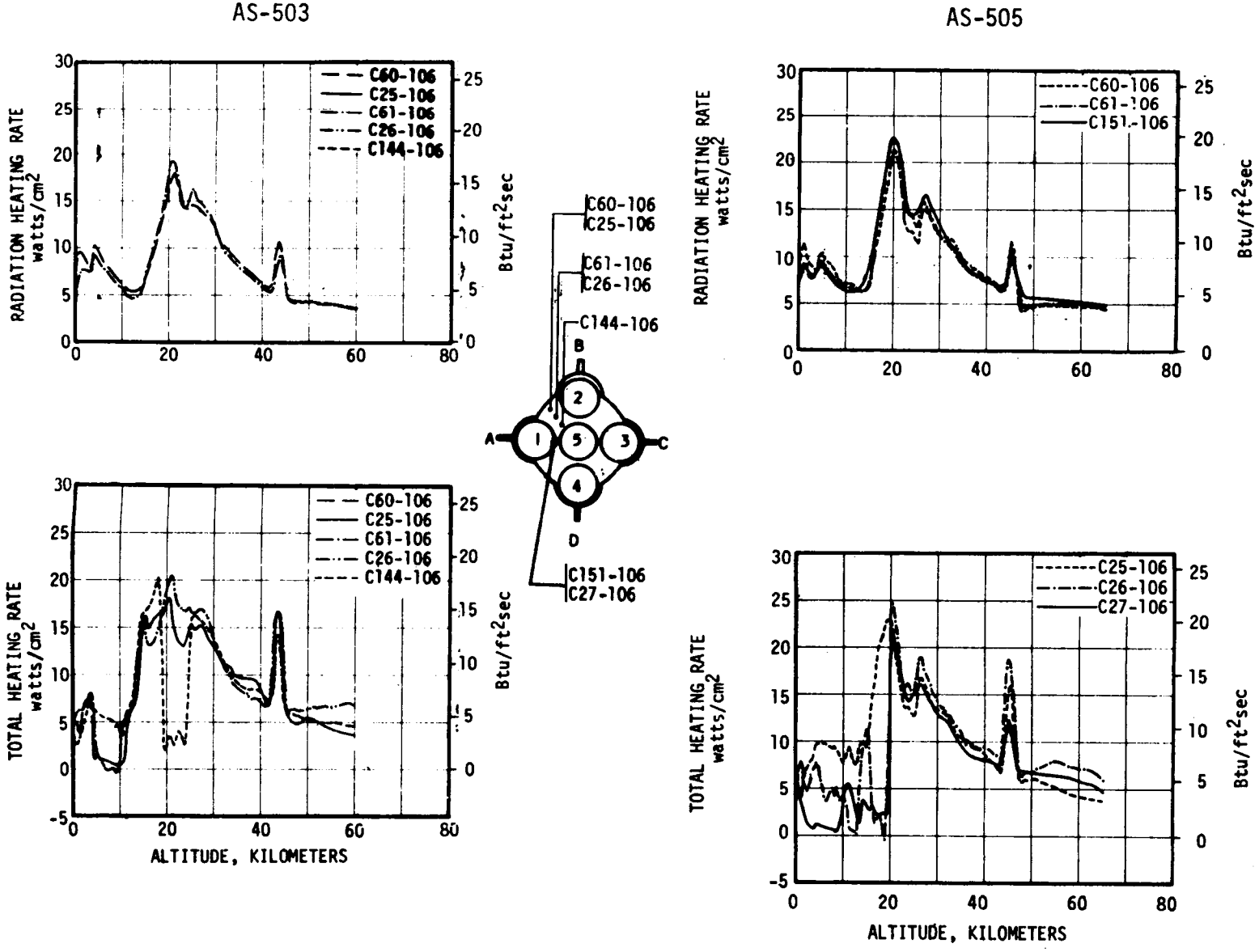

FIGURE 4.5-10 S-IC HEAT SHIELD HEATING RATES, AS-503 AND AS-505

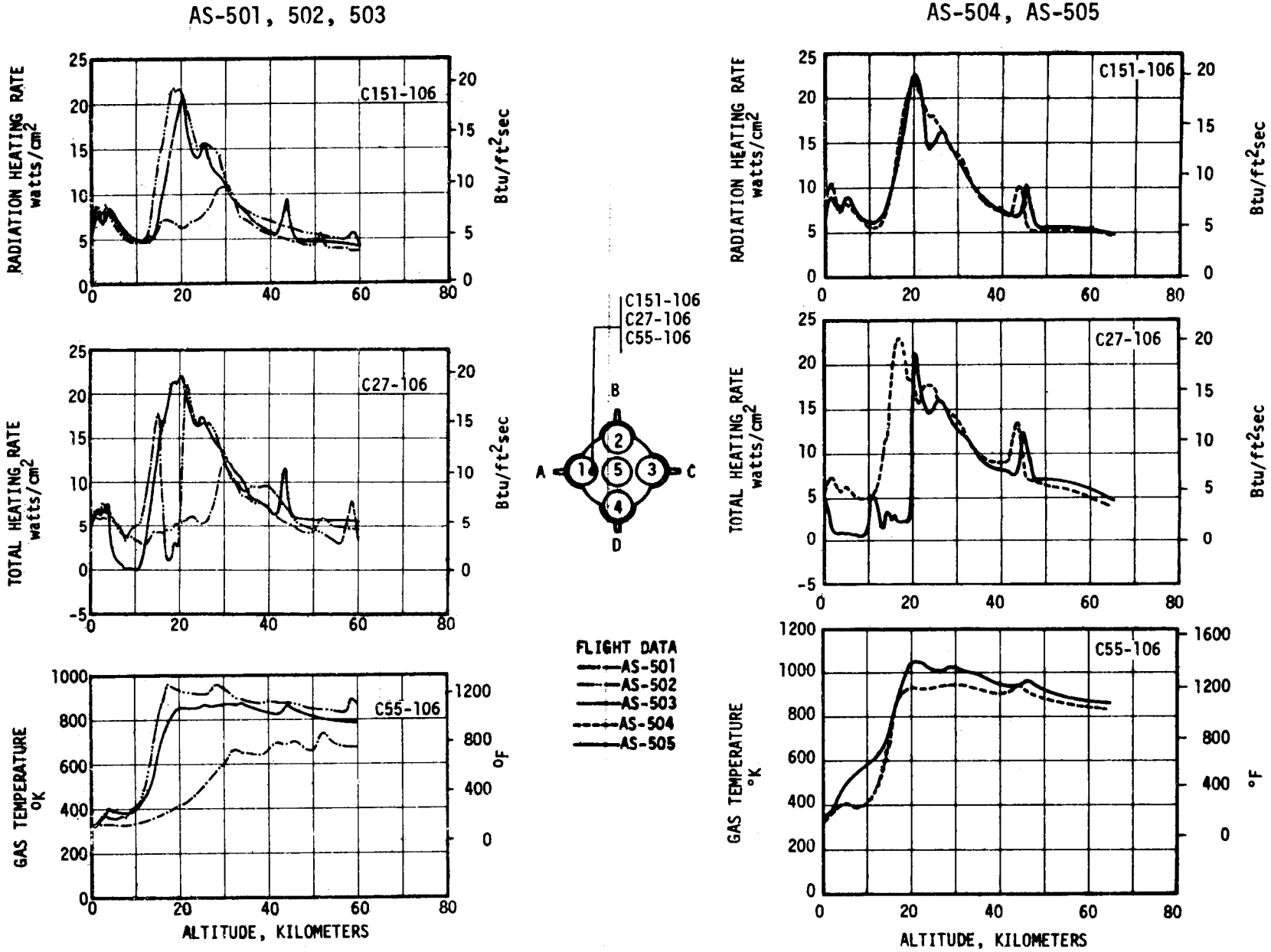

FIGURE 4.5-11 S-IC HEAT SHIELD ENVIRONMENT - r/R = 0.60 BETWEEN INBOARD AND OUTBOARD ENGINES - AS-501 THROUGH AS-505

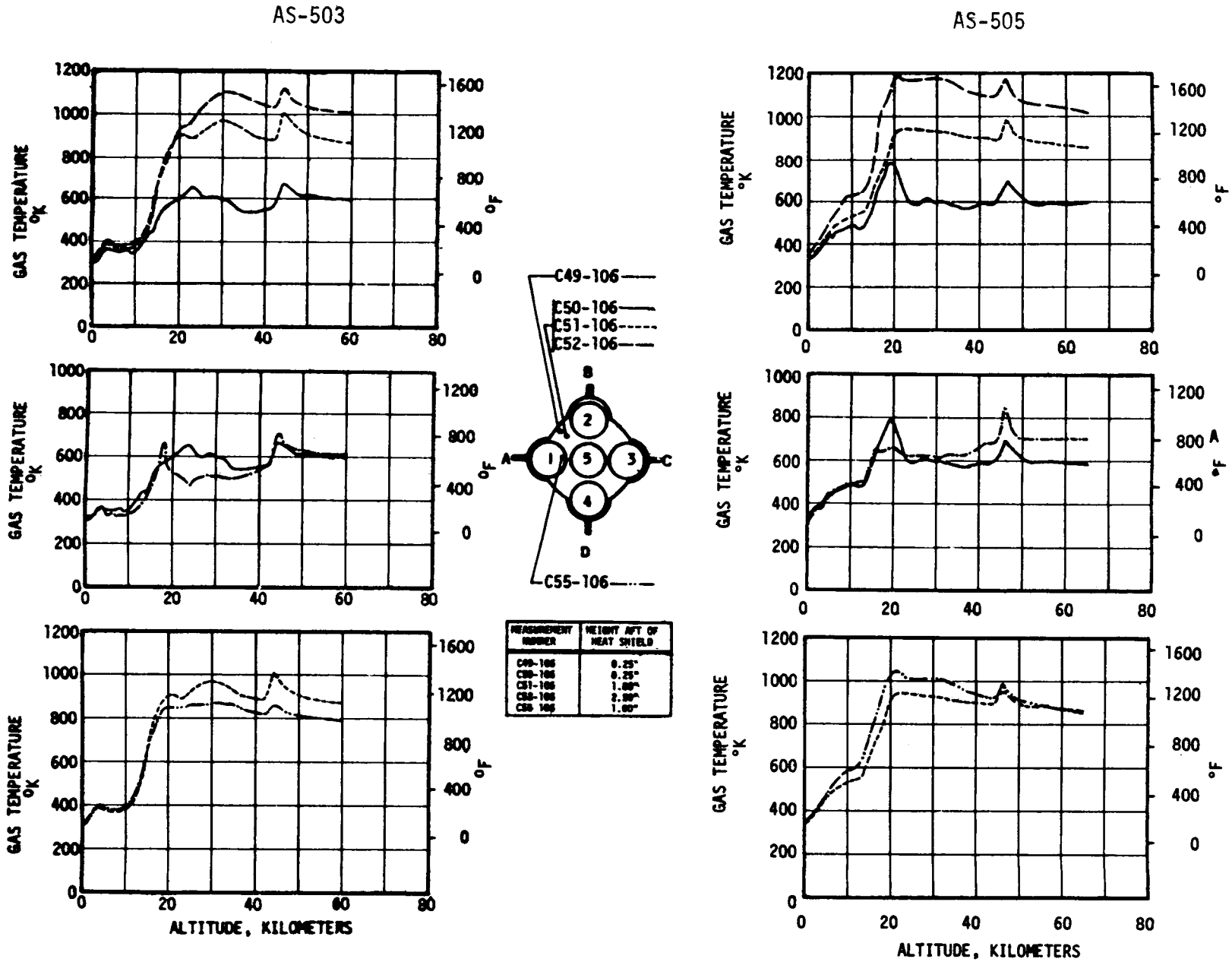

FIGURE 4.5-12 S-IC HEAT SHIELD GAS TEMPERATURE - AS-503 AND AS-505

AS-501, 502, 503

AS-504, AS-505

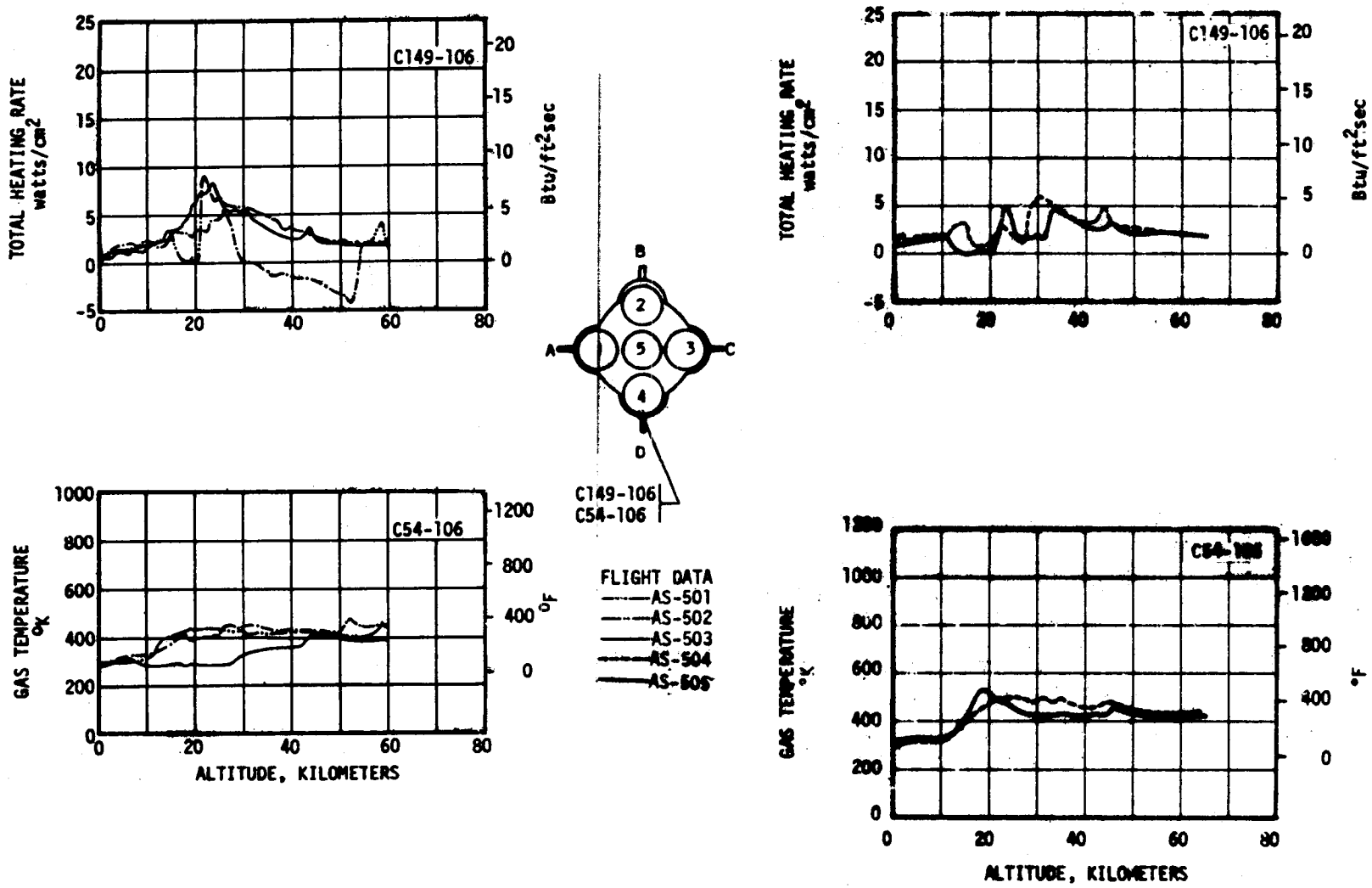

FIGURE 4.5-13 S-IC HEAT SHIELD ENVIRONMENT - BETWEEN OUTBOARD ENGINE AND ENGINE FAIRING - AS-501 THROUGH AS-505

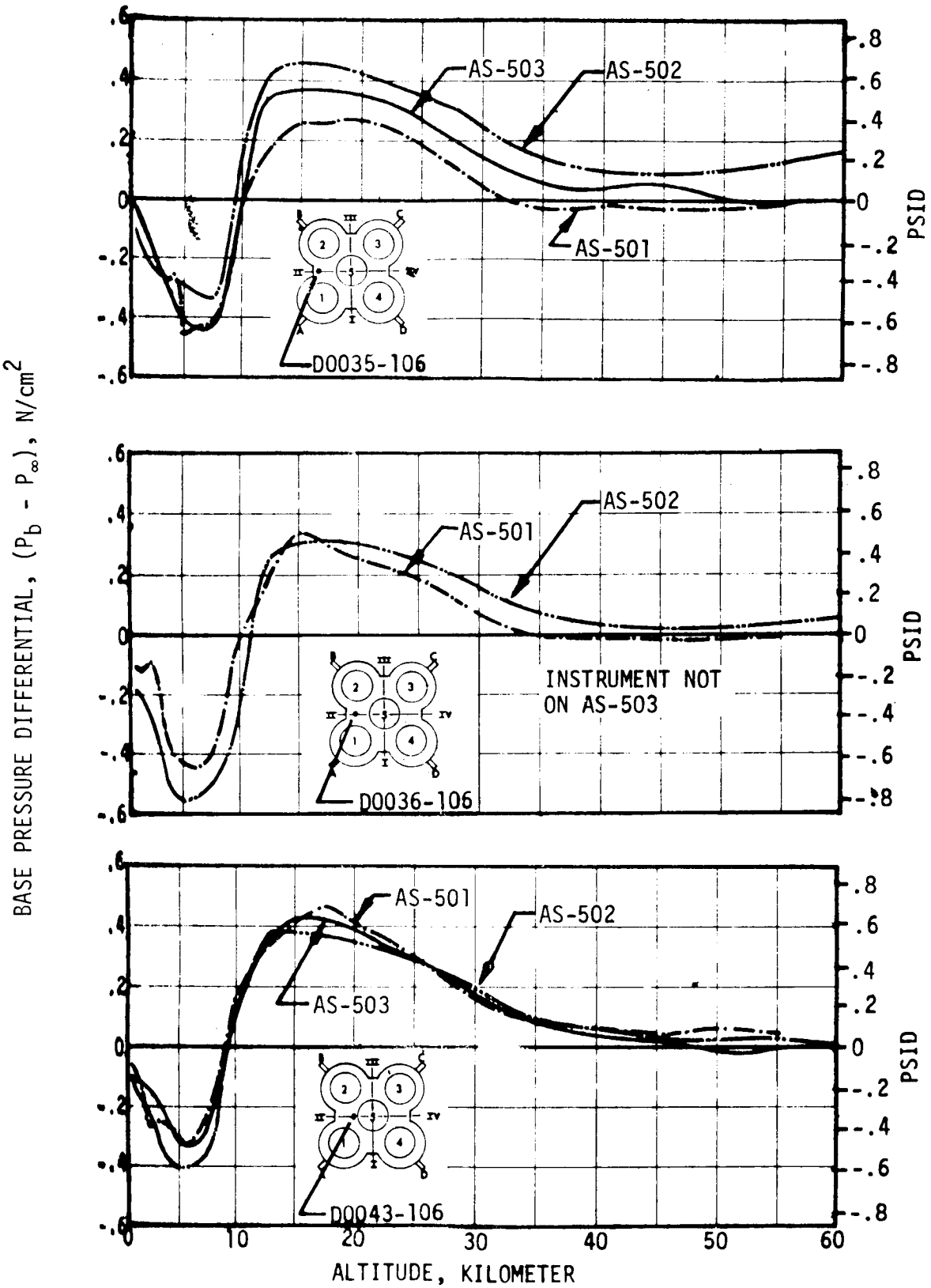

FIGURE 4.5-14. S-1C BASE PRESSURE DIFFERENTIAL

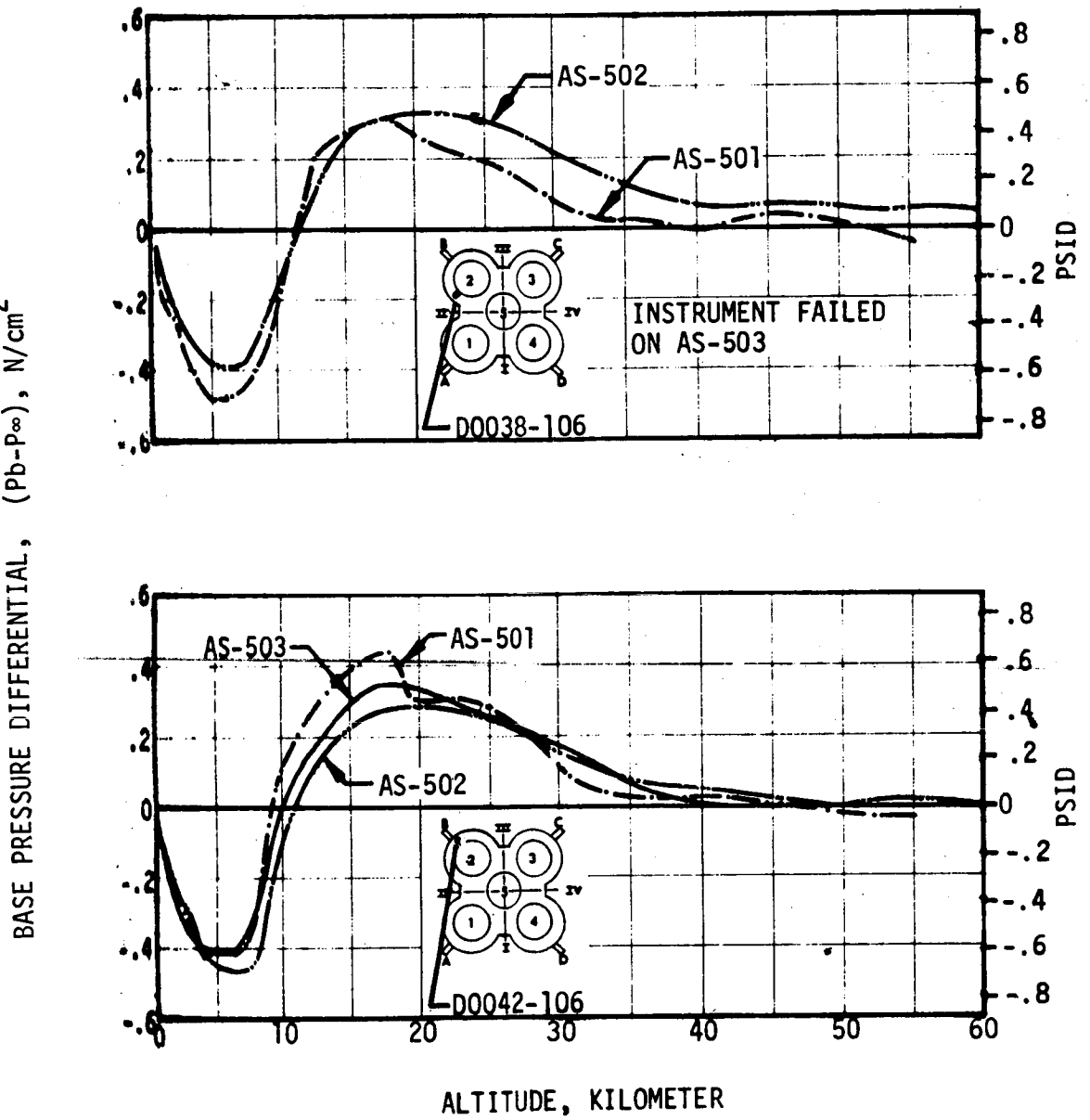

FIGURE 4.5-15. S-1C BASE PRESSURE DIFFERENTIAL

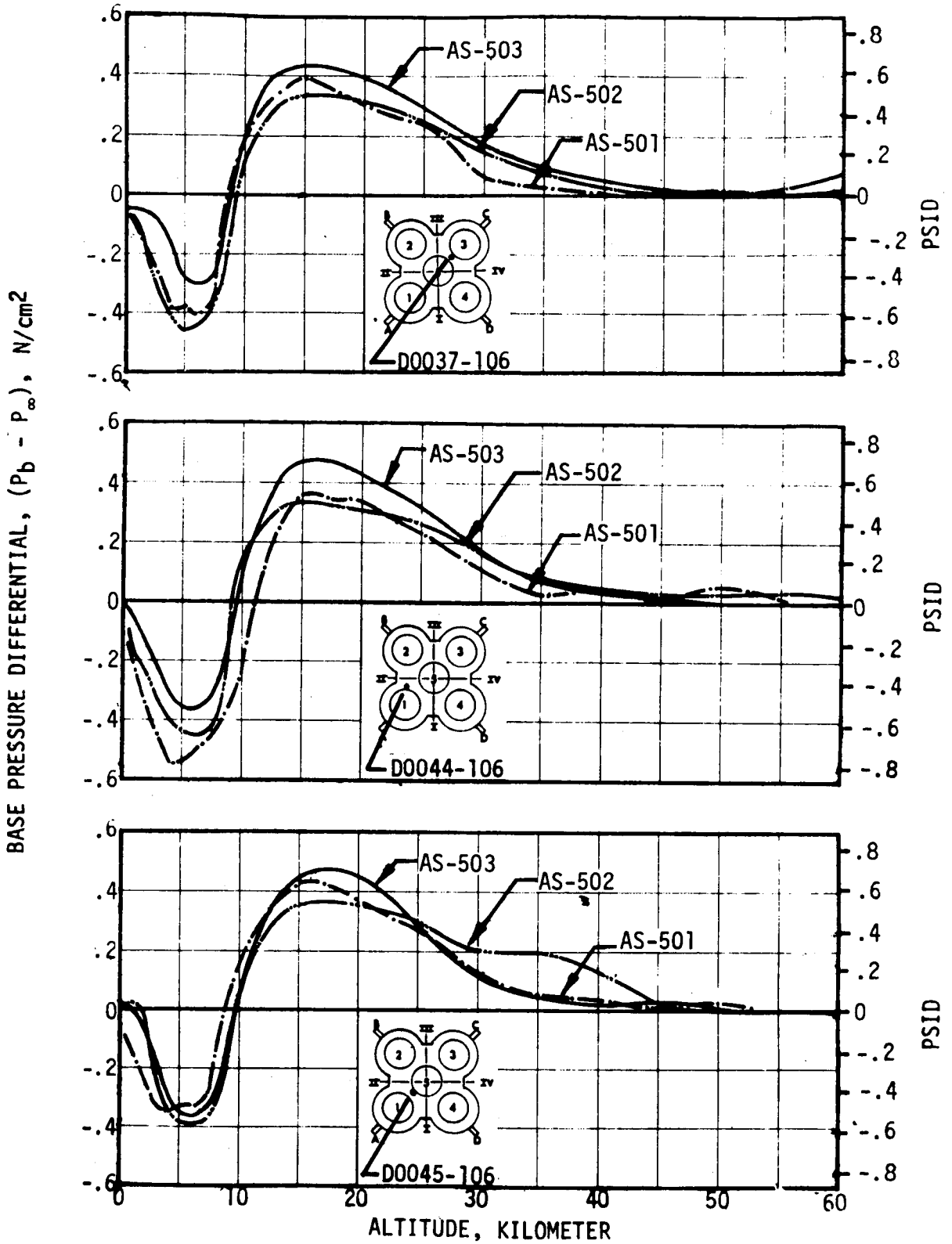

FIGURE 4.5-16. S-1C BASE PRESSURE DIFFERENTIAL

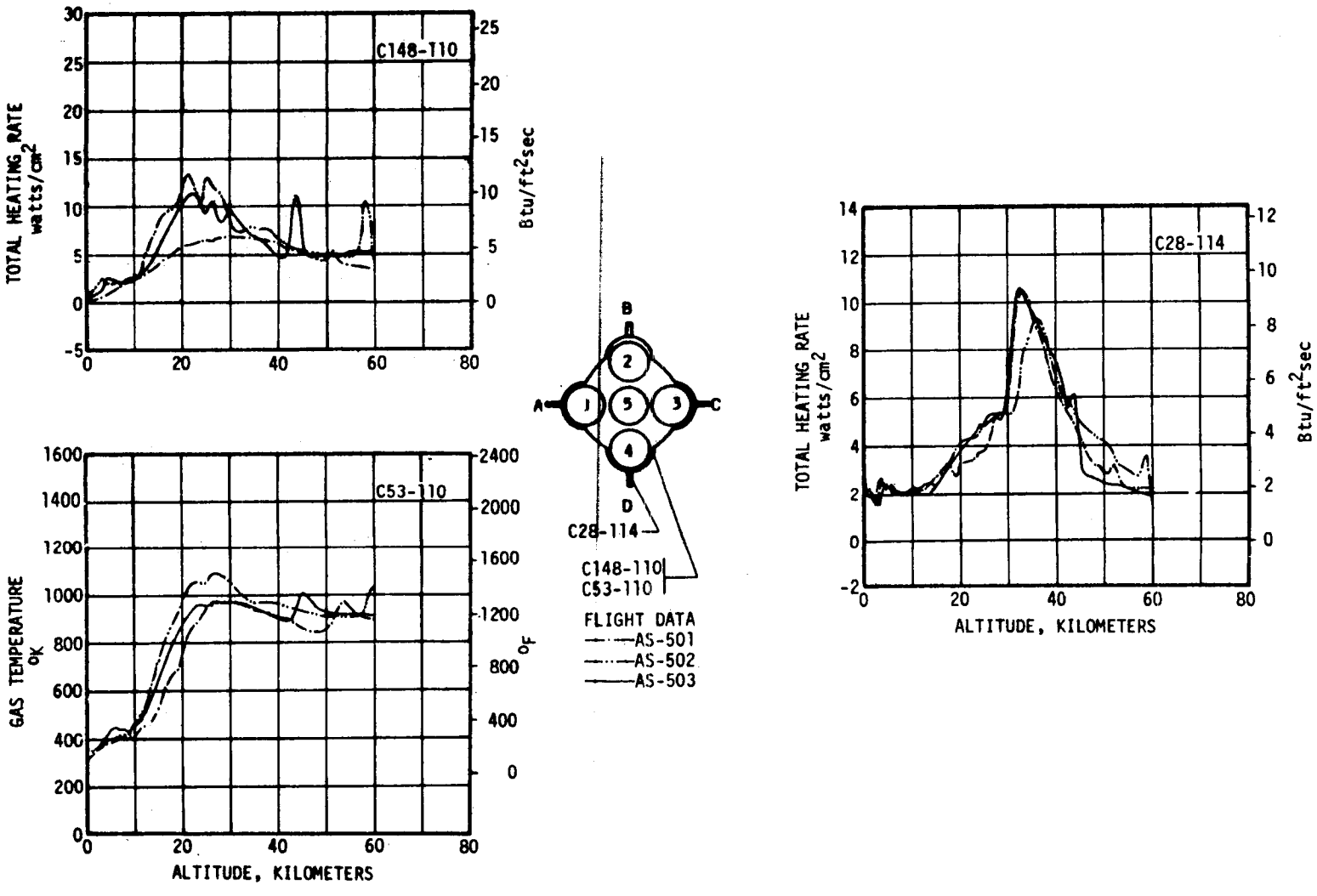

FIGURE 4.5-17 S-IC ENGINE FAIRING AND FIN TRAILING EDGE THERMAL ENVIRONMENT - AS-501 THROUGH AS-503

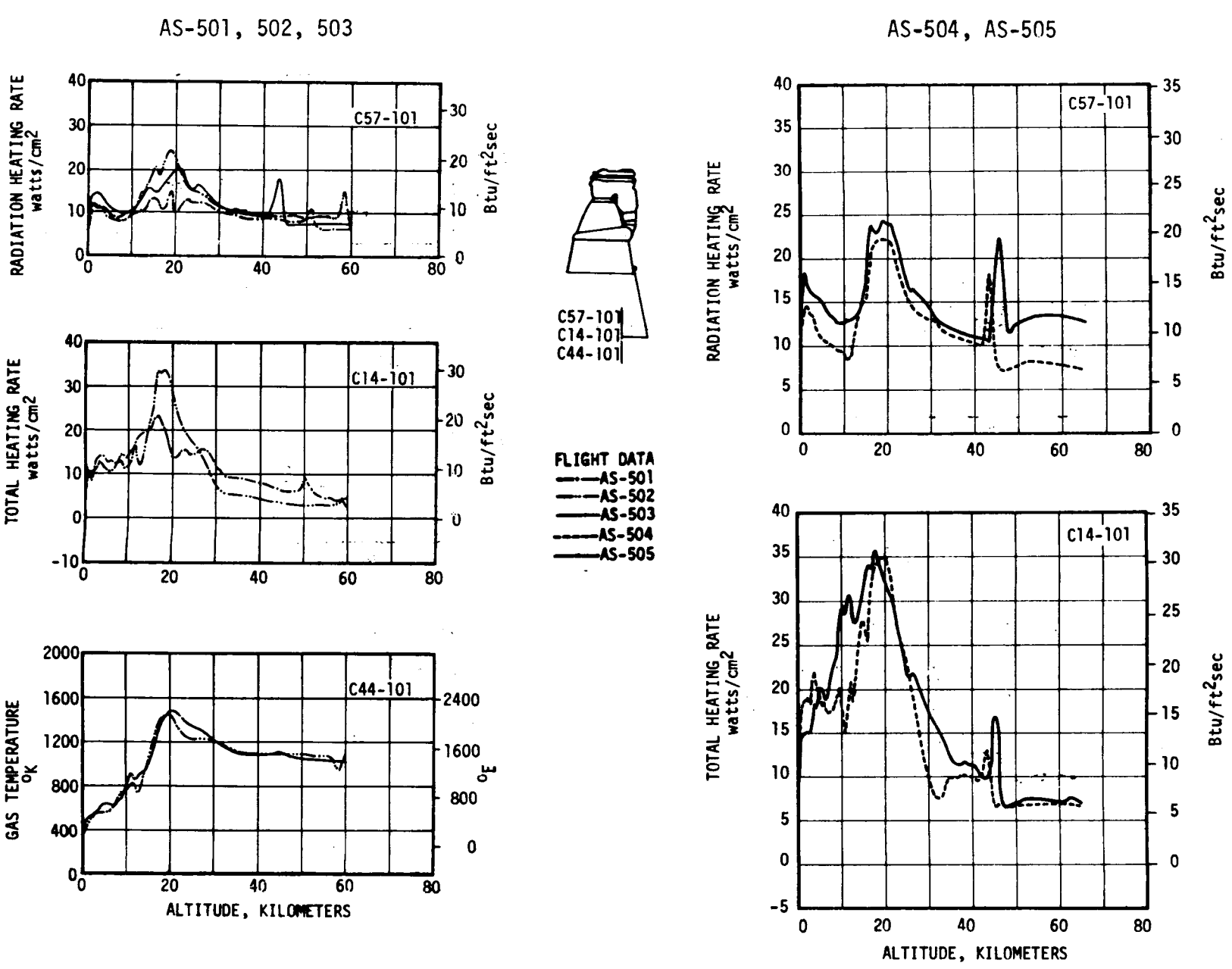

FIGURE 4.5-18 F-1 ENGINE ENVIRONMENT - OUTBOARD ENGINE EXIT PLANE FACING INBOARD - AS-501 THROUGH AS-505

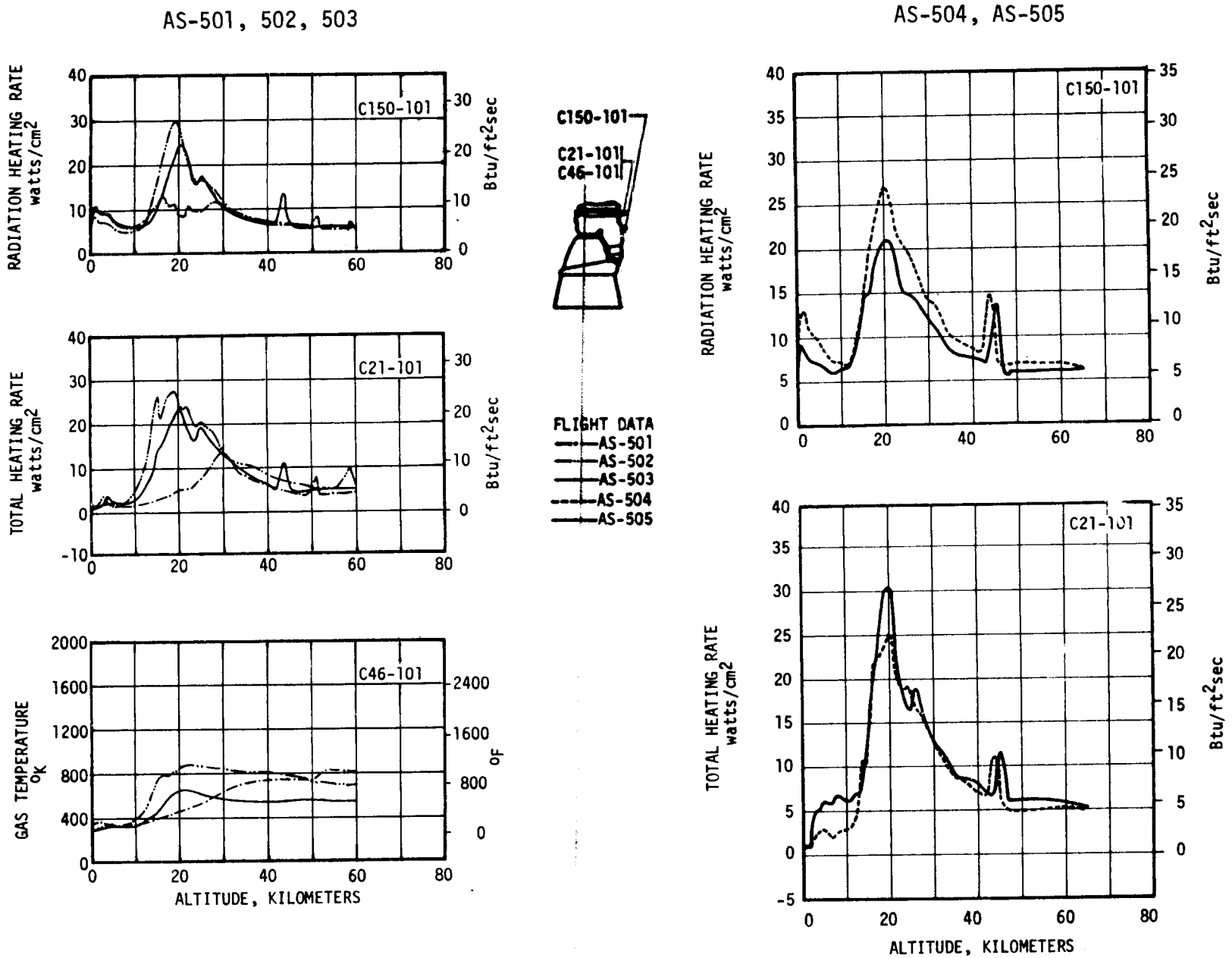

FIGURE 4.5-19 F-1 ENGINE ENVIRONMENT - OUTBOARD ENGINE NEAR HEAT SHIELD FACING OUTBOARD - AS-501 THROUGH AS-505

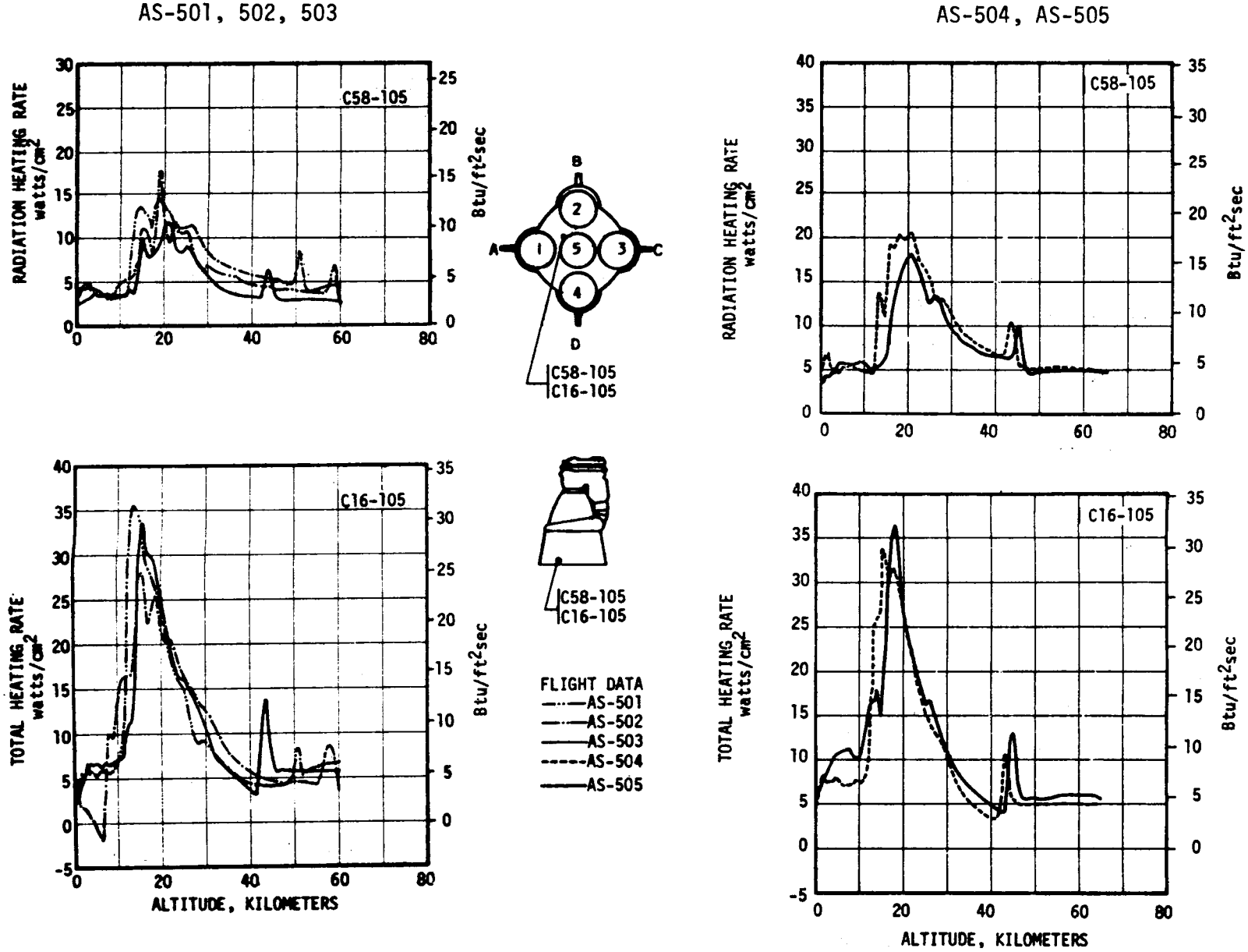

FIGURE 4.5-20 F-1 ENGINE ENVIRONMENT - INBOARD ENGINE EXIT PLANE FACING OUTBOARD BETWEEN TWO ENGINES - AS-501 THROUGH AS-505

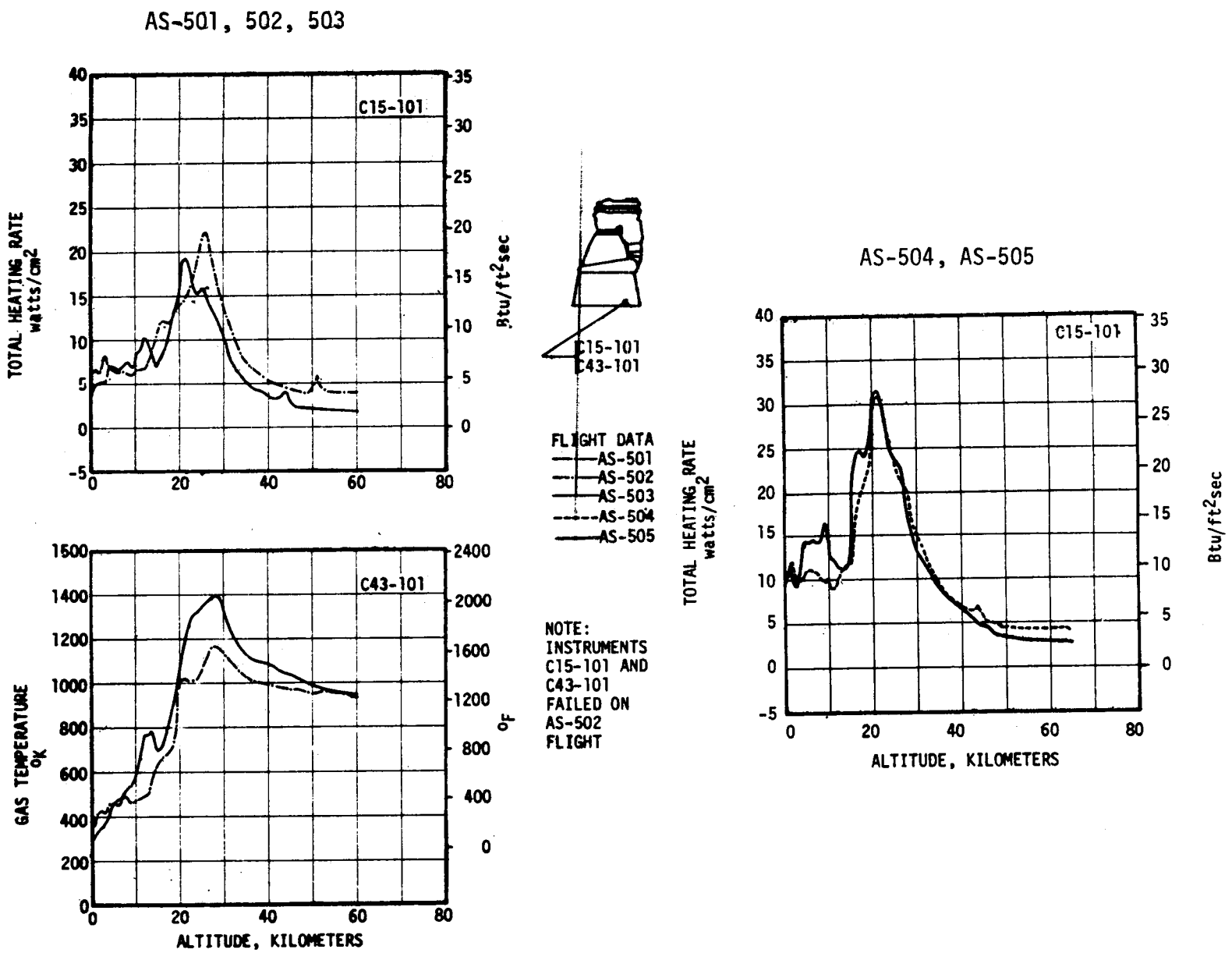

FIGURE 4.5-21 F-1 ENGINE ENVIRONMENT - OUTBOARD ENGINE EXIT PLANE FACING OUTBOARD ENGINE - AS-501 THROUGH AS-505

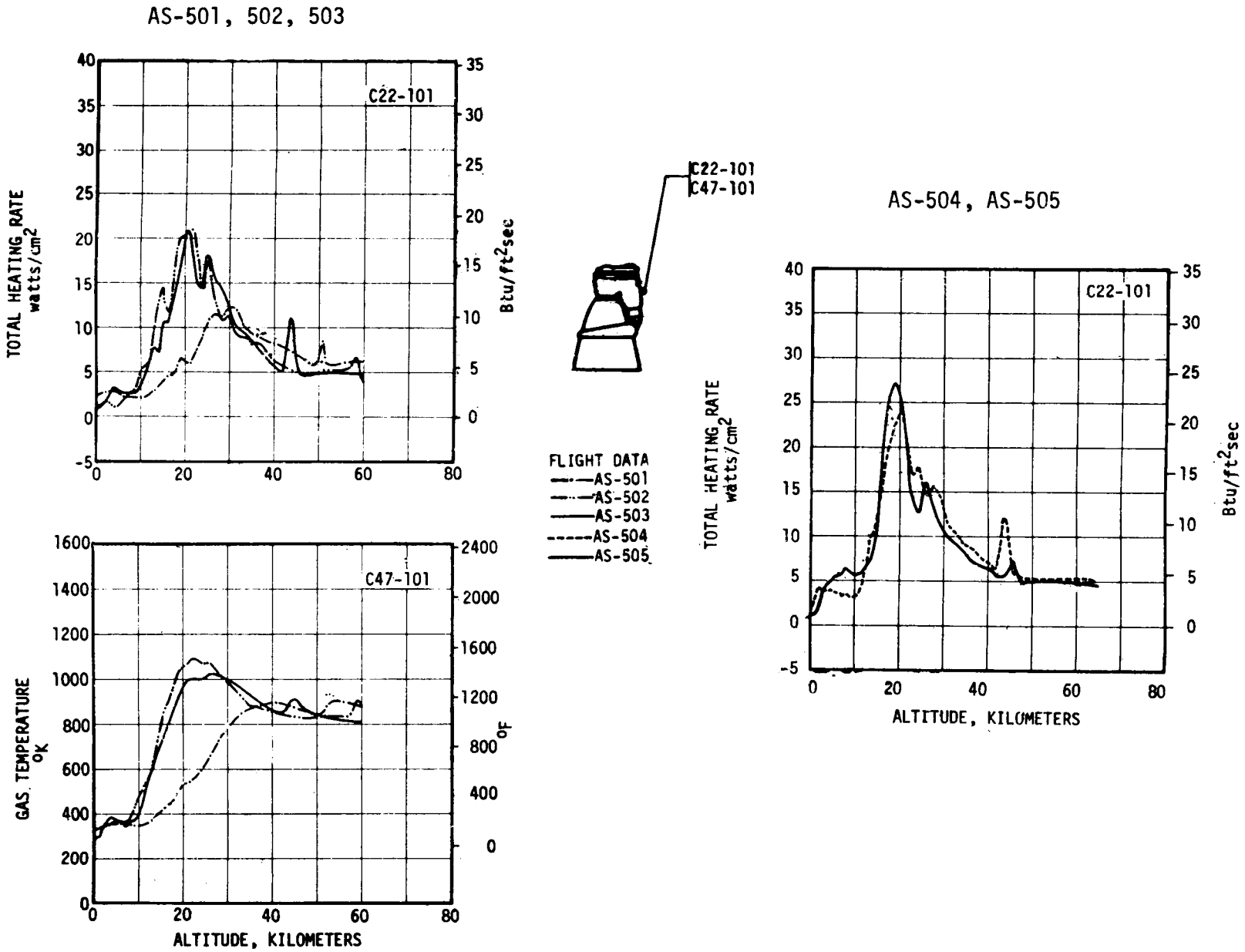

FIGURE 4.5-22 F-1 ENGINE ENVIRONMENT - OUTBOARD ENGINE NEAR HEAT SHIELD FACING INBOARD ENGINE - AS-501 THROUGH AS-505

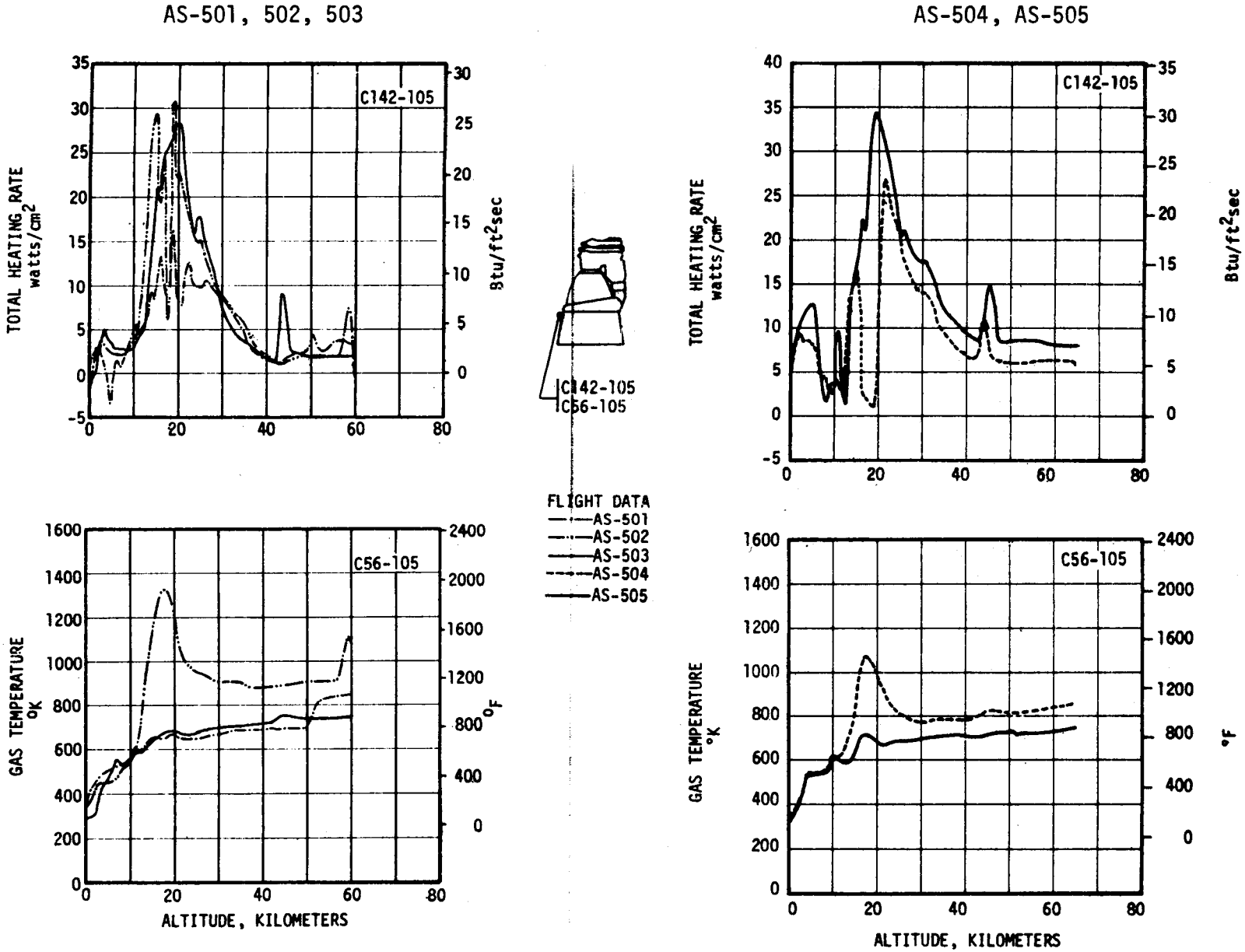

FIGURE 4.5-23 F-1 ENGINE ENVIRONMENT - INBOARD ENGINE MANIFOLD FACING OUTBOARD ENGINE - AS-501 THROUGH AS-505

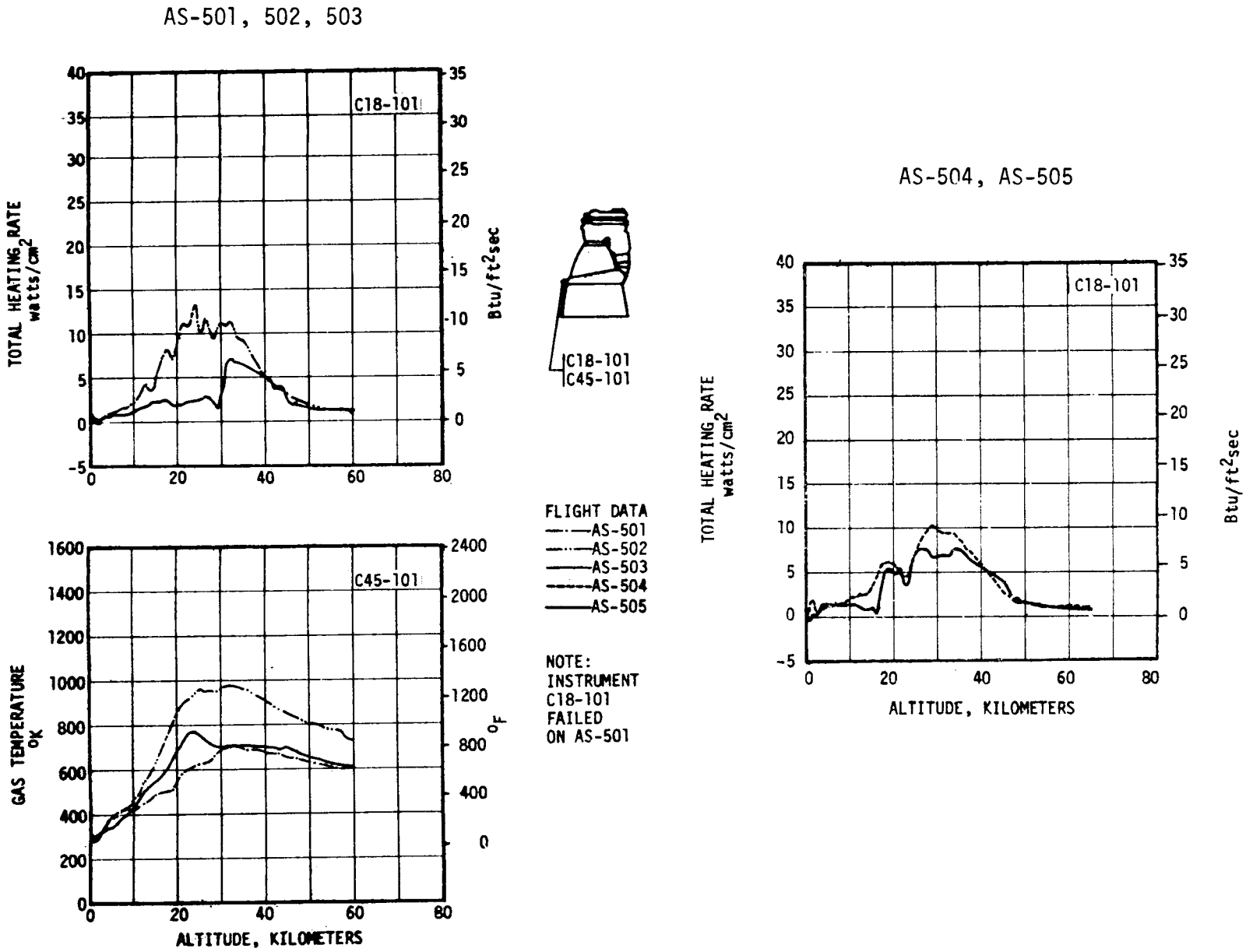

FIGURE 4.5-24 F-1 ENGINE ENVIRONMENT - OUTBOARD ENGINE MANIFOLD FACING OUTBOARD - AS-501 THROUGH AS-505

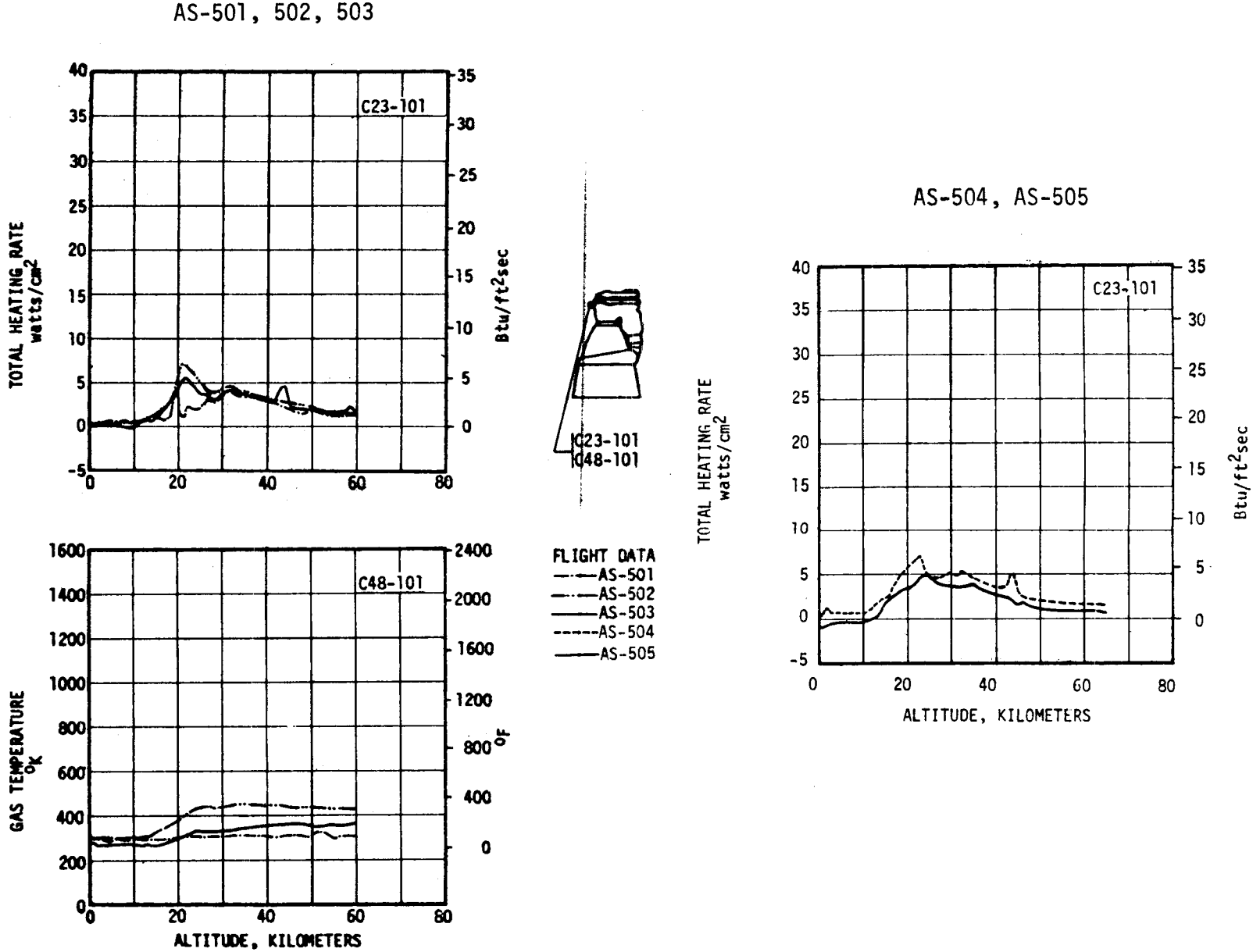

FIGURE 4.5-25 F-1 ENGINE ENVIRONMENT - OUTBOARD ENGINE NEAR HEAT SHIELD FACING OUTBOARD - AS-501 THROUGH AS-505

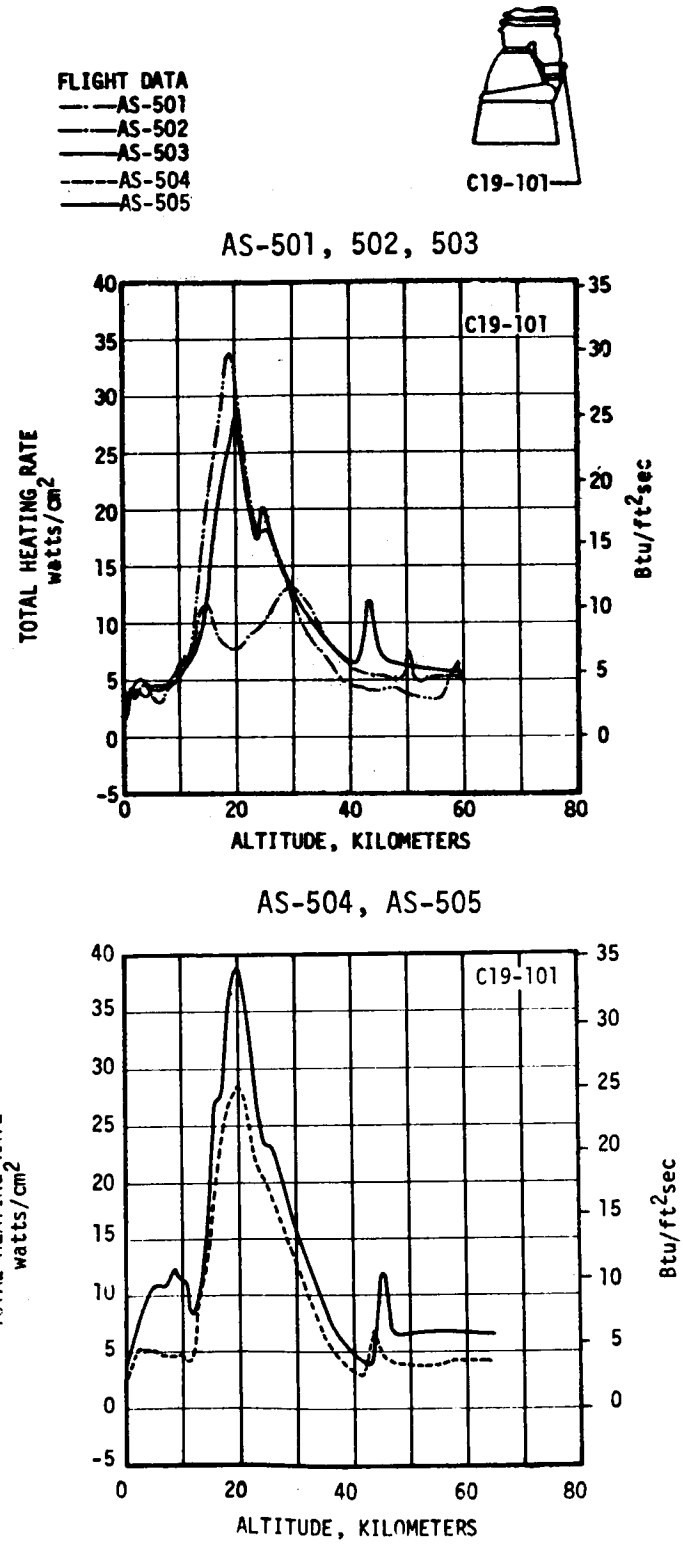

FIGURE 4.5-26 F-1 ENGINE ENVIRONMENT - OUTBOARD ENGINE FLEXIBLE MANIFOLD FACING INBOARD - AS-501 THROUGH AS-505

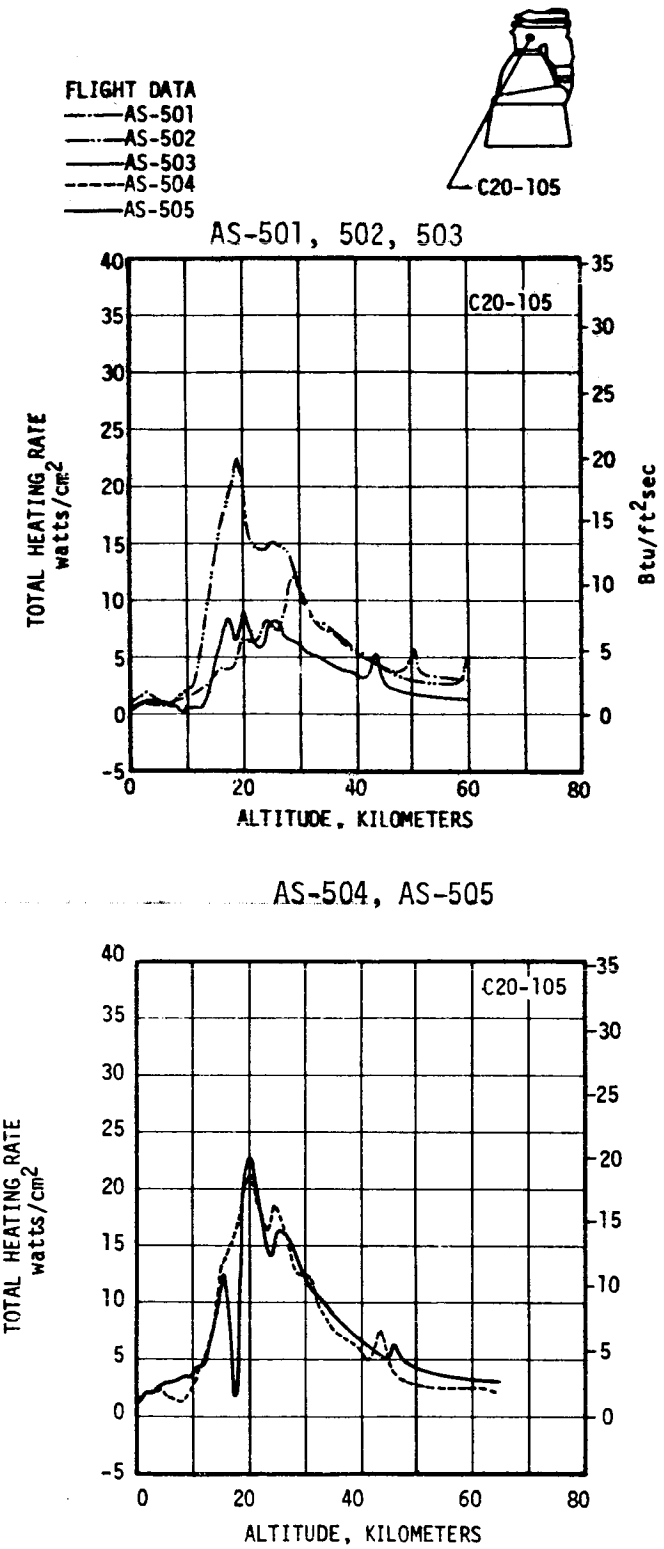

FIGURE 4.5-27 F-1 ENGINE ENVIRONMENT - INBOARD ENGINE NEAR HEAT SHIELD FACING OUTBOARD ENGINE - AS-501 THROUGH AS-505

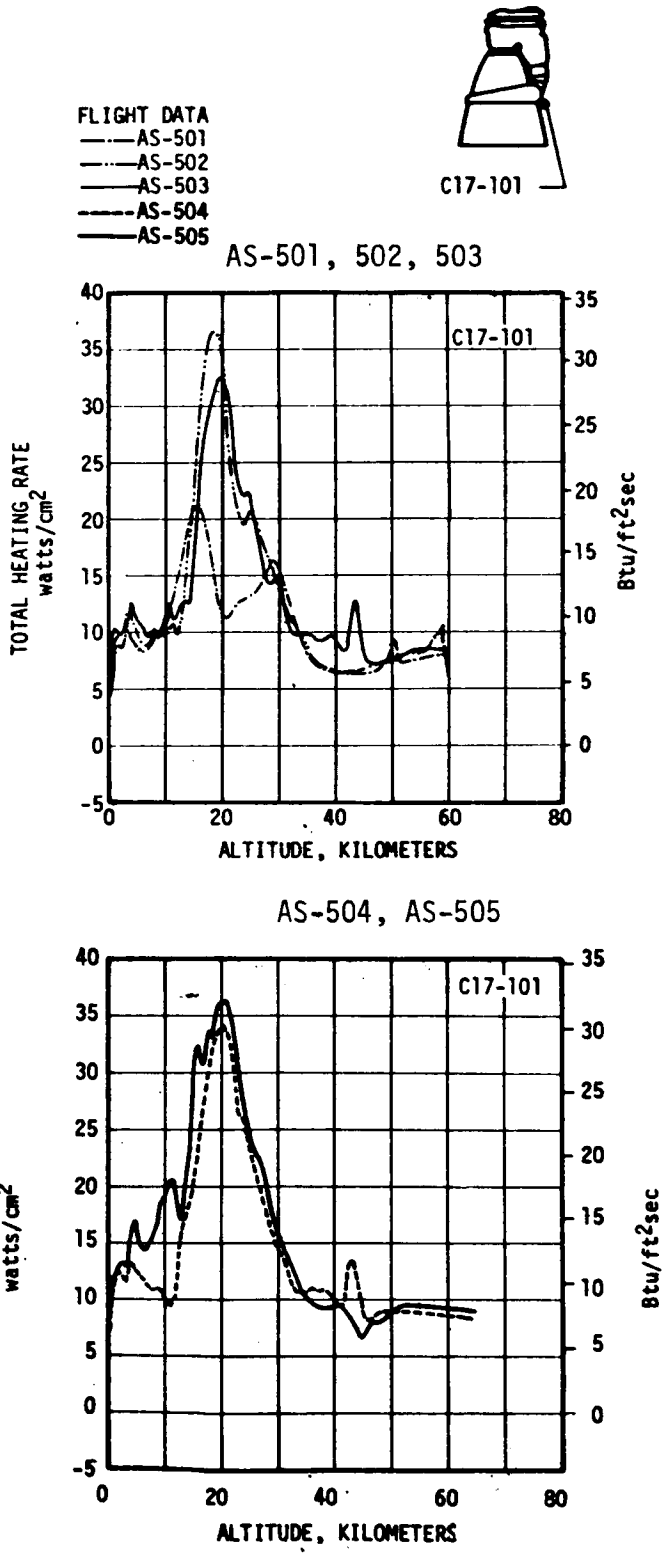

FIGURE 4.5- 28 F-1 ENGINE ENVIRONMENT - OUTBOARD ENGINE MANIFOLD FACING INBOARD - AS-501 THROUGH AS-505

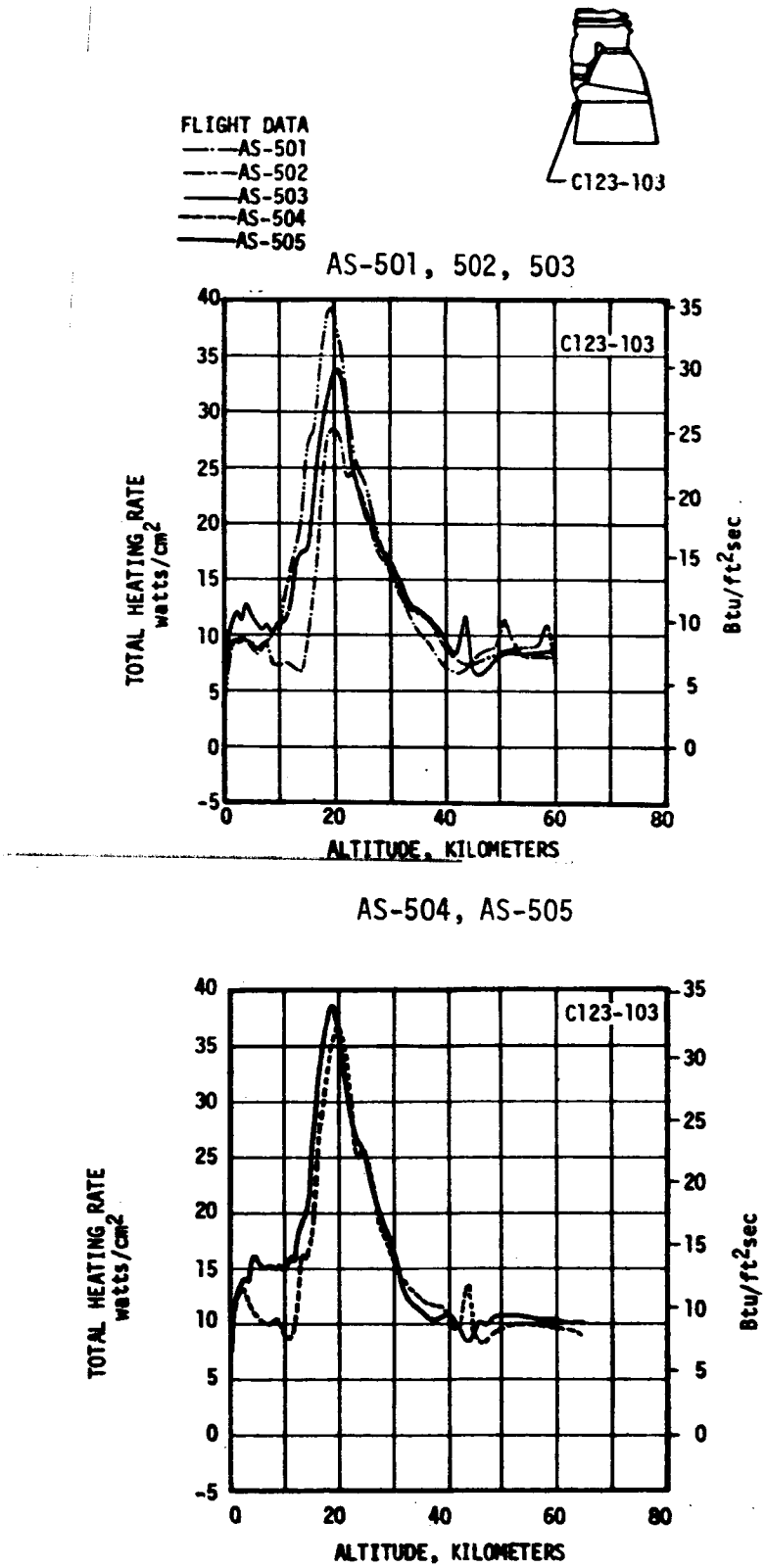

FIGURE 4.5- 29 F-1 ENGINE ENVIRONMENT - OUTBOARD ENGINE MANIFOLD FACING INBOARD - AS-501 THROUGH AS-505

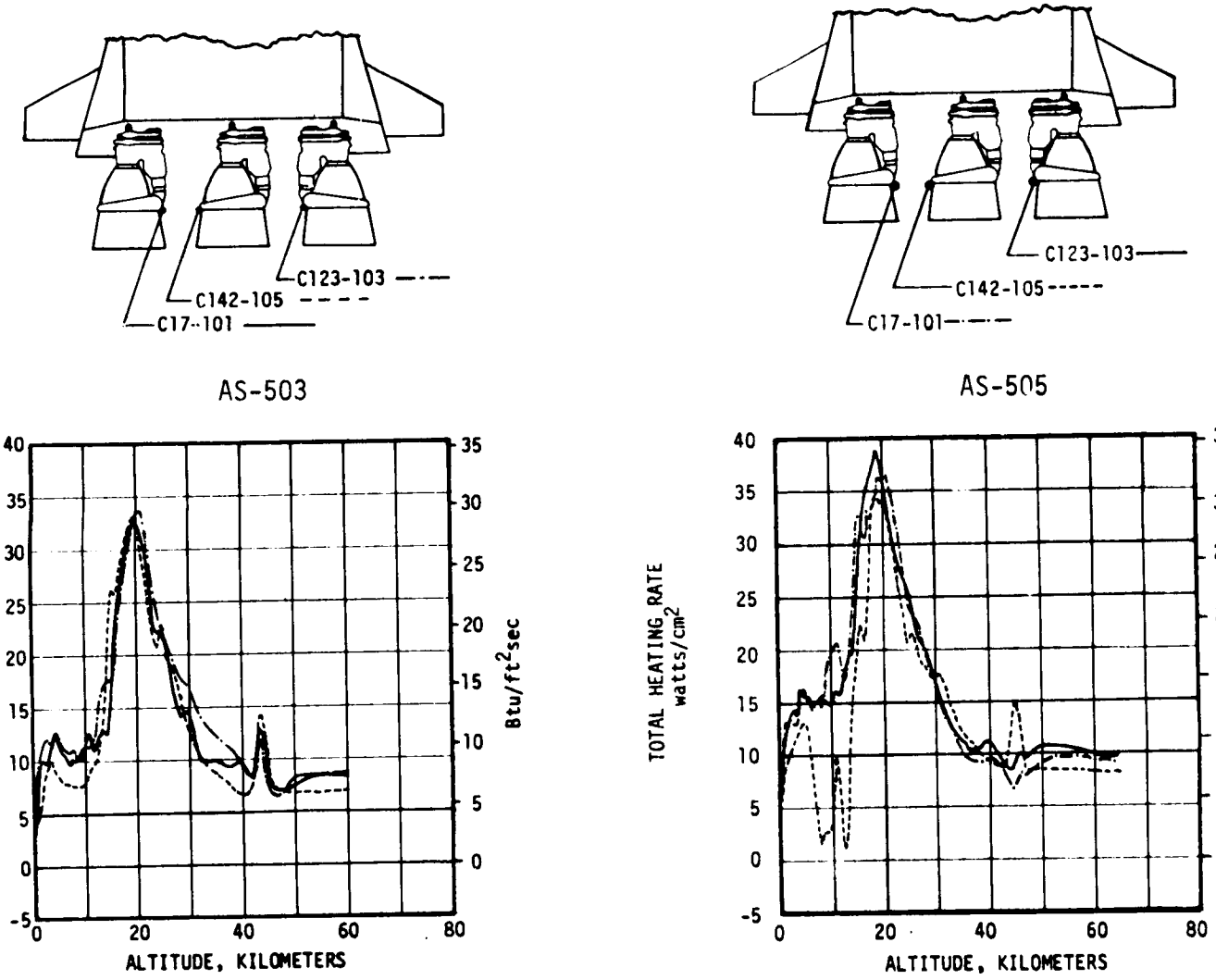

FIGURE 4.5- 30 F-1 ENGINE ENVIRONMENT - FLOW SYMMETRY, AS-503 AND AS-505

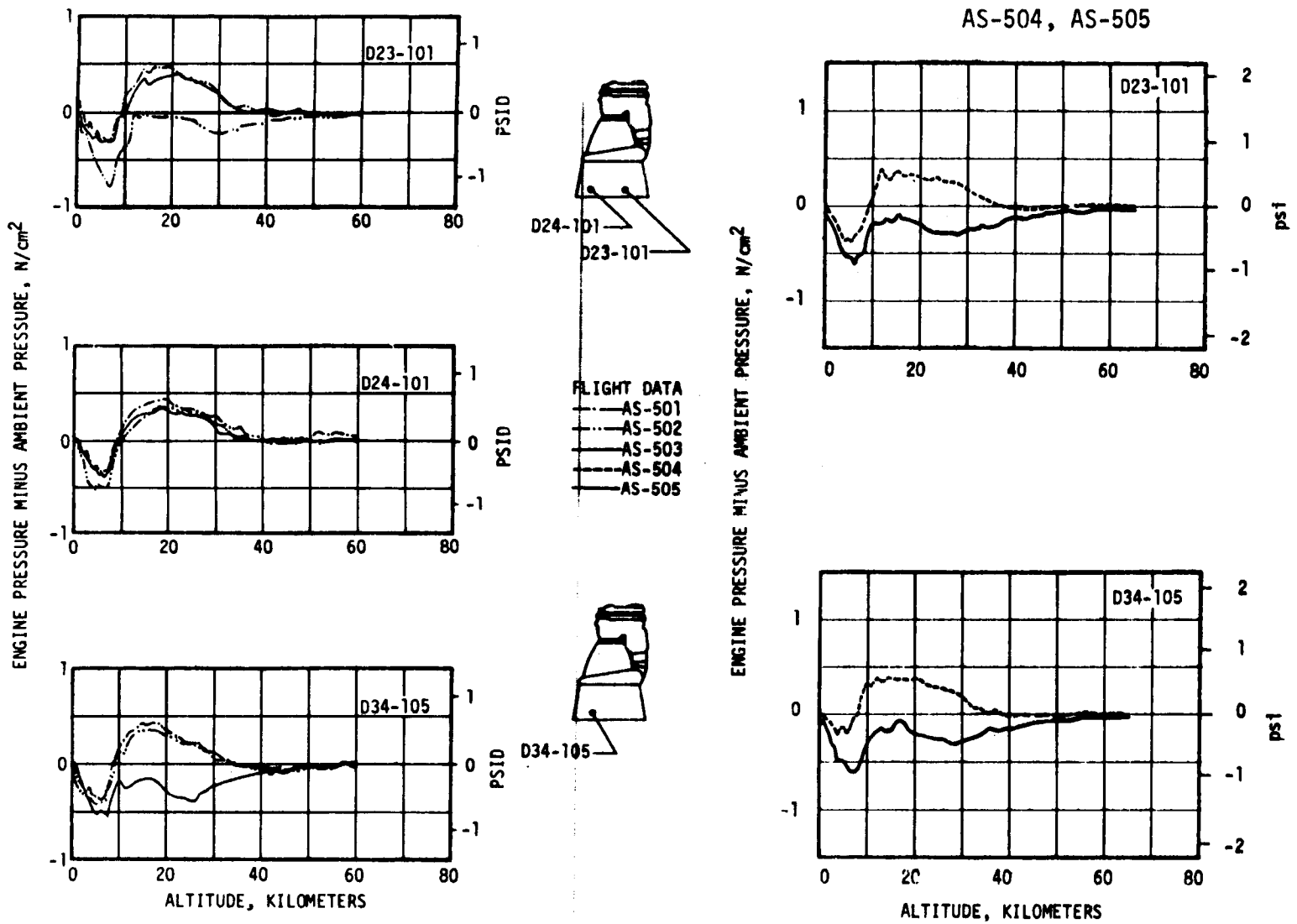

FIGURE 4.5- 31 F-1 ENGINE PRESSURE - INBOARD AND OUTBOARD ENGINE EXIT PLANE - AS-501 THROUGH AS-505

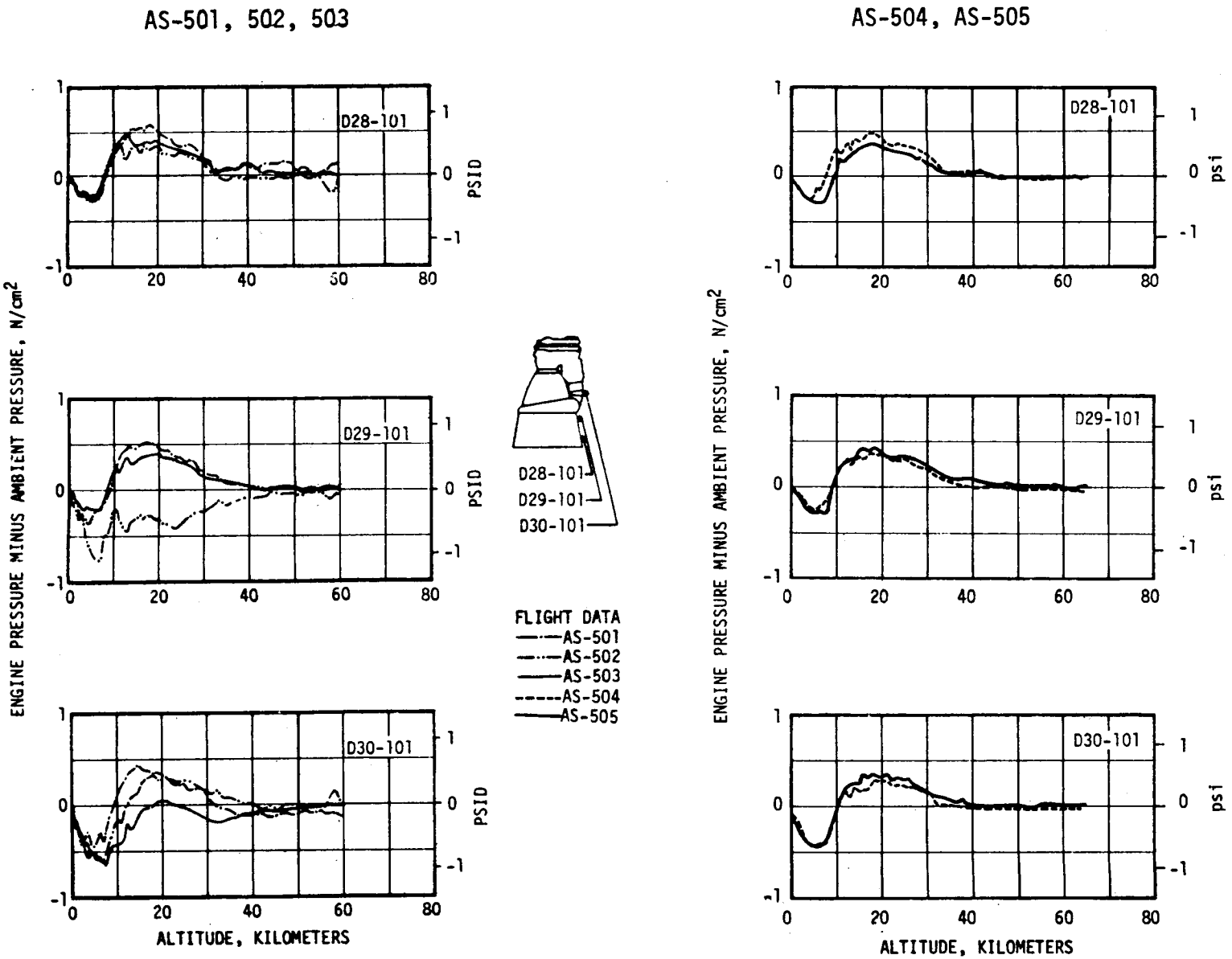

FIGURE 4.5-32 F-1 ENGINE PRESSURE AXIAL VARIATION ALONG OUTBOARD ENGINE FACING INBOARD - AS-501 THROUGH AS-505

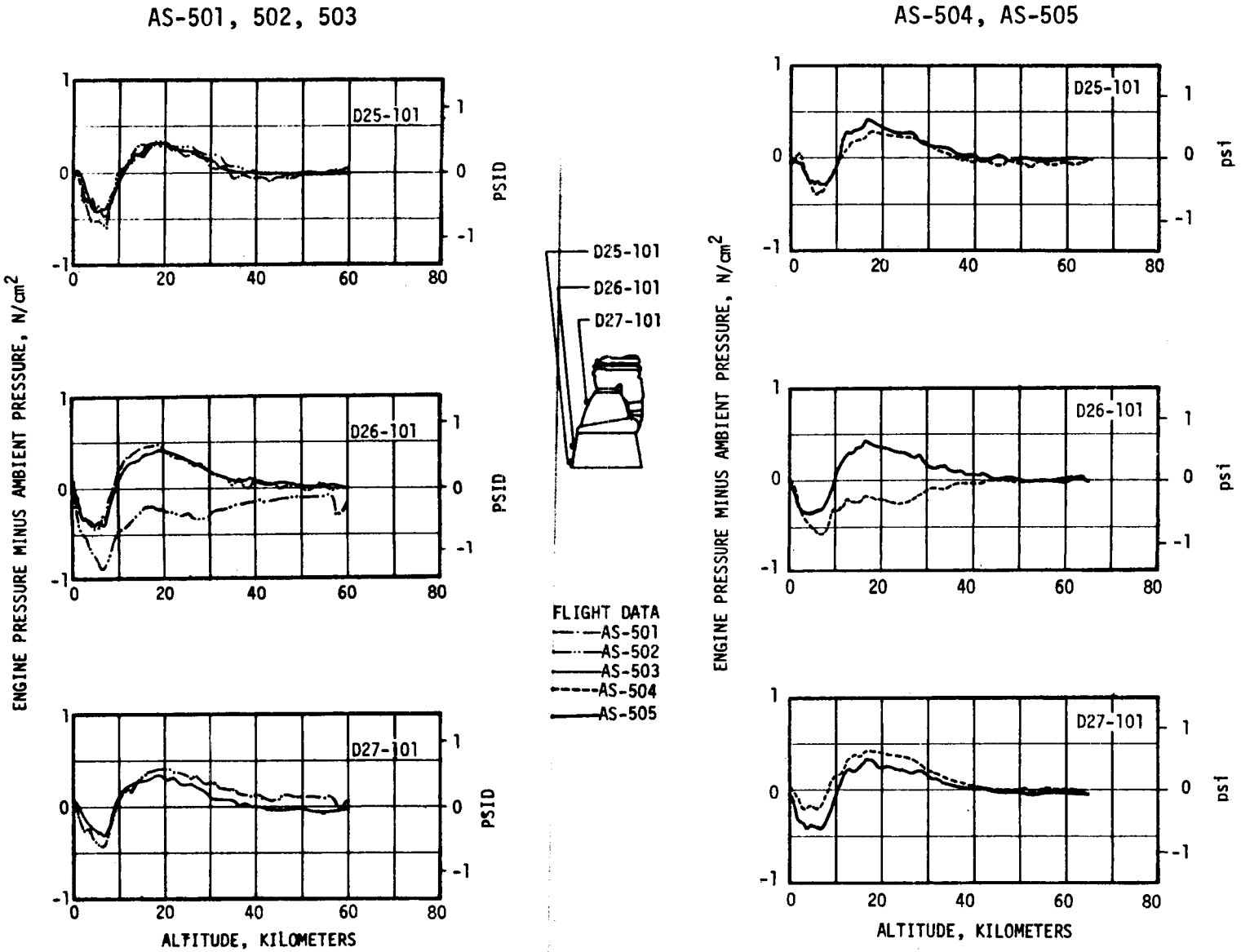

FIGURE 4.5-33 F-1 ENGINE PRESSURE - AXIAL VARIATION ALONG OUTBOARD ENGINE FACING OUTBOARD - AS-501 THROUGH AS-505

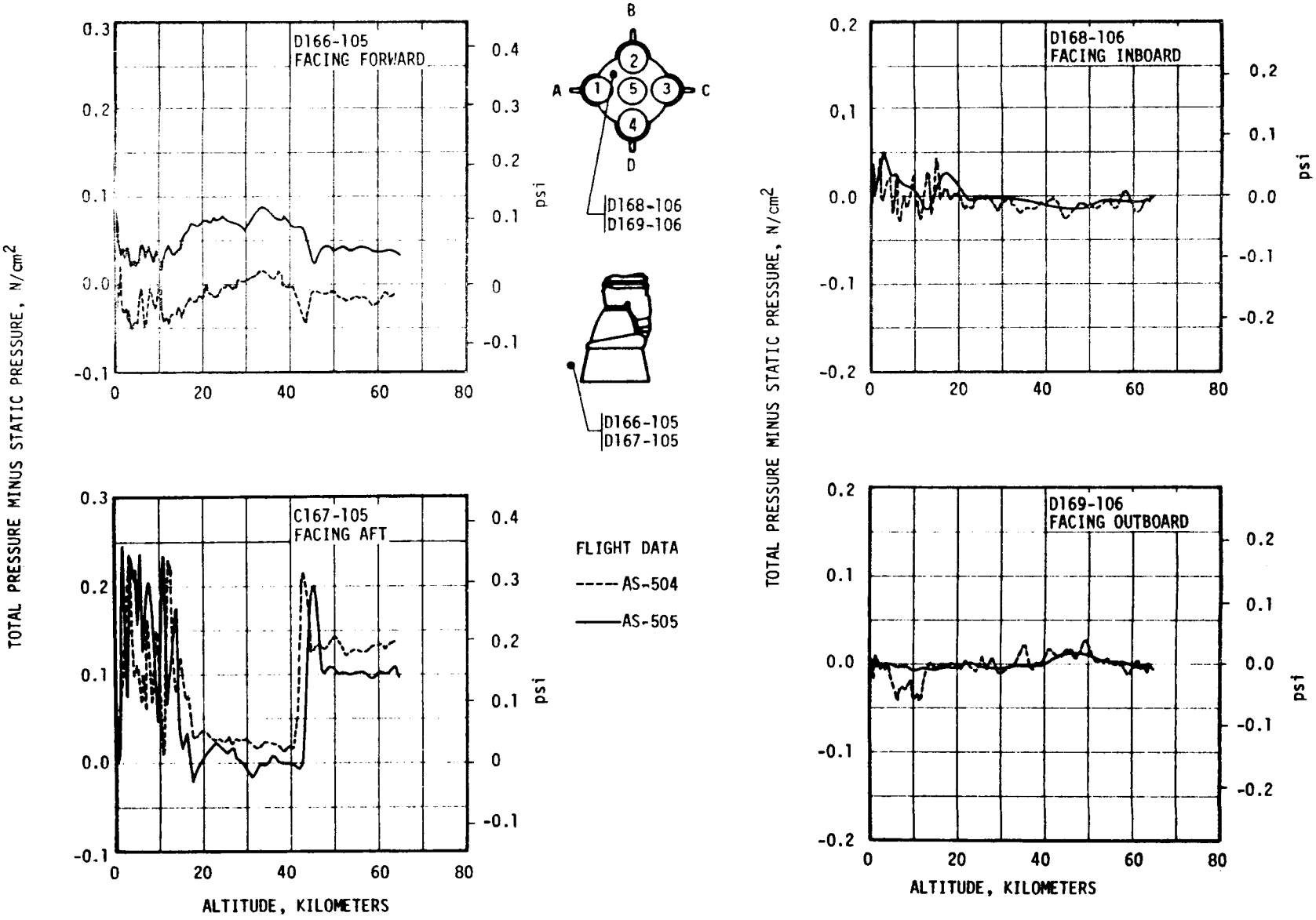

FIGURE 4.5-34 S-IC HEAT SHIELD AND ENGINE TOTAL PRESSURE - AS-504 AND AS-505

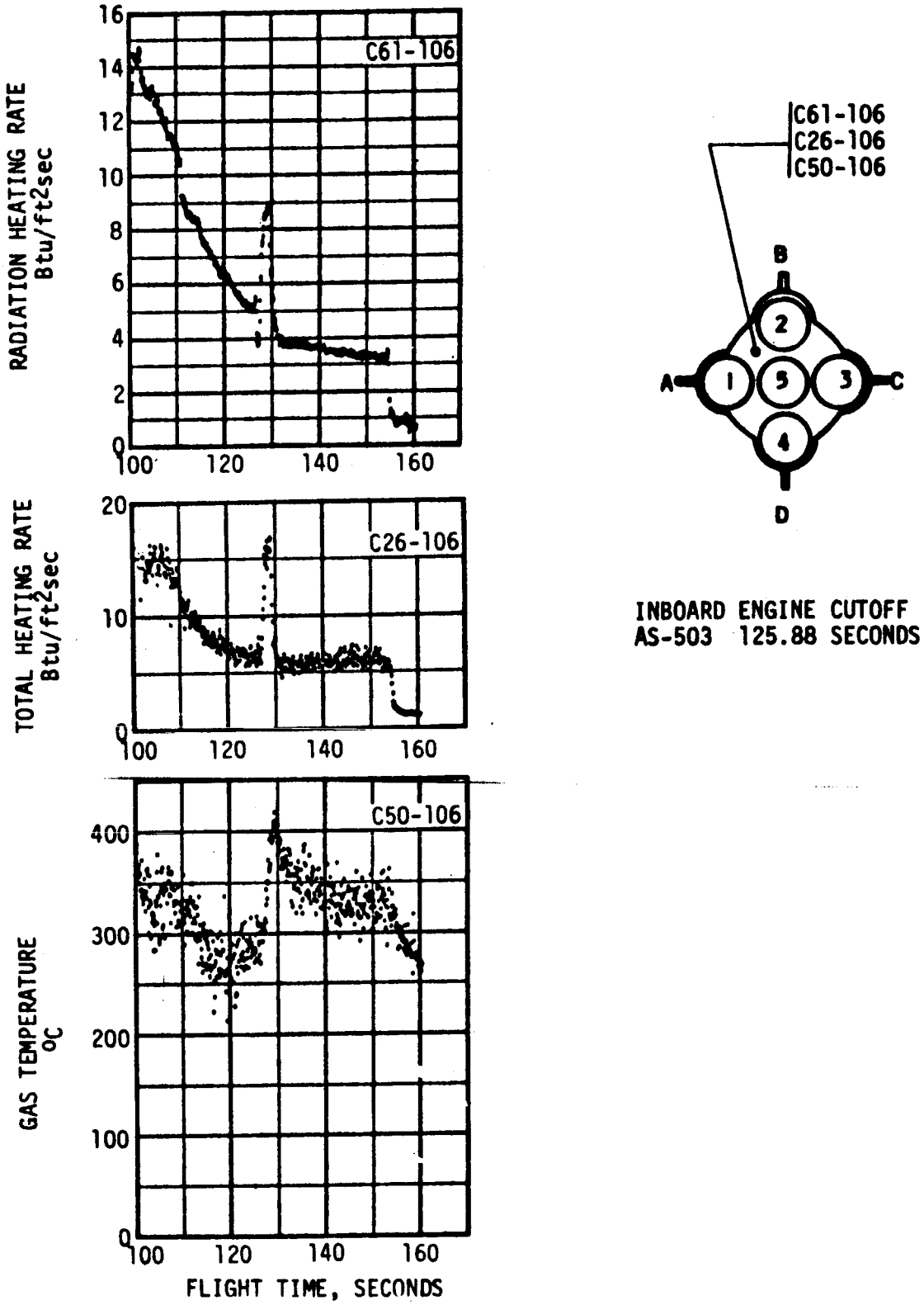

FIGURE 4.5-35 ENGINE OUT EFFECT ON HEAT SHIELD ENVIRONMENT

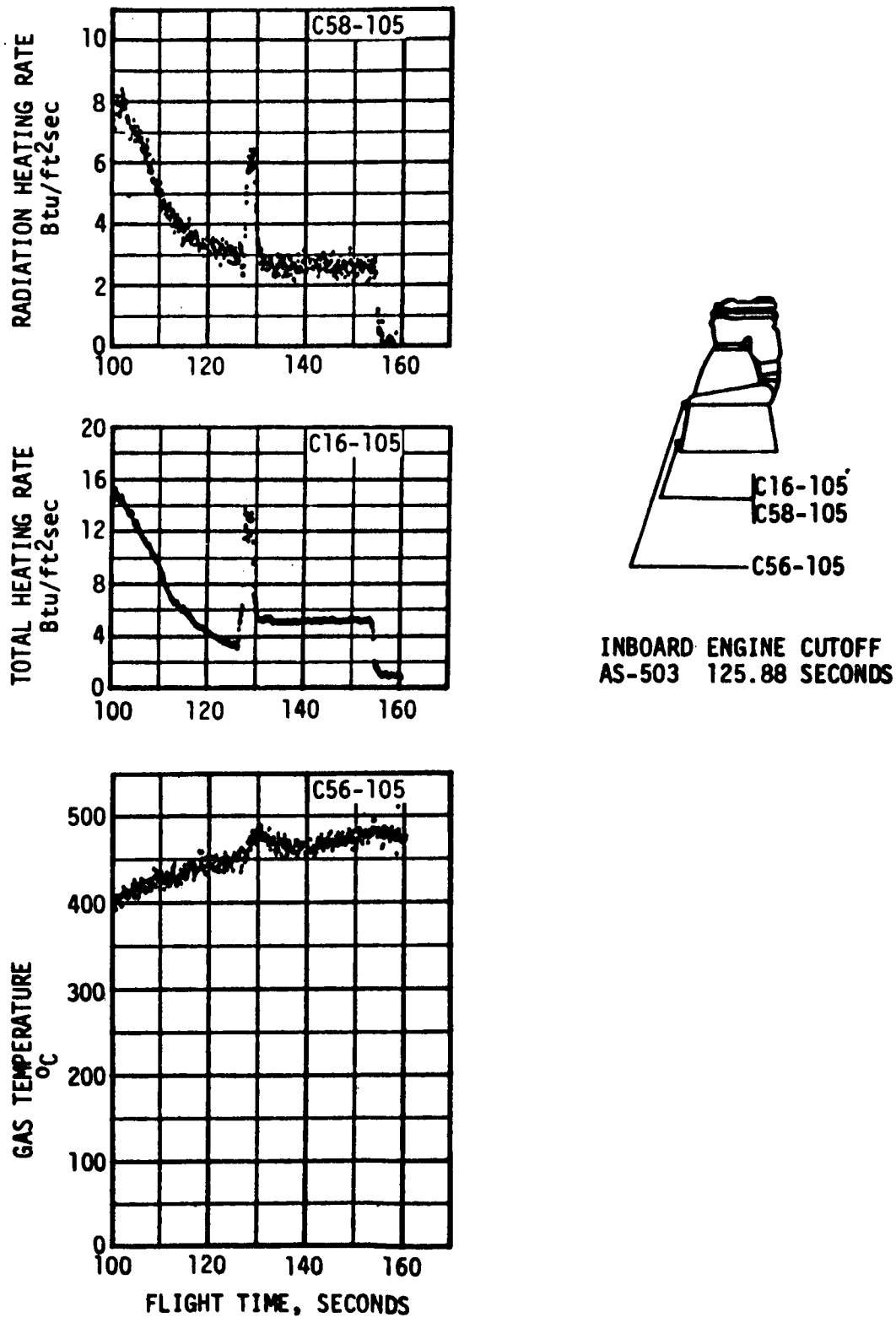

FIGURE 4.5-36 ENGINE OUT EFFECT ON CENTER ENGINE ENVIRONMENT

4.6 COMPARISON OF MODEL AND FLIGHT TEST RESULTS

Two comparisons are possible between the 1/45th scale short duration test results and the Saturn V/S-IC stage flight data. The AS-501 flight vehicle was flown with base flow deflectors and can be compared with the scoop and deflector model configuration designated $FS_1D_1SC_1N_1$-5. The base flow deflectors were removed on the AS-502 (and subsequent) flight vehicle. Flight data from AS-502 can be compared with data from the baseline model configuration designated FS_1N_1-5.

The model and flight data comparisons were enhanced by the close similarity in model and flight instrumentation locations; on the engines as well as the heat shield. The overall base geometry was simulated closely with the short duration model especially the external nozzle shape (the short duration model does not require cooling jackets for the hot flow nozzles therefore allowing good simulation of the engine external geometry). However, the small scale model created heating environments which contained significant scaling effects. Additional uncertainty in the validity of the comparisons occurs because of the poor simulation of turbine exhaust injection and instrumentation inaccuracies.

Heating Rates

Flight vehicle and model heat shield and center engine heating environments are compared in Figures 4.6-1 and 4.6-2, respectively. The heat shield comparisons in Figure 4.6-1 were made from data measured along a radial line between outboard engines. The center engine comparisons in Figure 4.6-2 were made from data measured near the nozzle exit plane facing outboard between two engines. In both figures, comparisons are made for the configuration with scoops and flow deflectors (AS-501 flight data compared to FS_1N_1-$5PL_1$ model data) and for the configuration without scoops and flow deflectors (AS-502 flight data compared to FS_1N_1-$5PL_1$ model data). The AS-501 flight vehicle did not have engine fairing scoops; however, the flow deflectors on the flight vehicle provided a scoop area to base area ratio closely approximated on the model with the D_1SC_1 scoop and deflector combination.

Radiation is expected to increase with increase in size such that the flight vehicle radiation is significantly higher than the model. Although the flight radiation data are higher than the model radiation data, as shown in the upper curve comparisons of Figures 4.6-1 and 4.6-2; no conclusions can be drawn from these comparisons because of the poor quality of the model radiation data. The model exhaust gases (GOX/ethylene) were not similar to the full scale and did not contain sufficient carbon to maintain correct similarity of emissivity with a LOX/RP-1 plume. The negligible radiation heating to the model heat shield and engines is caused by both scaling and non-simulation and therefore prevents any meaningful conclusions on the scalability of the radiation data.

Convective heating in the base is a function of size (the smaller the size, the larger the convective heating) and, consequently, the convective heating on the model was expected to be much larger than that experienced on the flight vehicle. Based upon simple turbulent and laminar theory scaling laws, the model data were expected to be between two and six times greater than the flight values. This trend is generally substantiated by the lower left curve comparisons on the heat shield and engine in Figures 4.6-1 and 4.6-2. However, it was impossible to define a scaling factor because of model and flight instrumentation inaccuracies and model simulation problems.

The model convective heating data did exhibit the same trend as the flight data when the scoops and flow deflectors were removed. The heat shield and center engine heating was increased with the removal of the flow deflectors. The trend may be more easily seen in the model data comparisons of Section 4.4, Figures 4.4-20 through 4.4-22.

Base Pressures

Average model base pressure, for model configurations with and without scoops and deflectors, is compared with AS-501 and AS-502 flight measured base pressure in Figure 4.6-3. The AS-501 pressure is higher than AS-502 as expected because of the flow deflectors. The effect of the flow deflectors on the model data is not as pronounced with approximately the same magnitude measured with both model configurations.

The trends of the base pressure minus ambient curves are very similar between the model and flight data; i.e., the base pressure is lower than ambient during aspiration and exceeds ambient after fully recirculated flow is established. The base pressure becomes equal to the ambient pressure at a higher altitude on the model than on the flight vehicle. The trend may be an indication that the flight vehicle plumes (with mixing and afterburning at the lower altitudes) impinge with each other earlier in flight causing recirculation into the base at the lower altitudes.

Gas Temperature

Gas recovery temperature in the base region was derived from heated base plate convective heating data at four test altitudes with the short duration model. These data were obtained for the model configuration without scoops and deflectors, and exhibited a considerable degree of scatter as discussed in Section 4.4.

4.6 (Continued)

The model recovery temperatures obtained by this method are compared with flight measured gas temperatures on the heat shield for the AS-501 and AS-502 flight in Figure 4.6-3. The flight data show large gradients in gas temperature near the heat shield and the accuracy of the model data is not good but it is evident that the flight and model data have comparable magnitudes of gas temperature at the higher altitudes.

Distributions Across Heat Shield

Flight and model data distributions across the heat shield are compared at 18,000 feet and 96,000 feet in Figures 4.6-4 and 4.6-5, respectively. Each figure contains both scooped and unscooped configuration data. The two altitudes were chosen as typical altitudes for aspirating flow through the base (18,000 feet) and fully recirculated flow into the base (96,000 feet).

The heating rate distribution comparisons are not conclusive although the trend exhibited by the low altitude model radiation (increase in the outboard direction) is as expected. The radial distributions in base pressure are very similar for the model and flight data at both altitudes and for the scooped and unscooped configuration.

WITH SCOOPS AND FLOW DEFLECTORS

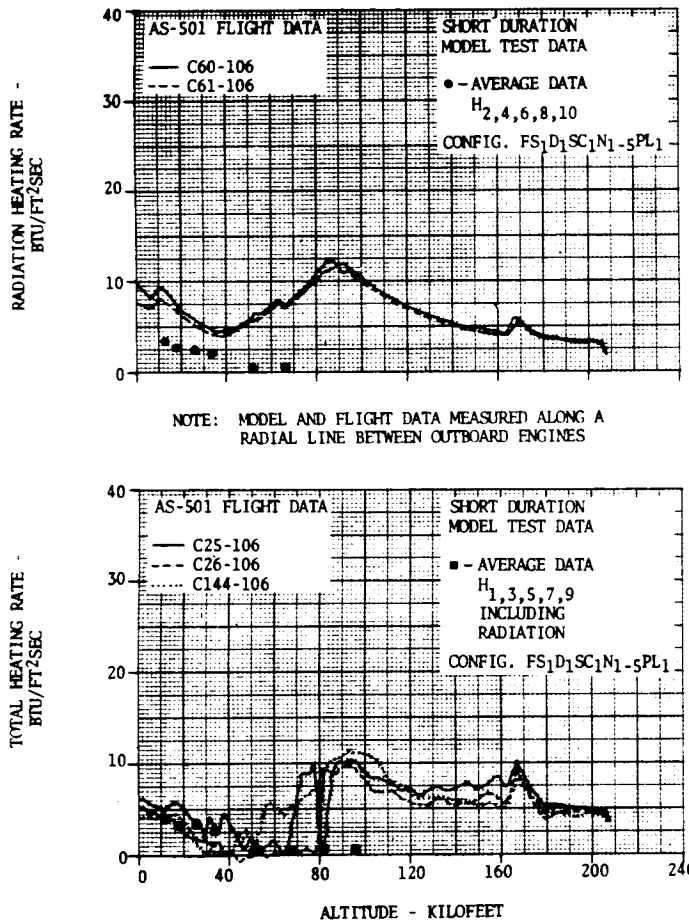

WITHOUT SCOOPS AND FLOW DEFLECTORS

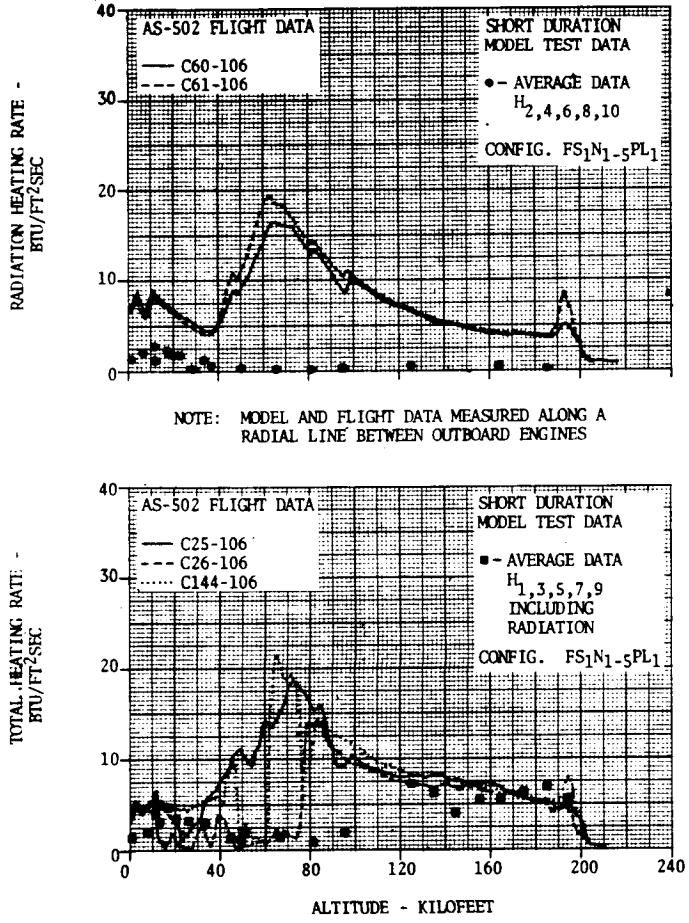

FIGURE 4.6-1. COMPARISON OF FLIGHT AND MODEL HEAT SHIELD ENVIRONMENTS

CENTER ENGINE HEATING ENVIRONMENTS

WITH SCOOPS AND FLOW DEFLECTORS

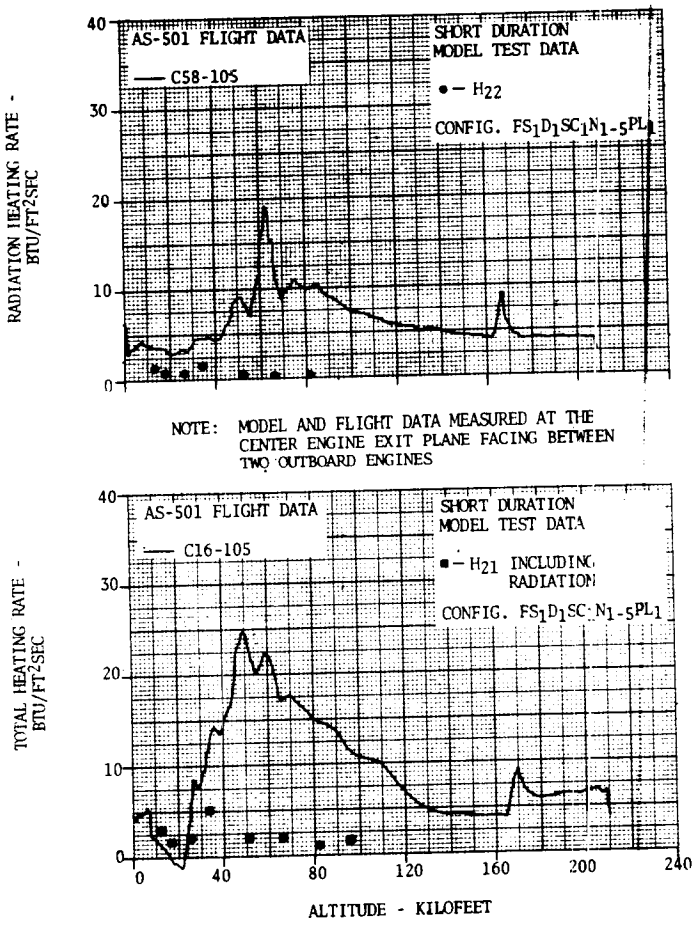

WITHOUT SCOOPS AND FLOW DEFLECTORS

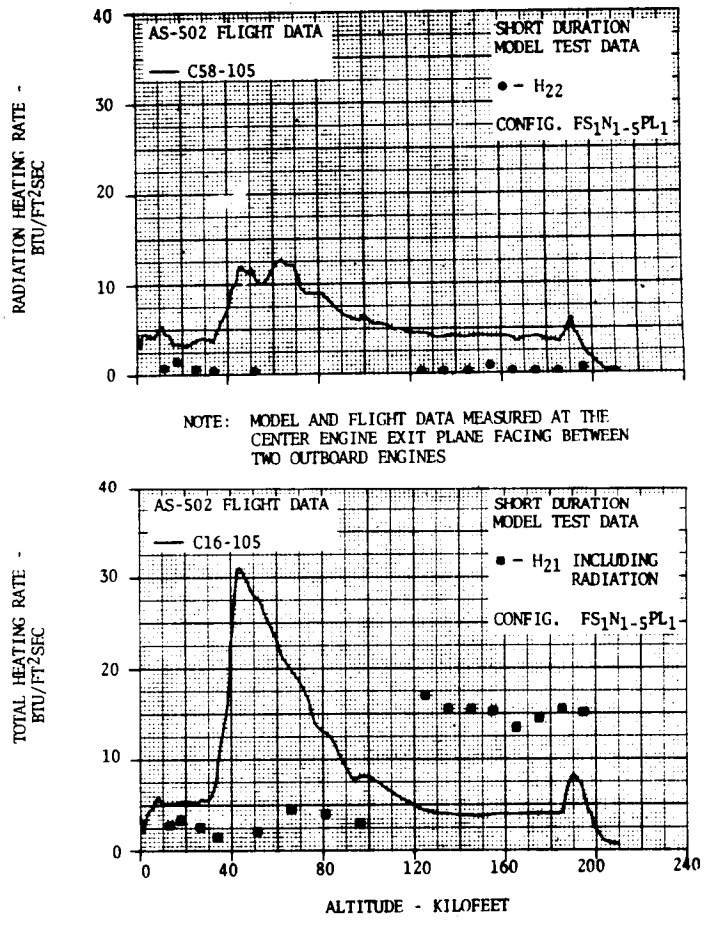

FIGURE 4.6-2. COMPARISON OF FLIGHT AND MODEL CENTER ENGINE ENVIRONMENTS

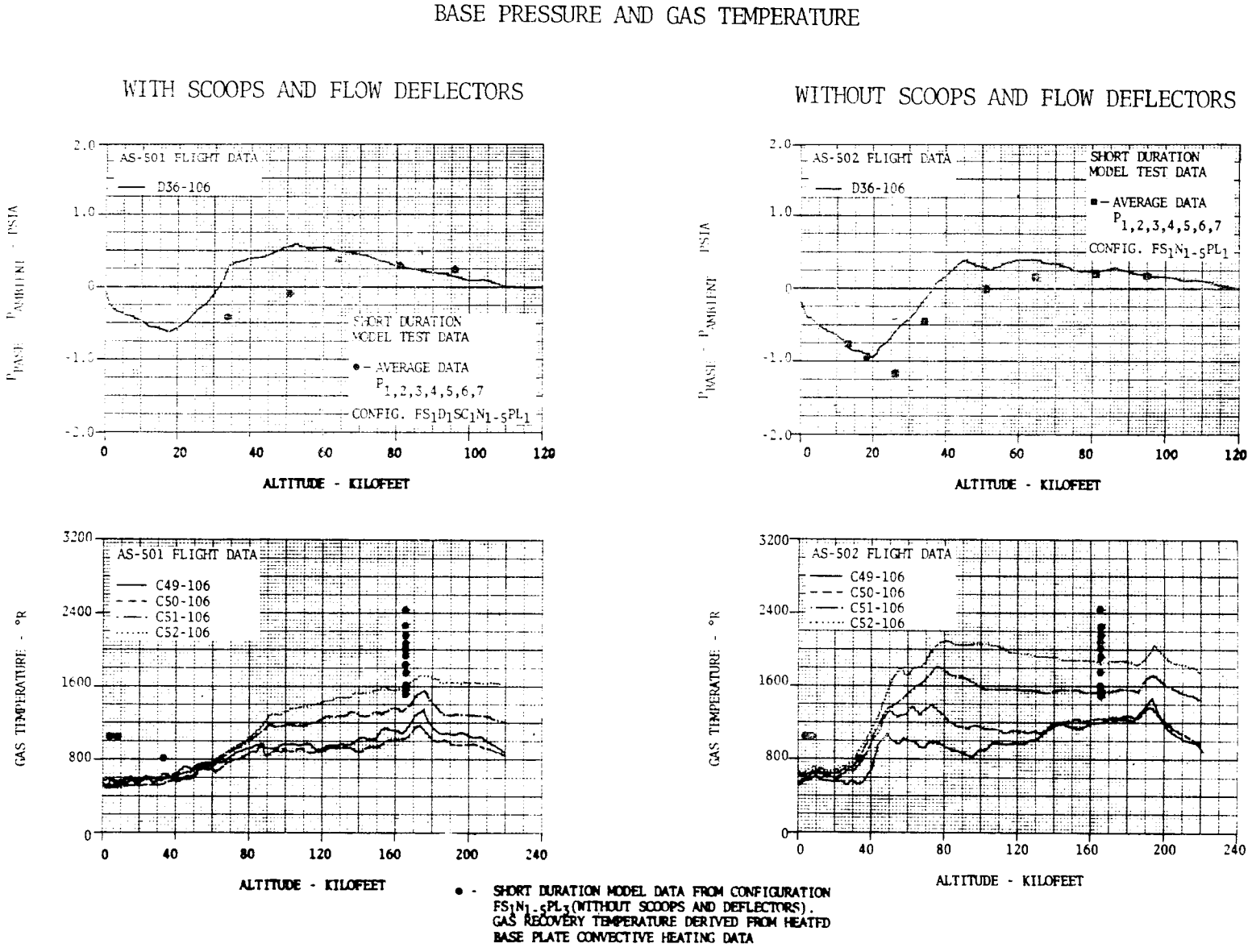

FIGURE 4.6-3. COMPARISON OF FLIGHT AND MODEL BASE PRESSURE AND GAS TEMPERATURE

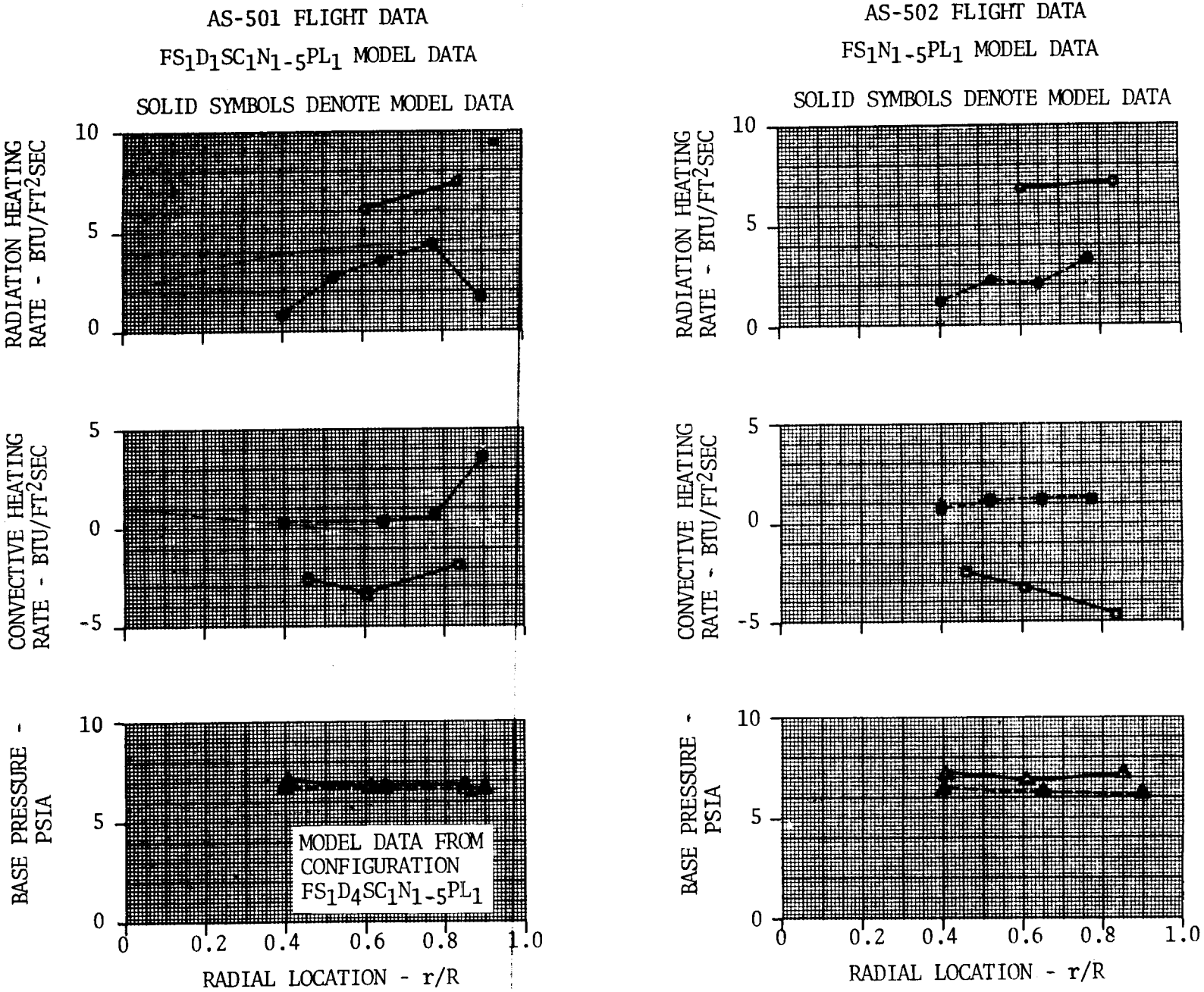

FIGURE 4.6-4. COMPARISON OF FLIGHT AND MODEL DATA DISTRIBUTIONS ACROSS HEAT SHIELD AT M = 0.8 (18,000 FEET) - ASPIRATING FLOW

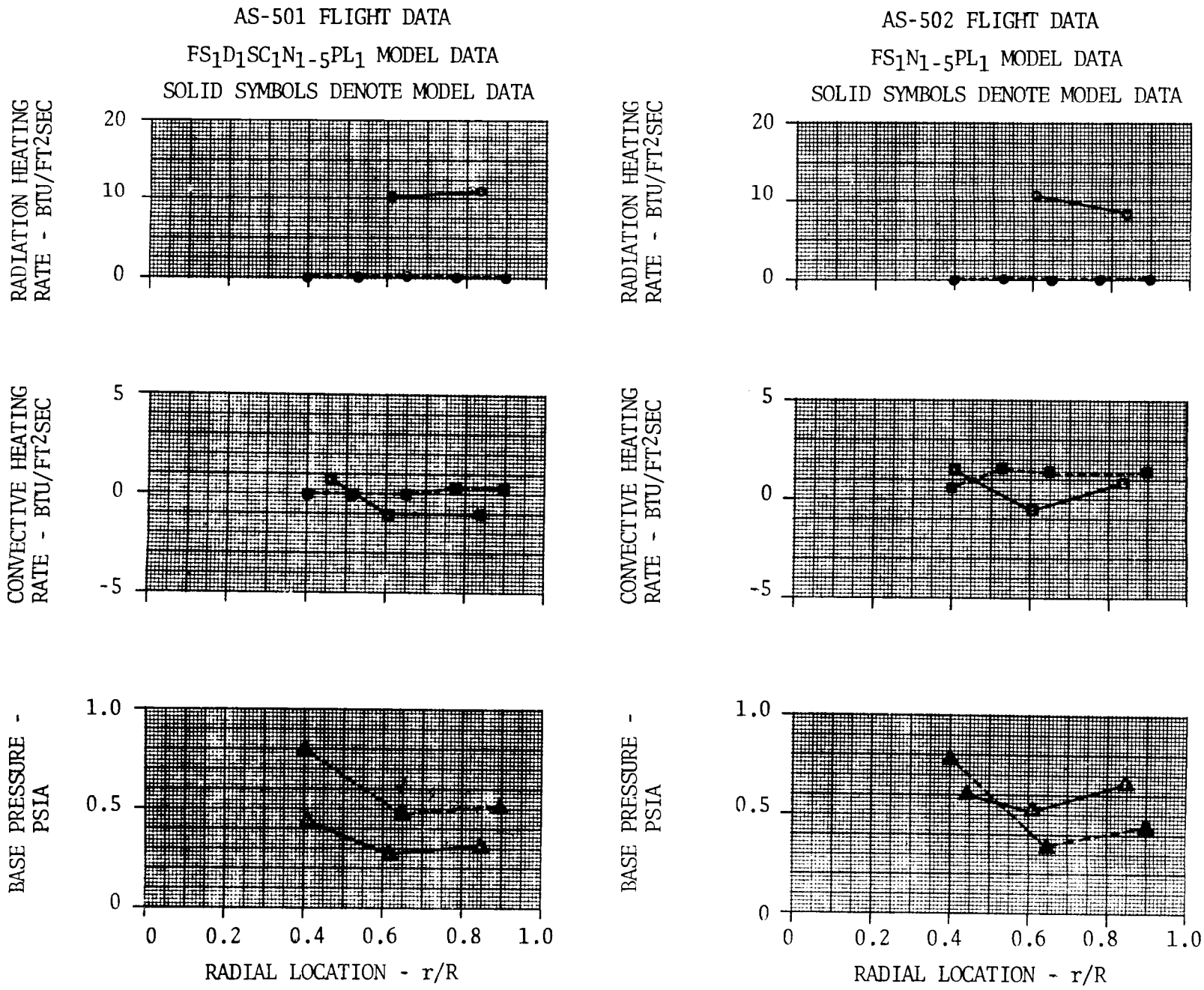

FIGURE 4.6-5. COMPARISON OF FLIGHT AND MODEL DATA DISTRIBUTIONS ACROSS HEAT SHIELD AT M = 3.5 (96,000 FEET) - FULLY RECIRCULATED FLOW

4.7 REFERENCES

4-1. Prozan, R. J.; "Development of a Method of Characteristics Solution for Supersonic Flow of an Ideal, Frozen, or Equilibrium Reacting Gas Mixture," LMSC/HREC A782535-A, April 1966.

4-2. Boeing Document D5-11287, "Analysis of Saturn S-IC Base Heating Environment," January 7, 1964.

4-3. NASA/MSFC Memo R-AERO-AT-65-28, "Sea Level Flame Model for the F-1 Engine: Design Criteria for Saturn V," Farmer, R. C.; October 12, 1965.

4-4. NACA TN 2836, "Radiant-Interchange Configuration Factors," Hamilton, D. C., and Morgan, W. R.; December 1952.

4-5. Boeing Document D5-15615, "Saturn V Model Base Heating Test Analysis (S-IC Stage), Volumes 1 and 2," August and October 1966, respectively.

4-6. Bogdan, L., "Measurement of Radiative Heat Transfer with Thin-Film Resistance Thermometers," CAL Report No. HM-1510-Y-9, July 1963.

4-7. Bogdan, L., "Heat Transfer Instrumentation," CAL Report WTH-021, March 1963.

4-8. Bogdan, L., "High-Temperature, Thin-Film, Resistance Thermometers for Heat Transfer Measurements," CAL Report No. HM-1510-Y-6, February 1963.

4-9. Skinner, G. T., "Analog Network to Convert Surface Temperature to Heat Flux," CAL Report No. 100, February 1960.

4-10. Boeing Document D5-15796-1, "Saturn V Aerothermodynamics Flight Evaluation - AS-501 through AS-503, June 19, 1969.

4-11. Boeing Document D5-15796-2, "Saturn V Aerothermodynamics Flight Evaluation-AS-504 and AS-505, November 14, 1969.

4-12. Rall, D. R., "Qualification Test Report-Radiation Heat Calorimeter Model R-2030-A-22," Report 64-282, October 1964, Hy-Cal Engineering, Santa Fe Springs, California.

4-13. Rall, D. R., "Qualification Test Report-Total Heat Calorimeter Model C-1147-A-ZZ," Report 64-182, October 1964, Hy-Cal Engineering, Santa Fe Springs, California.

4-14. Malone, E. W., "Heat Flux Measurements," Report D2-35057, January 1968, The Boeing Company, Seattle, Washington.

THIS PAGE LEFT BLANK INTENTIONALLY

CONTENTS

5.0 SATURN S-IV STAGE

5.1	S-IV STAGE PROTOTYPE CONFIGURATION	5-2
5.2	RL-10 ENGINE CHARACTERISTICS	5-6
5.3	PREDICTION METHODS	5-17
5.4	MODEL TESTS AND PARAMETRIC DATA	5-20
	5.4.1 1/10 SCALE S-IV 4-ENGINE COMBUSTION MODEL	5-20
	5.4.2 1/27.75 SCALE S-IV 4-ENGINE COLD FLOW MODEL	5-22
	5.4.3 1/10 SCALE S-IV 4-ENGINE HOT-FLOW MODEL SHORT DURATION	5-25
	5.4.4 1/10 SCALE S-IV 6-ENGINE HOT-FLOW SHORT DURATION	5-29
	5.4.5 MODEL TEST DATA COMPARISON	5-33
5.5	FLIGHT TESTS AND PARAMETRIC DATA	5-153
5.6	MODEL-FLIGHT DATA COMPARISONS	5-158
5.7	REFERENCES	5-162

5.0 SATURN S-IV STAGE

5.1 S-IV STAGE PROTOTYPE CONFIGURATION

The S-IV stage was the second stage of the Saturn I program. The primary objective of this program was the development of a two-stage launch vehicle. The program consisted of 10 vehicles which were divided into two main groups: Block I (SA-1 through SA-4) and Block II (SA-5 through SA-10). The Block I series utilized a dummy S-IV stage. The first active S-IV stage was flown on the SA-5 flight, January 29, 1964. The S-IV stage configuration used in the Block II series is shown in Figure 5.1-1.

The original design concept of the S-IV stage propulsion system had four uprated Pratt and Whitney RL-10A-3 engines (17,500 pounds thrust). This design was terminated in favor of a six-engine configuration using the standard RL-10A-3 engines (15,000 pounds thrust). The engines were circular arranged as shown in Figure 5.1-1. In the nominal positions the engines are canted outboard six degrees. Each engine is gimbal mounted on the stage thrust structure to provide engine thrust vectoring for vehicle altitude control and steering. (See Figure 5.1-2.) Two hydraulic actuators are utilized to gimbal each engine. All engines are gimbaled for pitch and yaw control and engines 1, 2, 3 and 4 are gimbaled for roll control.

A helium heater exhaust nozzle was located in the center of the heat shield. The helium heater is a low pressure combustor which burns oxygen and hydrogen at the following conditions: mixture ratio of one to one, chamber pressure of 7 psia, exhaust flow rate of 0.05 lb/sec, and exhaust total temperature of 800°F. The helium heater's purpose is to warm cold helium stored in high pressure spheres within the hydrogen tank for pressurization of the oxygen tank during flight. (See Figure 5.1-3.)

Additional information and flight objectives are contained in the MSFC Technical Information Summary for each flight. The preceding data were taken from Reference 5-1.

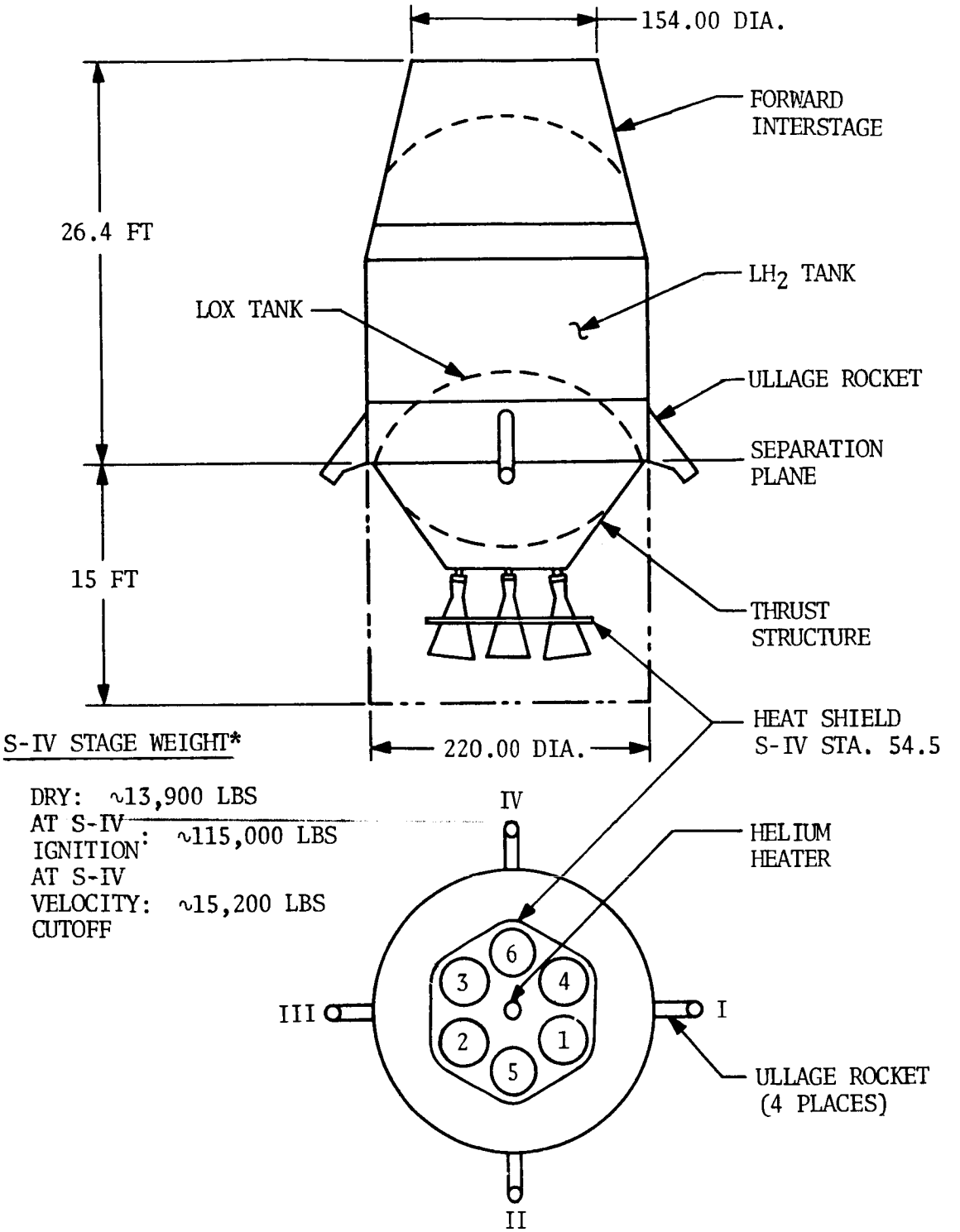

FIGURE 5.1-1. S-IV STAGE CONFIGURATION

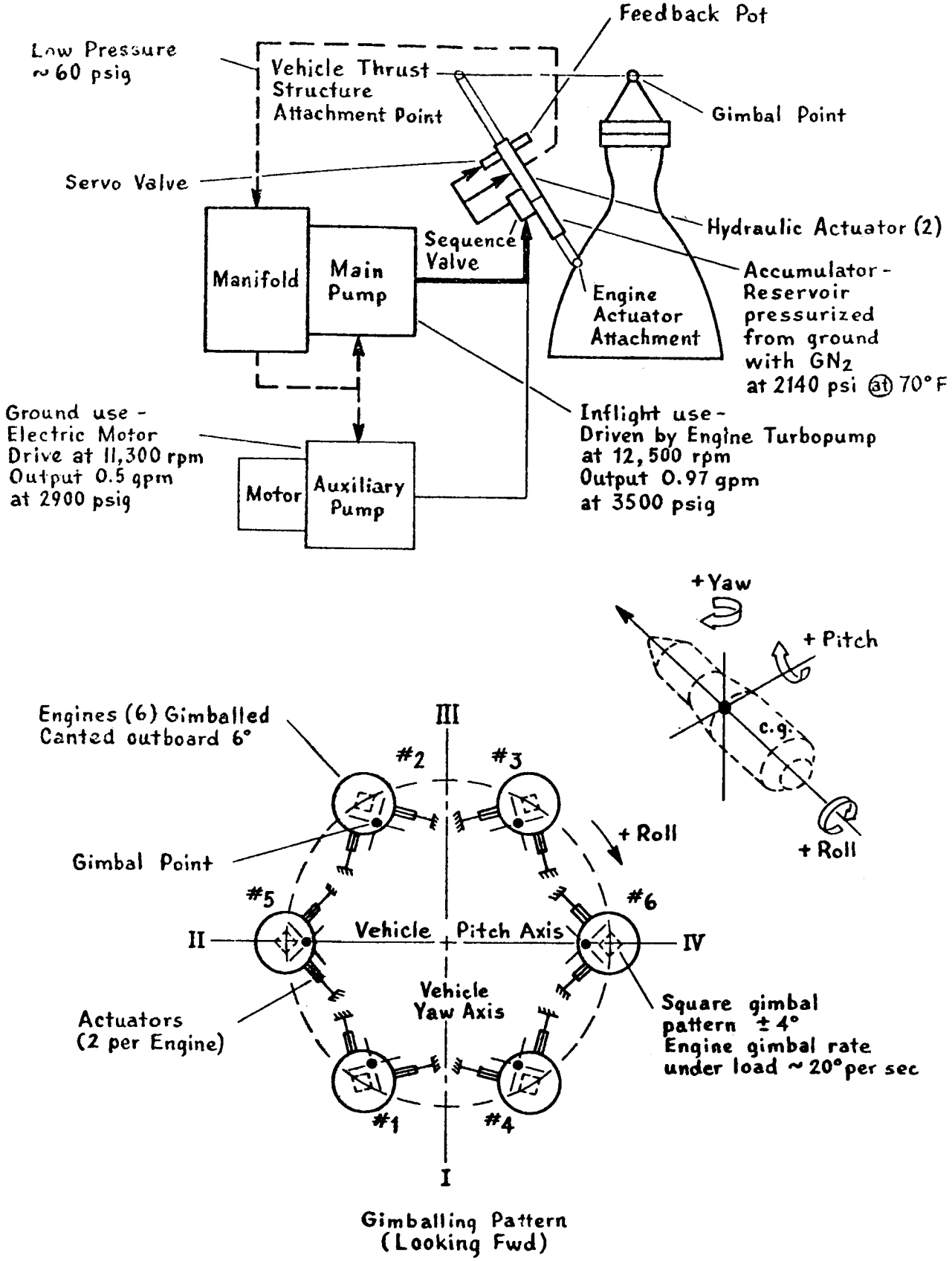

FIGURE 5.1-2. S-IV STAGE THRUST VECTOR CONTROL SYSTEM

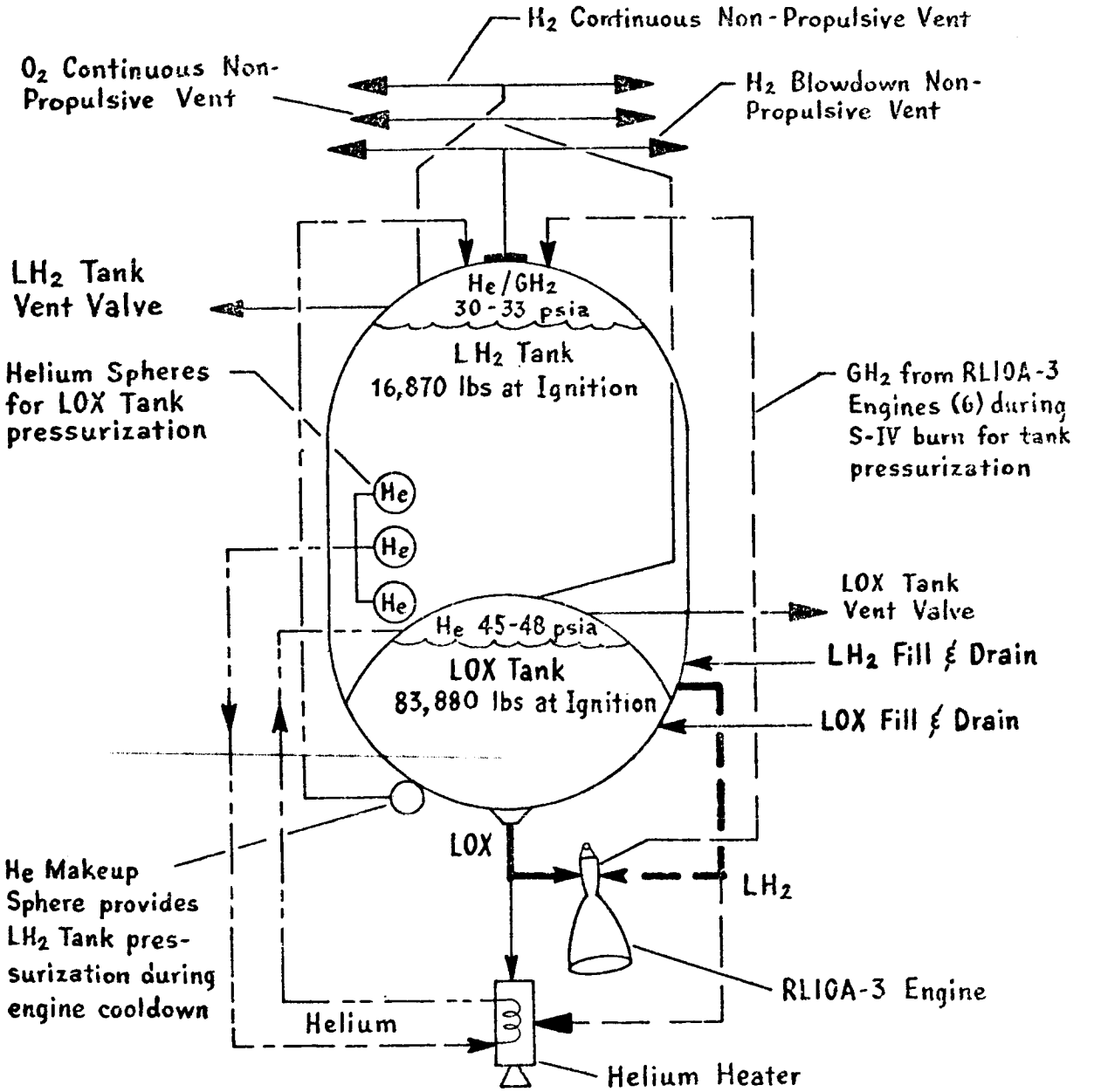

FIGURE 5.1-3. S-IV STAGE HELIUM HEATER

5.2 RL-10 ENGINE CHARACTERISTICS

The S-IV stage utilized six RL-10 engines in a circular arrangement. The engine system is shown in Figure 5.2-1. Each engine develops 15,000 pounds thrust using LOX-H_2 as propellants. The nominal engine operating characteristics are presented in the following table.

RL-10 ENGINE OPERATING CHARACTERISTICS

Chamber Pressure	300 psia
Chamber Temperature	5240°F
Oxidizer Fuel Weight Ratio, O/F	5.0
Nozzle Expansion Ratio	40

The RL-10 engine exit plane conditions and the exhaust plumes have been determined and reported in Reference 5-2. Data from this reference are presented in Figures 5.2-2 through 5.2-9. The nozzle exit plane and exhaust plume flow properties are based on shifting equilibrium during an isentropic expansion. Static pressure, static temperature, molecular weight, and effective specific heat ratio are presented in Table 5.2-1 as a function of Mach number. The equilibrium gas flow properties were used to determine the flow field for the nozzle contour shown in Figure 5.2-2. The distribution of Mach number, static pressure, static temperature, and effective specific heat ratio across the nozzle exit plane are presented in Figures 5.2-3 through 5.2-6, respectively.

Using the exit plane flow properties, a method of characteristics axisymmetric solution of the exhaust plume flow field was obtained. The Mach number distribution for an altitude of 160,000 feet is shown in Figure 5.2-7, and plume boundaries at altitudes between 80,000 and 250,000 feet are shown in Figure 5.2-8. The exhaust plume boundaries based on one-dimensional equilibrium gas flow within the nozzle and perfect gas properties beyond the nozzle exit plane are presented in Figure 5.2-9.

TABLE 5.2-1. RL-10 ENGINE EQUILIBRIUM EXHAUST GAS PROPERTIES

MACH NUMBER	PRESSURE PSIA	TEMPERATURE °R	MOLECULAR WEIGHT LB/LB MOLE	EFFECTIVE SPECIFIC HEAT RATIO, γ^*
0.0	3.00×10^{2}	5240	11.9436	1.1675
0.5	2.59×10^{2}	5139	11.9623	1.1700
1.0	1.70×10^{2}	4847	12.0087	1.1785
1.5	8.85×10^{1}	4392	12.0574	1.1942
2.0	3.89×10^{1}	3829	12.0859	1.2143
2.5	1.57×10^{1}	3247	12.0946	1.2327
3.0	6.24	2713	12.0959	1.2494
3.5	2.53	2254	12.0961	1.2672
4.0	1.07	1874	12.0961	1.2847
4.5	4.86×10^{-1}	1566	12.0961	1.3007
5.0	2.35×10^{-1}	1319	12.0961	1.3143
5.5	1.20×10^{-1}	1122	12.0961	1.3250
6.0	6.50×10^{-2}	963	12.0961	1.3334
6.5	3.69×10^{-2}	835	12.0961	1.3399
7.0	2.17×10^{-2}	730	12.0961	1.3451
7.5	1.33×10^{-2}	643	12.0961	1.3490
8.0	8.36×10^{-3}	570	12.0961	1.3522
8.5	5.40×10^{-3}	509	12.0961	1.3555
9.0	3.57×10^{-3}	456	12.0961	1.3588
9.5	2.41×10^{-3}	411	12.0961	1.3617
10.0	1.67×10^{-3}	373	12.0961	1.3642

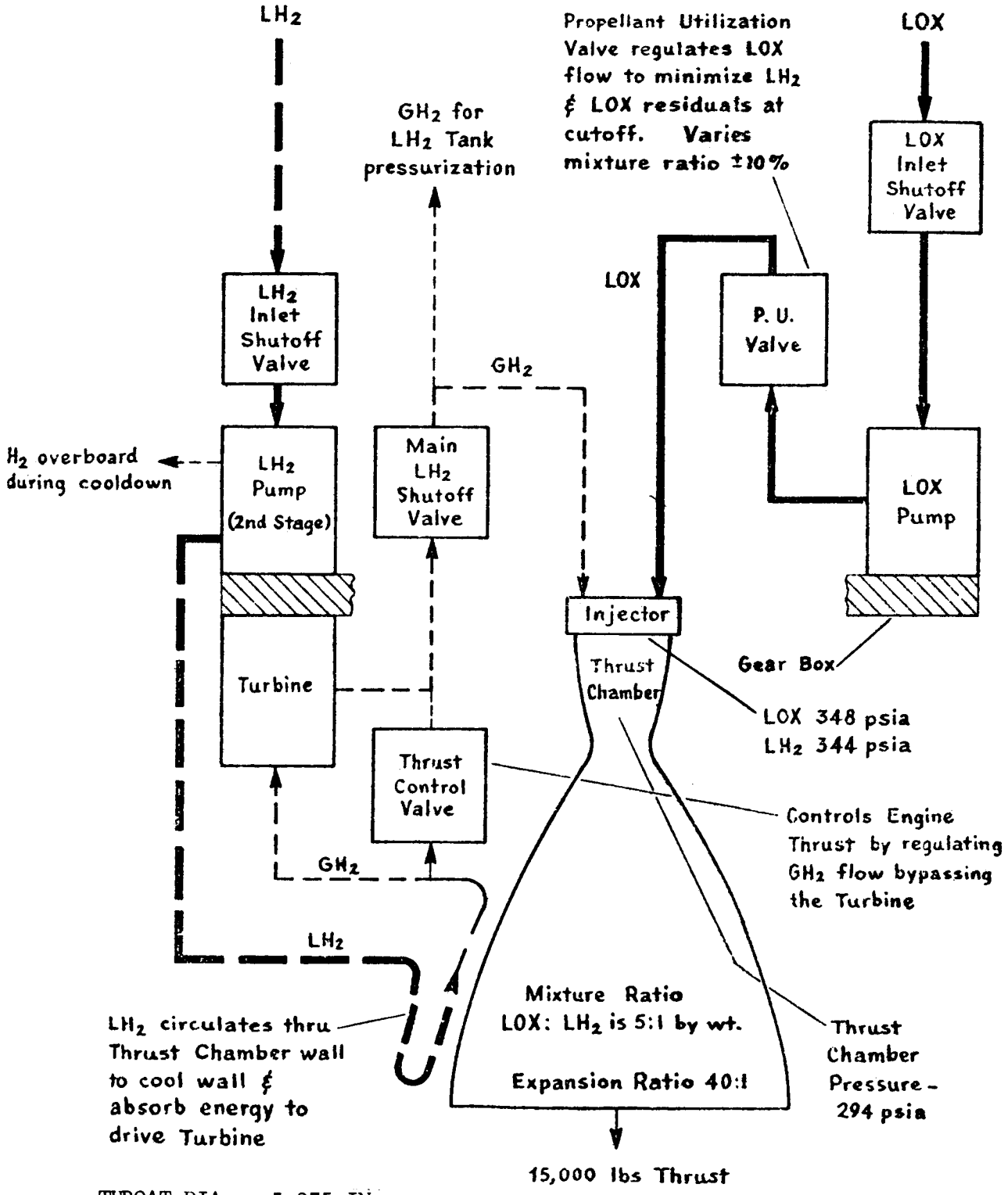

FIGURE 5.2-1. S-IV STAGE RL-10 ENGINE SYSTEM

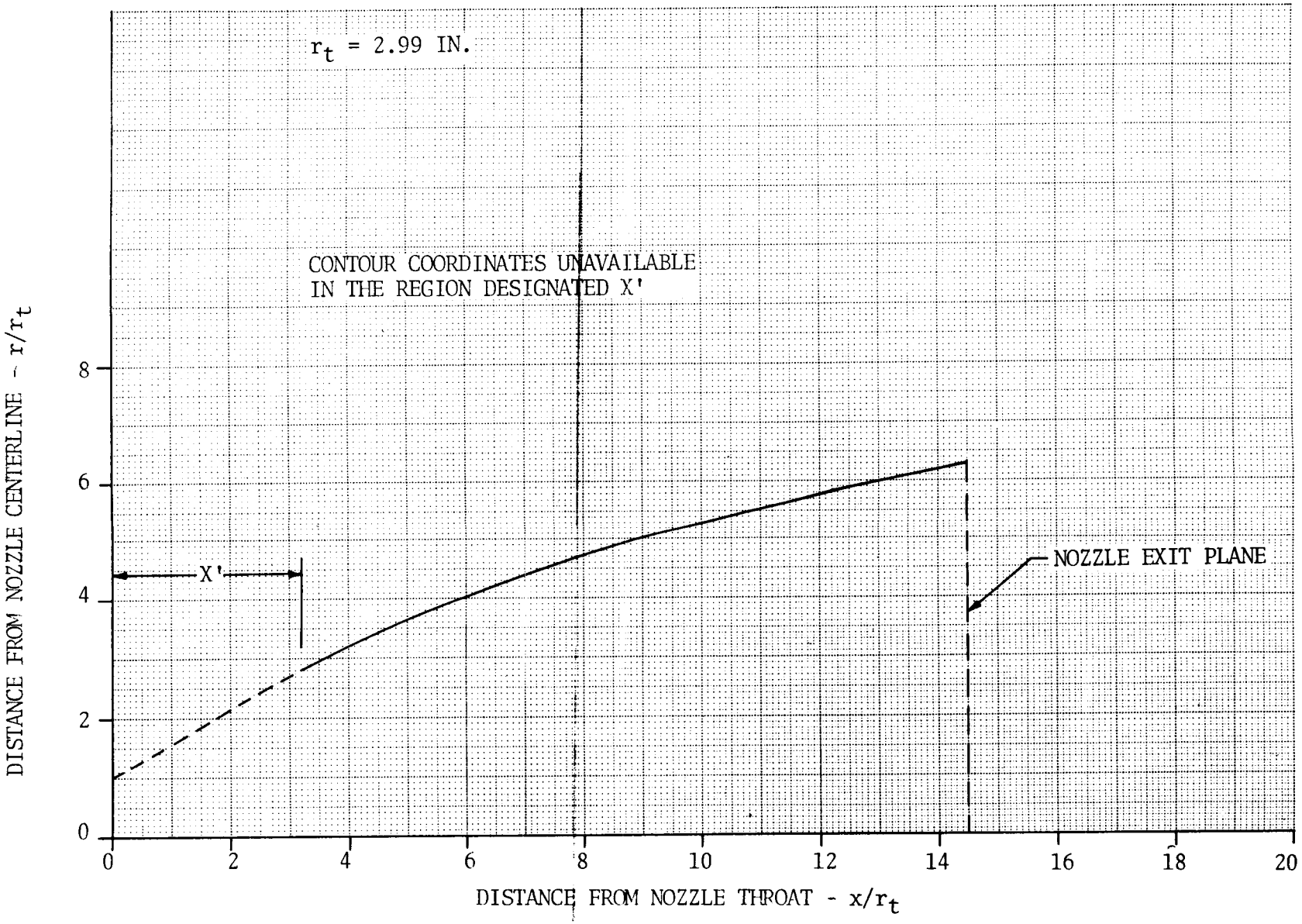

FIGURE 5.2-2. SATURN S-IV RL-10 ENGINE NOZZLE CONTOUR

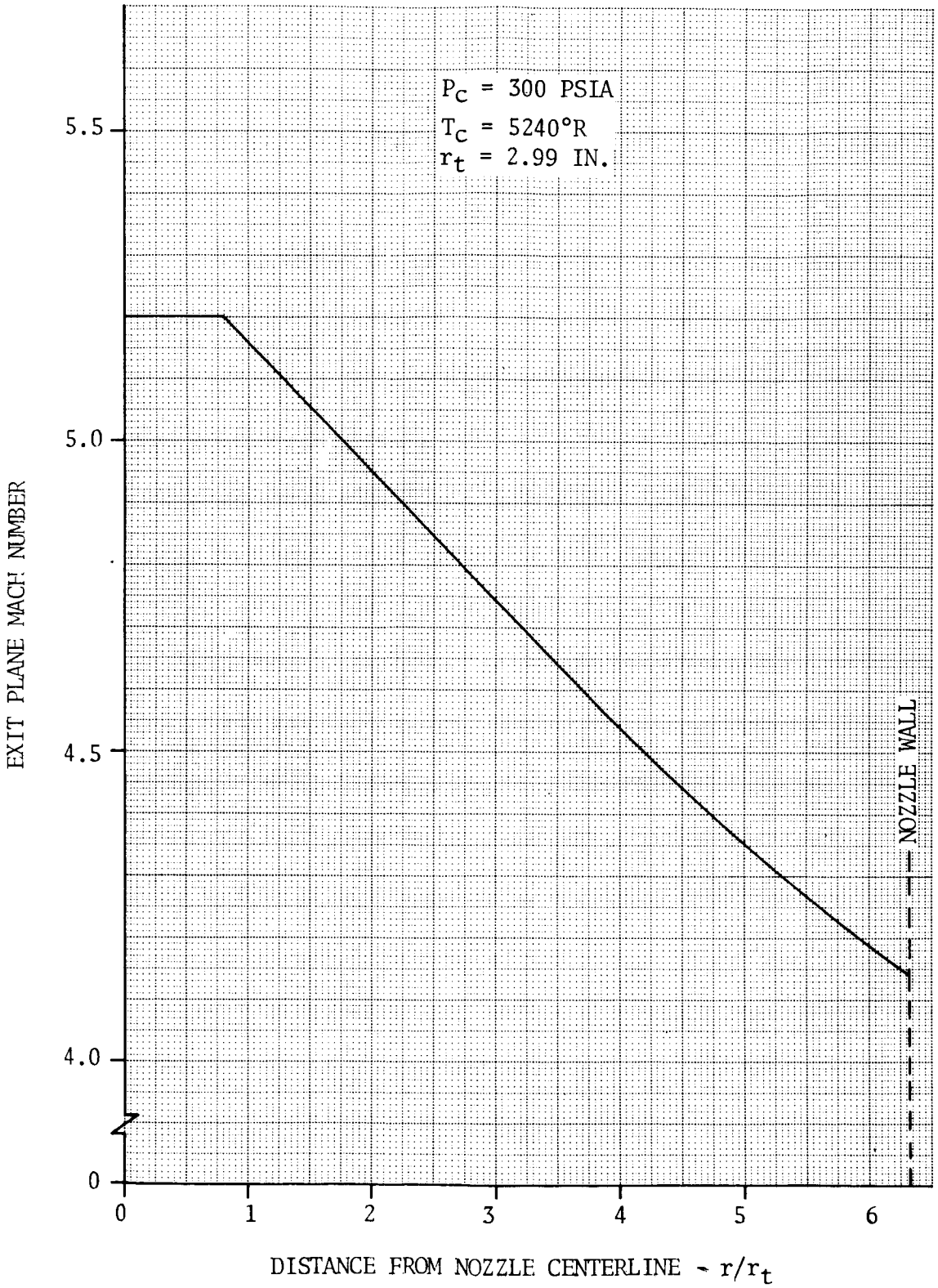

FIGURE 5.2-3. S-IV STAGE RL-10 ENGINE EXIT PLANE MACH NUMBER DISTRIBUTION

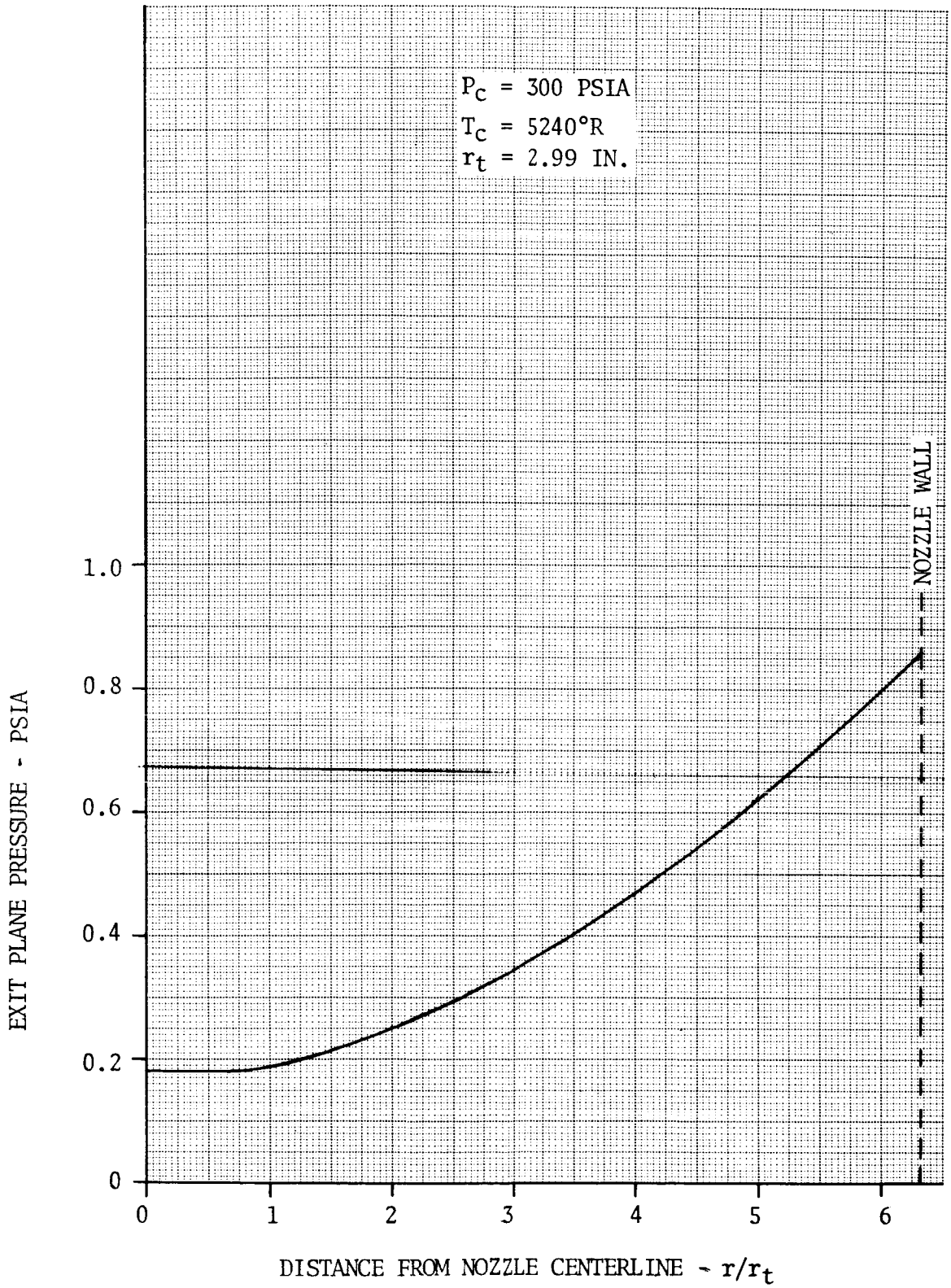

FIGURE 5.2-4. S-IV STAGE RL-10 ENGINE EXIT PLANE PRESSURE DISTRIBUTION

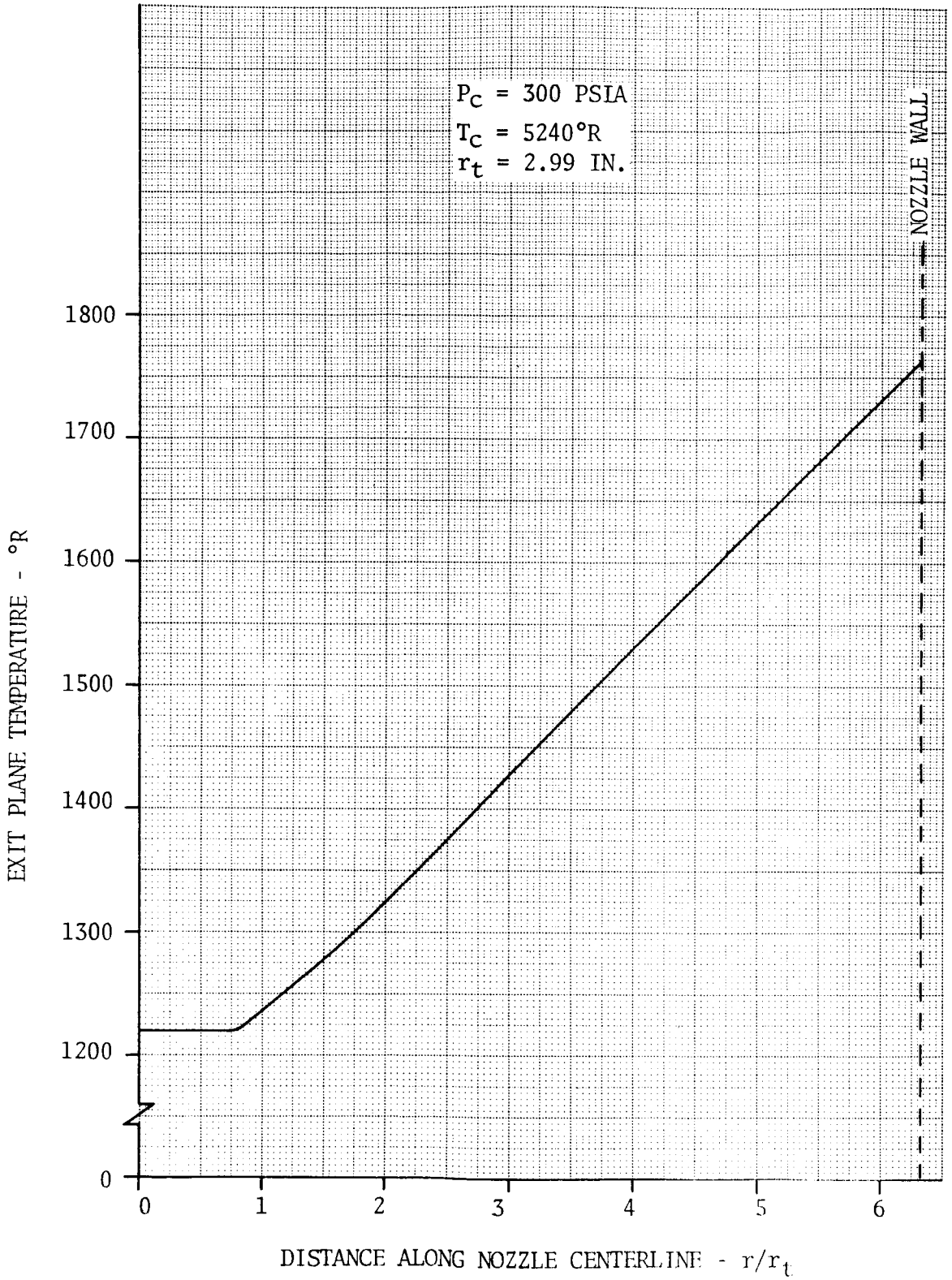

FIGURE 5.2-5. S-IV STAGE RL-10 ENGINE EXIT PLANE TEMPERATURE DISTRIBUTION

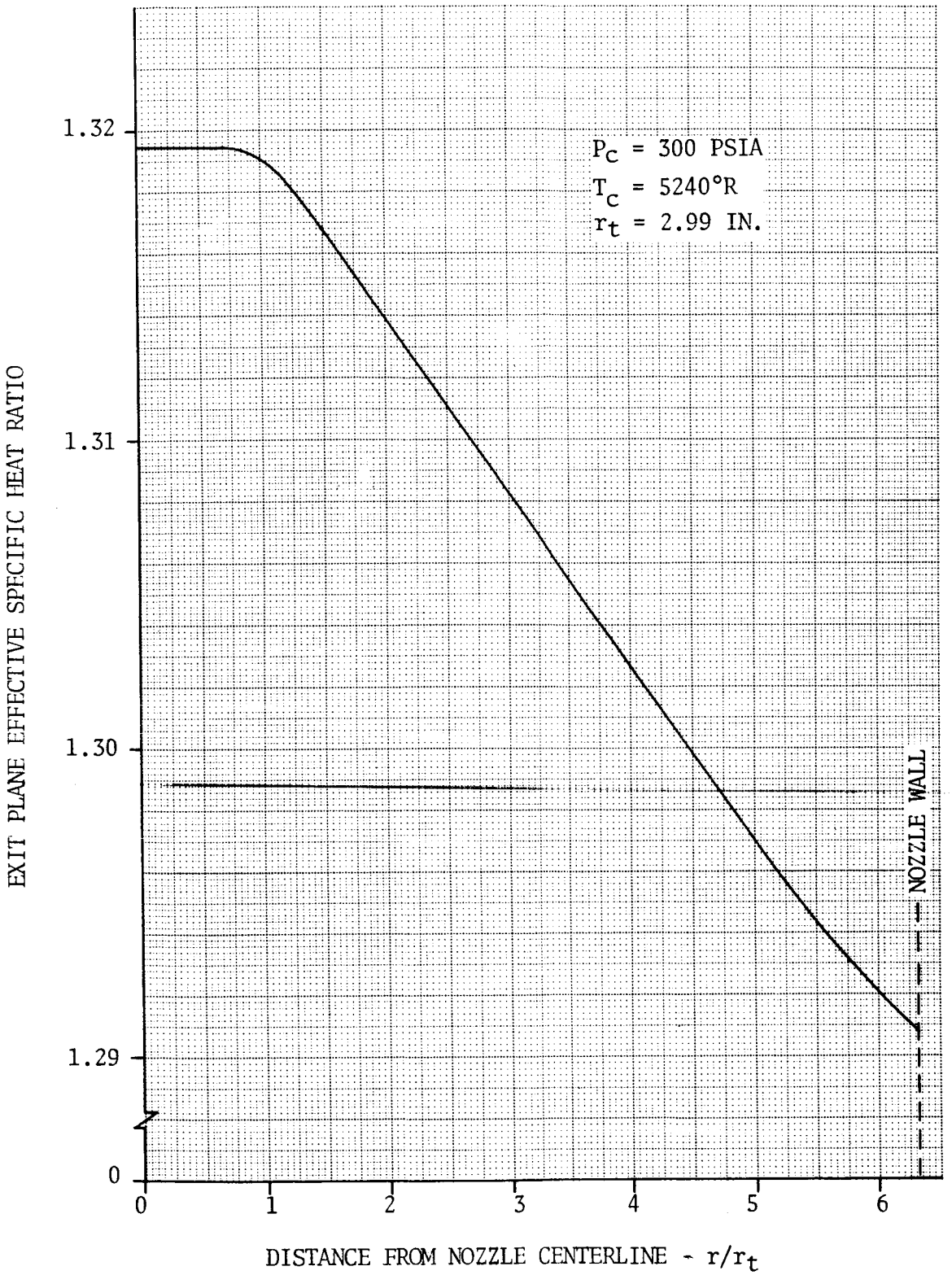

FIGURE 5.2-6. S-IV STAGE RL-10 ENGINE EXIT PLANE EFFECTIVE SPECIFIC HEAT RATIO DISTRIBUTION

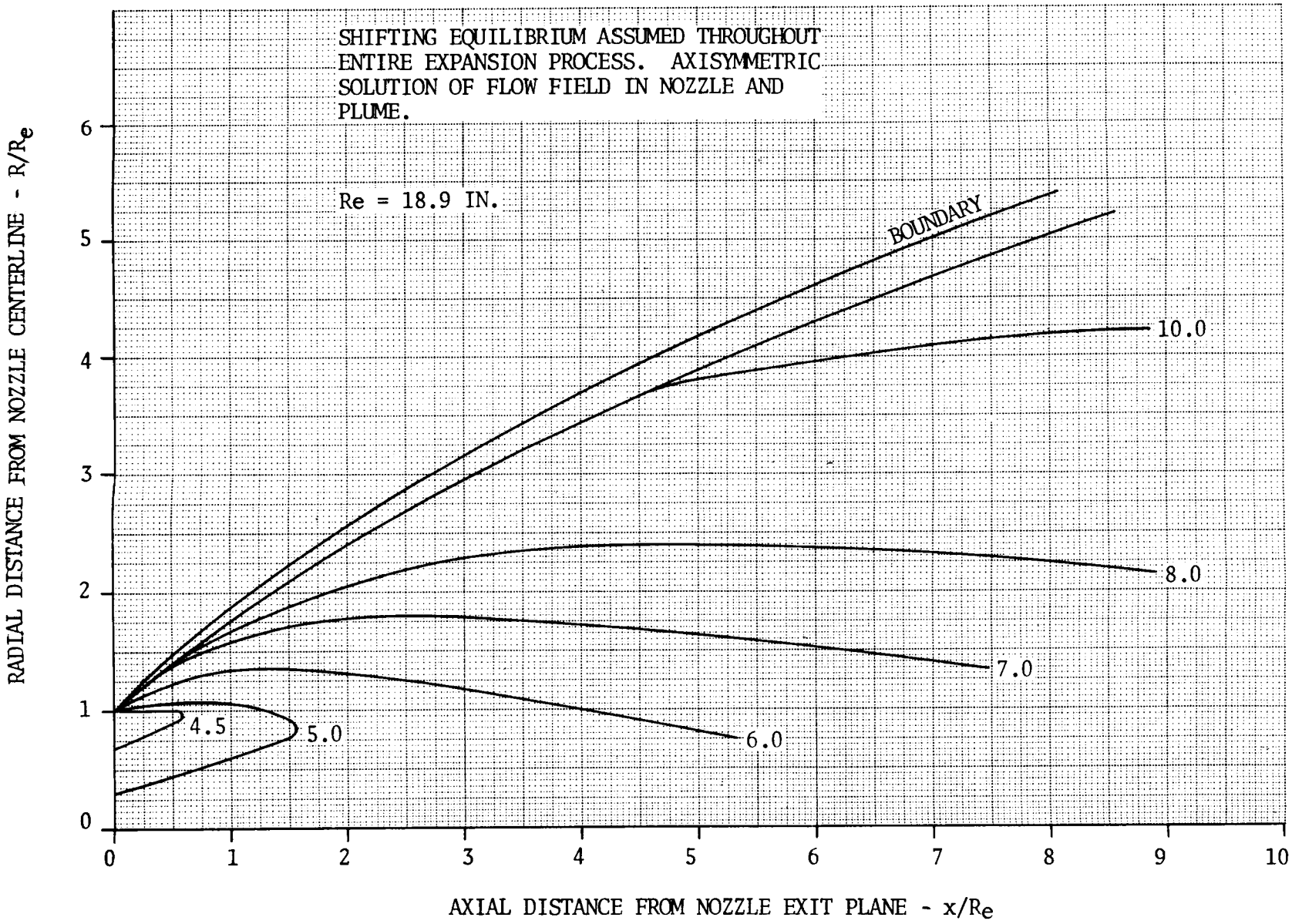

FIGURE 5.2-7. S-IV STAGE RL-10 ENGINE EXHAUST PLUME - 160,000 FEET

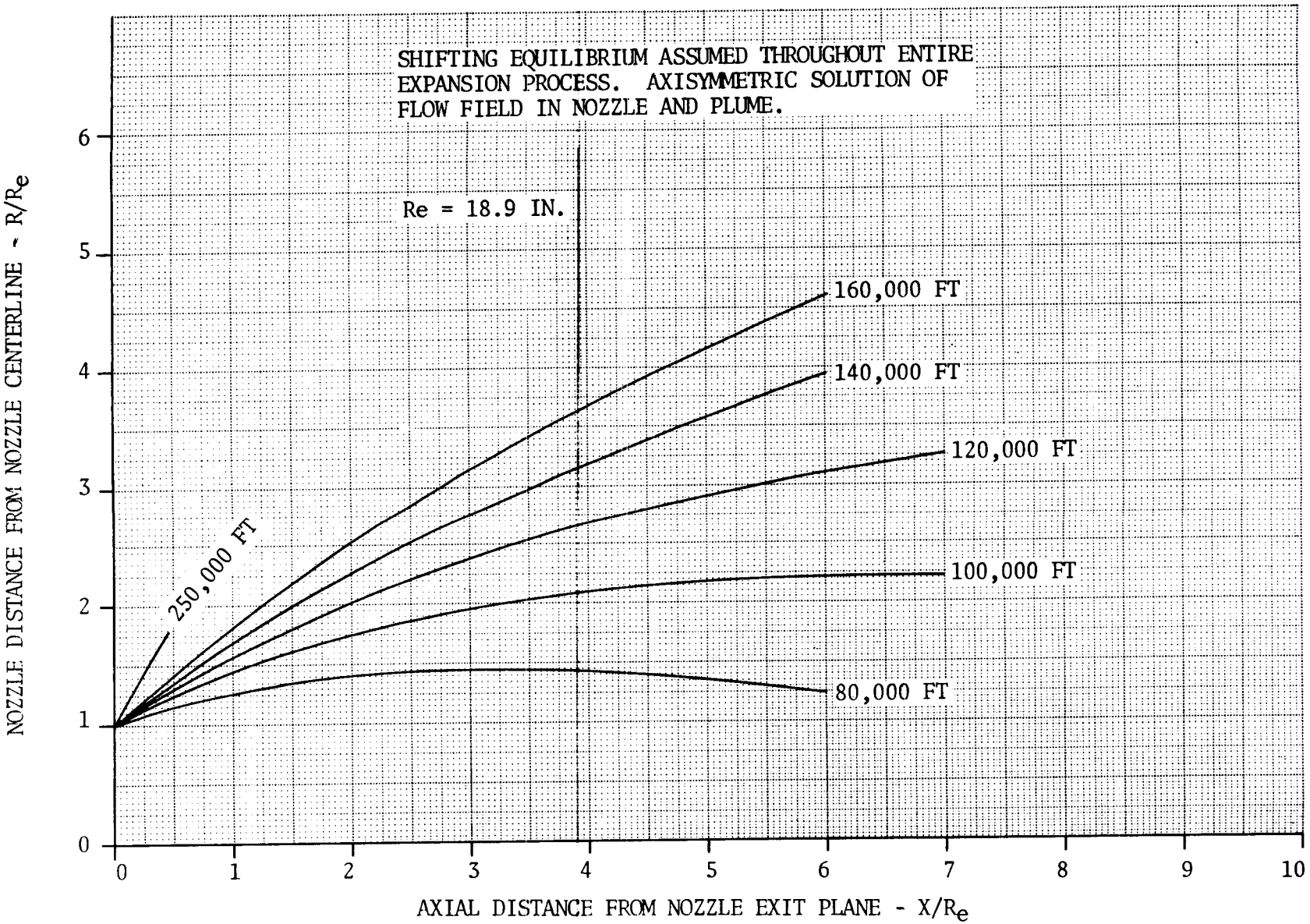

FIGURE 5.2-8. S-IV STAGE RL-10 ENGINE EXHAUST PLUME BOUNDARIES FOR VARIOUS ALTITUDES

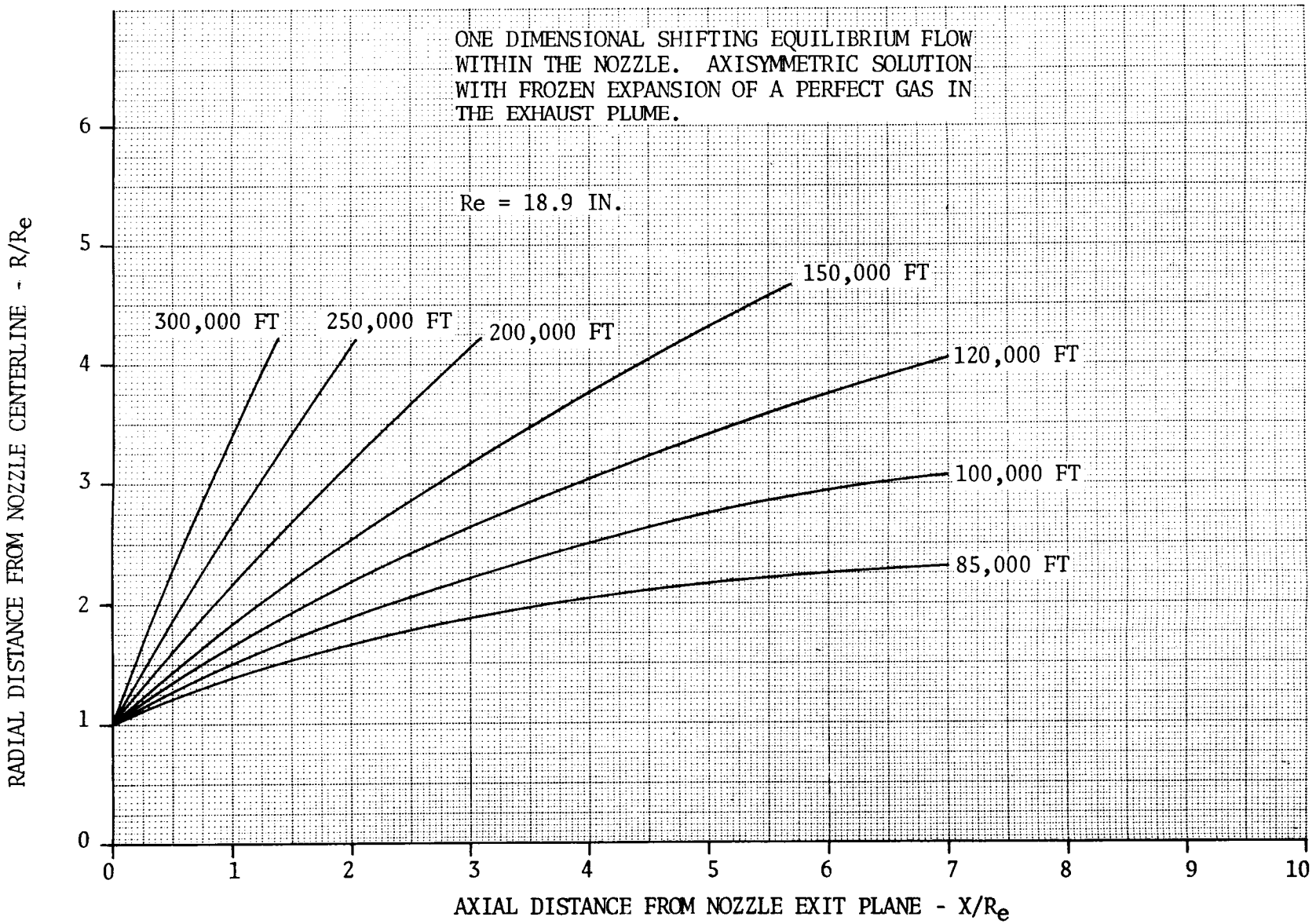

FIGURE 5.2-9. S-IV STAGE RL-10 ENGINE EXHAUST PLUME BOUNDARIES FOR VARIOUS ALTITUDES

5.3 PREDICTION METHODS

The S-IV base region design heating rates were primarily based on model test data. Convection, caused by flow reversal, was shown in early analyses to be the major heat source but analytical techniques were not available to provide a confident solution to the problem. Exhaust gas radiation was not significant because of the highly expanded, low density, non-luminous plumes (which are composed of hydrogen gas and water vapor with a very low emissivity).

Radiation

Although radiation was not a significant design consideration, detailed analytical predictions of the radiation heat flux on the base of the S-IV stage were made and reported in References 5-3 through 5-5. The procedure used in these predictions involved a determination of total incident radiation of various base locations from the RL-10 exhaust plume intersection regions as well as the supersonic core regions. The procedure is described in detail in Reference 5-3 and the results of the analytical prediction are shown in Figure 5.3-1. The bottom curve represents the calculated energy from the intersecting regions only. The center curve and upper curve consider contributions from the intersecting regions and supersonic core assuming beam lengths of $X/D \leq 4$ and $X/D \leq 25$, respectively. The top curve of Figure 5.3-1 was thought to be the realistic heat flux on the S-IV stage base. The design criteria value of 0.5 Btu/ft^2sec was based upon experimental data measured by a radiometer with a 2.5 inch circular field of view normal to the RL-10 exhaust plume and centered approximately 5 inches downstream of the nozzle. Details of these experiments are contained in Reference 5-6.

Convection

Prototype design convective heating was based upon model heating rates determined from 1/10 scale long duration "combustion model" and short duration "shock tube" model tests. The scale models that were tested to establish the design environment are described in Reference 5-7 and discussed in detail in Subsection 5.4. The relationship between model and full scale base thermal environments is discussed in Reference 5-8. It was concluded in this reference that model convective heating rate will be essentially equal to prototype convective heating rate up to a wall tempera ture of about 1000°R if the model is a geometric scale of the prototype and operates with combustion at the same chamber pressure as the prototype.

The heat flux data measured during model testing are "cold wall" values; that is, the calorimeter surface temperatures rise only a few degrees during the short test duration. Heating rates experienced during flight are the result of both the convective inputs (base recirculation) and radiation losses due to radiation from the hot face of the heat shield. The heat shield attains a surface temperature of approximately 1200°F. Also, the first two flights of the S-IV carried a back-up LOX tank pressurization system in the event of helium heater malfunction. Therefore, the heat shield had to be designed to withstand heating rates associated with an inoperable helium heater.

5.3 (Continued)

To avoid undue conservatism, it was necessary to translate the cold wall heat fluxes to equivalent hot wall values. This was accomplished by the following equation:

$$\frac{\dot{q}_{\text{hot wall}}}{\dot{q}_{\text{cold wall}}} = \frac{(T_{\text{gas}} - T_{\text{hot wall}})\ (W\ c_p)_{\text{copper calorimeter}}}{(T_{\text{gas}} - T_{\text{cold wall}})\ (W\ c_p)_{\text{copper calorimeter}}}$$

where: $\dot{q}$ = heating rate, Btu/ft^{2}sec

T_{gas} = 3600°F

$T_{\text{hot wall}}$ = 1500°F at q = 3.0 Btu/ft^{2}sec

$T_{\text{cold wall}}$ = 87°F (measured during tests)

$(W\ c_p)_{\text{copper calorimeter}}$ = Equal values for either test since the same calorimeters were used and the specific heat of copper is essentially constant over the temperature range of 70-1500°F.

This results in a ratio of two-thirds (hot wall heat flux to cold wall heat flux). Applying this to the cold wall heating rate of 3.0 Btu/ft^{2}sec at the center of the heat shield results in an equivalent hot wall value of 2.0 Btu/ft^{2}sec, which, by coincidence, closely equals the cold wall heat flux with helium heater effects. The final design of the heat shield was therefore based on a heat flux of 2.0 Btu/ft^{2}sec which was expected to be somewhat conservative because of the helium heater effects. While there was a reduction in heating rate radially, tests on heat shield materials showed that the final design could not benefit appreciably by this variation.

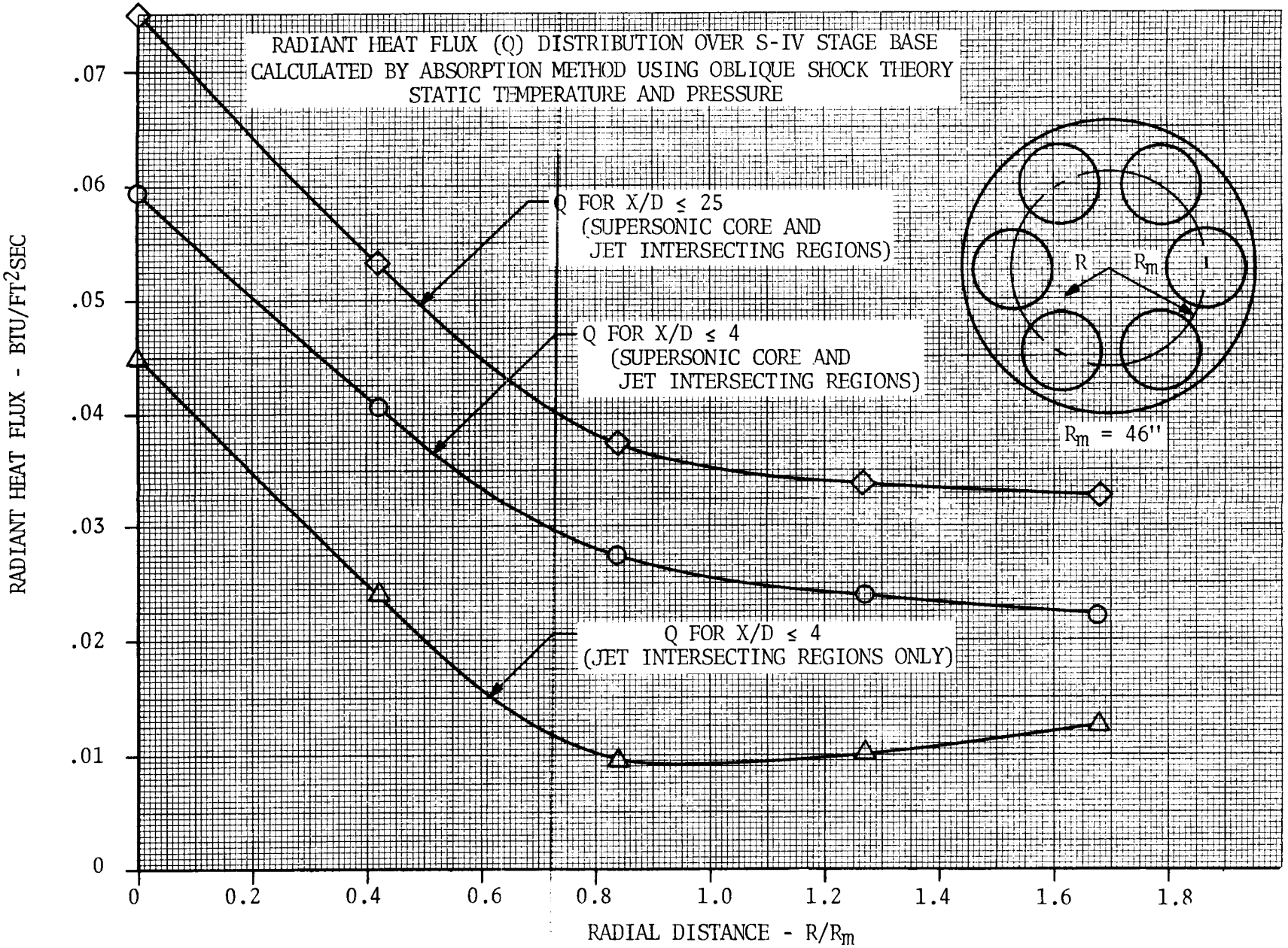

FIGURE 5.3-1. PREDICTED RADIANT HEAT FLUX DISTRIBUTION OVER S-IV STAGE BASE

5.4 MODEL TESTS AND PARAMETRIC DATA

Four major model test programs were conducted on the four- and six-engine configurations. (See Table 5.4-1.) The first two programs used a 1/10 scale four-engine combustion model and a 1/27.5 four-engine cold flow model. These models were tested between February and October 1961 at Arnold Engineering Development Center (AEDC) and FluiDyne Engineering Company (FEC). During this period a 1/10 scale four-engine shock tube model was tested at Cornell Aeronautical Laboratory (CAL). The first series of tests using this model were to verify the short-duration techniques and provide base region heating and pressure data. The second series of testing used the same model with minor modifications to provide data to determine the effects of Reynolds number and temperature on the base heating. After the S-IV base configuration was changed to the six-engine arrangement, a 1/10 scale shock tube model was tested at CAL. The original test program was completed in February 1962 and additional tests were conducted during May and October 1962. These tests provided data to be used in the design of the stage and to verify trends which were indicated by the four-engine model test data. A second series of tests were conducted later (full-scale flight tests had already been made) to provide supplementary pressure data for trajectory and performance analyses. Also, additional information was desired to define the effects of the helium heater exhaust flow on the heat shield heating rates and base flow field characteristics.

5.4.1 1/10 Scale S-IV Four-Engine Combustion Model

The purpose of these tests was to evaluate the reverse flow and heating phenomena in the base region of the original, four-engine, Saturn S-IV stage by measuring pressure and heat flux distribution on a 1/10 scale model with gaseous hydrogen/oxygen rocket engines. The model was tested (1) at approximately 143,000 feet to investigate base pressure and heat flux distribution in the base region, and (2) from 118,500 feet to 152,500 feet to investigate base pressure distribution as a function of altitude. All data have been normalized to a chamber pressure of 350 psia to permit direct comparison between various tests. Data presented in this section are representative data taken from Reference 5-9. These data show general magnitudes, trends and parameter effects. Complete data presentation and detail descriptions are contained in Reference 5-9.

Model Description and Test Conditions

A 1/10 scale model of the original Saturn S-IV stage base region presented in Figure 5.4-1 was used in these tests. This model was tested in the T-3 test cell in the Rocket Test Facility (RTF) at Arnold Engineering Development Center (AEDC) between March and May 1961. The model consisted of four gaseous hydrogen-oxygen rocket engines, a heat shield, secondary exhaust nozzle and secondary exhaust nozzle diverter. The engines were water cooled and operated at a nominal chamber pressure of 350 psia with an oxidizer-to-fuel weight ratio of 5.0. The engines had the same nozzle area ratio as the prototype. Each engine was canted 4 degrees outboard at the zero gimbal position and could be shifted ±5.66 degrees in the pitch and yaw directions to simulate maximum gimbaling. A small supersonic nozzle was positioned in the center of the heat shield to simulate the prototype helium heater nozzle.

5.4.1 (Continued)

A 90-degree cone acting as a flow diverter could be attached to the helium heater nozzle to divert the flow outward parallel to the heat shield surface. The nozzle and diverter configuration is presented in Figure 5.4-2.

The heat shield was instrumented with 20 pressure transducers, a traversing pressure probe and 22 calorimeters as shown in Figure 5.4-3. The calorimeters were of the transient (slug) type and were insulated from the surrounding heat shield structure by 0.031-inch air gaps and later by Min-k. Eleven (11) of the calorimeters had gold faces and the other half were painted black to determine the radiative and convective heat fluxes. Detailed descriptions of these instruments are contained in Reference 5-9. The amount of radiant heat flux was to have been determined by the differences between the heat fluxes indicated by the high absorptivity calorimeters which measured total heat flux and the low absorptivity gold plated calorimeters which measured primarily convective heat flux. The test results indicated that these differences were very small and sometimes negative. The quality of the reflectivity of the gold calorimeters was initially poor and deteriorated during the tests.

Model Test Parametric Data

The purpose of these tests was to evaluate the reverse flow and heating phenomena in the base region. The objectives for this evaluation were to determine the effects of secondary exhaust, engine gimbaling, and altitude.

Secondary Exhaust

The distributions of steady-state heat flux in the base region with and without secondary exhaust and secondary exhaust with diverter are shown in Figure 5.4-4. All heat flux values are hot-wall heat fluxes, and average values are given. The attempt to show a unique difference between the results obtained with the two methods of insulation (Min-K and air gap) was inconclusive. The distribution of base static pressure with and without secondary exhaust and secondary exhaust with diverter is presented in Figure 5.4-5.

Gimbaling

The engines could be shifted ±5.66 degrees in the pitch and yaw directions to simulate maximum gimbaling as shown in Figure 5.4-6. Heat flux and static pressure as a function of radial position are presented in Figure 5.4-7 through Figure 5.4-10 for the various gimbal conditions. All gimbaling runs were performed with secondary exhaust without diverters.

Altitude

The effect of altitude (120,000 to 150,000 feet) on the radial distribution of base pressures is shown in Figure 5.4-11.

5.4.2 1/27.75 Scale S-IV Four-Engine Cold Flow Model

The basic objective of these tests was to define the flow field in the base region of the original, four-engine, Saturn S-IV stage by determining static and total pressure distributions. Data presented in this section are representative data taken from References 5-9 through 5-11, and show general mangitudes and parameter effects. Complete data presentation and data descriptions are contained in the references.

Model Description and Test Conditions

FluiDyne Engineering Corporation designed and fabricated a 1/27.75 S-IV four-engine scale model. This model was tested at the Medicine Lake Laboratory of the FluiDyne Engineering Corporation (FEC) and at the Rocket Test Facility (RTF) at Arnold Engineering Development Center (AEDC) between February and October 1961. The model consisted of four conical nozzles, a chamber, a heat shield, and a secondary exhaust nozzle and diverter. A schematic of the model base is presented in Figure 5.4-12. The nozzles were designed to operate on 2000°R air at 87 psia with an expansion ratio of 10.4. At AEDC the maximum air supply temperature was 1000°R. This temperature required a supply pressure of 84 psia and a nozzle expansion ratio of 9.7; therefore, the simulation was not exact. The same was also true for simulating with unheated air which also required a nozzle expansion ratio of 9.7. Nozzle data for the cold flow model test are presented in the following table.

COLD FLOW NOZZLE DATA

Expansion Ratio	10.4
Exit Diameter	1.440"
Throat Diameter	0.445"
Exit Mach Number	3.97
Working Gas	Air
Nozzle Length (exit to effective gimbal point)	2.516"
Quantity	4
Geometry	Conical
Cone Wall Thickness	0.06"
Divergence Half Angle	11.7°

A removable nozzle in the center of the heat shield was used to simulate the helium heater exhaust by injecting ambient air into the base. A small flow diverter could be soldered to the heat shield above the helium heater nozzle to divert the secondary exhaust out along the heat shield. The helium heater exhaust nozzle and the diverter are presented in Figure 5.4-13.

5.4.2 (Continued)

The instrumentation on the heat shield consisted of six flush mounted static and four total pressure taps (1/16 inch aft of surface) positioned as shown in Figure 5.4-14. A static pressure tap located in the center of the heat shield was interchangeable with either a convergent-divergent nozzle or a total pressure tube. Five separate total pressure tubes could replace the helium heater nozzle with the location of the ends of the tubes at distances of 0, 0.295, 0.590, 0.885, and 1.380 inches aft of the heat shield surface. A total pressure rake was mounted between two nozzles with the tubes located in the vent area as shown in Figure 5.4-15. The helium heater nozzle was also used to measure the pressure at the center of the heat shield.

Model Test Parametric Data

These tests were conducted to determine the effects of the recirculation of exhaust gases into the base region. Objectives of the tests were to determine the altitude above which the base pressure remains constant (critical altitude), effects of heat shield locations, gimbaling, lip configuration, one engine not operative, secondary exhaust, chamber pressure, and chamber temperature.

The repeatability of the data is good as shown in Figure 5.4-16.

Critical Altitude

Early theory and experiments predicted that the base pressure would become constant after a critical altitude was reached. Base pressure data verify that the base pressure becomes independent of increasing altitude, but only after a triple reversal of the base pressure has occurred as seen in Figure 5.4-17.

Heat Shield Location

The purpose of varying the heat shield location was to alter the vent area ratio, A_C/A_L - the ratio of the nozzle exit plane reverse flow area to the lateral vent area. The heat shield pressure distribution for the ratio of A_C/A_L varying from 0.7 to 1.3 at an altitude of 150,000 feet is presented in Figure 5.4-18. At this altitude where the flow is not choked, the pressure distribution is not appreciably affected by A_C/A_L over the range tested. It is seen that the center base pressure increases as the lateral area is decreased.

Gimbaling

With four different mounting plates the engines could be gimbaled into any of the gimbal positions shown in Figure 5.4-19. Normally, the engines were canted four degrees radially from the model centerline. The pressure distributions due to gimbaling are compared to that of the gimbal null position (4° radial cant with model centerline) in Figures 5.4-20 through 5.4-24. The pressure distribution along a diameter perpendicular to the

gimbal direction is not altered significantly as shown in Figure 5.4-20. The pressure distribution parallel to the gimbal direction shifts the distribution in the direction of the gimbal as shown in Figure 5.4-21. Along a diameter not perpendicular or parallel to the gimbal direction, the same effect is noticed considering the parallel and normal components of the gimbal. (See Figures 5.4-22 and 5.4-23.) The effect of roll on the pressure distribution is presented in Figure 5.4-24.

Heat Shield Lip Configuration

The lip configuration of the heat shield could be modified with three different lips. (See Reference 5-11.) The lip configuration and the data from this configuration are presented in Figure 5.4-25. These data indicated that the lip configuration had no effect on the base pressure distribution; therefore, the other two lip configurations were not tested.

Secondary Exhaust

The effects of the helium heater exhaust simulation is presented in Figure 5.4-26. A flow diverter was placed over the helium heater exhaust nozzle to determine its effect on the base pressure. These data are also presented in Figure 5.4-26.

One Engine Inoperative

For the condition of one engine inoperative the reverse flow flows out around the inoperative engine, relieving the base pressure. As a result, the base pressure is very close to ambient as shown in Figure 5.4-27.

Chamber Temperature

The center base pressures for two altitude traverses, one with a chamber temperature of 1000°R and the other at ambient temperature, are compared in Figure 5.4-28. The chamber temperature effect on the heat shield pressure distribution at an altitude of 150,000 feet is presented in Figures 5.4-29 and 5.4-30. The chamber temperature traverse at 150,000 feet presented in Figure 5.4-31 indicates the effect on the pressures in the vent area above the heat shield. Rake pressures at an altitude traverse for two chamber temperatures are presented in Figure 5.4-32. Since the local flow directions are not parallel to the rake total pressure tubes, the indicated rake pressure may differ from the true total pressure.

Chamber Pressure

The possibility of simulating altitude by increasing the chamber pressure instead of decreasing the ambient pressure was investigated. A chamber pressure traverse for P_{CELL}/P_{CH} simulating altitudes above the critical altitude is presented in Figure 5.4-33. This simulation of altitude may be good below the critical altitude as well as above it as seen in Figure 5.4-34. Points A, B and C are defined in Figure 5.4-17.

5.4.3 1/10 Scale Four-Engine Hot-Flow Model - Short Duration

A four-engine 1/10 scale shock tube model was tested at Cornell Aeronautical Laboratory (CAL) during 1961. These tests were to verify the short duration techniques and provide base region pressure and heating data. Later a modified model was tested to determine the effects of Reynolds number and temperature on base heating. Data presented in this section are representative data taken from References 5-12 through 5-15. These data show general magnitudes, trends and parameter effects. Complete data presentation and detail descriptions are contained in the references.

Model Description and Test Conditions

The short-duration rocket combustion model employed in these tests was a 1/10 scale version of the S-IV four-engine stage. The model consisted of a combustion chamber, heat shield, four engine nozzles and a secondary exhaust nozzle. The first series of tests used a constant volume combustor and a constant pressure combustor was used in the second series. Descriptions of these combustors are contained in References 5-14 and 5-15, respectively. The model base configuration is shown in Figure 5.4-35. The engine nozzles were scaled versions of the Pratt and Whitney RL-10A-3 uprated rocket engines and were canted outboard 4 degrees. The helium heater exhaust nozzle was set in the center of the heat shield. A diverter was used on some tests to divert the secondary exhaust flow outward parallel to the heat shield. The secondary exhaust nozzle and diverter are shown in Figure 5.4-36. Cold hydrogen was used to simulate the hydrogen-rich combustion products of the prototype heater exhaust. The model engine and exhaust parameters are presented in the following table.

MODEL ENGINE AND EXHAUST PARAMETERS

Model Engine	
Chamber Pressure	350 psia
Chamber Temperature	5260°R
O/F Ratio	5.0
γ	1.28
M_{ex}	4.30
P_{ex}	0.637 psia
Gas Composition	62.5% H_2O_2 37.5% H_2
Helium Heater	
Chamber Pressure	15 psia
Chamber Temperature	530°R
Exhaust Composition	100% H_2
Exit Area	0.229 in^2

The instrumentation for the first series of tests consisted of pressure transducers and heat transfer gages as shown in Figure 5.4-37. Pressure and heat transfer probes were also used to survey the exit conditions of the nozzles. For the second series of tests the heat shield was instrumented for pressure, temperature and heat transfer as shown in Figure 5.4-38. A single pressure transducer was installed in the heat shield on the model centerline for a cross check on the extensive pressure data obtained in the first series of tests. Eleven (11) chromel-alumel thermocouples were imbedded in the heat shield to measure the local heat shield temperature. Heat transfer rates were determined by a technique that relies on sensing the transient surface temperature of the model heat shield. The sensing element is a thin film platinum strip fused on a flat pyrex substrate. The film temperature is equal to the instantaneous surface temperature. The output of the heat transfer gage is fed through an analog network which converts the signal from one representing temperature to one directly proportional to the instantaneous heat transfer rate.

Model Test Parametric Data (First Series)

Data were obtained to determine the variation of base pressure and heat transfer with altitude and the effect of base plate height, secondary exhaust flow with and without diverter, and combustor pressure. A constant volume combustor was used in these tests as described in Reference 5-14.

Variation with Altitude and Radial Distance

Test data were taken with the base plate at two axial locations. The standard base plate height (2.26 inches from nozzle exit) is shown in Figure 5.4-35. The second base plate position was 3.12 inches from the nozzle exit.

The standard configuration was run at an altitude of 200,000 feet several times. The base pressure and heat transfer distribution from these repeat runs are shown in Figure 5.4-39 and provide an indication of the repeatability of data.

The base pressure distributions across the base are shown for the two base plate configurations in Figures 5.4-40 and 5.4-41. Heat transfer data taken from the altitude series are presented in Figure 5.4-42 and 5.4-43 and indicate the same trends with altitude as the pressure data.

Effect of Base Plate Height

The effects of base plate height (2.26 and 3.12 inches from nozzle exit) on base pressure and heat transfer are shown in Figures 5.4-44 and 5.4-45, respectively. The actual difference in height was small and a large influence would not be expected. These two sets of data were taken at slightly different rocket chamber conditions which tend to obscure any comparison. By plotting the ratio base static pressure/chamber pressure, the effect of these differences should be minimized.

5.4.3 (Continued)

Effect of Secondary Exhaust

To simulate the secondary exhaust, room temperature hydrogen was injected into the center of the base. Two cases were investigated, 1) hydrogen was injected directly into the base region, and 2) a flow diverter was used to turn the flow parallel to the base plate. The secondary exhaust effects (with and without diverter) on the base pressure and heat transfer distribution are presented in Figures 5.4-46 and 5.4-47, respectively.

Effect of Variable Chamber Pressure

A range of combustor pressures ranging from 1/3 to 5 times the nominal design were tested. The effect of varying chamber pressure on the local base pressure is shown in Figures 5.4-48 and 5.4-49 for both the case of a constant ratio of ambient static to chamber pressure and for a constant ambient static pressure, respectively. In both cases, there are large differences in base static pressure/chamber pressure ratio with the highest chamber pressure showing the lowest value. This shows a very significant chamber pressure or Reynolds number effect since the base pressure has been non-dimensionalized by dividing through by the chamber pressure.

The effect of chamber pressure on base heat transfer measurements are presented in Figures 5.4-50 through 5.4-52. The effect for the case of a constant ratio of ambient static to chamber pressure and for a constant ambient pressure are presented in Figure 5.4-50 and 5.4-51, respectively. Heat transfer data at the constant ratio of ambient to chamber pressure is replotted in Figure 5.4-52 as a function of chamber pressure. The heat transfer data have been correlated with the local base pressure and are presented in Figure 5.4-53. These data fall on a straight line with a slope of 0.96.

Model Test Parametric Data (Second Series)

Data were obtained from the second series of tests using the constant pressure combustor as described in Reference 5-15. These data indicate the effects of chamber pressure and temperature; and the base recovery temperature based on model test data was determined.

Recovery Temperature

The technique employed to determine the recovery temperature consisted of simultaneously heating the heat shield and gages to consecutively higher temperatures and recording the corresponding heat transfer rates. Plots of heat transfer versus gage temperature were then made with the purpose of extrapolating the data to zero heat transfer rate and recording the intersecting point on the abscissa of gage temperature as the indicated recovery temperature. It was not possible to maintain the heat shield and gage temperatures exactly equal except at room temperature; therefore, the gages were in most cases only nominally equal in temperature to the heat shield. Typical data obtained by this technique are shown in Figure 5.4-54, additional data are contained in Reference 5-15.

5.4.3 (Continued)

Effect of Chamber Pressure

The base heat shield heat transfer rates are presented as a function of the combustion chamber pressure at various values of r/r_o in Figure 5.4-55. These heat transfer rates are also presented in Figure 5.4-56 as a function of the local heat shield pressure. The effect of chamber pressure on the recovery temperature for various ratios of r/r_o is presented in Figure 5.4-57. The slope of the curves give the variation of recovery temperature with chamber pressure at each gage location. The actual values of recovery temperatures expressed as a percentage of the combustion chamber temperature are shown in Figure 5.4-58 as a function of combustion chamber pressure. These data were obtained at a constant ratio of chamber pressure to ambient pressure (P_c/P_∞) of $106x10^3$ (which corresponds to P_c = 350 psia at 200,000 feet). This ratio represents conditions normally referred to as a "choked base flow" for this model configuration.

Limited data were also obtained as a ratio of chamber pressure to ambient pressure of $11.3x10^3$ (which corresponds to P_c = 350 psia at 140,000 feet) at chamber pressures of 85, 200, 350, 525 and 700 psia and at several wall temperatures. Only the variation in recovery temperature with chamber pressure can be implied from these data and not actual values of recovery temperature. The upper graph of Figure 5.4-59 shows the variation in heat transfer rate with chamber pressure for several gage locations (or various ratios of r/r_o), at a fixed heat shield temperature of 530°R and $P_c/P_\infty = 11.3x10^3$. The recovery temperature as a function of chamber pressure for various ratios of r/r_o is also shown in the bottom graph of Figure 5.4-59. Data were obtained which show the effects of chamber pressure on the choking pressure ratio. While the data are limited, it appears that a trend toward increasing choking pressure ratio accompanies increases in chamber pressure. A plot of choking pressure ratio as a function of chamber pressure is shown in Figure 5.4-60.

Effect of Nozzle Wall Temperature

The effect of the initial nozzle wall temperature on base heat transfer rates and recovery temperatures were investigated. The heat shield and gage temperatures were maintained at ambient temperatures while the nozzle was heated to temperatures of 1460°R. The variation in heat transfer rate with nozzle wall temperature for heat transfer gages located at various radii from the center of the heat shield is presented in Figure 5.4-61.

A significant increase in heat transfer rate is observed as the nozzle wall temperature increases. These data obtained for the minimum (540°R) and maximum (1460°R) wall temperatures are presented in Figure 5.4-62 as a function of r/r_o. A uniform increase in heat transfer rate of approximately 40 percent is indicated across the heat shield for these conditions.

5.4.4 1/10 Scale Six-Engine Hot-Flow Model - Short Duration

Two series of tests were conducted using a 1/10 scale model of the Saturn S-IV six-engine configuration at the Cornell Aeronautical Laboratory. The first series of tests were completed in February 1962 and additional tests were conducted during May and October 1962. The second series were conducted later (full-scale flight tests had already been made) to provide supplementary pressure data for trajectory and performance analyses. Data presented in this section are representative data taken from References 5-16 and 5-17. These data show general magnitudes, trends, and parameter effects. Complete data presentation and detail descriptions are contained in the references.

Model Description and Test Conditions

The first series of tests utilized a 1/10 scale Saturn S-IV six-engine model configuration. The model consisted of six nozzles ($A/A^* = 39.87$) and an instrumented base plate which was shock mounted from the plenum chamber. The six-engine model used a constant pressure combustor. The hydrogen and oxygen gases are stored under pressure in separate tubes. A mylar diaphragm is mechanically ruptured, allowing the gases to mix and then be ignited prior to discharging through the nozzles. In the nominal position, the nozzles were canted radially outboard at an angle of 6 degrees. The model configuration (from the heat shield aft) used for the first series of tests is shown in Figure 5.4-63. This model was tested at the Cornell Aeronautical Laboratory for an altitude range of 120,000 to 220,000 feet, which was achieved by duplicating the ambient pressure. The second series of tests utilized a hexagonal shaped heat shield rather than the round heat shield used in the first series of tests as shown in Figure 5.4-64. The model engine parameters are presented in the following table.

MODEL ENGINE PARAMETERS

Propellants	Gaseous hydrogen/gaseous oxygen
PMR	5.5:1
P_c	300 psia
T_c	5600°R
γ	1.15
A/A^*	39.87
M_{ex}	4.17
P_{ex}	0.63 psia
T_{ex}	2240°R
Exhaust Composition	70% H_2O, 30% H_2

For helium heater exhaust simulation, a small section in the center of the base heat shield was replaced by a nozzle. This nozzle was fitted with a removable flow-diverter attachment, which diverted the flow outboard parallel to the heat shield. A schematic of the secondary flow arrangement is shown in Figure 5.4-65. A preheated hydrogen-nitrogen mixture was used to simulate the prototype helium heater exhaust flow.

5.4.4 (Continued)

The base of the model, which is located in the plane of the heat shield, was instrumented with heat transfer and pressure instrumentation as shown in Figure 5.4-66 for the first series of tests. Extensive pressure instrumentation was employed on the heat shield during the second series of tests. Twelve pressure transducers were located on radii between and in line with the model engines. Two redundant pressure tap locations were provided to check the base flow symmetry and to provide backup measurements for certain of the transducers. Two types of heat shield pressure probes were fabricated: 1) total pressure probe rakes of varying angle of attack, and 2) vertical (normal to the heat shield) pressure probes of varying heights (5/8", 1" and 1 3/4"). Six heat transfer gages measured the convective heat transfer rates to the heat shield along a ray between engines. Locations of these instruments are shown in Figure 5.4-67. A special heat-transfer gage capable of being externally heated was employed to measure the recovery temperature at the center of the base plate.

A specially made instrumented nozzle was employed in the base region. Static pressure orifices were located over the portion of the nozzle protruding into the base region and were oriented normal to the exterior nozzle contour. Rotation of the instrumented portion allowed the entire nozzle pressure profile to be determined.

Model Test Parametric Data (First Series)

The purpose of these tests was to determine base heating and pressure distribution over an altitude range of 140,000 feet to 220,000 feet. Data were obtained to determine the effects of altitude combustion chamber pressure, secondary flow, and gimbaling.

Radial Distribution

The distributions of static pressure, total pressure, and heat transfer rate across the base of the ungimbaled six-engine configuration, with no secondary flow, for an altitude of 220,000 feet are shown in Figure 5.4-68. These data have been normalized to the nominal 300 psi plenum pressure.

Altitude Series

1) Normal Combustor Operation

The effect of altitude on the base-static pressure at the various radial locations is shown in Figures 5.4-69 and 5.4-70. Base-total pressures for probe heights of 0.25 and 1.00 inches are presented in Figure 5.4-71 as a function of ambient pressure. Base heat-transfer rates as functions of ambient pressure and altitude are presented in Figure 5.4-72. These data are for the normal combustor operation and have been corrected to a plenum pressure of 300 psi.

5.4.4 (Continued)

2) Modified Combustor Operation

The effect of altitude on base-static pressure for the modified combustor operation is presented in Figures 5.4-73 and 5.4-74. Comparison of these data with similar data for normal combustor operation shows that although the center-base pressures are somewhat lower, the outboard pressures compare favorably with the normal operation. The lower center-base pressures may result from the fact that the modified combustor operation does not show the high initial overpressure characteristics of the normal operation. Heat transfer data obtained with modified combustor operation over a simulated altitude range of 160,000 to 220,000 feet are presented in Figure 5.4-75. These data indicate that with the modified combustor operation, there was no apparent altitude effect.

Details of the modified combustor operation are contained in Reference 5-16.

Effect of Combustion Chamber Pressure

The variable combustor chamber pressure series were run with two different sets of ambient conditions: 1) ambient or receiver tank pressure was the same at all combustion chamber pressures, 0.013 psia simulating 220,000 feet altitude, and 2) the ratio of plenum to ambient pressure was held constant for all runs. The ratio (2.3×10^5) corresponds to the basic condition of 300 psi plenum pressure and 220,000 feet altitude.

1) Constant Ambient Pressure

The radial variation of base-static pressure for normal combustion chamber pressures of 100, 200, 300 and 350 psi is shown in Figure 5.4-76. The effect of plenum pressure on base-total pressure is shown in Figure 5.4-77 for nominal plenum pressures of 100, 200, 300 and 350 psi. The radial variation of base heat transfer rates for the nominal 100, 200, 300 and 350 psi plenum pressures is shown in Figure 5.4-78. These data have been corrected to the desired nominal values.

2) Constant Ratio of Ambient Pressure to Plenum Pressure

The radial variations of static pressure, total pressure, and heat transfer rates for the nominal 100, 200, 300 and 350 psi plenum pressures are shown in Figures 5.4-79, 5.4-80, and 5.4-81, respectively. These data have been corrected to the desired nominal values.

The correlation between base static pressure and heat transfer for both sets of ambient conditions is shown in Figure 5.4-82 and 5.4-83.

5.4.4 (Continued)

Effects of Secondary Flow

The effects of injecting secondary flow into the base region are shown in Figures 5.4-84 through 5.4-90. The radial distribution of static pressure is presented in Figure 5.4-84. The radial distribution of total pressure for probe heights of 1/4, 5/8 and 1 inch are presented in Figure 5.4-85. The effect on static and total pressure of diverting the secondary flow radially is shown in Figure 5.4-86. A comparison of base pressure distribution (static and total) without secondary exhaust, with secondary exhaust, and with secondary exhaust with a diverter is presented in Figure 5.4-87. The radial distributions of heat transfer for secondary flow and secondary flow with a diverter are shown in Figure 5.4-88. Heat transfer data taken with secondary flow where the 5/8 and 1 inch total pressure probes were installed are presented in Figure 5.4-89. These data indicate that the probe height had no noticeable effect on the base heat transfer rates. A comparison showing the base heat transfer distributions without secondary flow; with secondary flow; and with secondary flow with a diverter is presented in Figure 5.4-90.

Effects of Gimbaling

A schematic of the S-IV six-engine gimbaling is presented in Figure 5.4-91. The effects of gimbaling on base static pressure are shown in Figures 5.4-92 through 5.4-95; total pressure, Figures 5.4-96 through 5.4-99; and heat transfer, Figures 5.4-100 through 5.4-103. These data are plotted in such a manner that the data are combined from comparison gimbaling runs to present distributions completely across the base on three different diameters. The base schematic on each plot shows the orientation of each engine for the model altitude plotted. All gimbaling runs were made with helium heater exhaust secondary flow without a diverter.

Model Test Parametric Data (Second Series)

The primary objective of these tests was to obtain base thrust and nozzle drag measurements. These data are discussed in detail in Reference 5-17. The secondary objectives were to define the effects of the helium heater exhaust flow, and to determine the base recovery temperature

Effect of Secondary Exhaust

The effect of the secondary exhaust flow on the base static pressure profiles along a ray between engines and along a ray in line with an engine are presented in Figures 5.4-104 and 5.4-105. Heat shield vertical probe pressure data along a ray between engines with and without secondary exhaust are presented in Figure 5.4-106 through 5.4-108.

Nozzle outer surface pressure profiles without and with secondary exhaust flow as functions of nozzle azimuth and height above the heat shield are shown in Figures 5.4-109 through 5.4-112.

5.4.4 (Continued)

The effect of the secondary exhaust on the heat shield heat-transfer rates is shown in Figure 5.4-113.

Recovery Temperature

Data obtained with the heated heat-transfer gage are shown as a function of gage temperature in Figure 5.4-114 along with an extrapolation of the data to an indicated recovery temperature of 2190°R.

5.4.5 Model Test Data Comparison

Different types of tests have been conducted using scale models of the S-IV stage. A partial listing of the different parameters and test conditions are presented in Table 5.4-2. Due to the different test conditions, it is difficult to make comparisons between the parameter data from each test. For general trends, a comparison of the helium heater exhaust effects on heating and pressure environments are compared in Figures 5.4-115 and 5.4-116, respectively. No attempt was made to isolate the parameter effect from the different test conditions at which these data were recorded.

TABLE 5.4-1. SUMMARY OF S-IV SCALE MODEL TESTS

TYPE OF TEST	LOCATION	NO. OF ENGINES	SCALE	ALTITUDE RANGE	DATE	REFERENCES
Combustion Model - Long Duration	AEDC	4	1/10	118,500 to 152,500 feet	1961	5-9
Cold Flow Model	AEDC & FEC	4	1/27.75	100,000 to 194,000 feet	1961	5-9 & 5-11
Hot-Flow Model - Short Duration	CAL	6	1/10	125,000 to 250,000 feet	1961	5-12 - 5-15
Hot-Flow Model - Short Duration	CAL	6	1/10	140,000 to 220,000 feet	1962	5-16 & 5-17

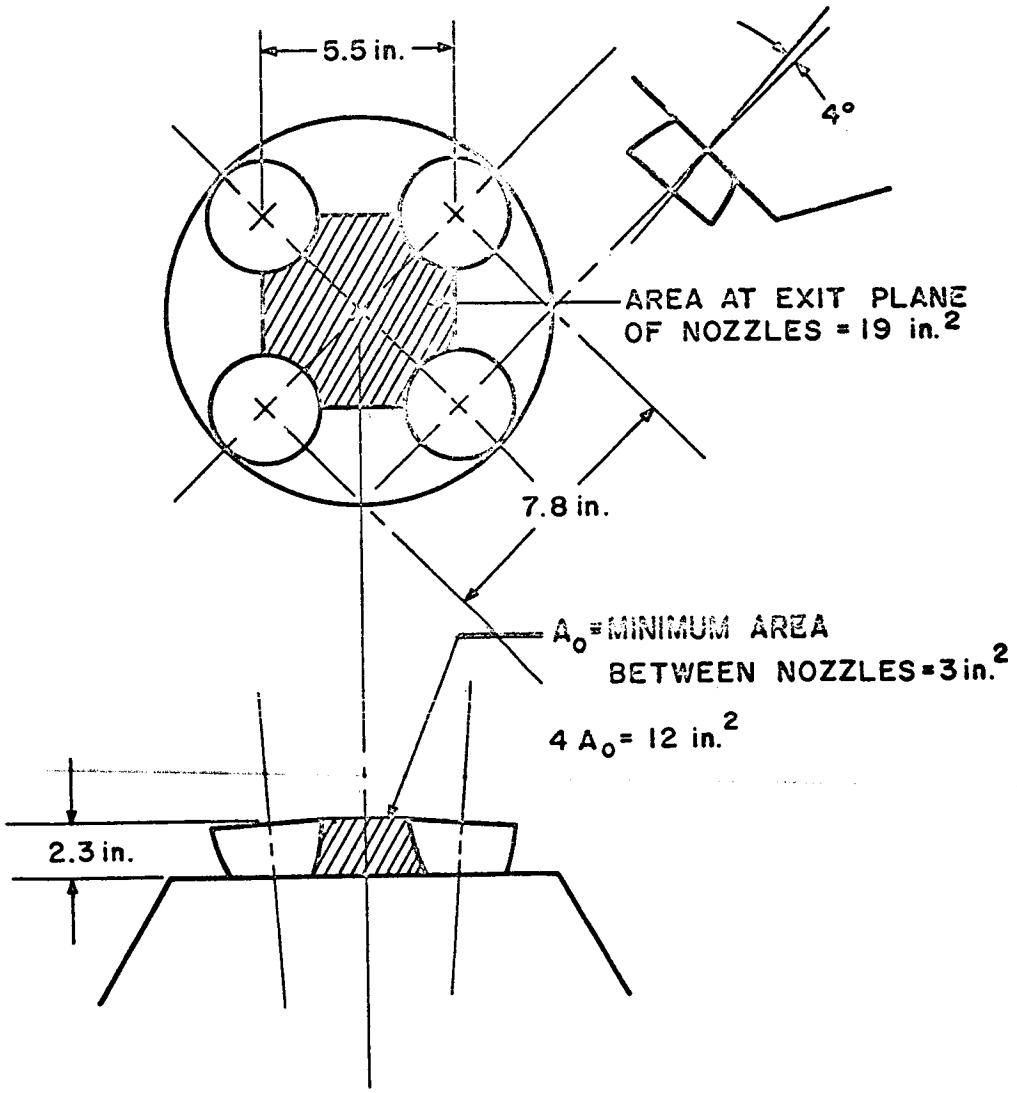

FIGURE 5.4-1. S-IV 4-ENGINE 1/10 SCALE COMBUSTION MODEL-BASE REGION CONFIGURATION

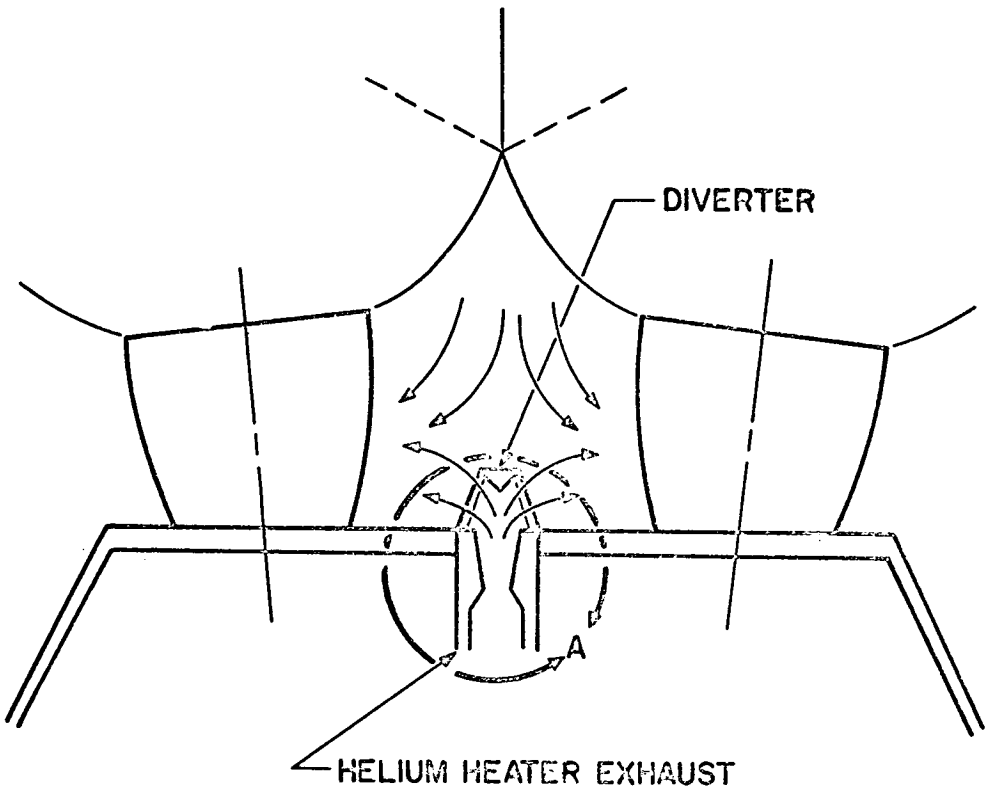

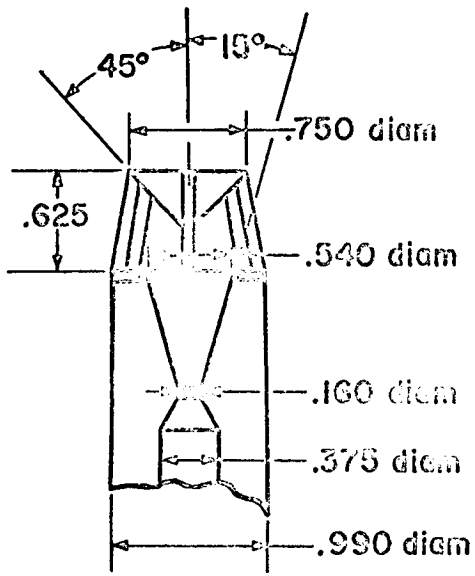

VIEW A

NOTE: DIMENSIONS ARE IN INCHES

FIGURE 5.4-2. S-IV 4-ENGINE 1/10 SCALE COMBUSTION MODEL - HELIUM HEATER EXHAUST NOZZLE AND DIVERTER

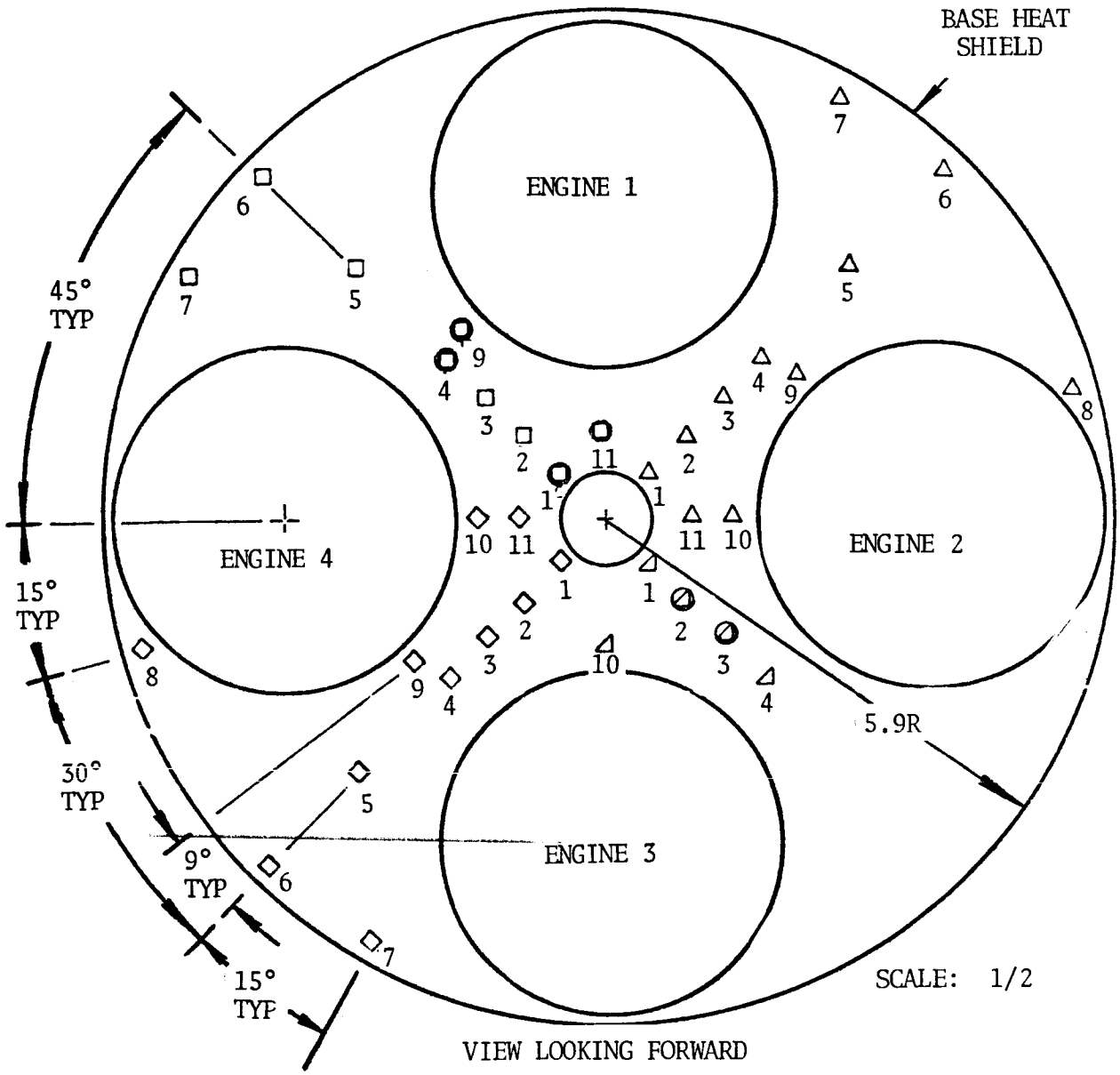

SYMBOL	TYPE OF INSTRUMENT	LOCATION	RADIUS (IN)
◇	BLACK CALORIMETER	1	0.750
		2	1.375
△	GOLD CALORIMETER	3	2.000
		4	2.625
□, ⊿	STATIC PRESSURE TAPS	5	4.125
		6, 7, 8	5.625
○	TOTAL PRESSURE PROBE (FACING CENTER)	9	2.800
		10	1.000
		11	1.500

NOTE: AXIAL TRAVERSING PROBE NOT SHOWN

FIGURE 5.4-3. S-IV 4-ENGINE 1/10 SCALE COMBUSTION MODEL - BASE HEAT SHIELD INSTRUMENTATION

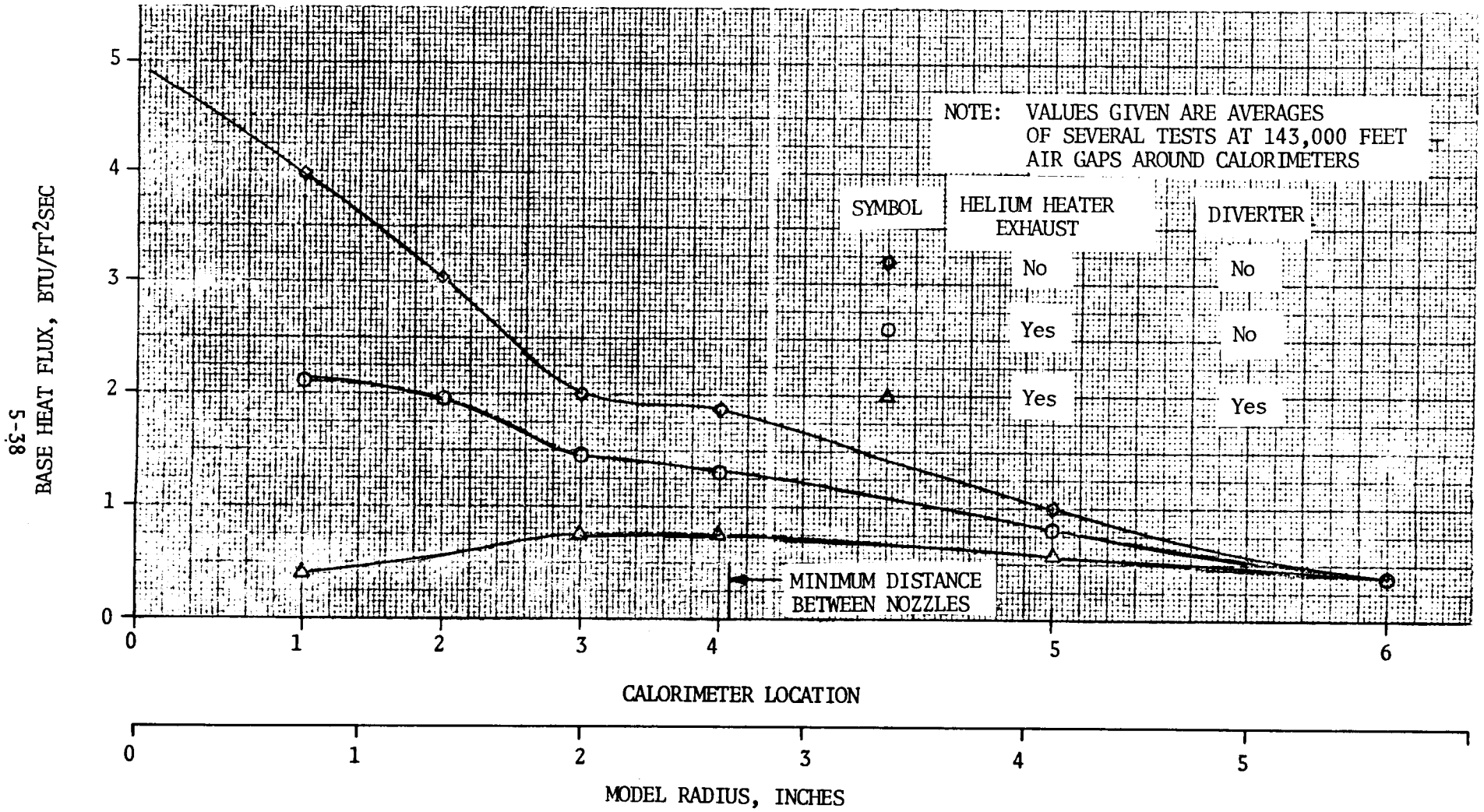

FIGURE 5.4-4. S-IV 4-ENGINE 1/10 SCALE COMBUSTION MODEL - EFFECT OF SECONDARY EXHAUST ON BASE HEAT FLUX DISTRIBUTION

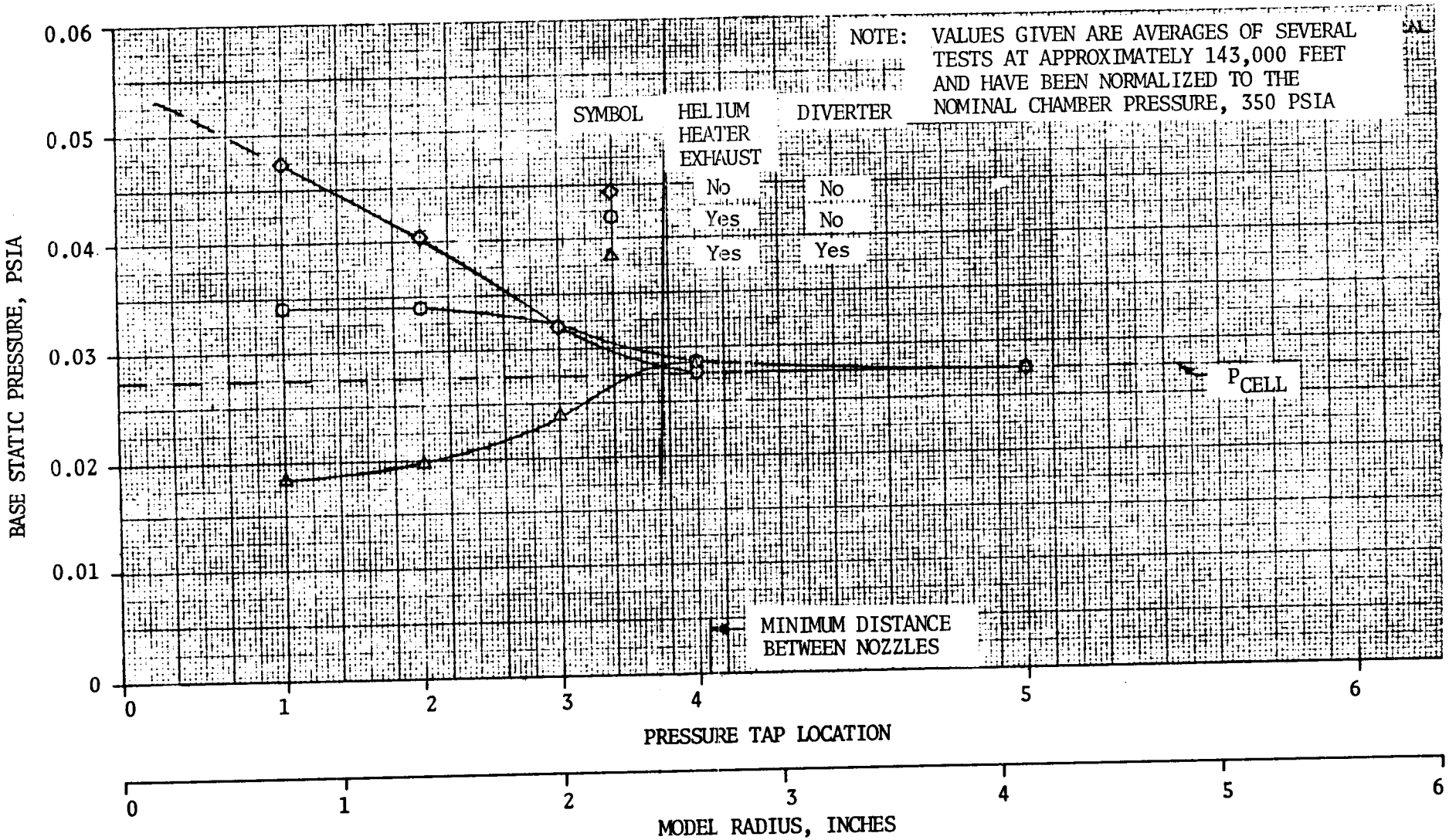

FIGURE 5.4-5. S-IV 4-ENGINE 1/10 SCALE COMBUSTION MODEL - EFFECT OF SECONDARY EXHAUST ON BASE STATIC PRESSURE DISTRIBUTION

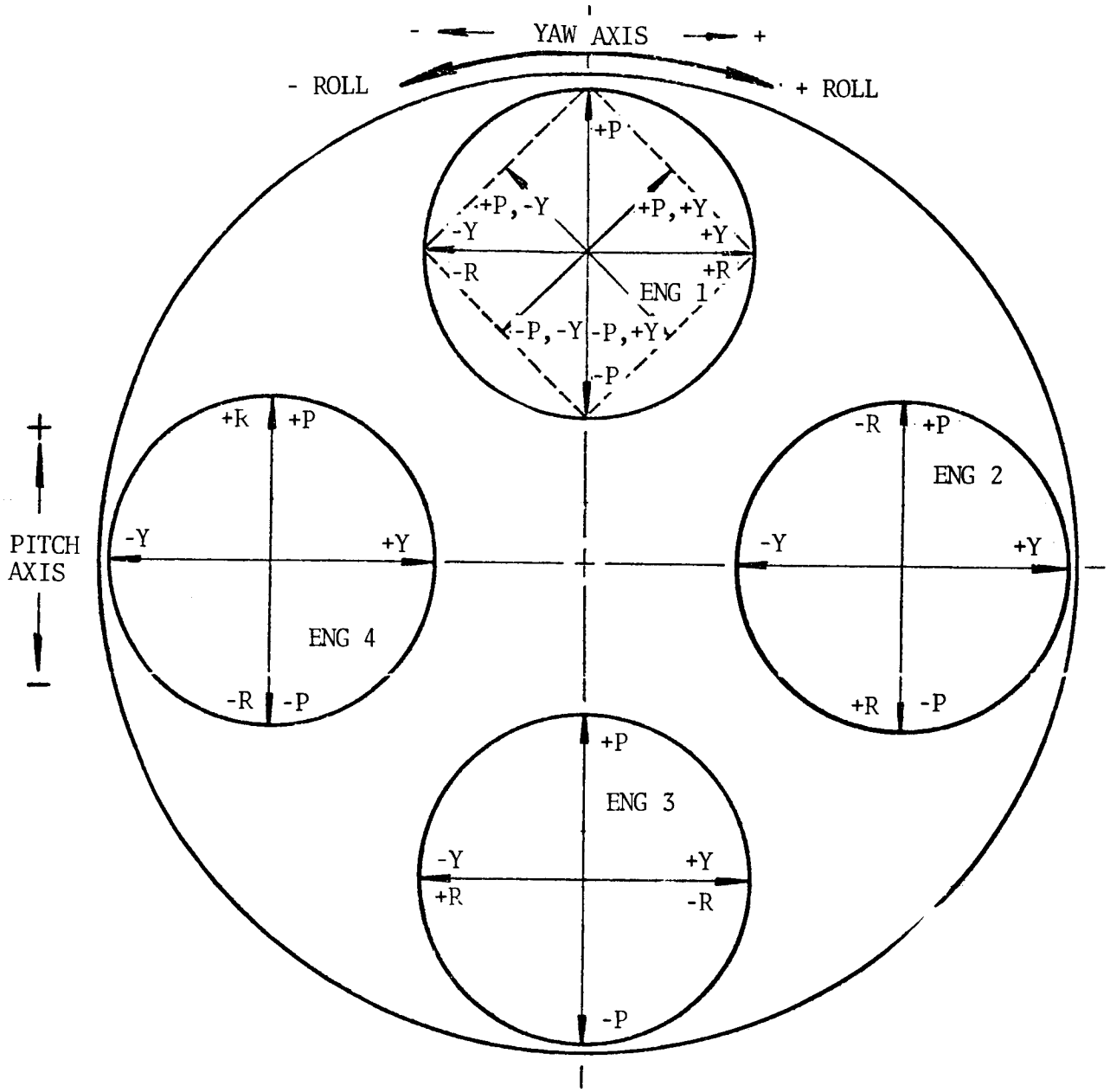

VIEW LOOKING FORWARD

P = PITCH Y = YAW R = ROLL
5.66° GIMBALLING INDICATED BY ARROW TOUCHING CIRCLE
4° GIMBALLING INDICATED BY ARROW NOT TOUCHING CIRCLE
DASHED LINE IS GIMBALLING PERIMETER, COMMON TO ALL ENGINES

FIGURE 5.4-6. S-IV 4-ENGINE 1/10 SCALE COMBUSTION MODEL - GIMBAL PATTERNS

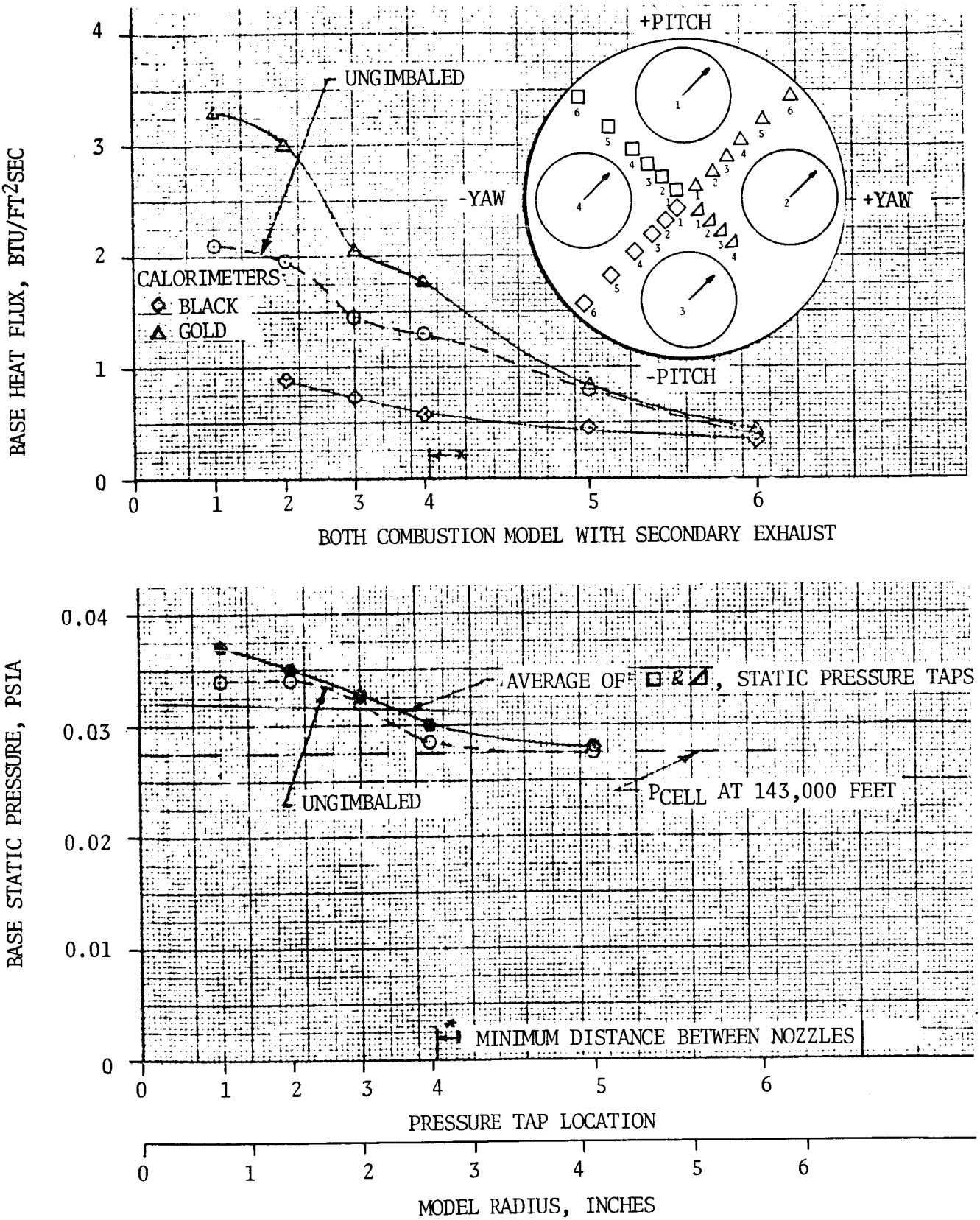

FIGURE 5.4-7. S-IV 4-ENGINE 1/10 SCALE COMBUSTION MODEL - BASE HEAT FLUX AND STATIC PRESSURE DISTRIBUTIONS FOR THE POSITIVE PITCH/POSITIVE YAW, 4° GIMBAL CONFIGURATION

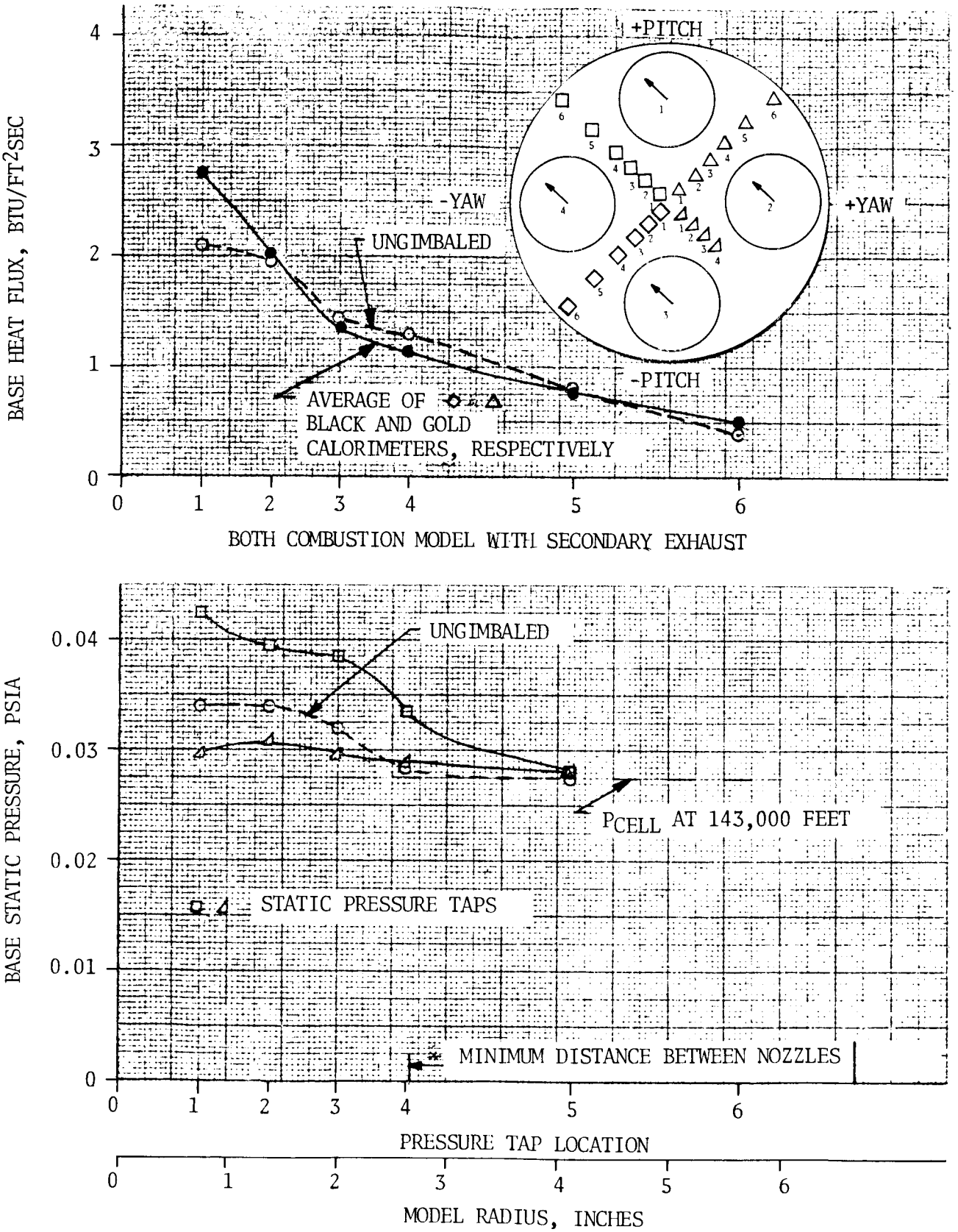

FIGURE 5.4-8. S-IV 4-ENGINE 1/10 SCALE COMBUSTION MODEL - BASE HEAT FLUX AND STATIC PRESSURE DISTRIBUTIONS FOR THE POSITIVE PITCH/NEGATIVE YAW, 4° GIMBAL CONFIGURATION

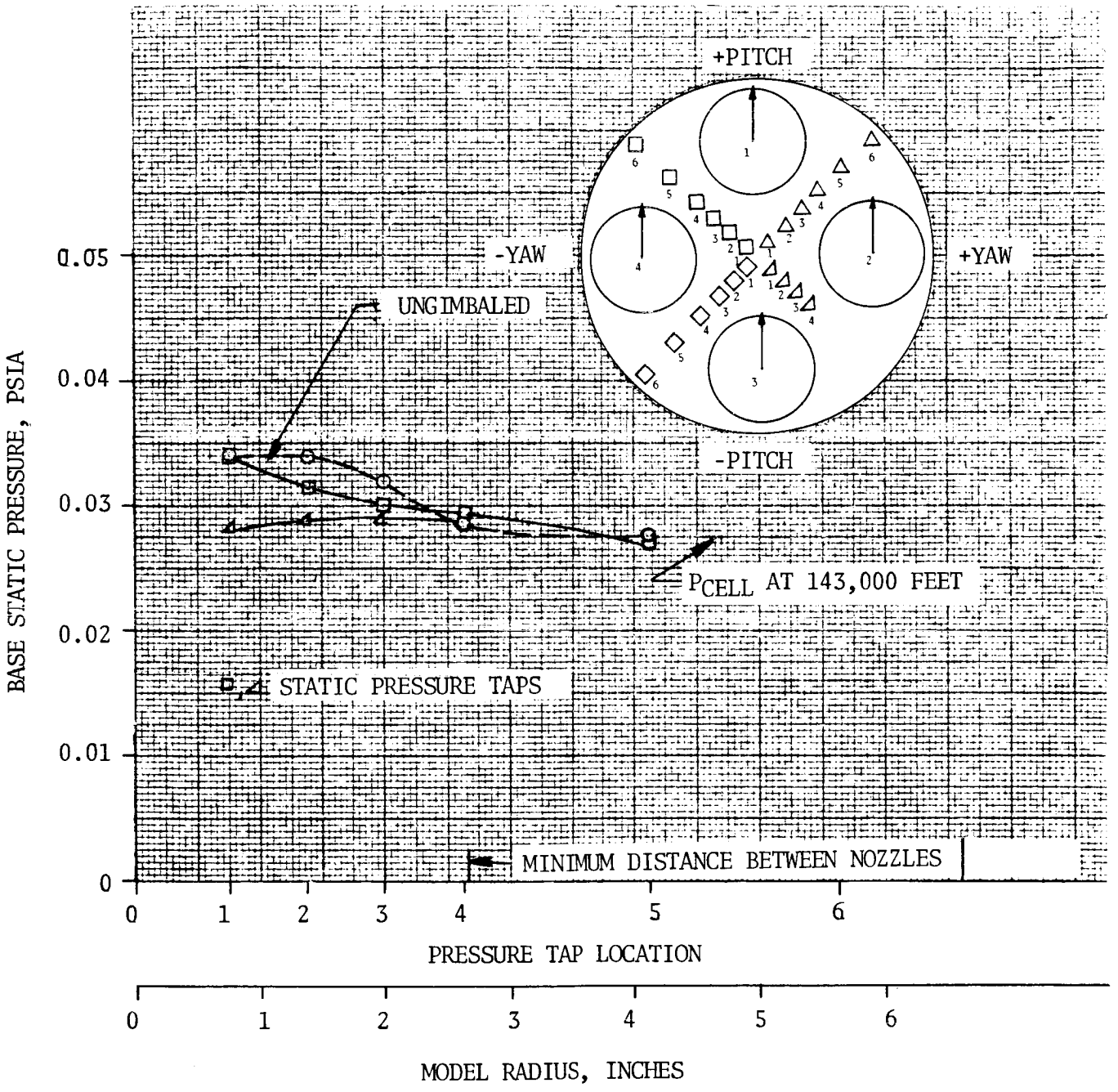

FIGURE 5.4-9. S-IV 4-ENGINE 1/10 SCALE COMBUSTION MODEL - BASE STATIC PRESSURE DISTRIBUTION FOR THE POSITIVE PITCH, 5.66° GIMBAL CONFIGURATION

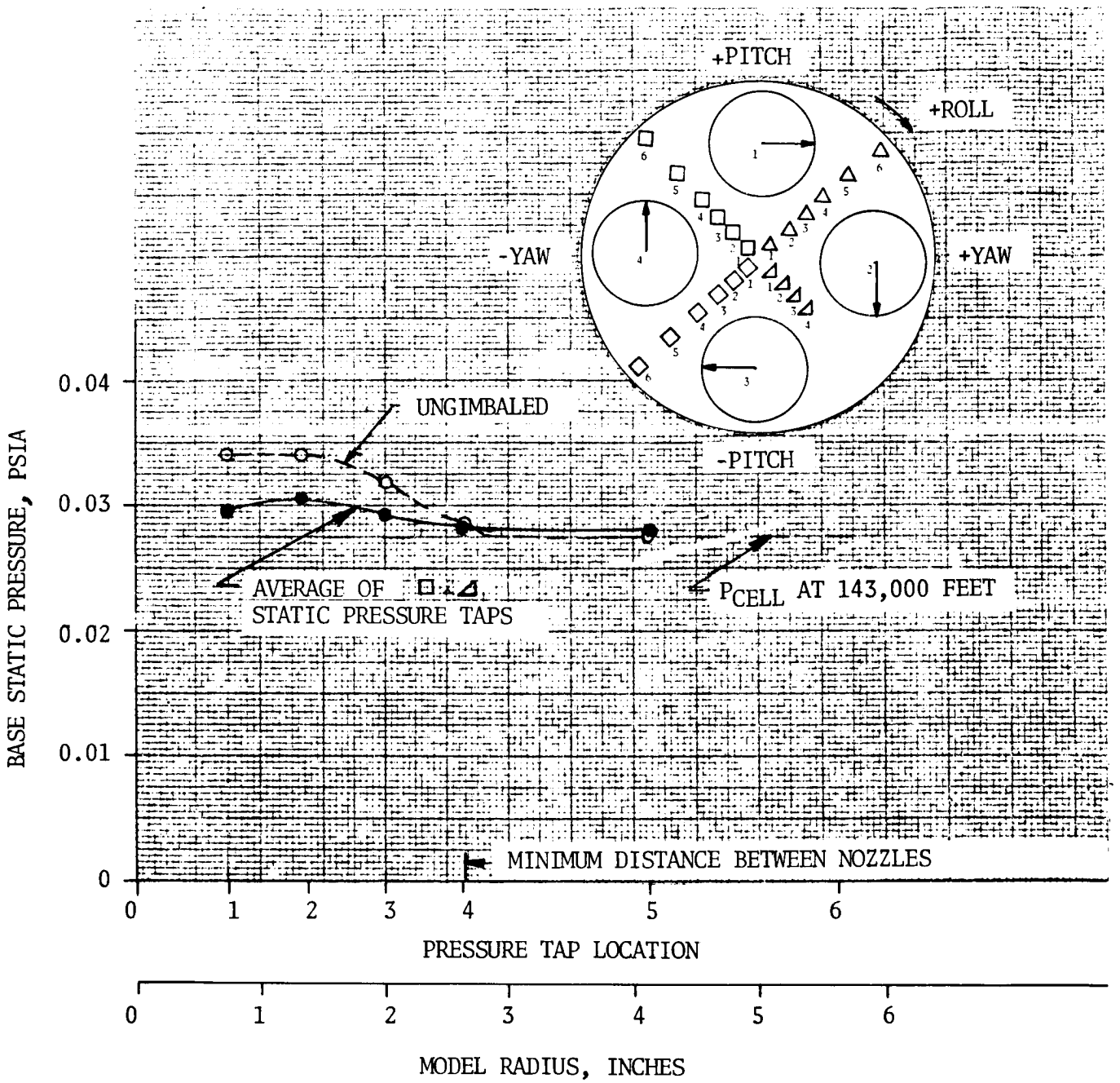

FIGURE 5.4-10. S-IV 4-ENGINE 1/10 SCALE COMBUSTION MODEL - BASE STATIC PRESSURE DISTRIBUTION FOR THE POSITIVE ROLL GIMBAL CONFIGURATION

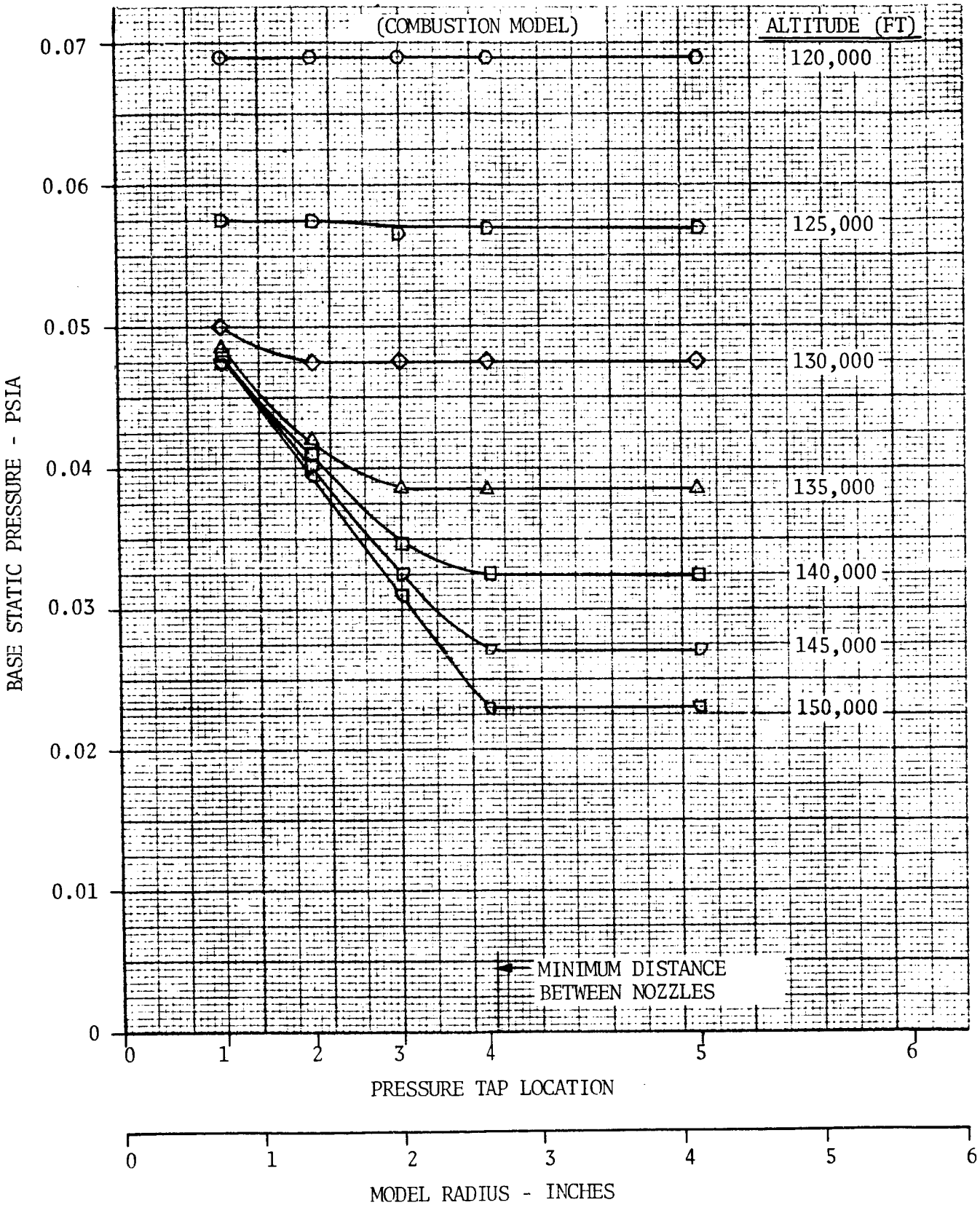

FIGURE 5.4-11. S-IV 4-ENGINE 1/10 SCALE COMBUSTION MODEL - EFFECT OF ALTITUDE ON BASE STATIC PRESSURE DISTRIBUTION

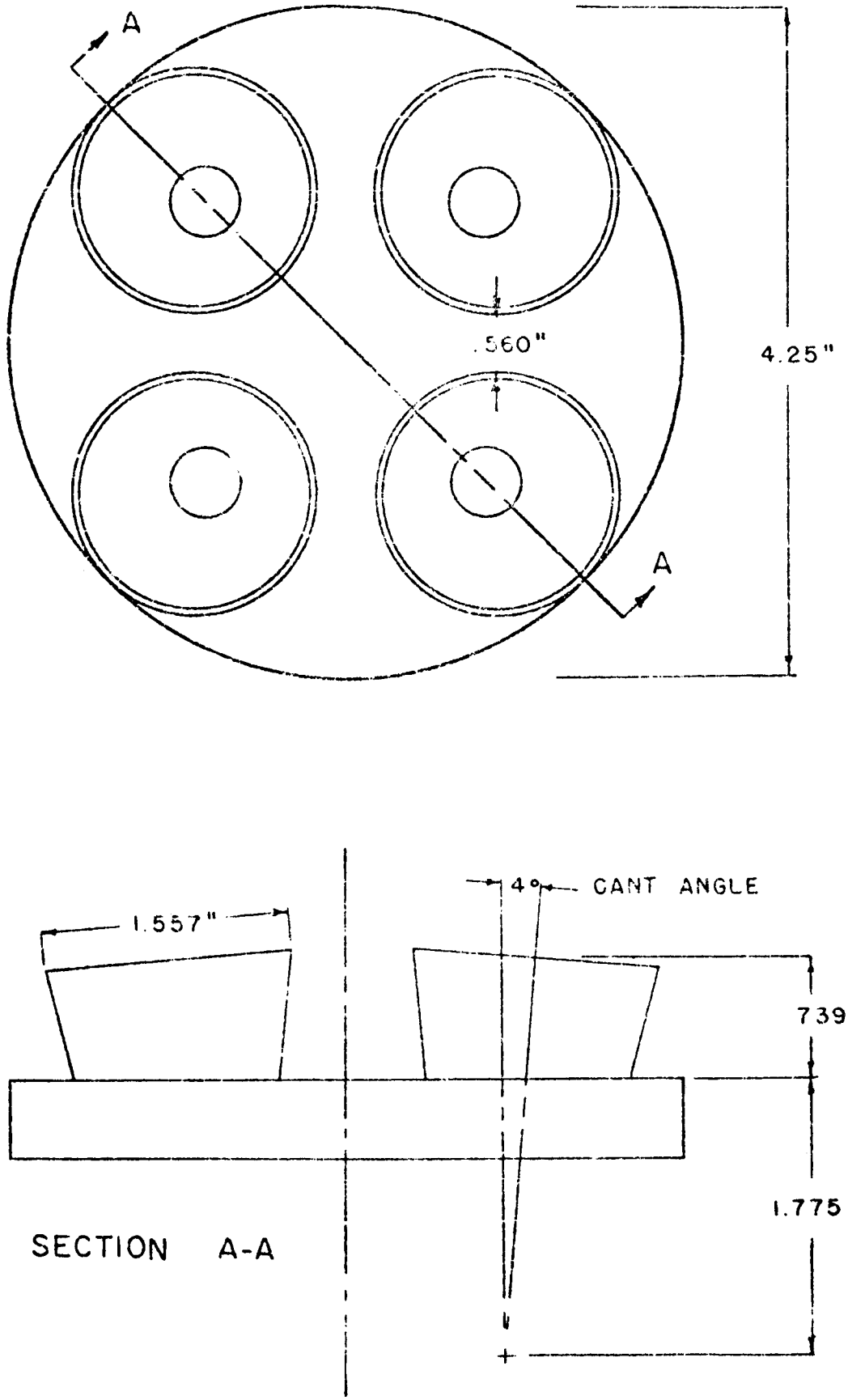

FIGURE 5.4-12. S-IV 4-ENGINE 1/27.75 SCALE COLD FLOW MODEL - BASE REGION CONFIGURATION

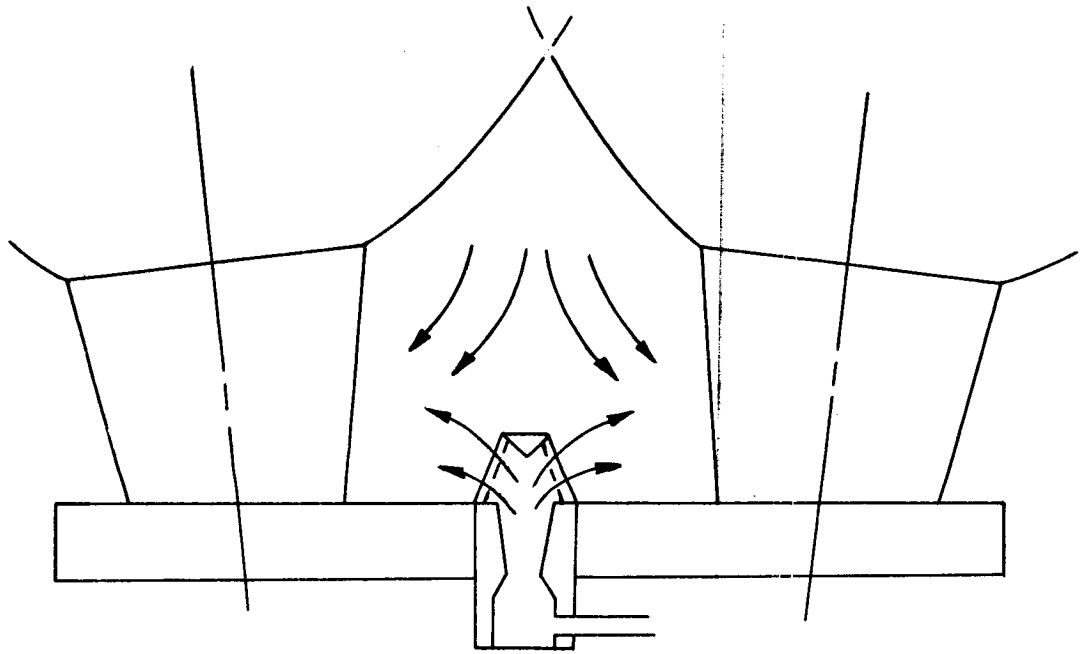

EXIT DIAMETER = .317 INCHES
A/A* = 5.856

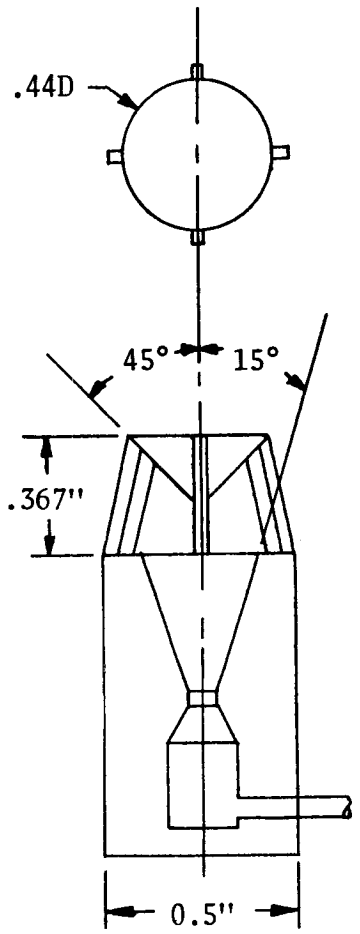

FIGURE 5.4-13. S-IV 4-ENGINE 1/27.75 SCALE COLD FLOW MODEL - HELIUM HEATER EXHAUST NOZZLE AND DIVERTER

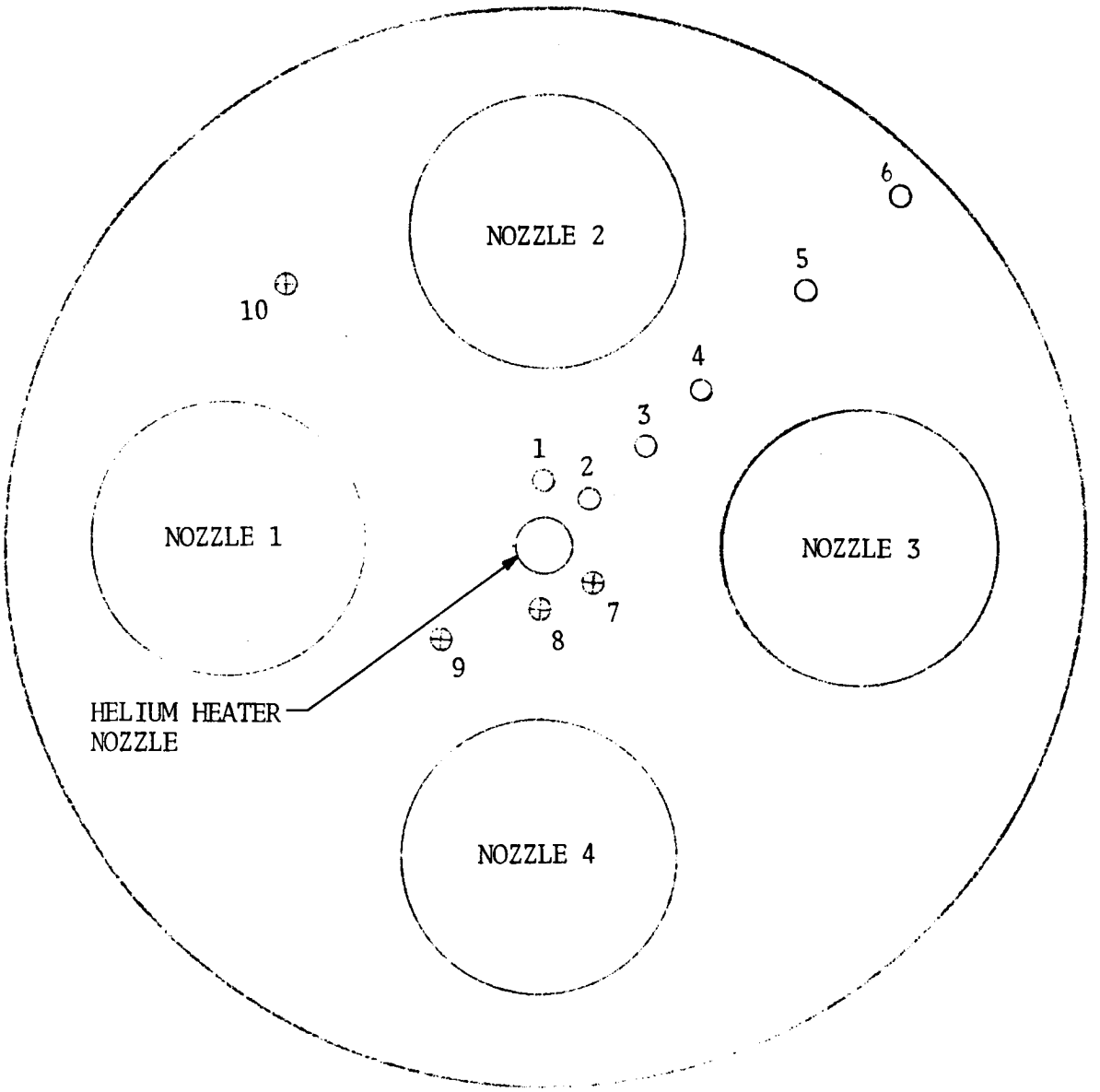

	Location	Radius (in)
○ Static Pressure Tap Location	1, 2, 7, 8	0.333
	3, 9	0.666
⊕ Total Pressure Tap Location	4	1.000
	5, 10	1.500
	6	2.000

NOTE: The inside diameters of the static taps are approximately 0.039 inches except number 5 which is 0.064 inches. The inside diameters of the total pressure taps are approximately 0.05 inches and are approximately 0.063 inches above the heat shield.

FIGURE 5.4-14. S-IV 4-ENGINE 1/27.75 SCALE COLD FLOW MODEL - BASE HEAT SHIELD INSTRUMENTATION

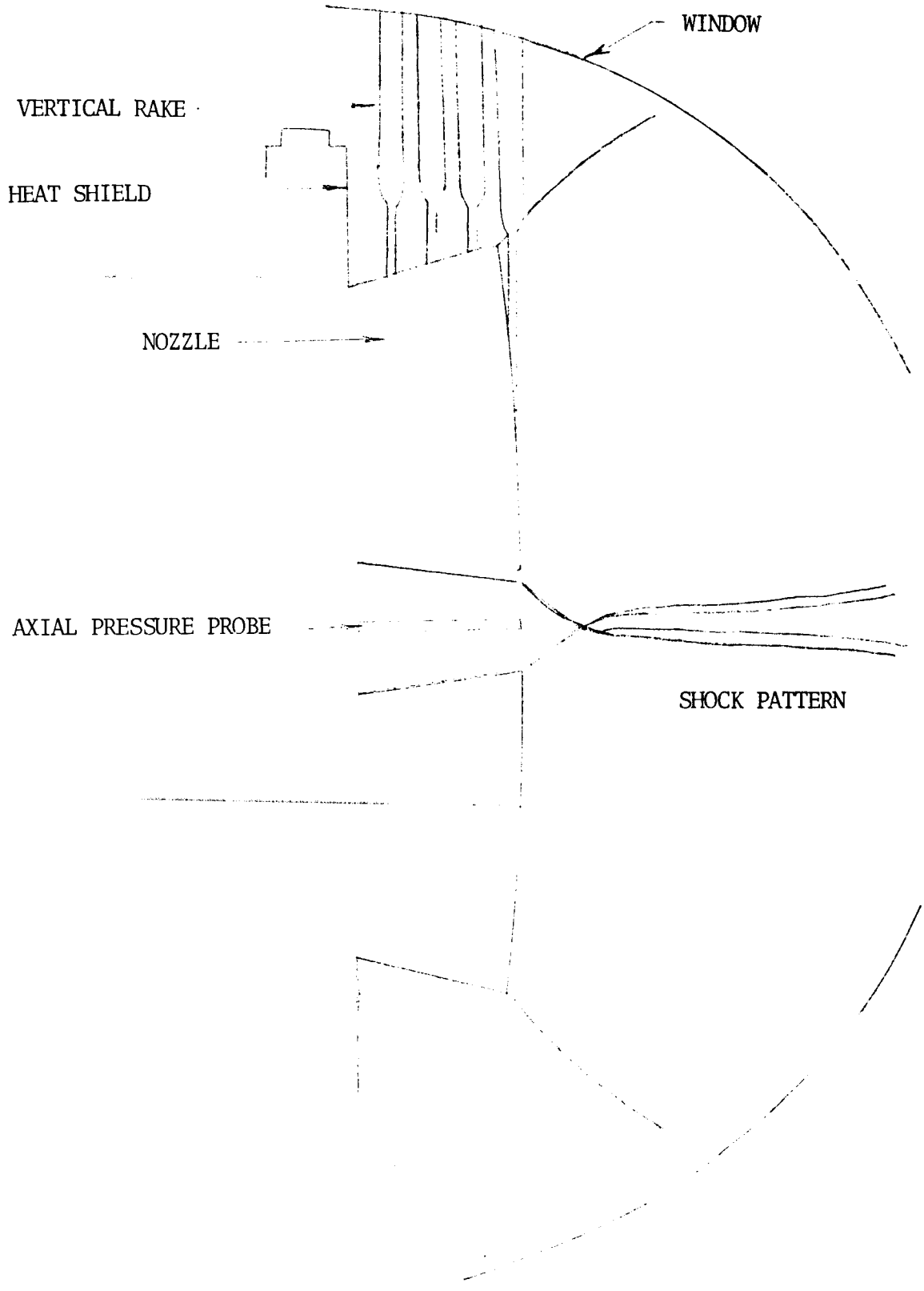

FIGURE 5.4-15. S-IV 4-ENGINE 1/27.75 SCALE COLD FLOW MODEL - BASE REGION INSTRUMENTATION

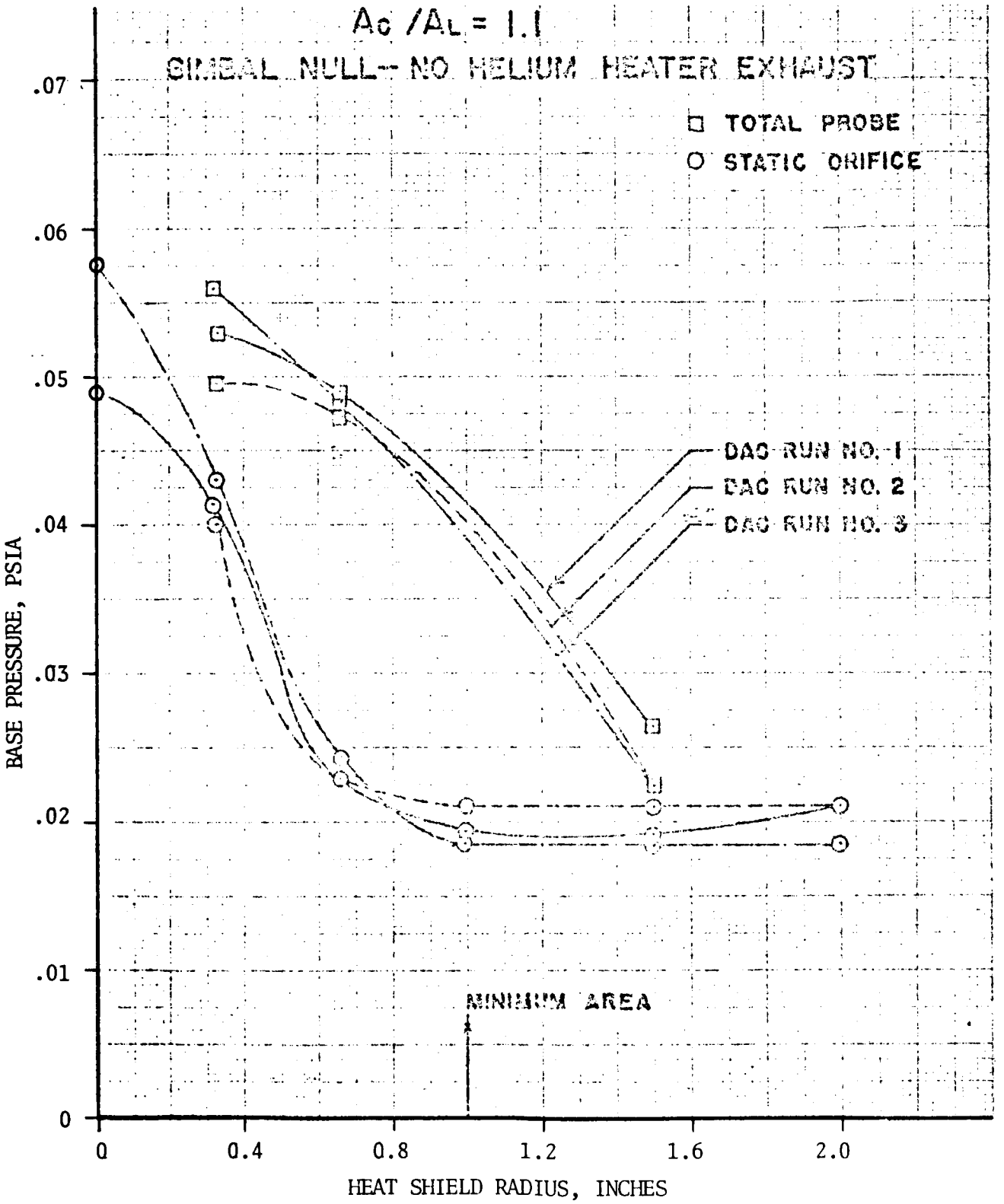

FIGURE 5.4-16. S-IV 4-ENGINE 1/27.75 SCALE COLD FLOW MODEL - REPEATABILITY OF BASE HEAT SHIELD PRESSURE DATA

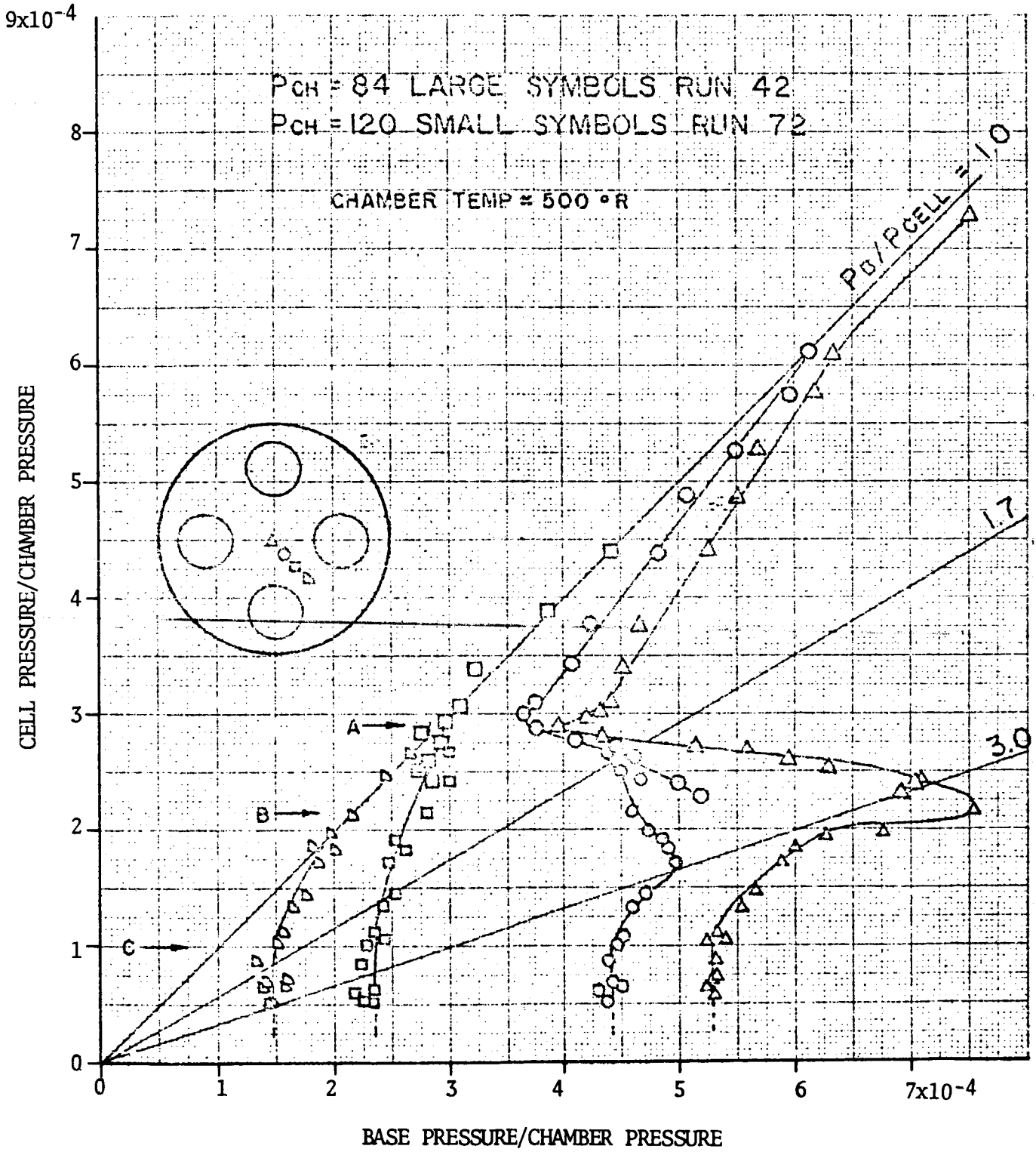

FIGURE 5.4-17. S-IV 4-ENGINE 1/27.75 SCALE COLD FLOW MODEL - ALTITUDE EFFECT ON BASE HEAT SHIELD PRESSURES

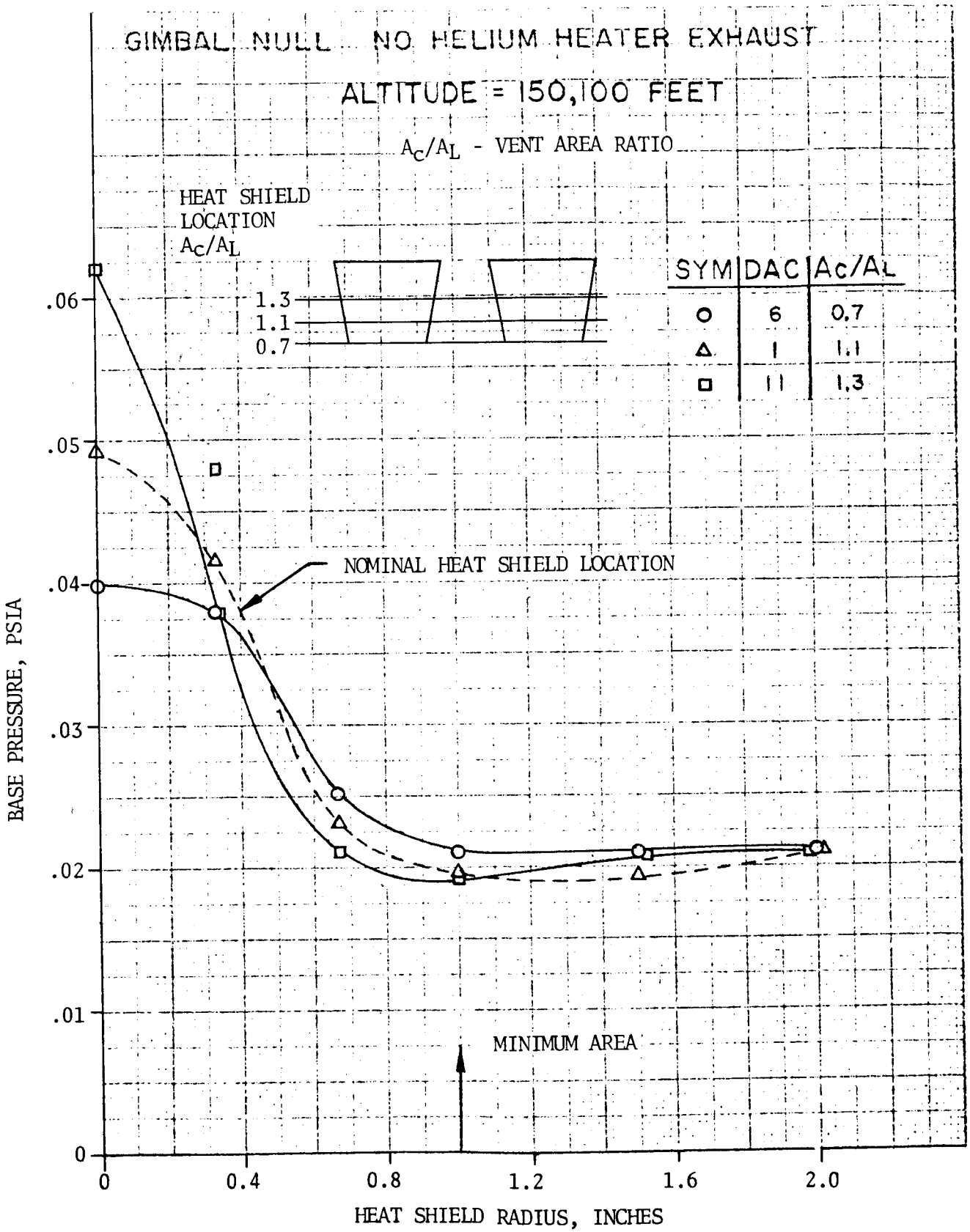

FIGURE 5.4-18. S-IV 4-ENGINE 1/27.75 SCALE COLD FLOW MODEL - EFFECT OF HEAT SHIELD LOCATION ON BASE HEAT SHIELD PRESSURE DISTRIBUTION

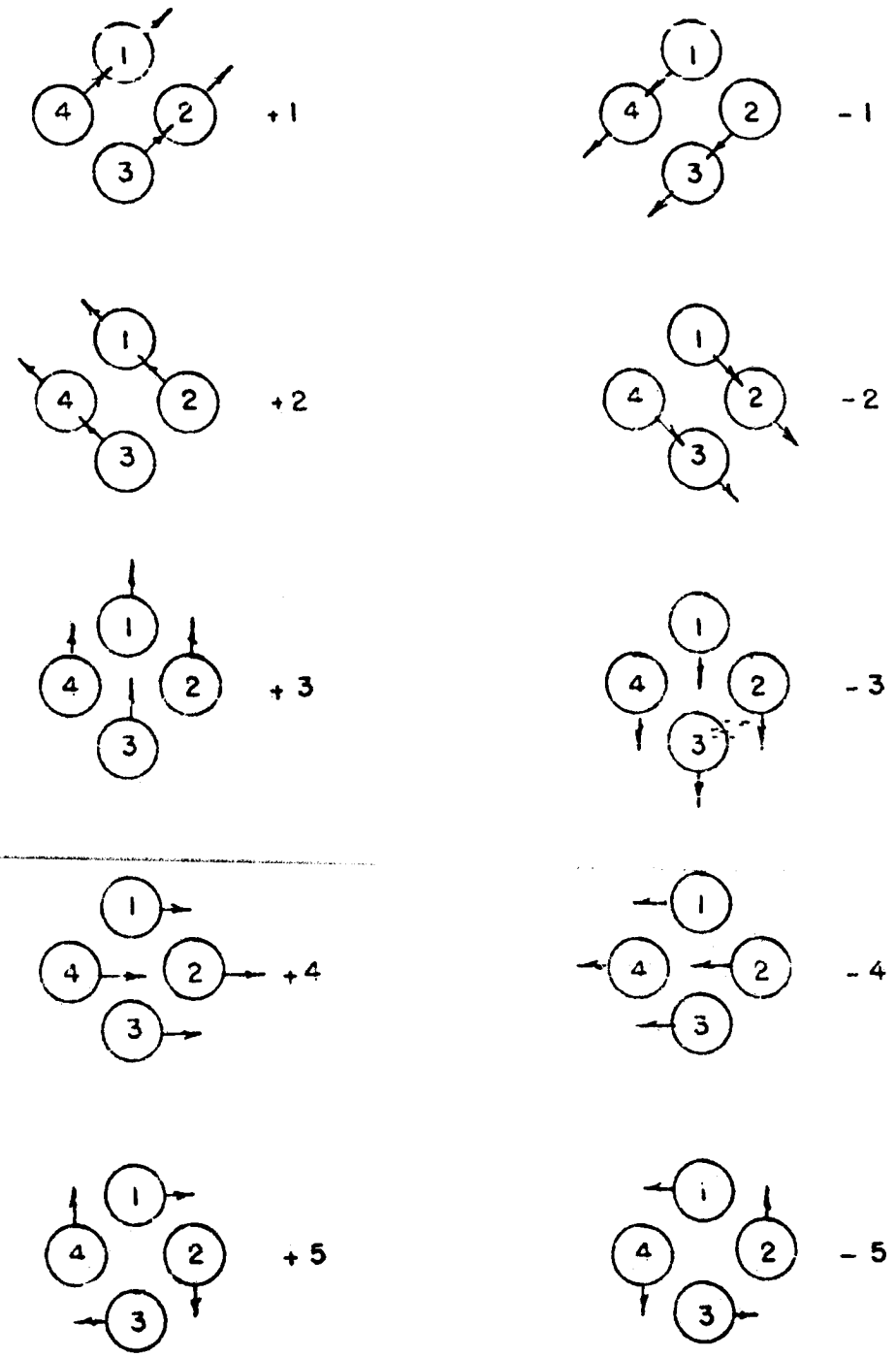

FIGURE 5.4-19, S-IV 4-ENGINE 1/27.75 SCALE COLD FLOW MODEL - GIMBAL PATTERNS

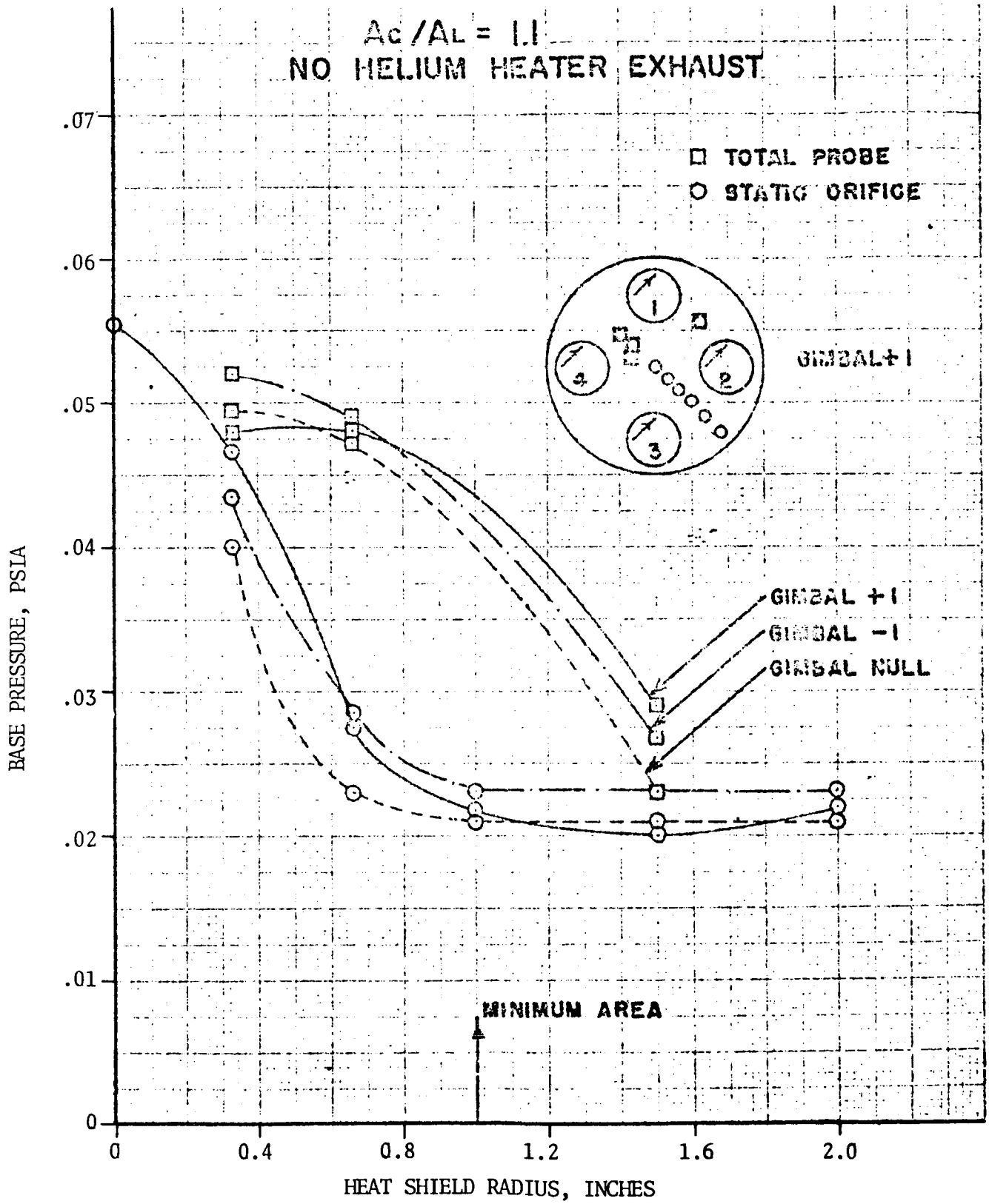

FIGURE 5.4-20. S-IV 4-ENGINE 1/27.75 SCALE COLD FLOW MODEL - EFFECT OF GIMBALLING ON BASE HEAT SHIELD PRESSURE DISTRIBUTION

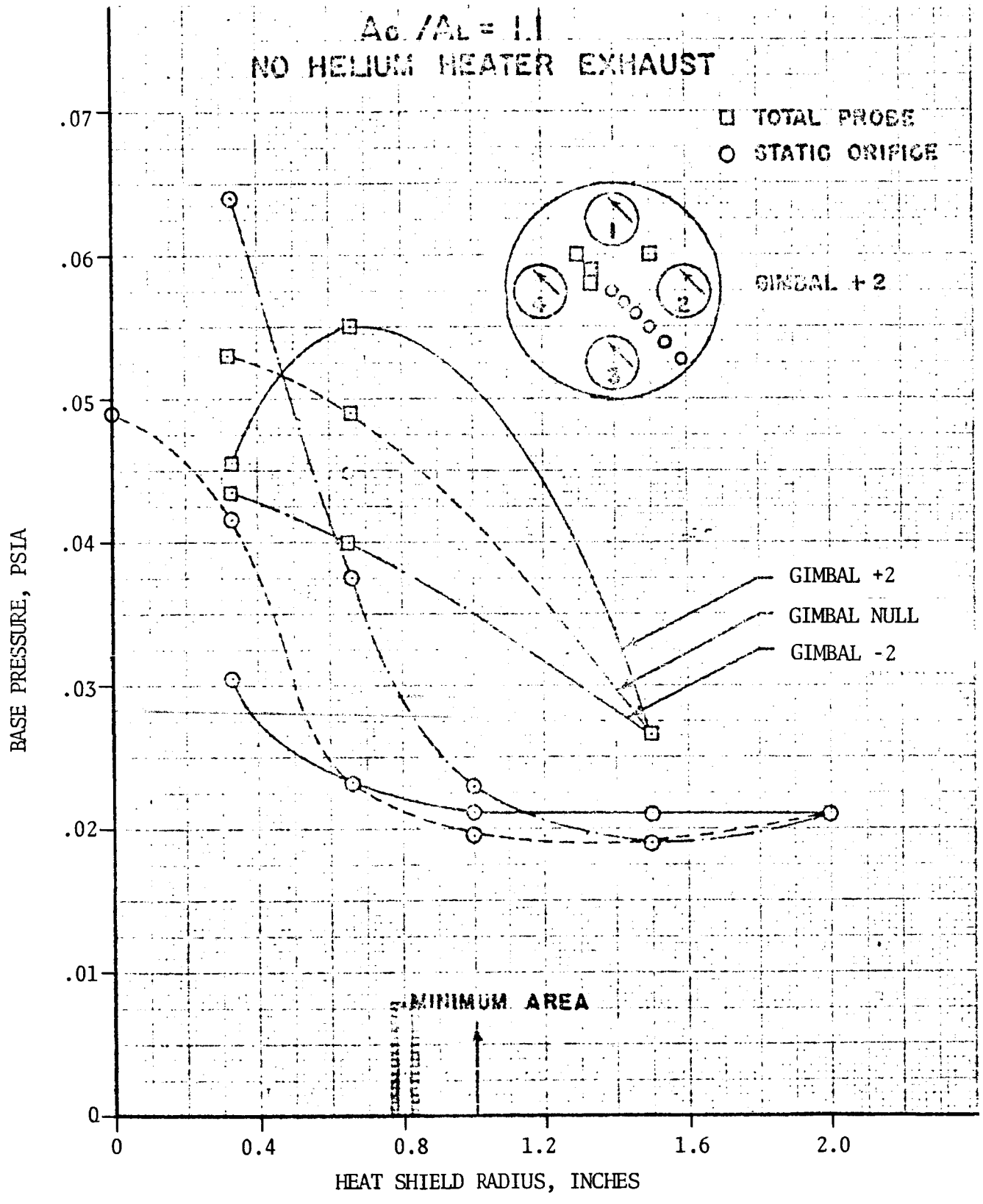

FIGURE 5.4-21. S-IV 4-ENGINE 1/27.75 SCALE COLD FLOW MODEL - EFFECT OF GIMBALLING ON BASE HEAT SHIELD PRESSURE DISTRIBUTION

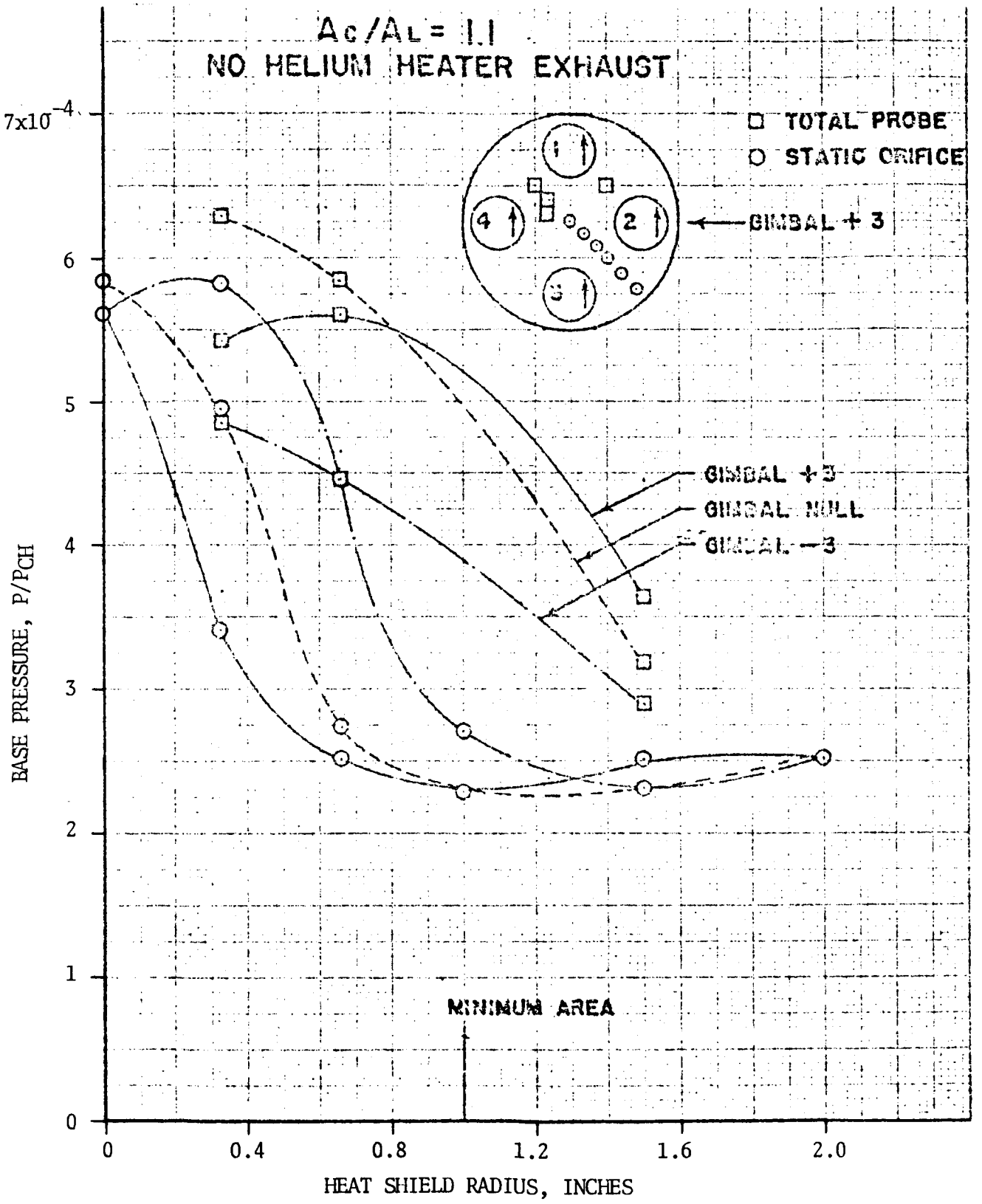

FIGURE 5.4-22. S-IV 4-ENGINE 1/27.75 SCALE COLD FLOW MODEL - EFFECT OF GIMBALLING ON BASE HEAT SHIELD PRESSURE DISTRIBUTION

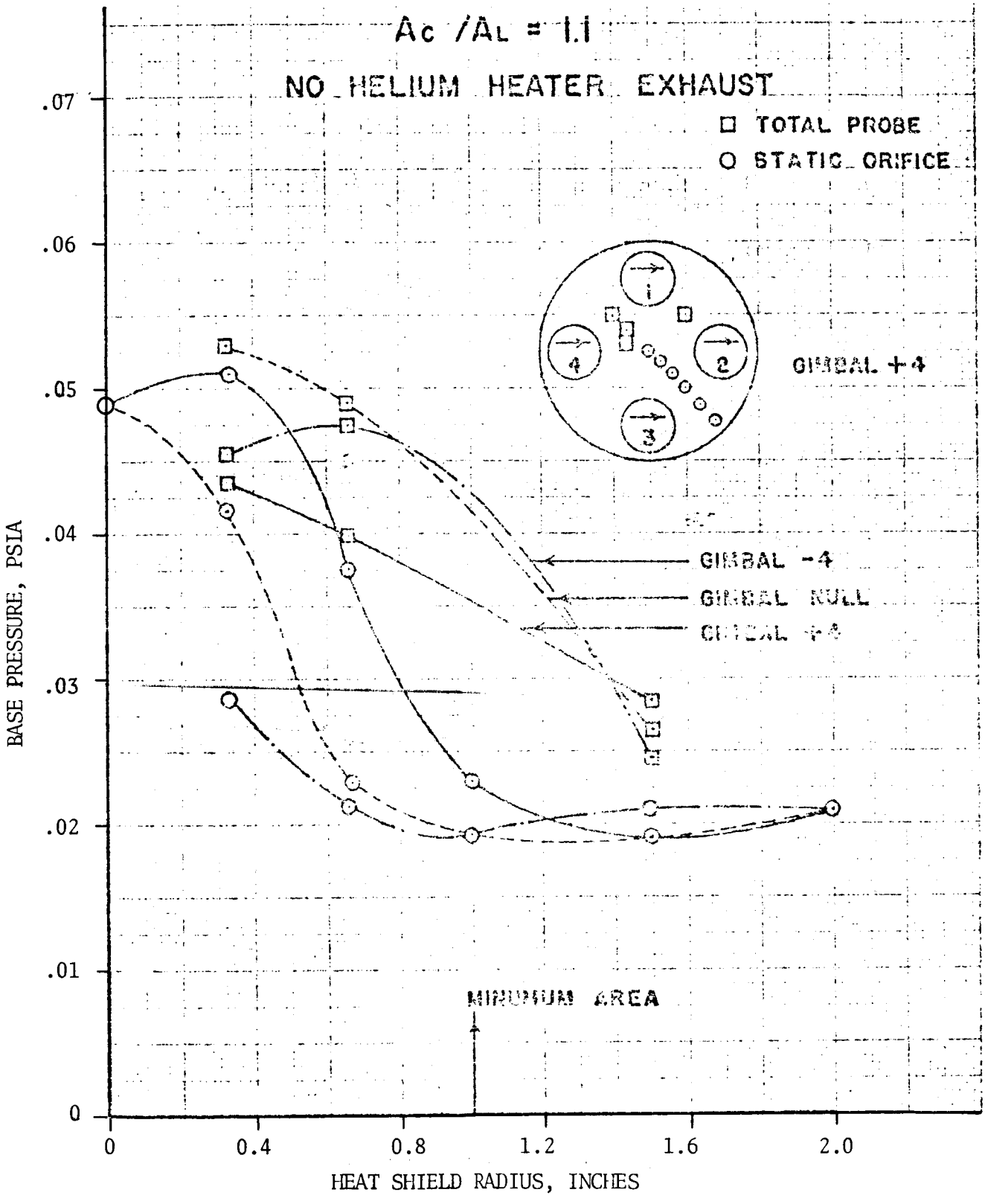

FIGURE 5.4-23. S-IV 4-ENGINE 1/27.75 SCALE COLD FLOW MODEL - EFFECT OF GIMBALLING ON BASE HEAT SHIELD PRESSURE DISTRIBUTION

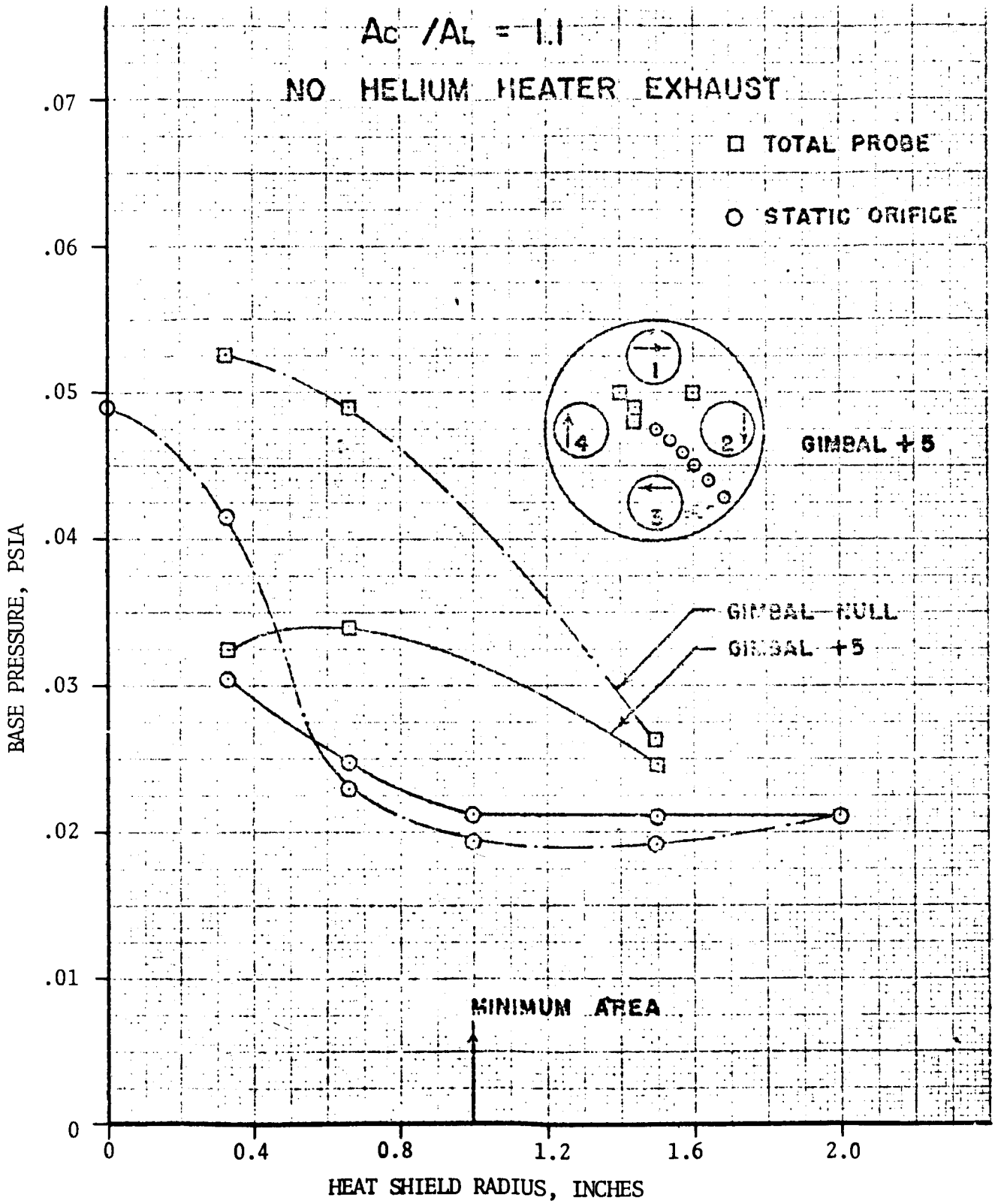

FIGURE 5.4-24. S-IV 4-ENGINE 1/27.75 SCALE COLD FLOW MODEL - EFFECT OF GIMBALLING ON BASE HEAT SHIELD PRESSURE DISTRIBUTION

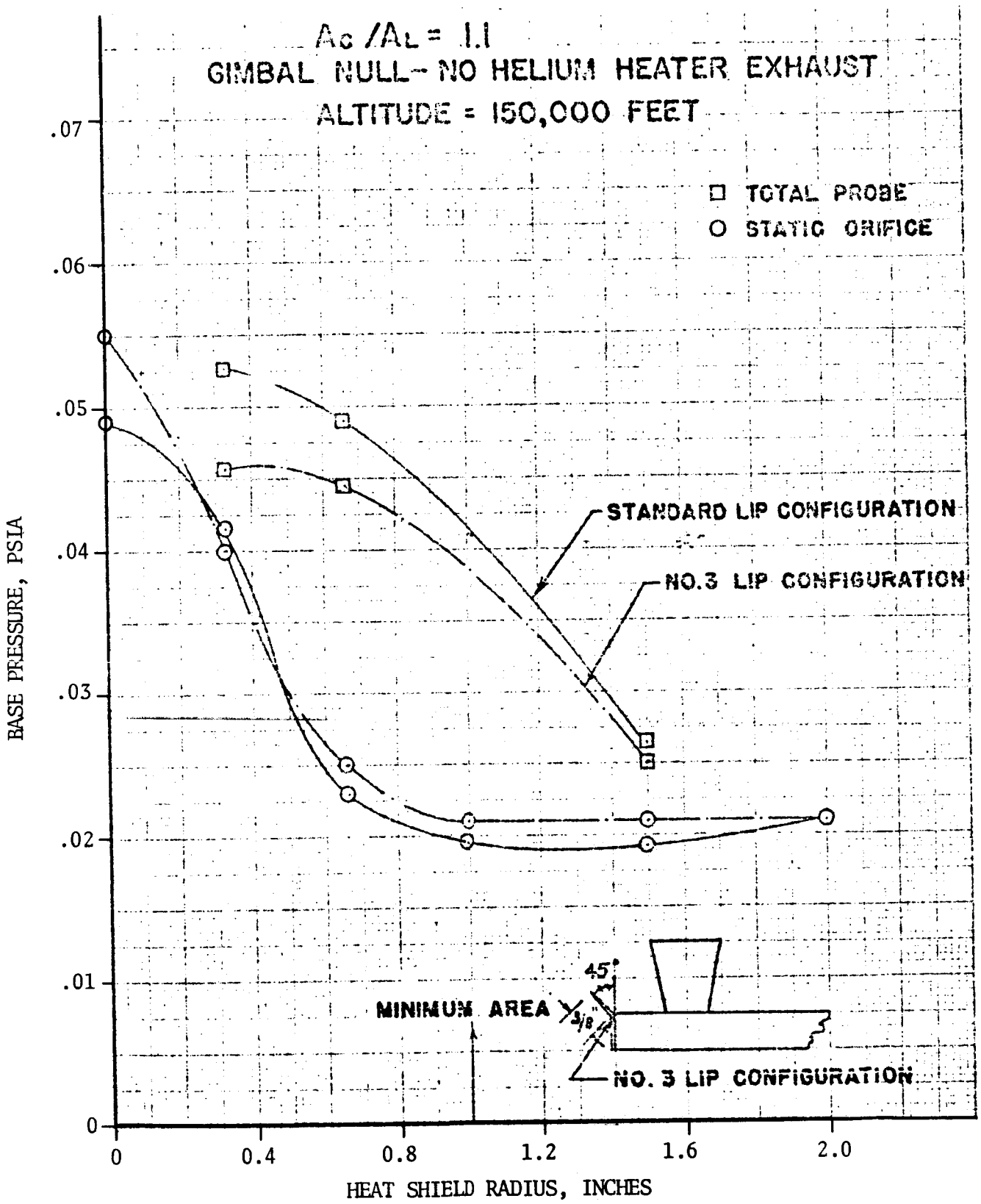

FIGURE 5.4-25. S-IV 4-ENGINE 1/27.75 SCALE COLD FLOW MODEL - EFFECT OF LIP CONFIGURATION ON BASE HEAT SHIELD PRESSURE DISTRIBUTION

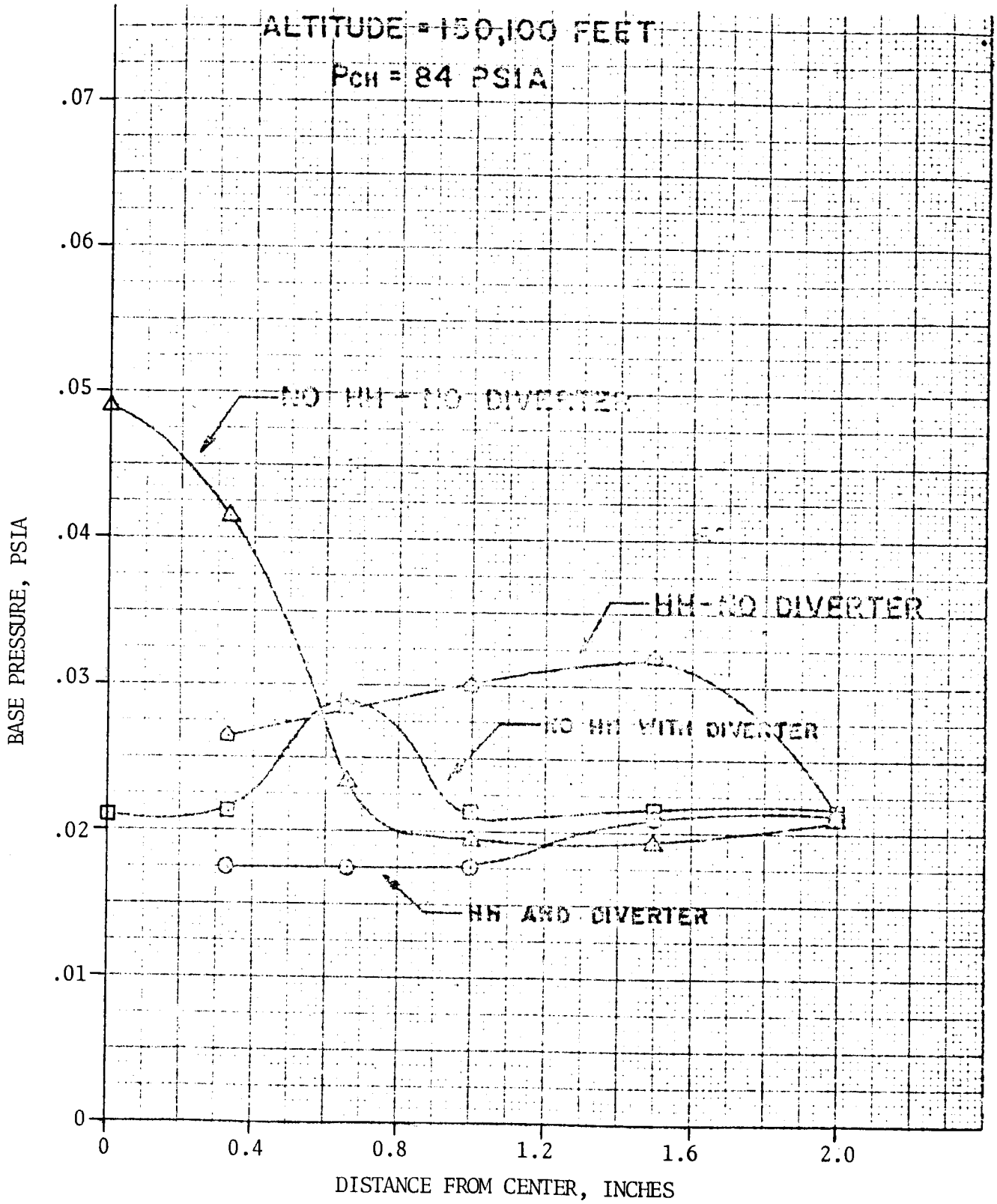

FIGURE 5.4-26. S-IV 4-ENGINE 1/27.75 SCALE COLD FLOW MODEL - EFFECT OF HELIUM HEATER EXHAUST AND DIVERTER ON BASE PRESSURE DISTRIBUTION

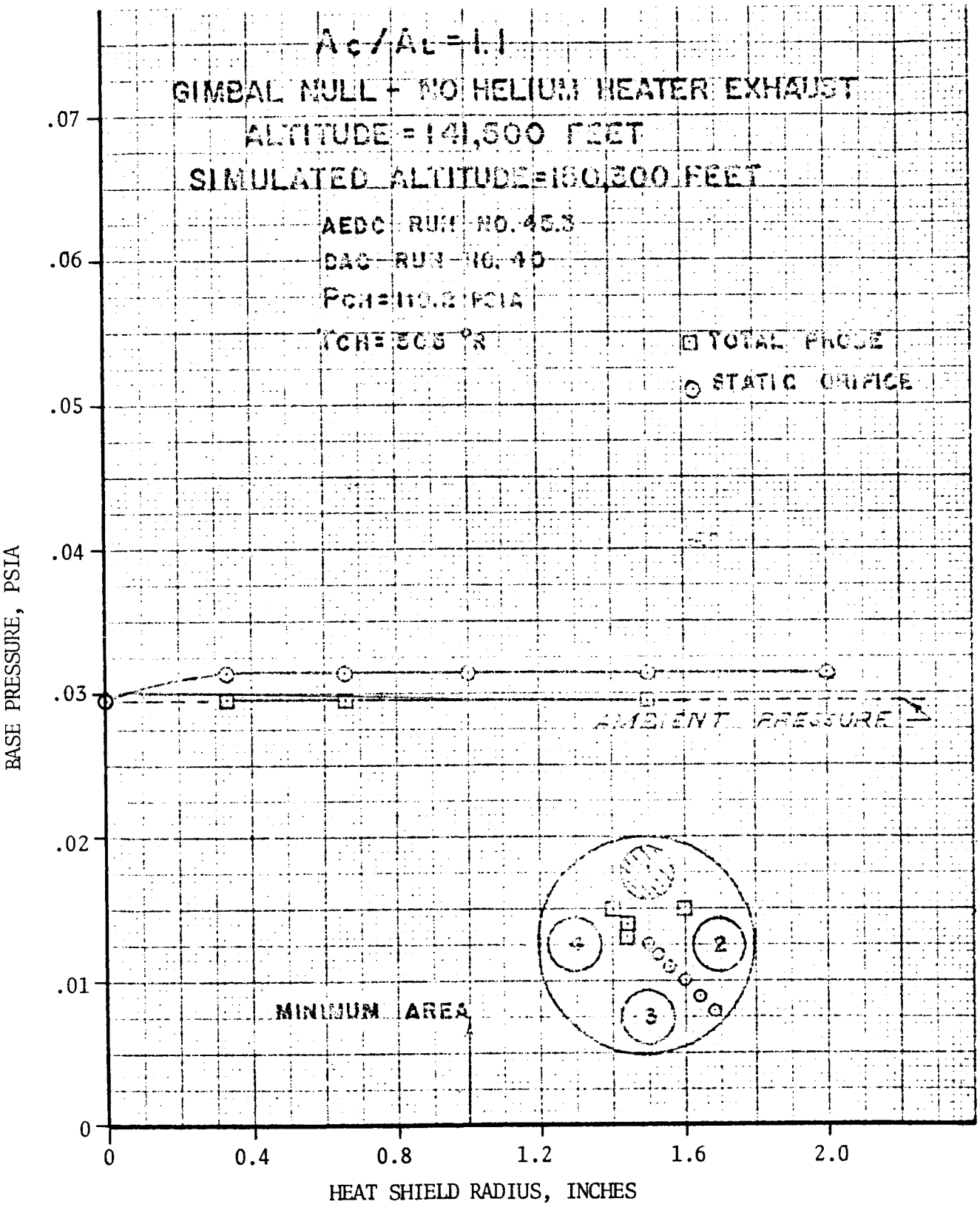

FIGURE 5.4-27. S-IV 4-ENGINE 1/27.75 SCALE COLD FLOW MODEL - BASE HEAT SHIELD PRESSURE DISTRIBUTION ONE ENGINE OUT CONFIGURATION

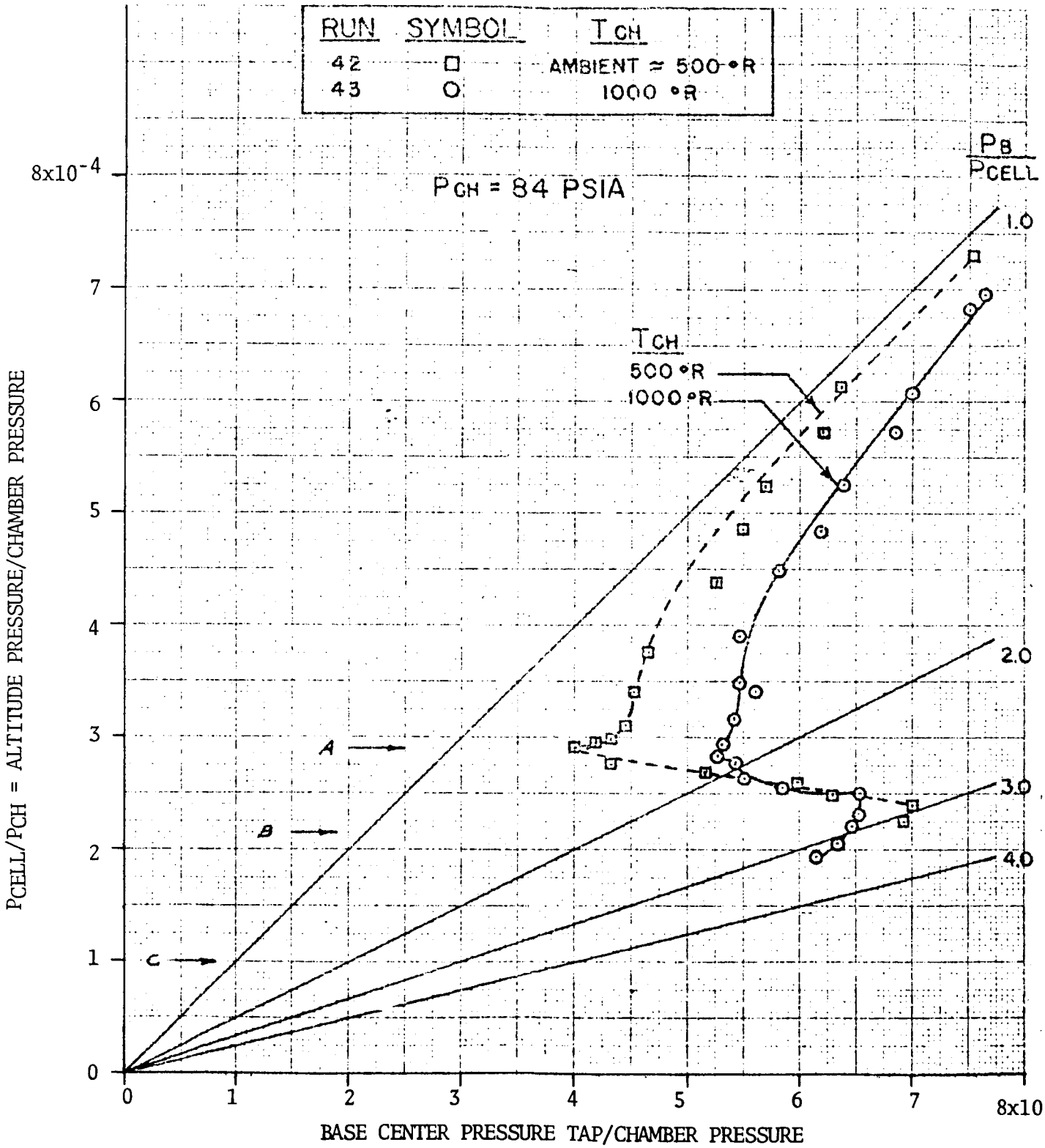

FIGURE 5.4-28. S-IV 4-ENGINE 1/27.75 SCALE COLD FLOW MODEL - EFFECT OF ALTITUDE AND CHAMBER TEMPERATURE ON THE BASE CENTER PRESSURE

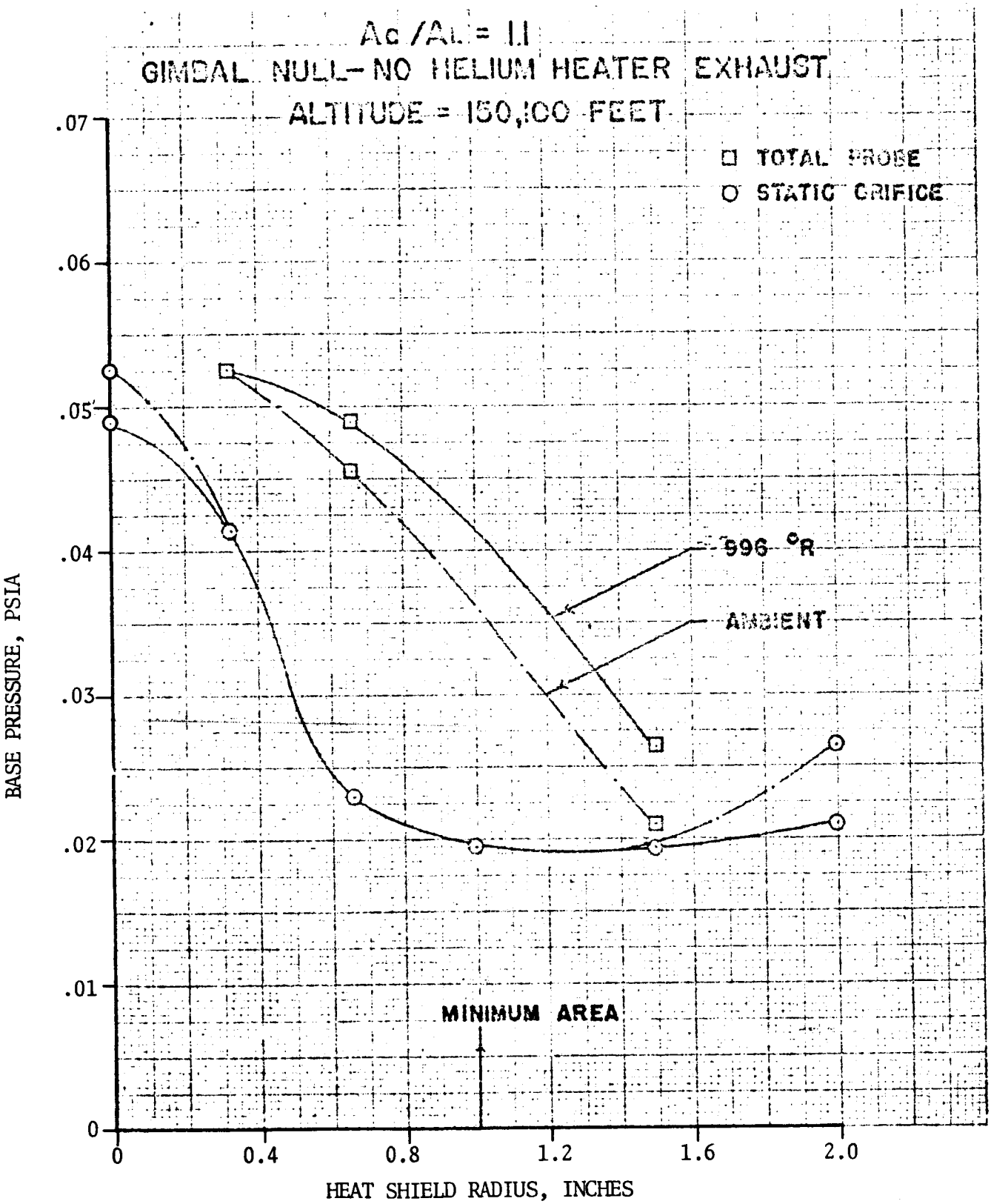

FIGURE 5.4-29. S-IV 4-ENGINE 1/27.75 SCALE COLD FLOW MODEL - EFFECT OF CHAMBER TEMPERATURE ON BASE HEAT SHIELD PRESSURE DISTRIBUTION

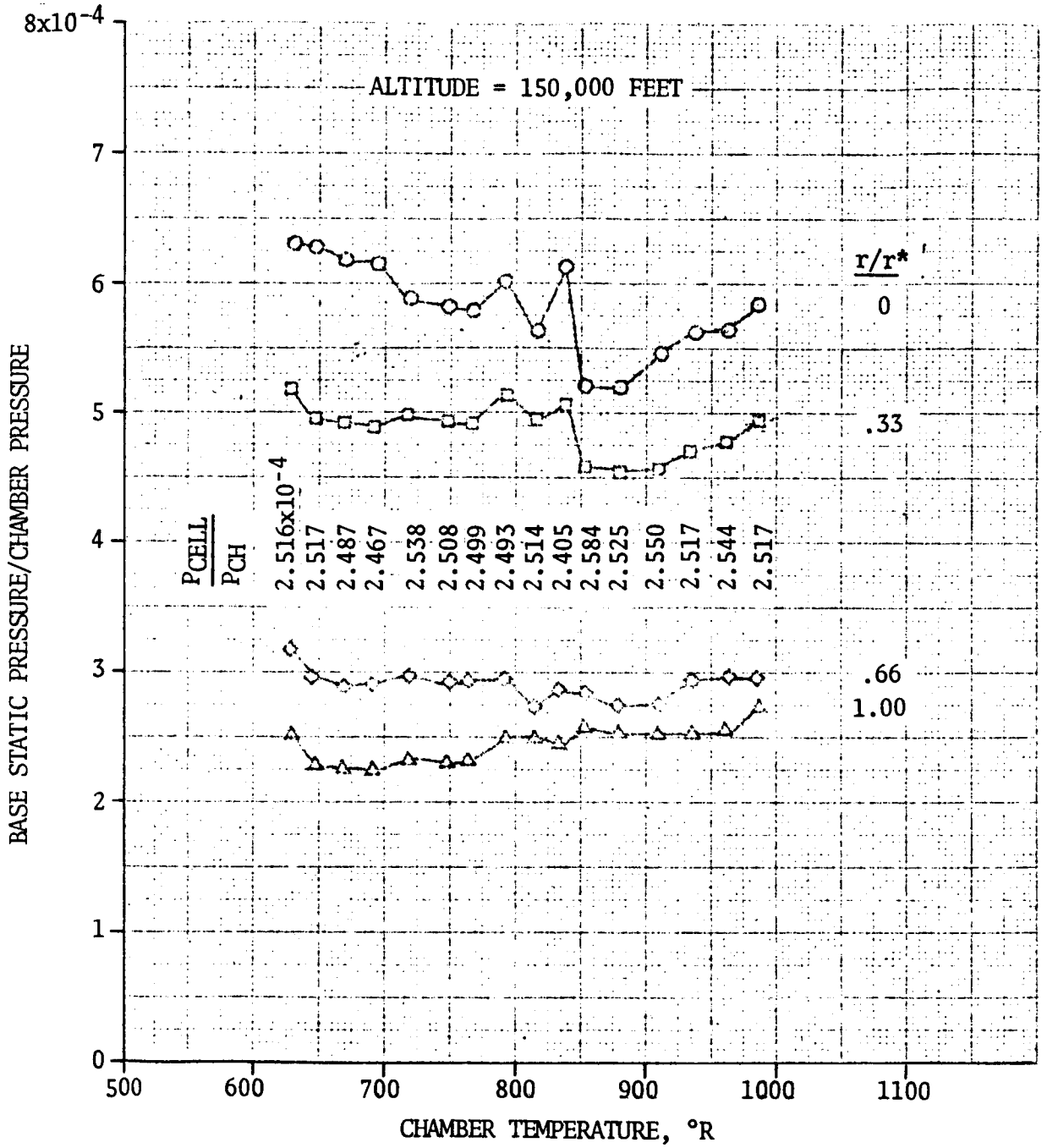

FIGURE 5.4-30. S-IV 4-ENGINE 1/27.75 SCALE COLD FLOW MODEL - EFFECT OF CHAMBER TEMPERATURE ON THE BASE PRESSURE DISTRIBUTION

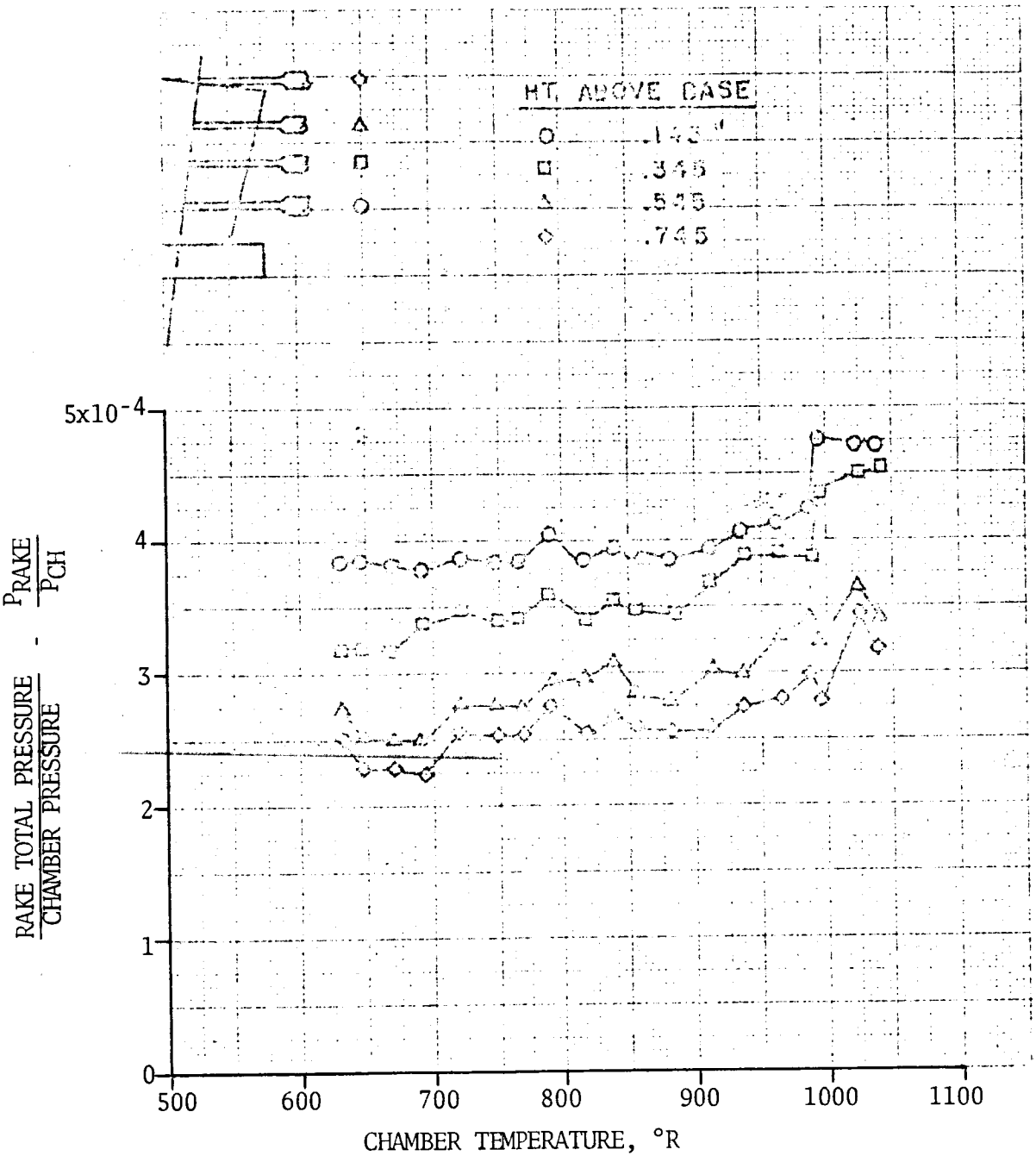

FIGURE 5.4-31. S-IV 4-ENGINE 1/27.75 SCALE COLD FLOW MODEL - EFFECT OF CHAMBER TEMPERATURE ON VENT AREA PRESSURE DISTRIBUTION

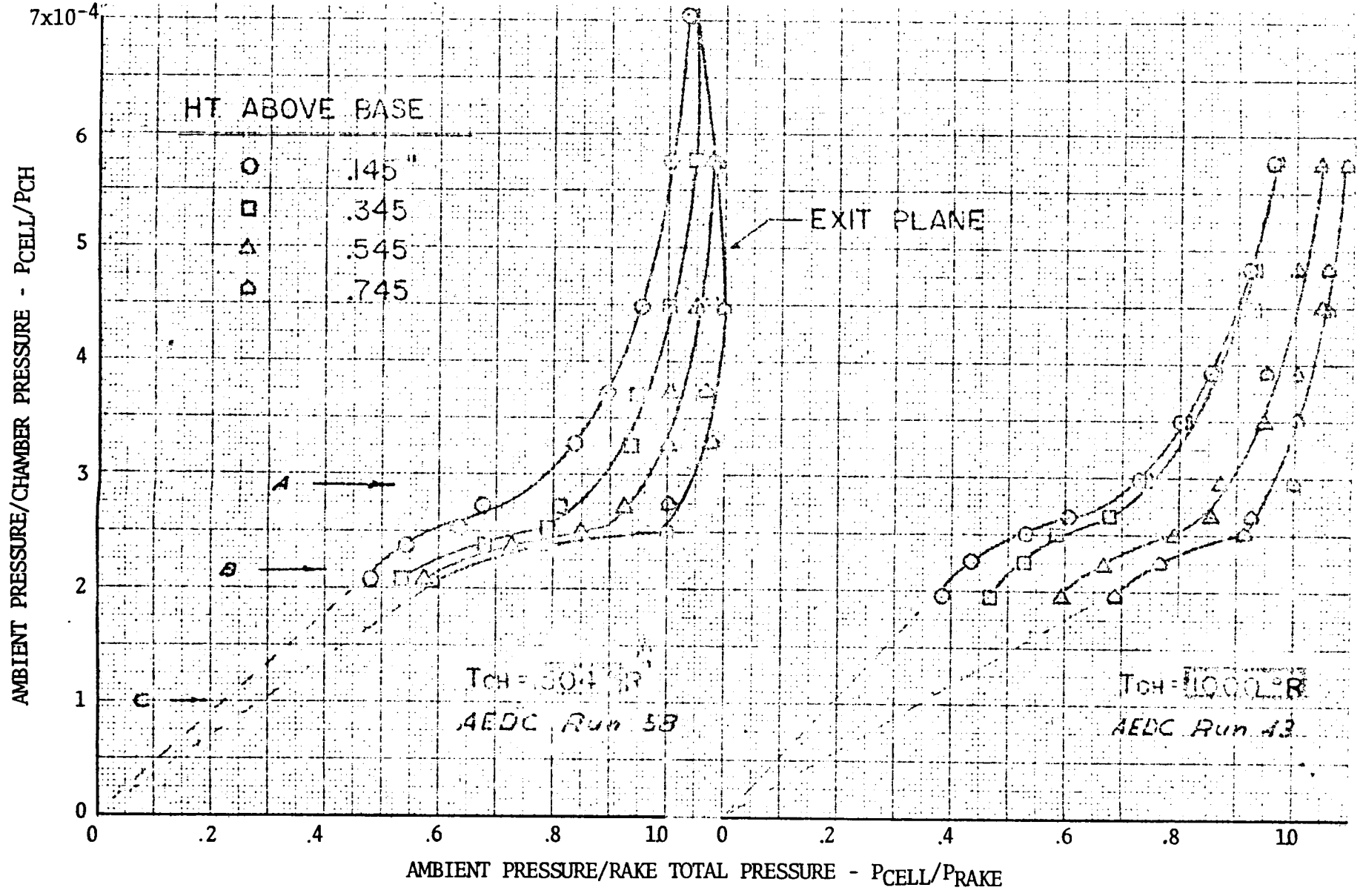

FIGURE 5.4-32. S-IV 4-ENGINE 1/27.75 SCALE COLD FLOW MODEL - VENT AREA PRESSURE DISTRIBUTION

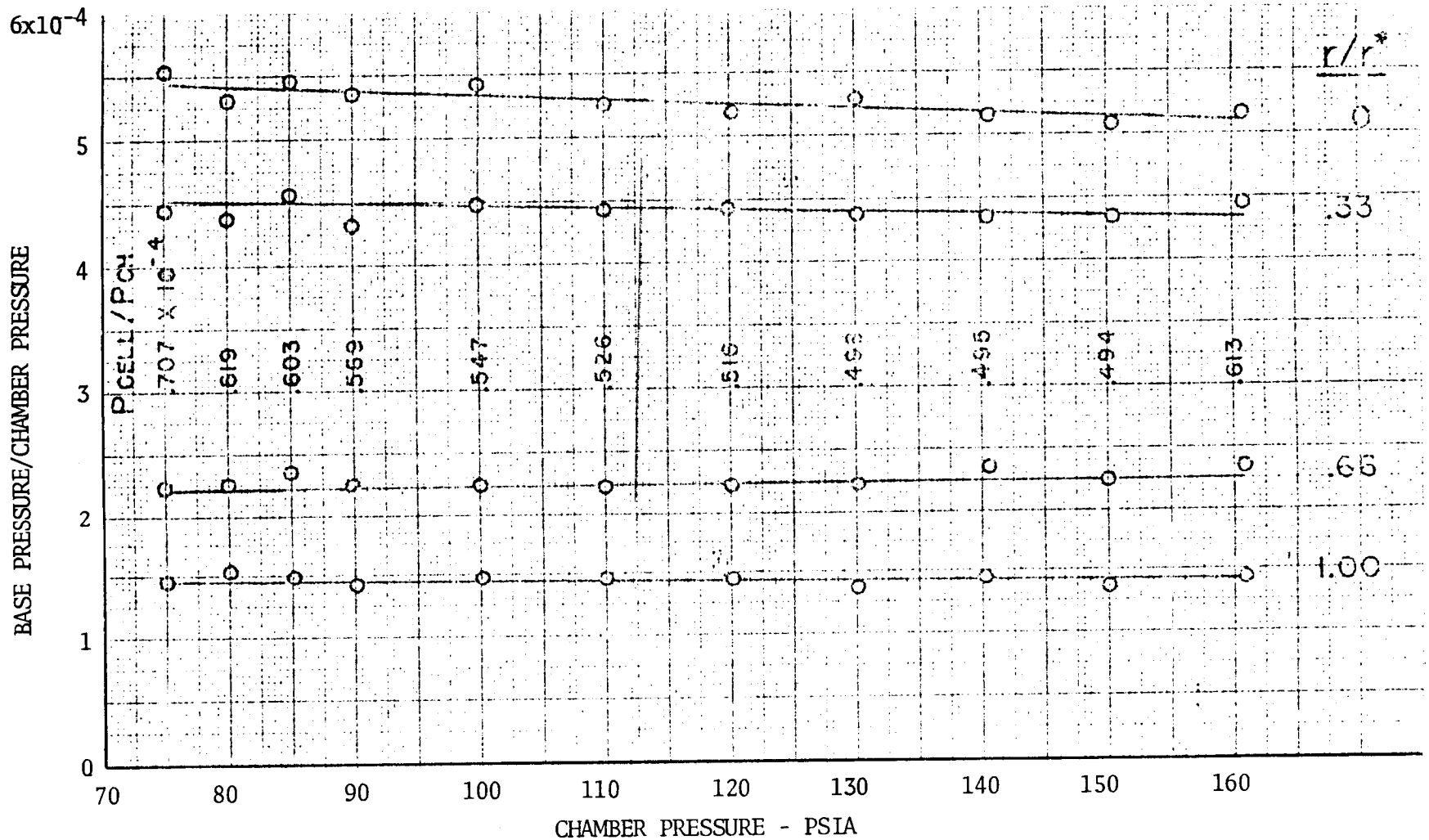

FIGURE 5.4-33. S-IV 4-ENGINE 1/27.75 SCALE COLD FLOW MODEL - EFFECT OF CHAMBER PRESSURE ON HEAT SHIELD PRESSURE DISTRIBUTION FOR ALTITUDES GREATER THAN CRITICAL

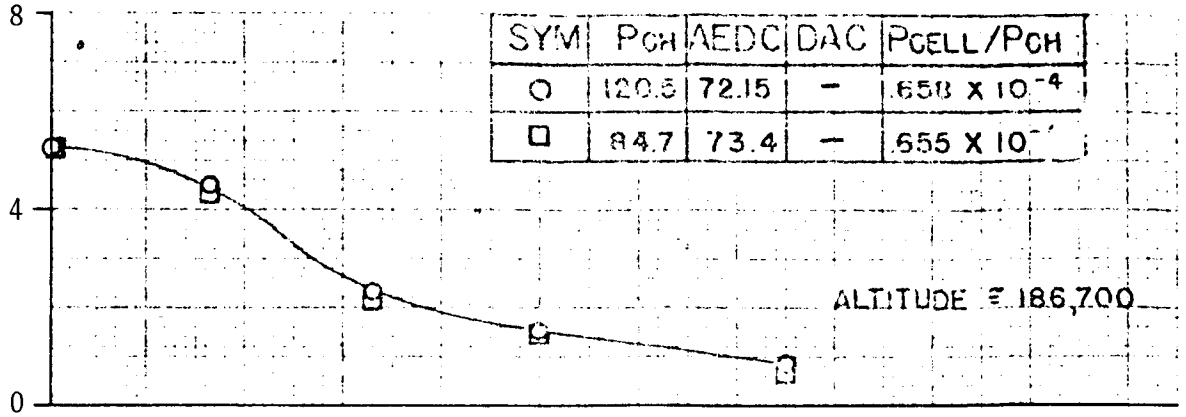

(A) ABOVE POINT C

NOTE: POINTS A, B AND C ARE DEFINED IN FIGURE 5.4-17.

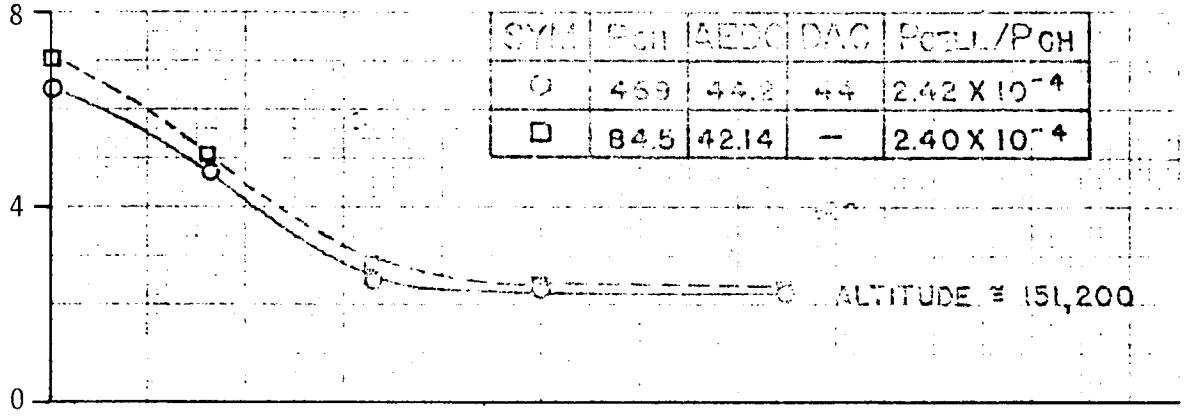

(B) BETWEEN POINTS A AND B

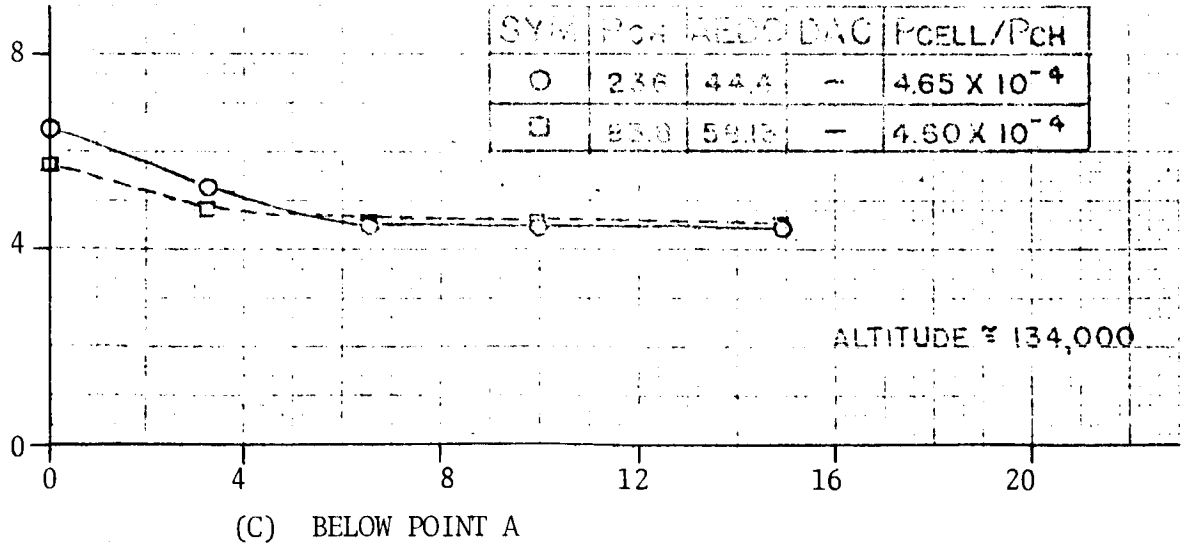

(C) BELOW POINT A

BASE PRESSURE / CHAMBER PRESSURE x 10^4

FIGURE 5.4-34. S-IV 4-ENGINE 1/27.75 SCALE COLD FLOW MODEL - EFFECT OF CHAMBER PRESSURE FOR ALTITUDES ABOVE AND BELOW THE CRITICAL ALTITUDE

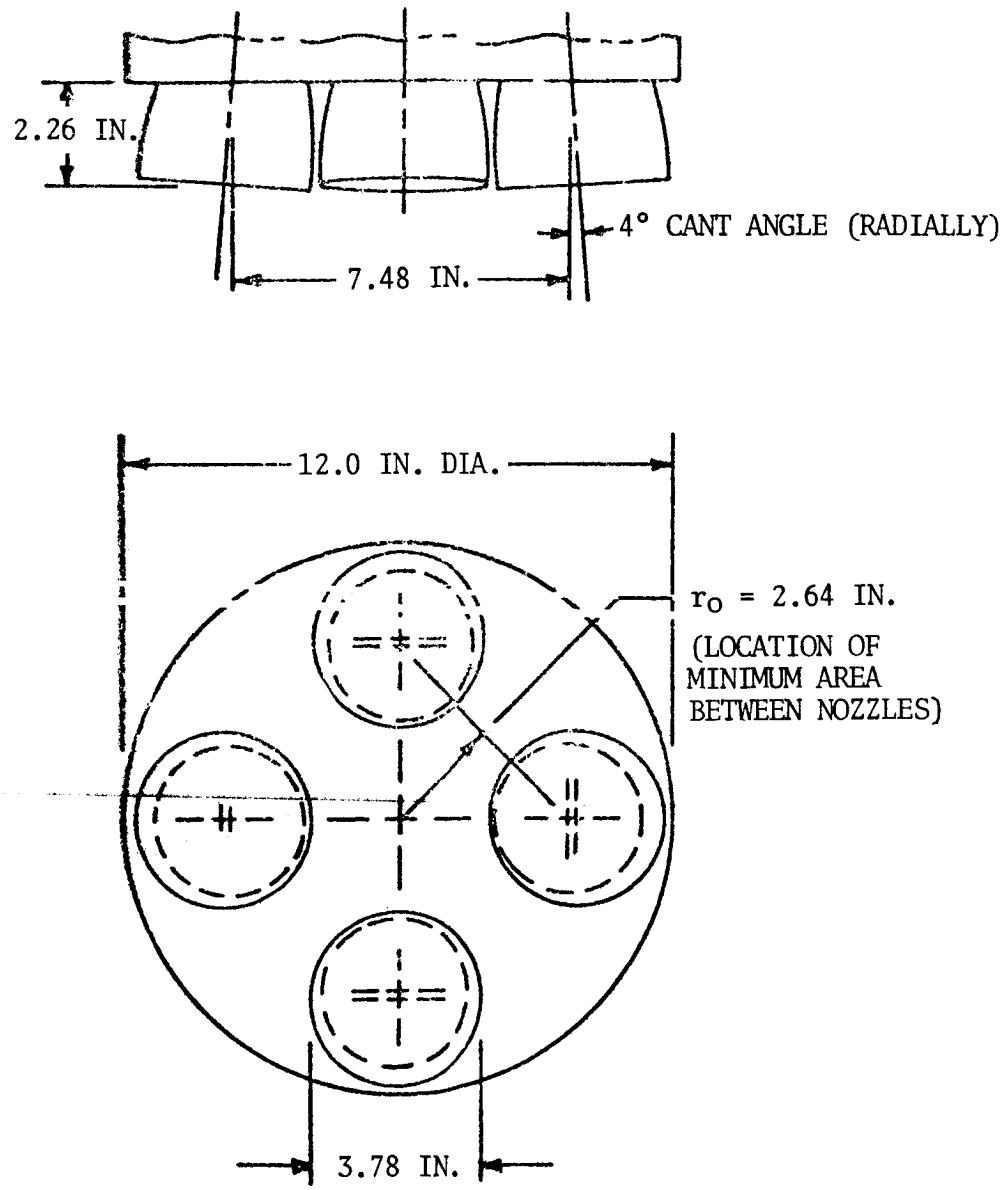

FIGURE 5.4-35. S-IV 4-ENGINE 1/10 SCALE SHOCK TUBE MODEL - BASE REGION CONFIGURATION

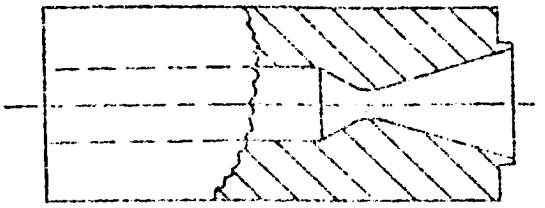

THROAT DIA. = 0.160 INCHES
EXIT DIA. = 0.540 INCHES

NOTE: HYDROGEN GAS, AT THE FOLLOWING CONDITIONS, WAS USED TO SIMULATE THE PROTOTYPE HELIUM HEATER EXHAUST. (SECONDARY EXHAUST)

CHAMBER TEMPERATURE: 530°R

CHAMBER PRESSURE: 15 PSIA

NOZZLE

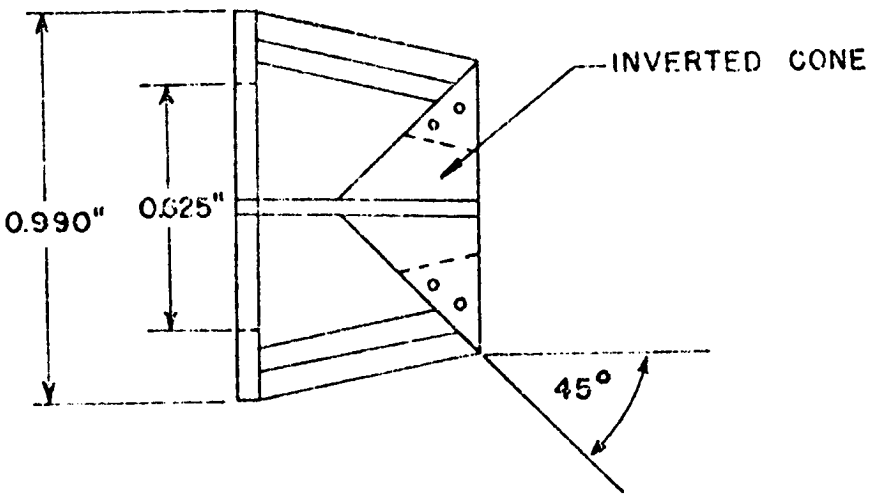

DIVERTER

FIGURE 5.4-36. S-IV 4-ENGINE 1/10 SCALE SHOCK TUBE MODEL - HELIUM HEATER EXHAUST NOZZLE AND DIVERTER

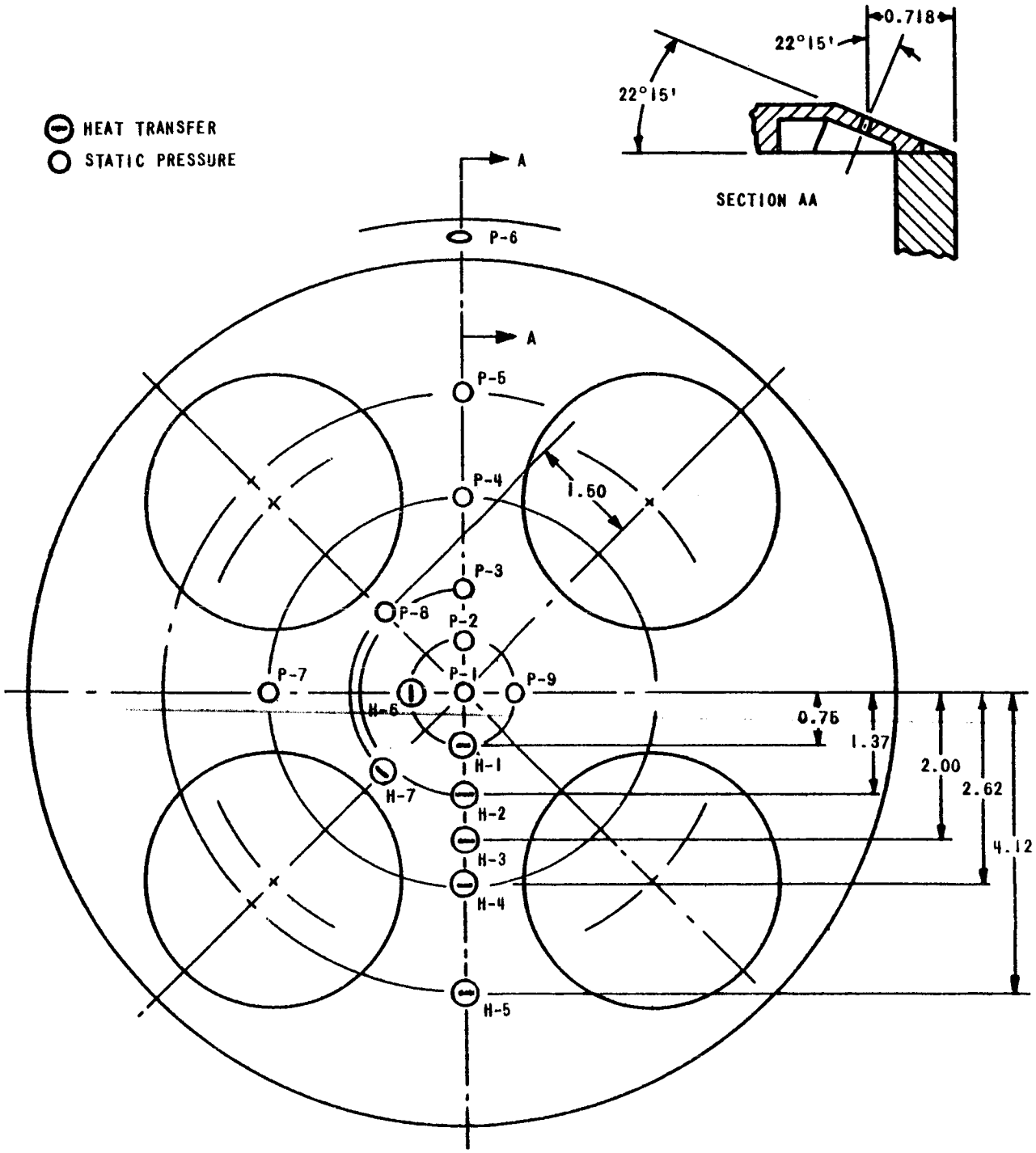

FIGURE 5.4-37. S-IV 4-ENGINE 1/10 SCALE SHOCK TUBE MODEL - BASE REGION INSTRUMENTATION (FIRST SERIES)

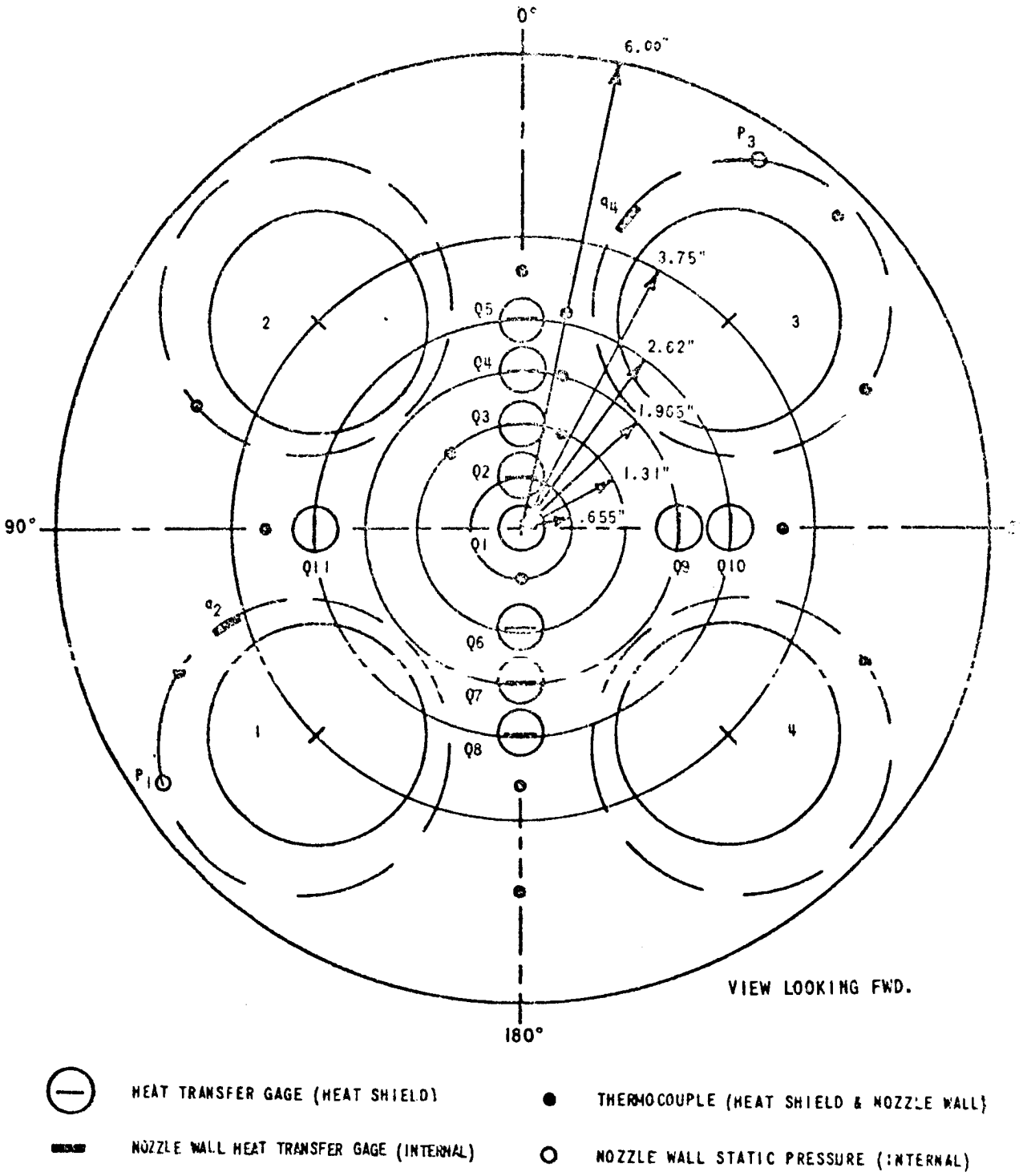

FIGURE 5.4-38. S-IV 4-ENGINE 1/10 SCALE SHOCK TUBE MODEL - BASE REGION INSTRUMENTATION (SECOND SERIES)

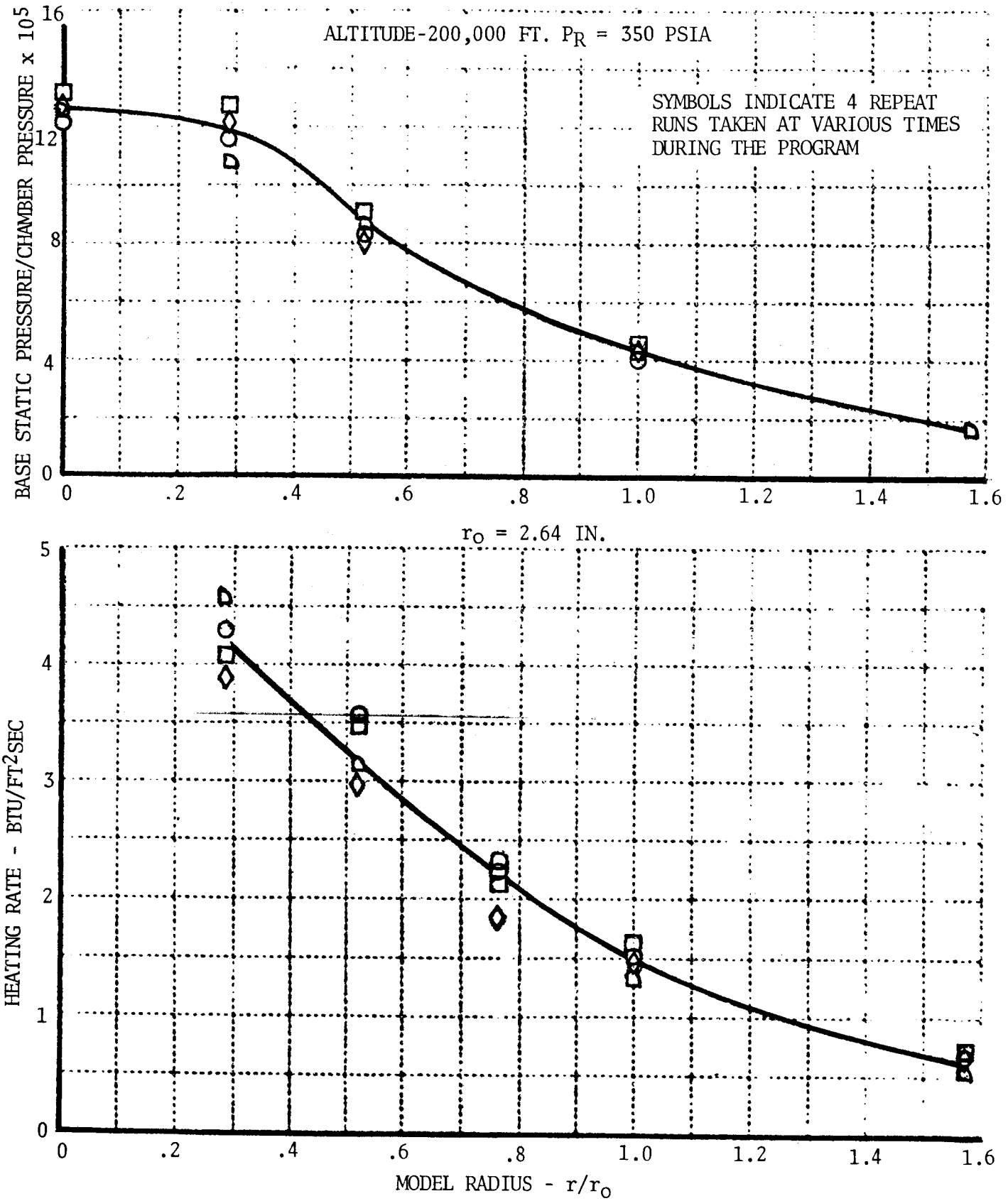

FIGURE 5.4-39. S-IV 4-ENGINE 1/10 SCALE SHOCK TUBE MODEL - DATA REPEATABILITY

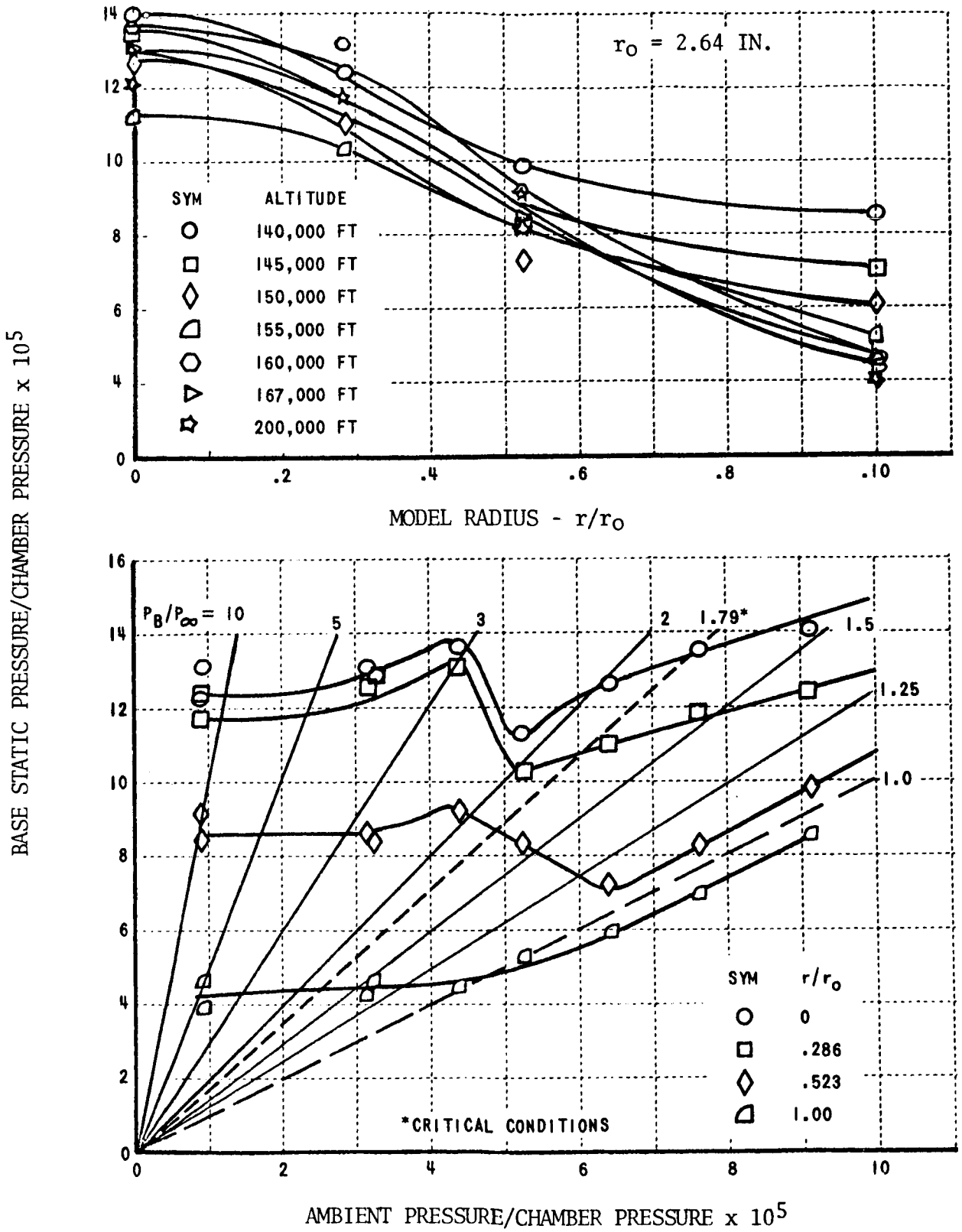

FIGURE 5.4-40. S-IV 4-ENGINE 1/10 SCALE SHOCK TUBE MODEL - EFFECT OF ALTITUDE ON BASE HEAT SHIELD PRESSURE DISTRIBUTIONS

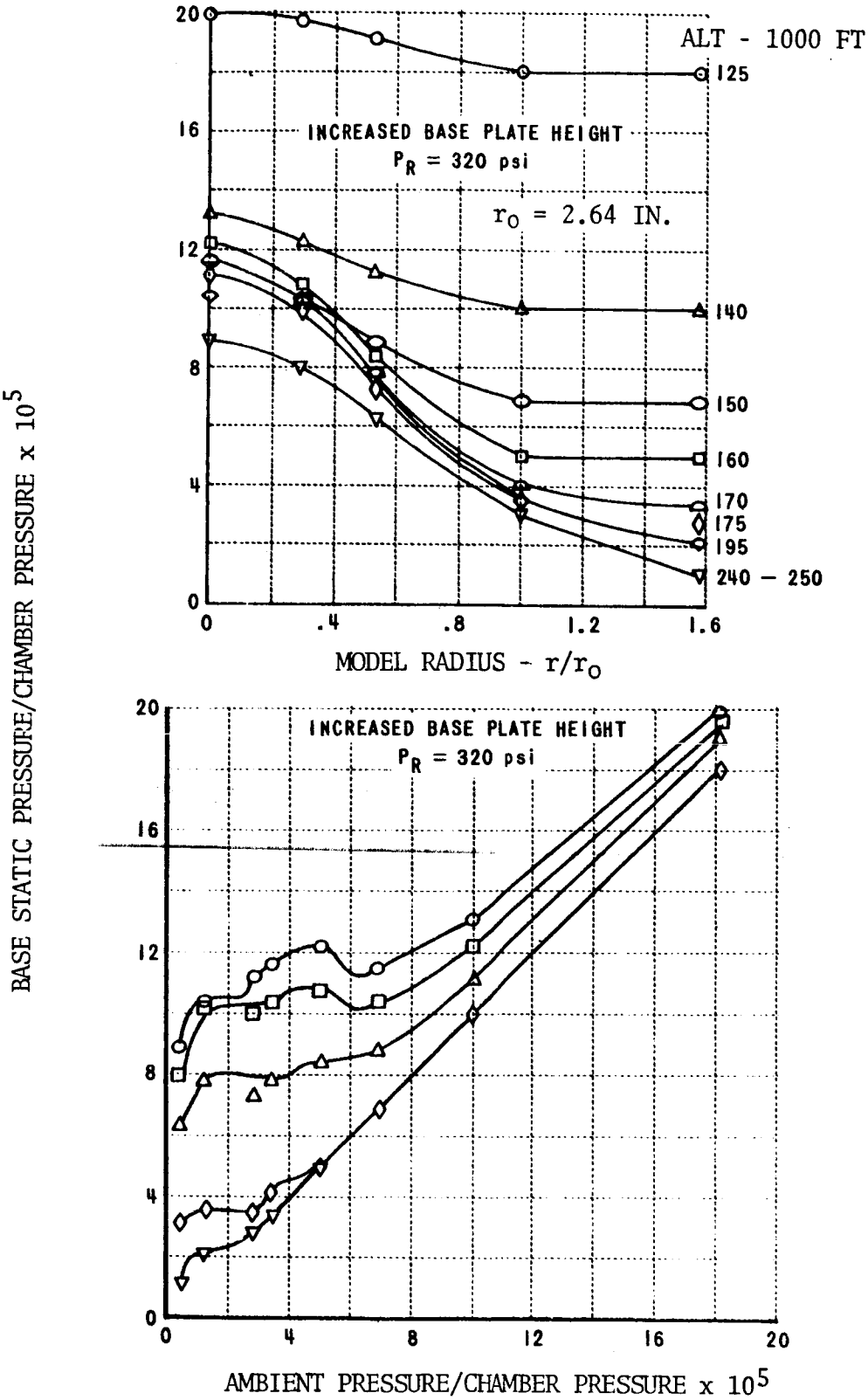

FIGURE 5.4-41. S-IV 4-ENGINE 1/10 SCALE SHOCK TUBE MODEL - EFFECT OF ALTITUDE ON BASE HEAT SHIELD PRESSURE DISTRIBUTIONS (INCREASED BASE PLATE HEIGHT)

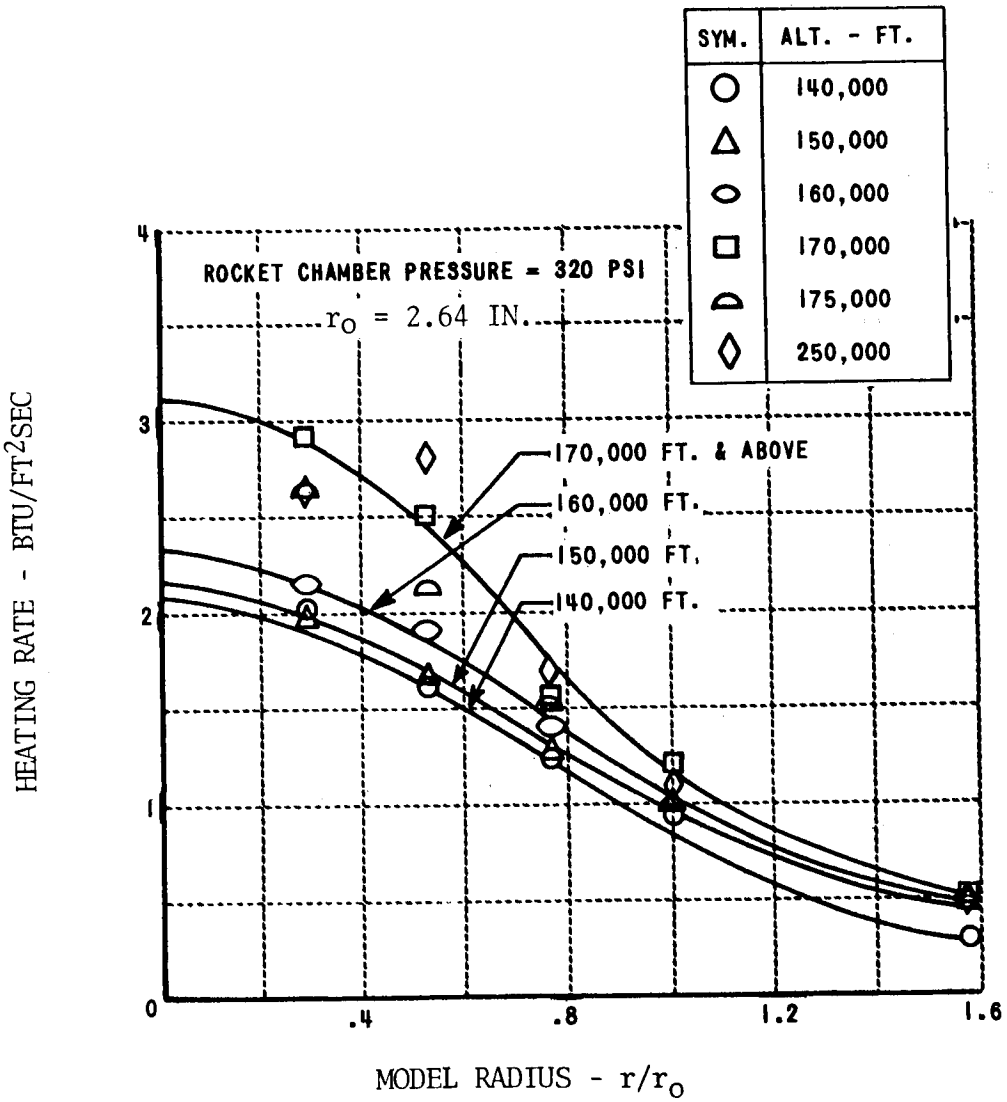

FIGURE 5.4-42. S-IV 4-ENGINE 1/10 SCALE SHOCK TUBE MODEL - EFFECT OF ALTITUDE ON BASE HEAT SHIELD HEAT TRANSFER DISTRIBUTION (INCREASED BASE PLATE HEIGHT)

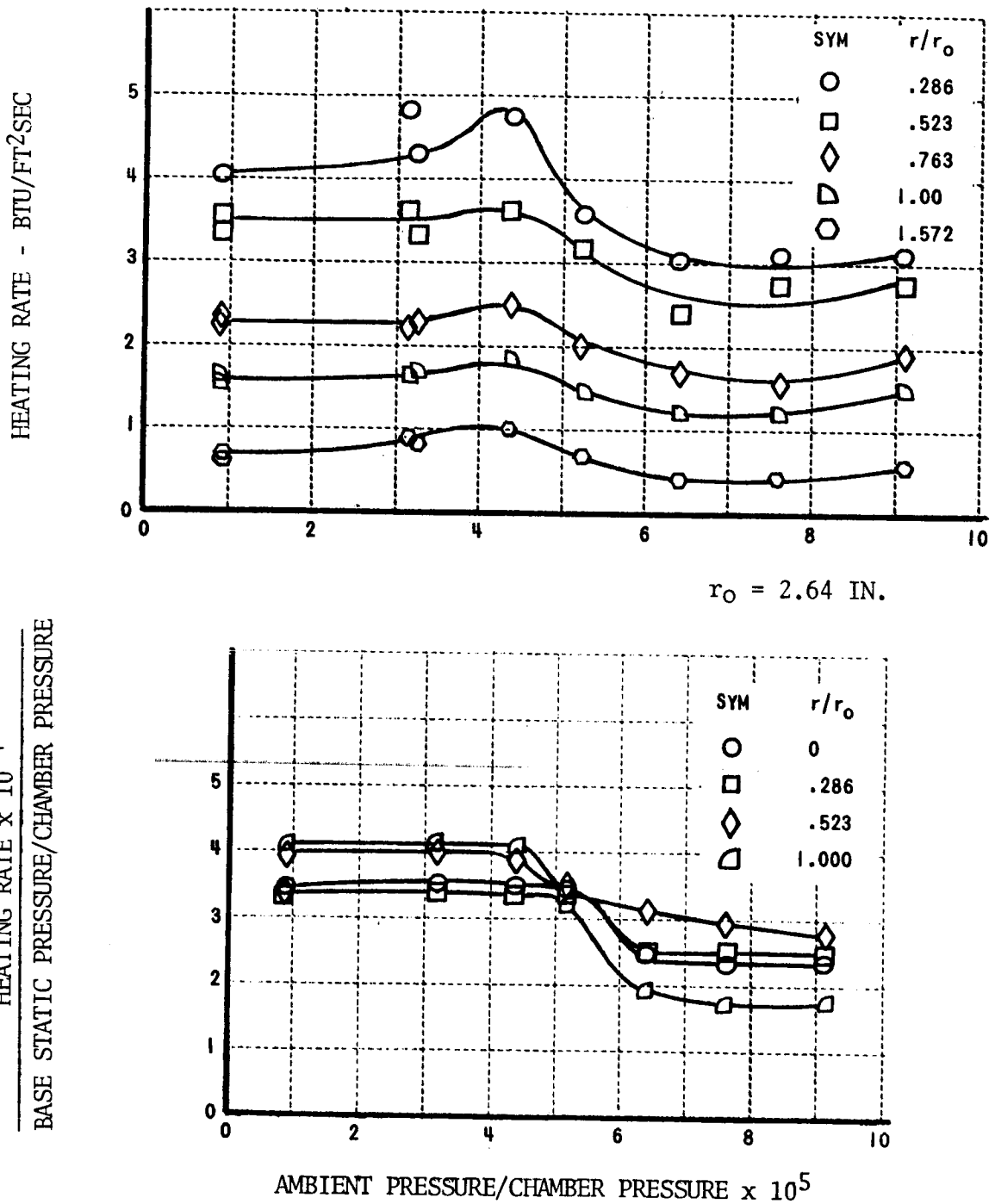

FIGURE 5.4-43. S-IV 4-ENGINE 1/10 SCALE SHOCK TUBE MODEL - CORRELATION OF BASE HEAT SHIELD HEAT TRANSFER AND AMBIENT PRESSURE

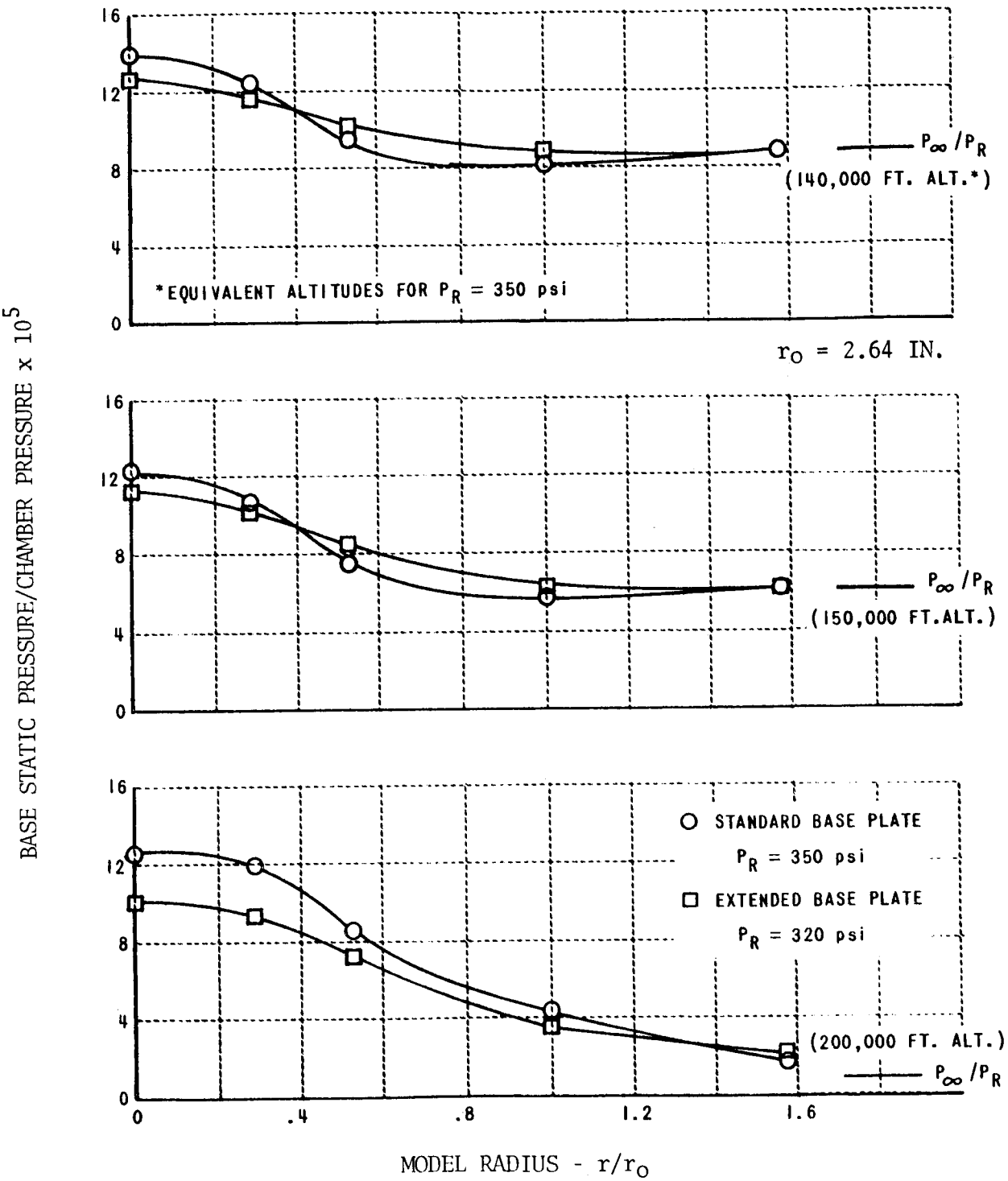

FIGURE 5.4-44. S-IV 4-ENGINE 1/10 SCALE SHOCK TUBE MODEL - EFFECT OF BASE PLATE LOCATION ON BASE PRESSURE DISTRIBUTIONS

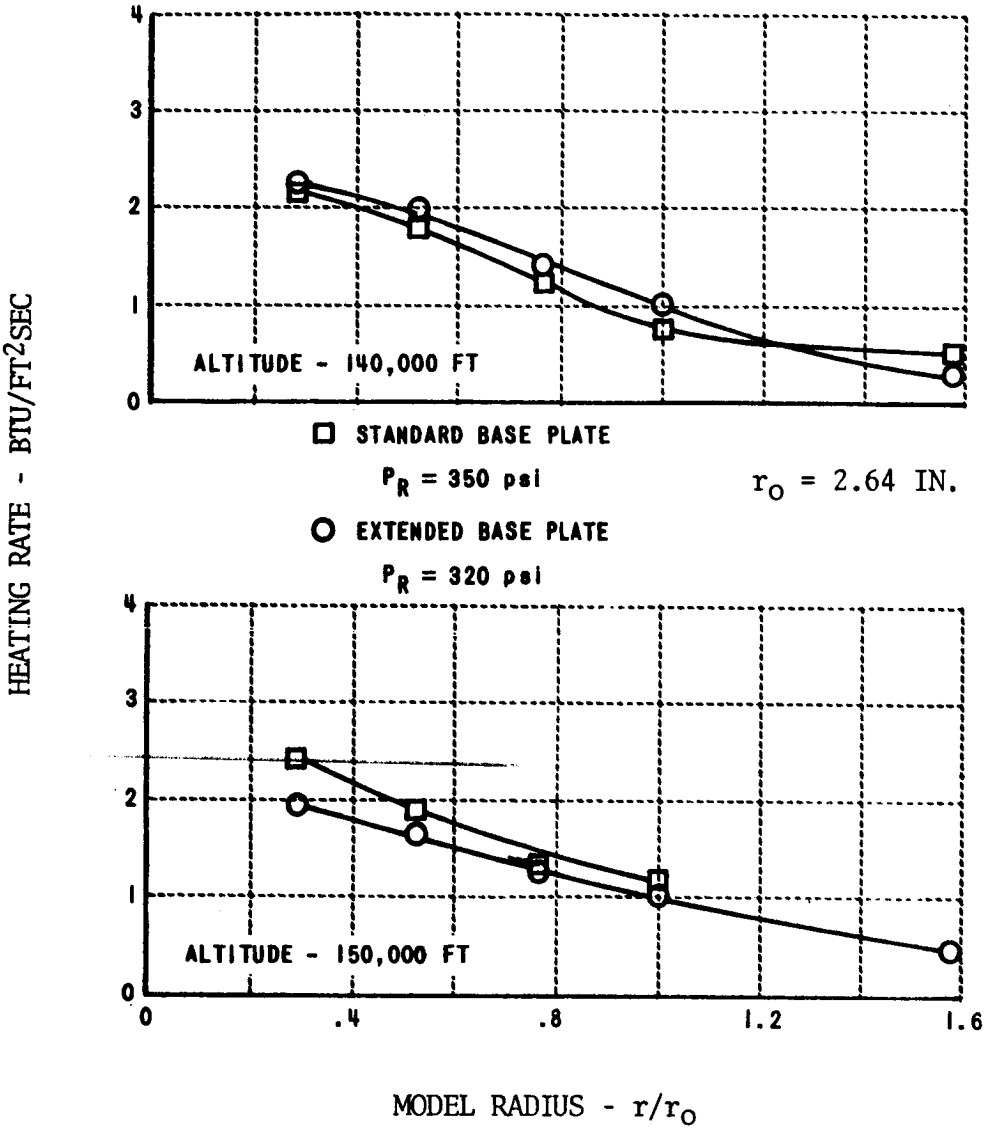

FIGURE 5.4-45. S-IV 4-ENGINE 1/10 SCALE SHOCK TUBE MODEL - EFFECT OF BASE PLATE LOCATION BASE HEATING RATES

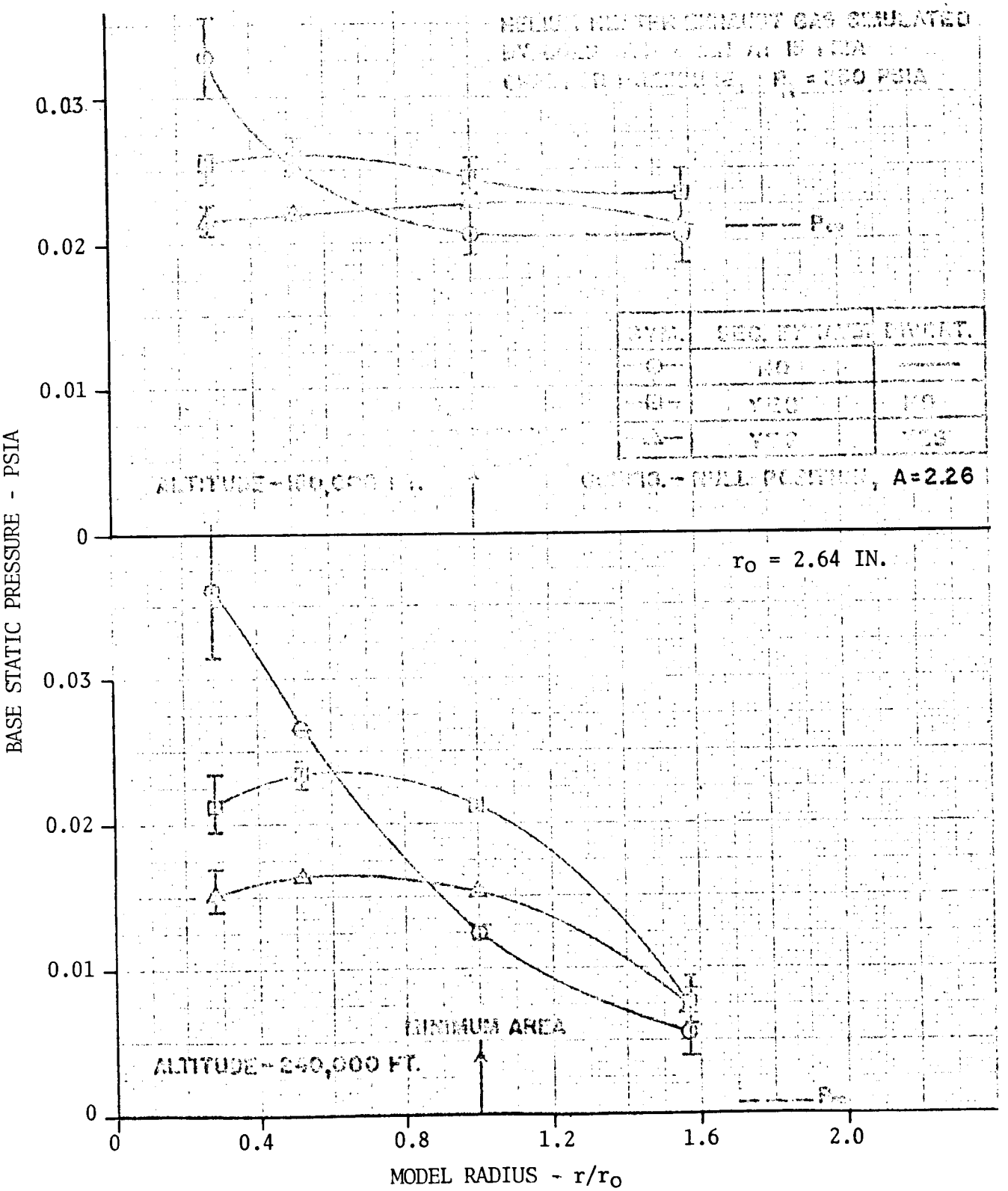

FIGURE 5.4-46. S-IV 4-ENGINE 1/10 SCALE SHOCK TUBE MODEL - EFFECT OF SECONDARY FLOW ON BASE HEAT SHIELD PRESSURE DISTRIBUTION

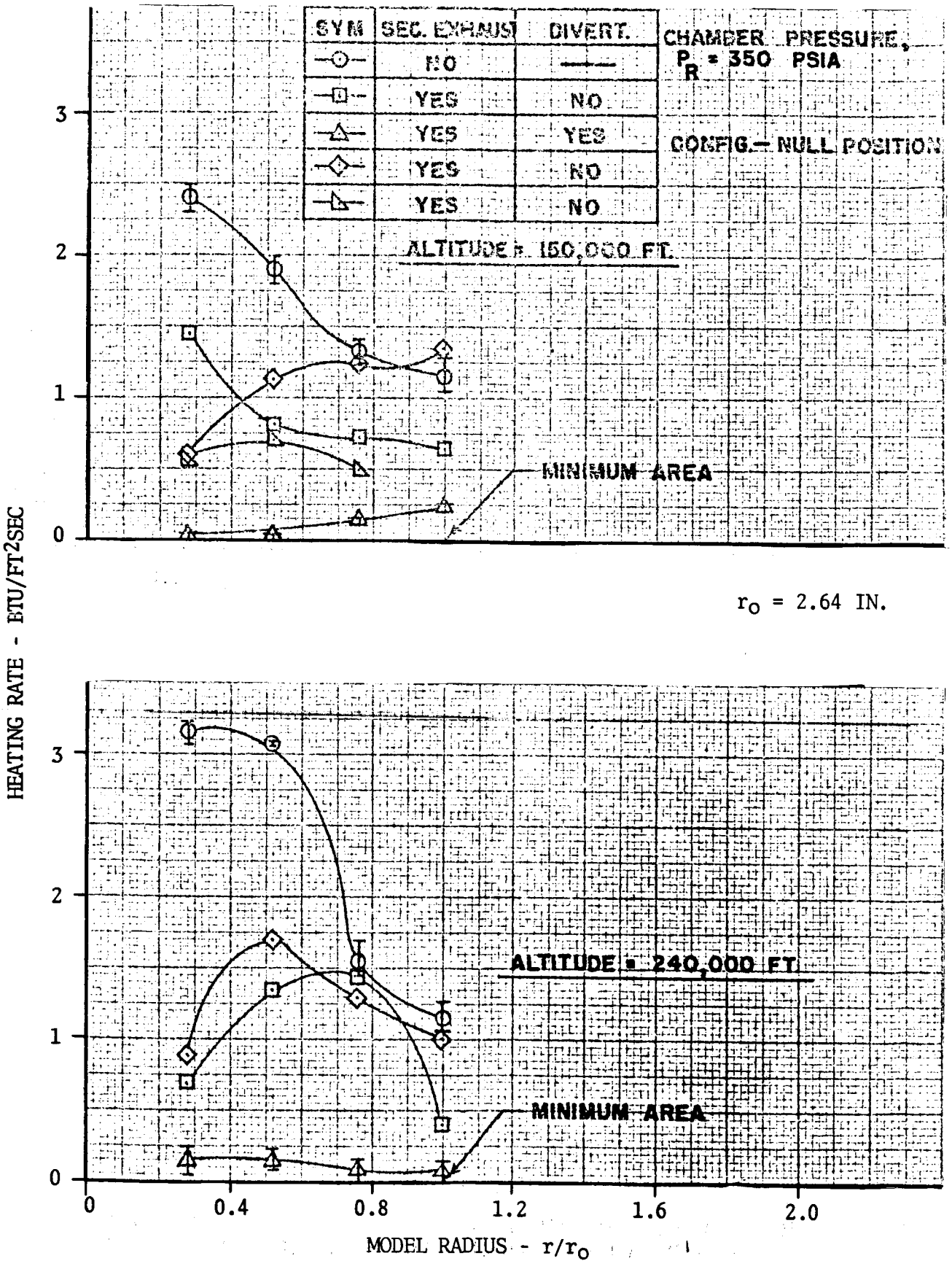

FIGURE 5.4-47. S-IV 4-ENGINE 1/10 SCALE SHOCK TUBE MODEL - EFFECT OF SECONDARY EXHUAST ON BASE HEAT SHIELD HEATING RATE

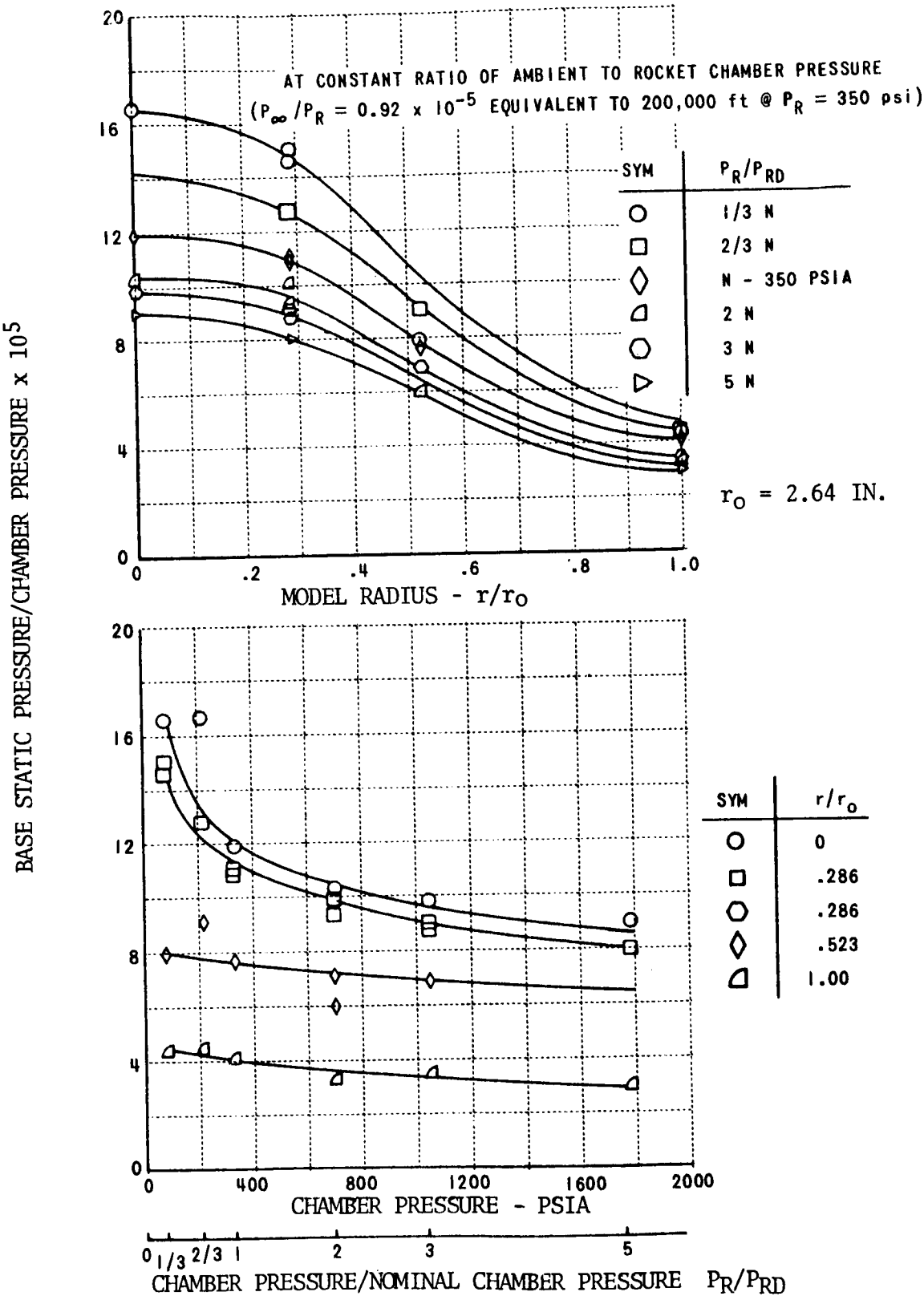

FIGURE 5.4-48. S-IV 4-ENGINE 1/10 SCALE SHOCK TUBE MODEL - EFFECT OF CHAMBER PRESSURE ON BASE HEAT SHIELD PRESSURE DISTRIBUTION

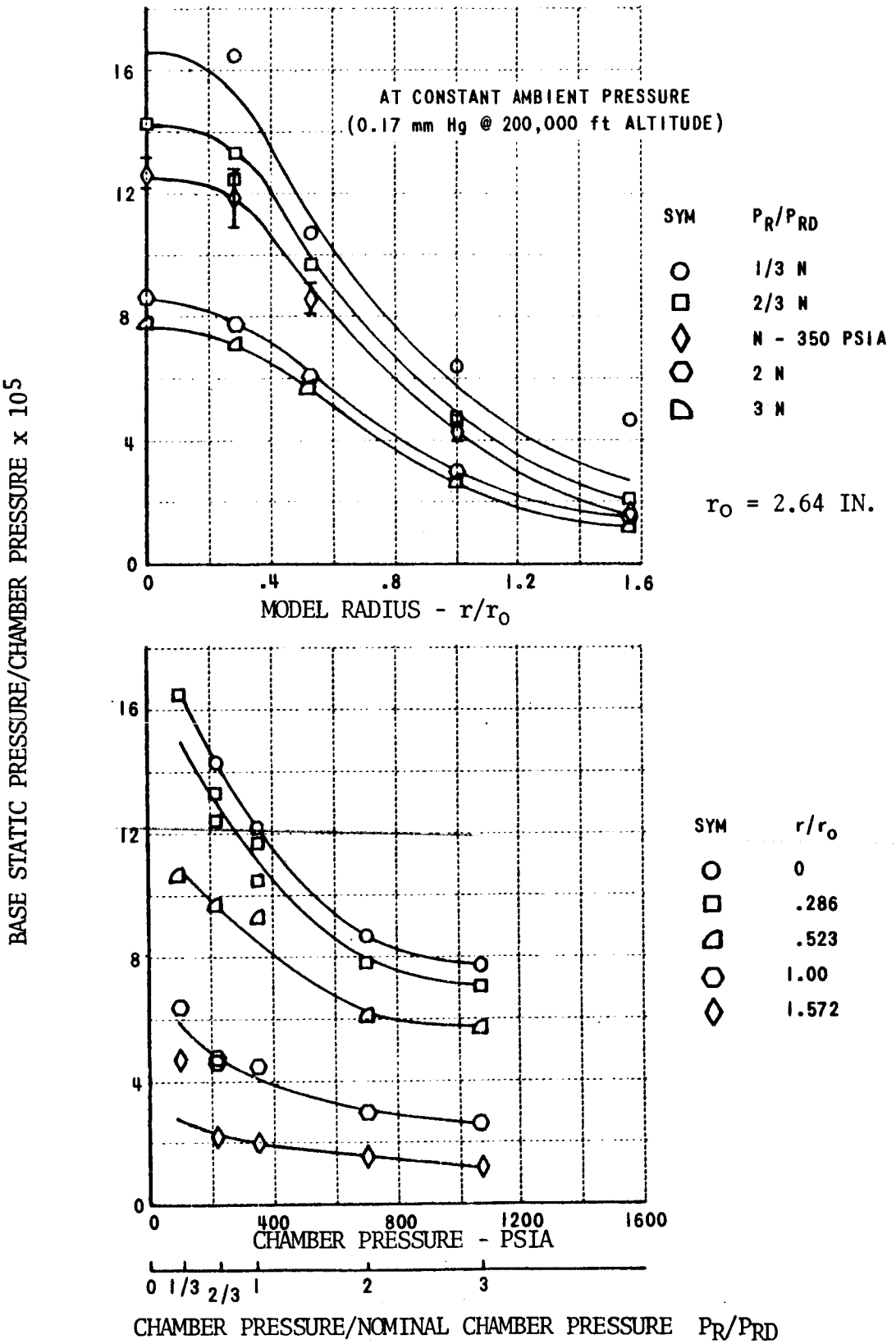

FIGURE 5.4-49. S-IV 4-ENGINE 1/10 SCALE SHOCK TUBE MODEL - EFFECT OF CHAMBER PRESSURE ON HEAT SHIELD PRESSURE DISTRIBUTION

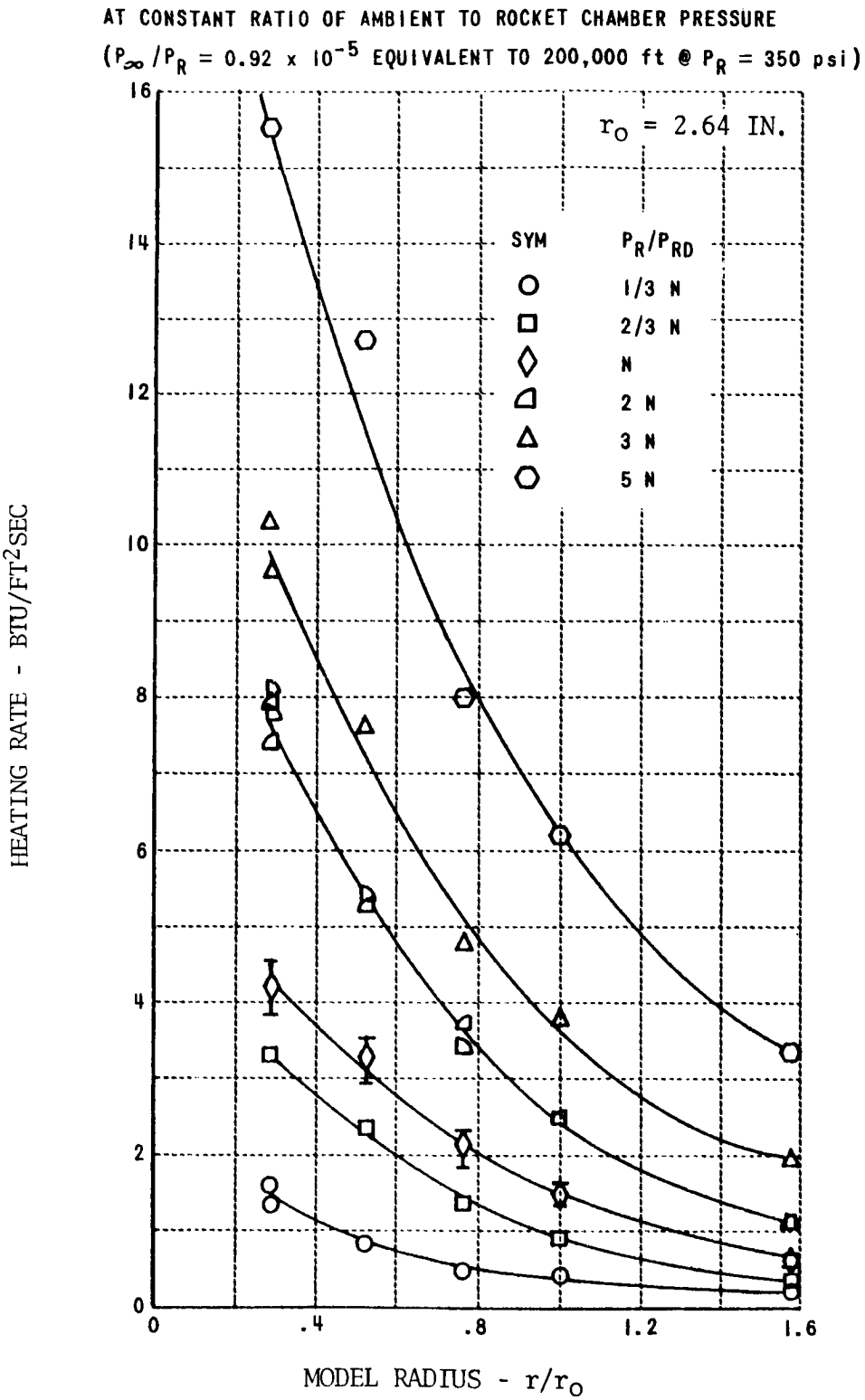

FIGURE 5.4-50. S-IV 4-ENGINE 1/10 SCALE SHOCK TUBE MODEL - EFFECT OF CHAMBER PRESSURE ON BASE HEAT TRANSFER

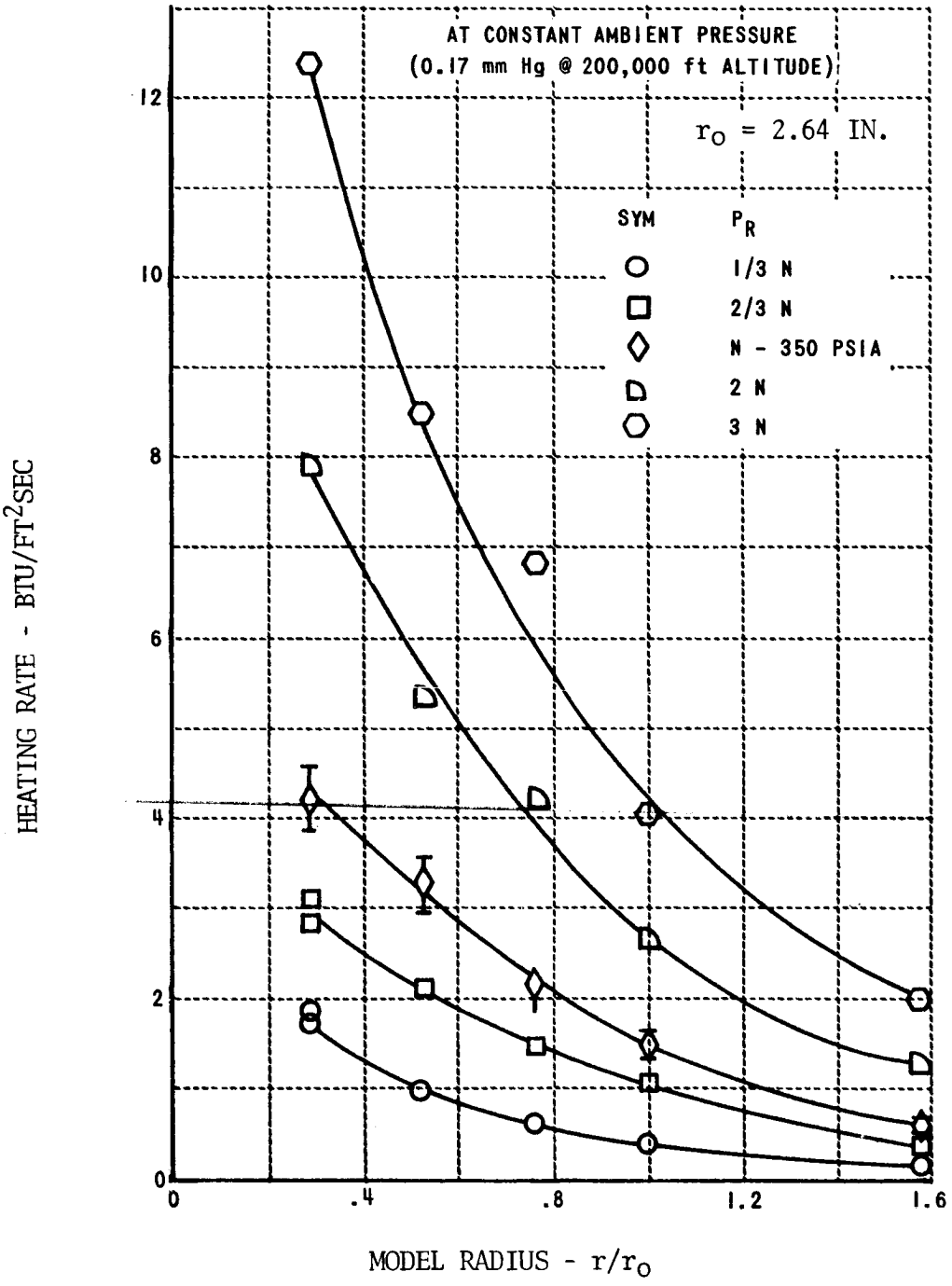

FIGURE 5.4-51. S-IV 4-ENGINE 1/10 SCALE SHOCK TUBE MODEL - EFFECT OF CHAMBER PRESSURE ON BASE HEAT SHIELD HEAT TRANSFER

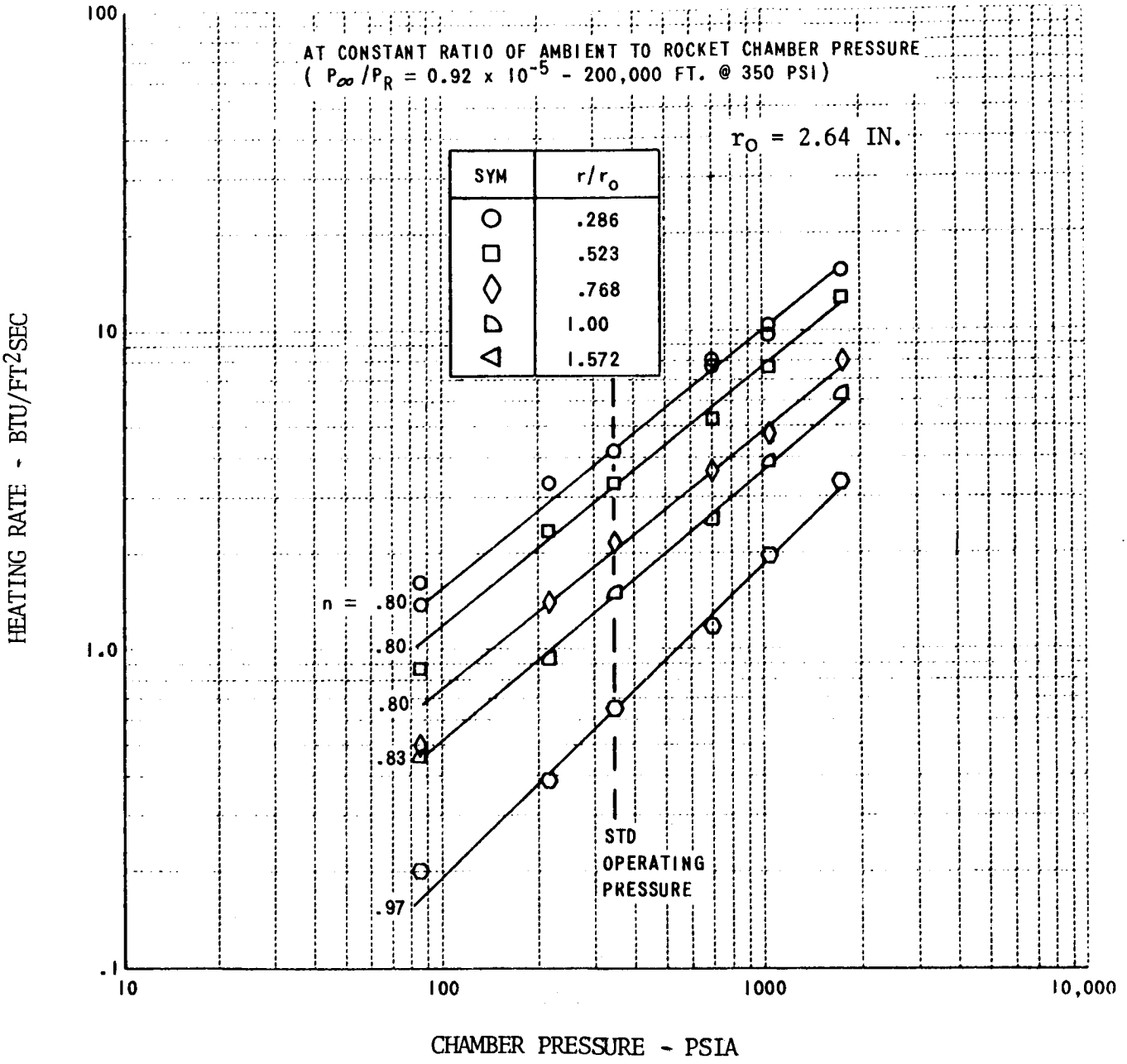

FIGURE 5.4-52. S-IV 4-ENGINE 1/10 SCALE SHOCK TUBE MODEL - EFFECT OF CHAMBER PRESSURE ON BASE HEAT SHIELD HEATING RATE

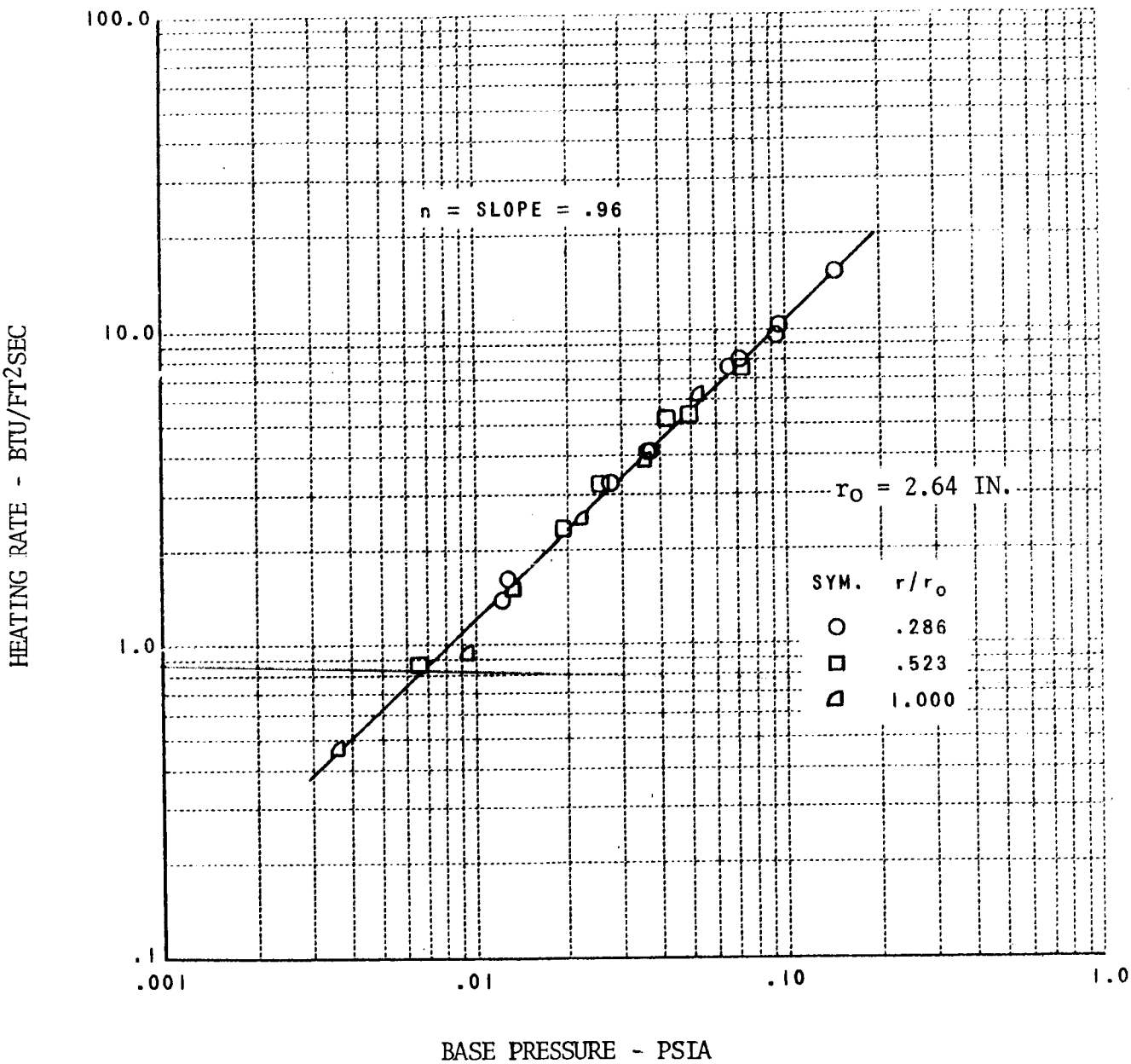

FIGURE 5.4-53. S-IV 4-ENGINE 1/10 SCALE SHOCK TUBE MODEL - CORRELATION OF HEAT TRANSFER RATE WITH BASE PRESSURE

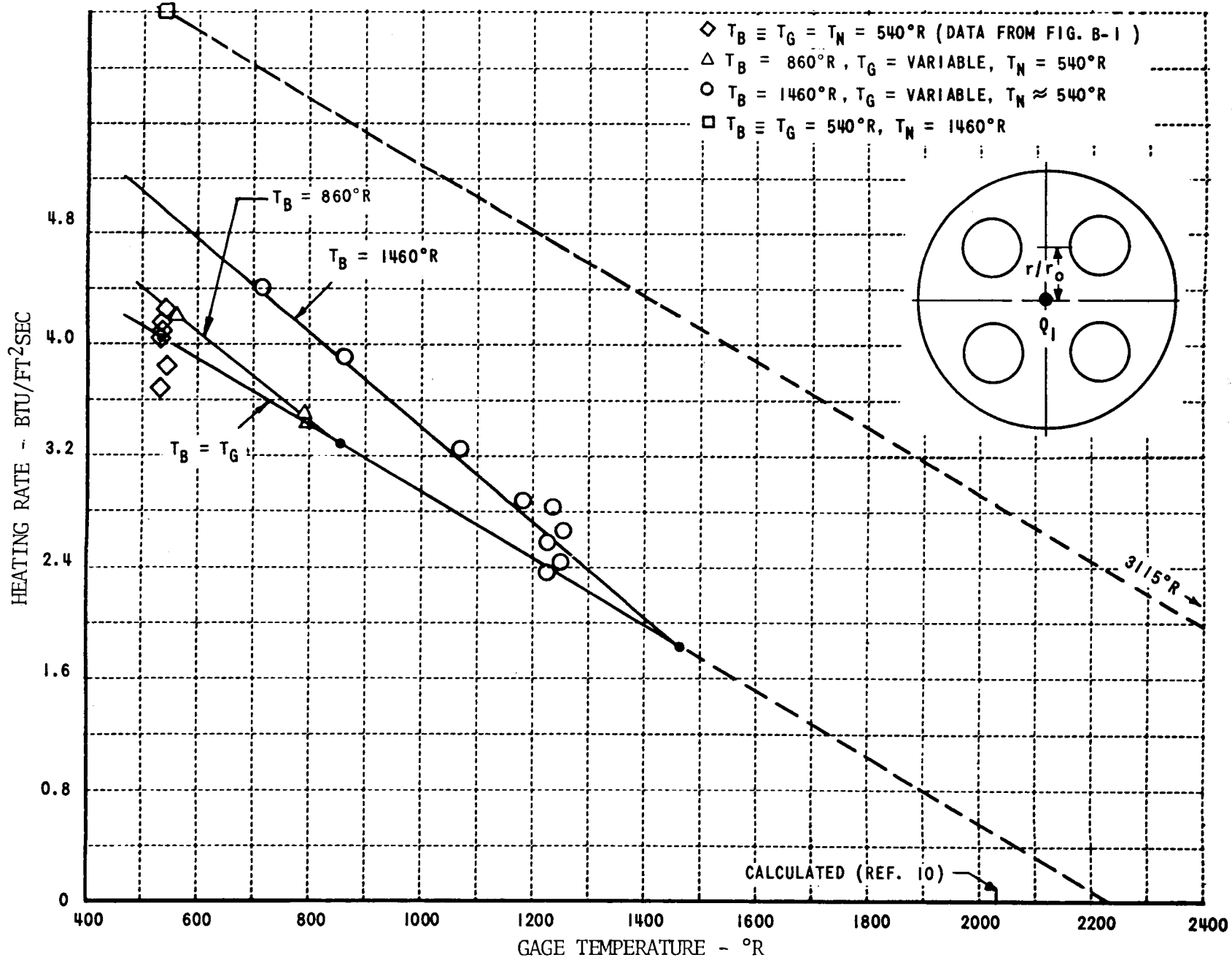

FIGURE 5.4-54. S-IV 4-ENGINE 1/10 SCALE SHOCK TUBE MODEL - BASE REGION RECOVERY TEMPERATURE

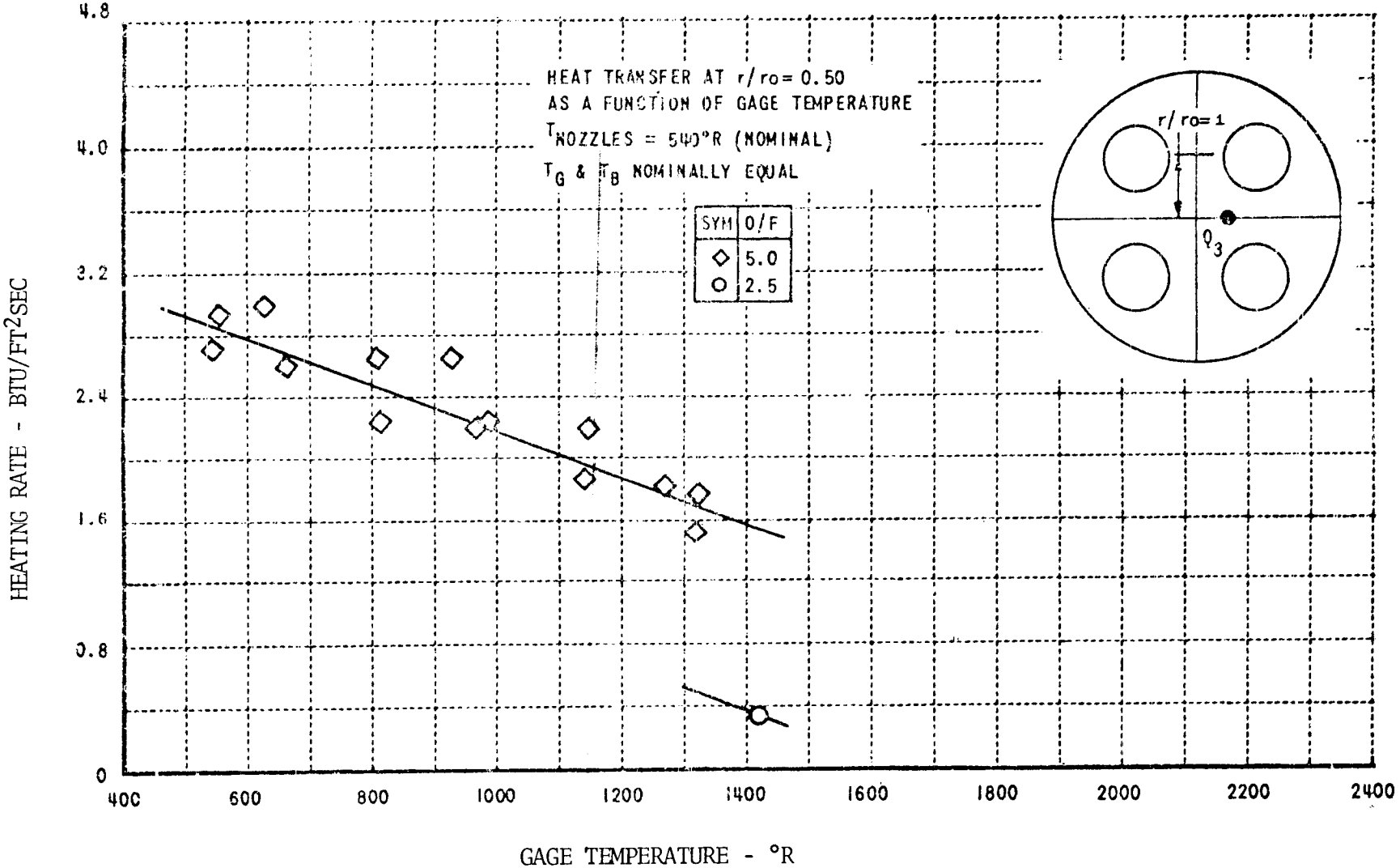

FIGURE 5.4- 54. S-IV 4-ENGINE 1/10 SCALE SHOCK TUBE MODEL - BASE REGION RECOVERY TEMPERATURE

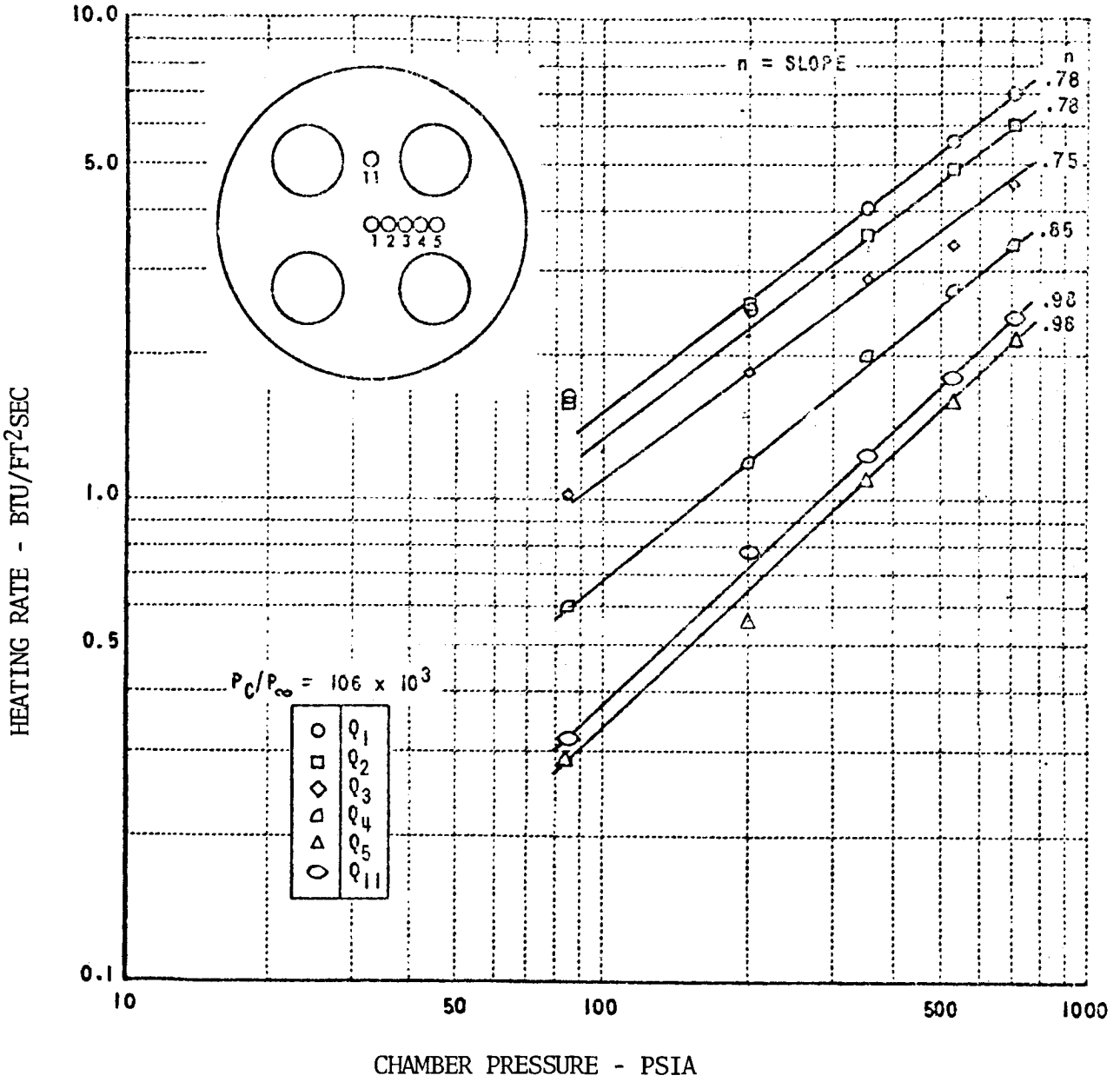

FIGURE 5.4- 55. S-IV 4-ENGINE 1/10 SCALE SHOCK TUBE MODEL - EFFECT OF CHAMBER PRESSURE ON BASE HEAT SHIELD HEAT TRANSFER RATE

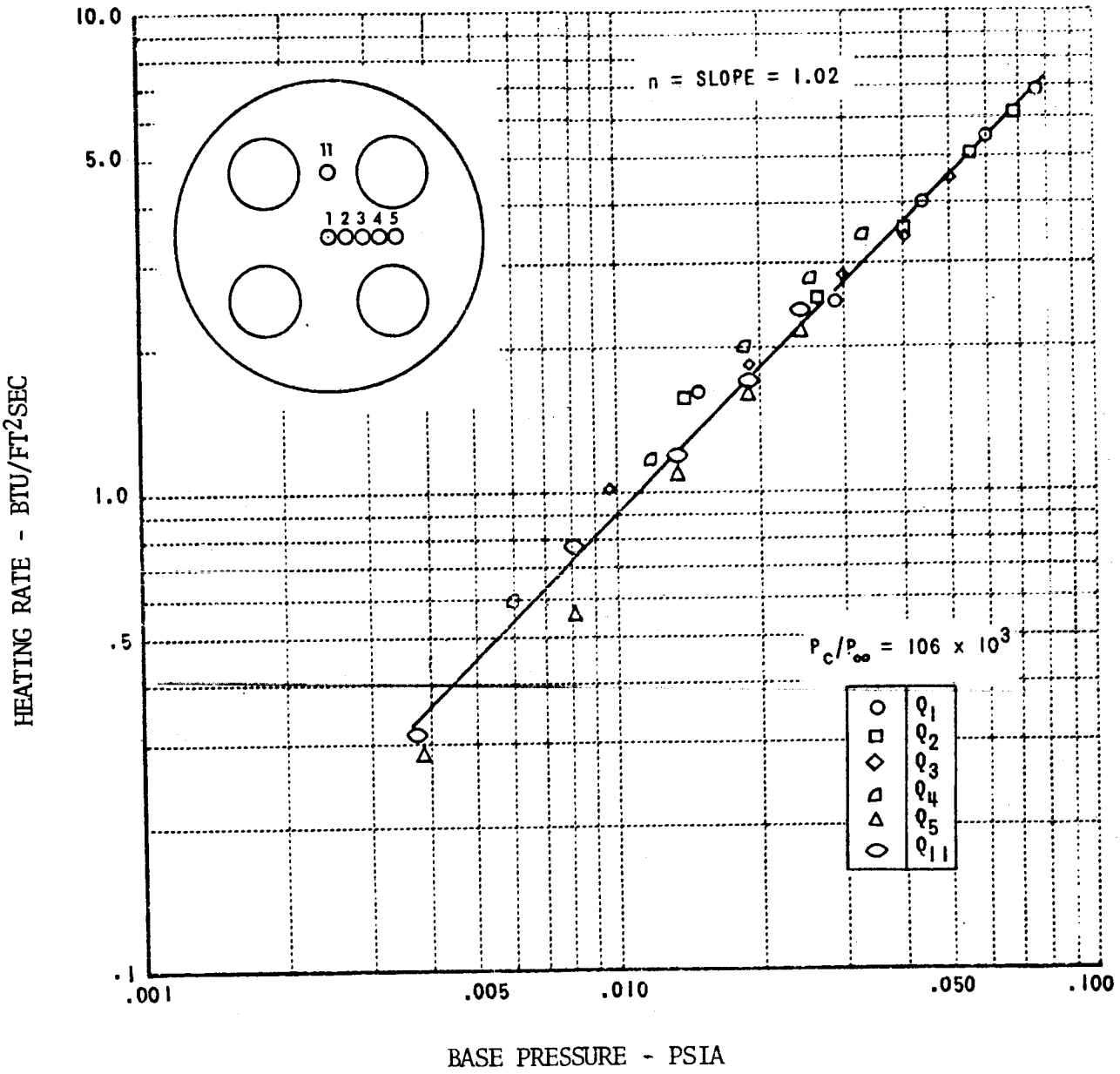

FIGURE 5.4- 56. S-IV 4-ENGINE 1/10 SCALE SHOCK TUBE MODEL - CORRELATION OF HEAT TRANSFER RATE WITH HEAT SHIELD PRESSURE

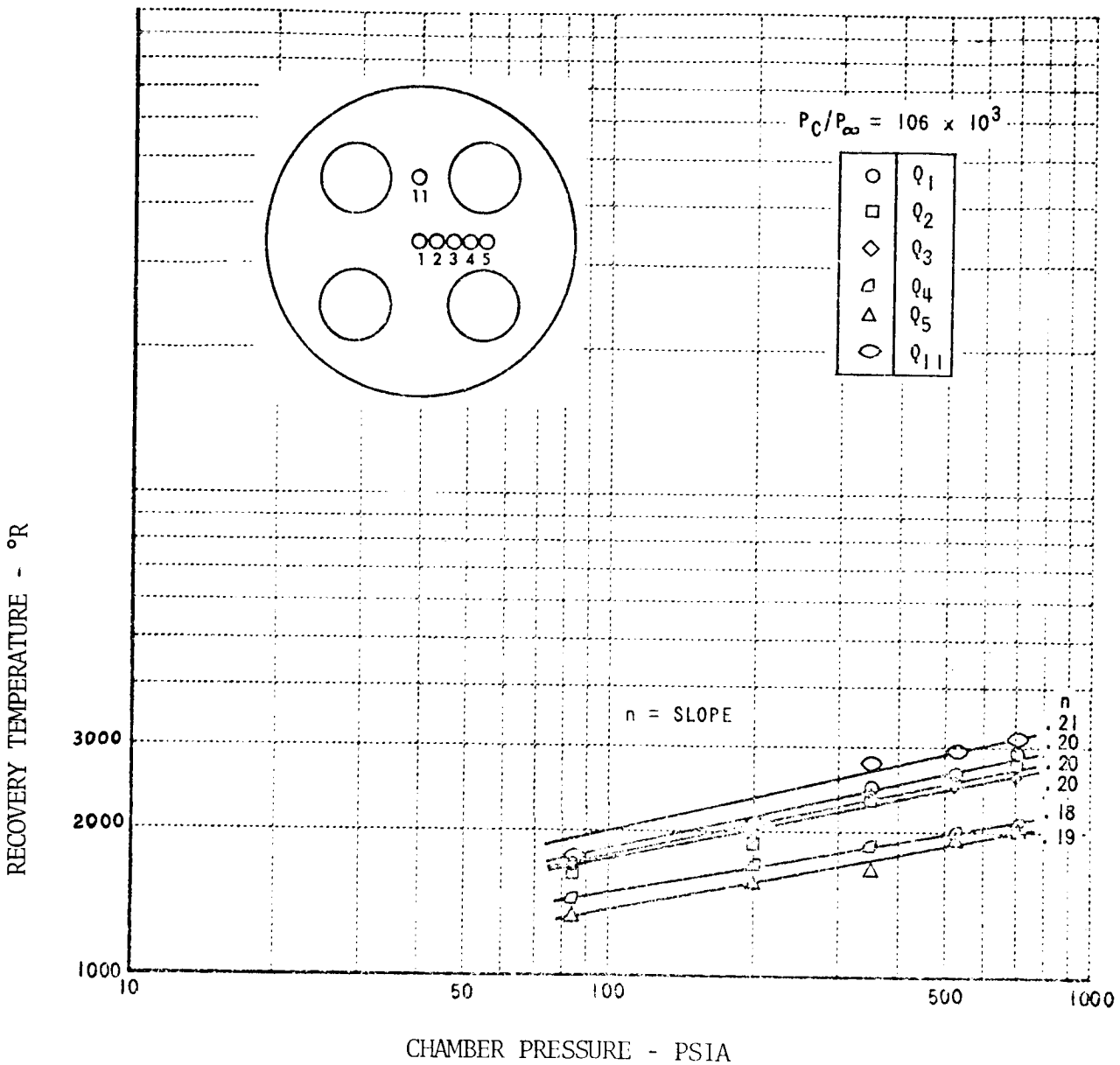

FIGURE 5.4-57. S-IV 4-ENGINE 1/10 SCALE SHOCK TUBE MODEL - EFFECT OF CHAMBER PRESSURE ON BASE REGION RECOVERY TEMPERATURE

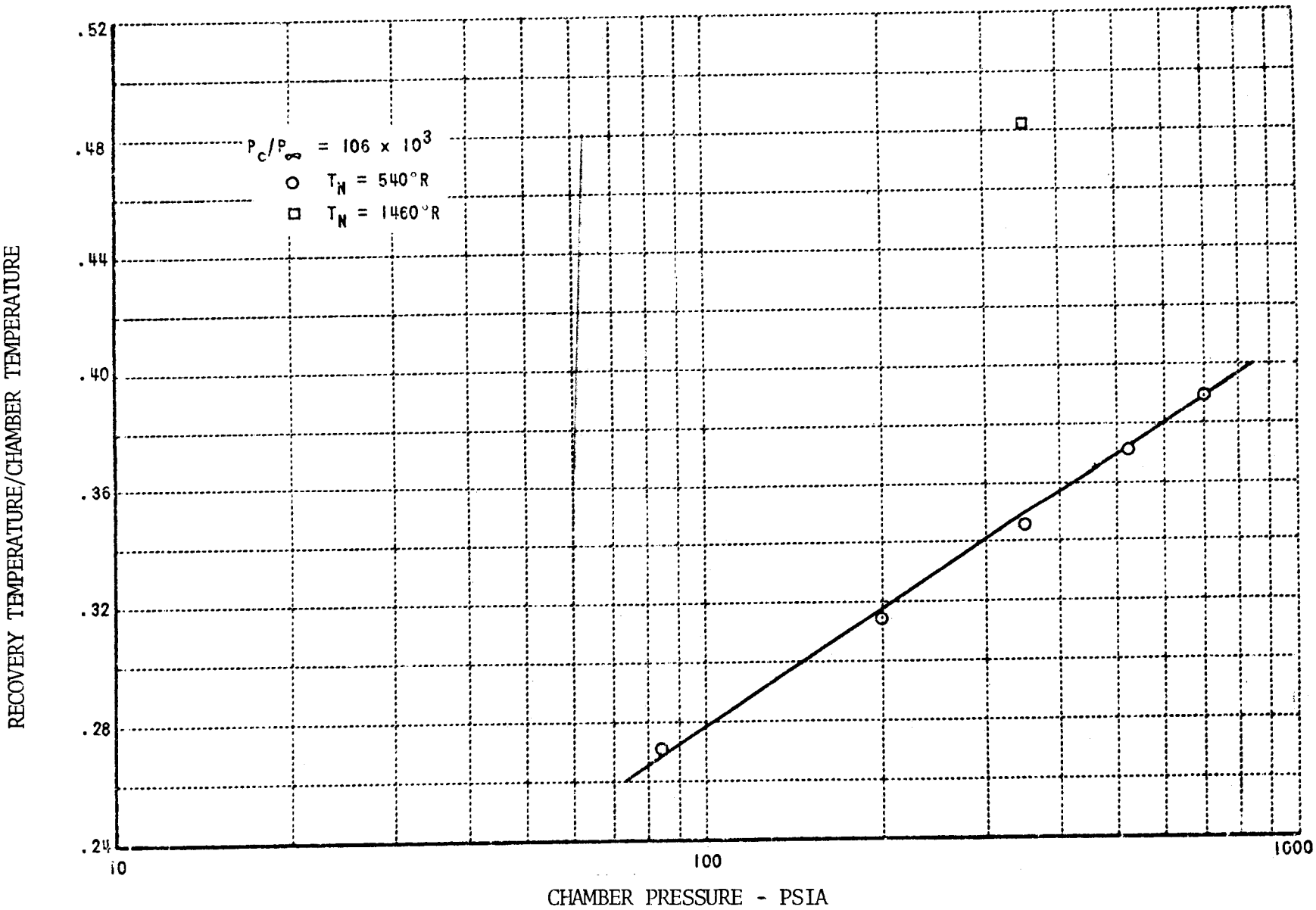

FIGURE 5.4-58. S-IV 4-ENGINE 1/10 SCALE SHOCK TUBE MODEL - EFFECT OF CHAMBER PRESSURE ON RECOVERY TEMPERATURE/ CHAMBER TEMPERATURE RATIO

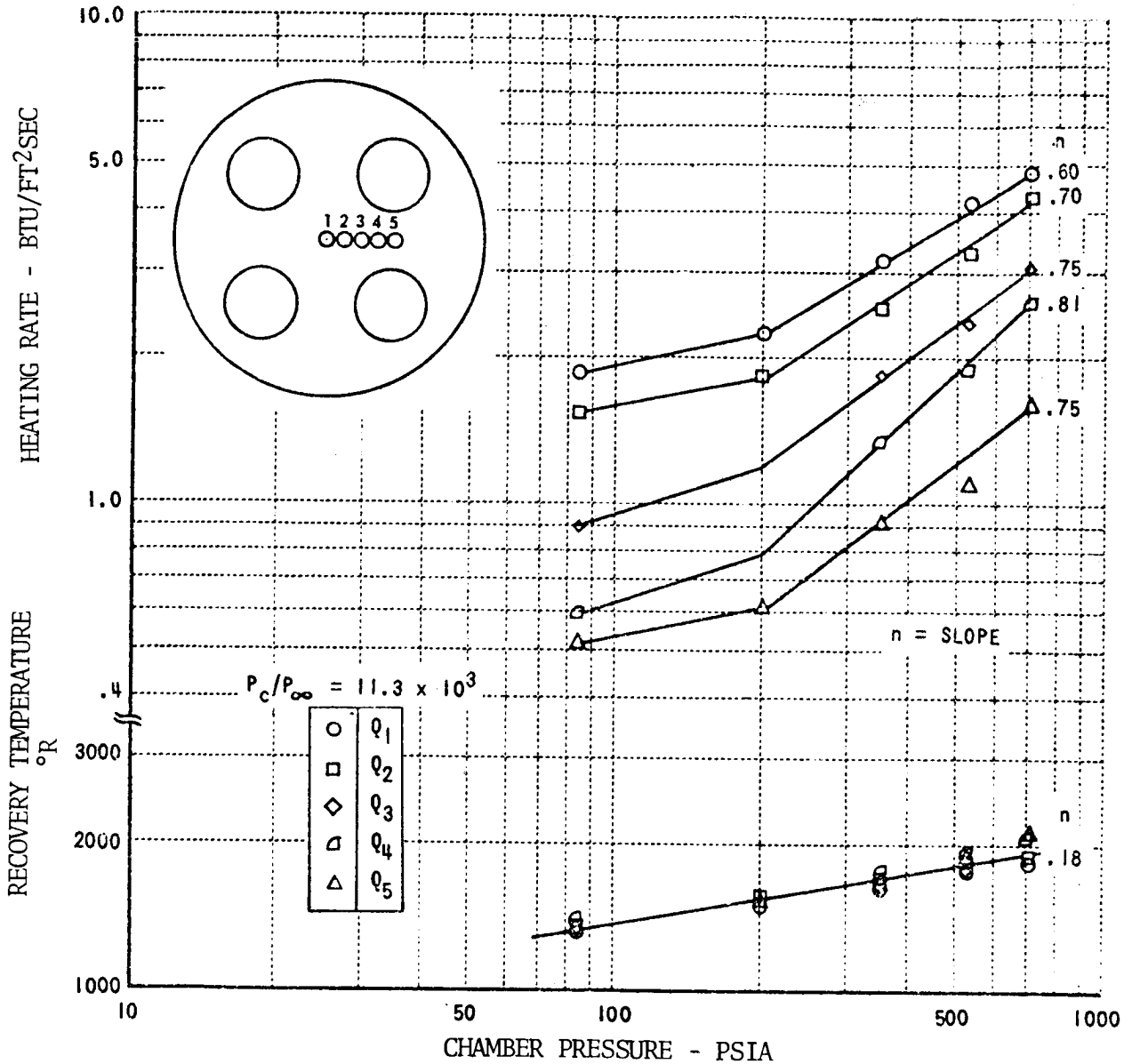

FIGURE 5.4-59. S-IV 4-ENGINE 1/10 SCALE SHOCK TUBE MODEL - EFFECT OF CHAMBER PRESSURE ON BASE REGION HEAT TRANSFER RATE AND RECOVERY TEMPERATURE AT P_C/P_∞ = 11.3 x 10^3

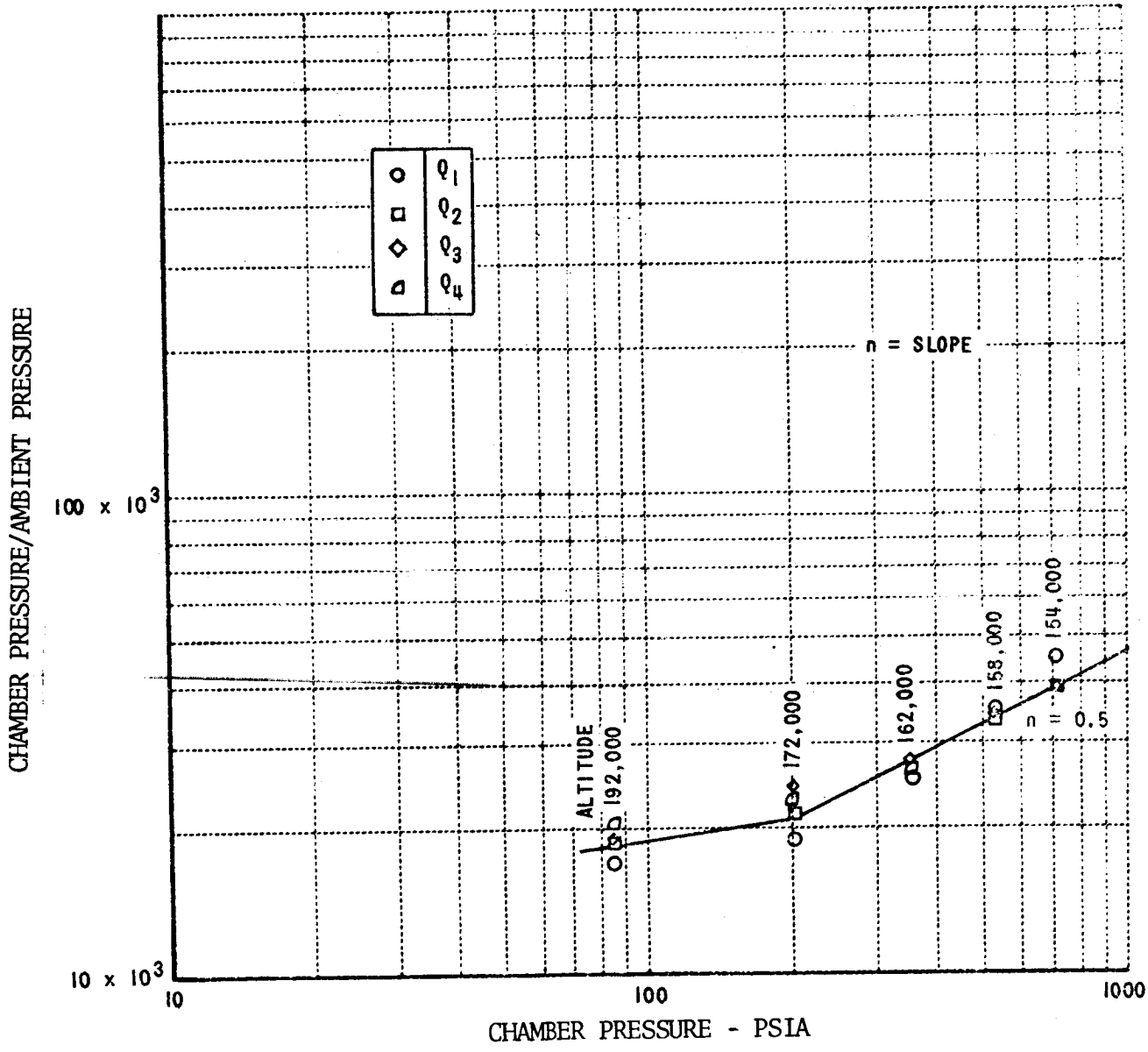

FIGURE 5.4-60. S-IV 4-ENGINE 1/10 SCALE SHOCK TUBE MODEL - EFFECT OF CHAMBER PRESSURE ON CHOKING ALTITUDE PRESSURE RATIO

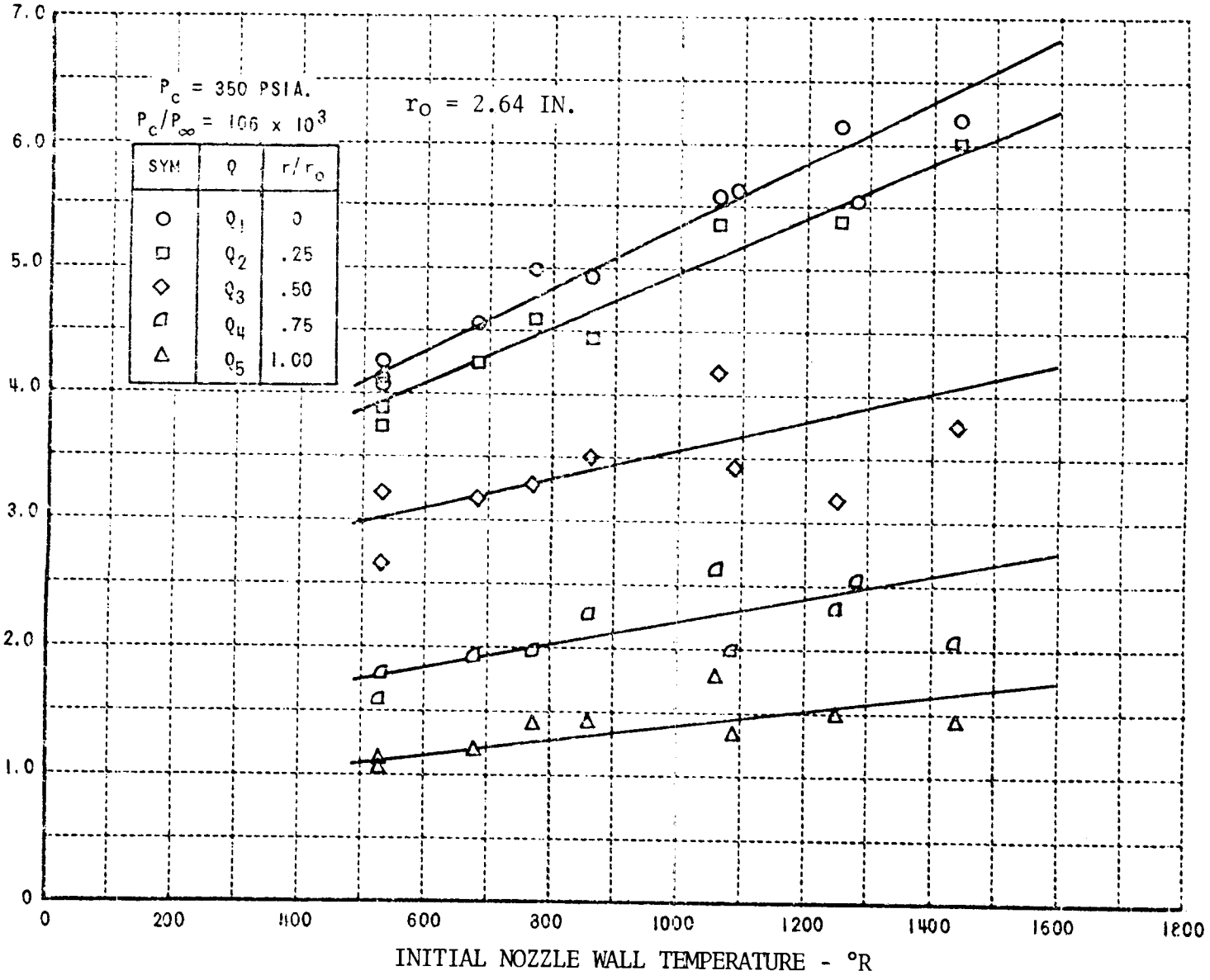

FIGURE 5.4-61. S-IV 4-ENGINE 1/10 SCALE SHOCK TUBE MODEL - EFFECT OF NOZZLE WALL TEMPERATURE ON BASE HEAT SHIELD HEAT TRANSFER RATES

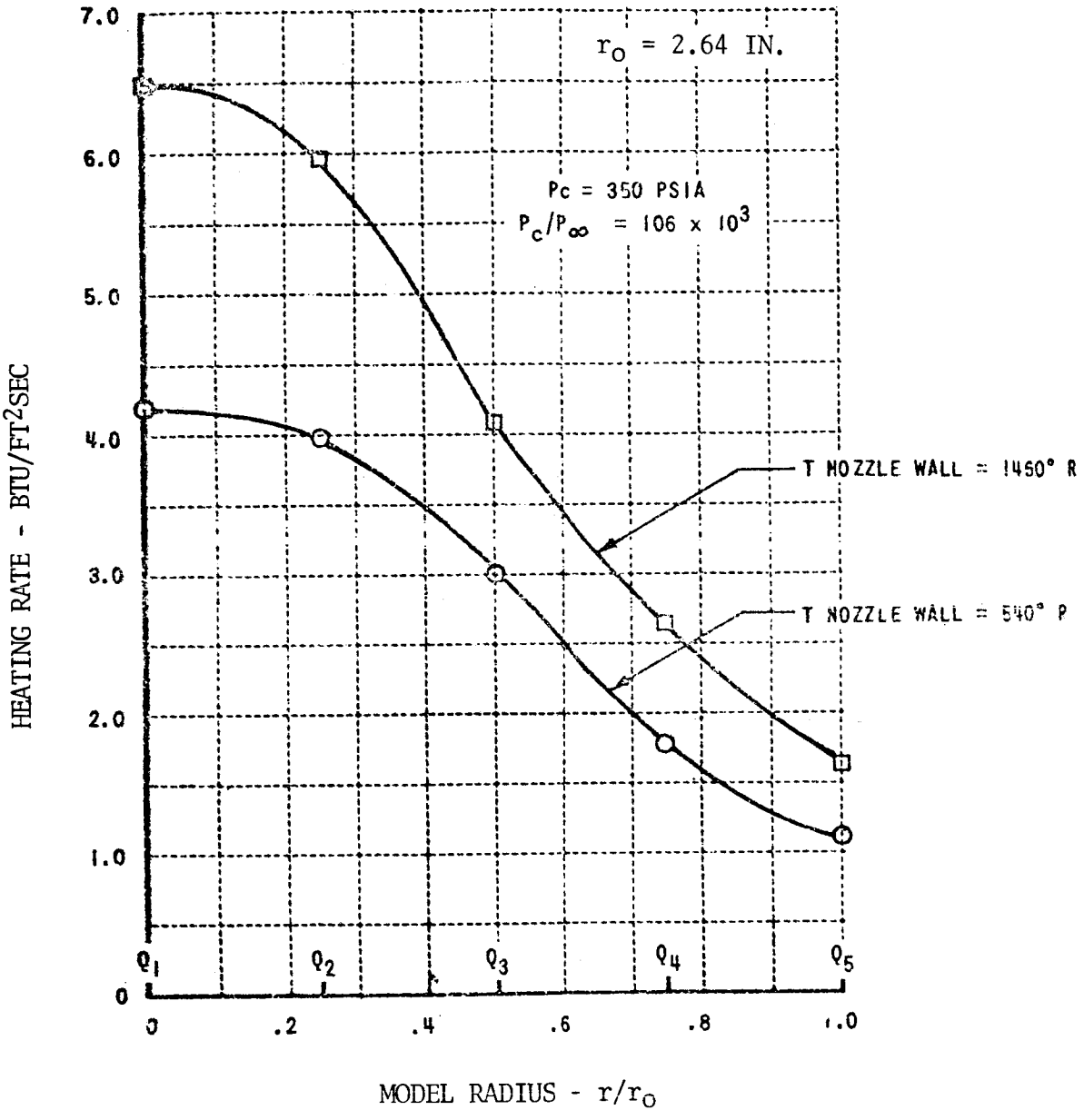

FIGURE 5.4-62. S-IV 4-ENGINE 1/10 SCALE SHOCK TUBE MODEL - EFFECT OF NOZZLE WALL TEMPERATURE ON BASE HEAT SHIELD HEAT TRANSFER RATES

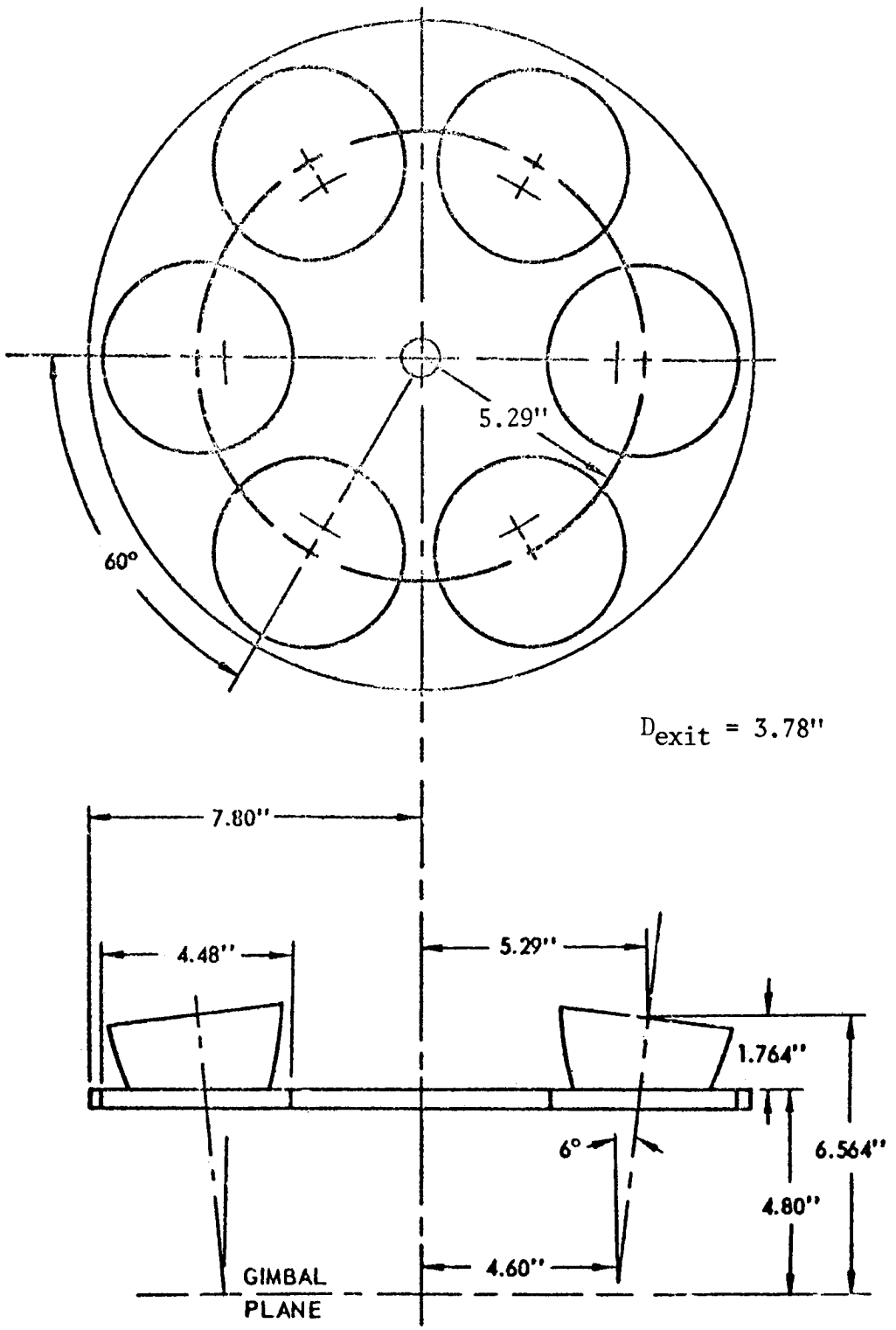

FIGURE 5.4-63. S-IV 6-ENGINE 1/10 SCALE SHOCK TUBE MODEL - BASE REGION CONFIGURATION (FIRST SERIES)

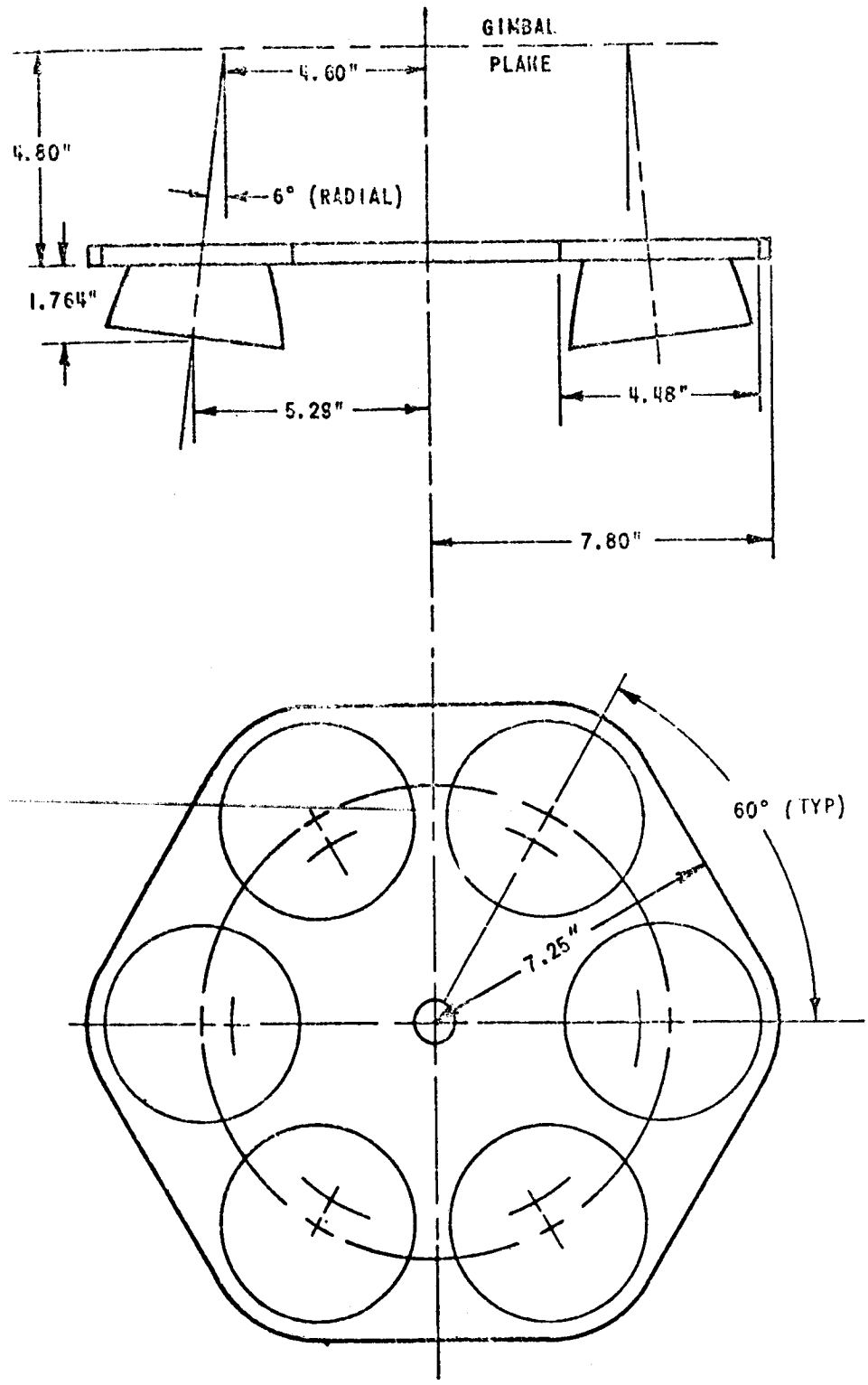

FIGURE 5.4-64. S-IV 6-ENGINE 1/10 SCALE SHOCK TUBE MODEL - BASE REGION CONFIGURATION (SECOND SERIES)

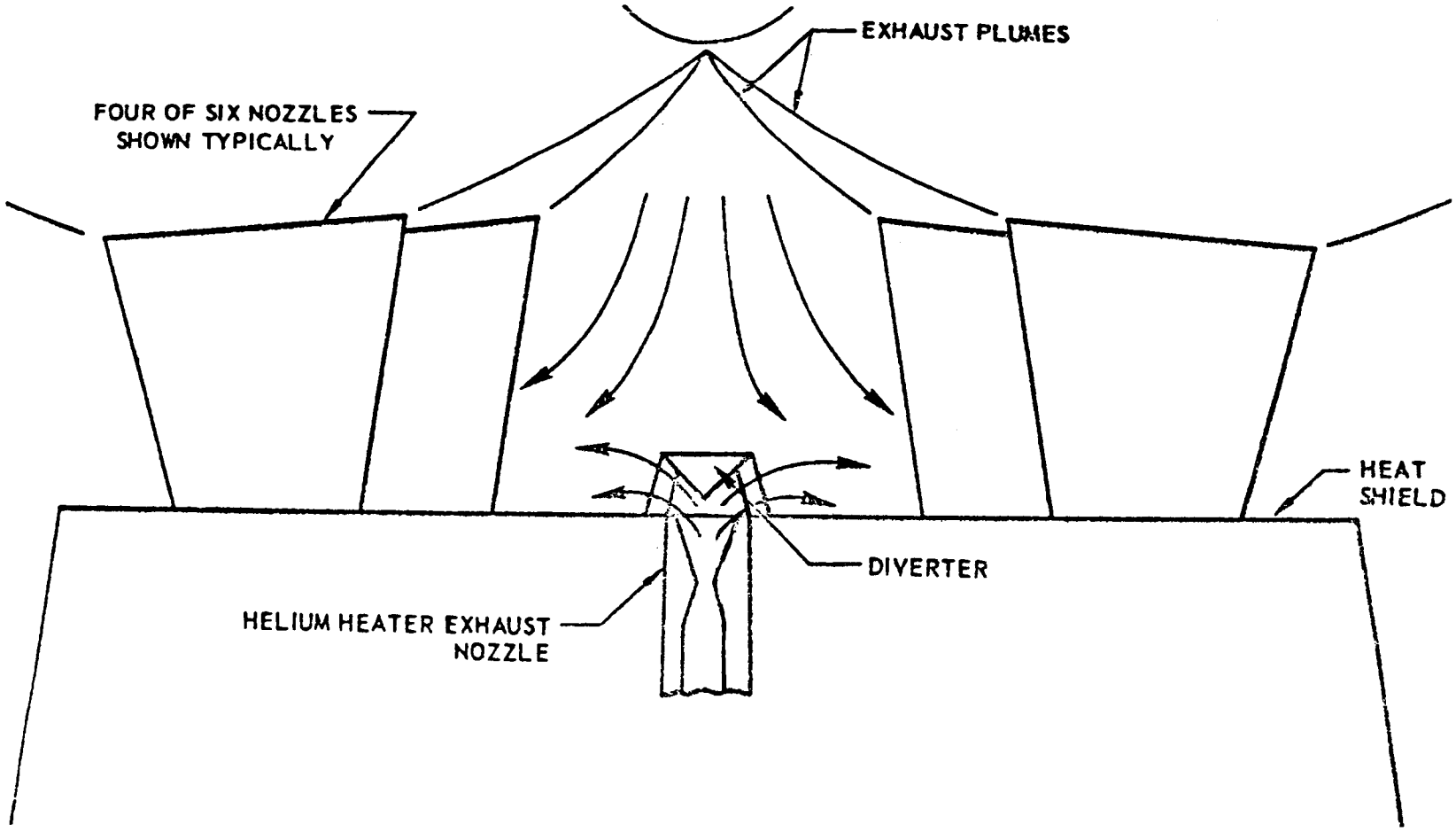

FIGURE 5.4-65. S-IV 6-ENGINE 1/10 SCALE SHOCK TUBE MODEL - HELIUM HEATER EXHAUST NOZZLE AND DIVERTER

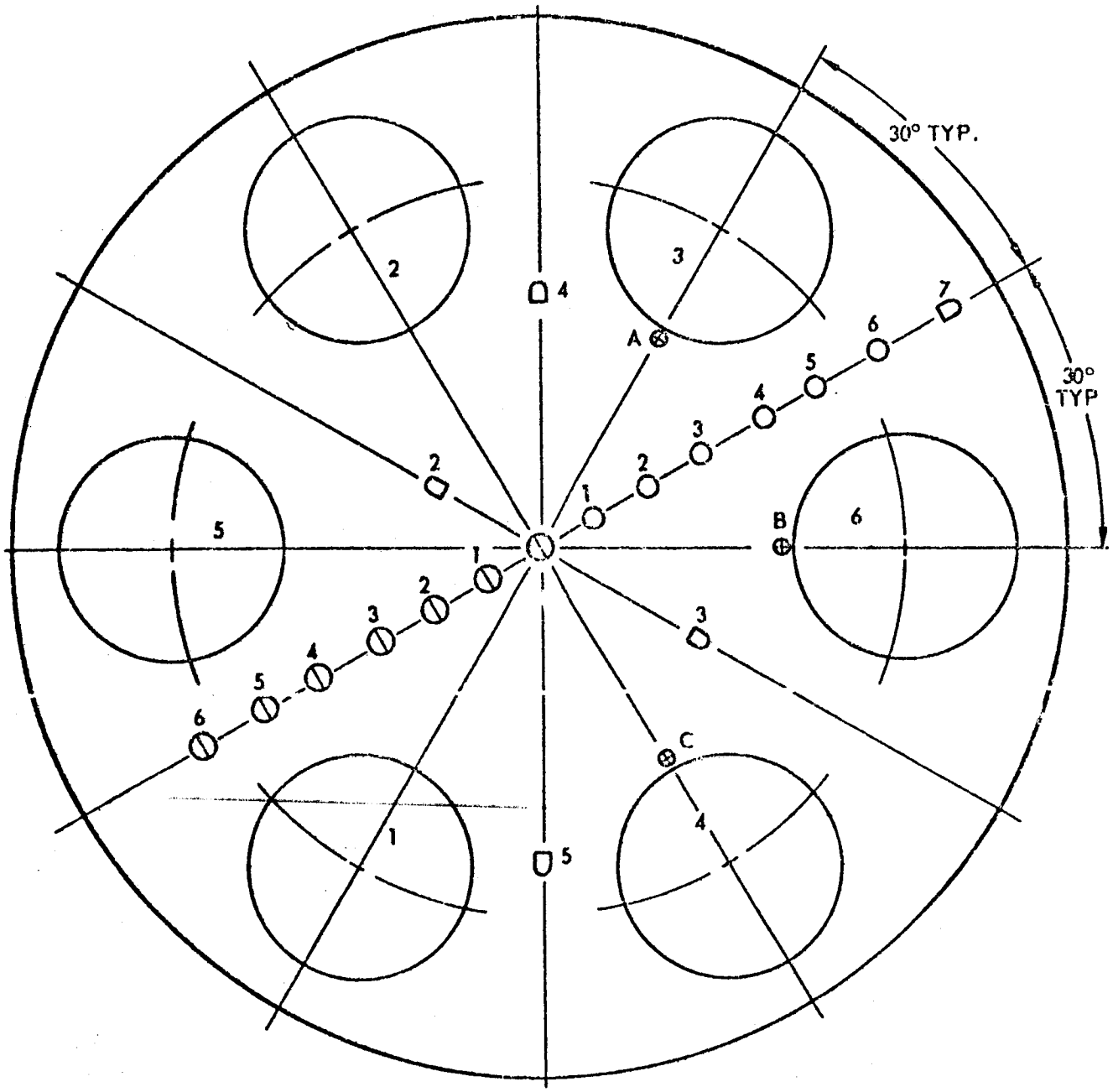

LOCATION	RADIUS (IN.)
1	1.00
2	1.62
3	2.25
4	3.35
5	4.50
6	5.75
7	7.25

O STATIC PRESSURE TAP
D TOTAL PRESSURE PROBE
⊕ NOZZLE SIDEWALL PRESSURE
⊖ HEAT TRANSFER GAGE

FIGURE 5.4-66. S-IV 6-ENGINE 1/10 SCALE SHOCK TUBE MODEL - BASE HEAT SHIELD INSTRUMENTATION (FIRST SERIES)

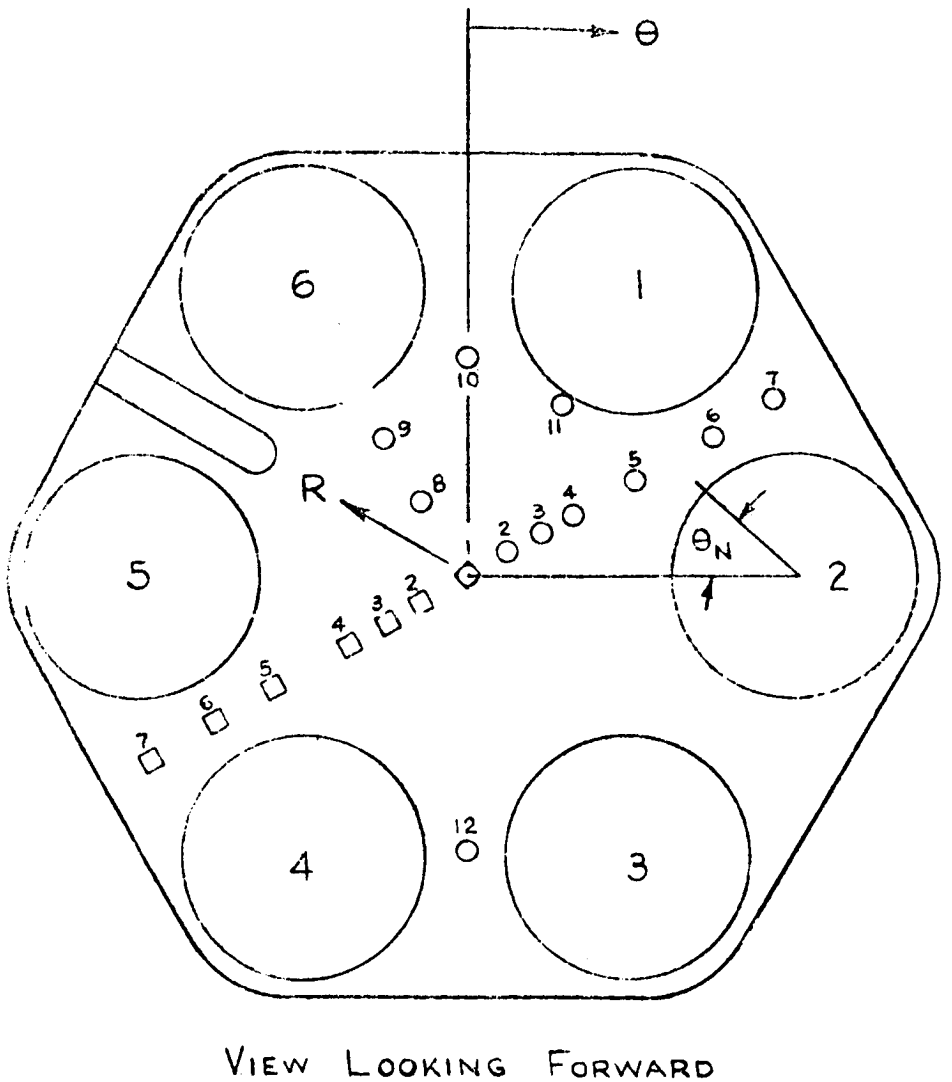

FIGURE 5.4-67. S-IV 6-ENGINE 1/10 SCALE SHOCK TUBE MODEL - BASE HEAT SHIELD INSTRUMENTATION (SECOND SERIES)

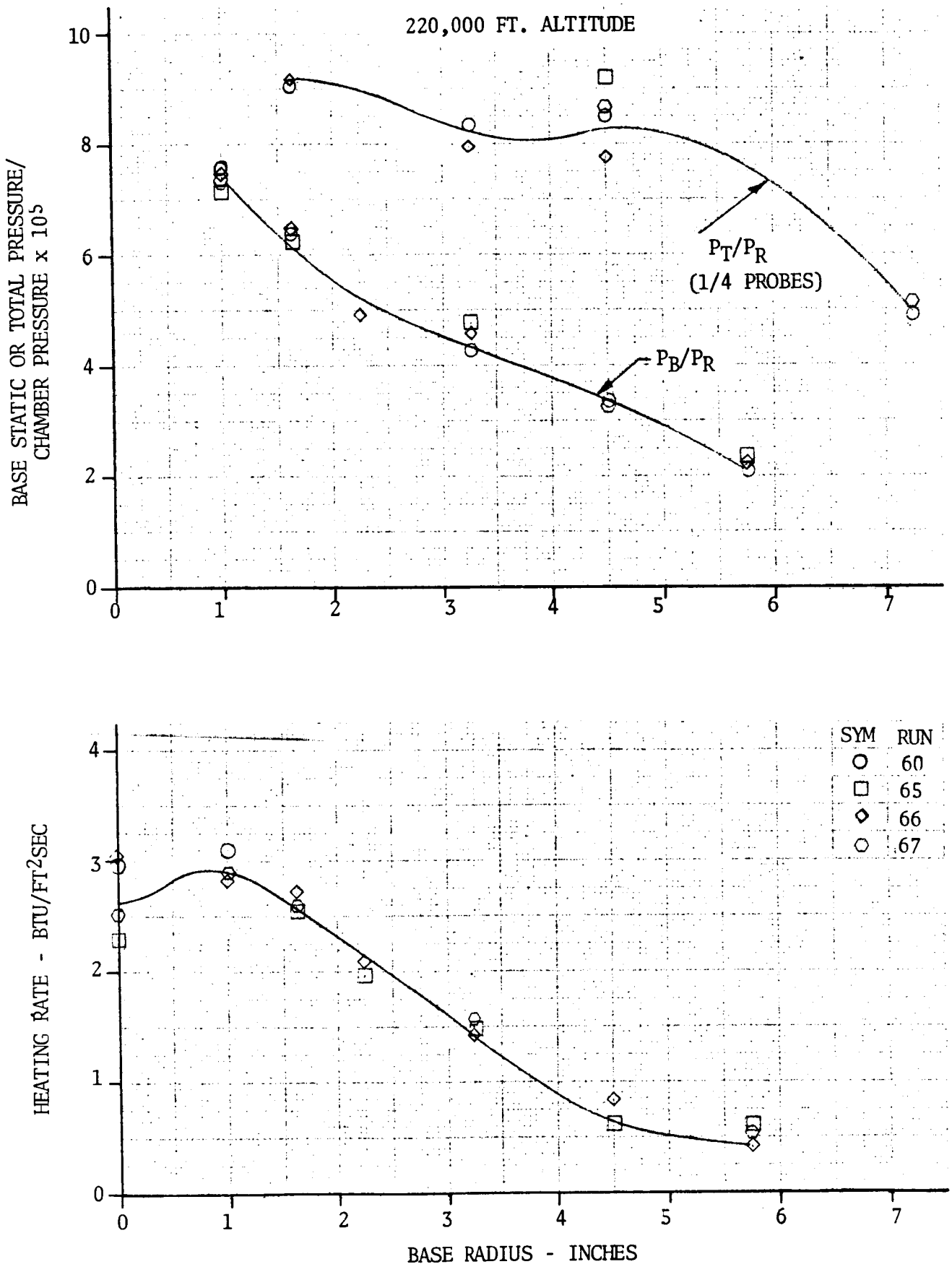

FIGURE 5.4-68. S-IV 6-ENGINE 1/10 SCALE SHOCK TUBE MODEL - BASE HEAT SHIELD RADIAL DISTRIBUTION OF NOMINAL STATIC AND TOTAL PRESSURE AND HEAT TRANSFER RATES

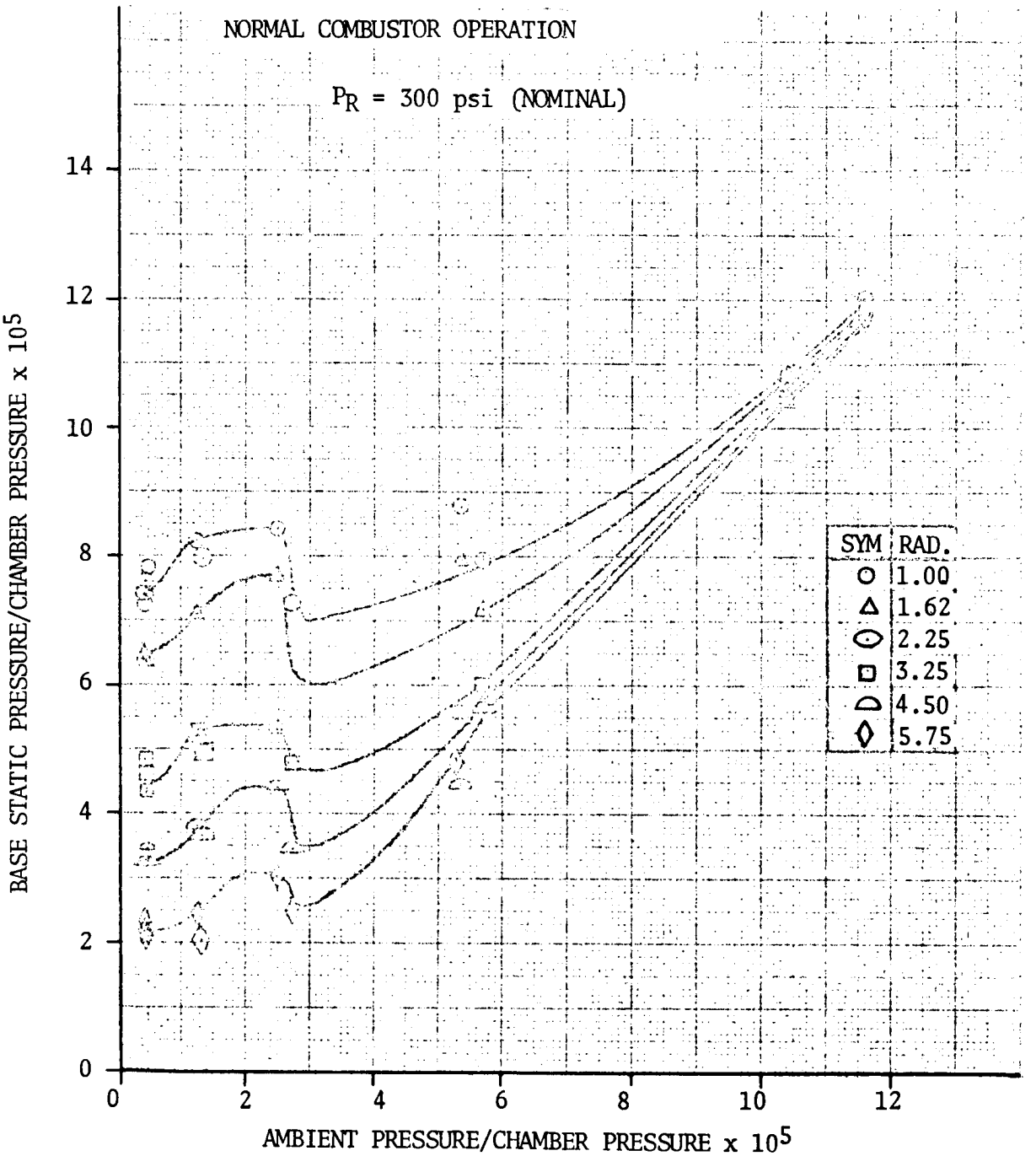

FIGURE 5.4-69. S-IV 6-ENGINE 1/10 SCALE SHOCK TUBE MODEL - EFFECT OF ALTITUDE ON BASE HEAT SHIELD STATIC PRESSURE

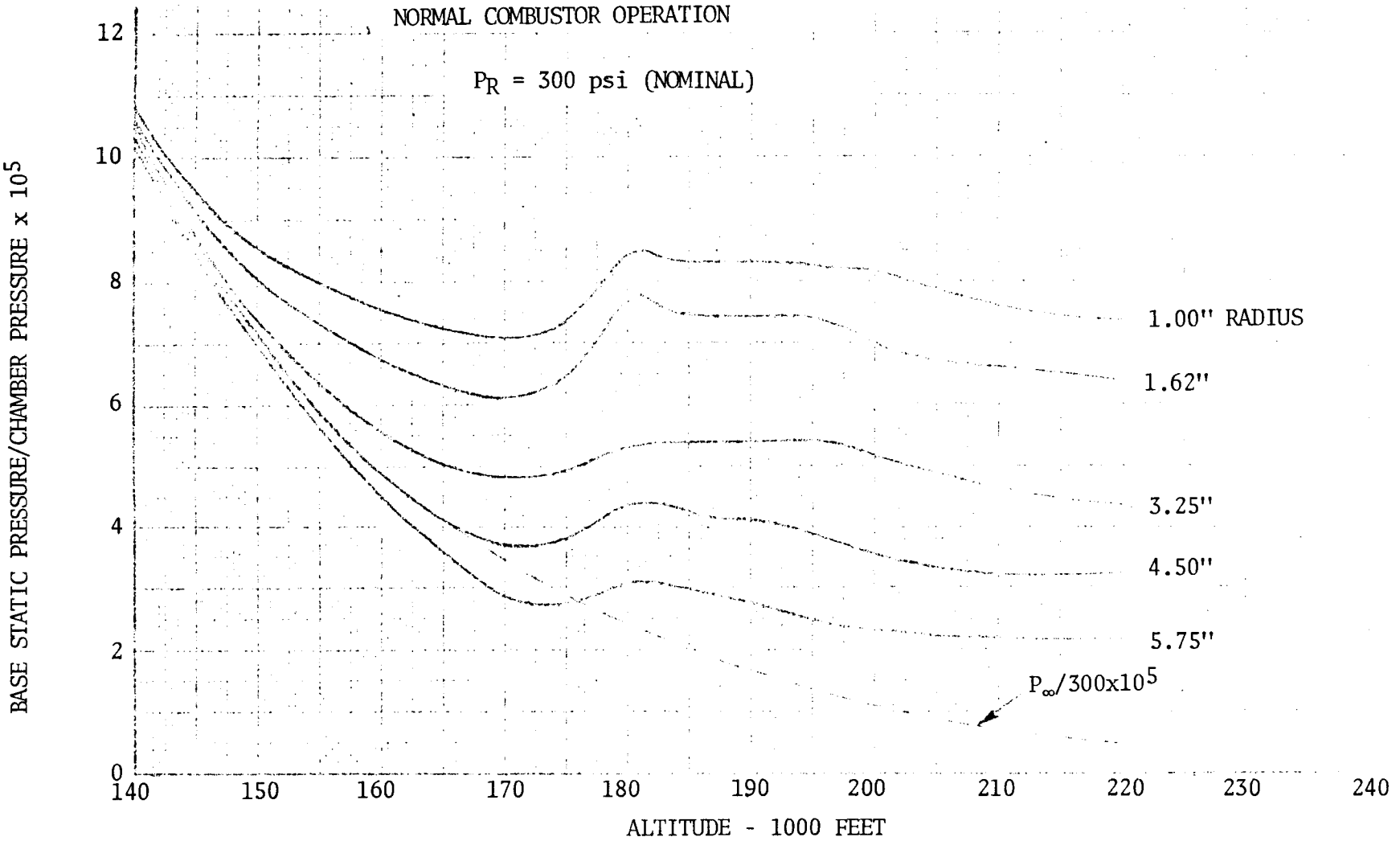

FIGURE 5.4-70. S-IV 6-ENGINE 1/10 SCALE SHOCK TUBE MODEL - EFFECT OF ALTITUDE ON BASE HEAT SHIELD STATIC PRESSURE DISTRIBUTION

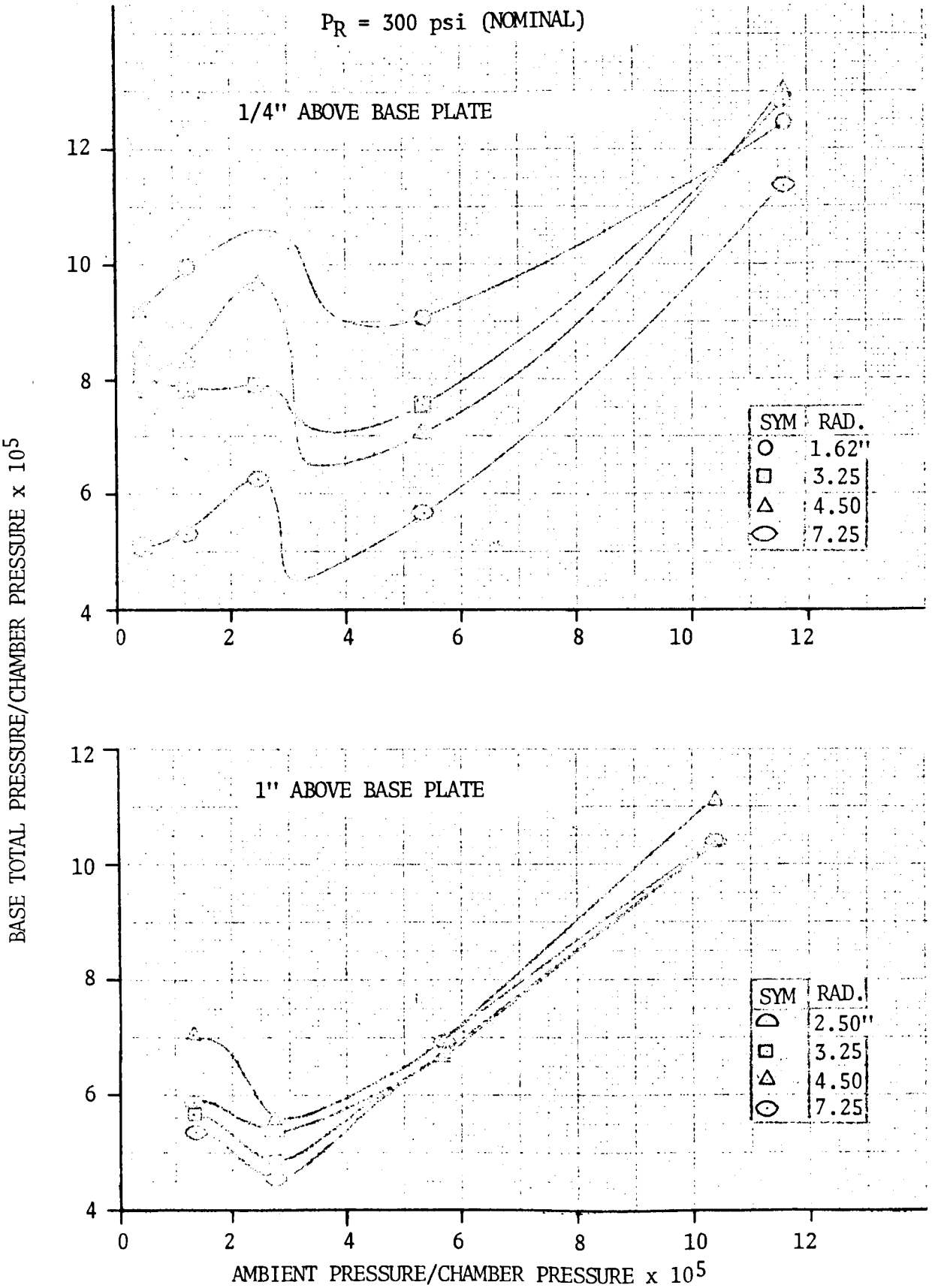

FIGURE 5.4-71. S-IV 6-ENGINE 1/10 SCALE SHOCK TUBE MODEL - EFFECT OF ALTITUDE ON BASE HEAT SHIELD TOTAL PRESSURE DISTRIBUTION

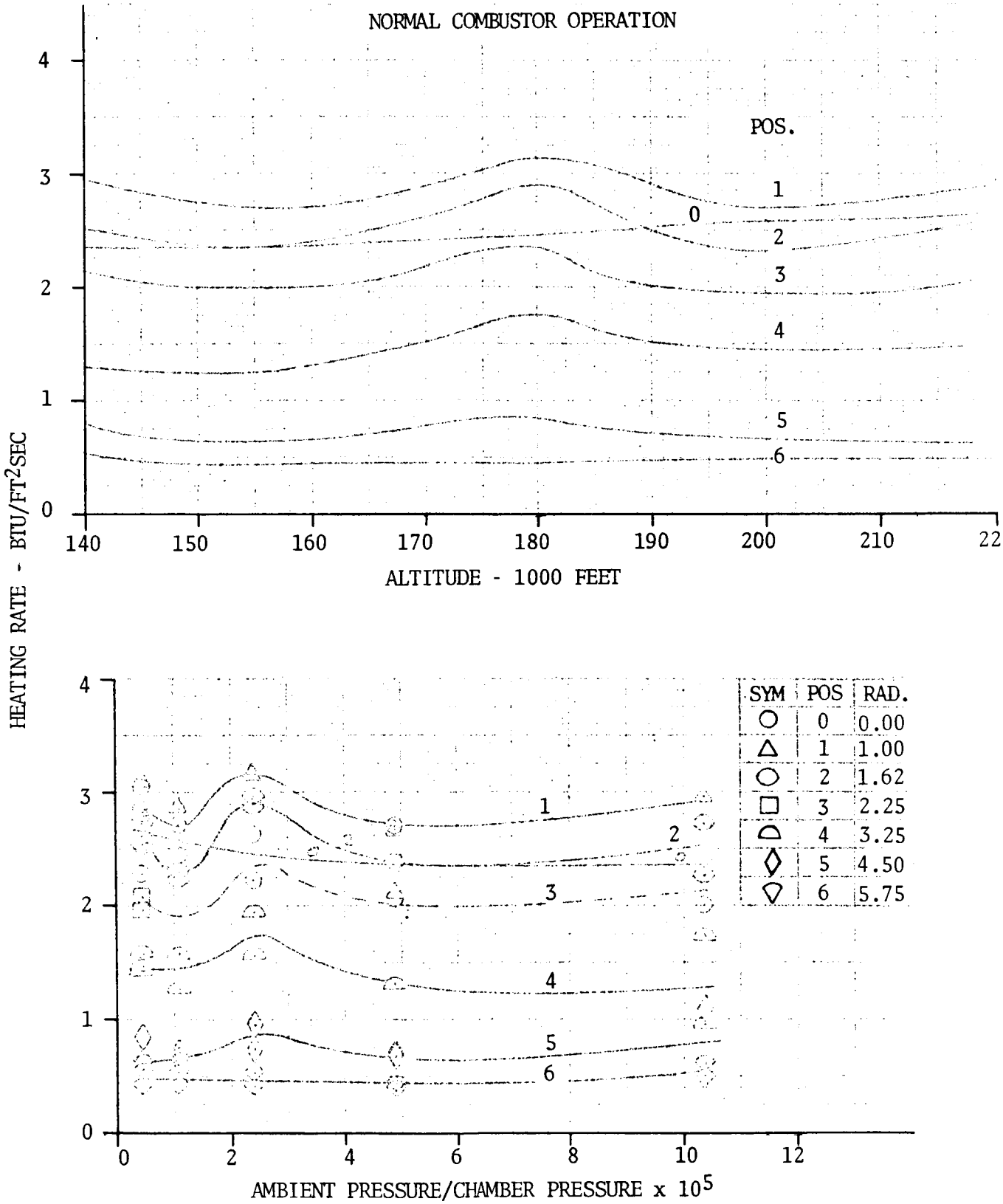

FIGURE 5.4-72. S-IV 6-ENGINE 1/10 SCALE SHOCK TUBE MODEL - EFFECT OF ALTITUDE ON BASE HEAT SHIELD HEAT TRANSFER RATES

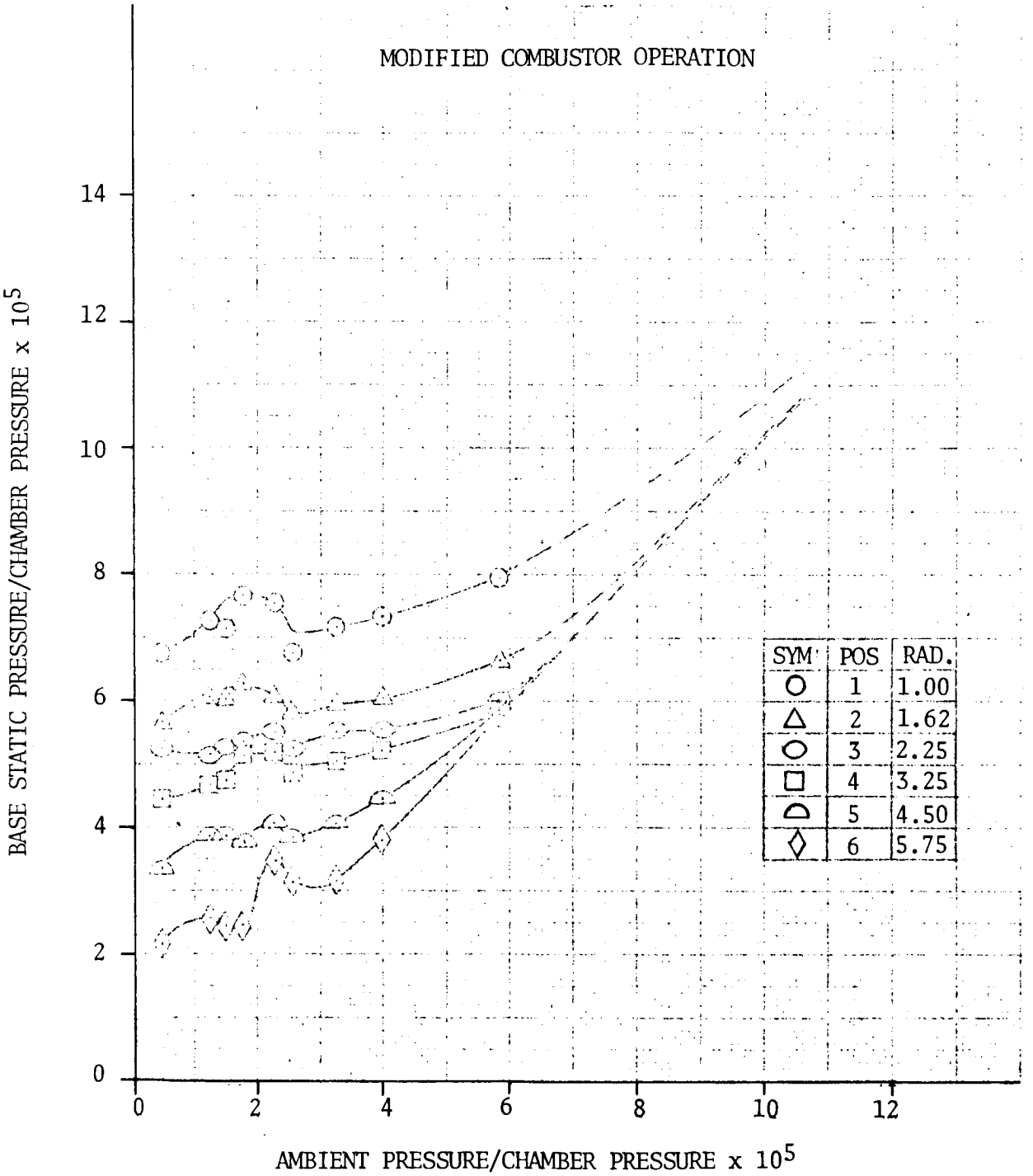

FIGURE 5.4-73. S-IV 6-ENGINE 1/10 SCALE SHOCK TUBE MODEL - EFFECT OF ALTITUDE ON BASE HEAT SHIELD STATIC PRESSURE

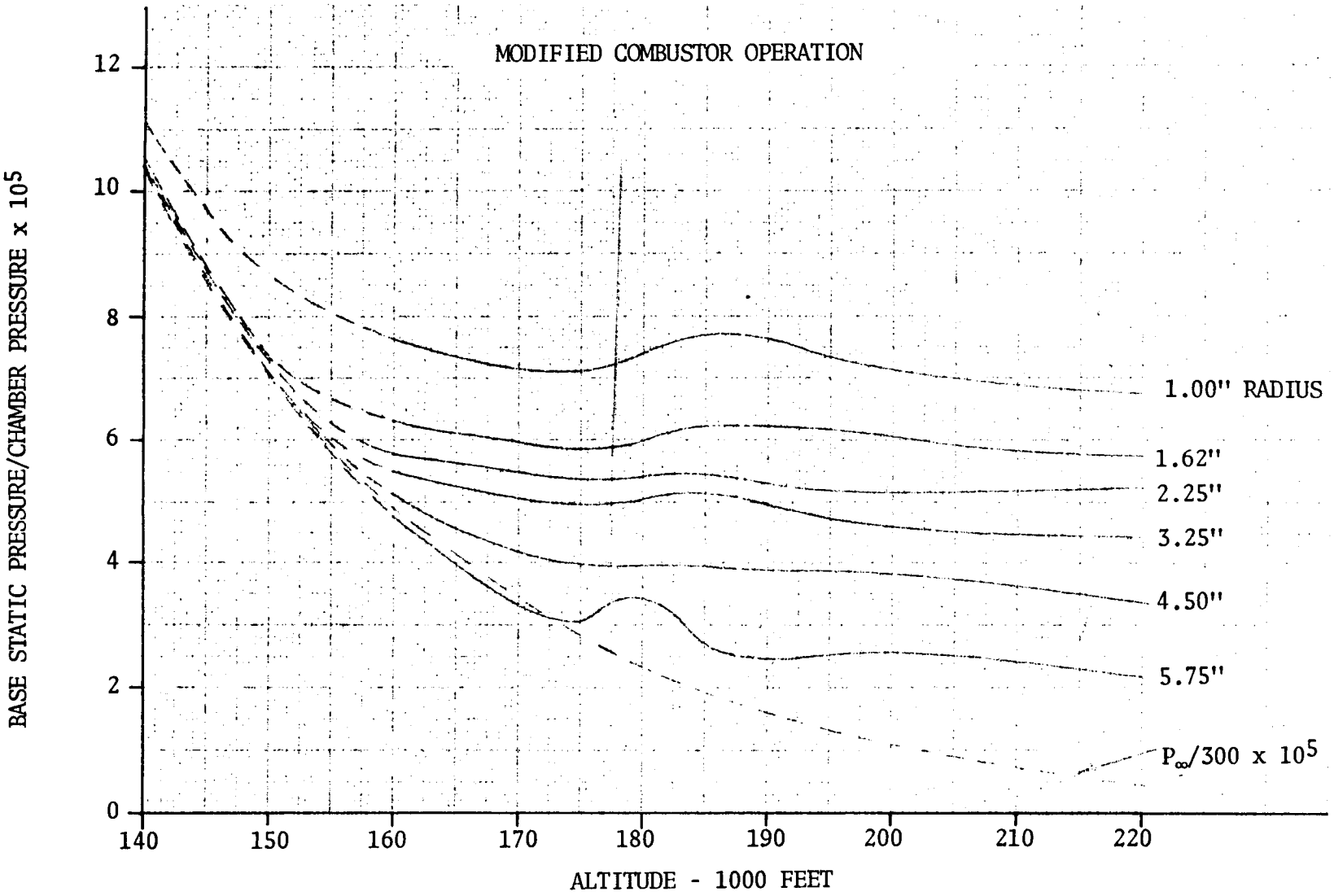

FIGURE 5.4- 74. S-IV 6-ENGINE 1/10 SCALE SHOCK TUBE MODEL - EFFECT OF ALTITUDE ON BASE HEAT SHIELD STATIC PRESSURE DISTRIBUTION

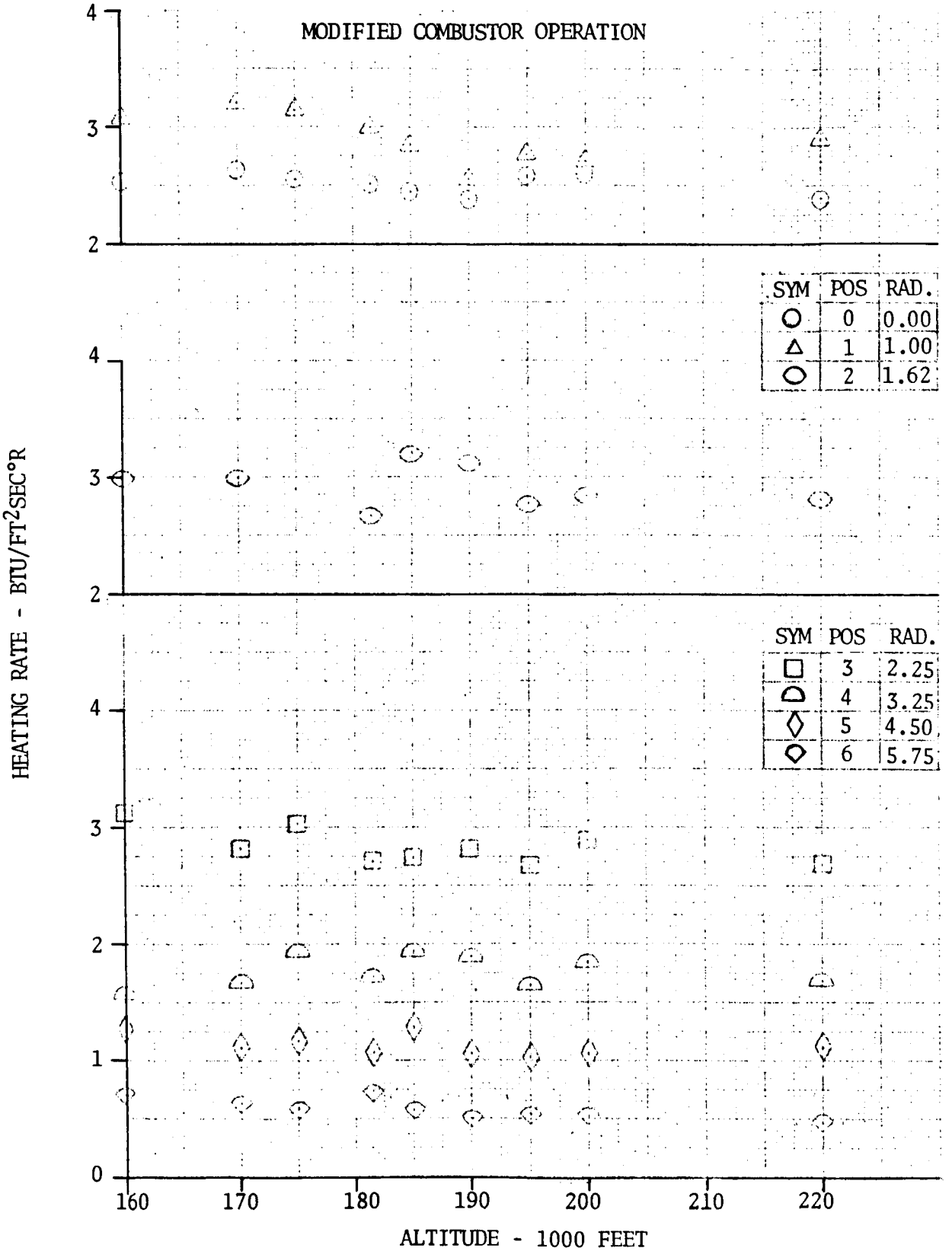

FIGURE 5.4-75. S-IV 6-ENGINE 1/10 SCALE SHOCK TUBE MODEL - EFFECT OF ALTITUDE ON BASE HEAT SHIELD HEAT TRANSFER RATES

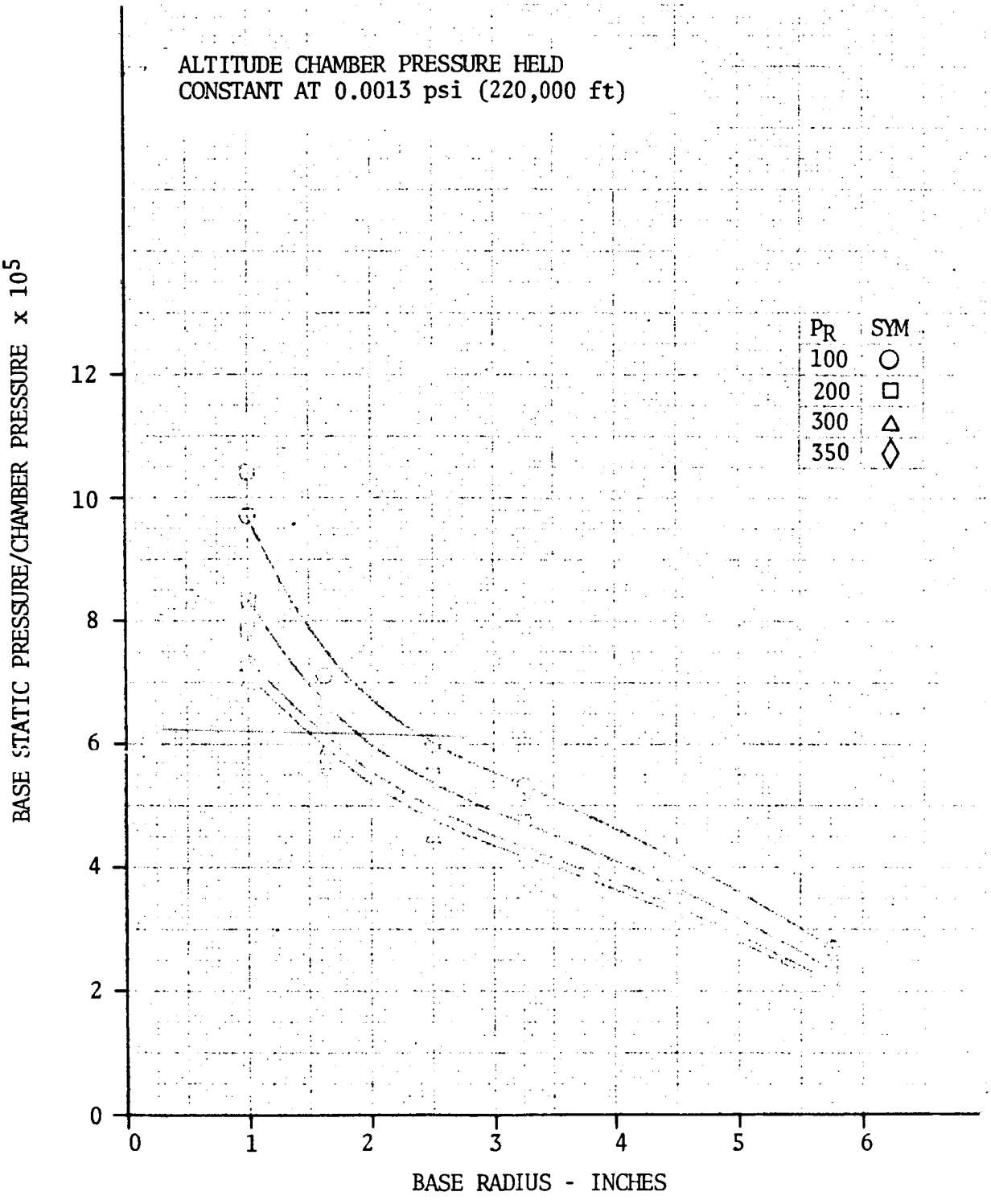

FIGURE 5.4- 76. S-IV 6-ENGINE 1/10 SCALE SHOCK TUBE MODEL - EFFECT OF CHAMBER PRESSURE ON BASE HEAT SHIELD STATIC PRESSURE DISTRIBUTION

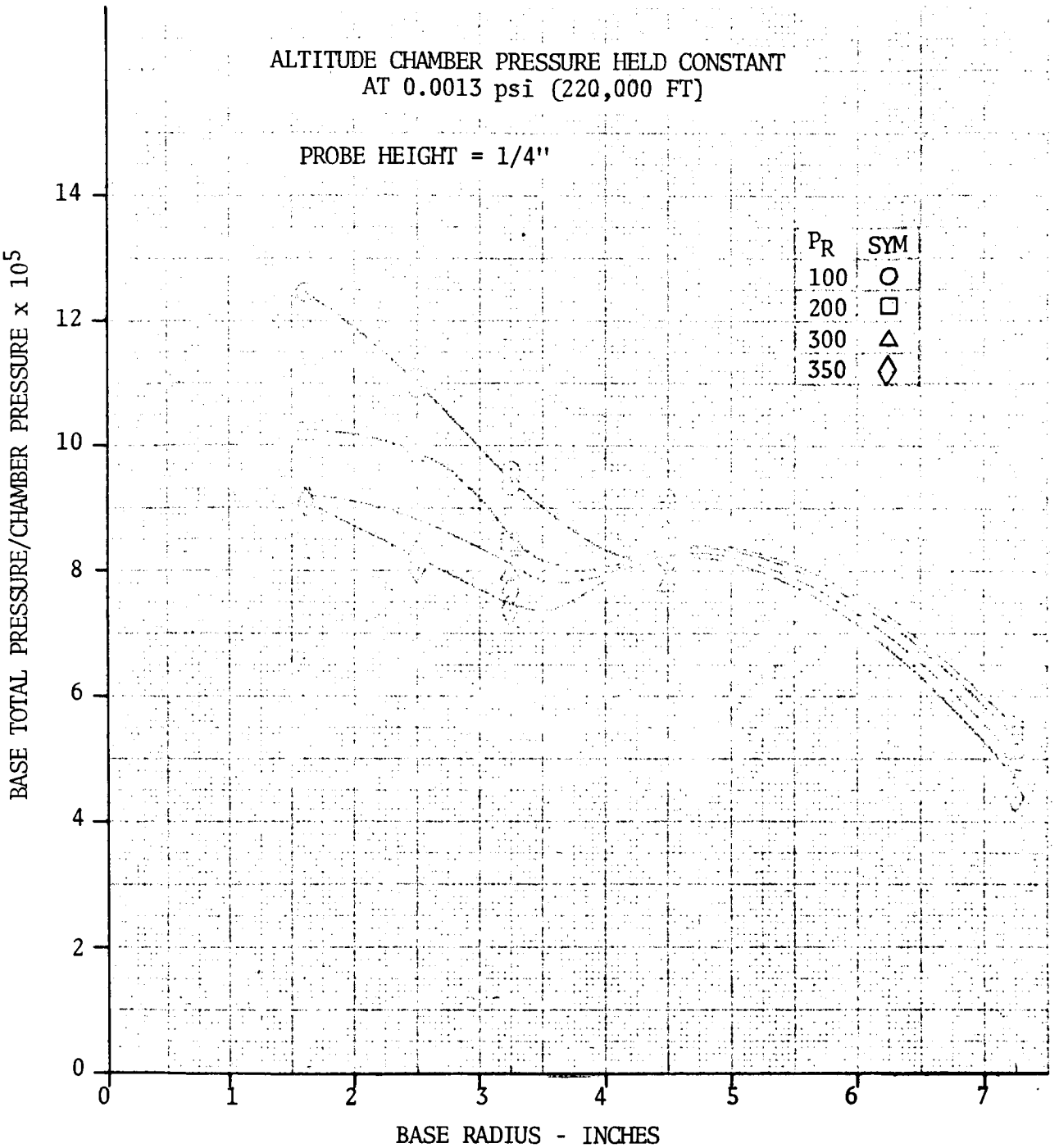

FIGURE 5.4-77. S-IV 6-ENGINE 1/10 SCALE SHOCK TUBE MODEL - EFFECT OF CHAMBER PRESSURE ON BASE TOTAL PRESSURE

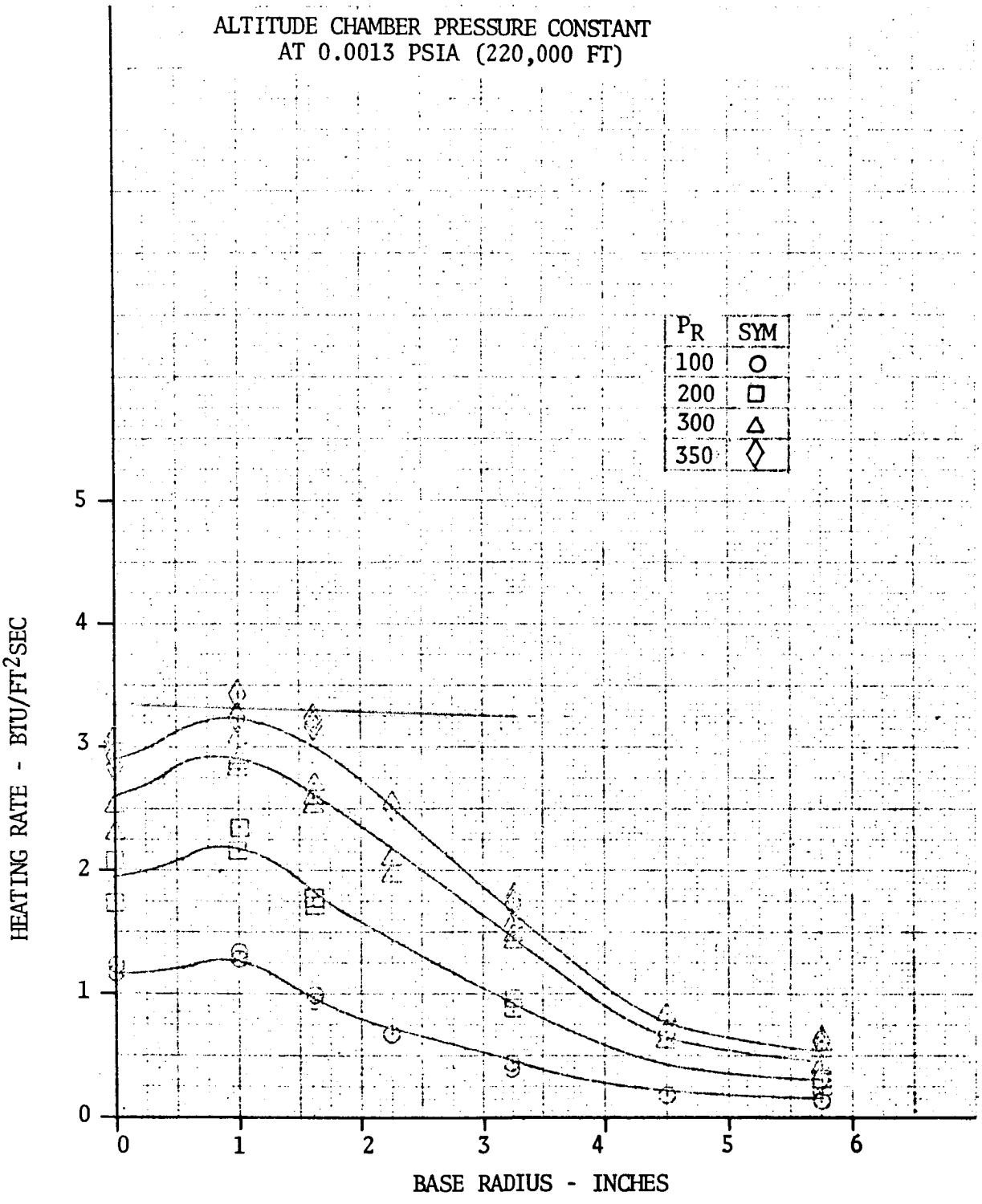

FIGURE 5.4-78. S-IV 6-ENGINE 1/10 SCALE SHOCK TUBE MODEL - EFFECT OF CHAMBER PRESSURE ON BASE HEAT TRANSFER RATES

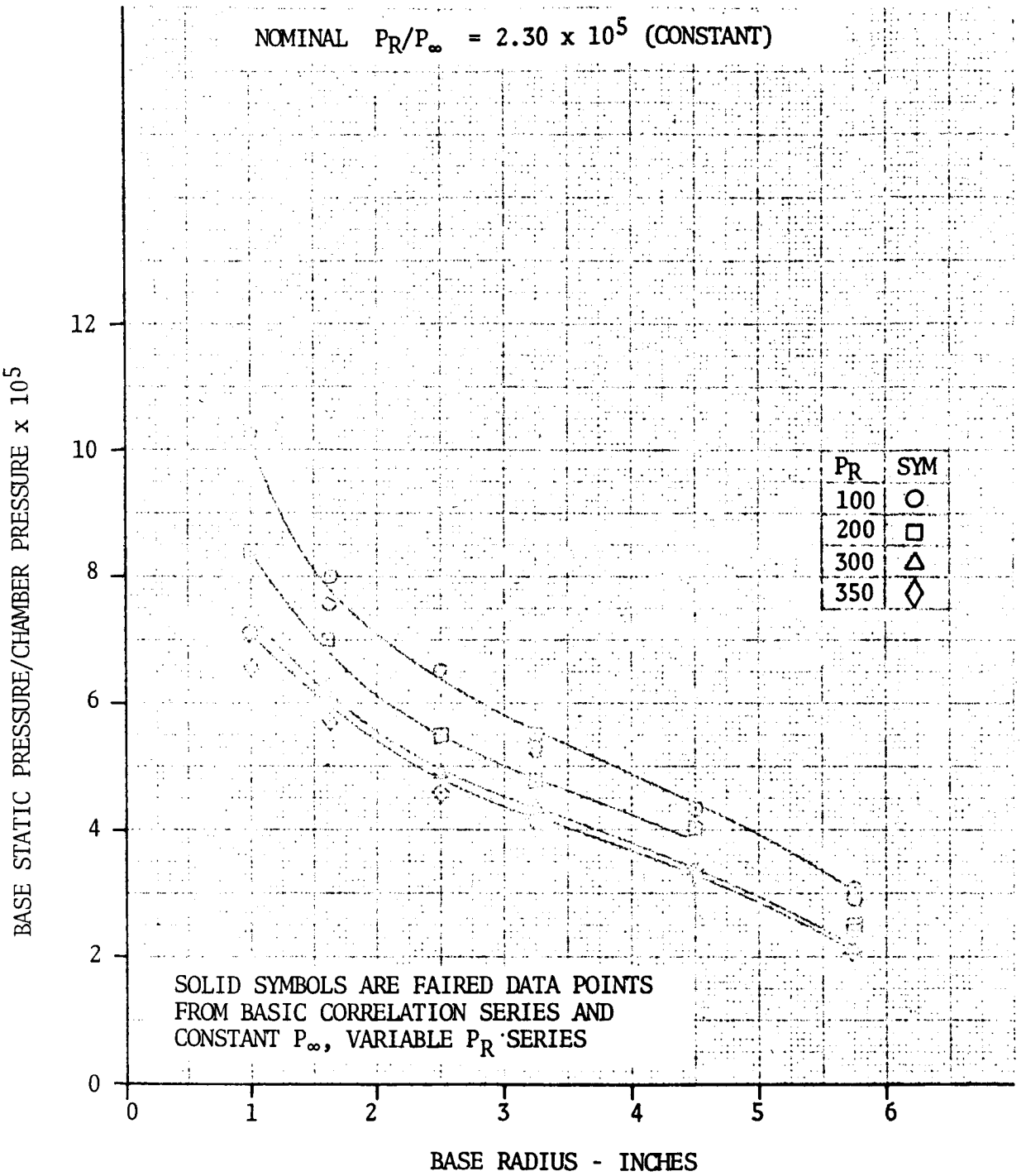

FIGURE 5.4-79. S-IV 6-ENGINE 1/10 SCALE SHOCK TUBE MODEL - EFFECT OF CHAMBER PRESSURE ON BASE STATIC PRESSURE

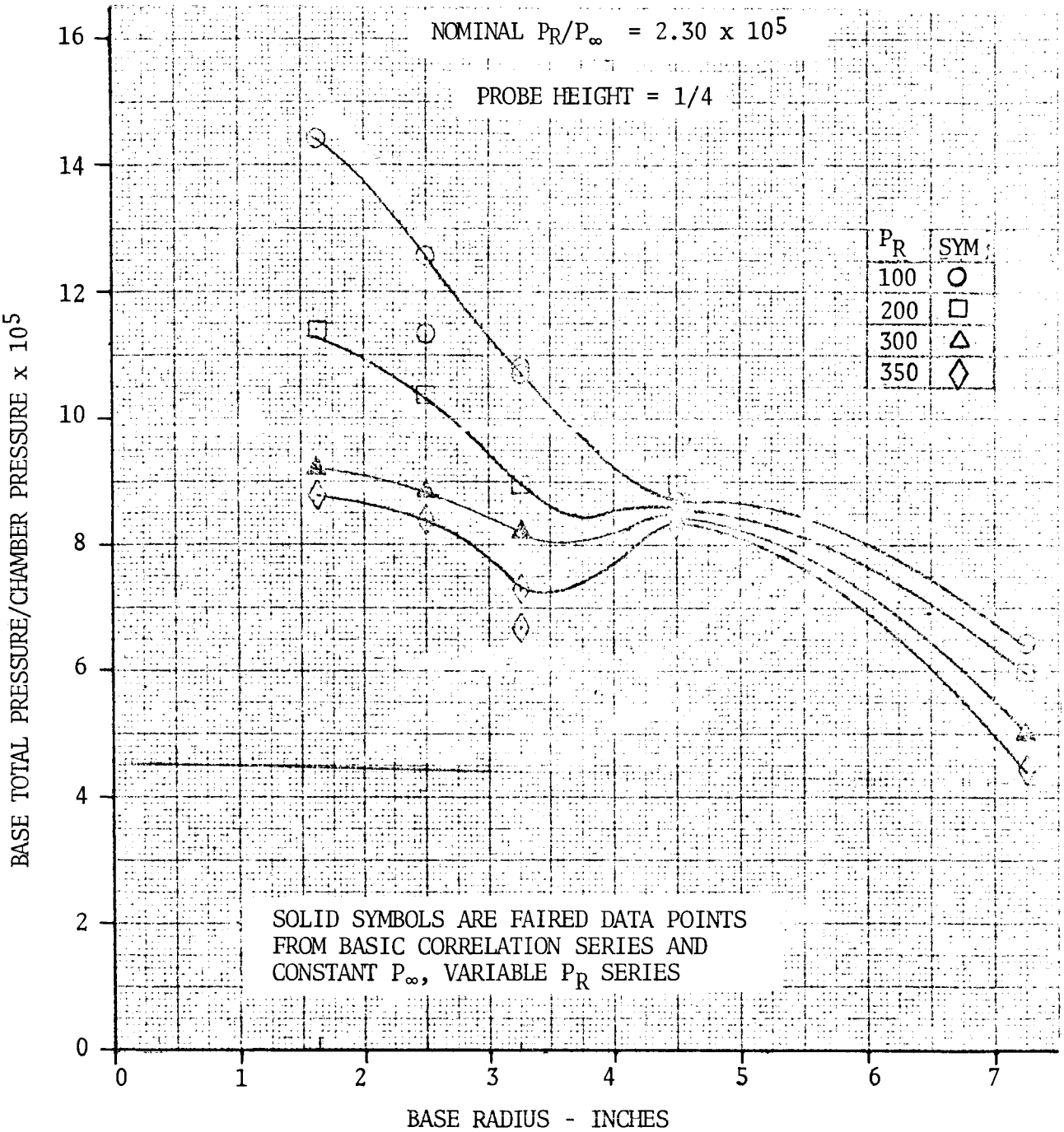

FIGURE 5.4-80. S-IV 6-ENGINE 1/10 SCALE SHOCK TUBE MODEL - EFFECT OF CHAMBER PRESSURE ON BASE TOTAL PRESSURE

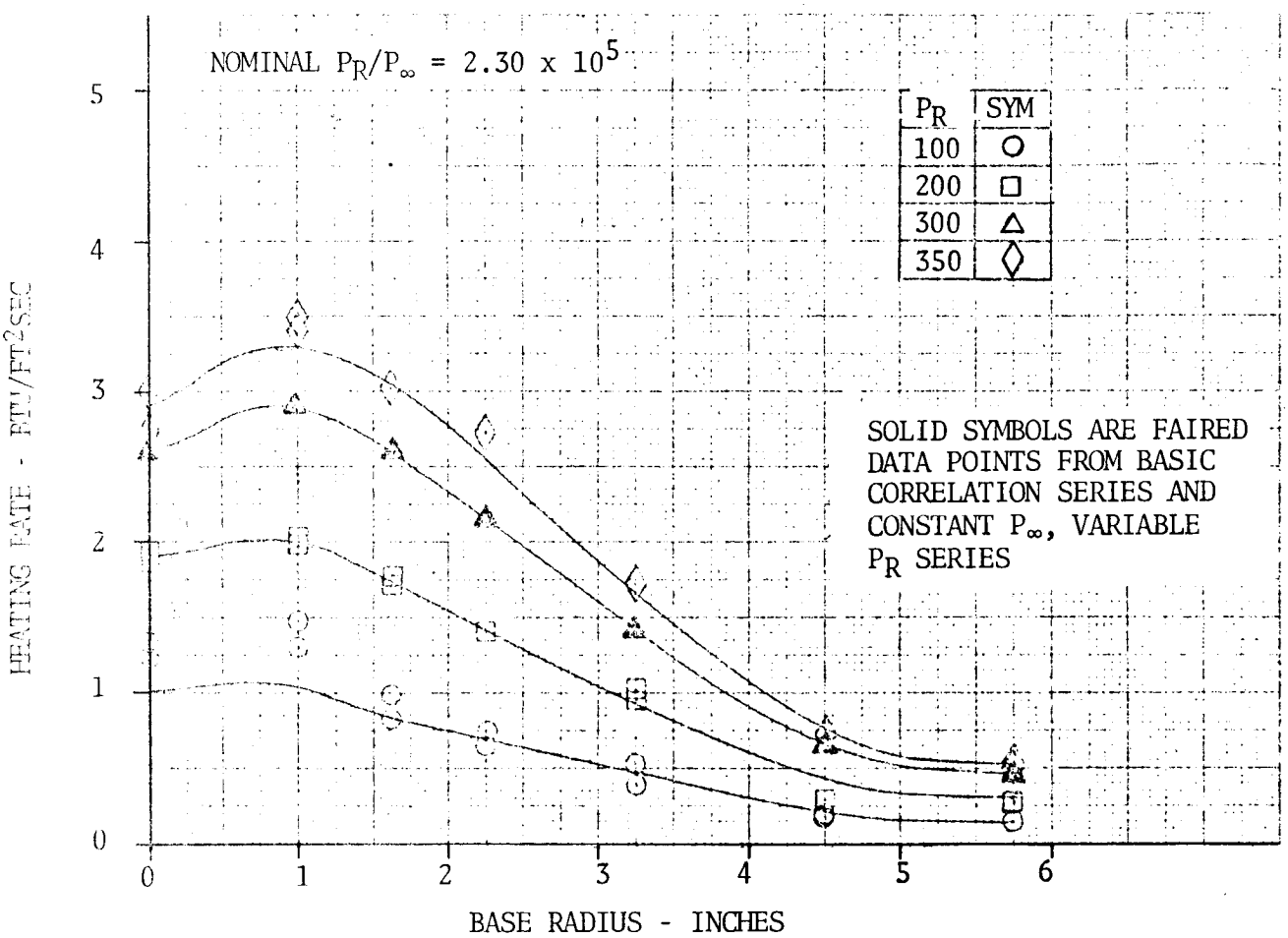

FIGURE 5.4-81. S-IV 6-ENGINE 1/10 SCALE SHOCK TUBE MODEL - EFFECT OF CHAMBER PRESSURE ON BASE HEAT TRANSFER RATES

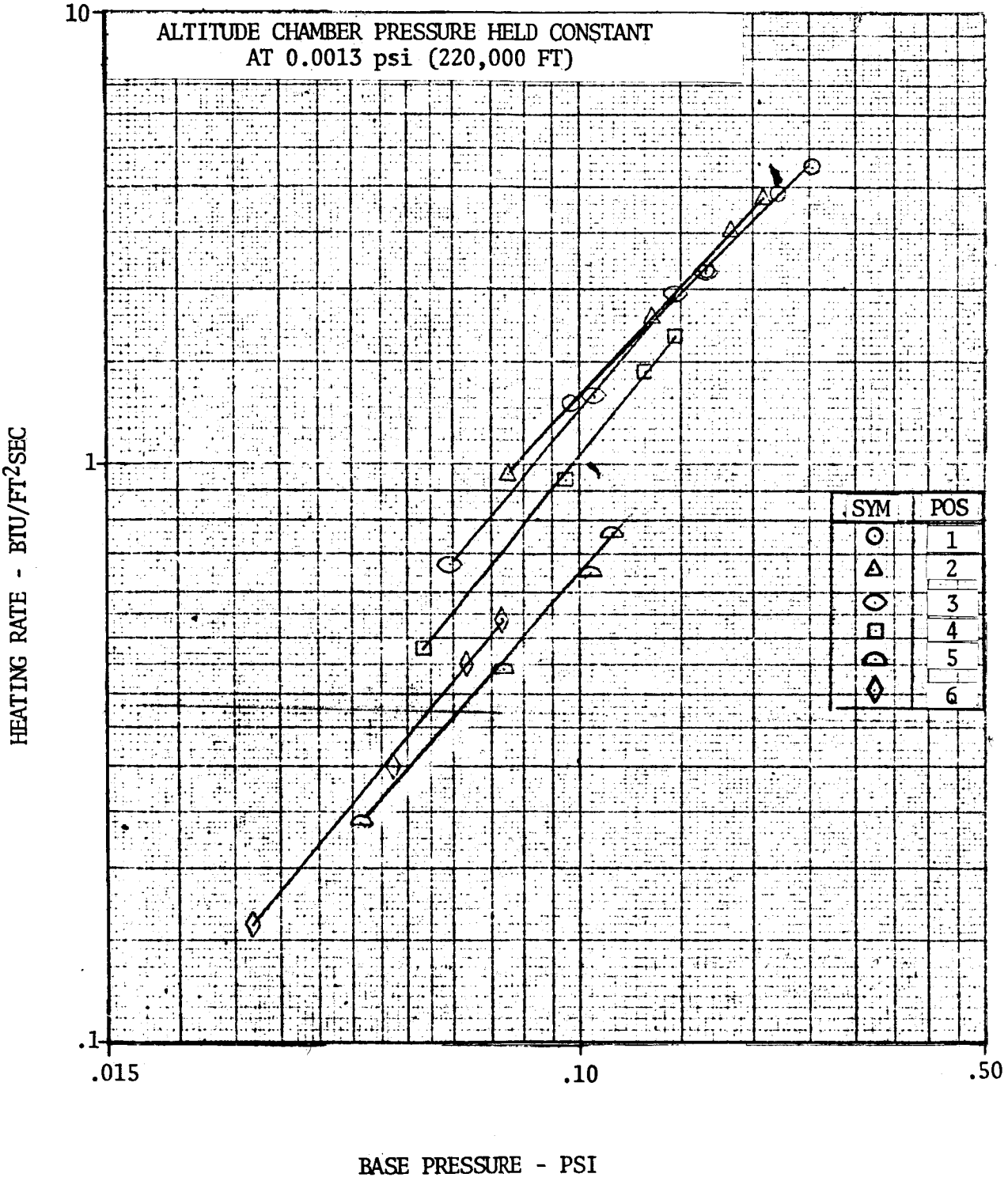

FIGURE 5.4-82. S-IV 6-ENGINE 1/10 SCALE SHOCK TUBE MODEL - CORRELATION OF BASE HEAT TRANSFER RATES WITH BASE PRESSURE

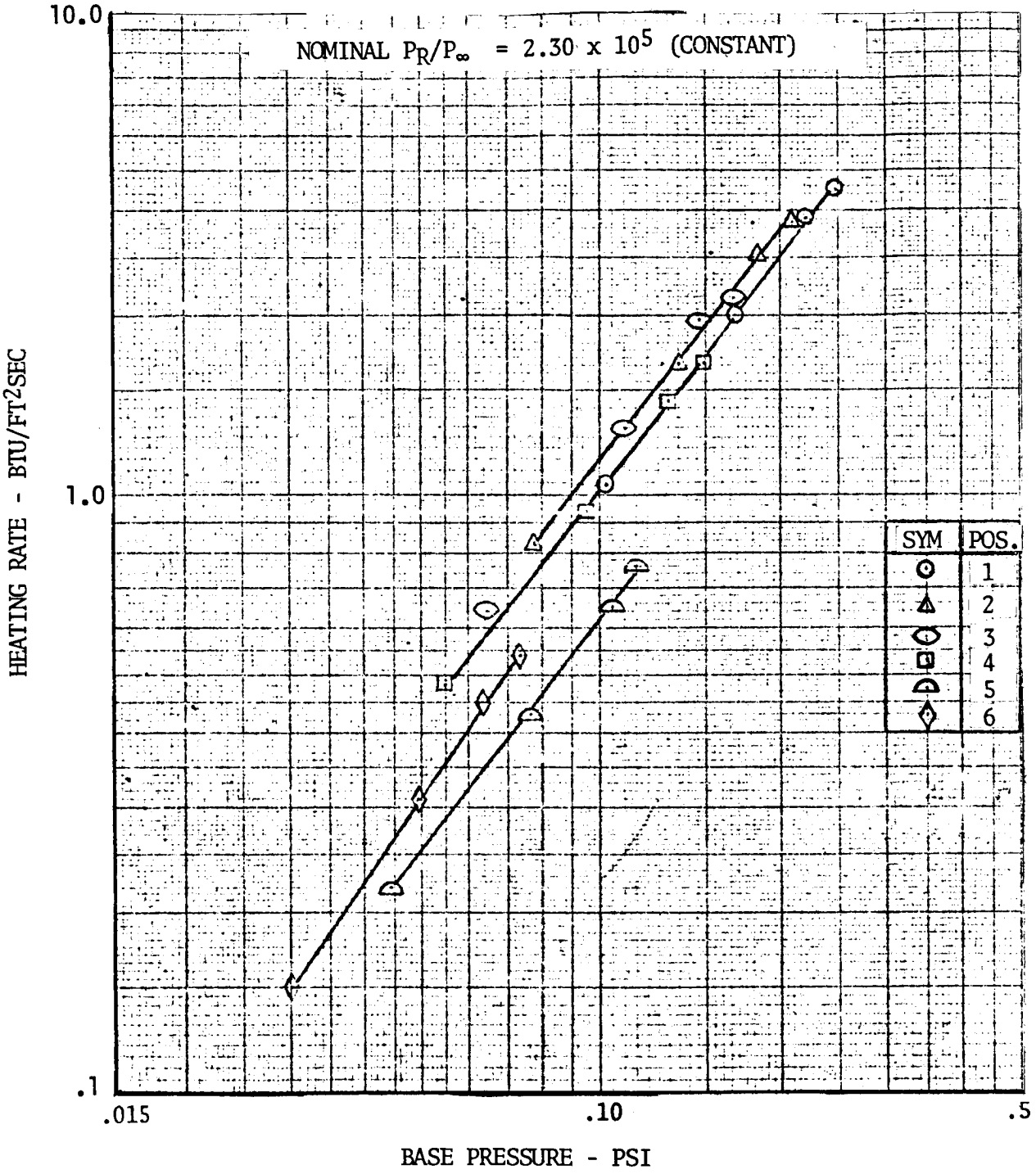

FIGURE 5.4-83. S-IV 6-ENGINE 1/10 SCALE SHOCK TUBE MODEL - CORRELATION OF BASE HEAT TRANSFER RATES WITH BASE PRESSURE

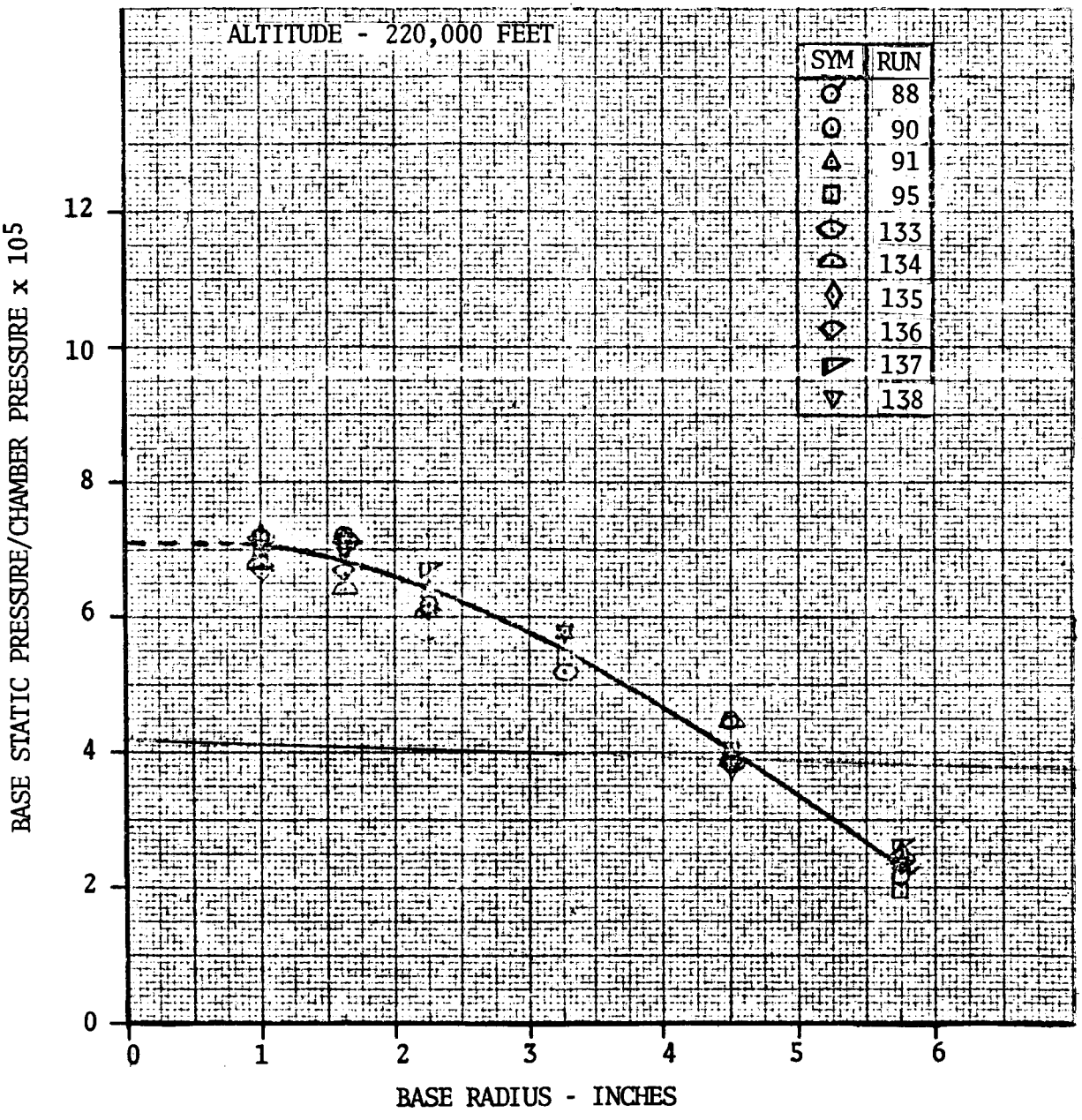

FIGURE 5.4-84. S-IV 6-ENGINE 1/10 SCALE SHOCK TUBE MODEL - BASE STATIC PRESSURE WITH SECONDARY EXHAUST

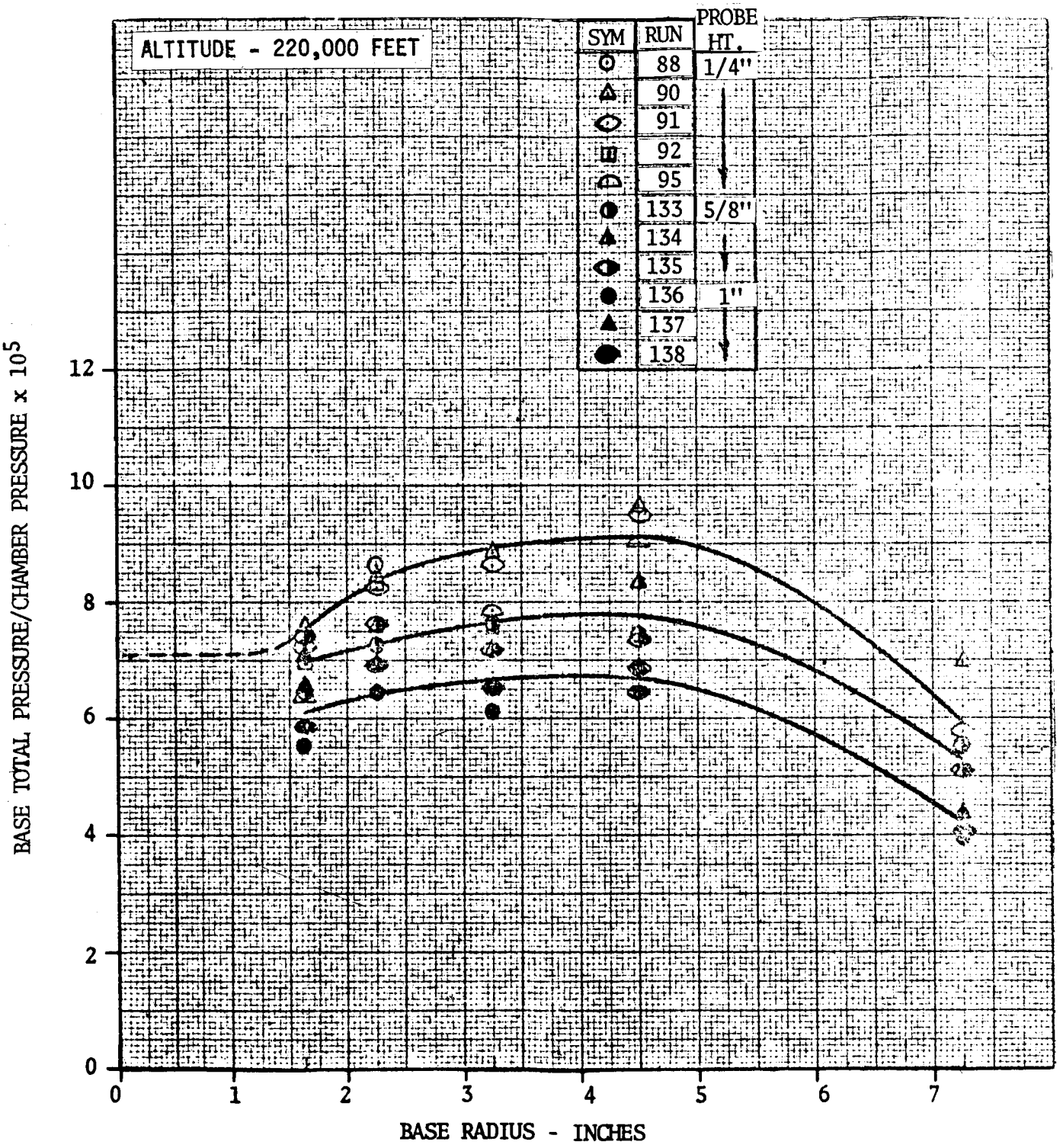

FIGURE 5.4-85. S-IV 6-ENGINE 1/10 SCALE SHOCK TUBE MODEL - BASE TOTAL PRESSURE WITH SECONDARY EXHAUST

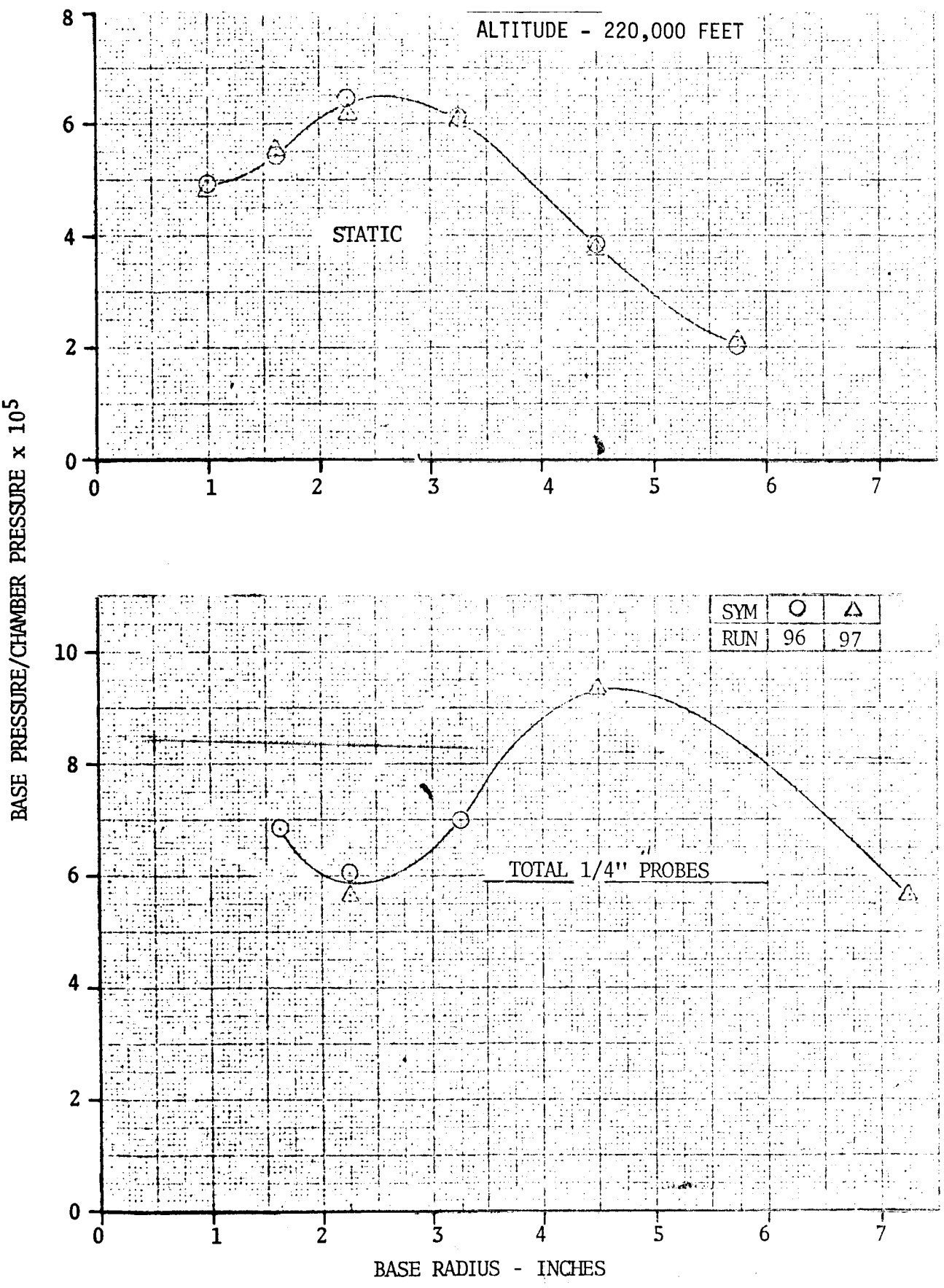

FIGURE 5.4-86. S-IV 6-ENGINE 1/10 SCALE SHOCK TUBE MODEL - BASE PRESSURES WITH SECONDARY EXHUAST AND DIVERTER

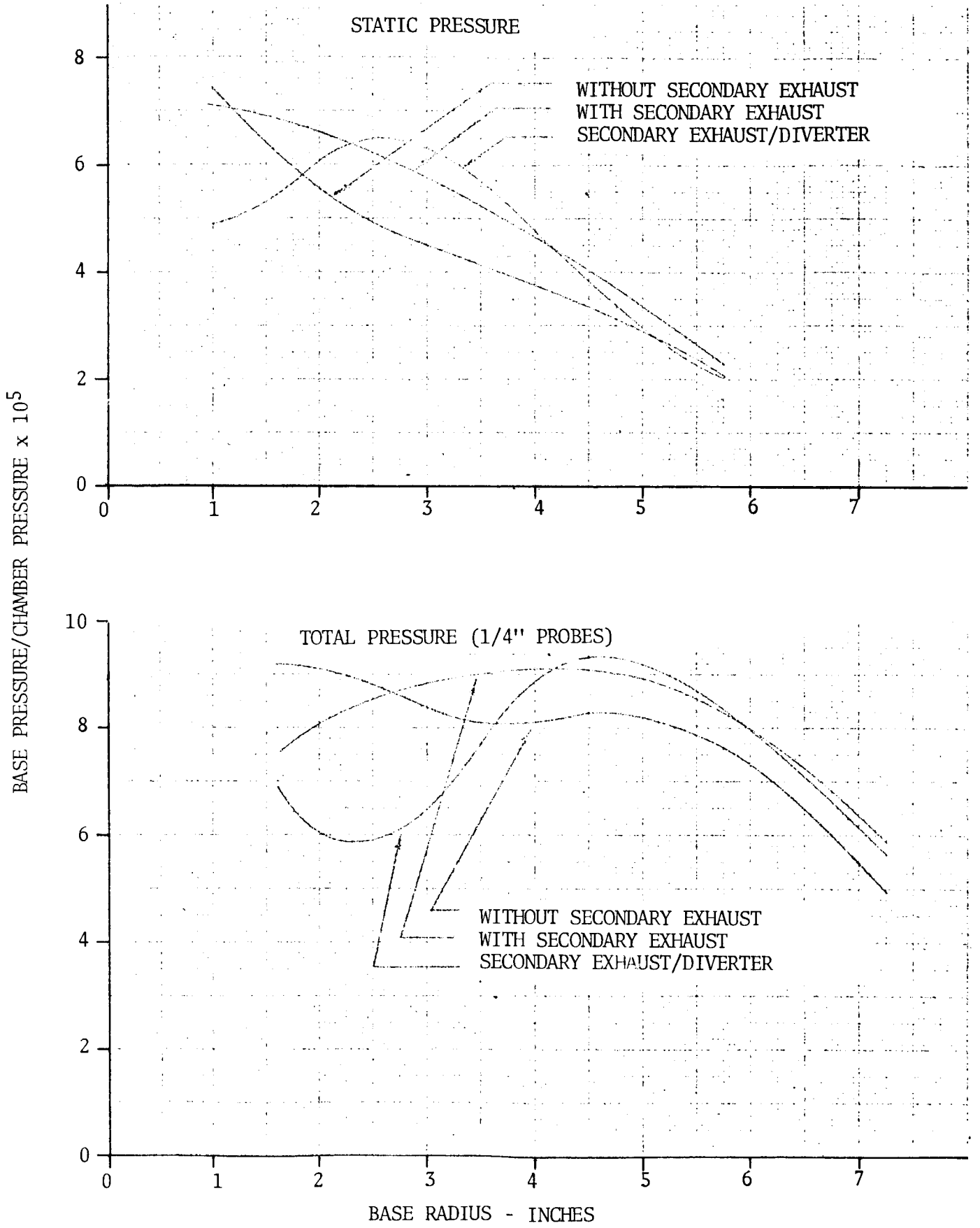

FIGURE 5.4-87. S-IV 6-ENGINE 1/10 SCALE SHOCK TUBE MODEL - EFFECTS OF SECONDARY EXHAUST ON BASE HEAT SHIELD PRESSURES

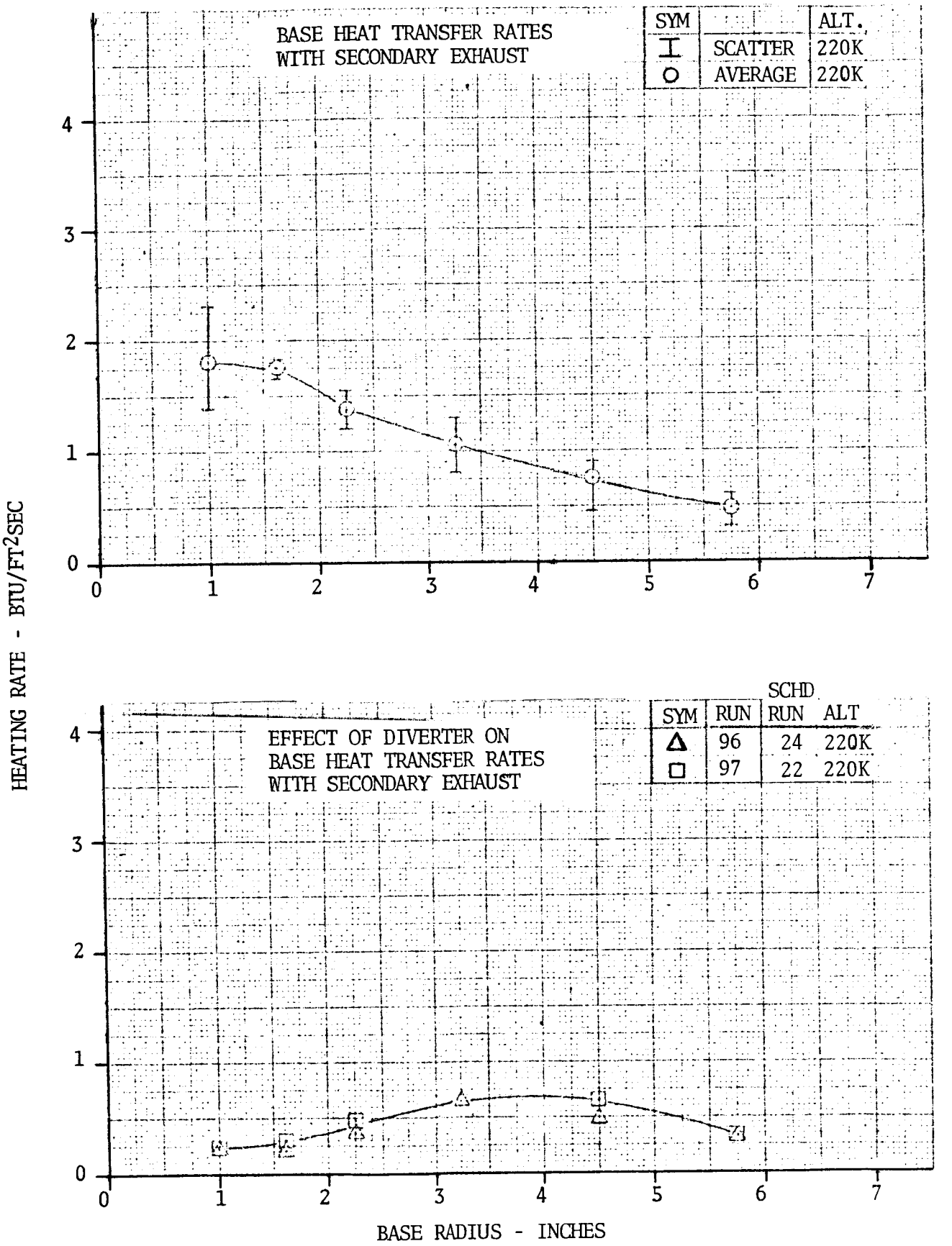

FIGURE 5.4-88. S-IV 6-ENGINE 1/10 SCALE SHOCK TUBE MODEL - EFFECT OF SECONDARY EXHAUST AND DIVERTER ON BASE HEAT SHIELD HEAT TRANSFER RATES

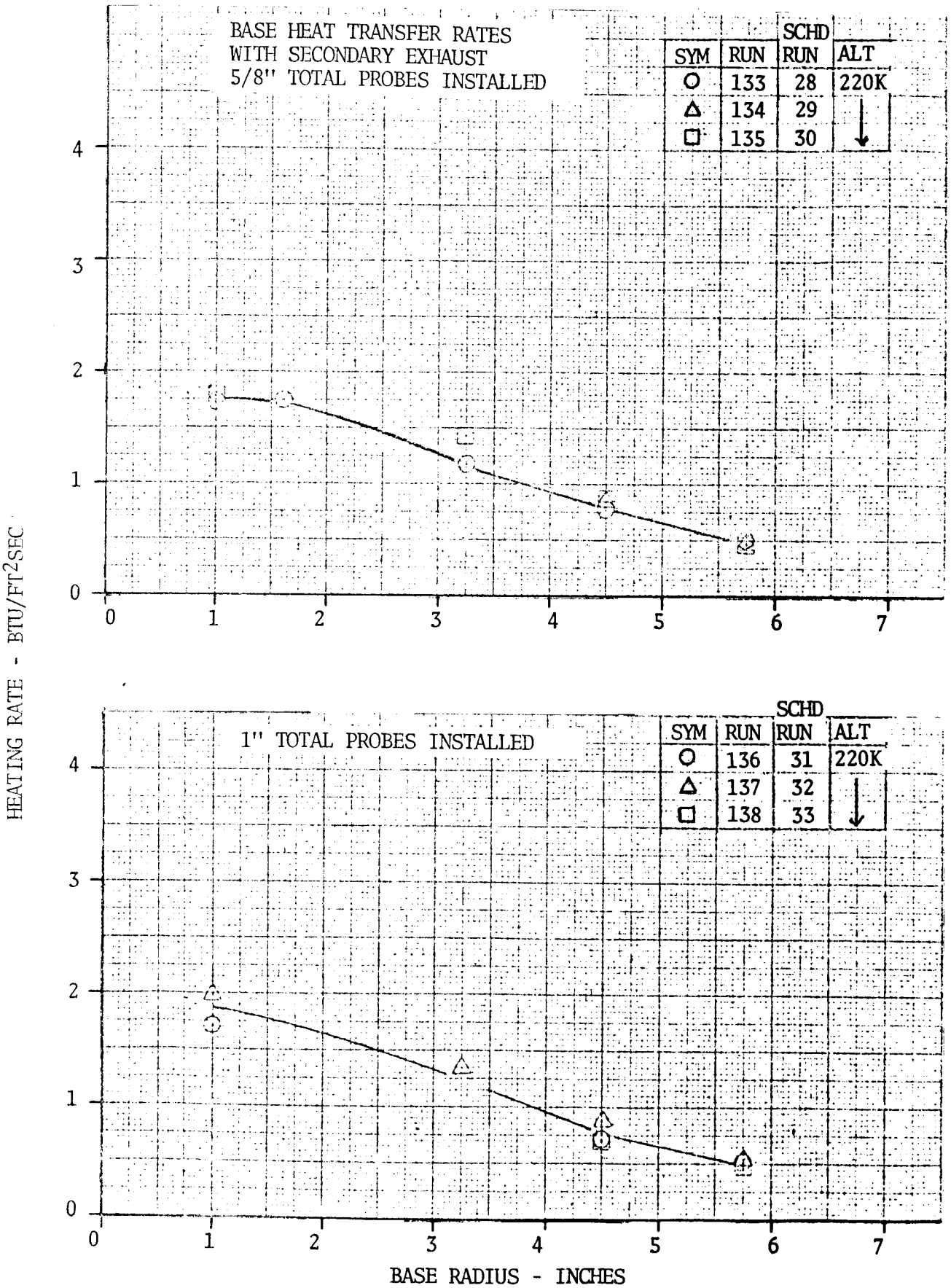

FIGURE 5.4-89. S-IV 6-ENGINE 1/10 SCALE SHOCK TUBE MODEL - EFFECTS OF SECONDARY EXHAUST ON BASE HEAT SHIELD HEAT TRANSFER RATES

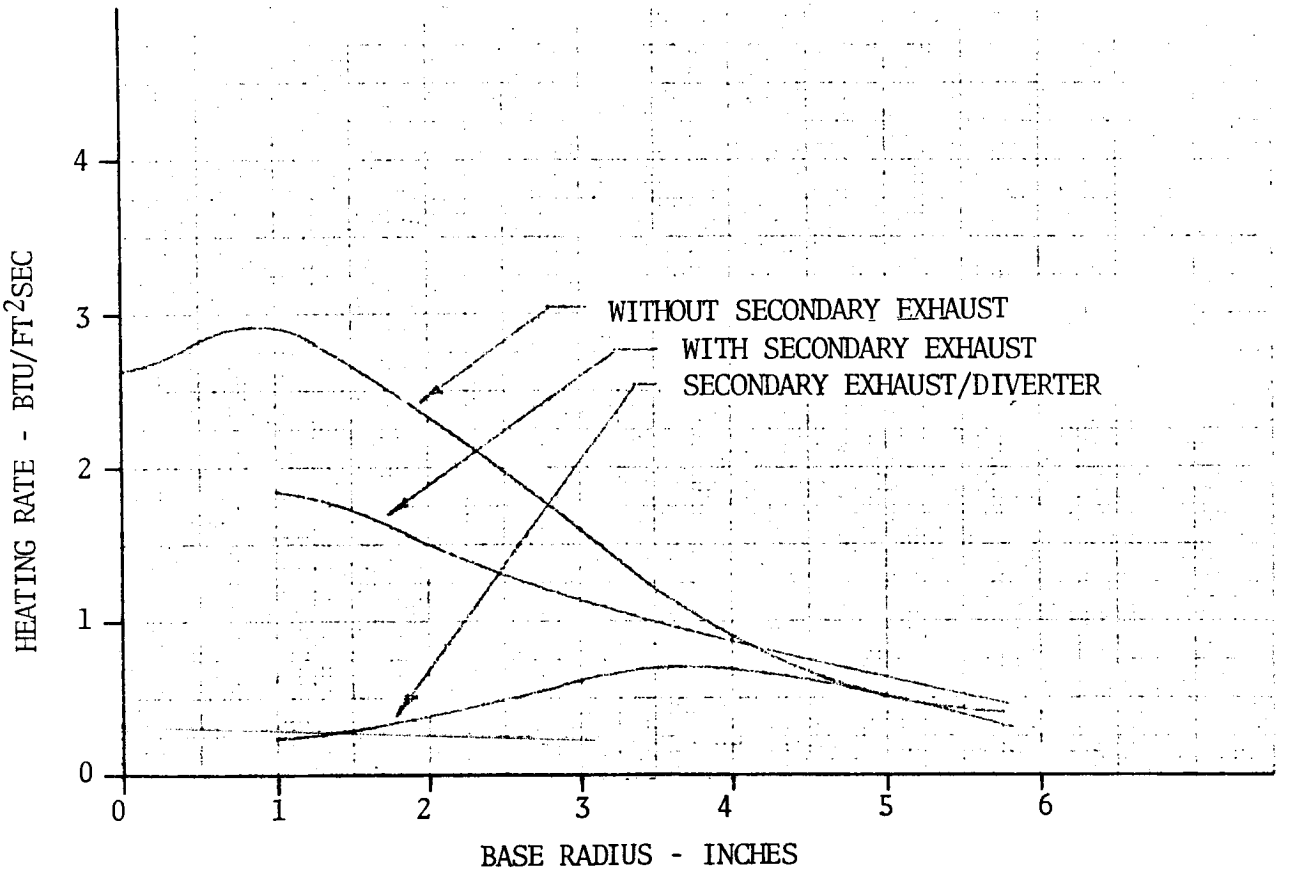

FIGURE 5.4-90. S-IV 6-ENGINE 1/10 SCALE SHOCK TUBE MODEL - EFFECTS OF SECONDARY EXHAUST ON BASE HEAT TRANSFER RATES

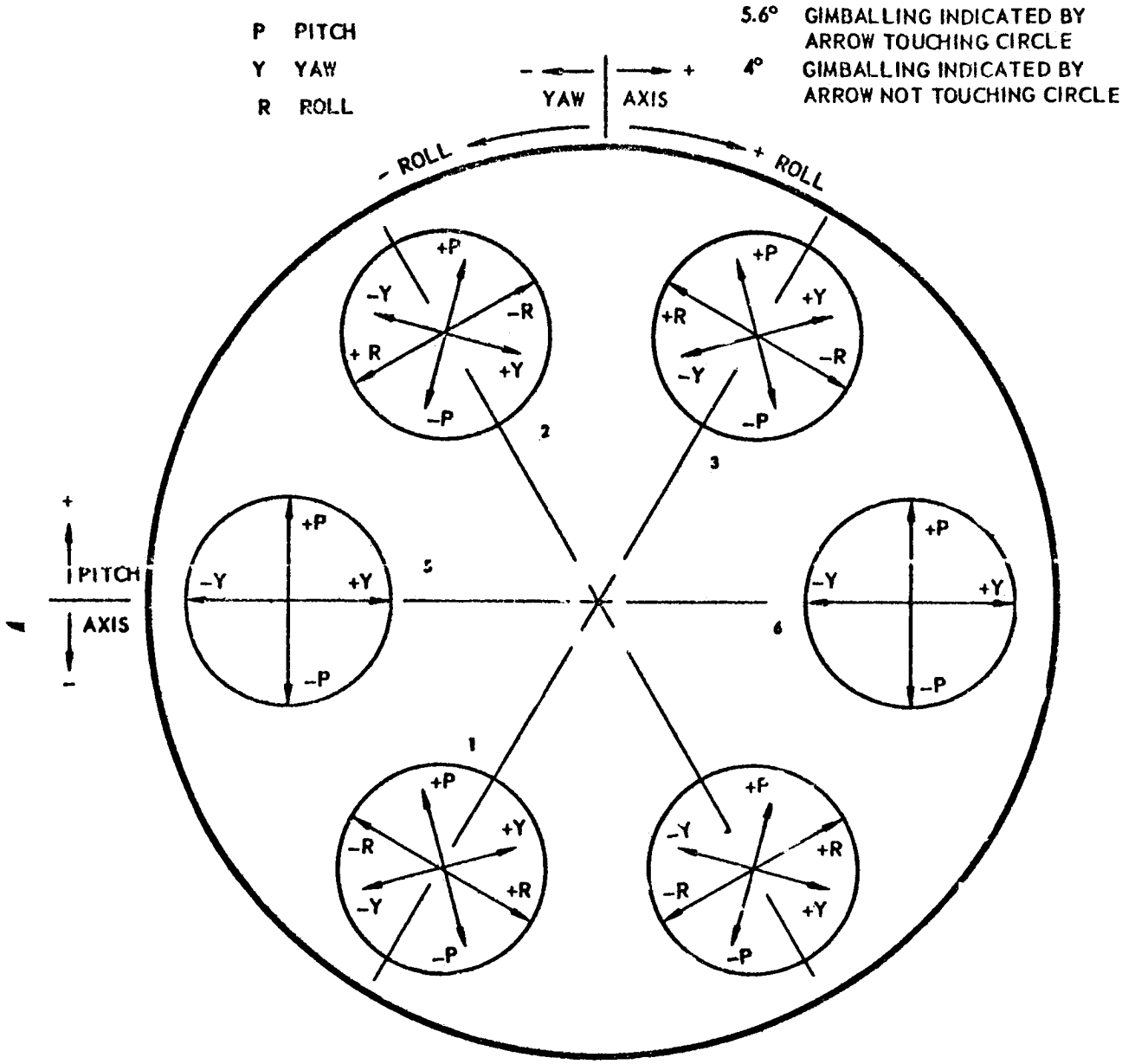

FIGURE 5.4-91. S-IV 6-ENGINE 1/10 SCALE SHOCK TUBE MODEL - GIMBAL PATTERNS

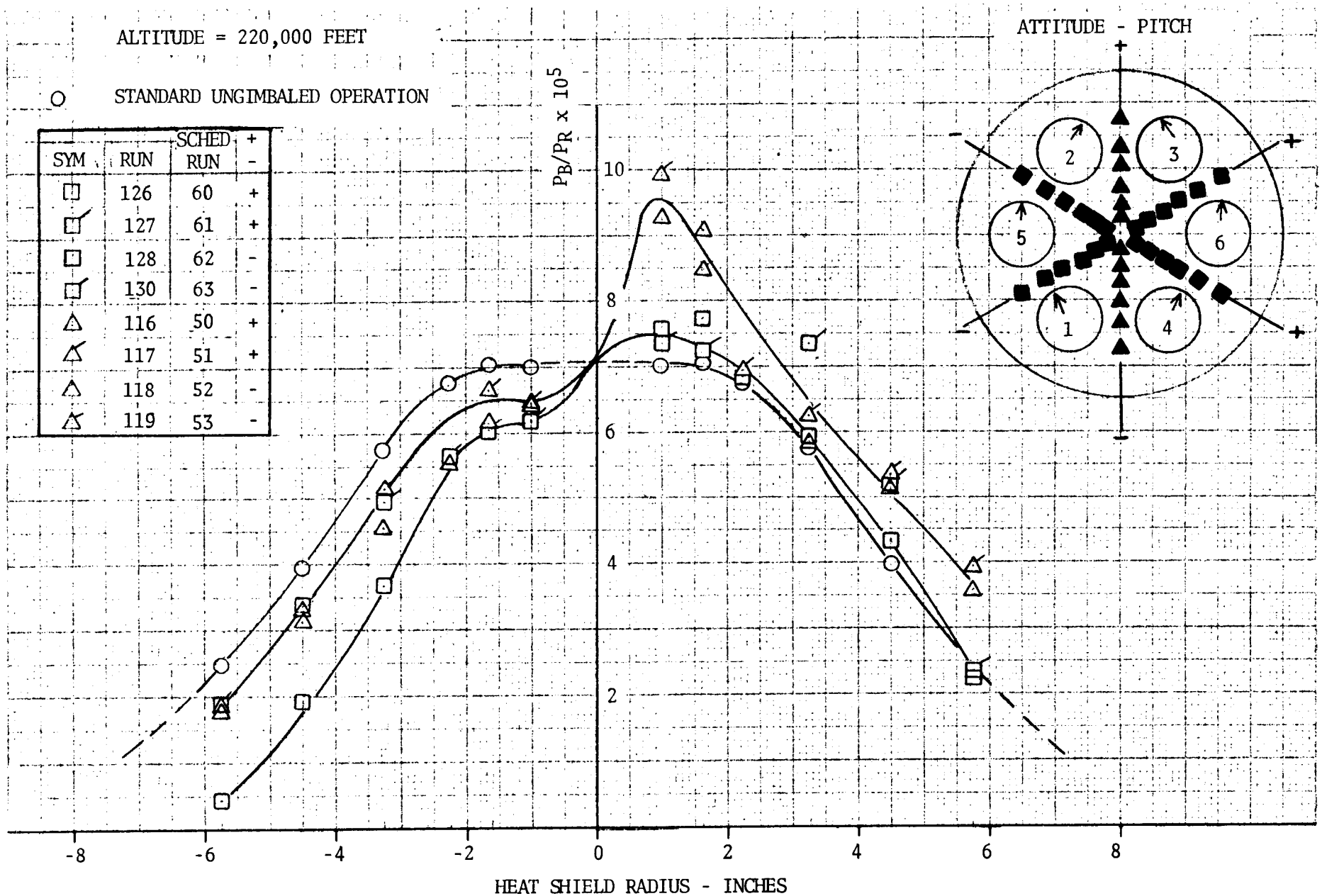

FIGURE 5.4-92. S-IV 6-ENGINE 1/10 SCALE SHOCK TUBE MODEL - EFFECT OF GIMBALLING ON BASE HEAT SHIELD STATIC PRESSURE DISTRIBUTION

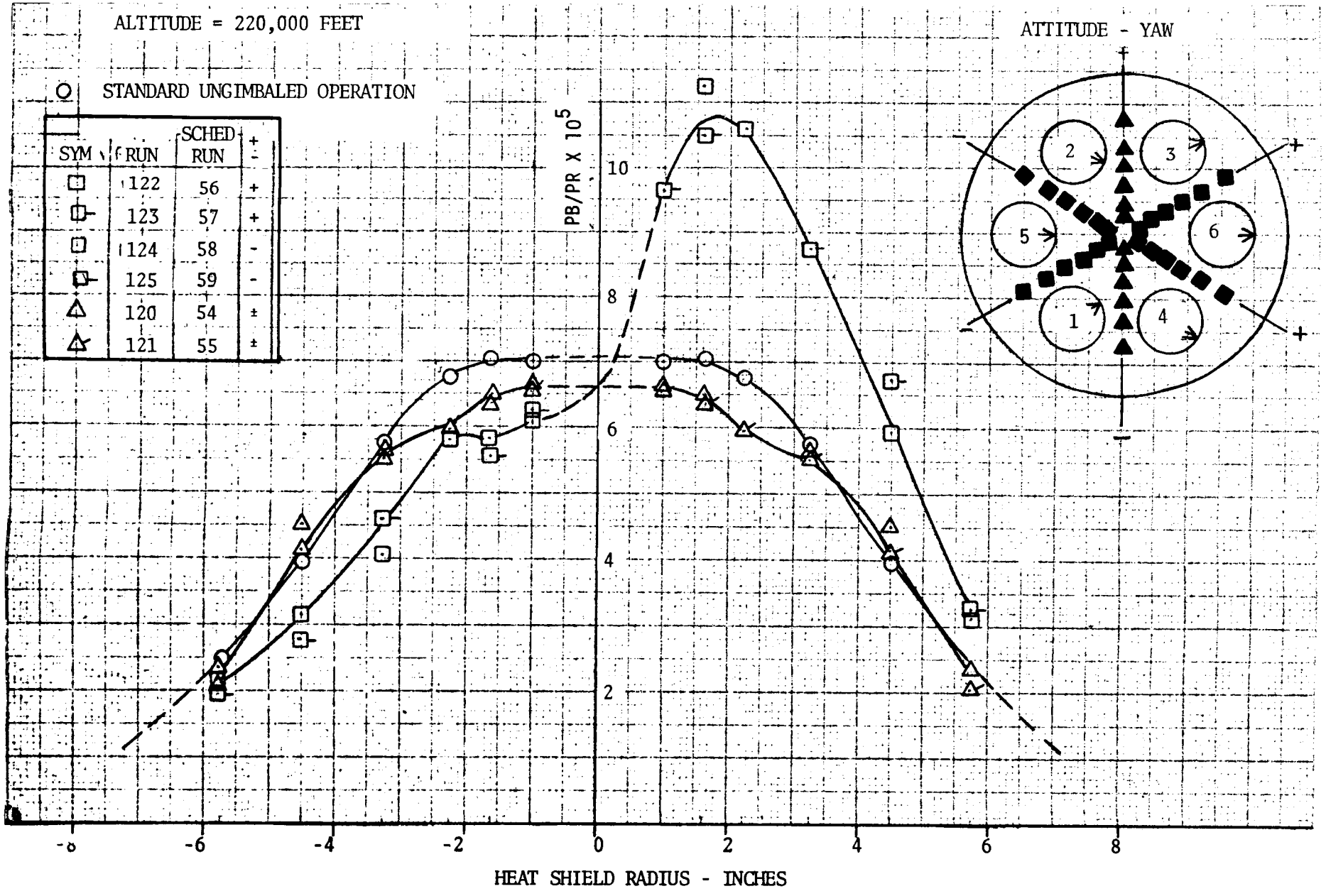

FIGURE 5.4-93. S-IV 6-ENGINE 1/10 SCALE SHOCK TUBE MODEL - EFFECT OF GIMBALLING ON BASE HEAT SHIELD STATIC PRESSURE DISTRIBUTION

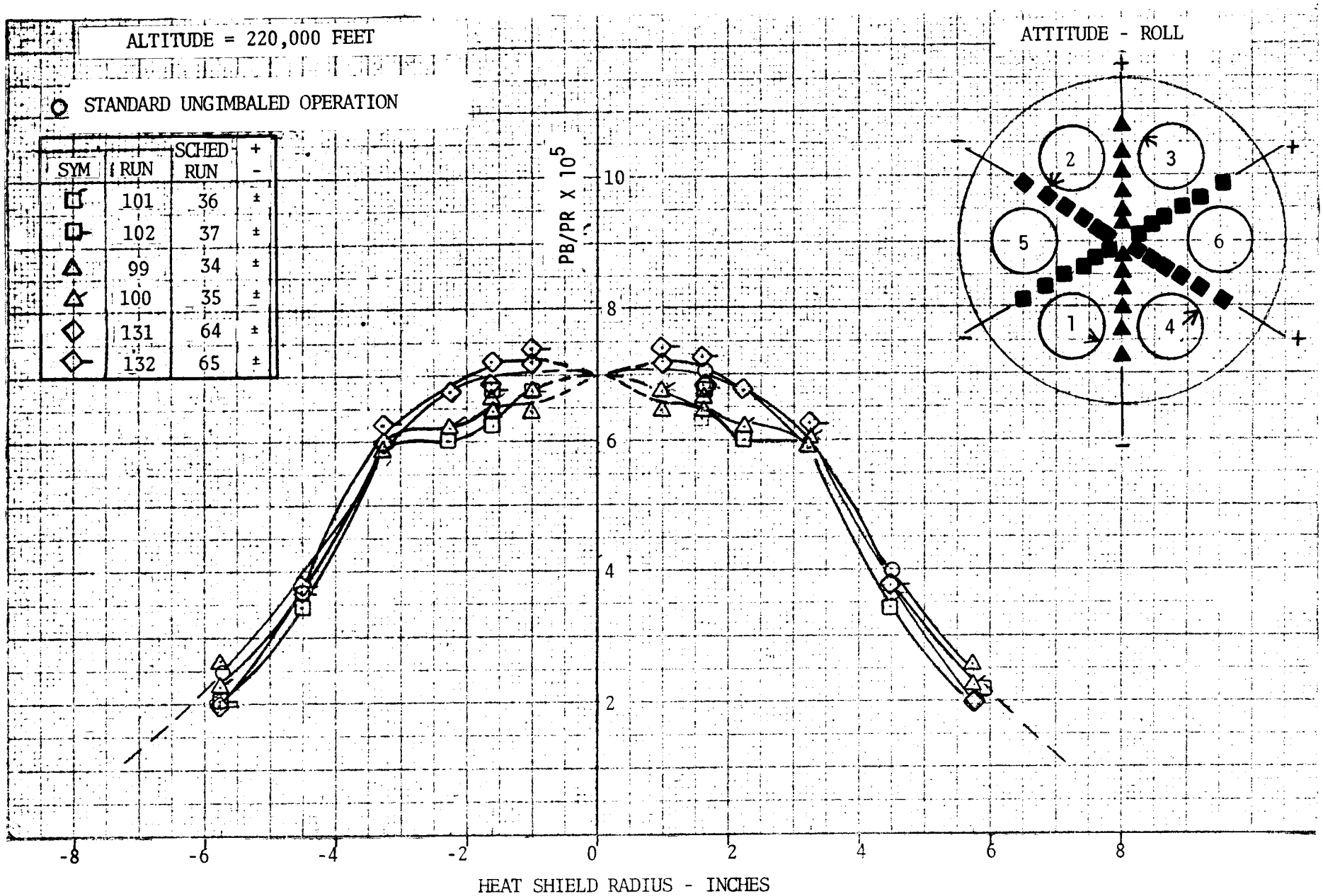

S-129

FIGURE 5.4-94. S-IV 6-ENGINE 1/10 SCALE SHOCK TUBE MODEL - EFFECTS OF GIMBALLING ON BASE HEAT SHIELD PRESSURE DISTRIBUTION

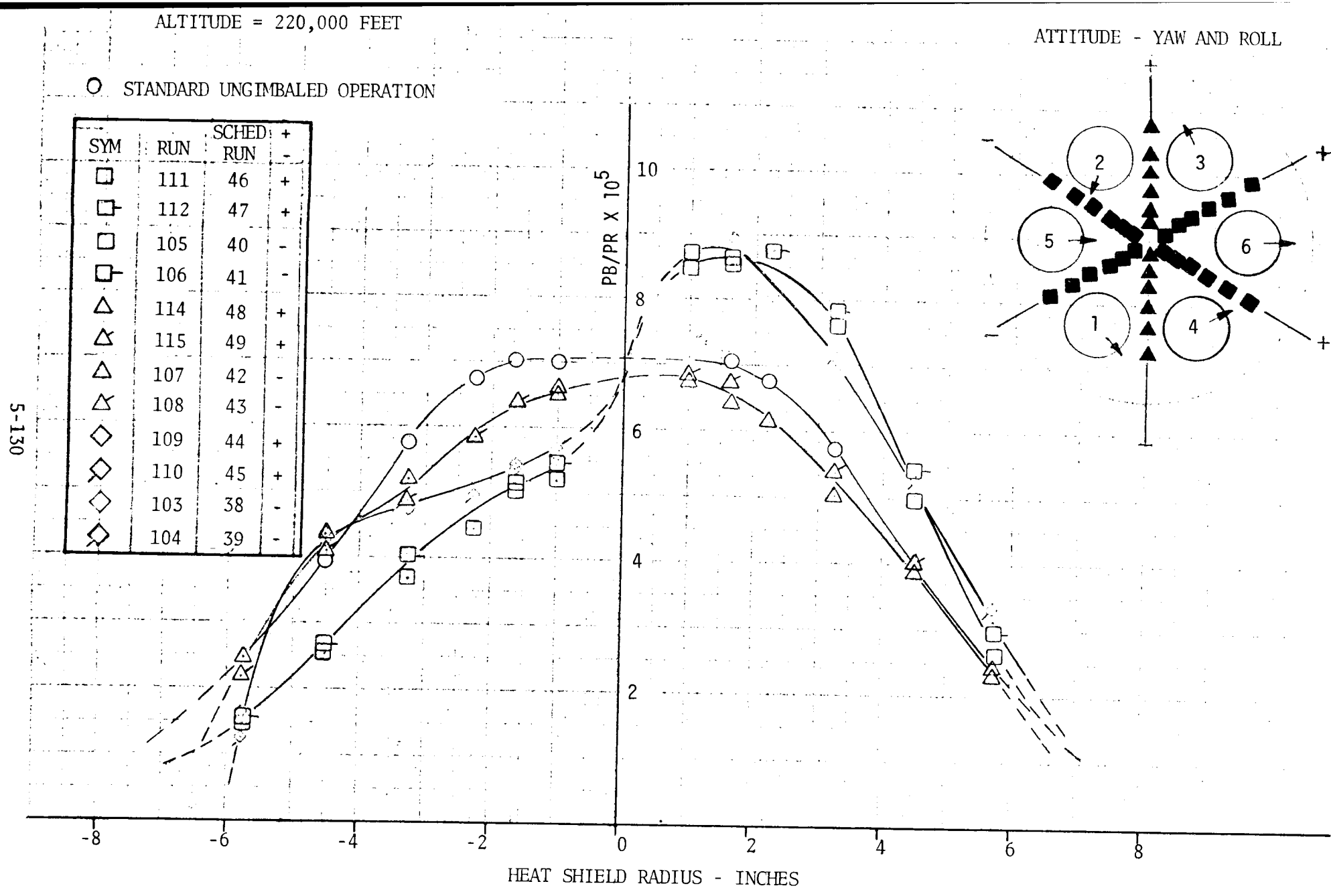

FIGURE 5.4-95. S-IV 6-ENGINE 1/10 SCALE SHOCK TUBE MODEL - EFFECT OF GIMBALLING ON BASE HEAT SHIELD STATIC PRESSURE DISTRIBUTION

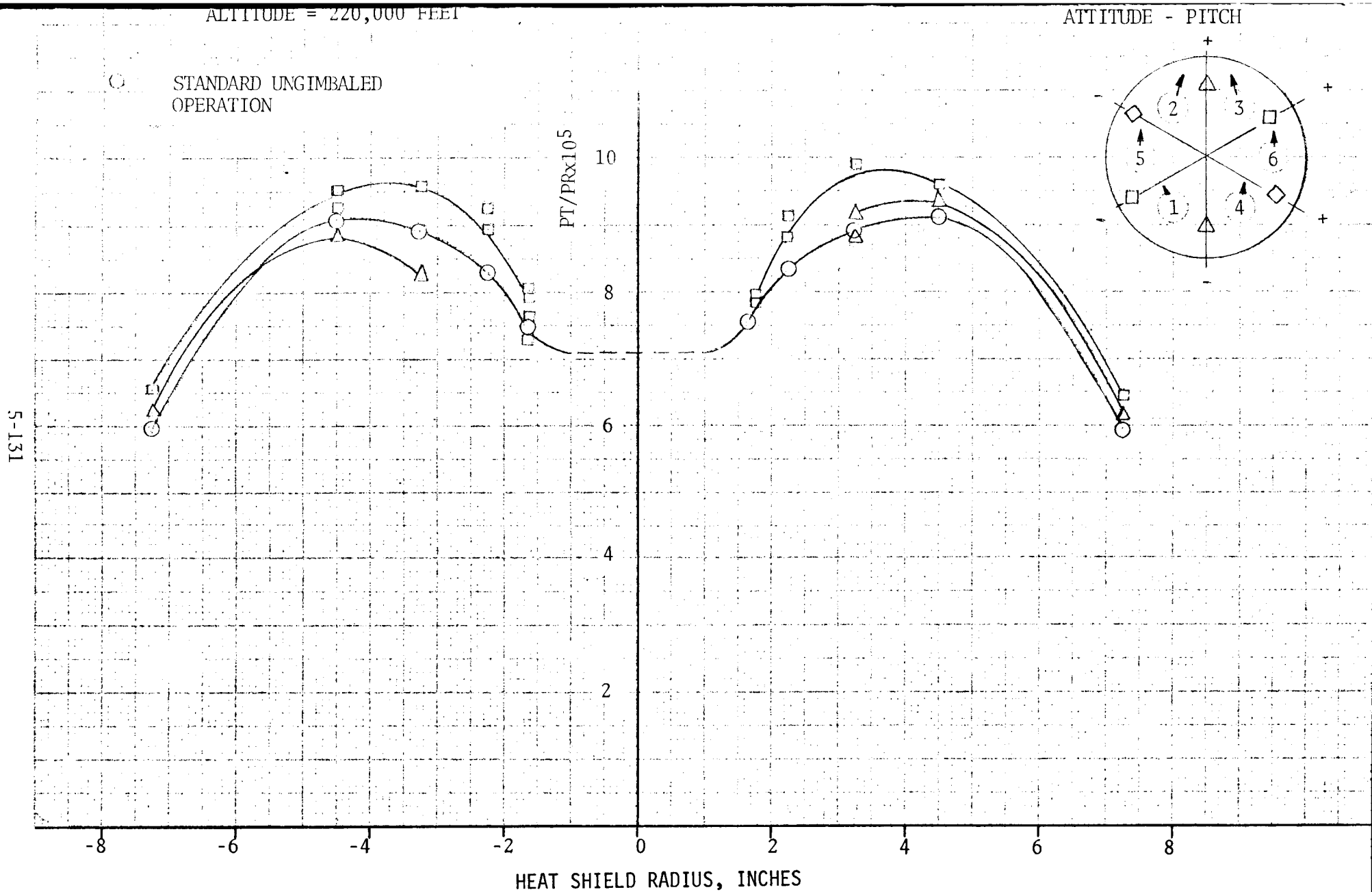

FIGURE 5.4-96. S-IV 6-ENGINE 1/10 SCALE SHOCK TUBE MODEL - EFFECTS OF GIMBALLING ON BASE HEAT SHIELD TOTAL PRESSURE DISTRIBUTION

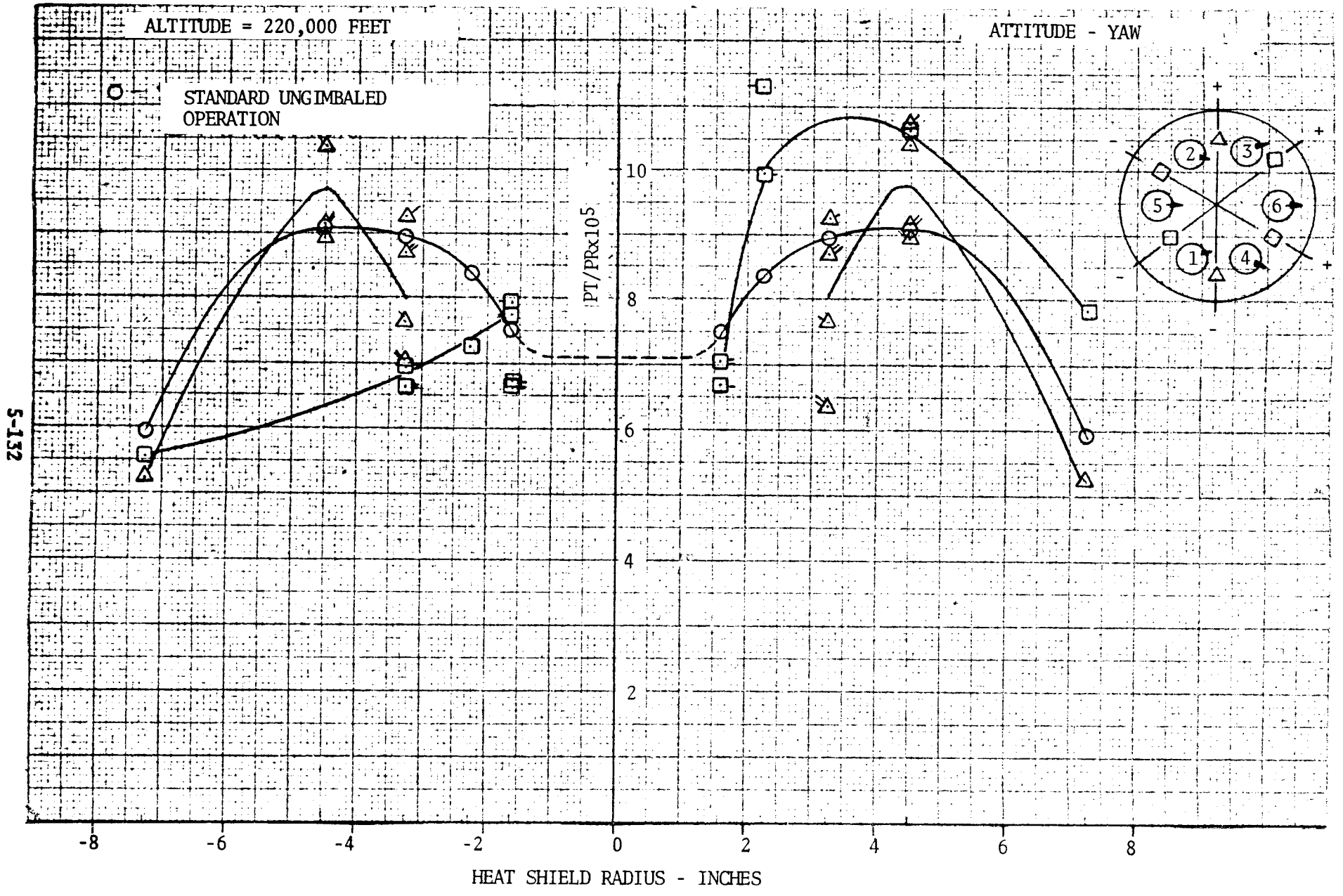

FIGURE 5.4-97. S-IV 6-ENGINE 1/10 SCALE SHOCK TUBE MODEL - EFFECT OF GIMBALLING ON BASE HEAT SHIELD TOTAL PRESSURE DISTRIBUTION

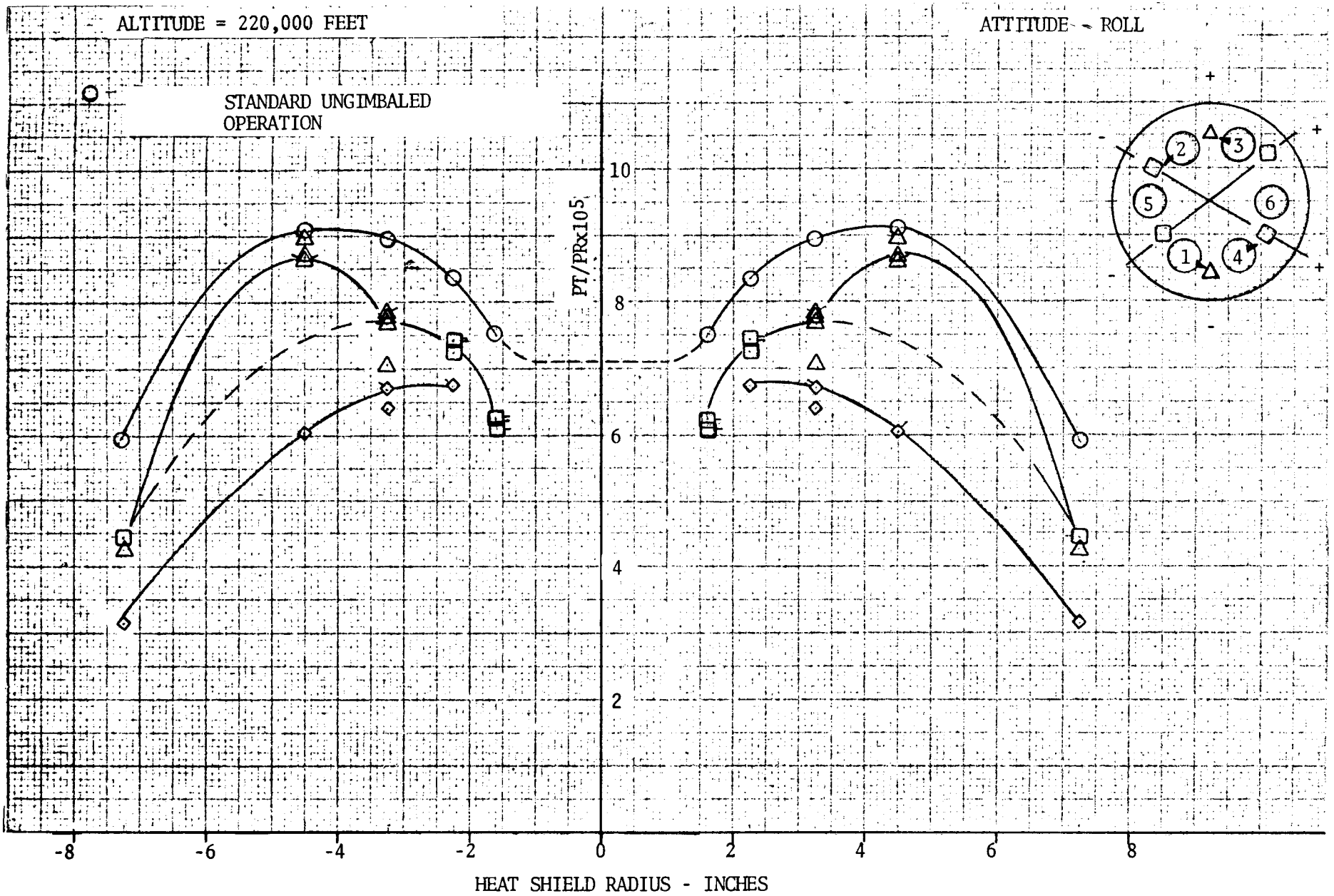

FIGURE 5.4-98. S-IV 6-ENGINE 1/10 SCALE SHOCK TUBE MODEL - EFFECT OF GIMBALLING ON BASE HEAT SHIELD TOTAL PRESSURE DISTRIBUTION

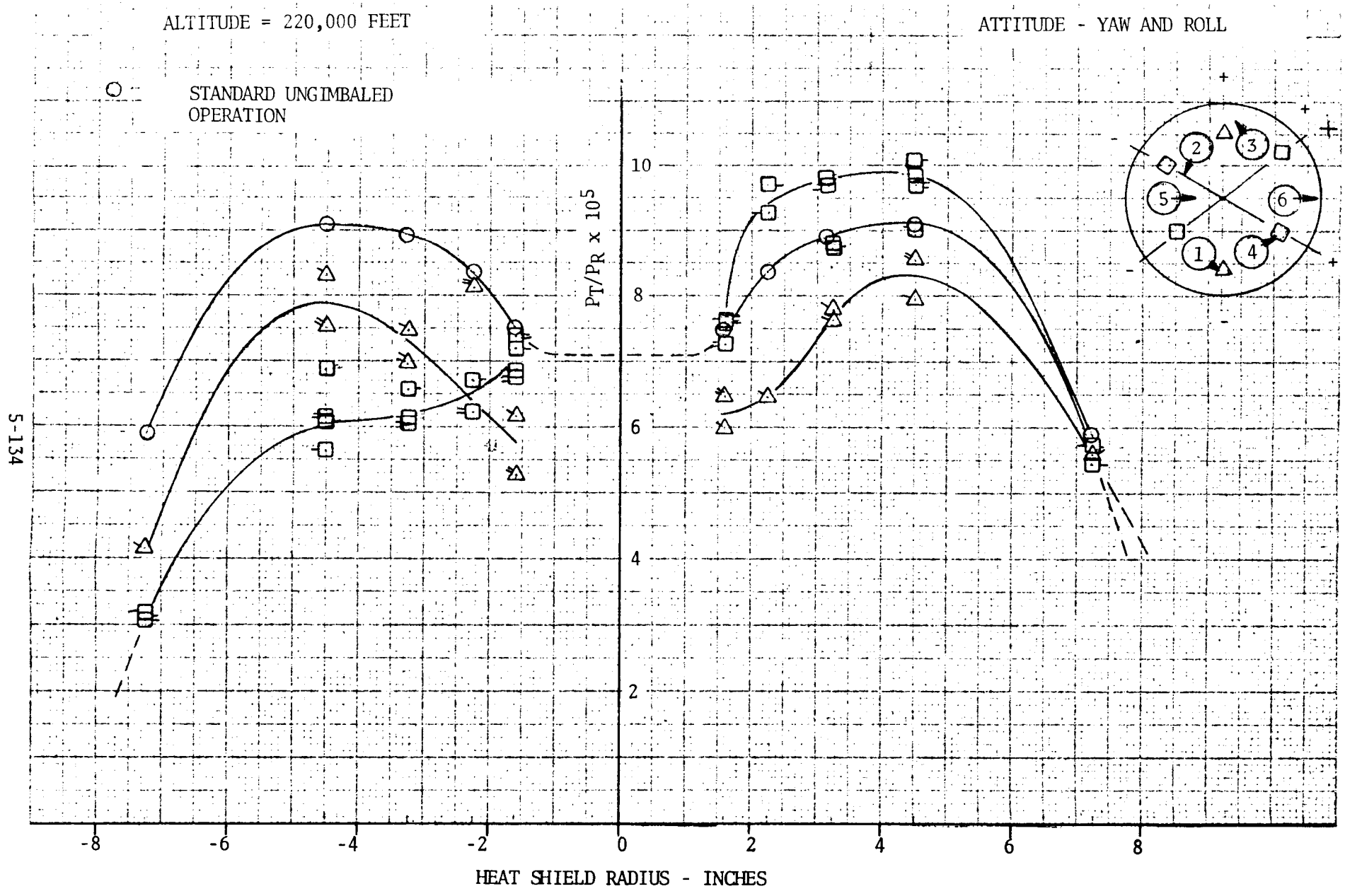

FIGURE 5.4-99. S-IV 6-ENGINE 1/10 SCALE SHOCK TUBE MODEL - EFFECT OF GIMBALLING ON BASE HEAT SHIELD TOTAL PRESSURE DISTRIBUTION

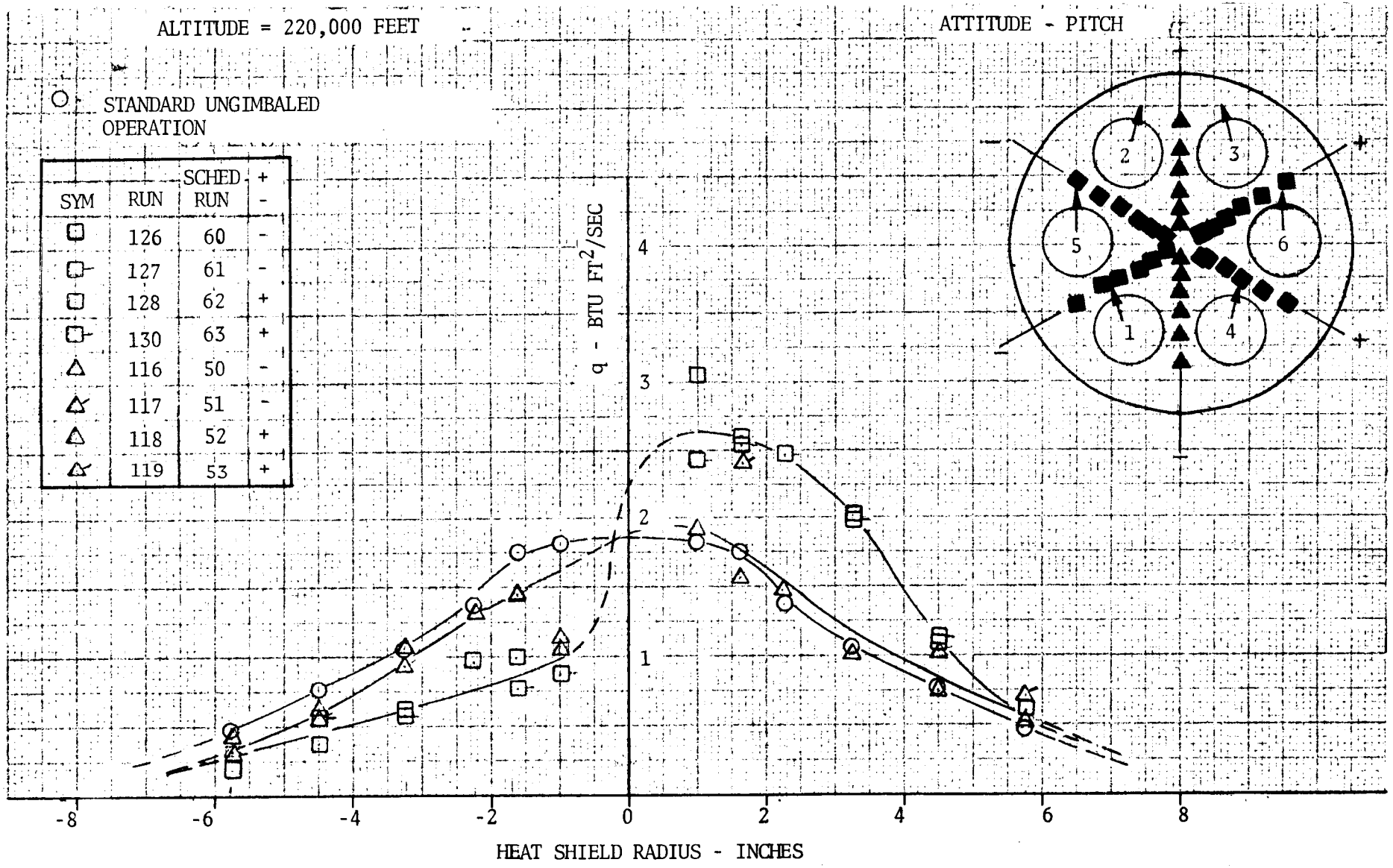

FIGURE 5.4-100. S-IV 6-ENGINE 1/10 SCALE SHOCK TUBE MODEL - EFFECT OF GIMBALLING ON BASE HEAT SHIELD HEAT FLUX DISTRIBUTION

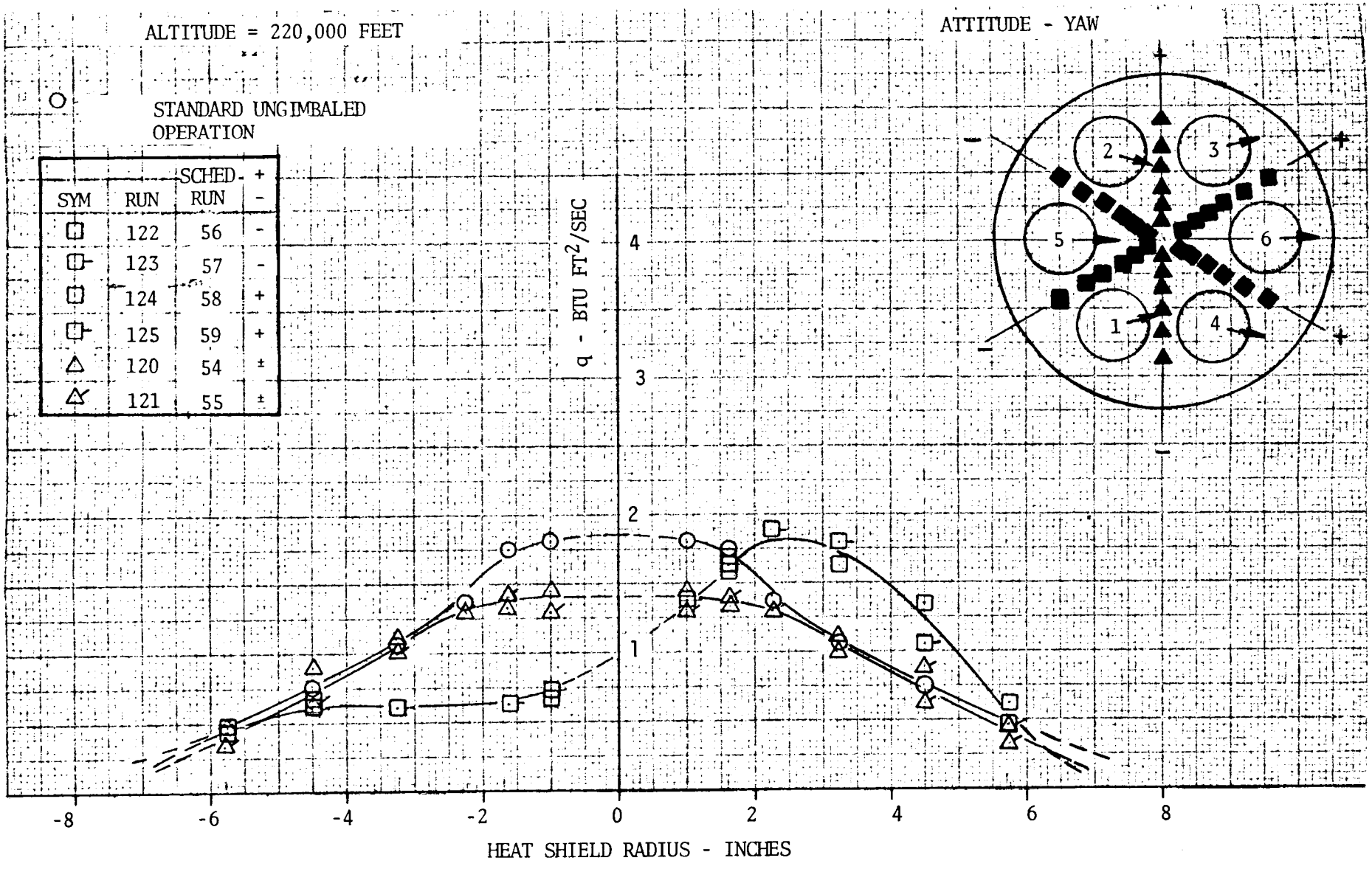

FIGURE 5.4-101. S-IV 6-ENGINE 1/10 SCALE SHOCK TUBE MODEL - EFFECT OF GIMBALLING ON BASE HEAT SHIELD TOTAL FLUX DISTRIBUTION

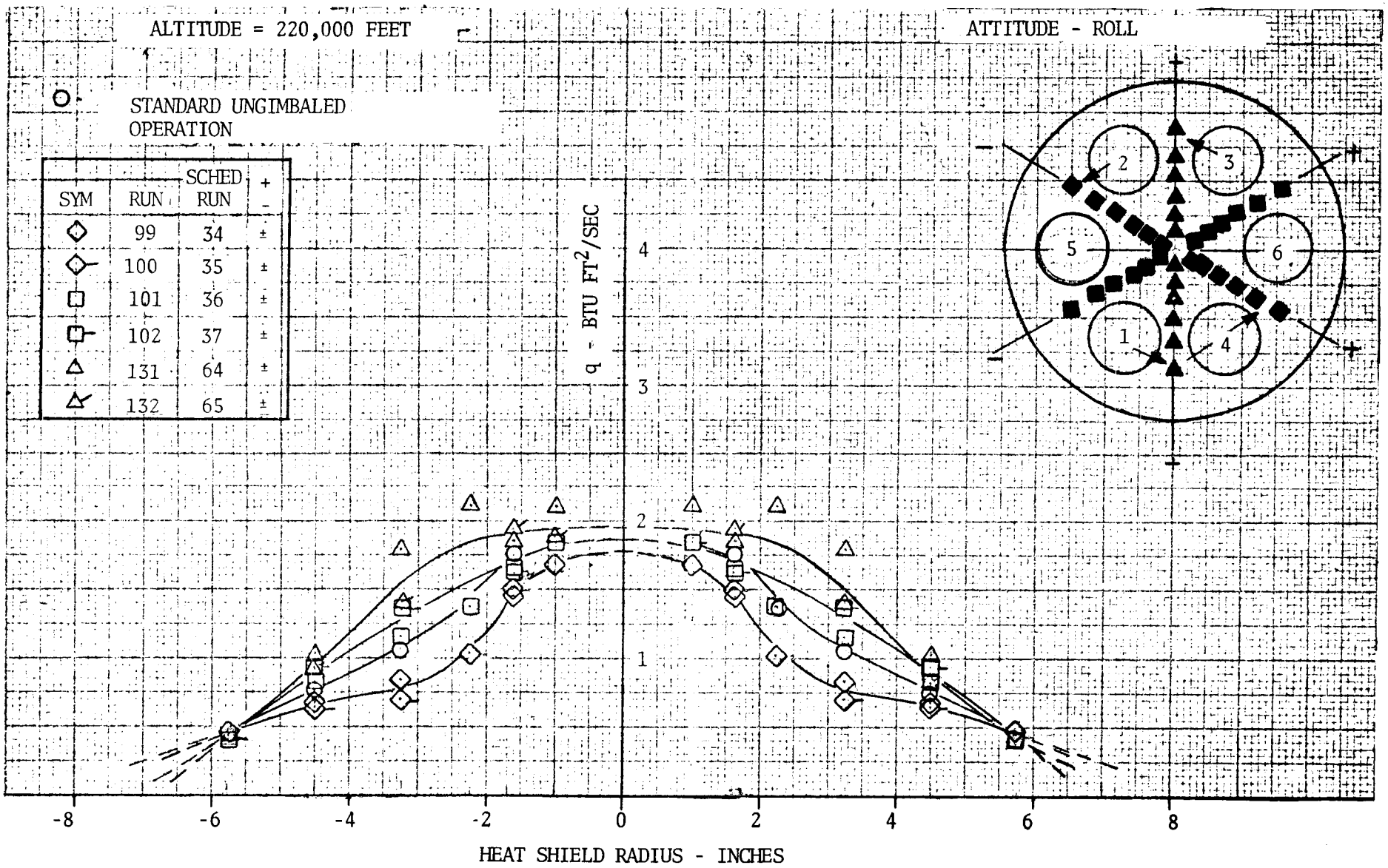

FIGURE 5.4-102. S-IV 6-ENGINE 1/10 SCALE SHOCK TUBE MODEL - EFFECT OF GIMBALLING ON BASE HEAT SHIELD HEAT FLUX DISTRIBUTION

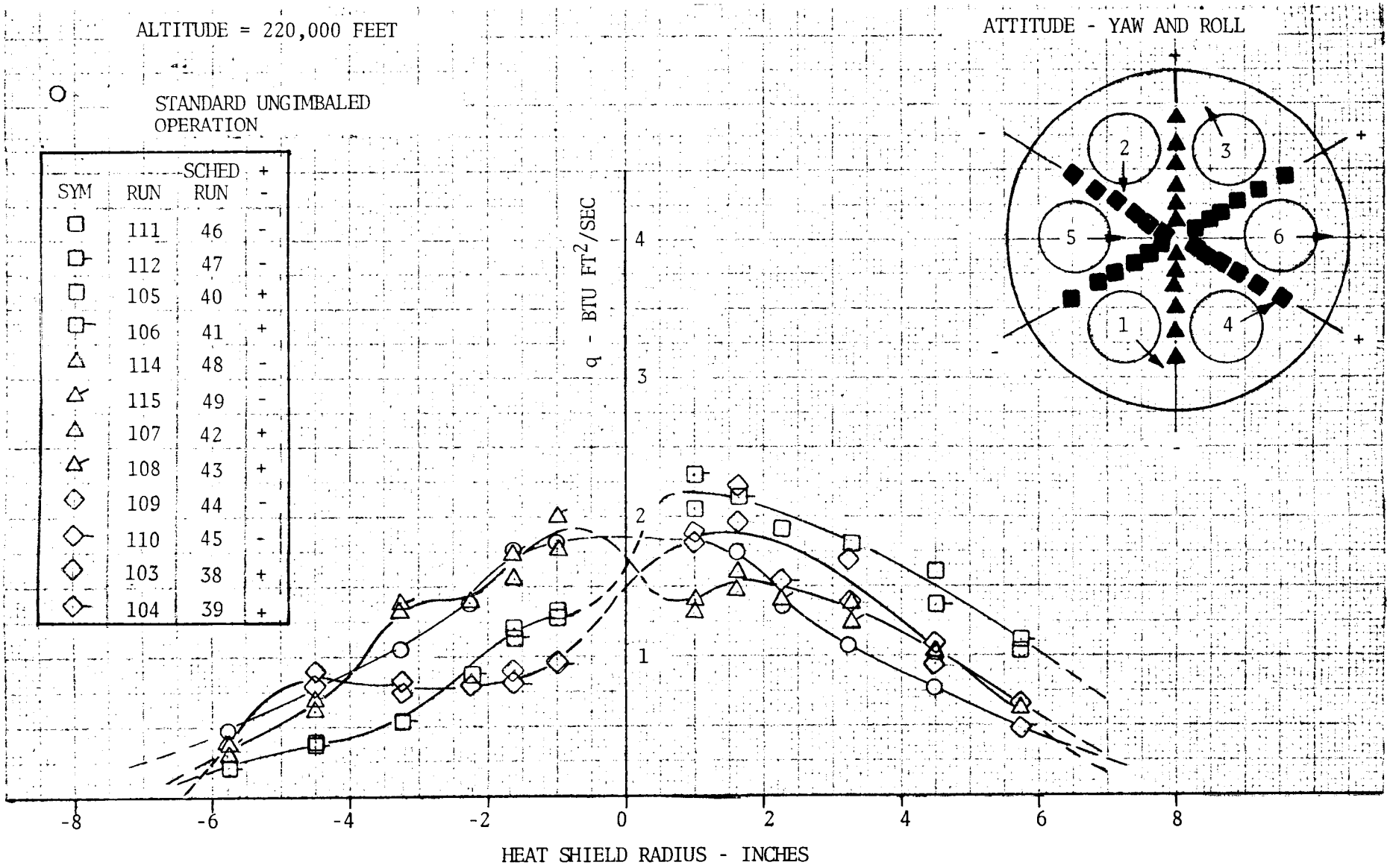

FIGURE 5.4-103. S-IV 6-ENGINE 1/10 SCALE SHOCK TUBE MODEL - EFFECT OF GIMBALLING ON BASE HEAT SHIELD HEAT FLUX DISTRIBUTION

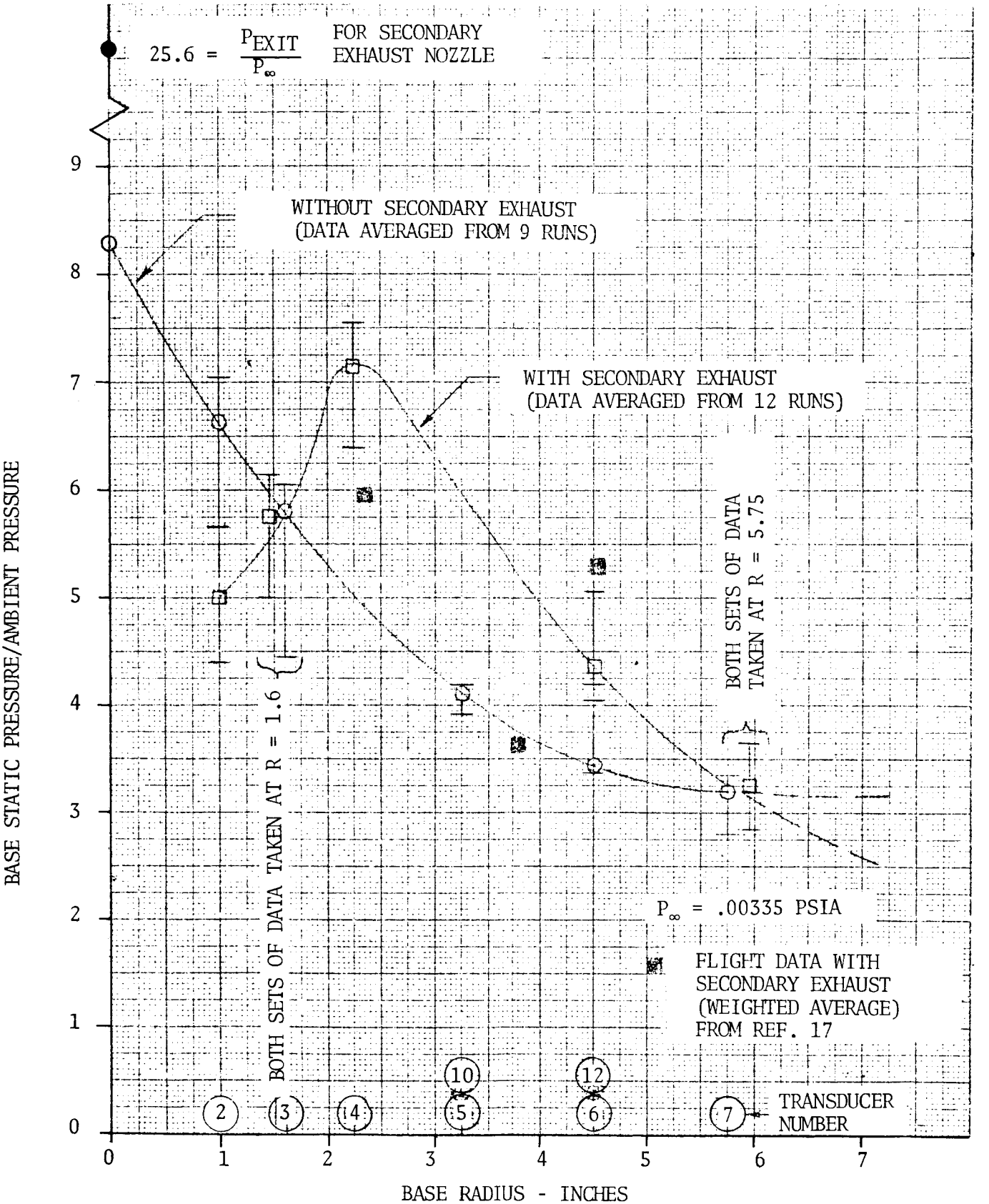

FIGURE 5.4-104. S-IV 6-ENGINE 1/10 SCALE SHOCK TUBE MODEL - EFFECT OF SECONDARY EXHAUST ON BASE HEAT SHIELD PRESSURE DISTRIBUTION

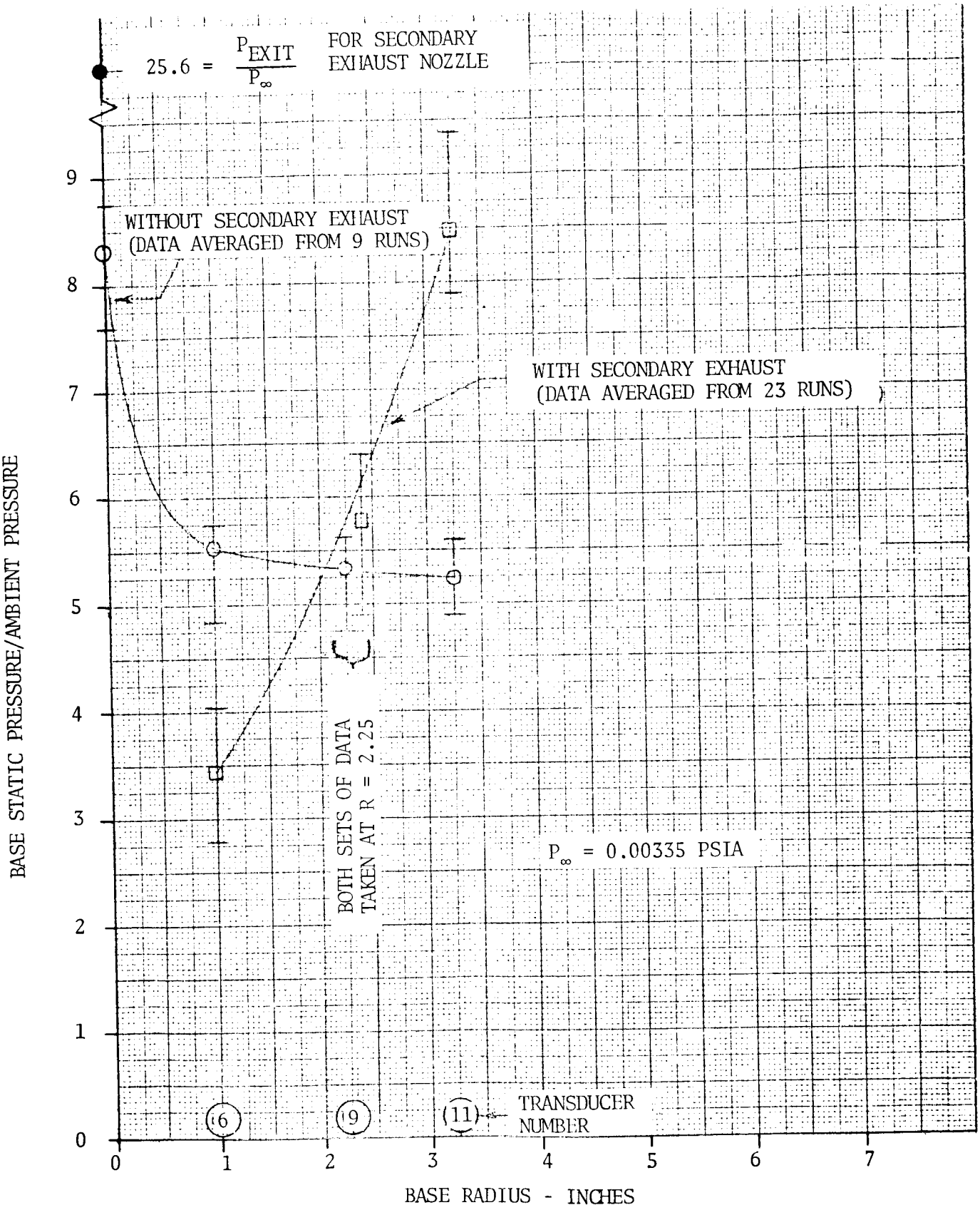

FIGURE 5.4-105. S-IV 6-ENGINE 1/10 SCALE SHOCK TUBE MODEL - EFFECT OF SECONDARY EXHAUST ON BASE HEAT SHIELD PRESSURE DISTRIBUTION

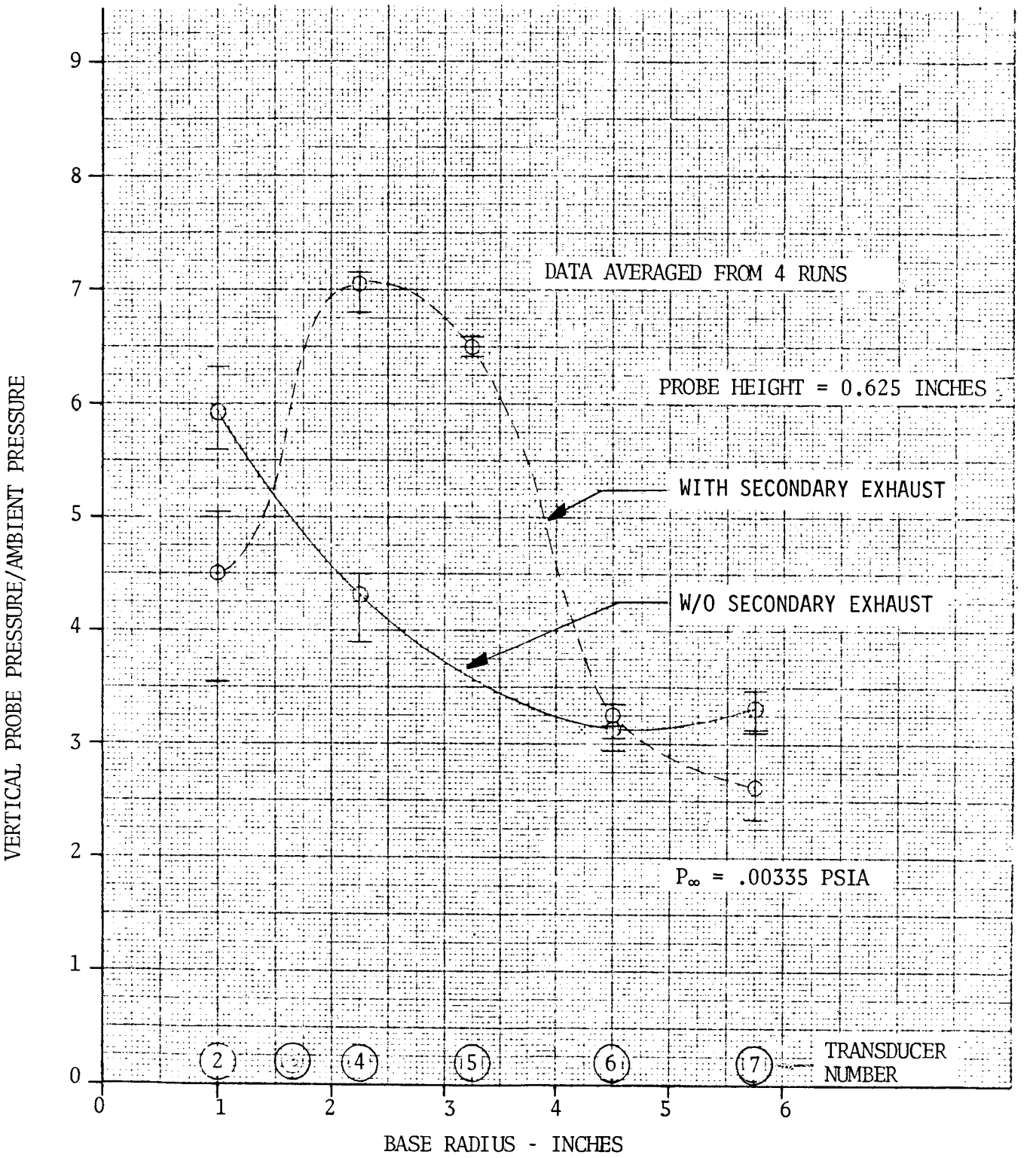

FIGURE 5.4-106. S-IV 6-ENGINE 1/10 SCALE SHOCK TUBE MODEL - EFFECTS OF SECONDARY FLOW ON HEAT SHIELD VERTICAL PROBE PRESSURES (ALONG A RAY BETWEEN ENGINES)

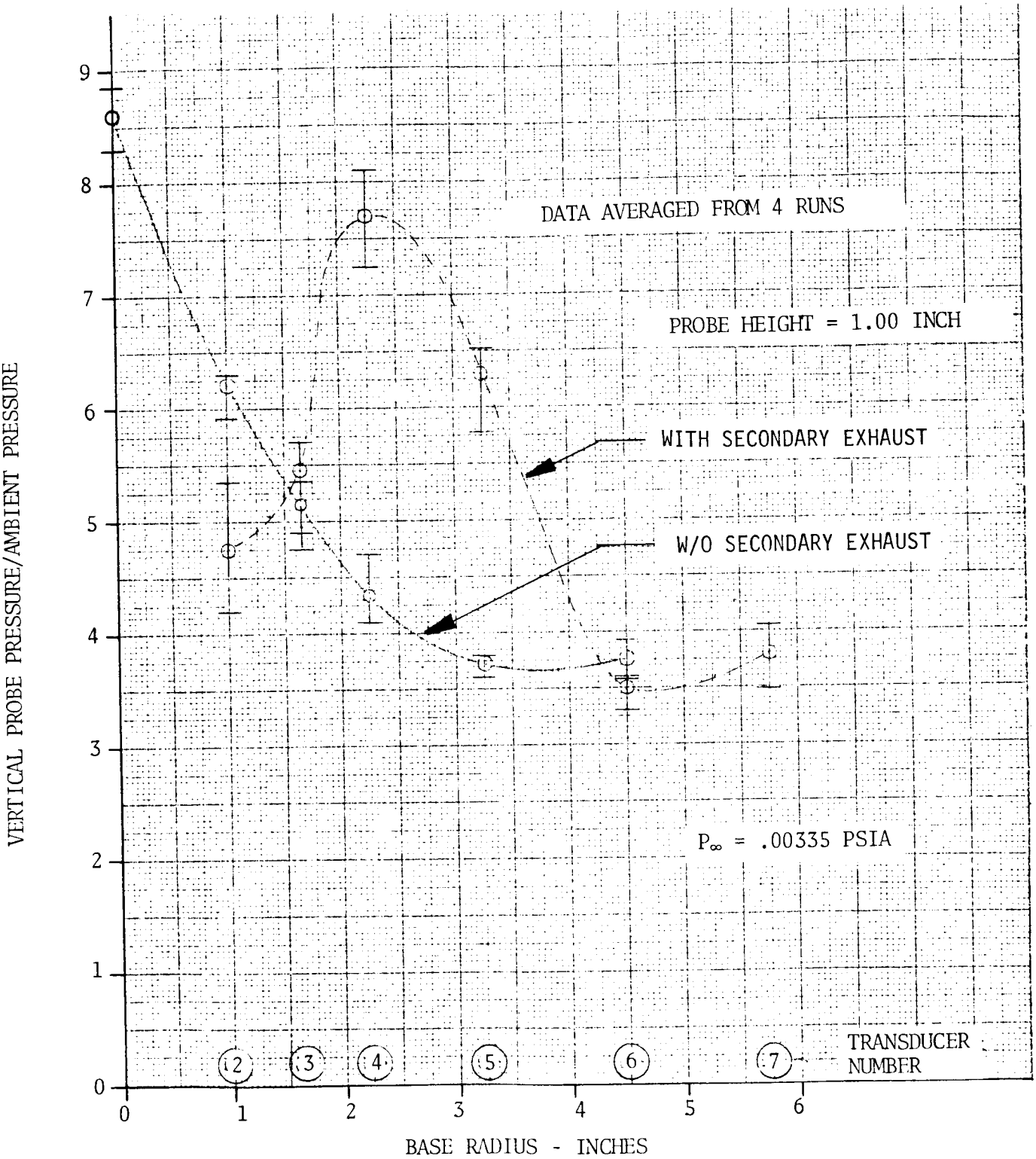

FIGURE 5.4-107. S-IV 6-ENGINE 1/10 SCALE SHOCK TUBE MODEL - EFFECTS OF SECONDARY FLOW ON HEAT SHIELD VERTICAL PROBE PRESSURES (ALONG A RAY BETWEEN ENGINES)

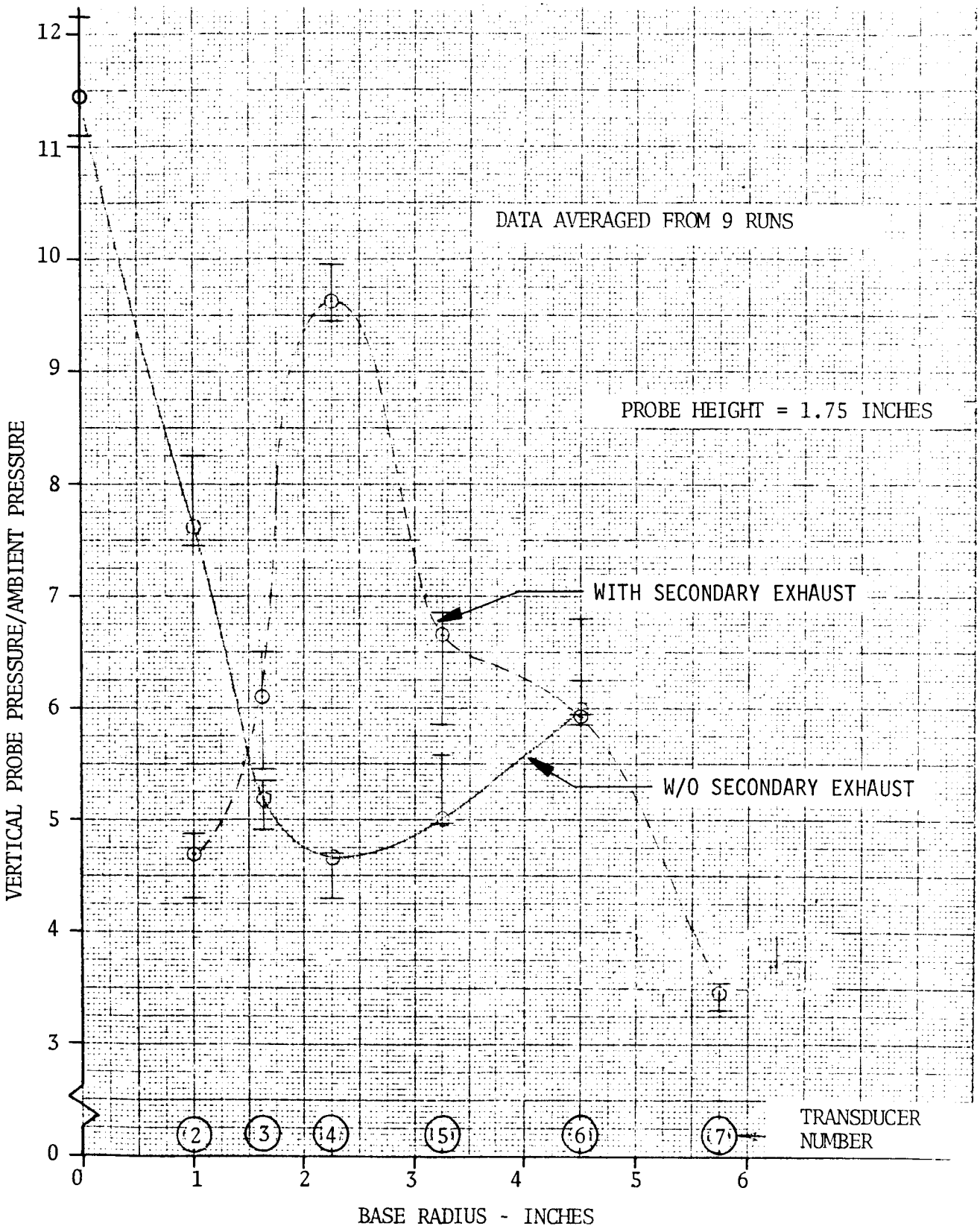

FIGURE 5.4-108. S-IV 6-ENGINE 1/10 SCALE SHOCK TUBE MODEL - EFFECTS OF SECONDARY EXHAUST ON HEAT SHIELD VERTICAL PROBE PRESSURES (ALONG A RAY BETWEEN ENGINES)

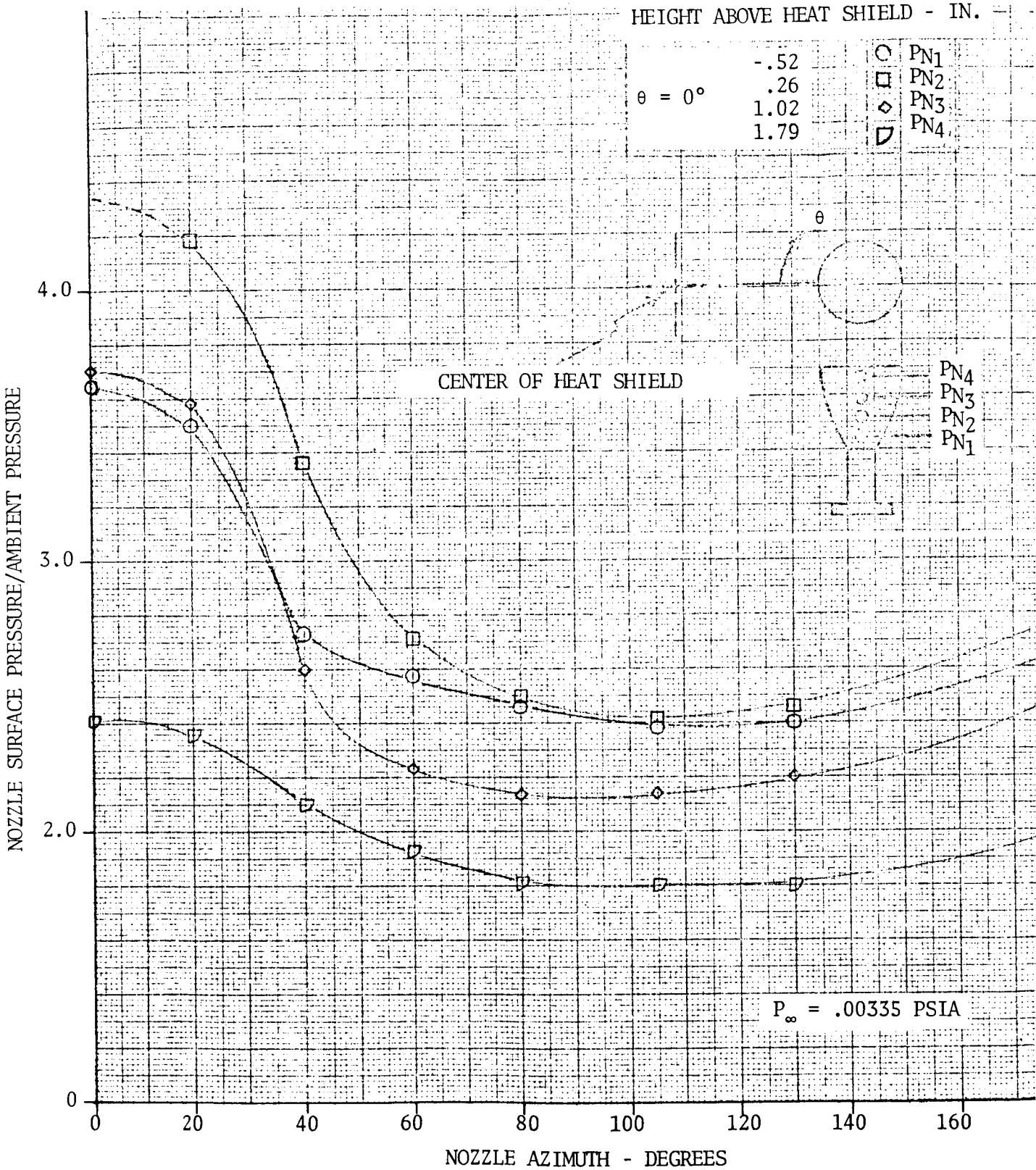

FIGURE 5.4-109. S-IV 6-ENGINE 1/10 SCALE SHOCK TUBE MODEL - NOZZLE SURFACE PRESSURE (NO SECONDARY EXHAUST)

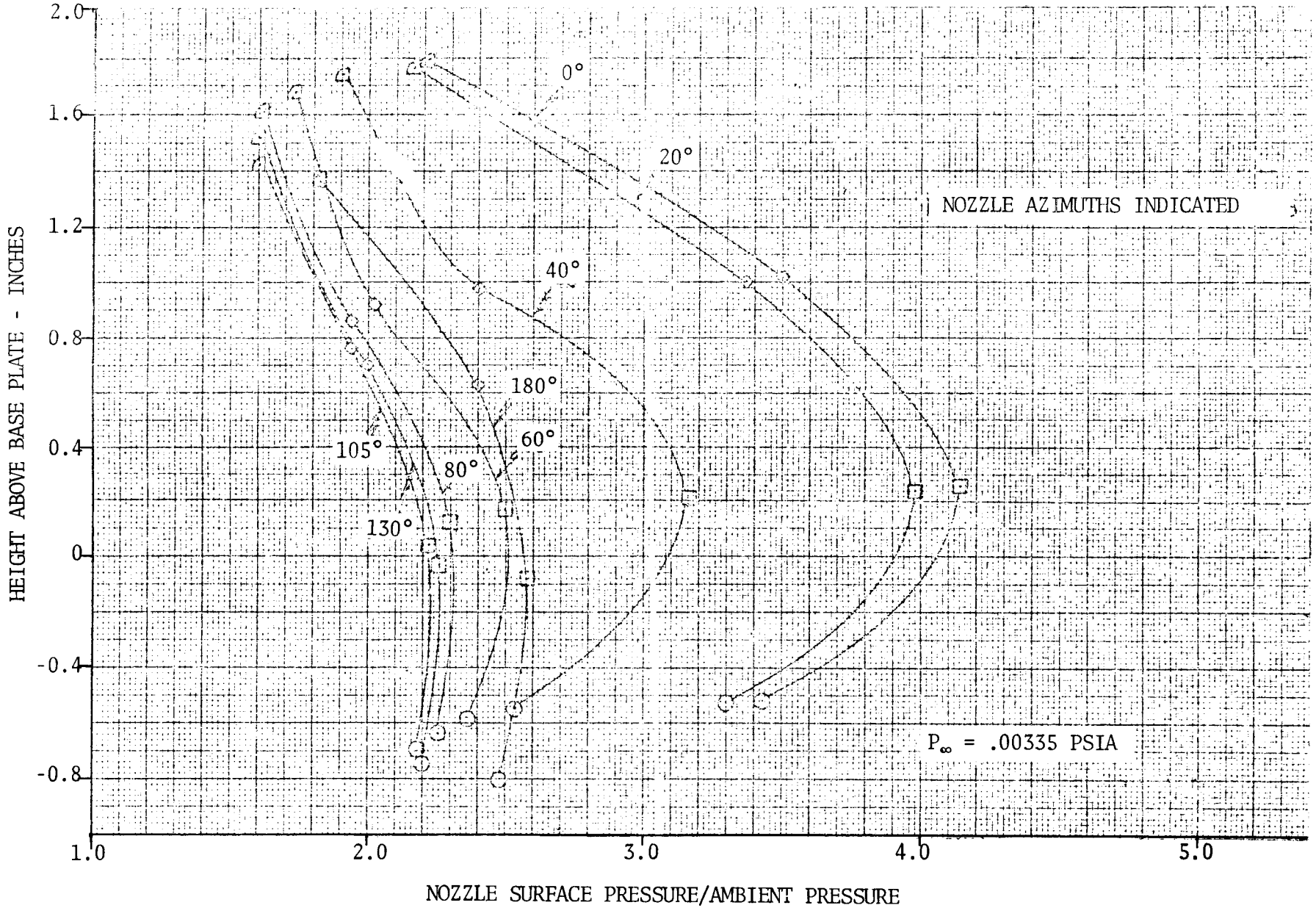

FIGURE 5.4-110. S-IV 6-ENGINE 1/10 SCALE SHOCK TUBE MODEL - NOZZLE SURFACE PRESSURE (NO SECONDARY EXHAUST)

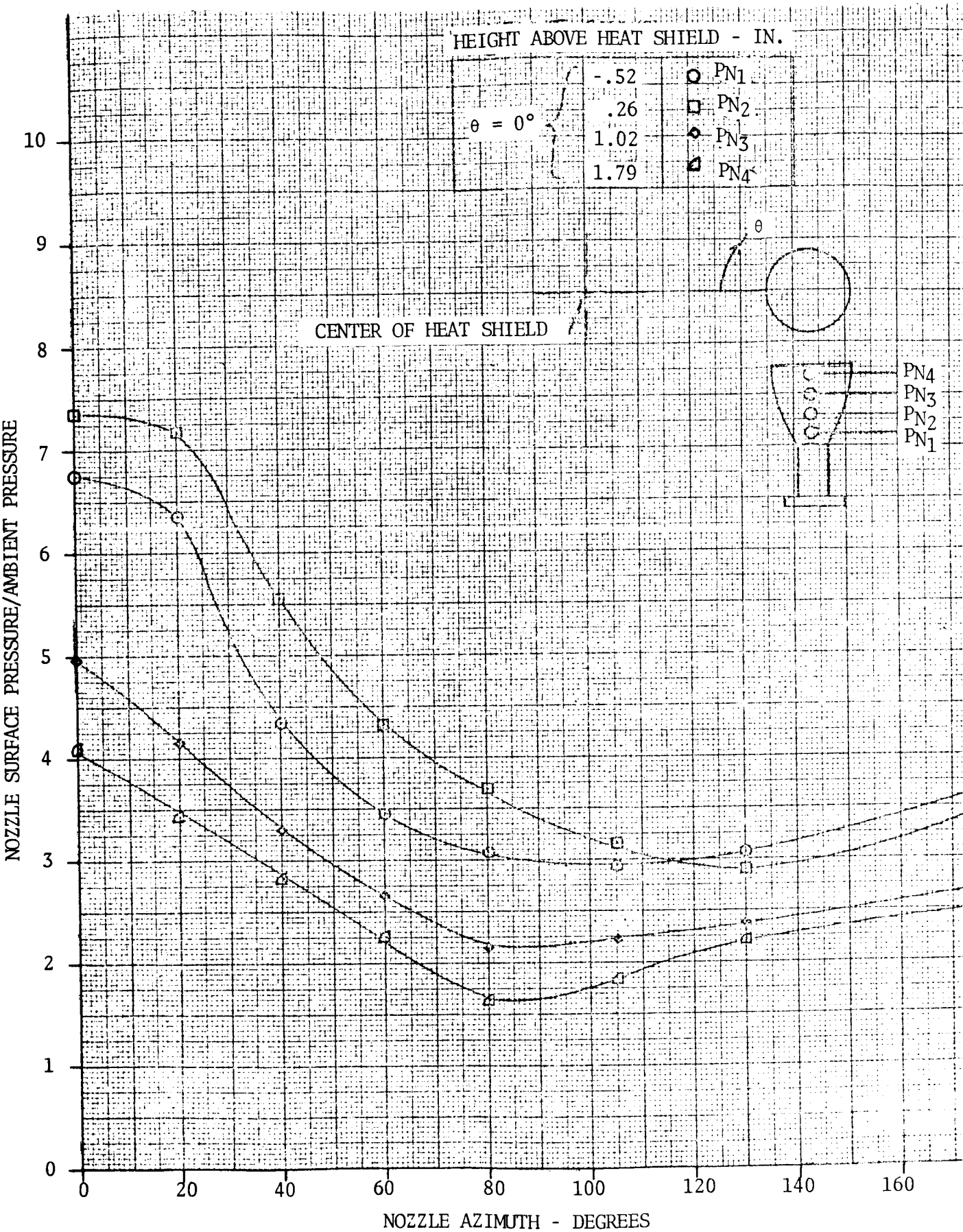

FIGURE 5.4-111. S-IV 6-ENGINE 1/10 SCALE SHOCK TUBE MODEL - NOZZLE SURFACE PRESSURE (WITH SECONDARY EXHAUST)

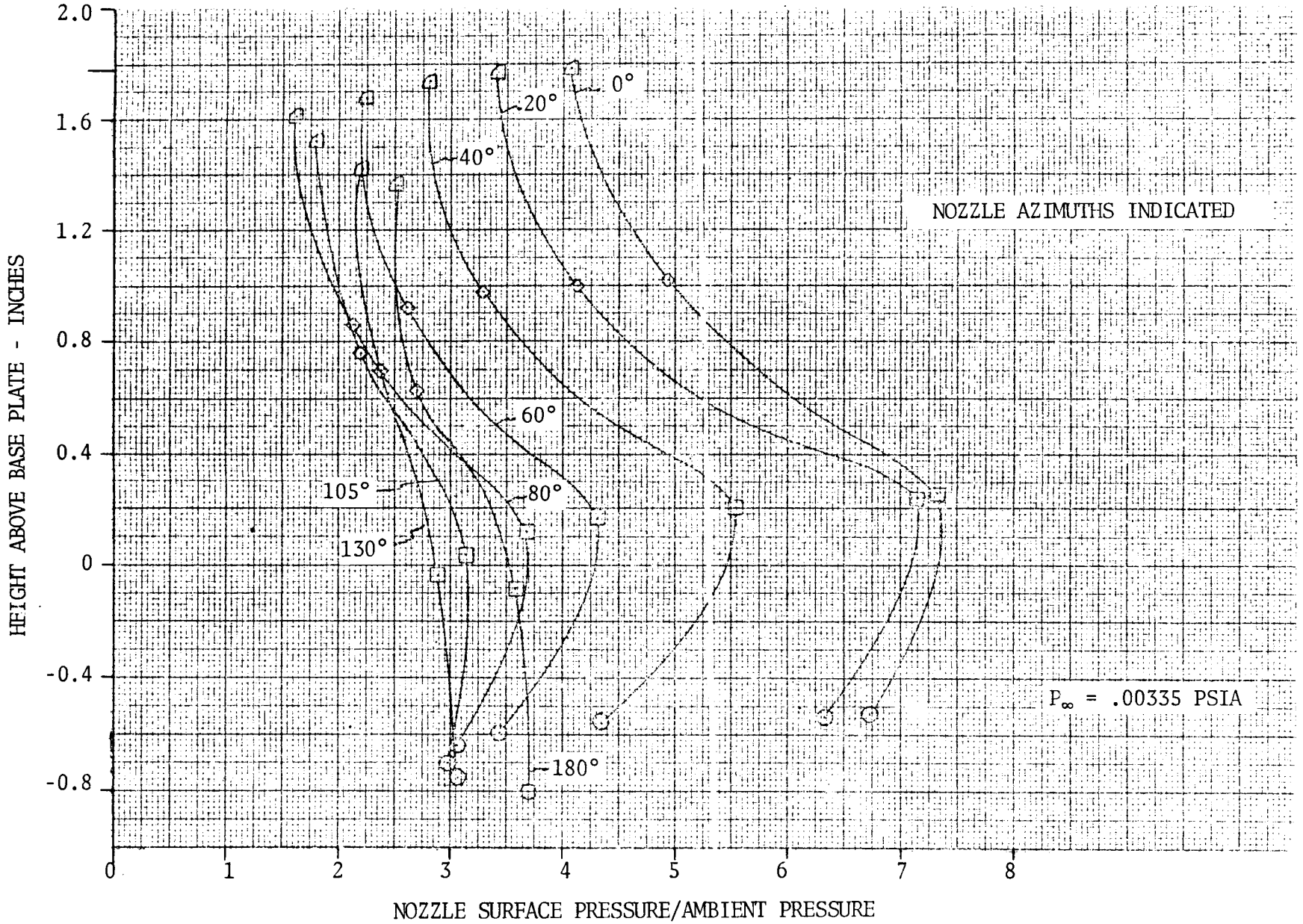

FIGURE 5.4-112. S-IV 6-ENGINE 1/10 SCALE SHOCK TUBE MODEL - NOZZLE SURFACE PRESSURE (WITH SECONDARY EXHAUST)

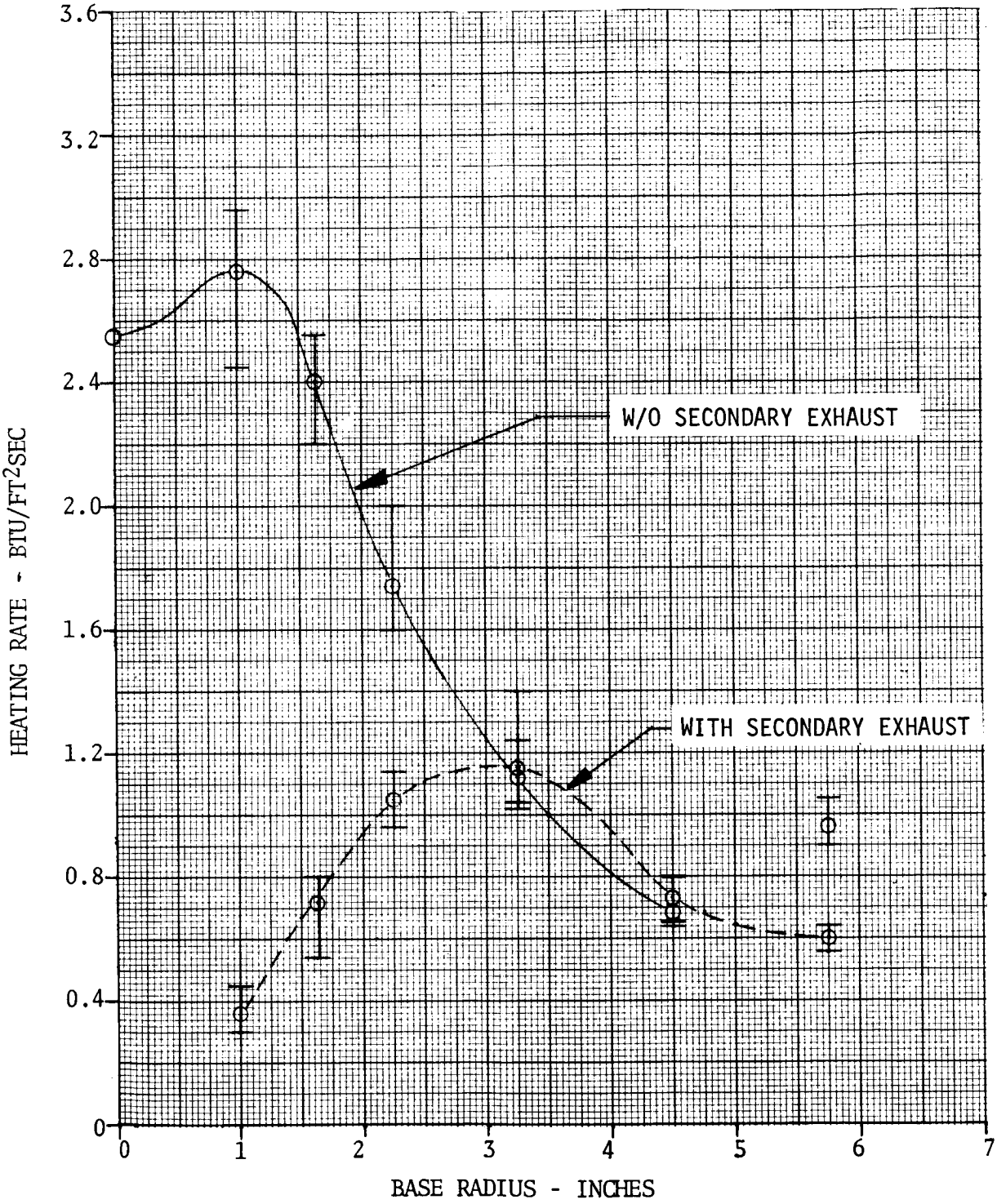

FIGURE 5.4-113. S-IV 6-ENGINE 1/10 SCALE SHOCK TUBE MODEL - EFFECT OF SECONDARY FLOW ON HEAT SHIELD HEAT TRANSFER RATES (ALONG A RAY BETWEEN ENGINES)

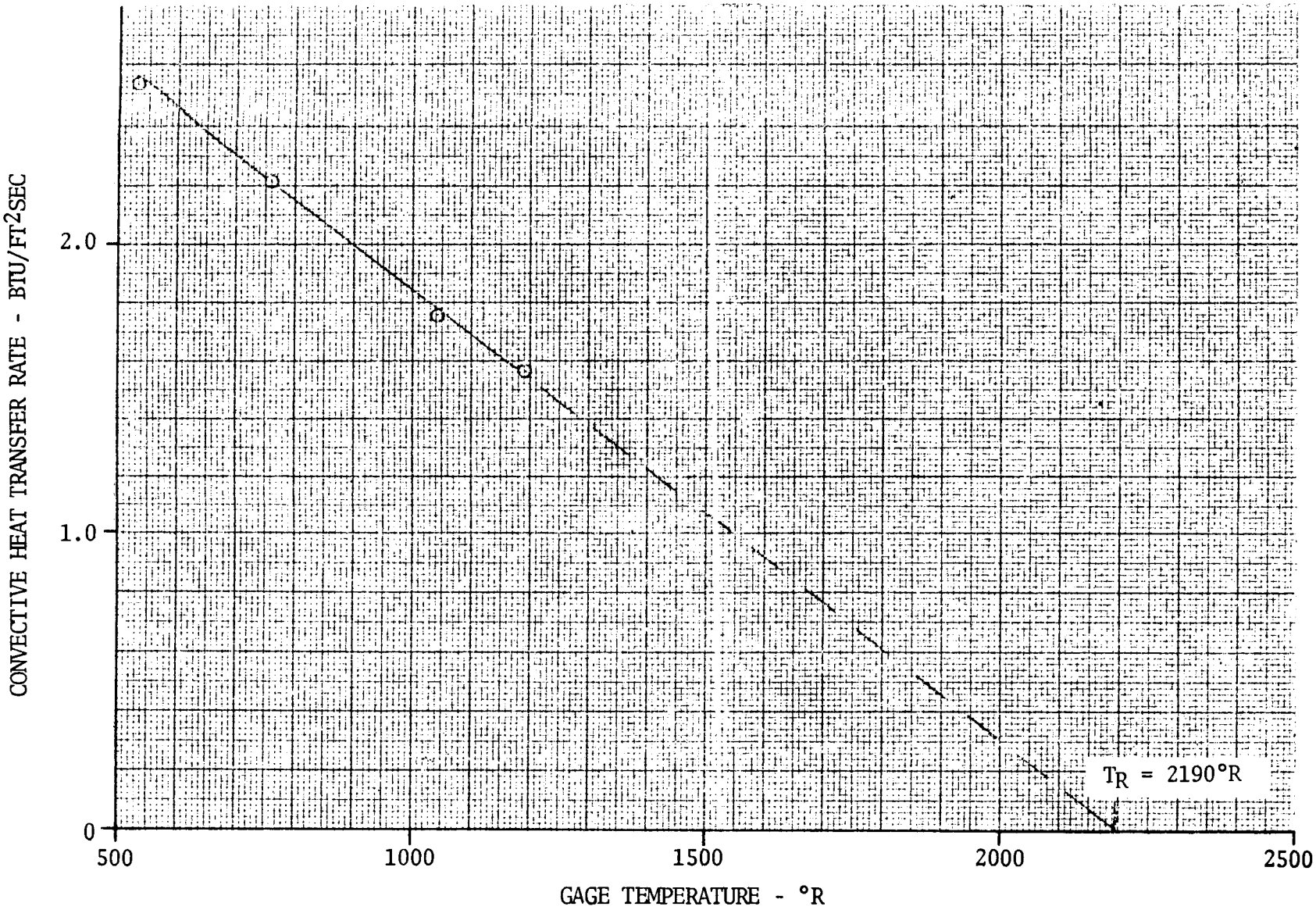

FIGURE 5.4-114. S-IV 6-ENGINE 1/10 SCALE SHOCK TUBE MODEL - HEAT SHIELD RECOVERY TEMPERATURE

TABLE 5.4-1. MODEL TEST COMPARISON

	1/10 COMBUSTION MODEL - AEDC	1/27.75 COLD FLOW MODEL - AEDC	1/10 SHOCK TUBE MODEL - CAL, 1ST SERIES	1/10 SHOCK TUBE MODEL - CAL, 2ND SERIES	1/10 SHOCK TUBE MODEL - CAL, 1ST SERIES	1/10 SHOCK TUBE MODEL - CAL, 2ND SERIES
NO. OF ENGINES	4	4	4	4	6	6
O/F RATIO	5.0		5.0	5.0	5.5:1	
HELIUM HEATER EXHAUST		AMBIENT AIR	15 PSIA 100% H_2 @ 530° R	NONE	PREHEATED HYDROGEN-NITROGEN MIXTURE	
GIMBALING	±5.66° & 4° ALL RUNS WITH HELIUM HEATER EXHAUST	±1, ±2, ±3, ±4, AND ±5	NONE	NONE	5.6° 4°	NONE
SCALE	1/10	1/27.75	1/10	1/10	1/10	1/10
PROPELLANT	LOX - H_2	AIR @ 1000° R NOMINAL	LOX - H_2	LOX - H_2	LOX - H_2	LOX - H_2
ENGINE CANT	4°	4°	4°	4°	6°	6°
CHAMBER PRESSURE	350 PSIA	84 PSIA	350 PSIA	350 PSIA	300 PSIA	300 PSIA
ALTITUDE						
TYPE OF TEST	LONG DURATION	COLD FLOW	SHORT DURATION (SHOCK TUBE)	SHORT DURATION	SHORT DURATION	SHORT DURATION
AREA RATIO	SAME AS PROTOTYPE	10.4			39.87	

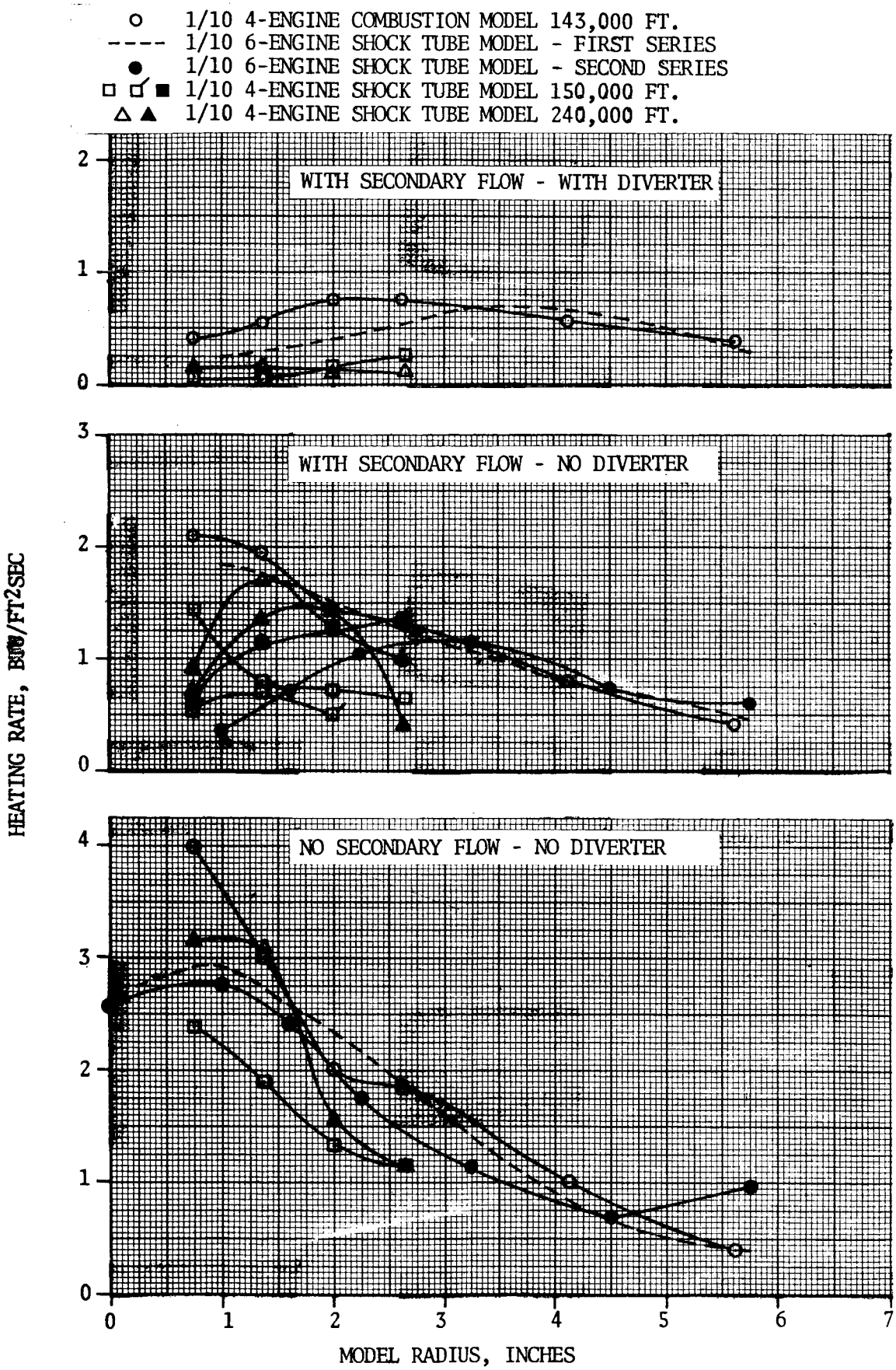

FIGURE 5.4-115. COMPARISON OF SECONDARY EXHAUST EFFECTS ON BASE HEAT SHIELD HEATING RATES

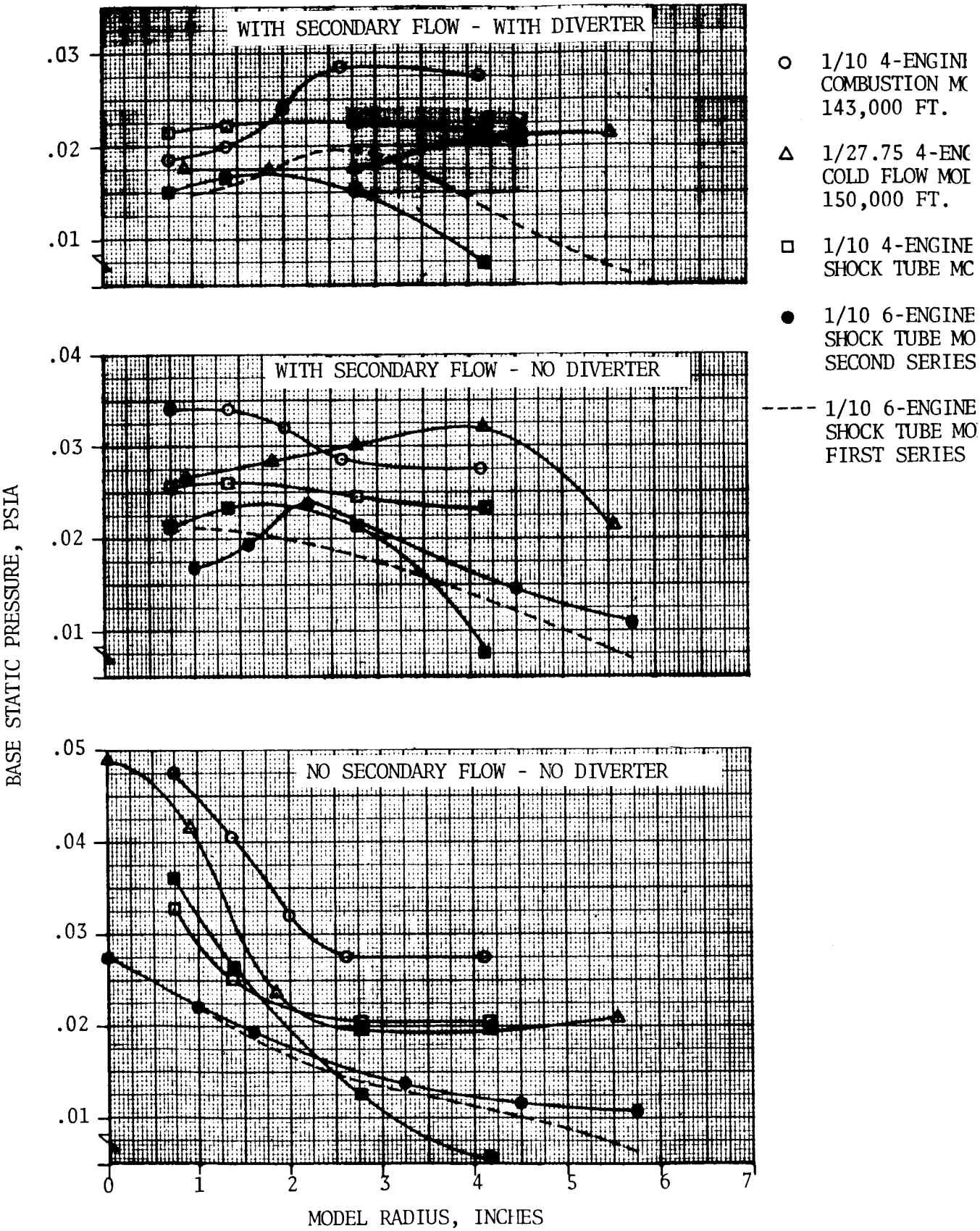

FIGURE 5.4-116. COMPARISON OF SECONDARY EXHAUST EFFECTS ON BASE HEAT SHIELD STATIC PRESSURE DISTRIBUTION

5.5 FLIGHT TESTS AND PARAMETRIC DATA

The S-IV stage was flown six times; the first on the SA-5 flight on January 27, 1964.

Instrumentation was located on the stages to obtain data to verify design adequacy and to provide, if possible, correlation with model data.

The first two stages (S-IV-5 and -6) were instrumented to determine the net heat flux to the heat shield by calorimeter measurements. The locations of the heat shield instrumentation for S-IV-5 and -6 are shown in Figure 5.5-1. The only significant differences between the first two flights were that slug-type calorimeters were used on S-IV-5 and asymptotic calorimeters were used on S-IV-6.

The second two stages (S-IV-7 and -9, which were flown out of order) did not record base region heating rates.

The S-IV-8 and -10 stages had three calorimeters and four pressure sensors. The range of the pressure sensors was 0 to 1 psia. This was unfortunate since the accuracy of the gages was approximately the same as the expected measurement (0.02 psia). The location of these instruments are shown in Figure 5.5-1.

Flight data for the S-IV stage base region are presented in Figure 5.5-2. The SA-5 flight data are different from the other flight data. This difference is believed to be caused by the change in instrumentation with the SA-6, -8 and -10 data being more reliable.

Attempts were made on the SA-5 flight to determine the convective and radiation heating rates by using black and gold surface calorimeters. The radiant heat flux was to be determined by measuring the difference between the high absorptivity black calorimeters, and the low absorptivity gold calorimeters which measure primarily convective heat flux. The gold calorimeter surfaces deteriorated during flight and the data from the calorimeters (black and gold) are approximately the same.

Average measured heat flux ranged from 0.68 to 1.14 watts/cm^2 with peak transients of 2.16 watts/cm^2 occurring at S-IV-6 engine start. (See Figure 5.5-2.) S-IV-8 flight data have similar trends and magnitudes as the S-IV-6 flight data. The average level of absorbed heat flux for each of the calorimeters was slightly higher on S-IV-10 than on S-IV-6 and S-IV-8. The rapid rise in heat flux measured by the inboard calorimeter on S-IV-10 beginning at 350 seconds is due to the helium heater cycling to single coil operation which results in a higher helium heater exhaust temperature. The decrease in heat flux of the inboard calorimeter at approximately 500 seconds is again due to a change in helium heater exhaust temperature which decreased due to hydrogen tank step pressurization at 491 seconds. (See Figure 5.5-2.)

5.5 (Continued)

Base pressure measurements, with a range of 0 to 0.7 N/cm^2 (1 psi), were flown for the first time on the S-IV-8 heat shield. The base pressure data show the effects of LOX chilldown gas on the compartment pressure and reveal the effect on base pressure of and retro rocket gas impingement after the heat shield clears the interstage. (See Figure 5.5-3.) Pressure levels were similar to model test data. The pressures measured were below the usual expected measurement accuracies so it is difficult to determine the actual force on the heat shield. However, they do indicate that the pressures are not significantly higher than the test results, and most likely, may be lower.

Four base pressure sensors (0 to 0.7 N/cm^2 measuring range) located on the S-IV-10 base heat shield failed to give useful data; they appear to have been plugged during most of the S-IV flight.

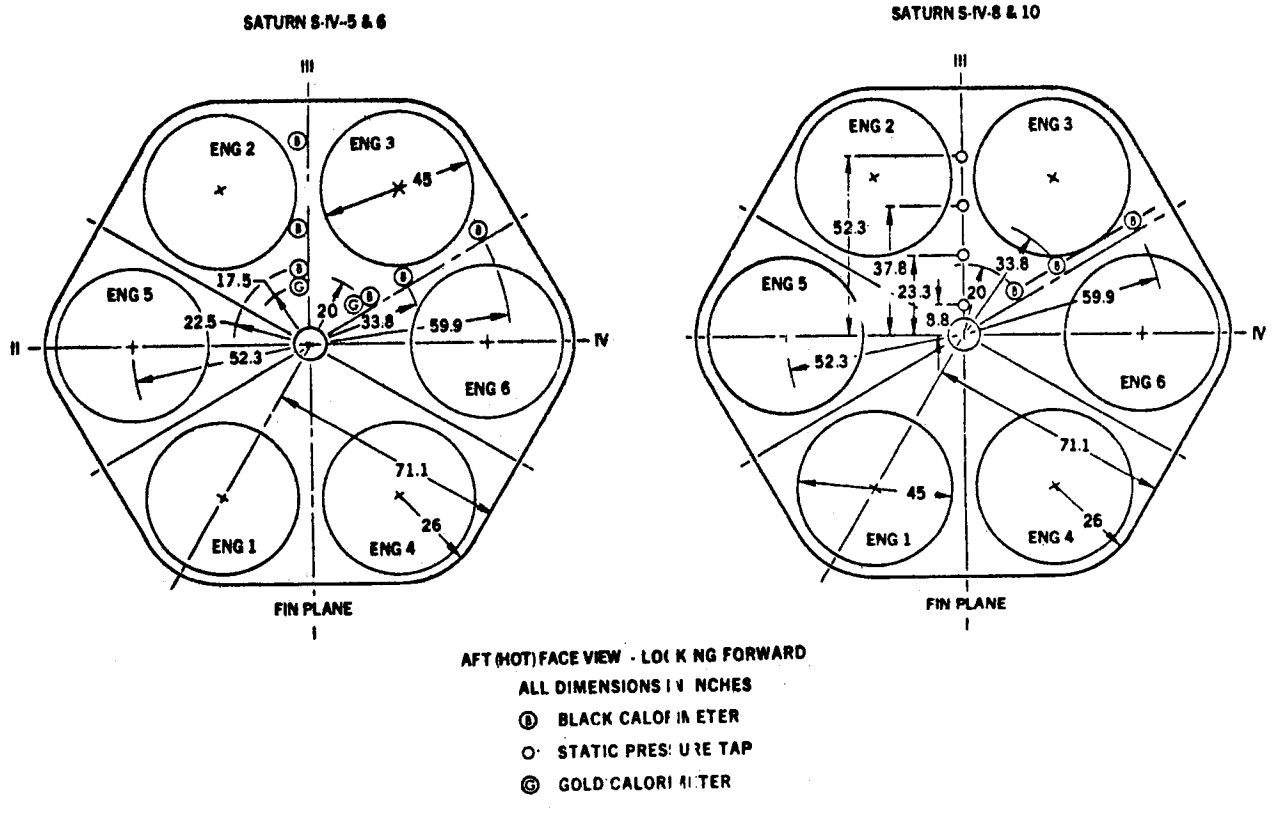

FIGURE 5.5-1. S-IV BASE HEAT SHIELD INSTRUMENTATION

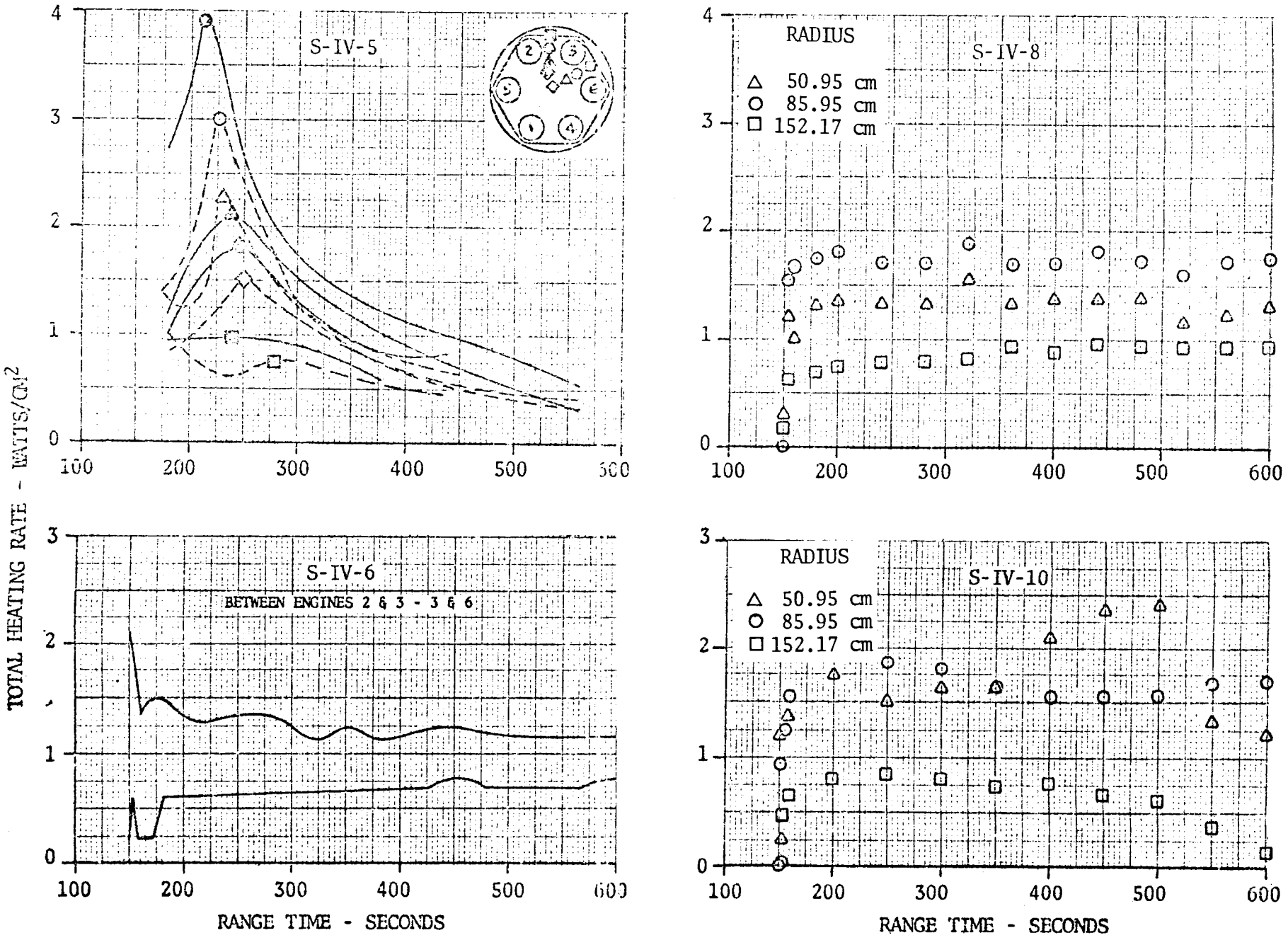

FIGURE 5.5.2 S-IV STAGE BASE REGION FLIGHT DATA

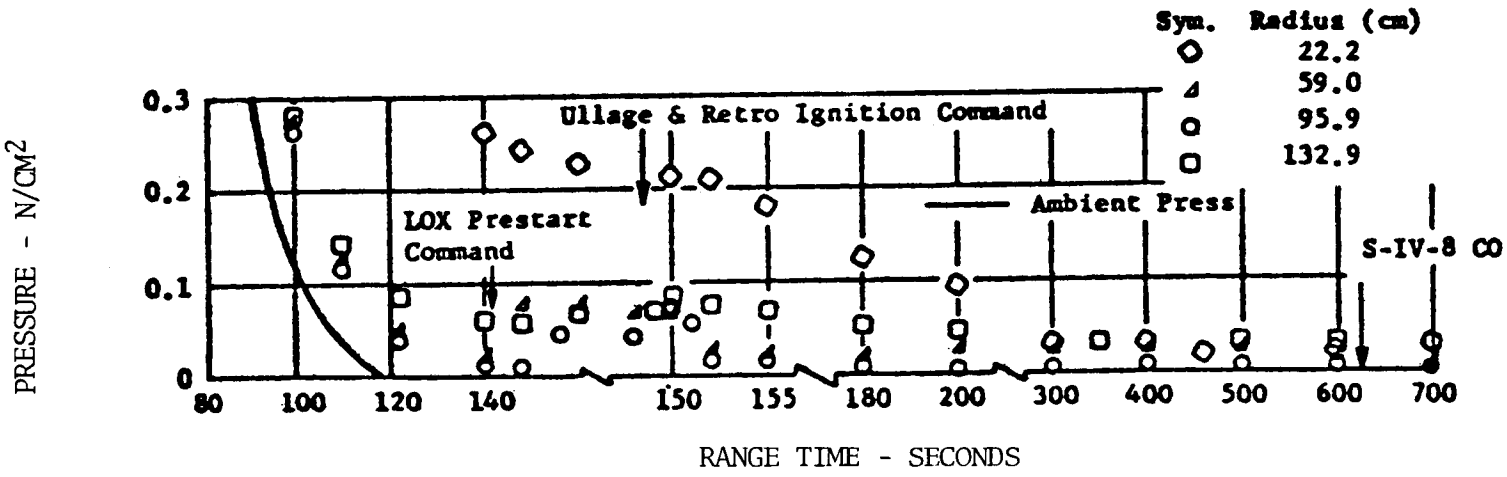

FIGURE 5.5-3. S-IV STAGE FLIGHT PRESSURE ENVIRONMENT

5.6 MODEL-FLIGHT DATA COMPARISON

This section presents comparison of flight data with selected model data. Parameter effects are included. The radial distribution of the heat flux for the S-IV-5 heat shield compared with model data are presented in the upper graph of Figure 5.6-1. A shift in the location of peak heating outboard as compared to the model data and a greater peak heating rate were experienced during the S-IV-5 flight. The radial distribution of the heat flux for the S-IV-6 heat shield compared to the six-engine shock tube model data with and without simulated helium heater secondary flow are shown in the lower graph of Figure 5.6-1. These comparisons were based on model test data taken from Reference 5-16.

Additional model data were determined from the second series of tests (Reference 5-17). These data are compared with the flight data from the S-IV-6 stage and are presented in Figures 5.6-2 and 5.6-3. The flight data/model data comparison without secondary exhaust is presented in Figure 5.6-2 and the comparison with secondary exhaust is presented in Figure 5.6-3. In general, the model data agree well with the flight data. Flight data without secondary exhaust was measured at the start of S-IV burn prior to the establishment of secondary flow.

S-IV-5

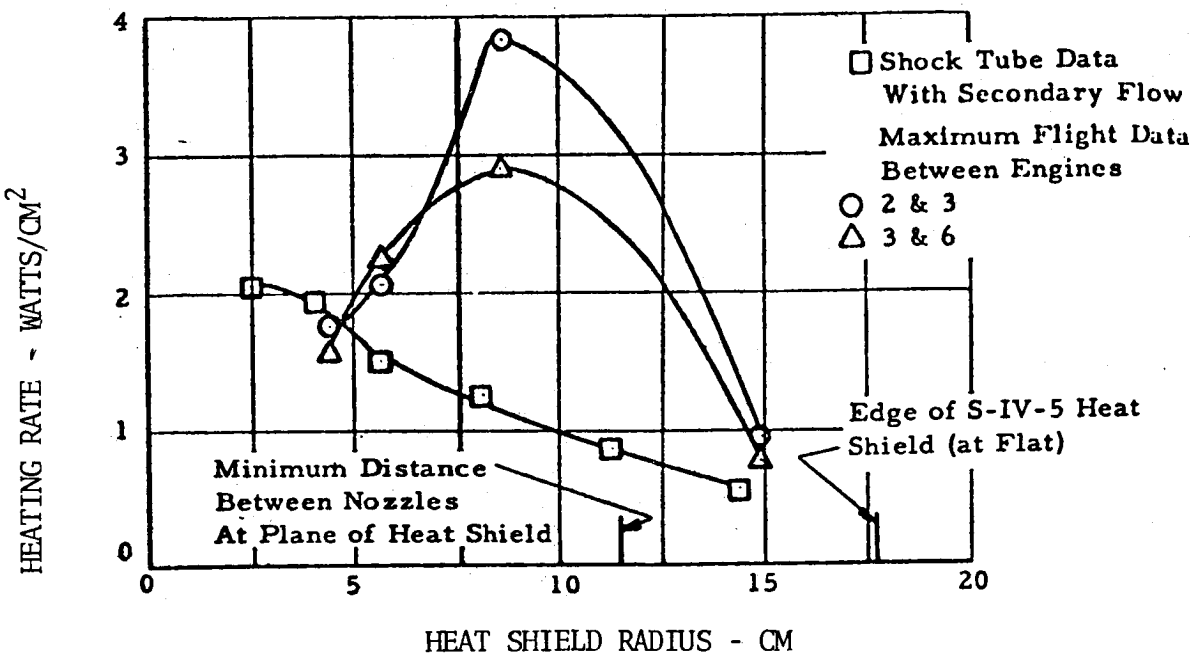

S-IV-6

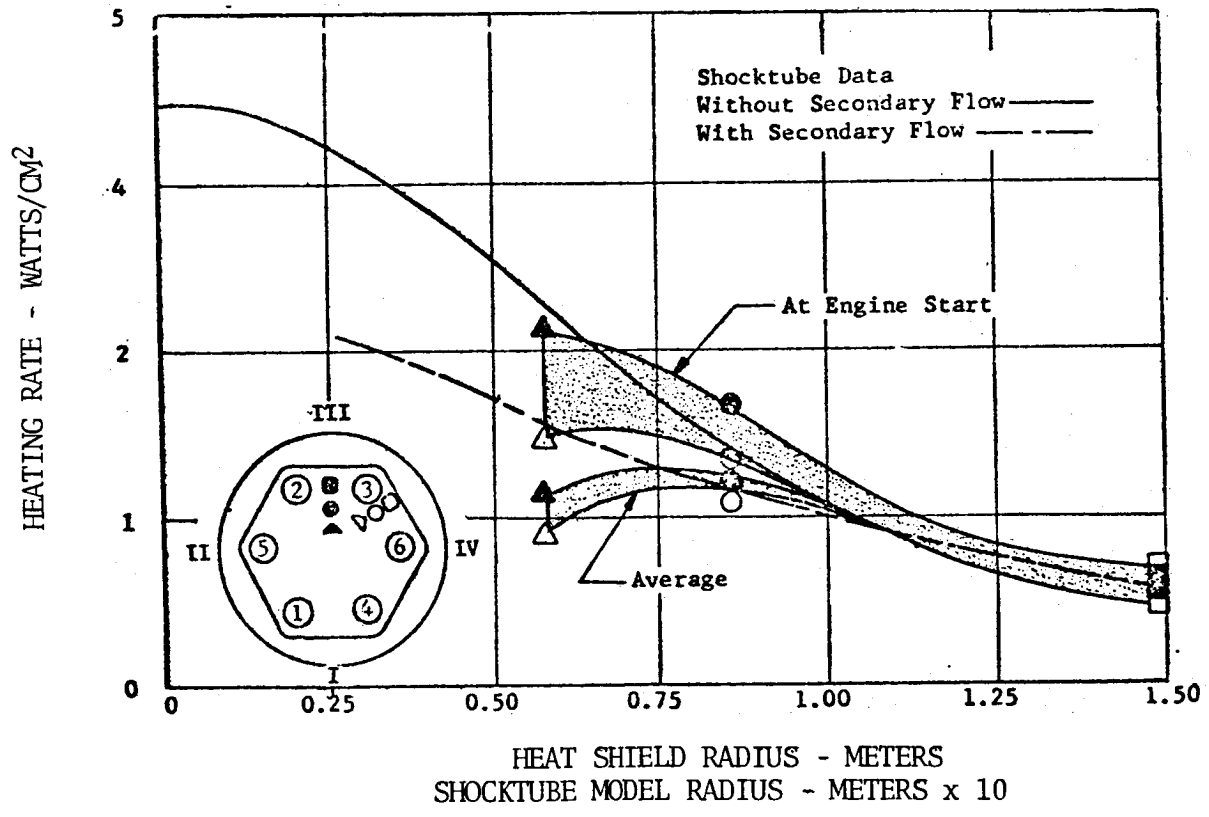

FIGURE 5.6-1. COMPARISON OF S-IV STAGE FLIGHT HEATING RATE WITH MODEL TEST DATA

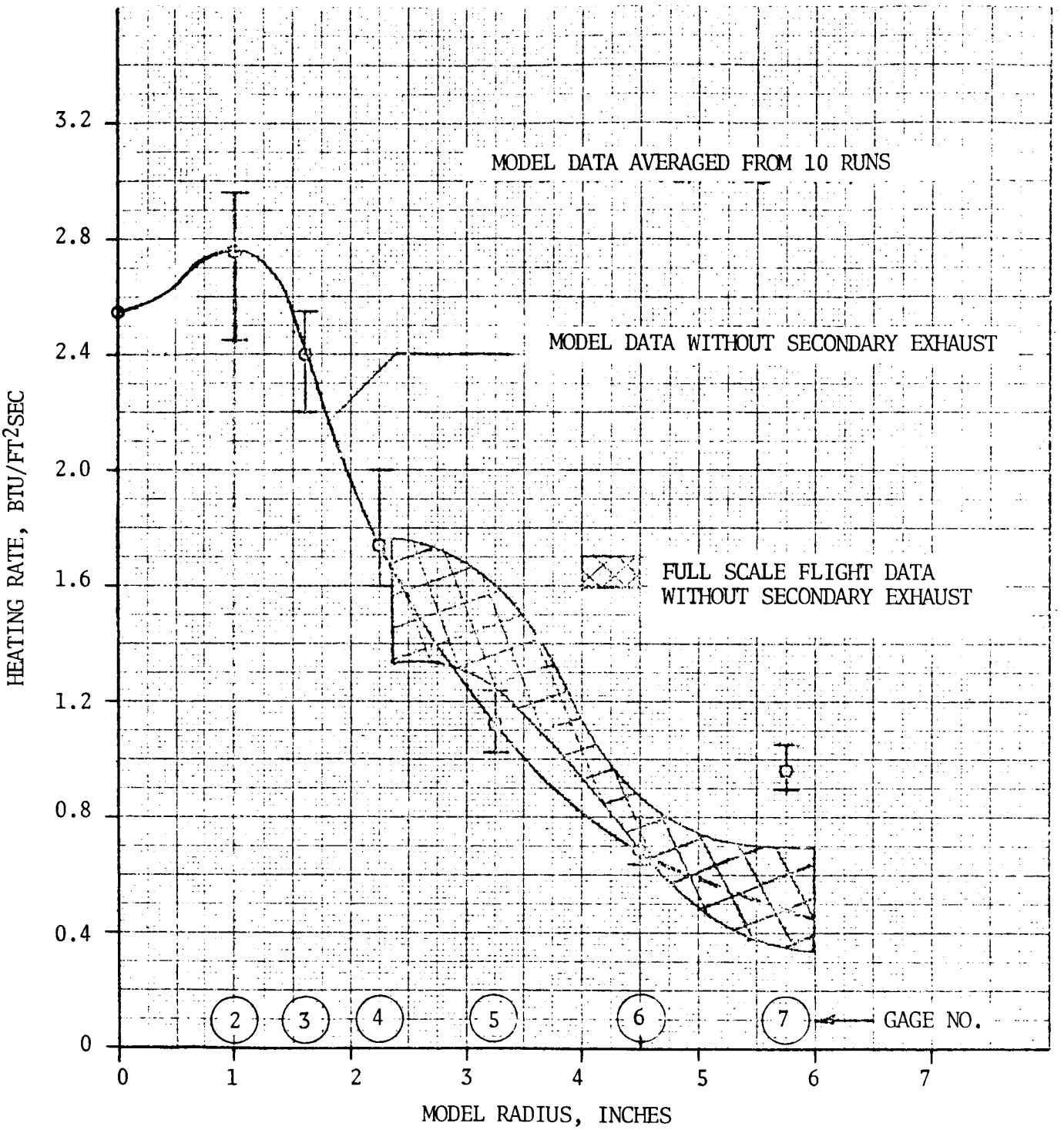

FIGURE 5.6-2. COMPARISON OF S-IV STAGE FLIGHT DATA AND MODEL TEST DATA - WITHOUT SECONDARY EXHAUST

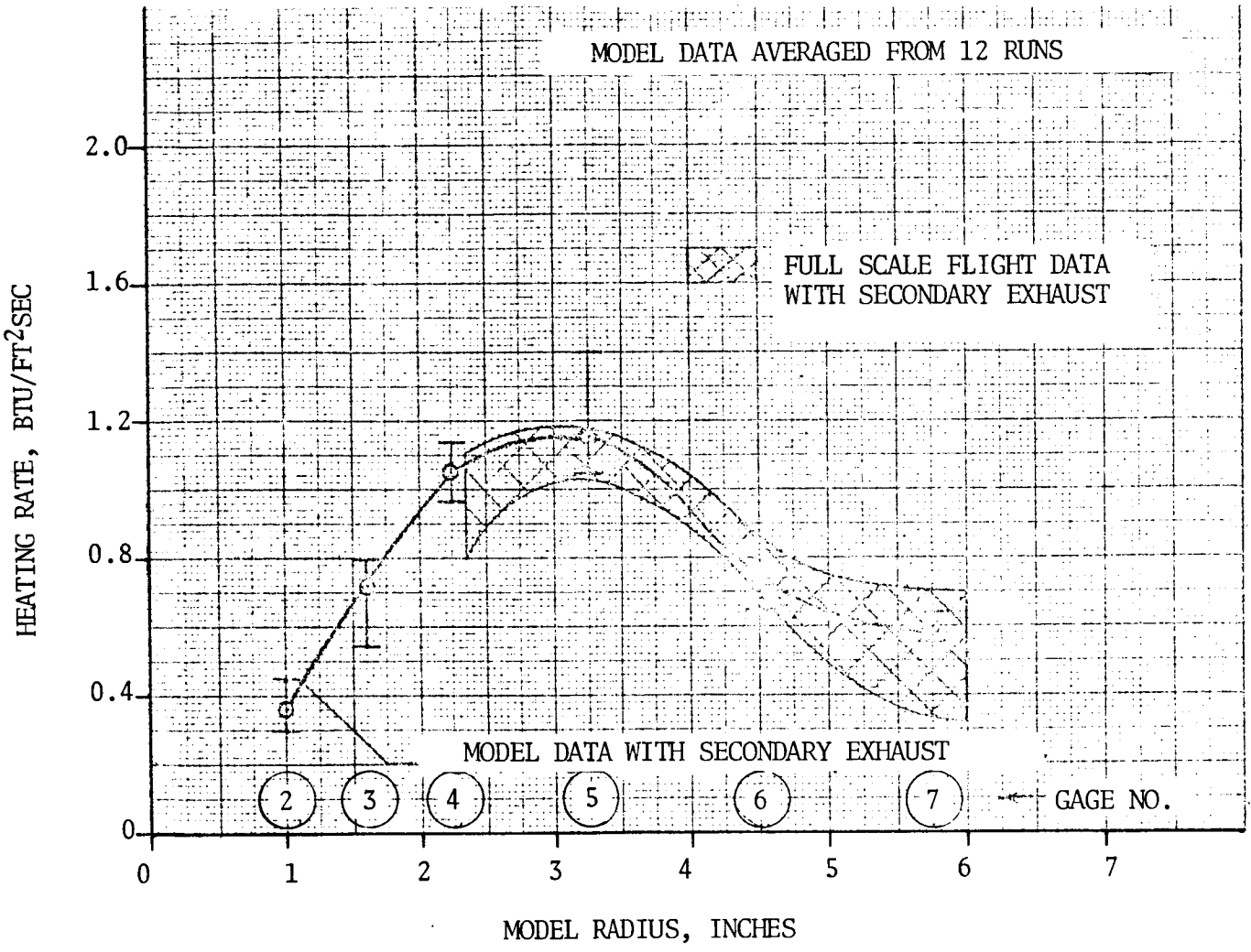

FIGURE 5.6-3. COMPARISON OF S-IV STAGE FLIGHT DATA AND MODEL TEST DATA - WITH SECONDARY EXHAUST

5.7 REFERENCES

5-1. MSFC Report R-ASTR-TJ-10-65, "SA-9 Technical Information Summary," February 1, 1965.

5-2. Douglas Memo AZ-260-S/PT-62-104, "Predicted Nozzle Exit Plane and Exhaust Flow Properties for the Saturn S-IV 15K Engines," March 13, 1962.

5-3. MSFC Memo R-AERO-AT-64-4, "Estimate of the S-IV Stage Base Radiation Heat Environment," February 6, 1964.

5-4. MSFC Memo M-AERO-A-28-63, "Thermal Environment Design Criteria of Saturn S-IV Base," originally dated March 22, 1963; Addendum A added April 11, 1963.

5-5. MSFC Unpublished Memo M-AERO-A-56-63, "Estimate of the Radiation Heat Flux on the Base of the Saturn S-IV Stage."

5-6. MSFC Memo M-AERO-A-83-63, "Radiation Measurements at the Exit of the RL-10 Engine," dated August 15, 1963.

5-7. Douglas Paper 3662, "The Saturn S-IV Stage Base Thermal Environment Flight and Scale Model Comparison," Dearing, D. L., January 24, 1966.

5-8. AIAA Paper No. 65-826, "Base Heating Scaling Criteria for a Four-Engine Rocket Cluster Operating at High Altitude," Sergeant, R. J., December 13-15, 1965.

5-9. Douglas Report SM-47340, "Saturn S-IV Stage Base Heating Test Summary Four-Engine Combustion and Cold Flow Models," September 1965.

5-10. MSFC Memo M-AERO-A-13-62, "Results of the Saturn S-IV Cold Flow Base Recirculation Tests Conducted at Arnold Engineering Development Center," March 6, 1962.

5-11. Douglas Report SM-37984, "Saturn S-IV Stage Base Heating Test Program - Cold Flow Model," July 1961.

5-12. MSFC Memo M-AERO-A-105, "Some Preliminary Results of the Cornell S-IV Base Heating Tests," November 29, 1961.

5-13. MSFC Memo M-AERO-A-9-62, "Some Results of the Cornell S-IV Base Heating Tests, Altitude Series," January 29, 1962.

5-14. CAL Report No. HM-1510-Y-1(I), "The Application of Short-Duration Techniques to the Experimental Study of Base Heating, Part I: High-Altitude Testing Technique and Experimental Results for a 4-Engine Rocket Configuration," April 1962.

5.7 (Continued)

5-15. CAL Report No. HM-1510-Y-1(II), "The Application of Short-Duration Technique to the Experimental Study of Base Heating, Part II: A Study of Reynolds Number and Temperature Effects on Base Heating for a Four-Engine Hot Rocket Configuration Operating at High Altitude," April 1965.

5-16. CAL Report No. HM-1510-Y-3, "High Altitude Base Heating and Pressure Distribution Investigation on the Saturn S-IV 6-Engine Stage Rocket Using Short-Duration Techniques," June 1963.

5-17. CAL Report No. HM-2045-Y-3, "High Altitude Base Region Thrust Investigations on a Saturn S-IV 6-Engine Stage Model Using Short Duration Techniques," September 1967.

THIS PAGE LEFT BLANK INTENTIONALLY

CONTENTS

6.0 SATURN S-II BASE ENVIRONMENT

6.1	S-II CONFIGURATION	6-2
6.2	J-2 ENGINE CHARACTERISTICS	6-4
6.3	PREDICTION METHODS	6-7
6.4	MODEL TEST AND PARAMETRIC DATA	6-14
6.5	FLIGHT TEST AND PARAMETRIC DATA	6-47
6.6	COMPARISON OF MODEL AND FLIGHT TEST RESULTS	6-61
6.7	REFERENCES	6-67

6.0 SATURN S-II STAGE

6.1 S-II CONFIGURATION

The S-II stage is the second stage of the Saturn V vehicle. Separation from the S-IC stage is accomplished using a dual-plane method. The first separation plane is at Station 0 (16 inches forward of the engine exit plane) and separation at this point may occur at altitudes as low as 53.4 KM. Approximately 30 seconds after first plane separation, when dynamic pressure has dropped to a negligible value, the interstage skirt is separated at Station 196 and falls away without any mechanical guidance.

Propulsion for the S-II stage is provided by a cluster of five Rocketdyne J-2 engines arranged as shown in Figure 6.1-1. A heat shield located at Station 44 (aft face) protects the components and structure in the base region from the recirculating exhaust gases of the engine cluster. Flexible curtains between the engines and the heat shield permit engine movement, and the outboard engines are gimbaled for control. Extreme engine movements from null (including over-shoot) are limited to 7.5 degrees in both pitch and yaw or 10.6 degrees resultant toward or away from the center engine (or in the plane normal to this movement). Because of engine and stage misalignments and deflection (compliance) of the thrust structure under load, the exact alignment of the engines is difficult to define. In order to assure that the thrust structure compliance does not cause engine deflections which increase the severity of the base environment, the outboard engines are precanted outboard under no load so that they will not be canted toward the center engine when thrust is applied. The initial precant angle was 1.8 degrees directly away from the center engine, but this has been changed to account for changes in the thrust structure flexibility. The precant angle was increased to 2.3 degrees on the 504 vehicle to compensate for the new thrust structure which was expected to be more flexible. Subsequent evaluation of the thrust structure compliance led to the reduction of the precant angle to 1.3 degrees on AS-505, and a further reduction to 0.6 degrees was required on AS-510 to prevent possible interstage collision.

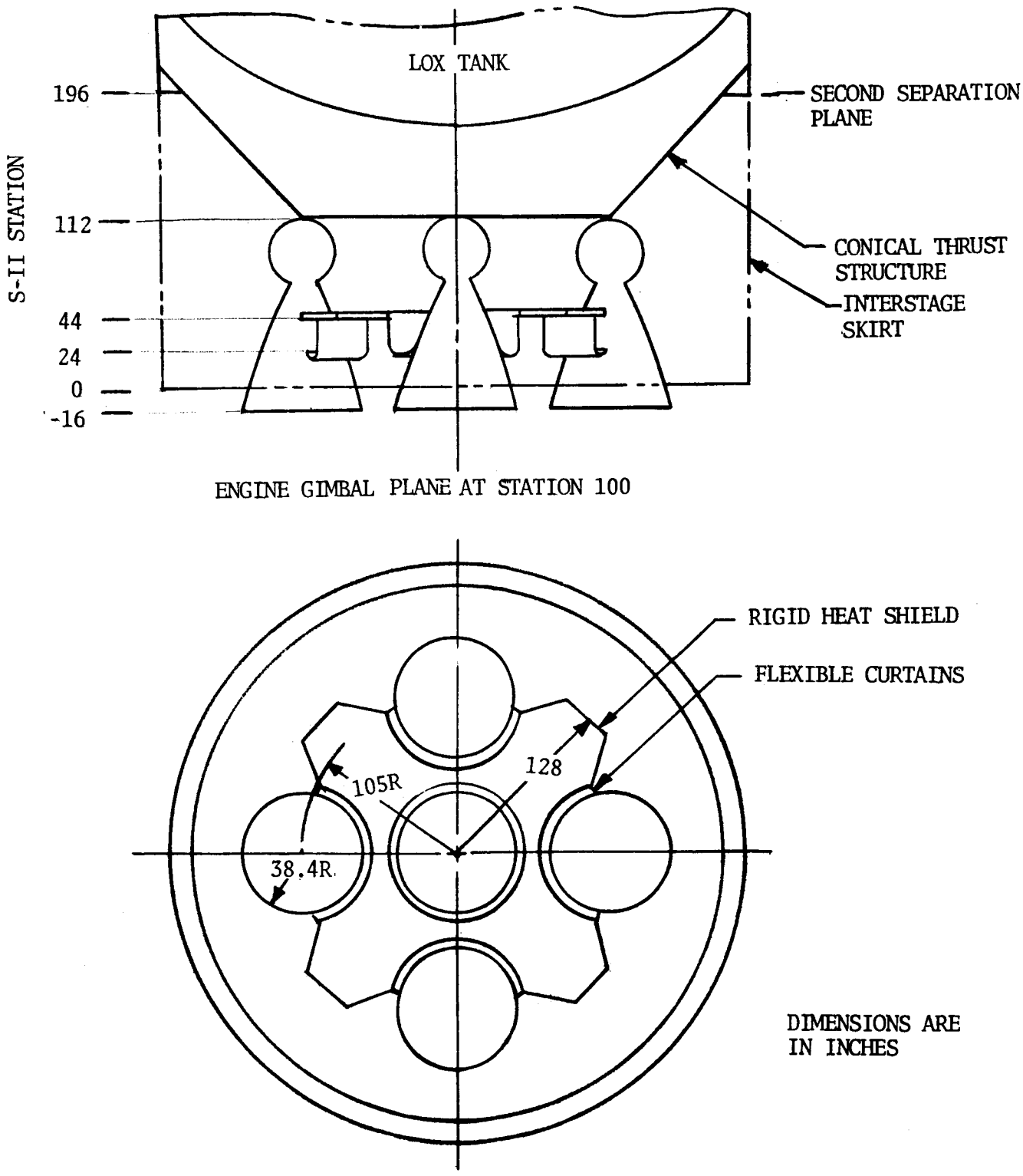

FIGURE 6.1-1. S-II BASE GEOMETRY

6.2 J-2 ENGINE CHARACTERISTICS

The J-2 engine used on the S-II stage was uprated during development by increasing chamber pressure and propellant flow rate. The final flight version produces 230,000 lbf at altitude with a nozzle stagnation pressure of 718 psia and an overall mixture ratio (oxygen/hydrogen) of 5.5. Although this mixture ratio is maintained for most of the stage operation, the engines are started at a propellant mixture (PMR) of 5.0 then switched to 5.5 with a later shift to 4.7 near the end of the flight. Another propulsion system variable which has been added in later flights is the center engine cutoff (CECO) to reduce the vehicle acceleration. The operation of the propulsion system can be varied to suit particular flight objectives, and some representative values of flight timing are outlined in Table 6.2-1.

TABLE 6.2-1. REPRESENTATIVE FLIGHT SCHEDULES

CONDITION	TIME FROM IGNITION (SECONDS)				
	SHIFT TO PMR = 5.5	INTERSTAGE SEPARATION	CECO	SHIFT TO PMR = 4.7	SHUT-DOWN
Design Nominal					
Case 1	2.5	30	-	280	374
Case 2	2.5	30	-	295	351
Design Engine-Out					
Case 1	2.5	30	-	350	467
Case 2	2.5	30	-	367	437
504 Flight	N/A	28.3	-	287.3	371.0
505 Flight	N/A	28.2	295.5	324.4	388.5

The J-2 engine has a regeneratively (hydrogen) cooled nozzle with an area ratio of 27.15. Turbine exhaust gases are introduced through 180 orifices between the tubes which form the nozzle wall in a plane approximately 48 inches forward of the exit (area ratio ≈ 13.2). Typical data which illustrate the mixture ratio effect and mass flow of the turbine exhaust are given in Table 6.2-2.

TABLE 6.2-2. NOMINAL J-2 ENGINE PROPELLANT FLOW RATES

	COMBUSTION CHAMBER	TURBINE EXHAUST	OVERALL ENGINE
Oxidizer Flow (lbm/sec)	454.39	3.49	457.88
Fuel Flow (lbm/sec)	79.54	3.71	83.25
Total Flow (lbm/sec)	533.93	7.20	541.13
Mixture Ratio (O/F)	5.71	0.94	5.50

6.2 (Continued)

Exhaust plume characteristics vary with mixture ratio and chamber pressure. Typical gas property variations for an overall mixture ratio of 5 are presented in Table 6.2-3, with corresponding plume isomachs shown in Figure 6.2-1. These data from Reference 6-1 were obtained using the last right running characteristic as a start line with smoothing of the flow directions near the nozzle centerline to eliminate negative flow angles. The Mach number along the start line varies from 3.39 at the lip to 4.1 on the axis.

TABLE 6.2-3. THERMODYNAMIC PROPERTIES - J-2 ENGINE PLUME

MACH. NUMBER	PRESSURE (PSF)	TEMPERATURE (°R)	SPECIFIC HEAT RATIO
5	63.4	1654	1.2937
6	16.7	1207	1.3184
7	5.5	915	1.3342
8	2.3	721	1.3438
9	0.97	579	1.3503
10	0.40	466	1.3551
12	0.05	331	1.3603
15	0.002	214	1.3642
20	0.0002	121	1.3670

Mixture Ratio = 5.17
Chamber Pressure = 680 psia
Chamber Temperature = 5958°R
Molecular Weight = 12.423

Propellant analysis based on equilibrium composition during expansion.

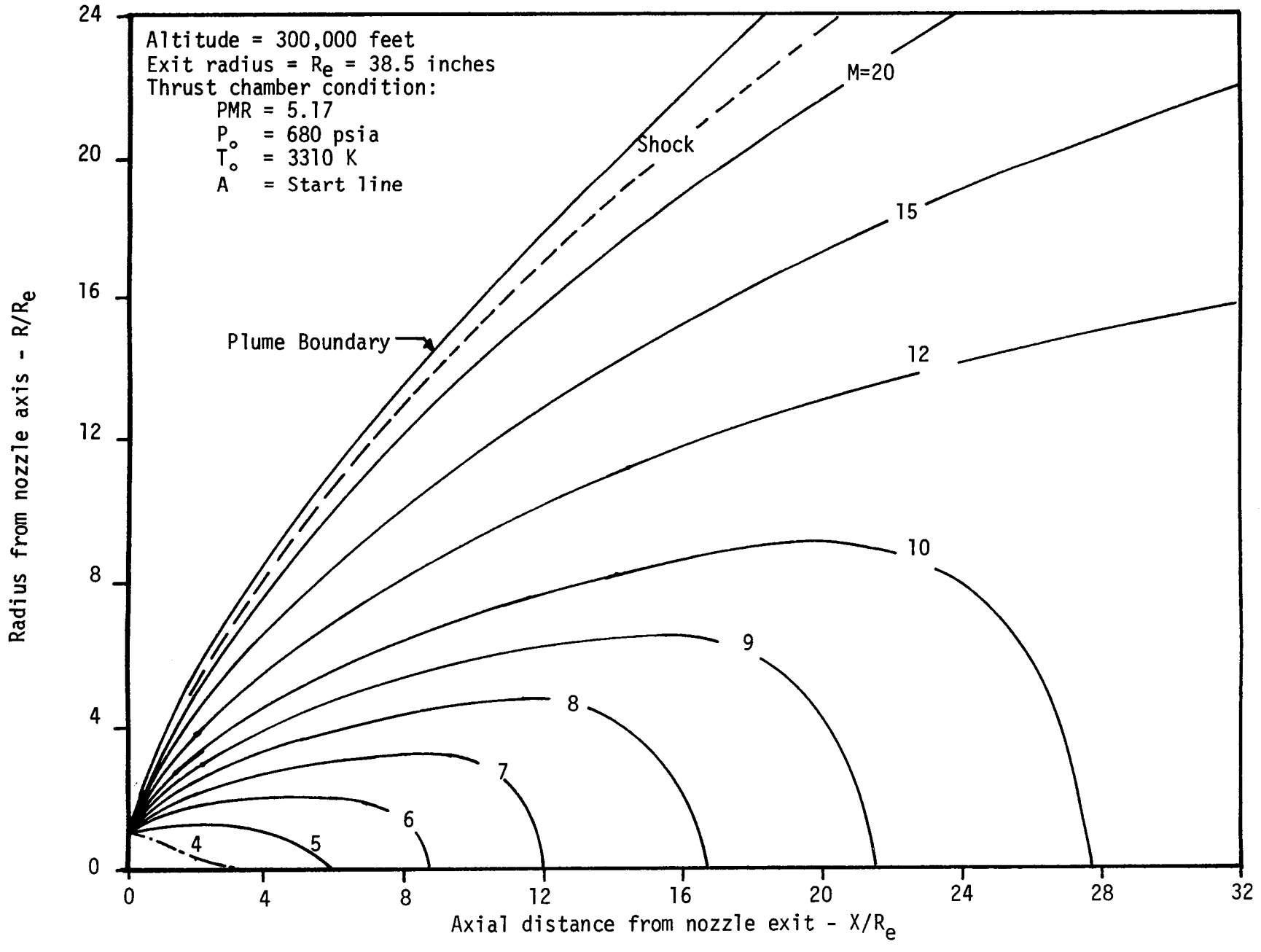

Figure 6.2-1 Typical J-2 engine plume.

6.3 PREDICTION METHODS

Pre-flight base heating predictions for the S-II stage were based on model test results for convection and analytical predictions of radiation.

Radiation

Because of the significant scale effects anticipated in the water vapor radiation from the exhaust plume, it was necessary to rely on analytical techniques to estimate the radiance to the heat shield. Two independent radiance estimates were made using different techniques. The design environment (Reference 6-2) was calculated by NAR using total emissivity data of Hottel, and later spot checks were made using a band model representative of the water vapor radiation with data averaged over 25 cm^{-1} spectral intervals.

The exhaust plume properties used in the total emissivity radiation prediction were determined by a method of characteristics for the free plume with estimates of properties in the interaction regions between plumes. The pressure and temperature in the interaction regions were assumed to be uniform normal to the impingement plane with variations in the axial direction.

The exhaust plume for the five-engine cluster used in the band model prediction was approximated by using an axisymmetric method-of-characteristics program with the flow configuration shown in Figure 6.3-1. The flow was expanded into a cone at the nozzle exit then turned into a cylinder with a radius equal to the distance from the nozzle axis to the impingement plane. It was necessary to use a 45 degree angle cone (Figure 6.3-2); rather than one approximating the free boundary so that an oblique shock could exist at the cone/cylinder corner. The arrangement of radial planes used in the flow field approximation is shown by Figure 6.3-3.

The points in the base region at which the radiant flux was calculated are illustrated in Figure 6.3-4 and a comparison of the band model results with the total emissivity calculation is presented in Table 6.3-1. In general, the predictions of the two methods are in good agreement.

Convection

Since the S-II stage operates at altitudes which cannot be conveniently duplicated in continuous flow test facilities, the short duration base heating test technique developed by Cornell Aeronautical Laboratory was used. Experience with the S-IV indicated that flight measurements were in reasonably good agreement with unscaled results from the 0.1 scale short duration model (Reference 6-3), so the same technique of using unscaled model data was chosen to define convective heating on the S-II. The opposing effects of scale on the heat transfer coefficient and recovery temperature produces characteristics similar to those depicted in Figure 6.3-5. Because of problems with the turbine exhaust simulation on the model and the apparent predominant effect of the turbine exhaust in cooling the reversed flow, the prediction method proved to be conservative.

6.3 (Continued)

During the model test program it was found that any inboard deflection of an outboard engine would cause an increase in convective heating in the base region. A full actuator movement (in one plane) of 7.5 degrees combined with the corresponding trim deflections from other engines caused the heat shield convective heating to increase approximately 400 percent. Even moderate deflections of less than 1 degree indicated significant increases in heating. Due to the sensitivity of the heating to gimbaling and the inability to characterize the deflection effects so that they could be systematically investigated, it was necessary to test failure cases and the resulting trim deflections for each failure mode likely to be of interest. Initially, generous 3-sigma control movements were included with trim and failure effects in the test patterns, but the high heating encountered caused a change to more realistic conditions. These included the failure condition to be tested with 3-sigma engine misalignments added along with the resultant trim deflections. After a time, the sensitivity to deflection caused a more thorough investigation of engine deflections, and it was found that structural compliance of the thrust cone caused significant inboard deflections which were added to the misalignment and trim deflections. The resulting high heating rates for the nominal and outboard-engine-out conditions caused concern that the heat shield design might be marginal, so the engines were precanted outboard.

TABLE 6.3-1. RESULTS OF RADIATION PREDICTIONS

POINT	COORDINATES[1] - INCHES			RADIATIVE FLUX - WATTS/CM^2	
	X	Y	Z	TOTAL EMISSIVITY REFERENCE 6-2	BAND MODEL REFERENCE 6-10
Heat Shield					
HS-1	52.5	0	-60	0.90	1.11
HS-2	70.7	-70.7	-60	1.18	1.14
Nozzle Exit[2]					
NE-1	66.6	0	0	4.20	4.41
NE-2	66.6	0	0	2.04	2.58
Thrust Structure[3]					
TS-1	140.0	-140.0	-212	0.17	0.15
TS-2	124.5	-124.5	-212	0.07	0.05
Interstage					
IS-1	140.0	-140.0	-16	0.73	0.79
IS-2	140.0	-140.0	-16	1.25	1.11

NOTES: (1) See Figure 6.3-4.
(2) Surface at NE-1 faces aft at the nozzle exit, while NE-2 faces laterally inboard.
(3) Without the interstage skirt in place.

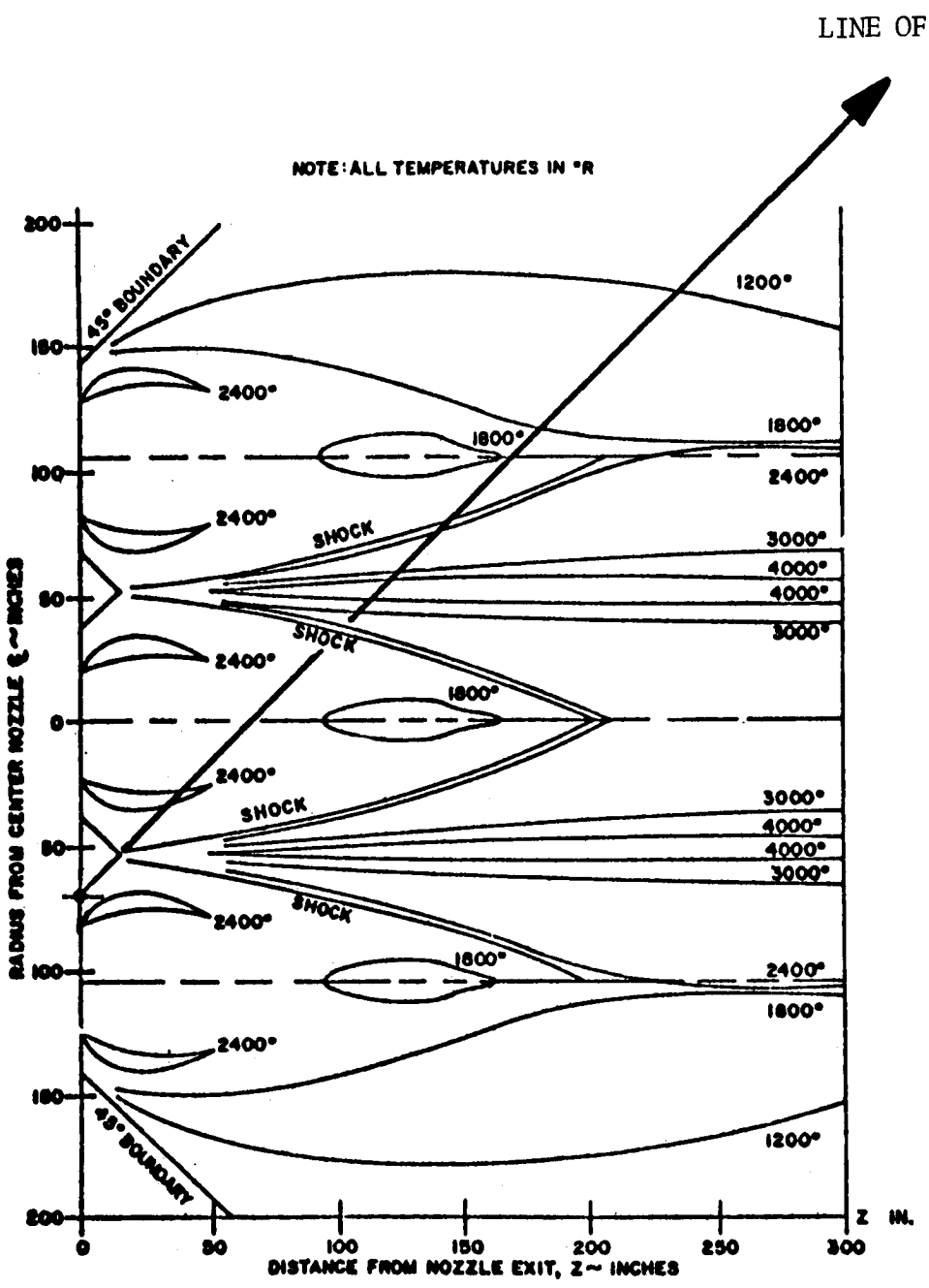

FIGURE 6.3-1. S-II RADIATION PREDICTION - TYPICAL FLOW FIELD SECTION ACROSS THREE NOZZLE EXITS

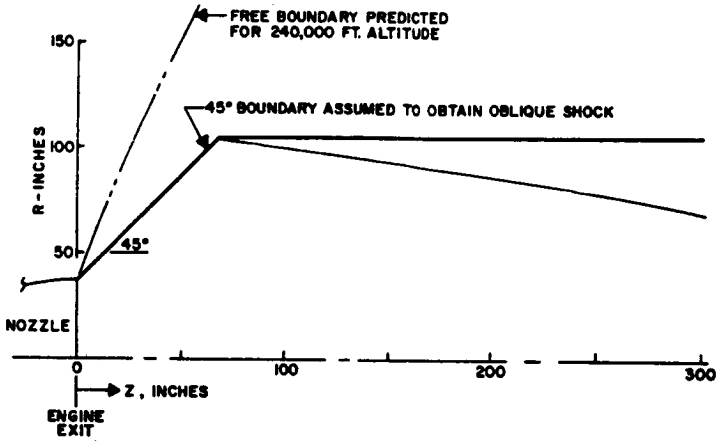

FIGURE 6.3-2. CONFIGURATION FOR AXISYMMETRIC FLOW FIELD APPROXIMATION

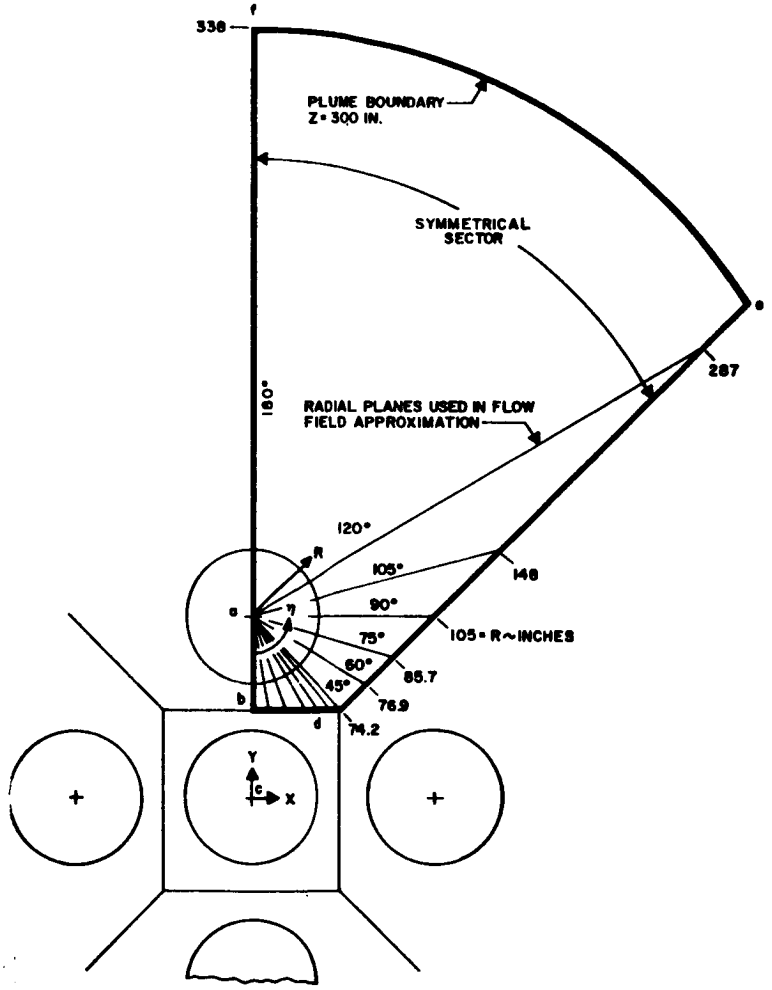

FIGURE 6.3-3. LOCATION OF PLANES USED IN APPROXIMATING THE S-II FLOW FIELD

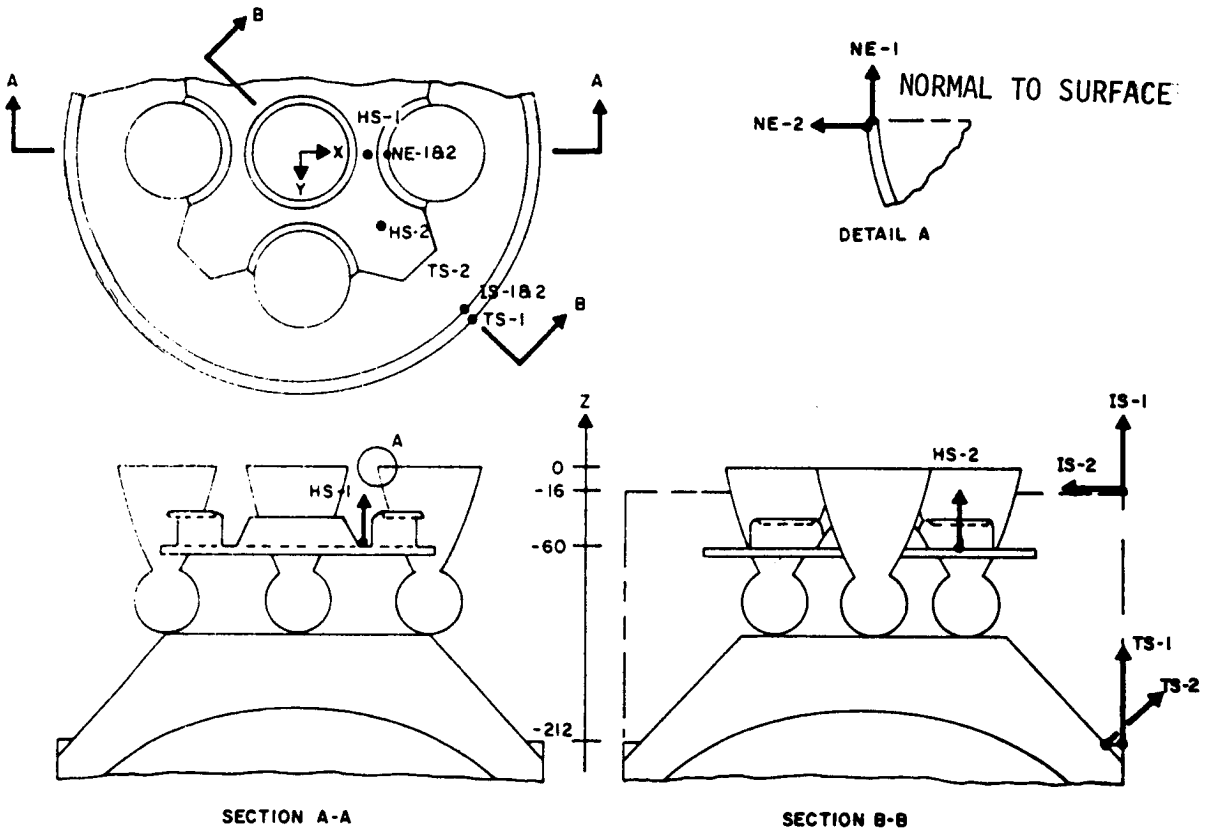

FIGURE 6.3-4. LOCATION OF POINTS IN THE BASE REGION AT WHICH BAND MODEL CALCULATIONS WERE MADE

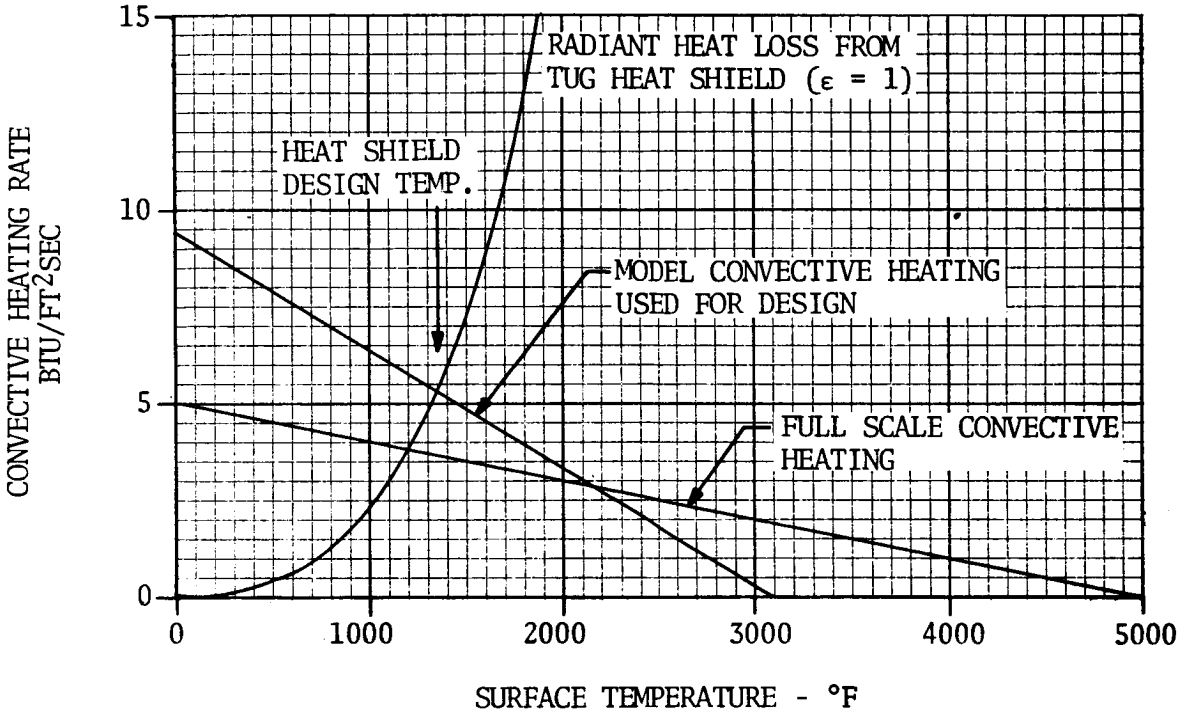

NOTE: This figure is an illustration only and should not be used for determining magnitudes of convective heating rate.

FIGURE 6.3-5. EXAMPLE OF ASSUMED MODEL AND PROTOTYPE HEATING

6.4 MODEL TESTS AND PARAMETRIC DATA

All base heating tests on the Saturn S-II were conducted using short-duration tests with no simulated external flow. Two models were used. First, a model in which the base geometry could be varied was tested in 1962 (Reference 6-4) to evaluate the effects of the number and spacing of the engines. Subsequent testing was performed using a model of the prototype base region. Tests of this model were conducted first at Cornell Aeronautical Laboratory during 1963 and 1964 (Reference 6-5) and then at the Impulse Base Flow Facility at MSFC in 1964 and 1965. Both of the test models were 0.04 scale and used scaled J-2 nozzle contours (area ratio of 27.5 and exit diameter of 3.08 inches).

Data from the two tests will be presented along with brief descriptions of the models. In presenting the data, effects of parametric variations will be emphasized rather than distributions of heating rates in the base region.

Parametric Model Tests

The parametric test model, Figure 6.4-1, was designed so that the engine and base spacing could be varied. There was a movable cylindrical skirt to simulate the interstage structure and a flame deflector to simulate the type heat shield under consideration for the S-II stage. In addition to the parametric variations available in the five-engine configuration, the center J-2 model nozzle could be removed for 4-engine tests. Due to the large number of variations tested, much of the data available came from a single run with no repeat runs to check the validity of the data. Since repeat runs of a given model configuration often exhibit data scatter of ±20 percent above the mean, caution should be used in evaluating the data as being an absolute indication of the parametric variation under consideration.

Model data were recorded by photographing oscilloscopes and was usually limited to about 20 measurements per test firing. Instrumentation on the model base consisted of 36 calorimeters and 41 surface pressures. In addition, a contoured strip was available for attachment to the exterior of the nozzles which had 27 calorimeters arranged in three rows. Calorimeters were the thin film type with a platinum resistance element deposited on a Pyrex substrate. Pressure measurements were made using piezo-electric transducers mounted to minimize acceleration effects from the model firing.

Parametric variations during the test included engine spacing, base location, interstage length, flame deflector position, ambient pressure, and combustion chamber pressure. Results of these variations taken from Reference 6-4 are presented in Figures 6.4-2 through 6.4-15. Brief comments on the results of each variation are presented below.

6.4 (Continued)

Engine Spacing

Results of varying the engine mounting circle diameter presented in Figures 6.4-2 and 6.4-3 illustrate the different characteristic distributions of heating and pressure and show a marked reduction of heating with increasing engine spacing on the four-engine configuration. The trend in heating rate on the five-engine configuration is not well defined due to lack of data, but the trend in base pressures indicates that the heating rates should be expected to decrease with increasing engine spacing.

Base Location

Effects of varying the position of the base forward of the nozzle exits are shown in Figure 6.4-4 for the five-engine configuration. This illustrates the increasing base pressure and heating rates which occur as vent areas between the engines are reduced by moving the base toward the nozzle exit plane. Results of the four-engine configuration, Figure 6.4-5, follow the same trend except for the case where the base is located at the nozzle exits. The shift in pressure distribution at this point and the slight reduction in heating rate may indicate a significant change in the base flow pattern, but since the data represent only one test run and the heating and pressure trends do not agree, no conclusion seems justified.

Interstage Length

As the interstage length is increased from flush with the base to a position in the plane of the nozzle exits an increase in base pressure would be expected, particularly in the outer portions of the base. This general trend is evident in the five-engine results, Figure 6.4-6, but in the outer areas of the four-engine base, Figure 6.4-7, insufficient pressure data are available and the trends in heating are not consistent. Much of the variation in the inner region of the base is likely to have resulted from run-to-run variations rather than the effect of the interstage.

Flame Deflector Position

In this configuration the flame deflector is sealed around the nozzles and represents a heat shield while the model base can be considered to represent the vehicle thrust structure. The important effects are the variation in base heating rates near the edge of the base and the effect of the interstage in increasing both base pressure and heating rates. These effects are illustrated in Figure 6.4-8 for the five-engine configuration, but since data on the four-engine configuration in Figure 6.4-9 are limited to the inner region of the base, the trend near the edge of the base was not documented.

6.4 (Continued)

Ambient Pressure

Base pressures and heating rates are presented in Figures 6.4-10 through 6.4-13, but no effects of pressure are apparent except in the outer base regions. This result is not unexpected since the range of altitudes for S-II operation did not go low enough for the ambient pressure to have a significant influence.

Combustion Chamber Pressure

Simulated model combustor pressure was varied from approximately 300 to 700 psia with representative effects on base pressure and heat transfer rate as shown in Figure 6.4-14. The indicated variation of base recovery temperature with chamber pressure and typical data taken for recovery temperature are illustrated in Figure 6.4-15. The variation in heating rate at each base temperature is an indication of the uncertainty in a particular measurement. Because of the uncertainty in recovery temperature on this test, results of the chamber pressure effects are not considered to be as accurate as those obtained later in the research test program reported in Reference 6-3.

Prototype Model Test

The prototype test model, Figure 6.4-16, was designed to simulate the flight configuration as closely as possible. Several components were simulated on the conical thrust structure and a removable interstage skirt was provided to simulate the base configuration during the time between first and second plane separations. The model was initially intended to operate at a propellant mixture ratio (PMR) of 5 with a nozzle stagnation pressure of 632 psia, but during the tests, mixture ratio of the model was varied from 4.5 to 5.5 with nozzle pressures of 546 to 715 psia to cover the range of PMR planned for the prototype.

Flexible rubber boots were used on the model to simulate the flexible heat shield curtains on the prototype and allow engine gimbaling to study various misalignment and malfunction control patterns. Preliminary tests were conducted with round heat shields representing full scale diameters of 210, 228, and 246 inches before the final 256-inch configuration shown in Figure 6.4-16 was chosen.

The prototype model was first tested at Cornell Aeronautical Laboratory (Reference 6-5) in a program consisting of approximately 350 runs and then it was transferred to MSFC for a test of approximately 700 runs. (MSFC results were used for design, but have not been published for other use.) Tests were primarily for heat transfer with comparatively little base pressure data taken. The large number of runs were required by the great number of configuration variables and the policy of making several repeat runs in tests at MSFC in an attempt to assure the data were representative. The regions of interest for heat transfer data were the nozzle walls, heat

shield, engine components forward of the heat shield, and the thrust structure. Tests with the interstage skirt indicated that its presence had a large effect on the thrust structure and region forward of the heat shield, but effects on the heat shield and nozzle walls were not significant and often difficult to define. The parametric variation which had the greatest effect on heating rates on the nozzles and heat shield aft surface was engine deflection. Approximately 30 deflection patterns were tested which represented engine and gimbal actuator failures as well as normal engine misalignments.

Since most of the engine deflection patterns represented assumed misalignments and actual control responses, there was generally no step-by-step variation of a single gimbal angle to evaluate its effect, so the results are difficult to characterize for general application. Considering this problem, the results to be presented are intended to demonstrate the general effect that was observed without going into details of specific deflection patterns. The parametric variations to be reviewed include the effect of heat shield size, interstage structure, turbo-pump exhaust simulation, outboard engine failure, single gimbal actuator failure, dual gimbal actuator failure, and variations in mixture ratio.

Heat Shield Size

Heat shield size was increased in an attempt to reduce heating rates in the thrust cone (structure) area since no thermal protection was planned for the structure and components mounted on the structure had relatively low temperature limits. Initial experiments used heat shield diameters of 210, 228 and 256 inches (full scale) with both flat and turned edges as shown in Figure 6.4-16. Based on the results of these tests, the 256-inch trapezoidal heat shield was chosen for the prototype and was used on almost all of the model tests at MSFC. During tests at CAL it was doubtful that steady flow was achieved on the thrust structure and the results of heat shield size on heating rate, shown in Figure 6.4-17, did not present a consistent trend. However, there was a general indication of a reduction in heating with increasing heat shield size, and tests indicated that heating with the smaller heat shield was more likely to increase with increasing altitude while the large heat shield did not indicate this trend. Later tests of longer duration at MSFC gave more confidence of steady flow being attained on the thrust cone and the measured heating rates were slightly higher, but there was no indication of a better definition of heat shield size effects.

Interstage Skirt

The interstage structure extends from the first separation plane, Station 0, to the second separation plane, Station 196, as indicated in Figure 6.4-16. Although there sometimes appear to be effects of the interstage on the heat shield aft side heating distribution, there was no consistent indication that the peak heating increased. The primary effect of the interstage is on the thrust cone heating rates as illustrated in Figure 6.4-18. It is

apparent that the interstage traps the flow off of the heat shield and directs it toward the thrust cone. The data shown are on a radial line between outboard engines where the heating is the highest. Lowest heating on the thrust cone is on a radial line through an outboard engine, but heating in this location is also increased significantly by the interstage.

Turbo-Pump Exhaust

The turbo-pump exhaust injection into the J-2 nozzle described in Section 6.2 was simulated on the nozzle by fifty 0.067-inch diameter holes drilled normal to the nozzle wall. Hydrogen heated to the estimated turbine exhaust gas temperature (1140°R) was used in the model simulation. The mass flow rate was simulated assuming an orifice discharge coefficient of 0.88 with sonic flow and a 16 psia stagnation pressure. Simulation of the mass flow rate with the lower molecular weight hydrogen causes an increase in the injection velocity and momentum and increases the relative volume in the base region. Simulation was also doubtful because of the probable different effects the injection would have on the nozzle and full scale boundary layer and possible separation and reattachment. In addition to these theoretical inaccuracies in simulation, it was also difficult to time the flow of heated hydrogen to correspond to the short test event. If the hydrogen arrived too soon, it flowed into the base region causing instrumentation problems and required more time for the initiation of steady flow when the combustor fired. This is particularly important in regard to the thrust cone heating. Because of the piping the gas passed through on the way to the manifold around the model nozzle, there was a tendency for the gas to cool, but three turbine exhaust qualification runs indicated the desired temperature could be maintained by using a supply reservoir temperature of 1460°R. The effects of the simulated turbine exhaust in lowering the peak heating rates are illustrated in Figures 6.4-19 through 6.4-22, but possible increases in some regions are also indicated in Figures 6.4-21 and 6.4-22. Although turbine exhaust injection is expected to lower the base recovery temperature since it cools the plume boundary, it was decided to base the S-II thermal environment on testing without the simulated injection because of the difficult and questionable simulation and the expected increase in recovery temperature with scale due to boundary layer effects.

Outboard Engine Failure

The significant effects resulting from an outboard engine failure are due to the engine deflections required for trim rather than the absence of the outboard exhaust plume. Experimental outboard engine failure patterns and the resulting increase in peak heat shield heating are illustrated in Figure 6.4-23. As the engines deflect, the location of the peak heating on the heat shield moves in the direction of the inboard deflection component and occurs at a smaller radius from the base center.

6.4 (Continued)

Single Actuator Failure

Deflection patterns which were tested as being representative of a single actuator failure at 7.5, 5, and 3 degrees are shown in Figure 6.4-24 as cases 3C, 5, 6 and 6A. In addition, three variations of combined engine misalignment and thrust structure compliance patterns (Cases 9, 9A and 9B) are considered as being representative of the type of flow pattern resulting from single actuator failures. As the gimbal angle increases, the peak heating moves across the heat shield (towards the outboard engine at which the maximum deflection component is pointed) and finally occurs on the flexible curtain attachment flange at the nozzle for the maximum angle tested. To illustrate this effect, results are presented in Figure 6.4-24 for both the rigid heat shield and the flexible curtain attachment flange. The results presented for the heat shield illustrate the most significant effect of a single actuator failure, but other effects have been observed. Heat rates on the nozzle wall increase for failures which direct the engine inboard, and increases in thrust cone heating have been noted when the failure directs the engines outboard.

Dual Actuator Failure

Movement of both actuators in an inboard direction causes significant increases in heating on the heat shield and center nozzle. In the extreme case of 7.5-degree deflection in pitch and yaw, plume impingement on the center nozzle was evident on the model, and good correlation was obtained between the peak measured heating and predictions using stagnation point heat transfer analysis. The effects of dual actuator deflection on the heat shield are illustrated in Figure 6.4-25. As in the case of a single actuator failure, the point of peak heating moves from the rigid portion of the heat shield to the flexible curtain at large deflection angles. Effects of dual actuator movement on the environment of the center nozzle are illustrated in Figure 6.4-26. The extremely high heating rates near the nozzle lip rapidly decrease as the distance from the plume impingement point increases, so there is no appreciable increase in heating on the forward portion of the nozzle.

Mixture Ratio

As the mixture ratio is increased on the J-2 engine, the total propellant flow rate also increases, so the chamber pressure varies with mixture ratio as indicated in Table 6.4-1. The resulting heating rate variations will be affected by both the pressure and temperature change. Test results were conclusive from a qualitative standpoint that the heating rates and base pressure increase with mixture ratio, but quantitative results were not significant since test-to-test variations in heating are comparable to a significant portion of the anticipated variation in heating.

TABLE 6.4-1. EFFECT OF MIXTURE RATIO CHANGE ON S-II BASE ENVIRONMENTS

PMR	PREDICTED NOZZLE PRESSURE - P_O - PSIA	STAGNATION TEMPERATURE - T_O - °R	$P_O/P_O(5.0)$	$T_O/T_O(5.0)$
4.5	546	5626	0.865	0.947
4.7	584	5717	0.924	0.970
5.0	632	5891	1.000	1.000
5.5	715	6101	1.131	1.042

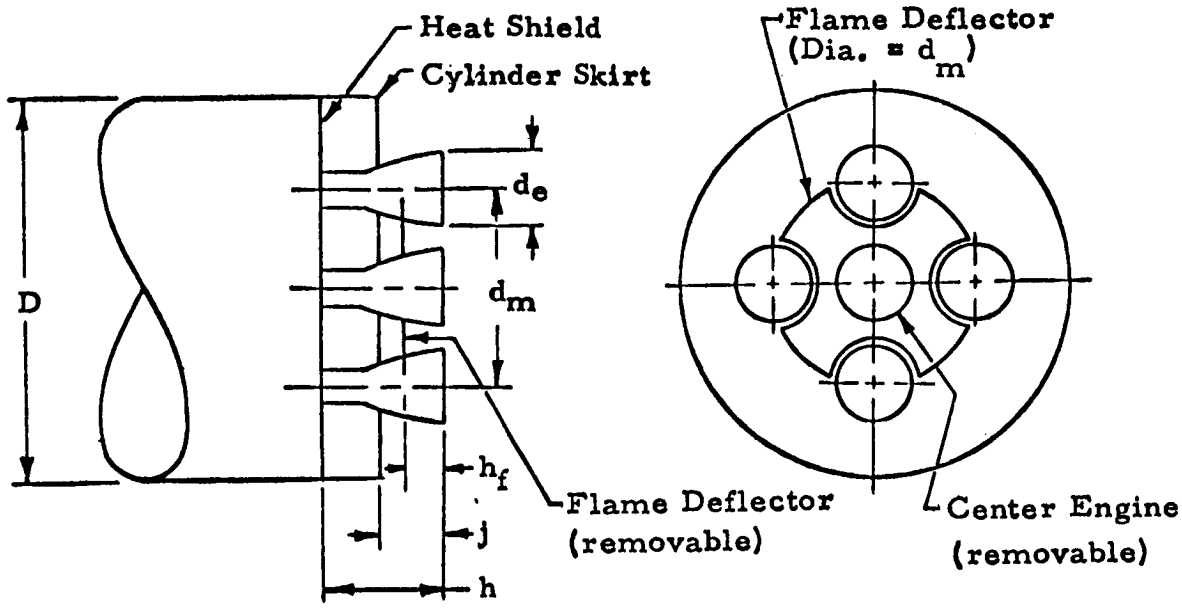

Nominal Configuration

Dimension	Model Scale Inches	Full Scale Inches	Dimensionless Ratio
D	15.64	396	
d_e (I.D.)	3.08	77	d_e/D = 0.1944
d_m	8.40	210	d_m/D = 0.5303
h	1.72	43	h/D = 0.1086
j	1.72	43	j/D = 0.1086

Chamber pressure = P_R = 632 psia
No Flame Deflector
Five Engines

FIGURE 6.4-1. SATURN S-II PARAMETRIC MODEL ARRANGEMENT

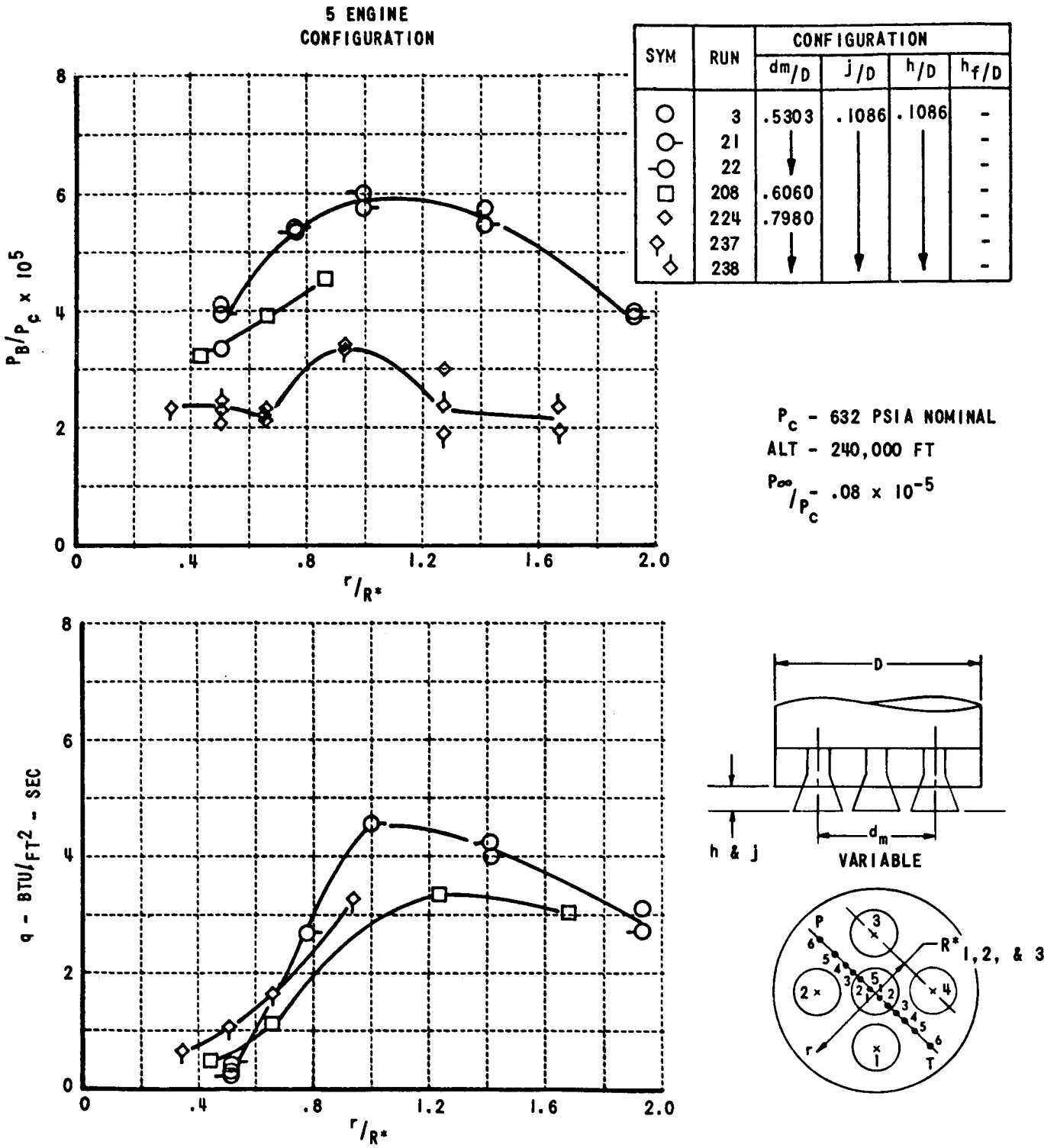

FIGURE 6.4-2. EFFECT OF ENGINE MOUNTING CIRCLE DIAMETER ON BASE PRESSURE AND HEAT TRANSFER (5 ENGINE)

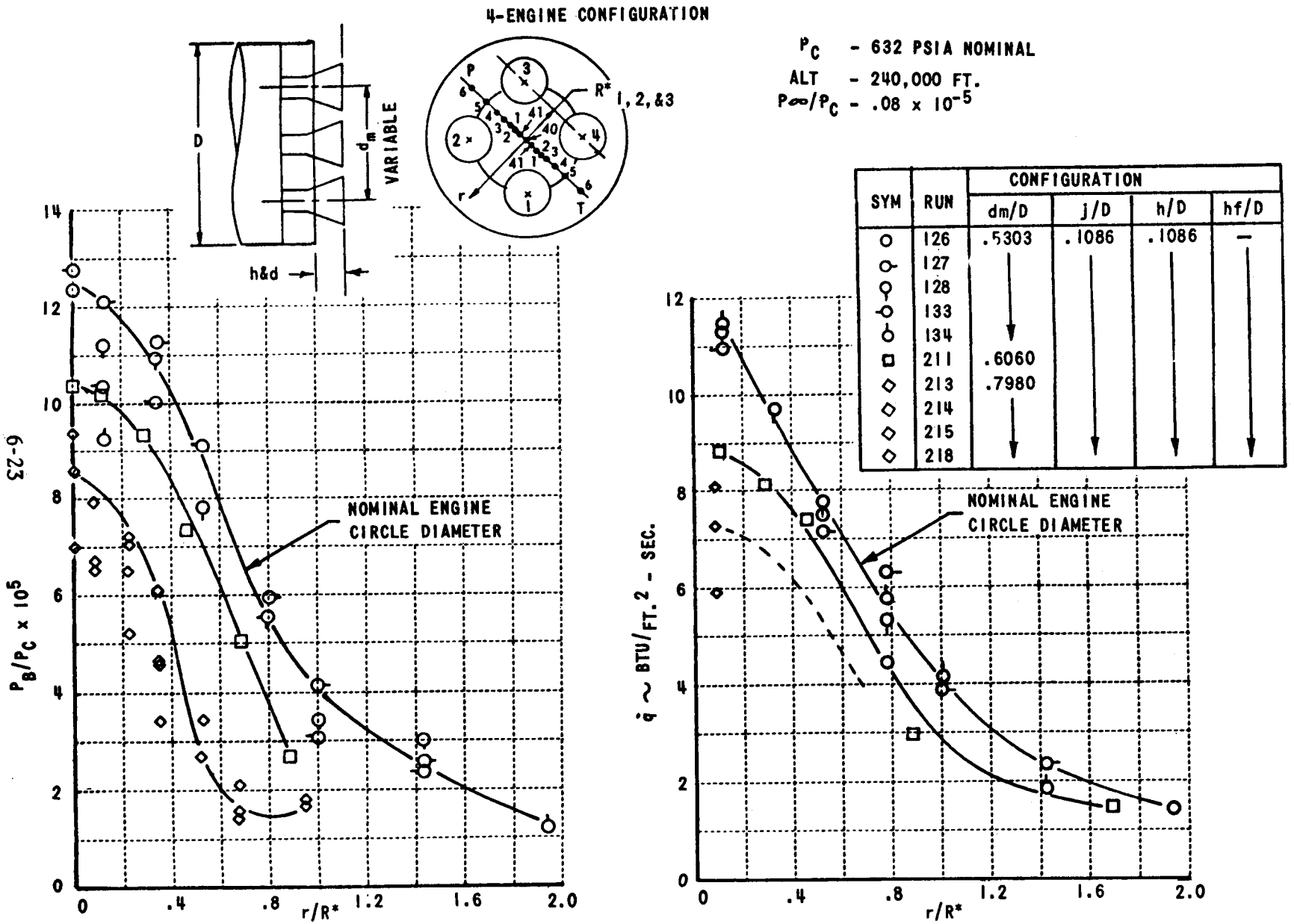

FIGURE 6.4-3. EFFECT OF ENGINE MOUNTING CIRCLE DIAMETER ON BASE PRESSURE AND HEAT TRANSFER (4 ENGINE)

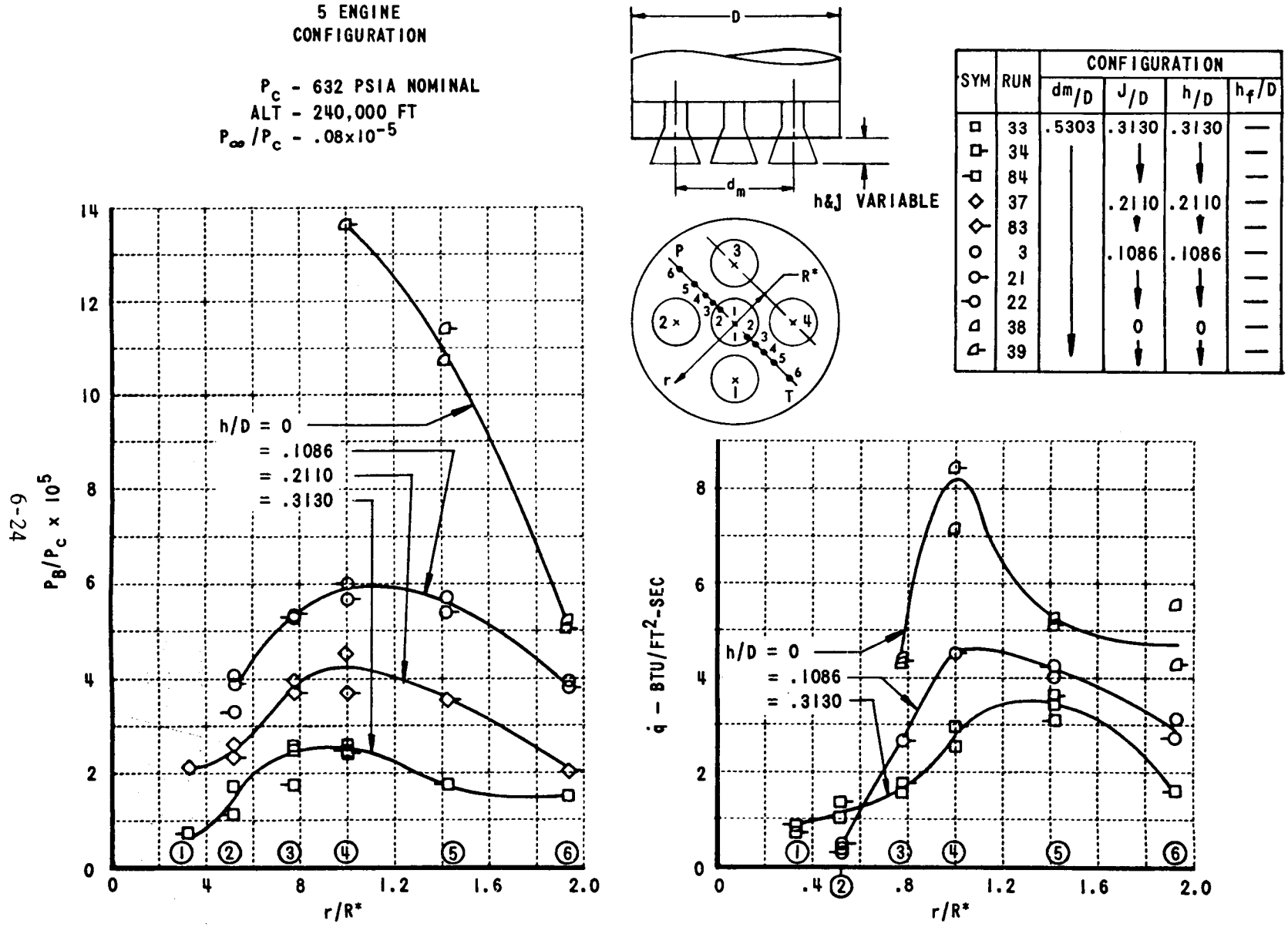

FIGURE 6.4-4. EFFECT OF BASE LOCATION ON BASE PRESSURE AND HEAT TRANSFER (5 ENGINE)

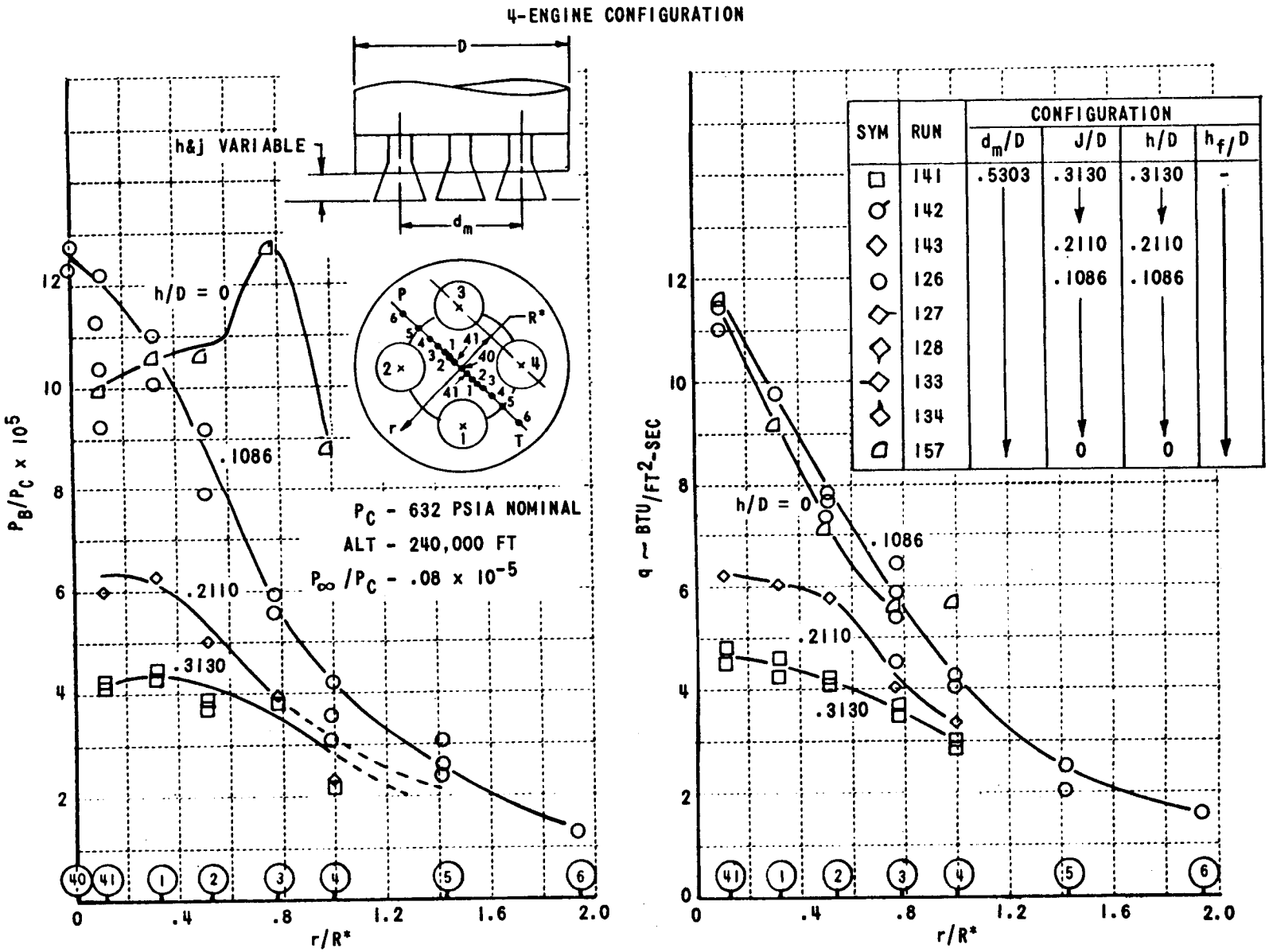

FIGURE 6.4-5. EFFECT OF BASE LOCATION ON BASE PRESSURE AND HEAT TRANSFER (4 ENGINE)

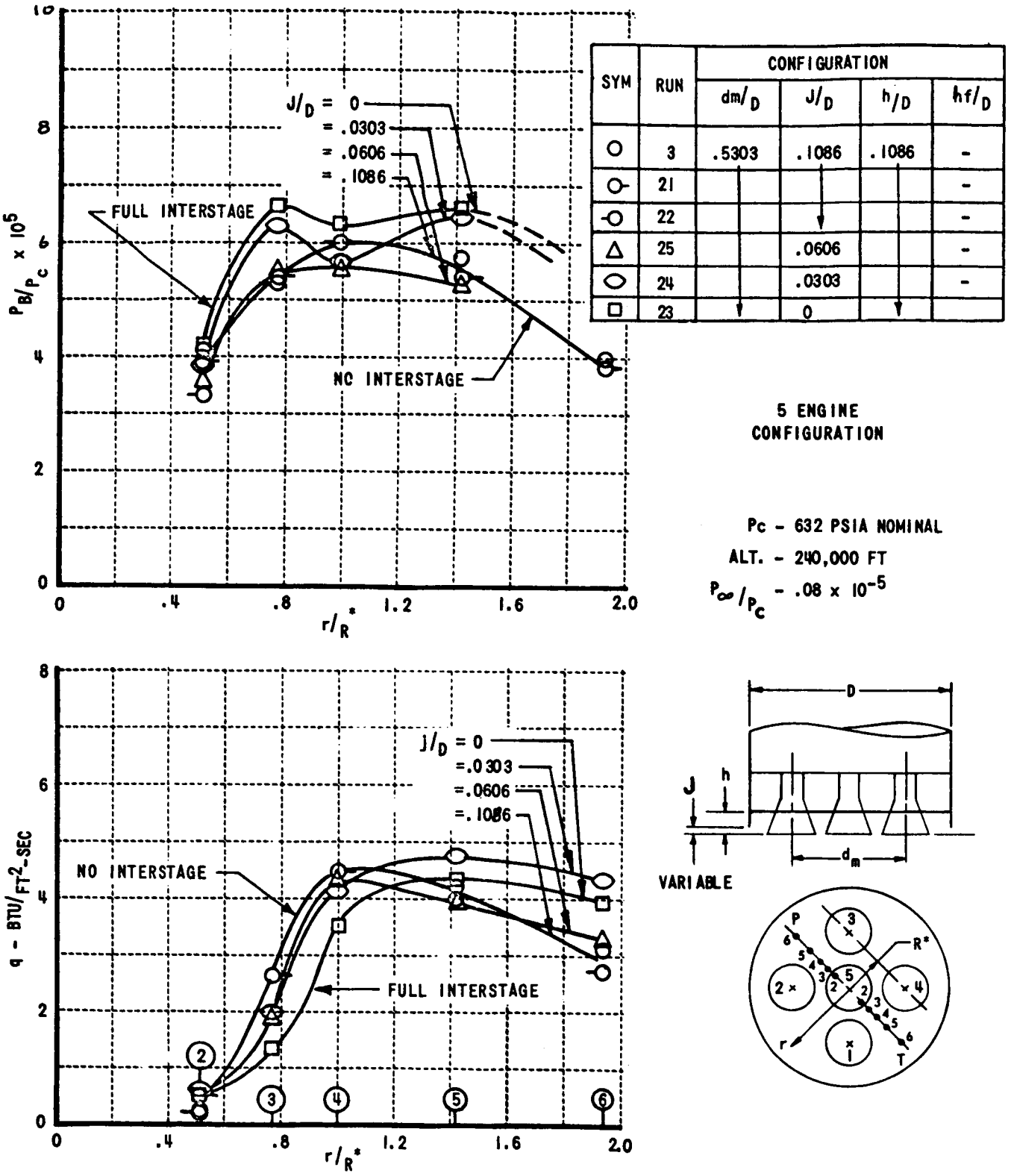

FIGURE 6.4-6. EFFECT OF INTERSTAGE LENGTH ON BASE PRESSURE AND HEAT TRANSFER (5 ENGINE)

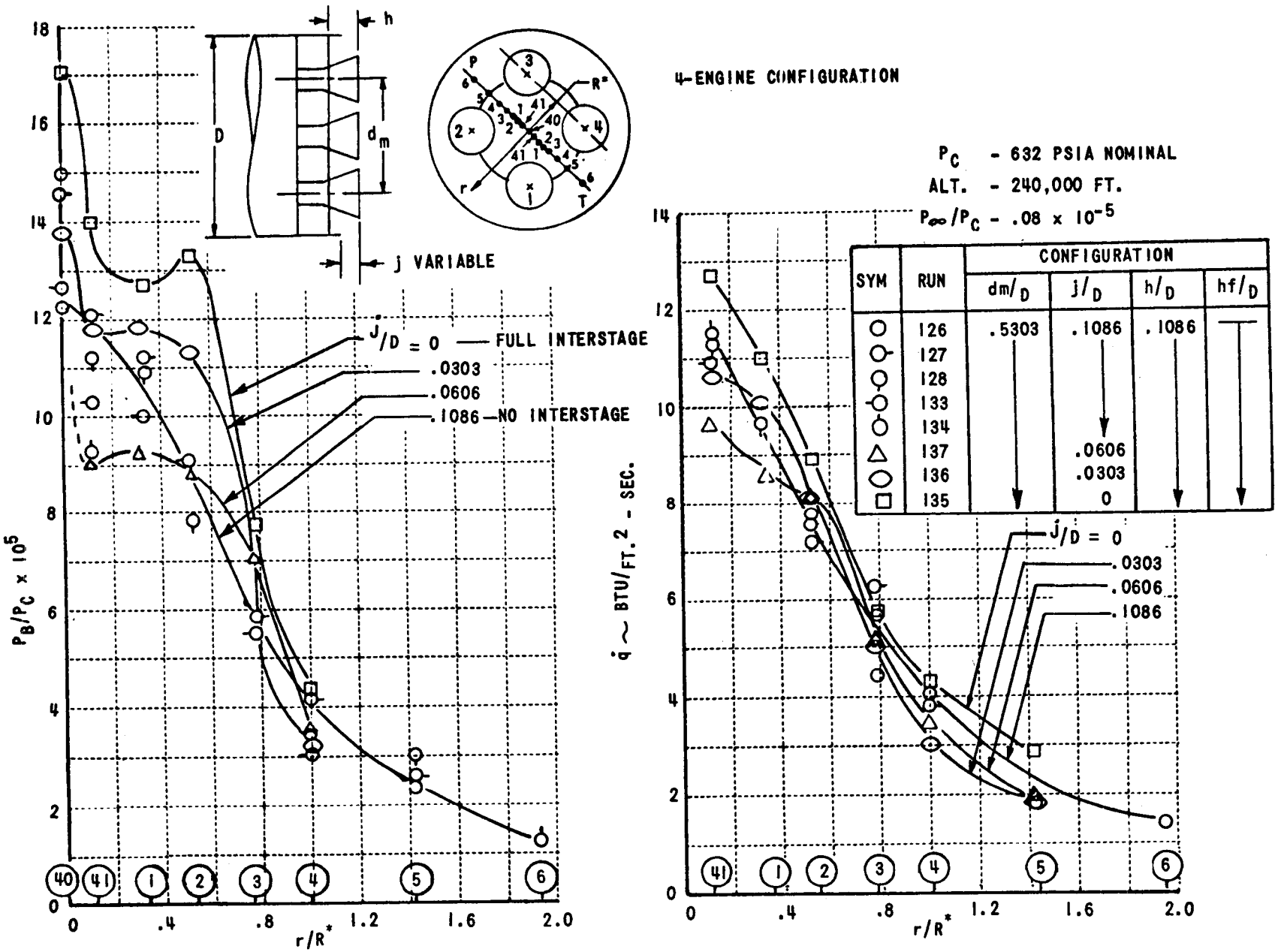

FIGURE 6.4-7. EFFECT OF INTERSTAGE LENGTH ON HEAT TRANSFER AND BASE PRESSURE (4 ENGINE)

SYM (AVE)	RUNS	CONFIGURATION			
		d_m/D	j/D	h/D	h_f/D
○	55,56,58,86,100	.5303	0	.3130	.2110
△	59,91,94				.1086
◇	95,99				0
□	57,61,87,88		.3130		.2110
▷	90,92,93,108,109				.1086
◇	98				0

5 ENGINE CONFIGURATION

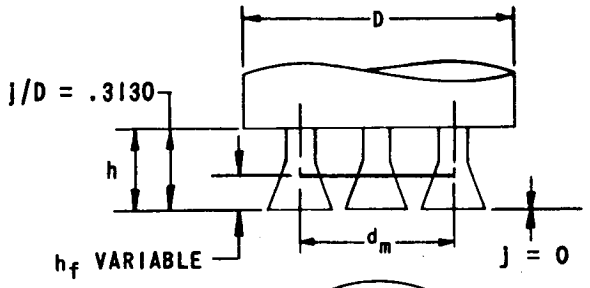

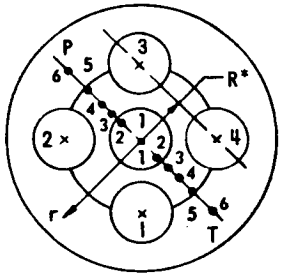

SOLID SYMBOLS ARE FLAME DEFLECTOR DATA

P_c - 632 PSIA NOMINAL
ALT - 240,000 FT
P_∞ / P_c -.08x10^{-5}

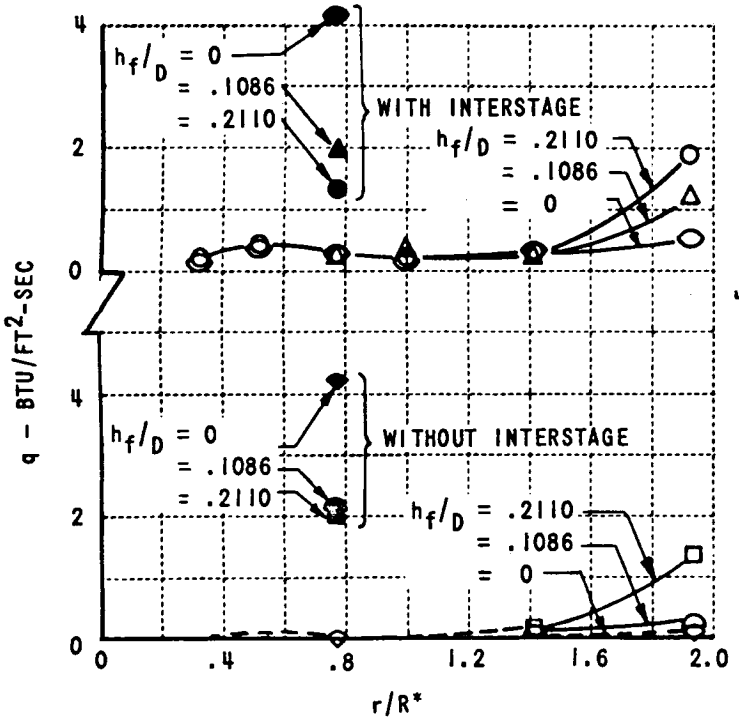

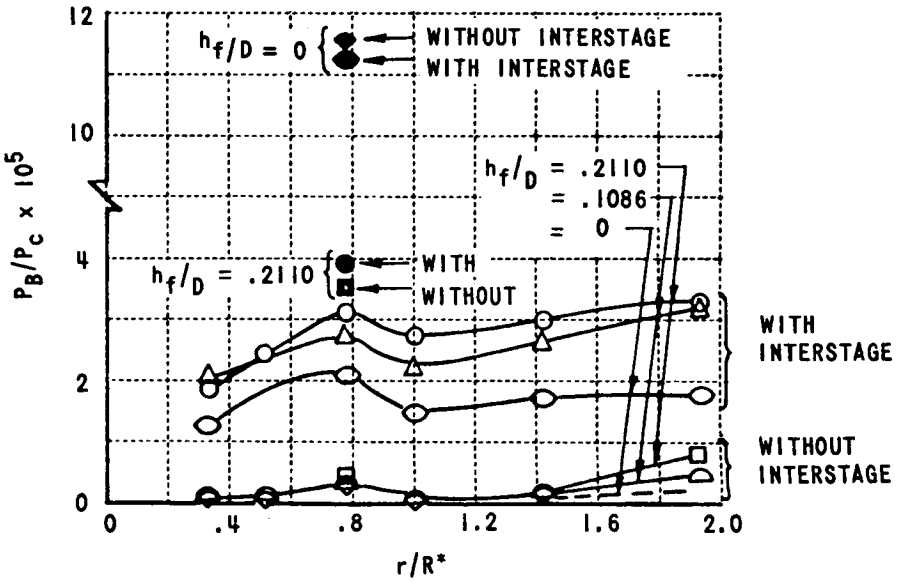

FIGURE 6.4-8. EFFECT OF FLAME DEFLECTOR (NO GAP) POSITION ON BASE PRESSURE AND HEAT TRANSFER (5 ENGINE)

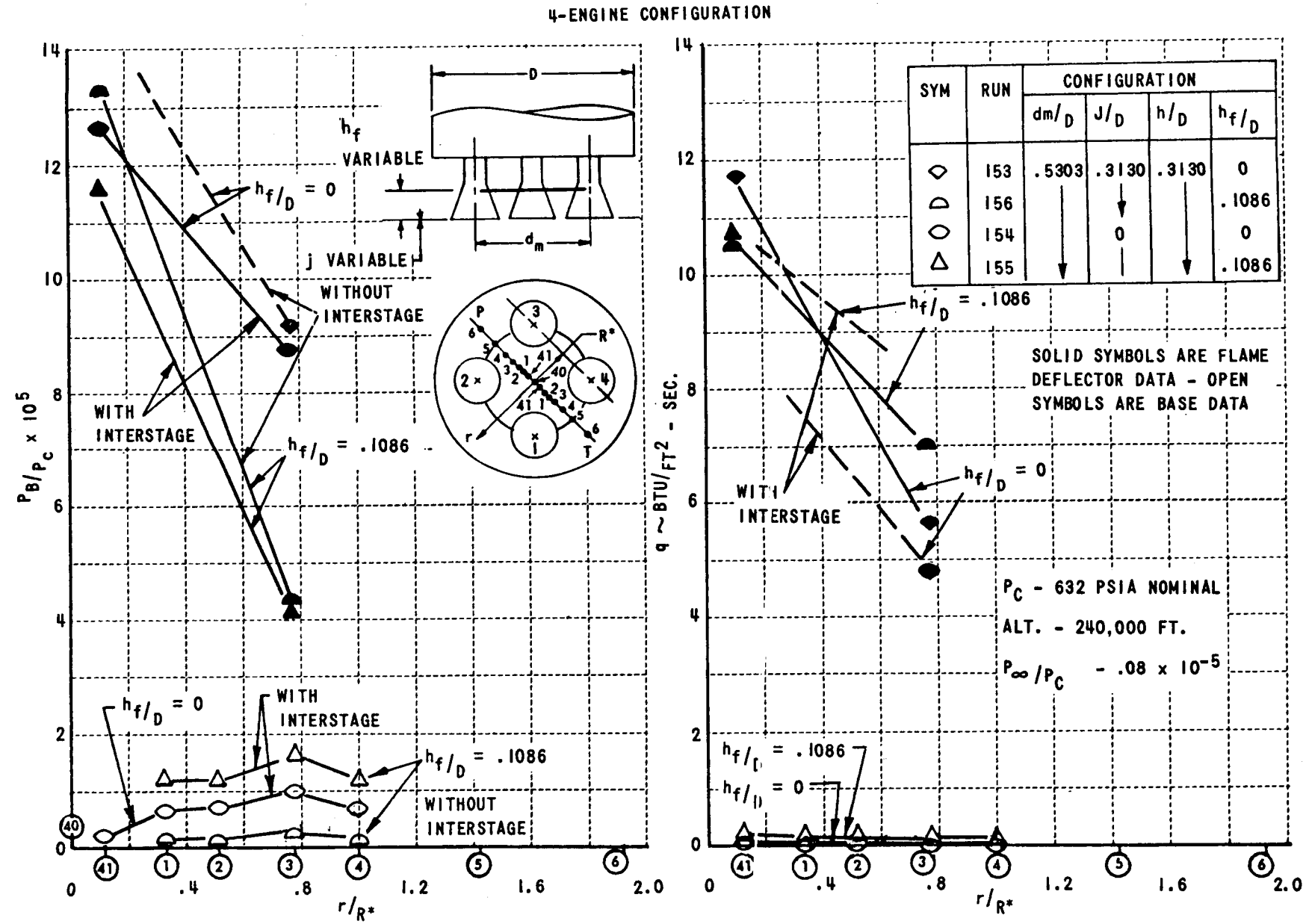

FIGURE 6.4-9. EFFECT OF FLAME DEFLECTOR (NO GAP) POSITION ON BASE PRESSURE AND HEAT TRANSFER (4 ENGINE)

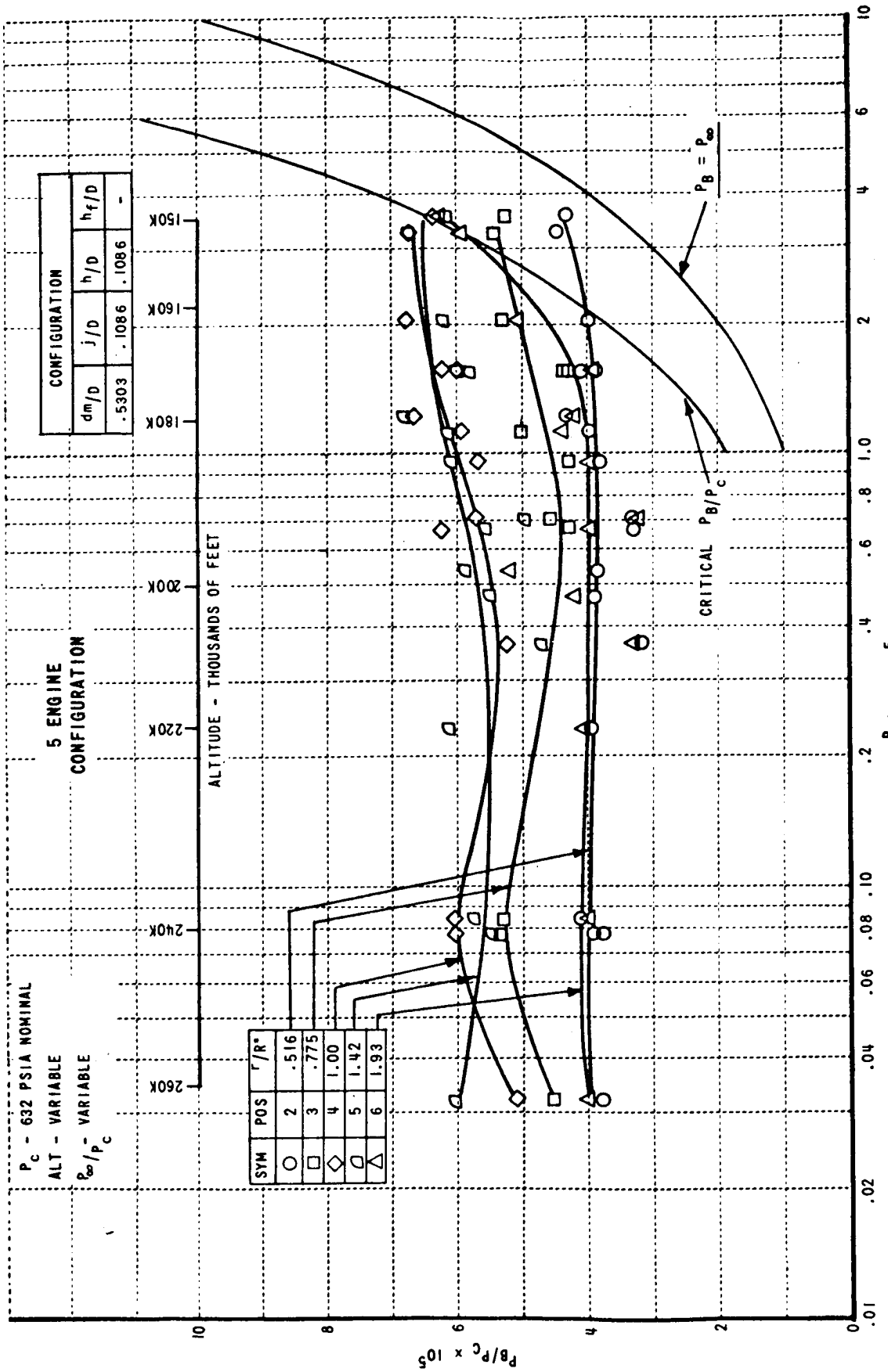

FIGURE 6.4-10. EFFECT OF AMBIENT PRESSURE ON BASE PRESSURE (5 ENGINE)

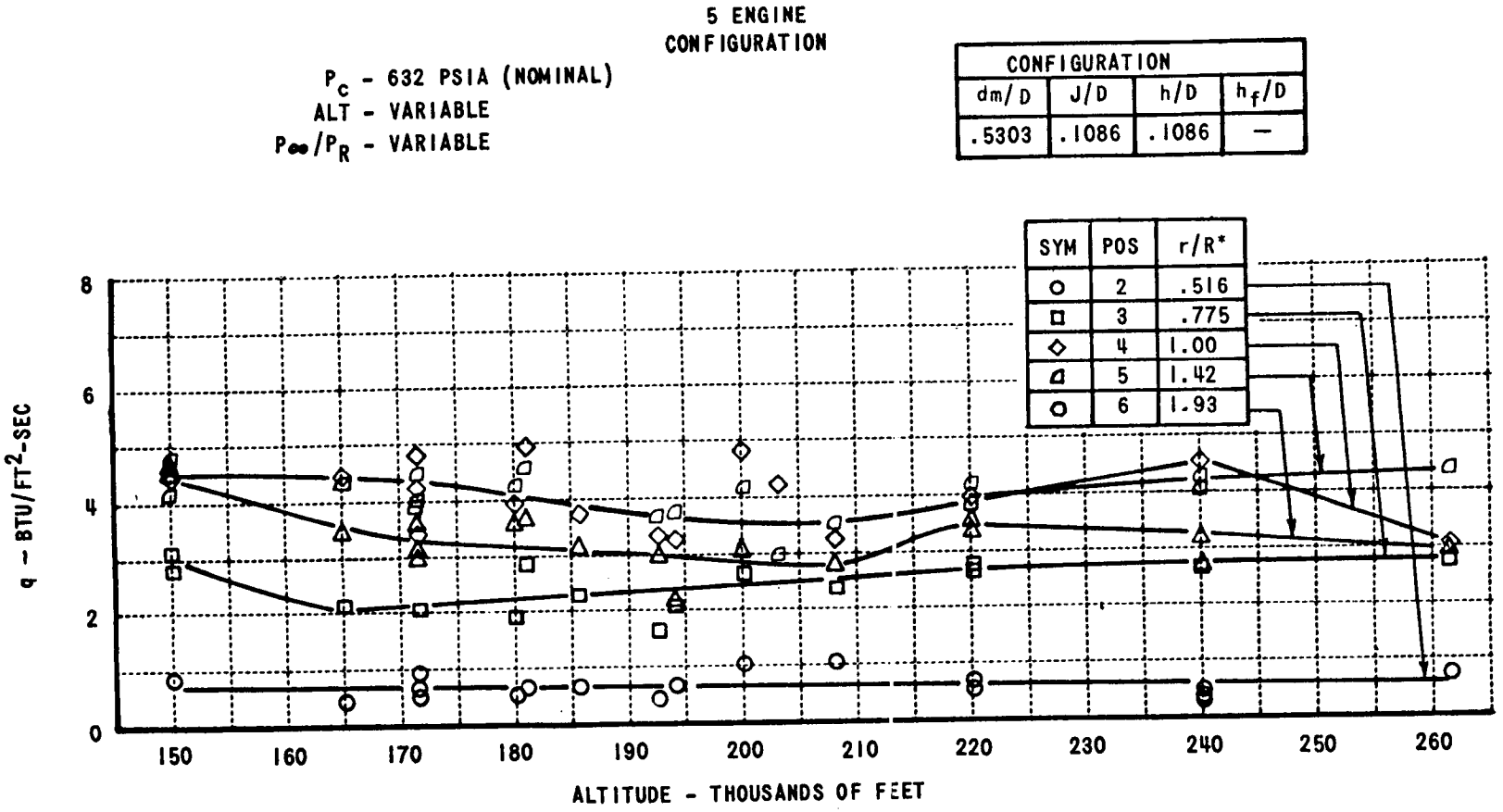

FIGURE 6.4-11. EFFECT OF ALTITUDE ON BASE HEAT TRANSFER RATES (5 ENGINE)

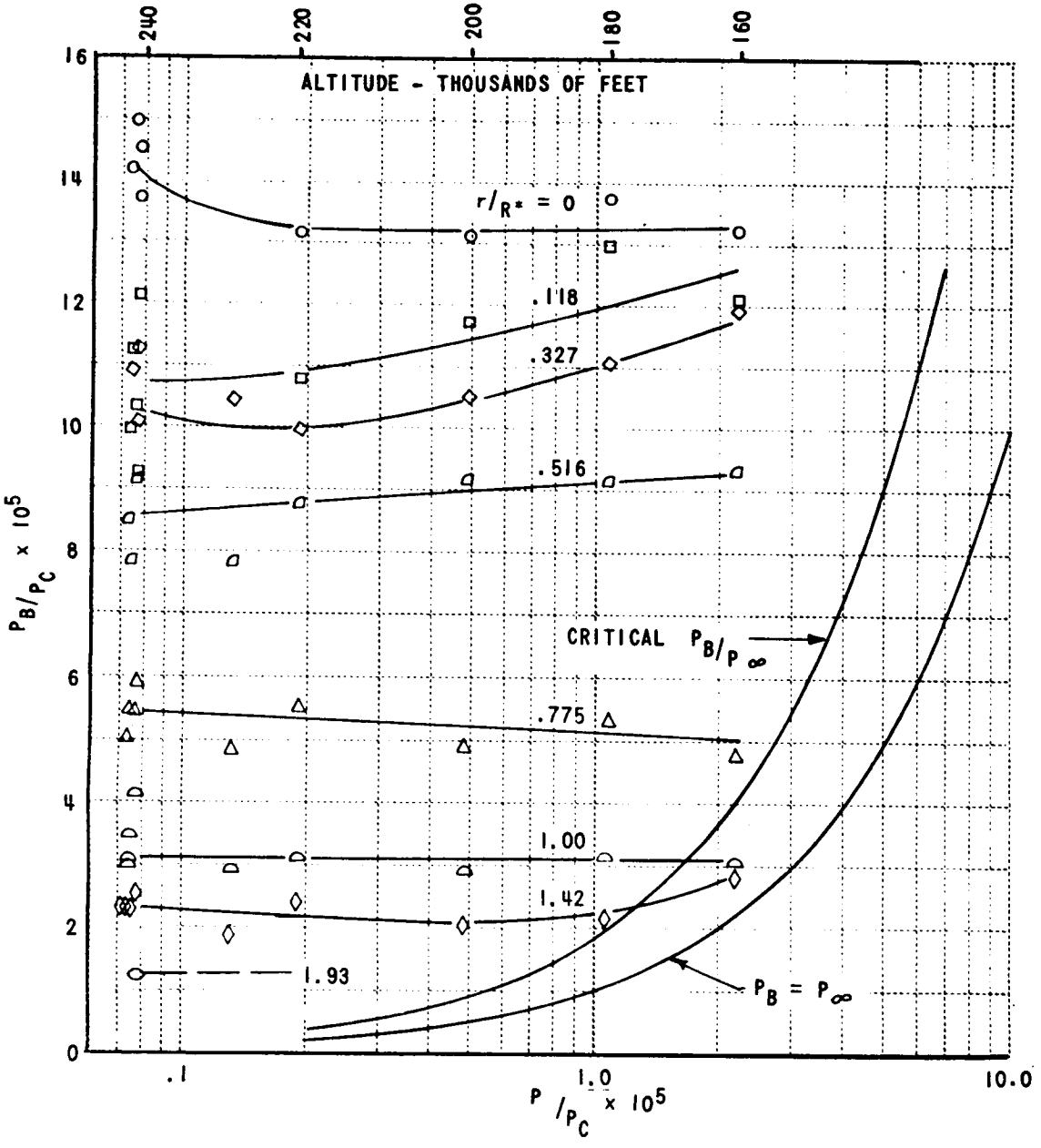

4-ENGINE CONFIGURATION

CONFIGURATION			
d_m/D	j/D	h/D	h_f/D
.5303	.1086	.1086	—

P_C - 632 PSIA NOMINAL

ALT. - VARIABLE

P_∞/P_C - VARIABLE

SYM	POS.	r/R^*
○	40	0
□	41	.118
◇	1	.327
⌐	2	.516
△	3	.775
⌒	4	1.000
◇	5	1.420
⬭	6	1.980

FIGURE 6.4-12. EFFECT OF ALTITUDE ON BASE PRESSURE (4 ENGINE)

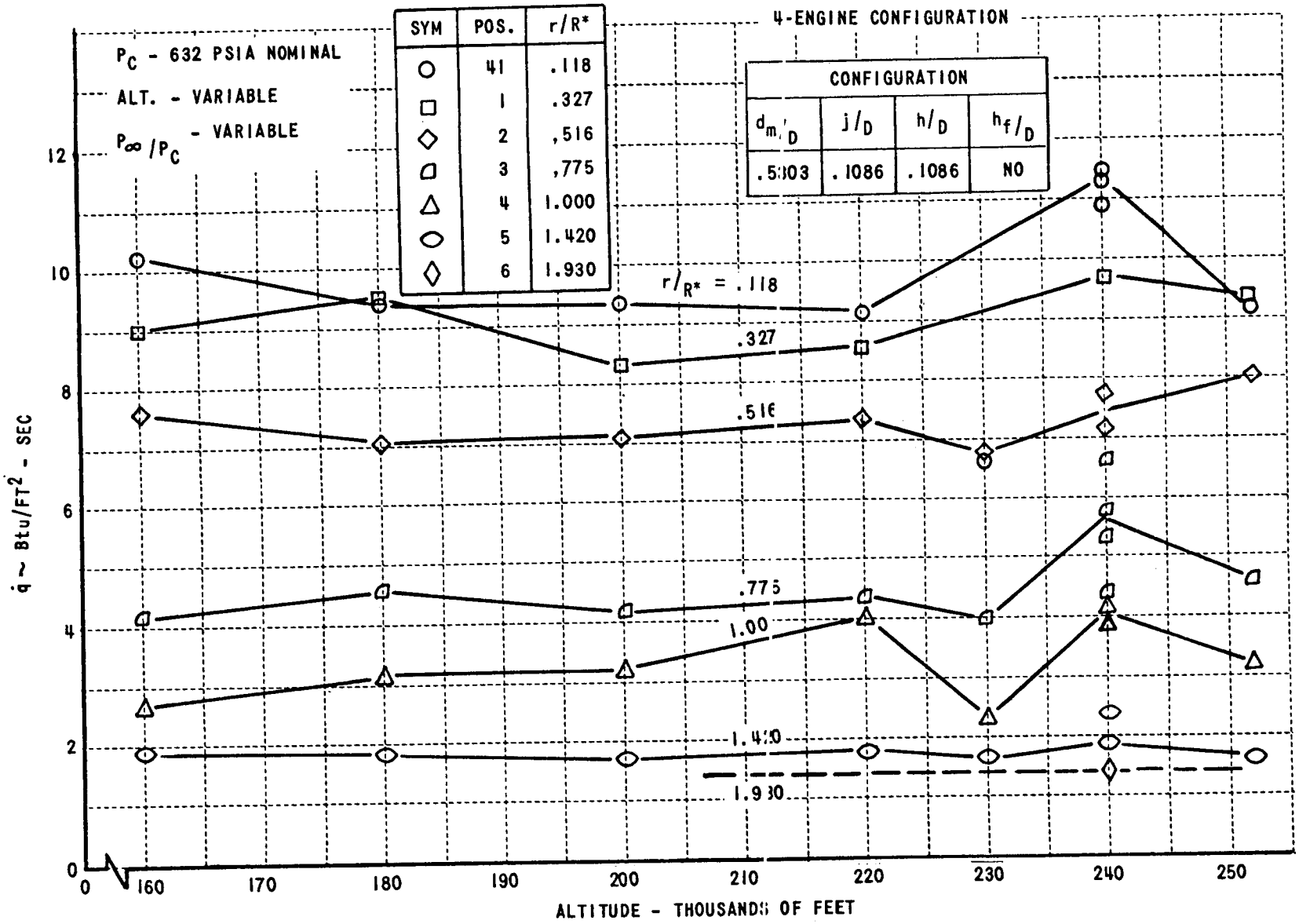

FIGURE 6.4-13. EFFECT OF ALTITUDE ON BASE HEAT TRANSFER (4 ENGINE)

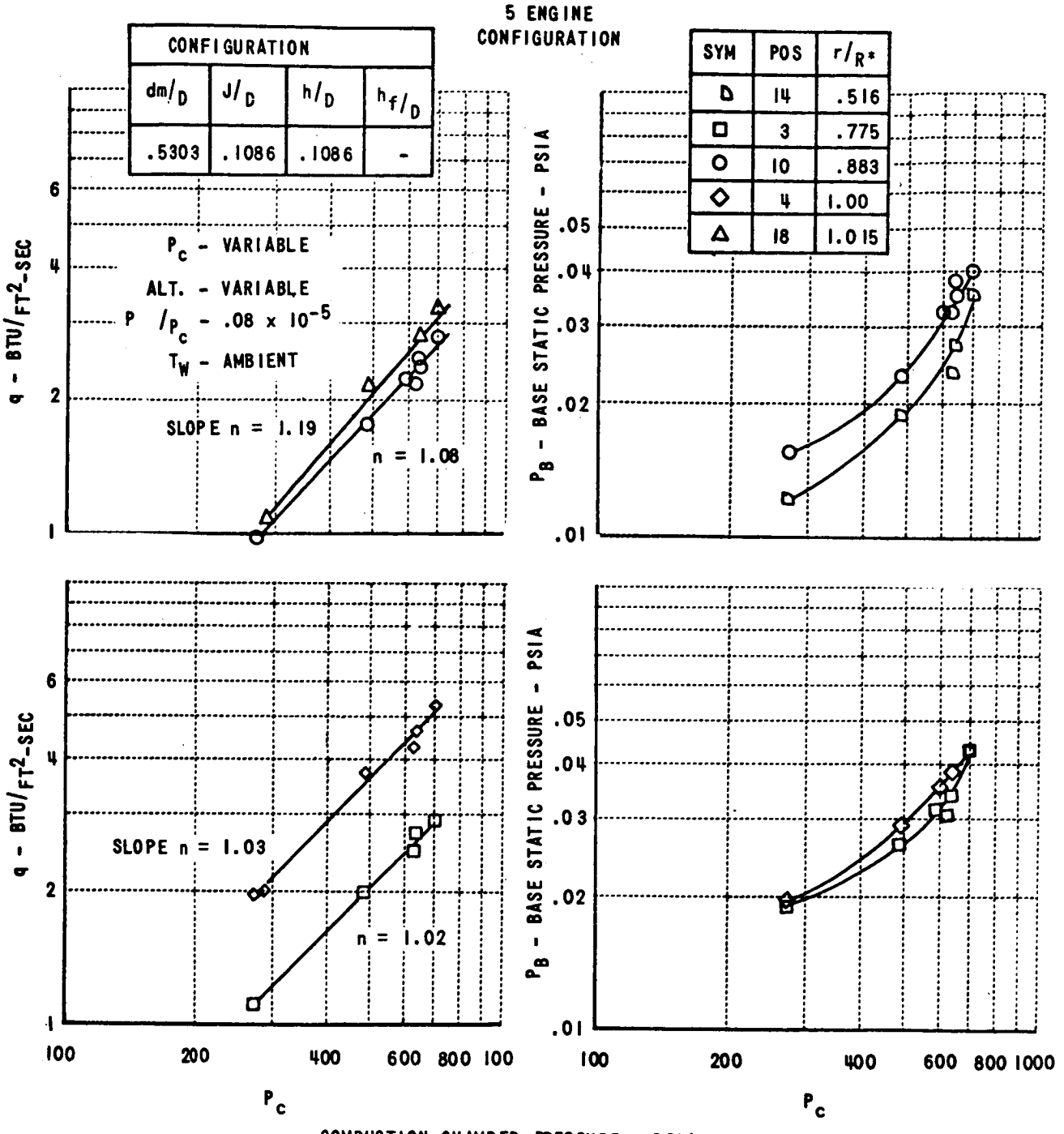

FIGURE 6.4-14. EFFECT OF COMBUSTION CHAMBER PRESSURE ON BASE HEAT TRANSFER AND PRESSURE (5 ENGINE)

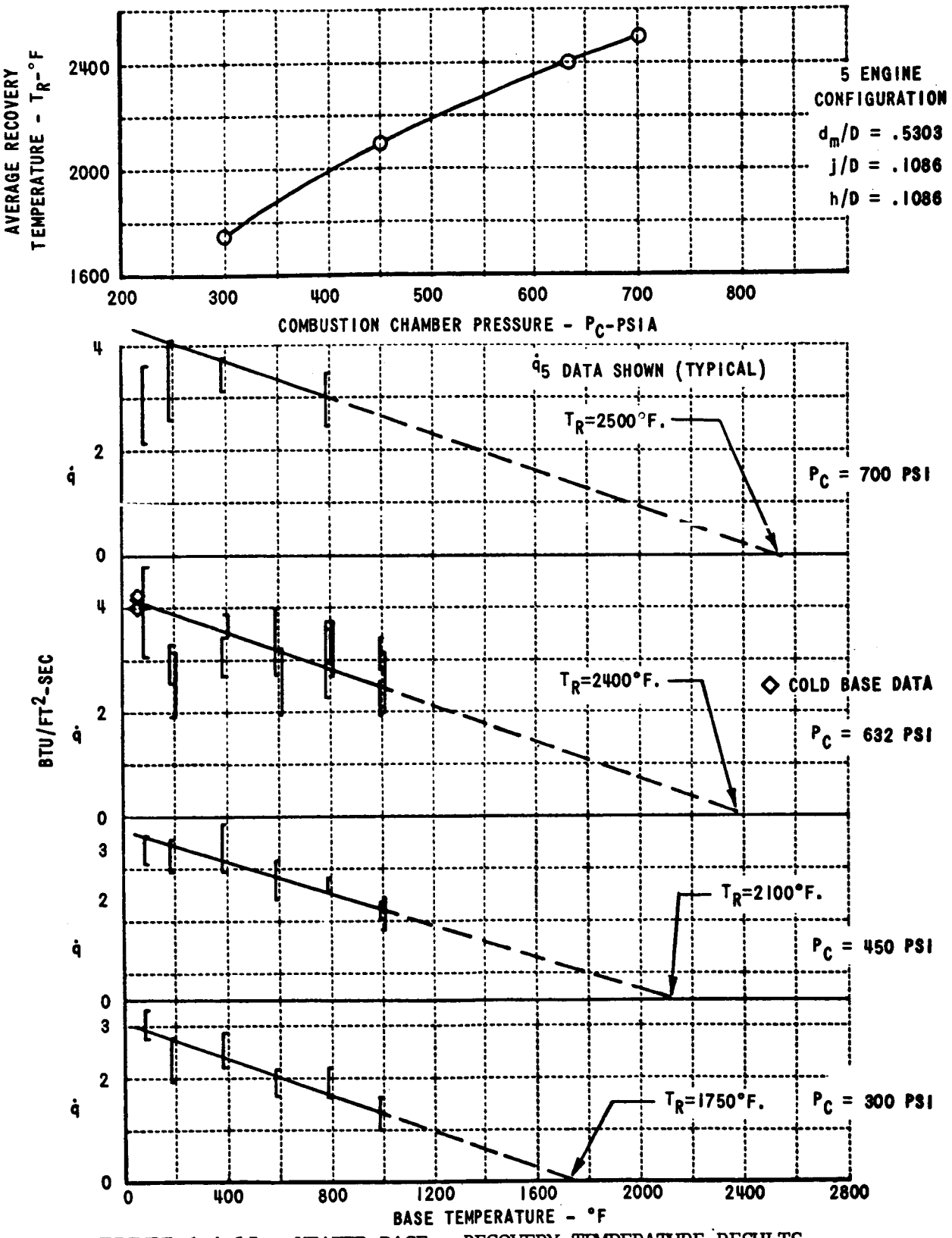

FIGURE 6.4-15. HEATED BASE - RECOVERY TEMPERATURE RESULTS (5 ENGINE)

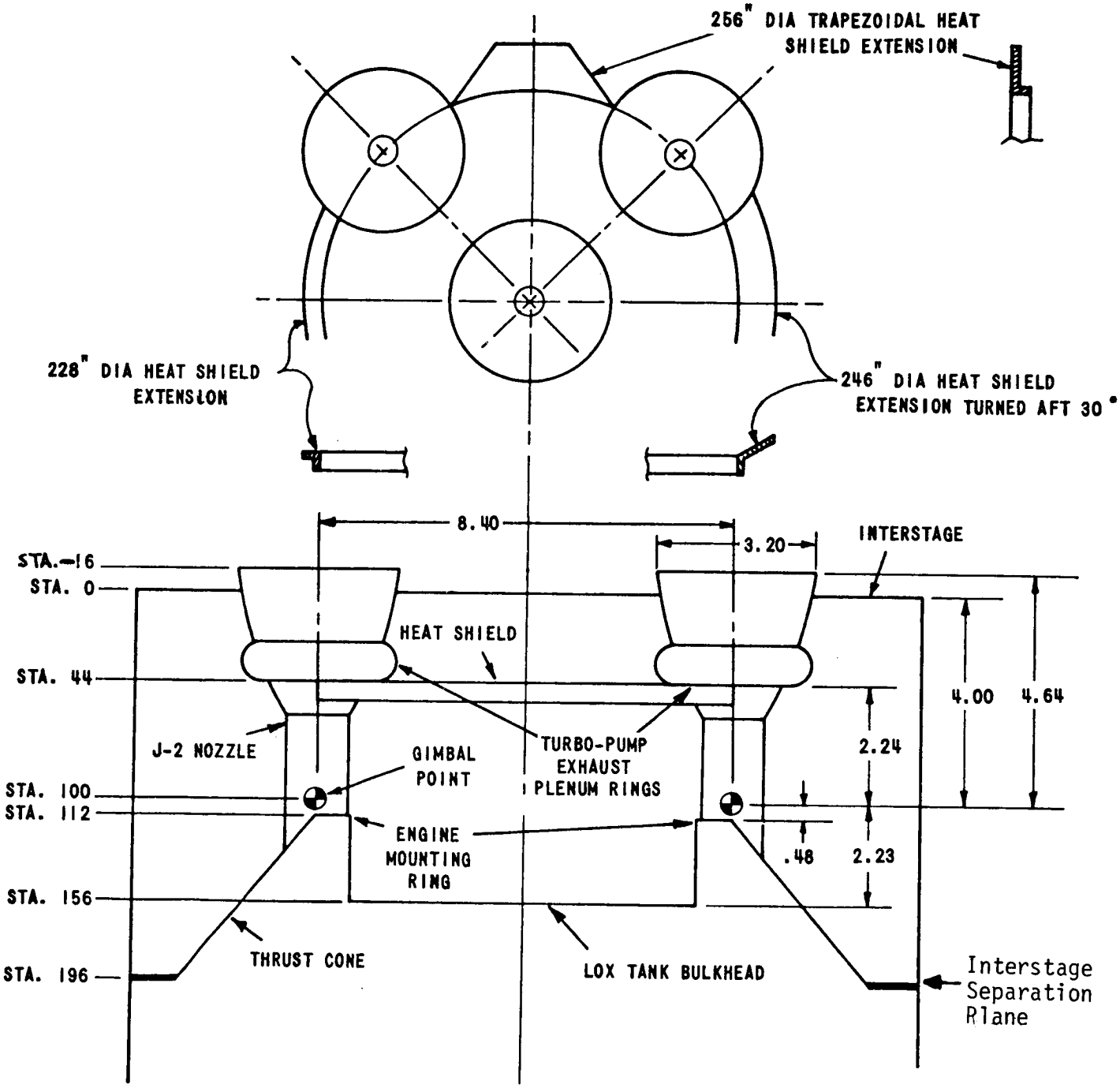

FIGURE 6.4-16. S-II PROTOTYPE MODEL SCHEMATIC

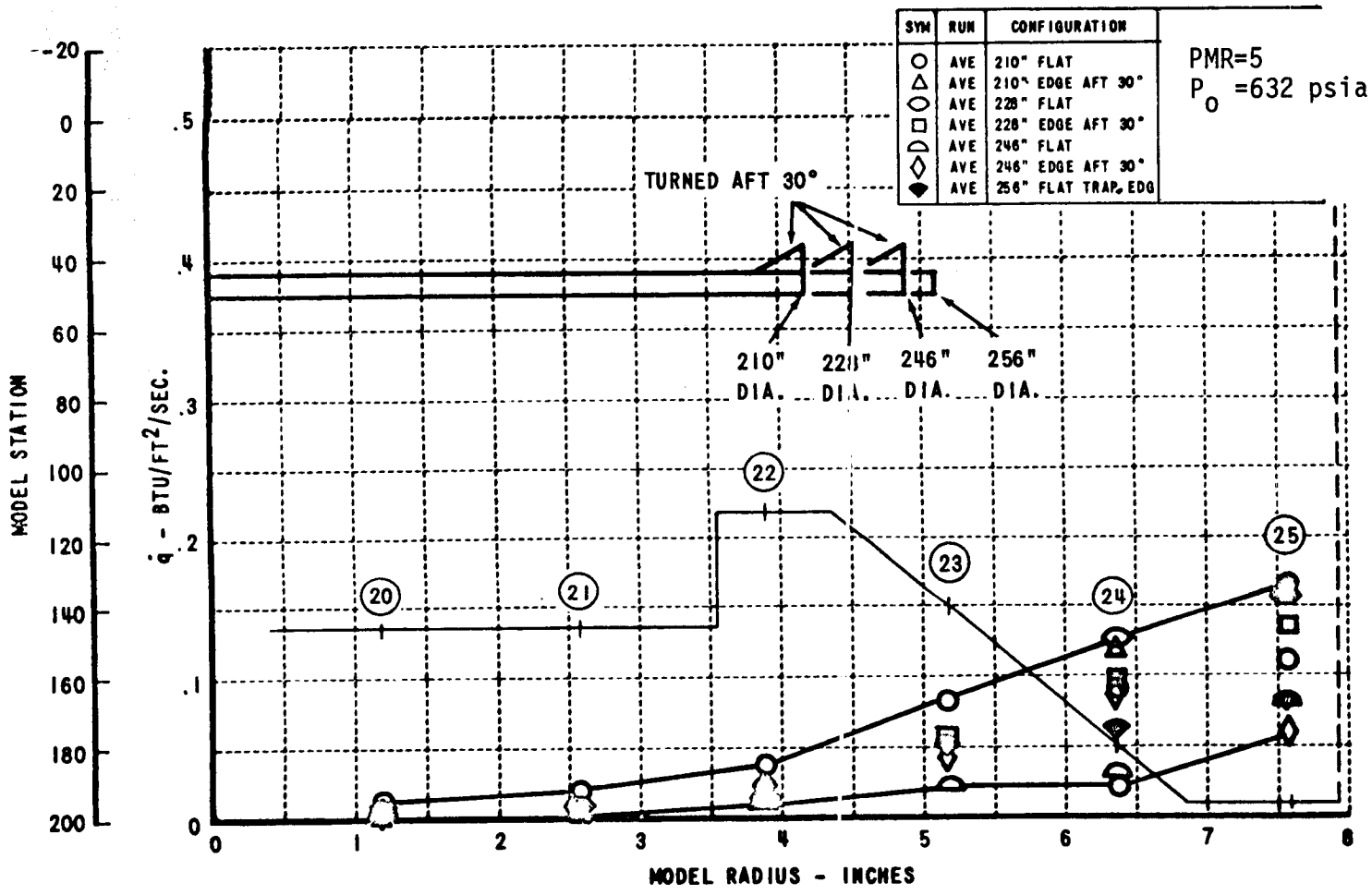

FIGURE 6.4-17. EFFECT OF HEAT SHIELD EDGE CONFIGURATION ON BASE REGION HEAT FLUX

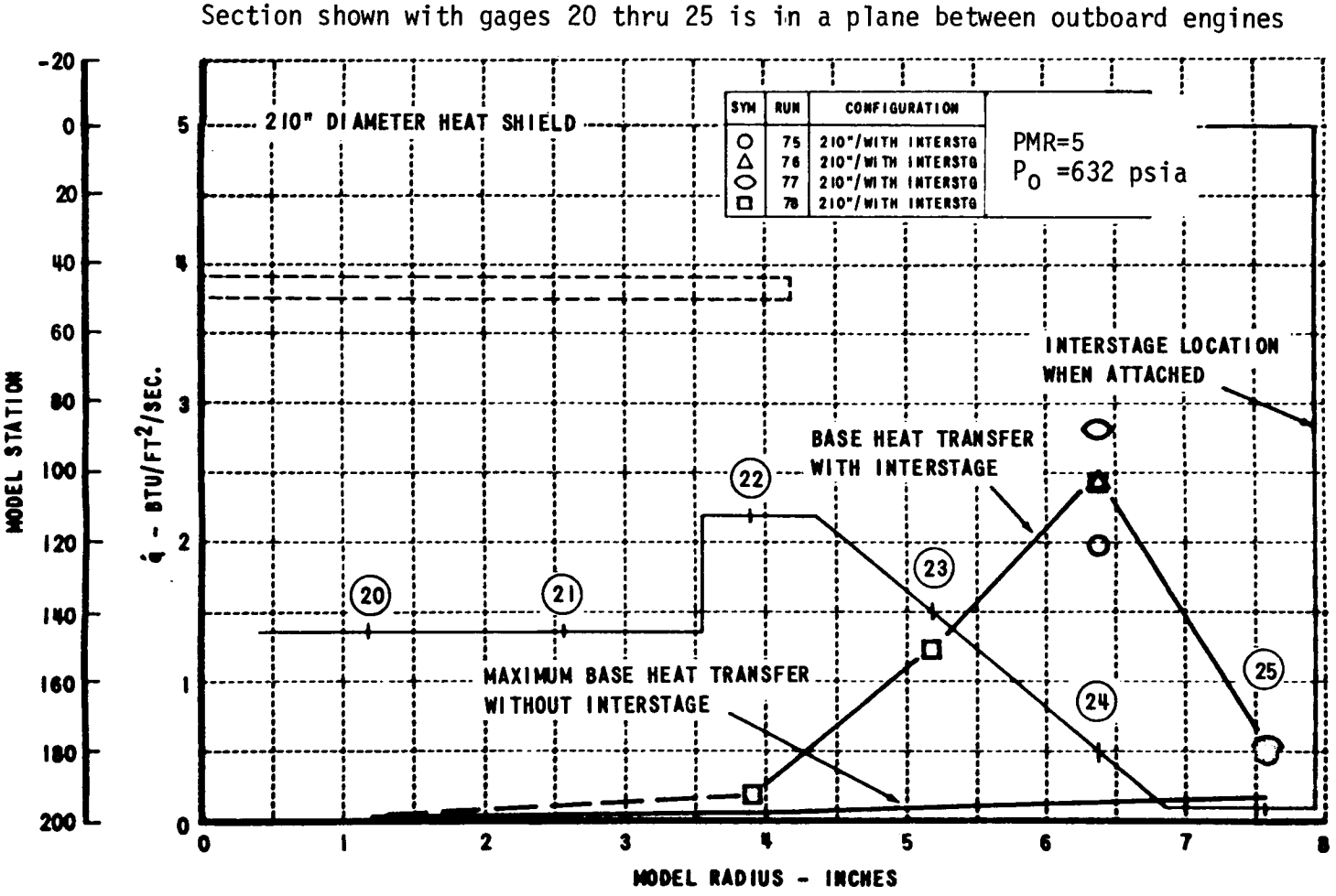

FIGURE 6.4-18. EFFECT OF INTERSTAGE ON BASE HEAT TRANSFER RATES

Section shown with gages 20 thru 25 is in a radial plane between outboard engines.

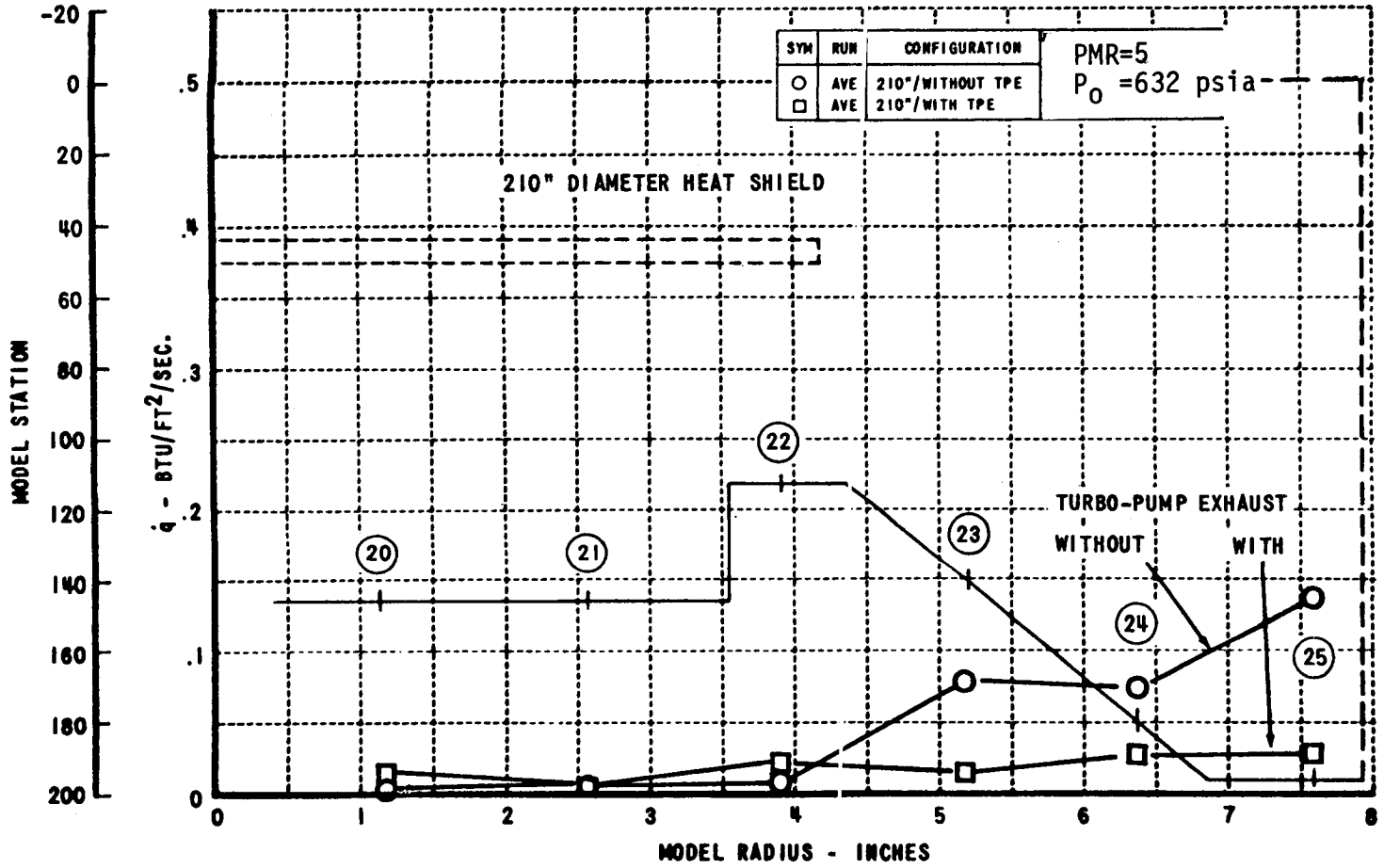

FIGURE 6.4-19. EFFECT OF TURBO-PUMP EXHAUST (TPE) ON BASE REGION HEAT FLUX

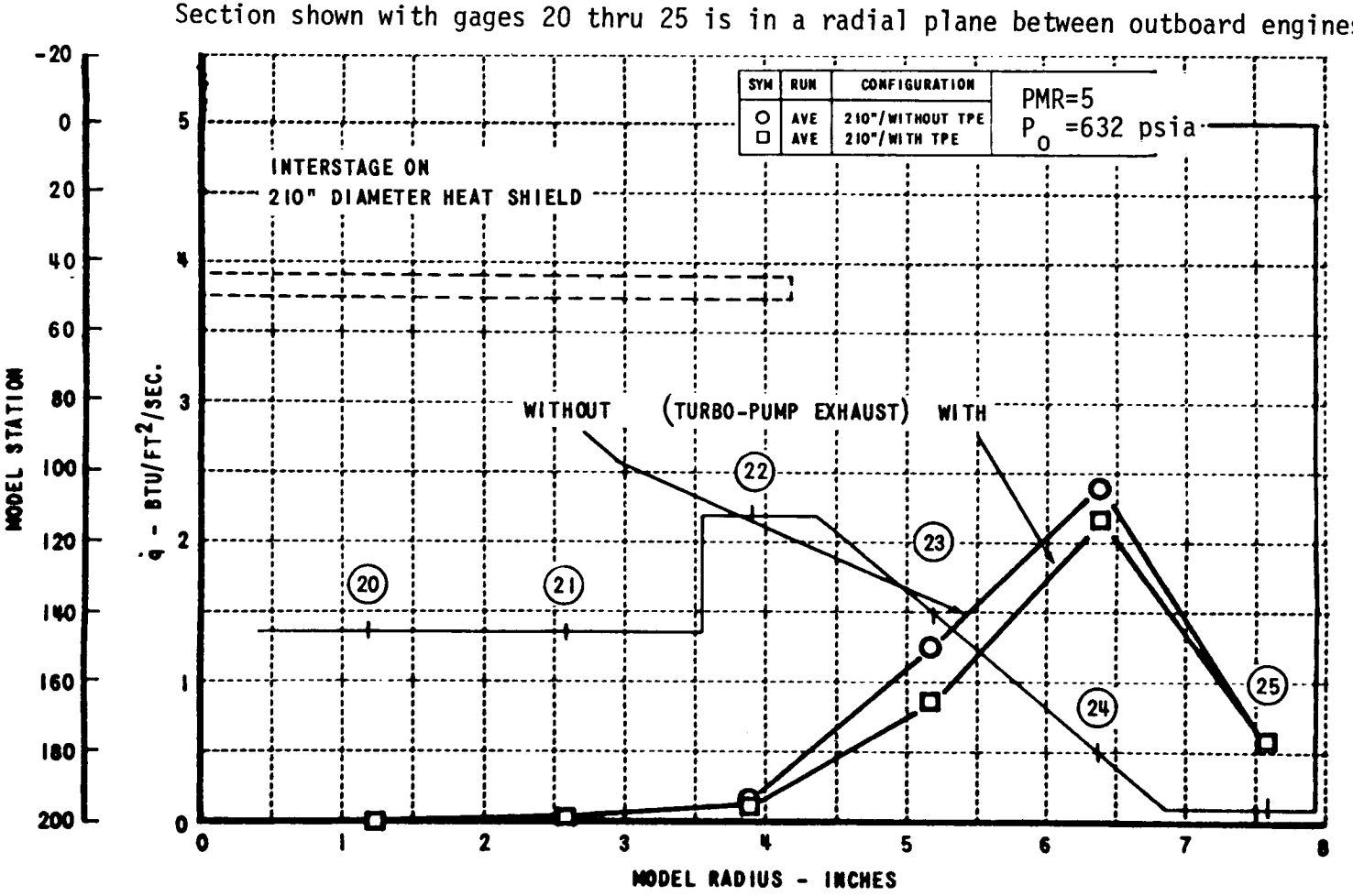

FIGURE 6.4-20. EFFECT OF TURBO-PUMP EXHAUST (TPE) ON BASE REGION HEAT FLUX

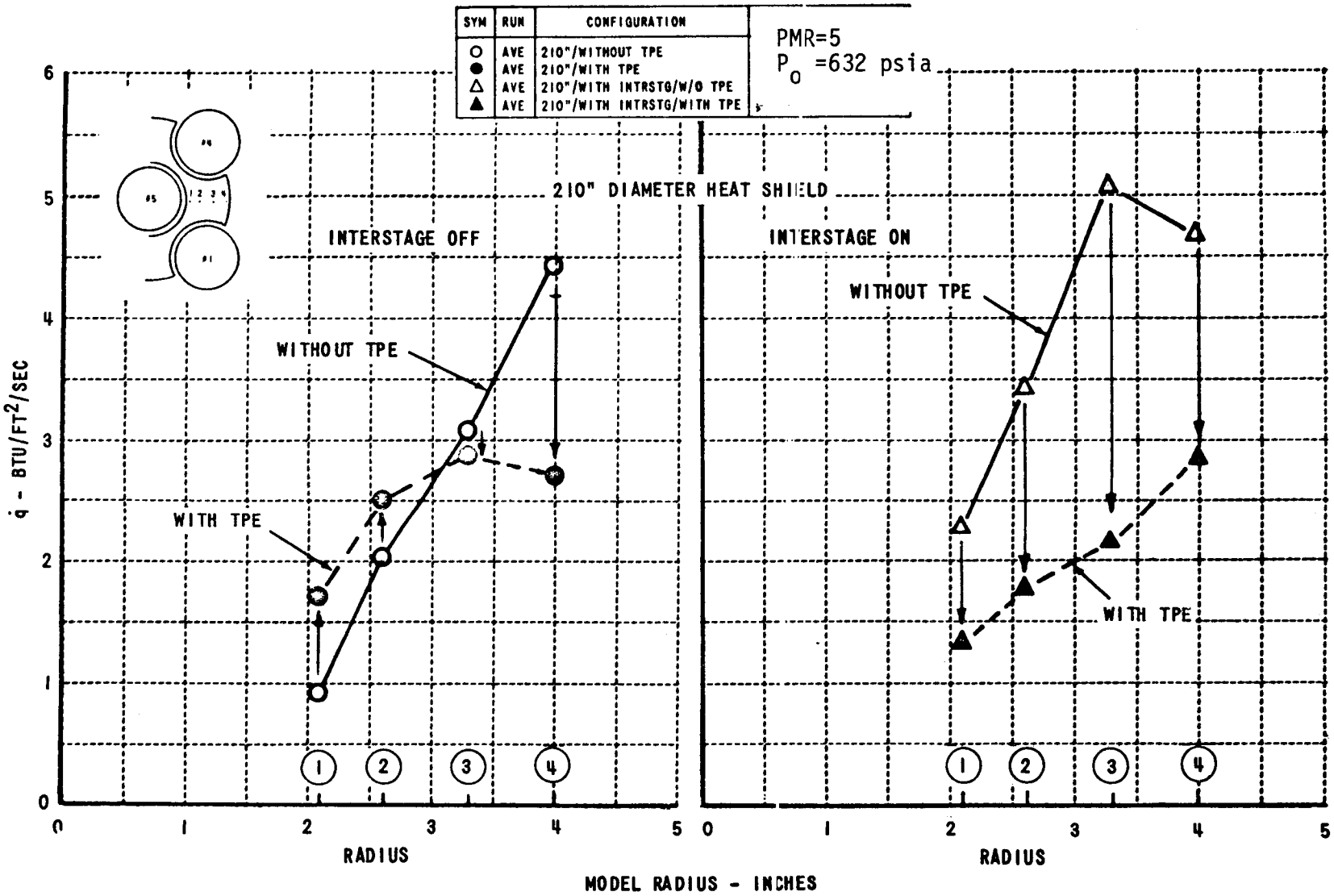

FIGURE 6.4-21. EFFECT OF TURBO-PUMP EXHAUST (TPE) ON HEAT SHIELD HEAT FLUX

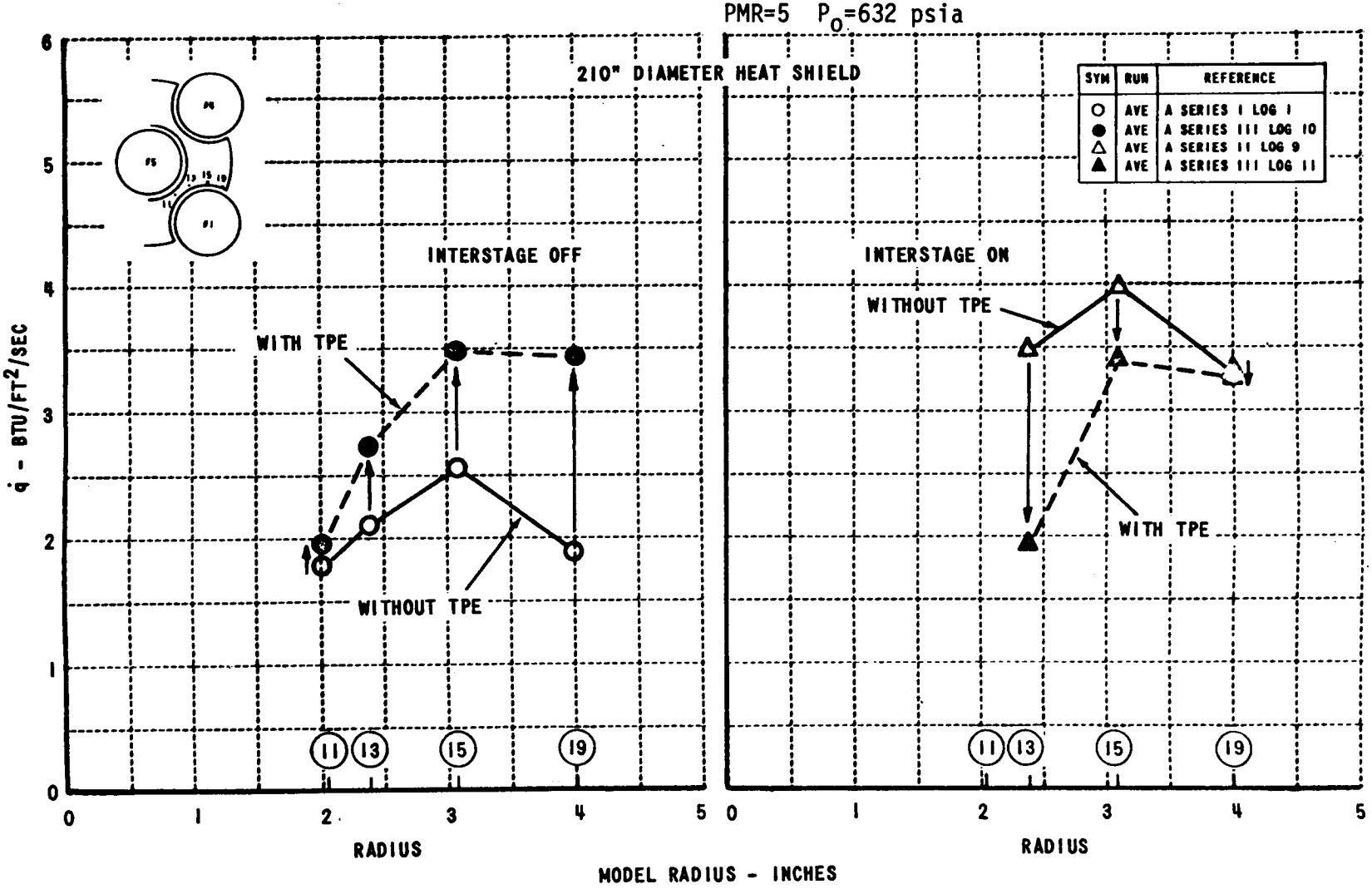

FIGURE 6.4-22. EFFECT OF TURBO-PUMP EXHAUST (TPE) ON HEAT SHIELD HEAT FLUX

Model Engine-Out Deflection Patterns

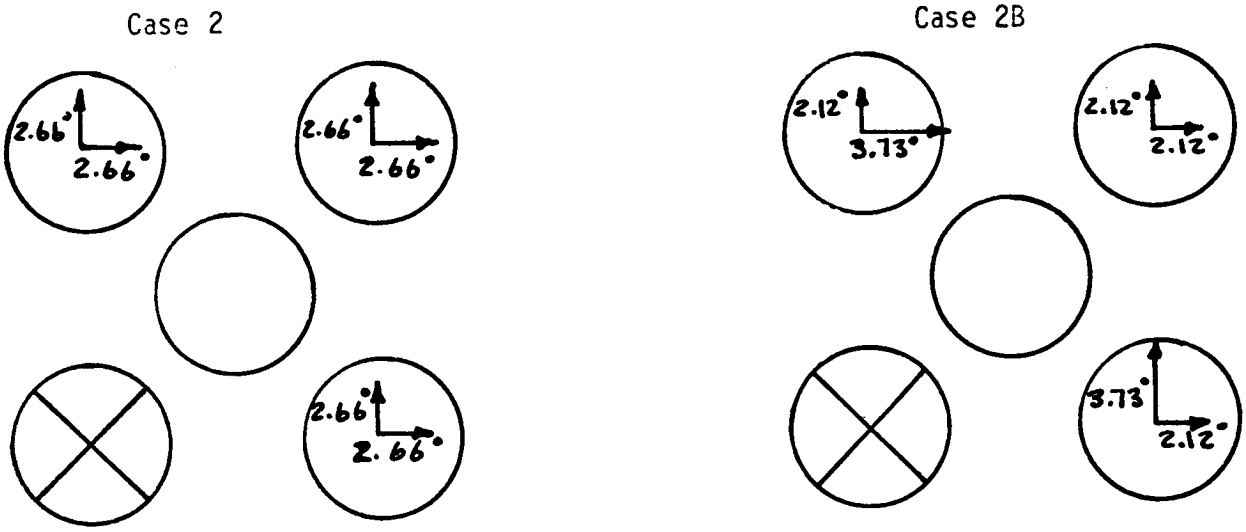

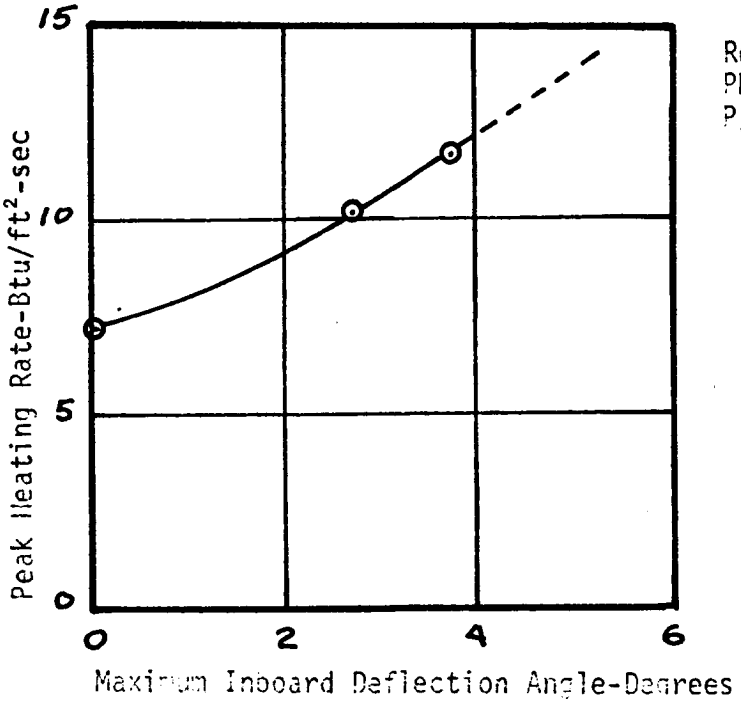

Figure 6.4-23 Effects of outboard engine failure on the maximum heat shield heating rate.

Model Deflection Patterns

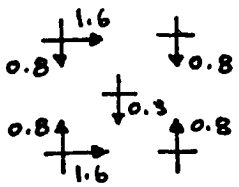

Case 9

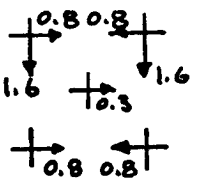

Case 9A

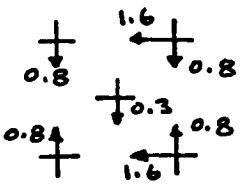

Case 9B

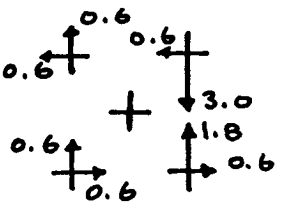

Case 6

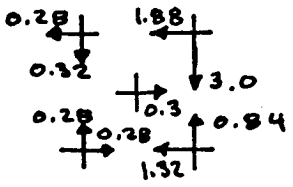

Case 6A

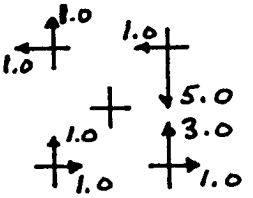

Case 5

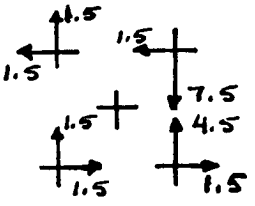

Case 3C

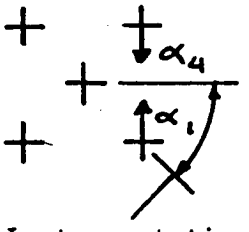

Instrumentation in this octant.

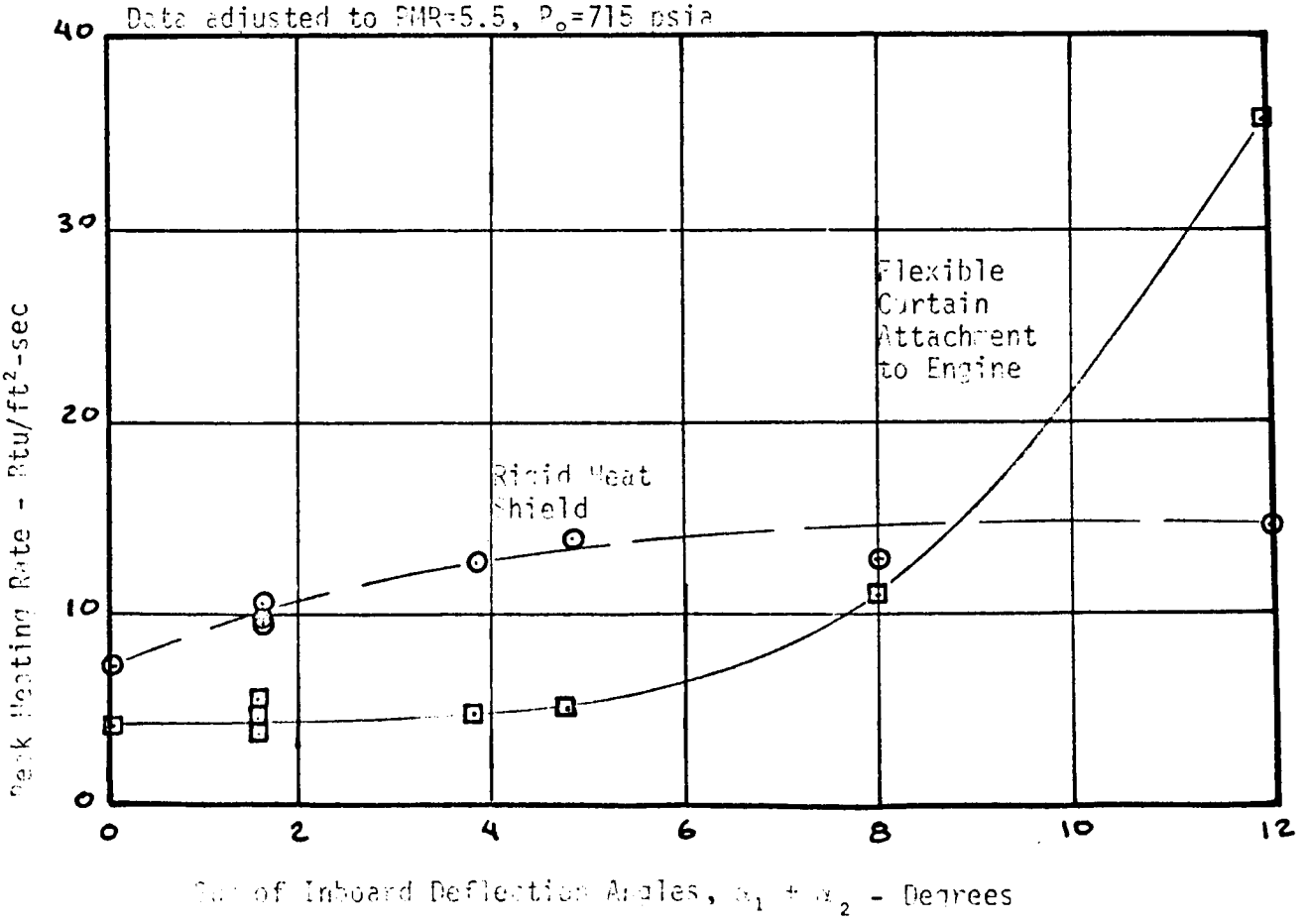

Figure 3.4-24 Effects of single actuator failure inboard on heat shield heating rates.

Model Deflection Patterns

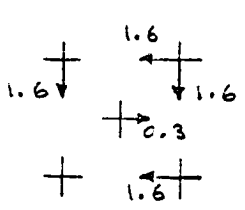

Case 8

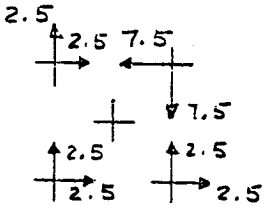

Case 4Aa

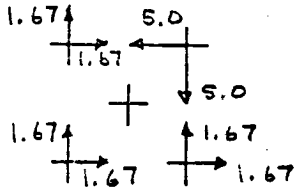

Case 7

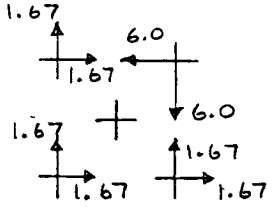

Case 11

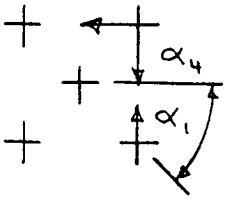

Peak heating in this octant

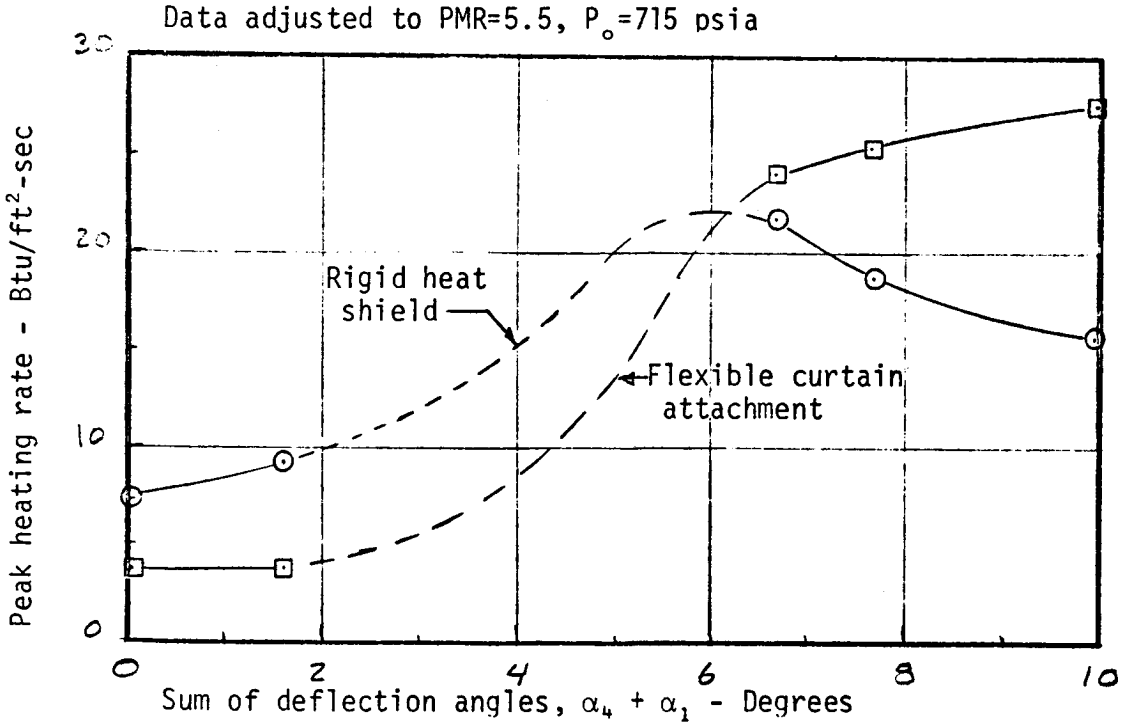

Figure 6.4-25 Effects of dual actuator failure on heat shield heating rates.

Symbol	$\beta_p = \beta_y$
⊙	7.5
◇	6
⊡	5

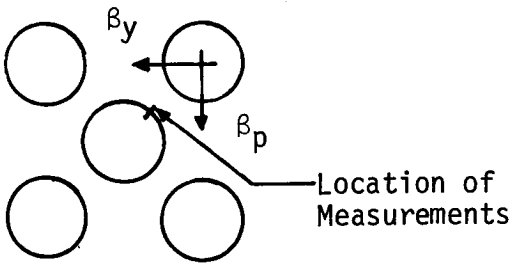

Data adjusted to PMR=5.5, P_o=715 psia

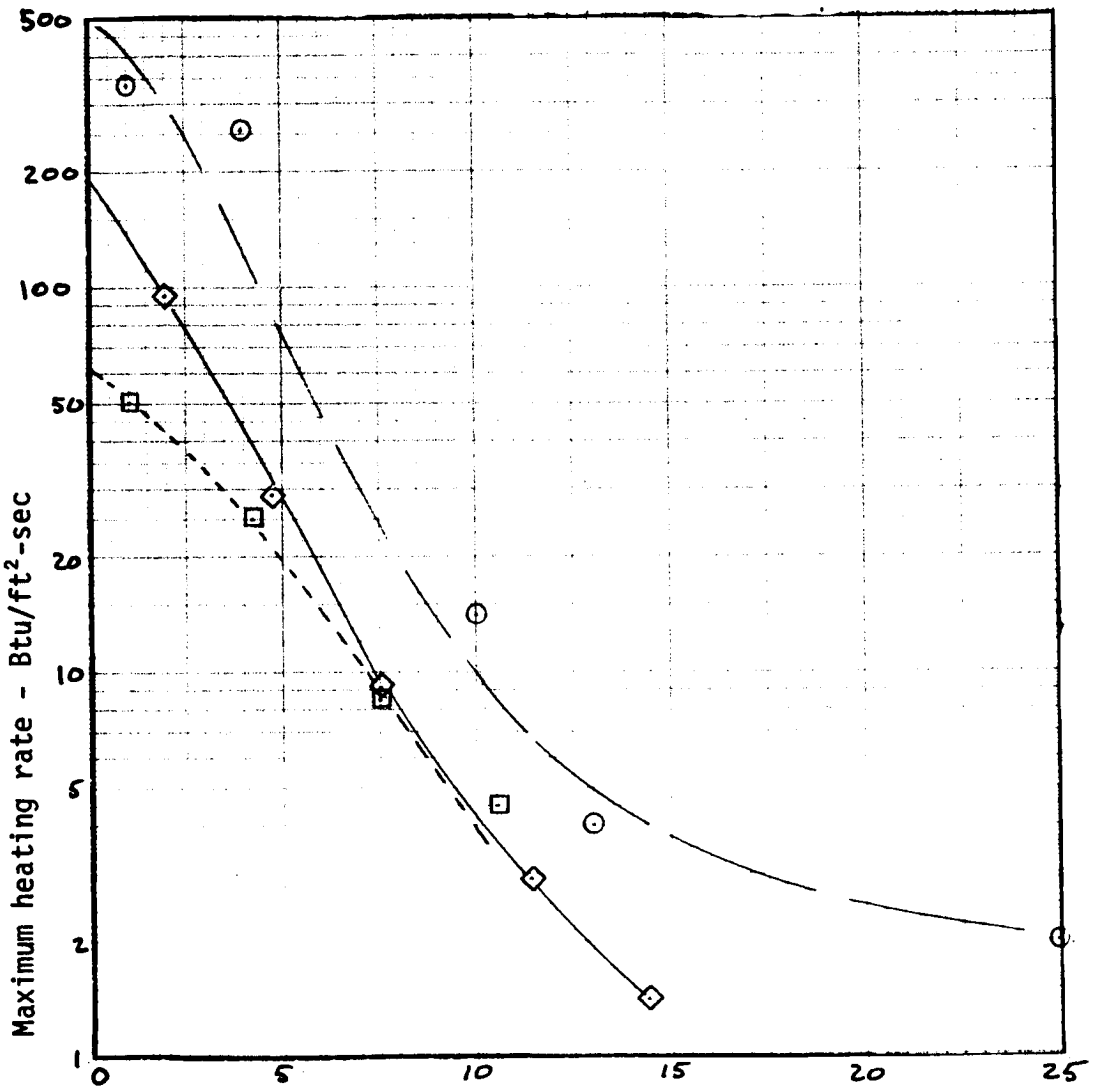

Figure 6.4-26 Effects of dual actuator failure on center nozzle heating.

6.5 FLIGHT TEST AND PARAMETRIC DATA

S-II base environment instrumentation consisted of pressure transducers, total and radiation calorimeters, gas temperature probes, and structural temperature sensors. The first five vehicles (AS-501 through AS-505) had extensive instrumentation, but the instrumentation was very limited on subsequent flights. The quality of the flight data was generally good. The design of the gas temperature probes did not permit a direct gas temperature measurement, but the correction procedures used to estimate gas temperatures from the probe temperature appear to give results which are consistent with other heating measurements.

In presenting the flight results, the pressure, interstage effect, and gas temperature results will be reviewed first, then the radiation and total heating results for the heat shield and thrust structure will be reviewed. The results presented are taken primarily from the first five vehicles, (References 6-6 and 6-7) but experience in later flights is summarized where significant differences have been noted.

Pressure

The pressures on the aft face of the heat shield shown in Figure 6.5-1 are constant to slightly decreasing through most of the flight following the transient caused by interstage separation approximately 30 seconds after ignition. The PMR shift and consequent chamber pressure reduction produce a marked drop in the 450 to 500 second range. On AS-505, the PMR shift was preceded by CECO at about 460 seconds which also caused an appreciable drop.

The interstage separation can cause opposite effects as illustrated on instrument D95 (Figure 6.5-1). On AS-505 there is a pronounced rise which is counter to most interstage separation results, but this effect was also noted on total heating rates on other flights. This apparent anomaly may be caused by changes in the pressure distribution since most evidence points to a general pressure drop in the base region after interstage separation. The drop in pressure after the second separation is most pronounced forward of the heat shield as illustrated in Figure 6.5-2.

Interstage Separation

More detailed records of the base environment during interstage separation are presented in Figure 6.5-3. In these data the separation process is shown to have a pronounced transient effect which is particularly noticeable in the pressure. The slower response of the calorimeters and gas temperature probe tend to attenuate the rapid changes, but the more sensitive radiation calorimeter shows a marked change.

6.5 (Continued)

Gas Temperature

Gas temperature on the aft face of the heat shield is measured with unshielded probes extending approximately 2 inches from the heat shield. The probes have a high heat capacity and emissivity, so a large discrepancy exists between the probe indicated temperature and the gas recovery temperature. To correct the probe indication to the gas recovery temperature, assumptions must be made to evaluate the convective and radiative heat gain and the radiation and conduction heat losses. Since heating rates and recovery temperatures vary in the base region, each probe must be corrected differently. The procedure used in making the corrections is outlined in Reference 6-8, and typical results are shown in Figure 6.5-4.

There is a definite increase in recovery temperature caused by CECO as illustrated on AS-505 (Figure 6.5-4) and a decrease in recovery temperature due to the lower mixture ratio after PMR shift. On AS-507 the engine precant was reduced from 2.3 to 1.3 degrees to bring the engines to a more nearly null position during firing and a definite increase (to 856°K) was noted in the recovery temperature during five-engine operation. On AS-508 it appeared that a steady state engine deflection caused a more severe thermal environment and CECO occurred prematurely at 330 seconds so the flight was longer than nominal. The maximum temperatures recorded on AS-508 were as follows:

Condition	Predicted Recovery Temperature
Before CECO	910°K (1180°F)
After CECO	1045°K (1420°F)
After PMR Shift	940°K (1230°F)

These are the highest temperatures recorded to date.

Heat Shield Heating Rates

Since the incident radiation on the heat shield was expected to be fairly uniform, only two radiation calorimeters were installed on the heat shield for the first five flights. The indicated incident radiation shown in Figure 6.5-5 indicates little variation in the peak heating rates. The radiation calorimeters generally show a gradual response which is particularly apparent in the slow initial rise, and the delay in dropping to an equilibrium value after the PMR shift.

Recent evaluation of this behavior (Reference 6-9) presents convincing evidence that it is caused by gradual heating of the radiometer quartz window by both convection and radiation beyond the window cut-off ($\approx$3.5 μm). Radiation from the heated window is then added to the plume radiation transmitted by the window, so the calorimeter indication changes gradually in response to the window temperature variation. The example analyzed indicated

6.5 (Continued)

that the total plume radiation (both long and short wave length) is 30 to 40 percent less than the calorimeter indication. Due to variations in the correction with instrument location and flight time which have not been computed, it was not practical to correct the flight data to be presented, so the results shown in Figures 6.5-3 and 6.5-5 are indicated values. No analysis has been made of possible errors in the thrust cone radiation presented in Figure 6.5-10.

Variations in radiation are caused by the PMR shift and by engine shutdown on flights AS-502 and AS-505. On AS-502, Engines 2 and 3 shut down at approximately 413 seconds causing a large drop on instrument C665 (adjacent to Engine 2) and a small dip followed by a rise on instrument C692. The rise on C692 must be attributed to deflection of Engines 1 and 4, but it is difficult to interpret due to the response of the radiometer to window heating.

The center engine cut-off on AS-505 causes a definite drop on both radiation instruments followed by a further drop at PMR shift. Due to the rapid response of the calorimeter at this point and the general rise in total heating at CECO, this decrease is attributed to a radiation decrease rather than changes in the window temperature.

Representative total heating rates for AS-501 through AS-505 are presented in Figures 6.5-6 through 6.5-9. These data have not been corrected to cold wall conditions, but the calorimeters remain relatively cool, so the correction would be small. The results indicate much more variation than the radiation. This could be caused by variations in engine performance and alignment which would affect both the overall heating and the distribution of heating rates. The divergence in trends caused by interstage separation noted earlier in the heat shield aft face pressures is also apparent in the total heating rates.

The reduction of heating resulting from the PMR shift is apparent in all total heating rates, but an increase in heating as a result of CECO on AS-505 is not consistently indicated. Although there is no pronounced decrease in total heating due to CECO, some instruments do not show an increase. For example the maximum increase is indicated on C687 (Figure 6.5-8) while C720 (also Figure 6.5-8) in the same area, shows a very slight declining trend. This indicates a definite shift in distribution, but there is no evidence of an increase in peak heating.

Shutdown of Engines 2 and 3 on AS-503 causes both increases and decreases in heating depending upon position. Instruments C721 and C858 are between Engines 2 and 3 so they (Figure 6.5-7) indicate a drastic drop in heating, while instruments C687 and C720 between Engines 1 and 4 indicate an increase in heating (Figure 6.5-8).

6.5 (Continued)

The only total heating calorimeter on AS-506 through AS-509 (C722) indicated somewhat higher heating rates than the maximum of 3 watts/cm^2 noted on AS-503 (Figure 6.5-6). When precant was reduced on AS-507, the C722 heating rate reached a peak of 3 watts/cm^2 compared to approximately 2.7 watts/cm^2 on flights AS-504 and AS-505 which had a similar thrust structure and the higher precant (precant was increased to 2.3 degrees with the new thrust structure on AS-504 and was reduced to 1.3 degrees on AS-507). On AS-509, C722 indicated a peak of 3.22 watts/cm^2 after the premature CECO.

The heating rate on the forward face of the heat shield was measured on AS-504 and AS-505 (Calorimeter C723, Figure 6.5-9). The results indicated the expected significant effect of the interstage skirt, but a large increase was also noted after interstage separation on AS-504. It is suspected that this peak was caused by leakage at the flexible curtain around Engine 4 because of improper lacing of the curtain to the heat shield. This would allow leakage which could be modulated by small engine gimbal movements.

Thrust Cone Heating Rates

The thrust cone total and radiation heating rates are presented in Figure 6.5-10. They indicate significant convective heating with the interstage in place, particularly near the middle of the thrust cone (C666 and C821). After interstage separation the total heating rates are so low that it is difficult to evaluate the relative effects of convective and radiant heating. The results indicate a reduction in heating at the PMR shift and a transient increase on C688 for AS-502. This increase was associated with hot gas leakage forward of the heat shield from the failure of Engine 2.

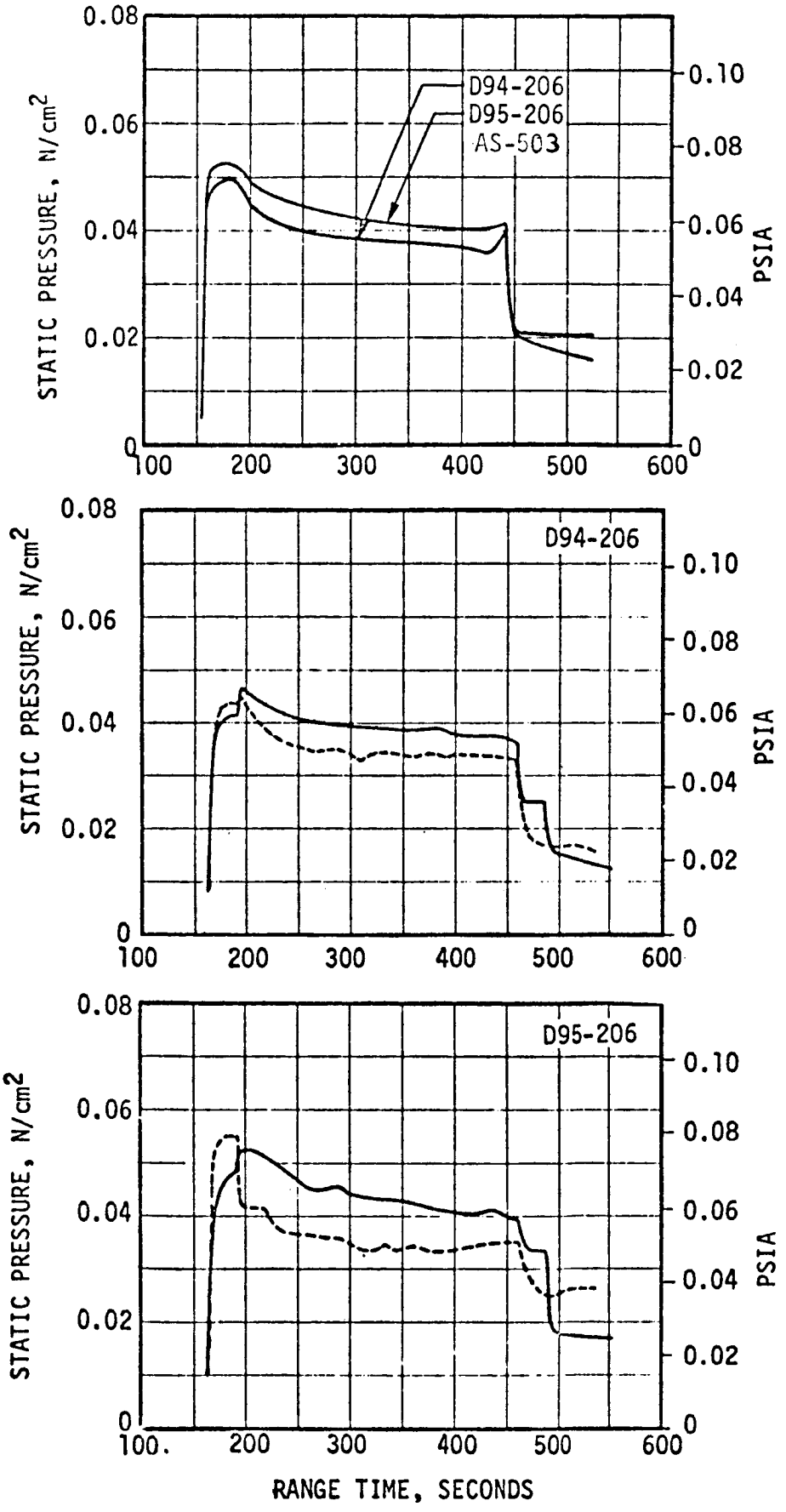

Inst.	Radius Inches	Angle Degrees
D95	85	270
D94	85	90

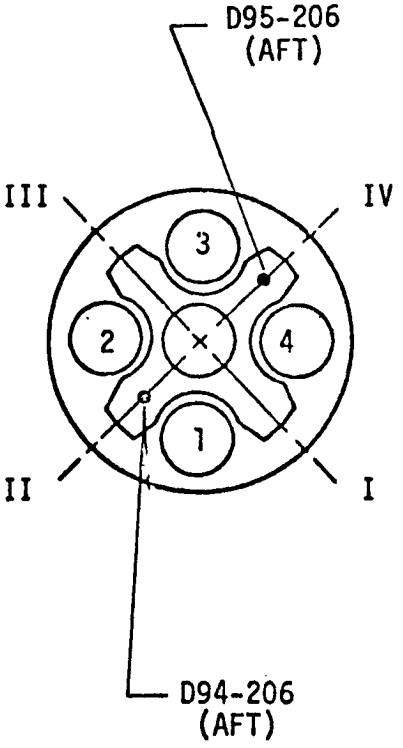

FLIGHT DATA

-----AS-504

——AS-505

FIGURE 6.5-1 STATIC PRESSURES ON THE HEAT SHIELD AFT FACE.

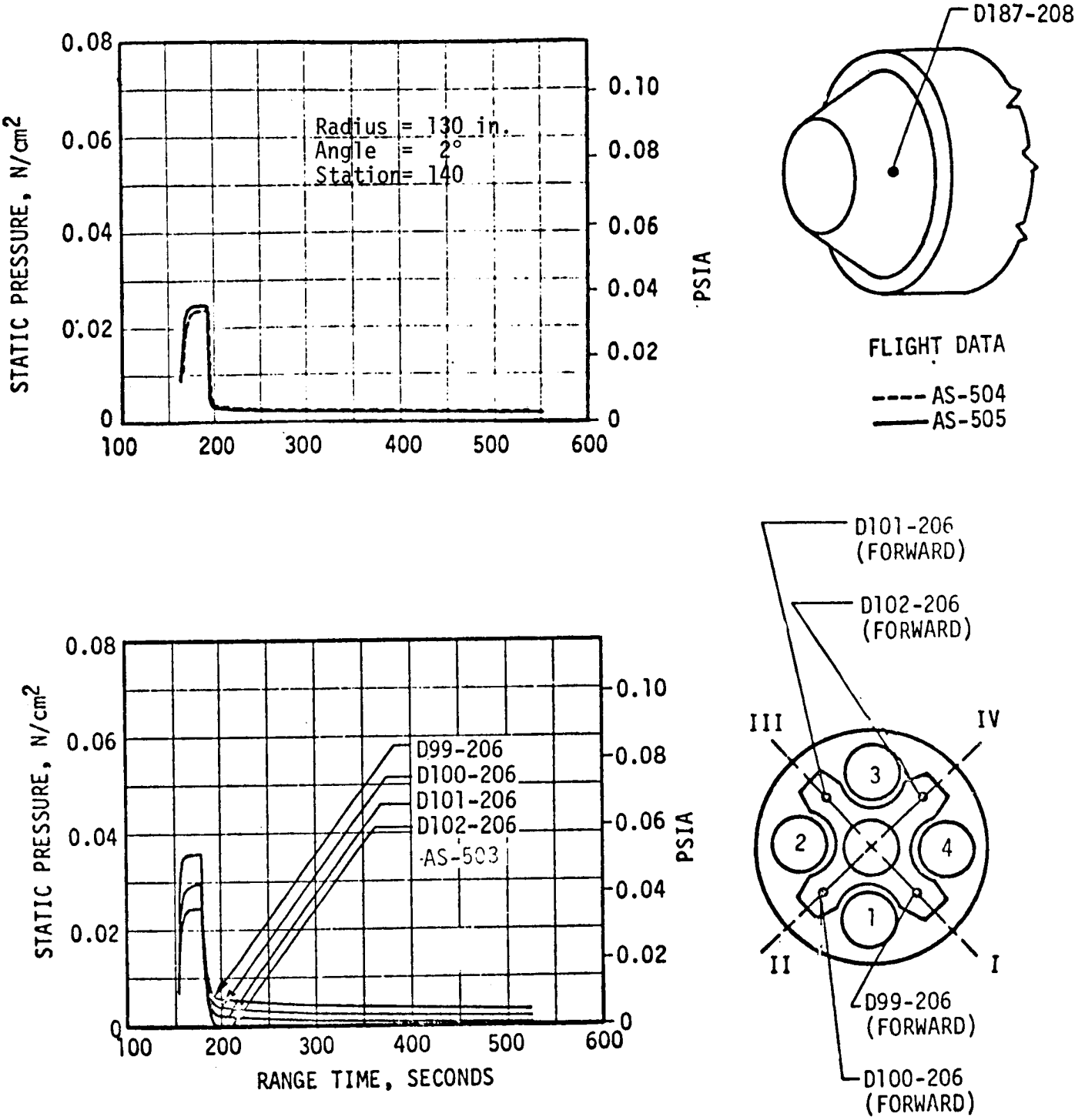

R = 85 inches on D99 thru D102

FIGURE 6.5-2 STATIC PRESSURES FORWARD OF THE HEAT SHIELD.

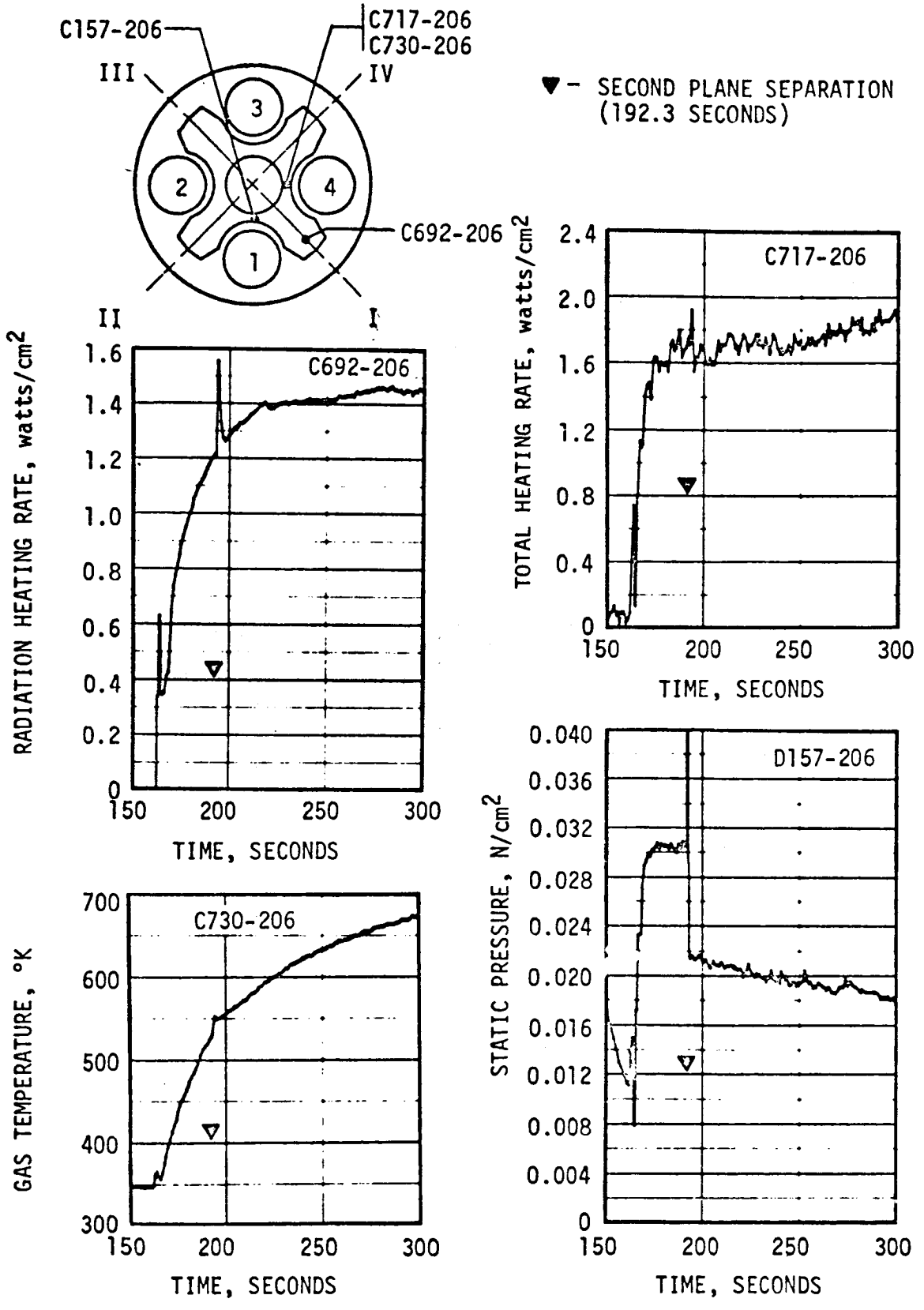

FIGURE 6.5-3 TYPICAL BASE REGION ENVIRONMENT DURING INTERSTAGE SEPARATION (AS-505)

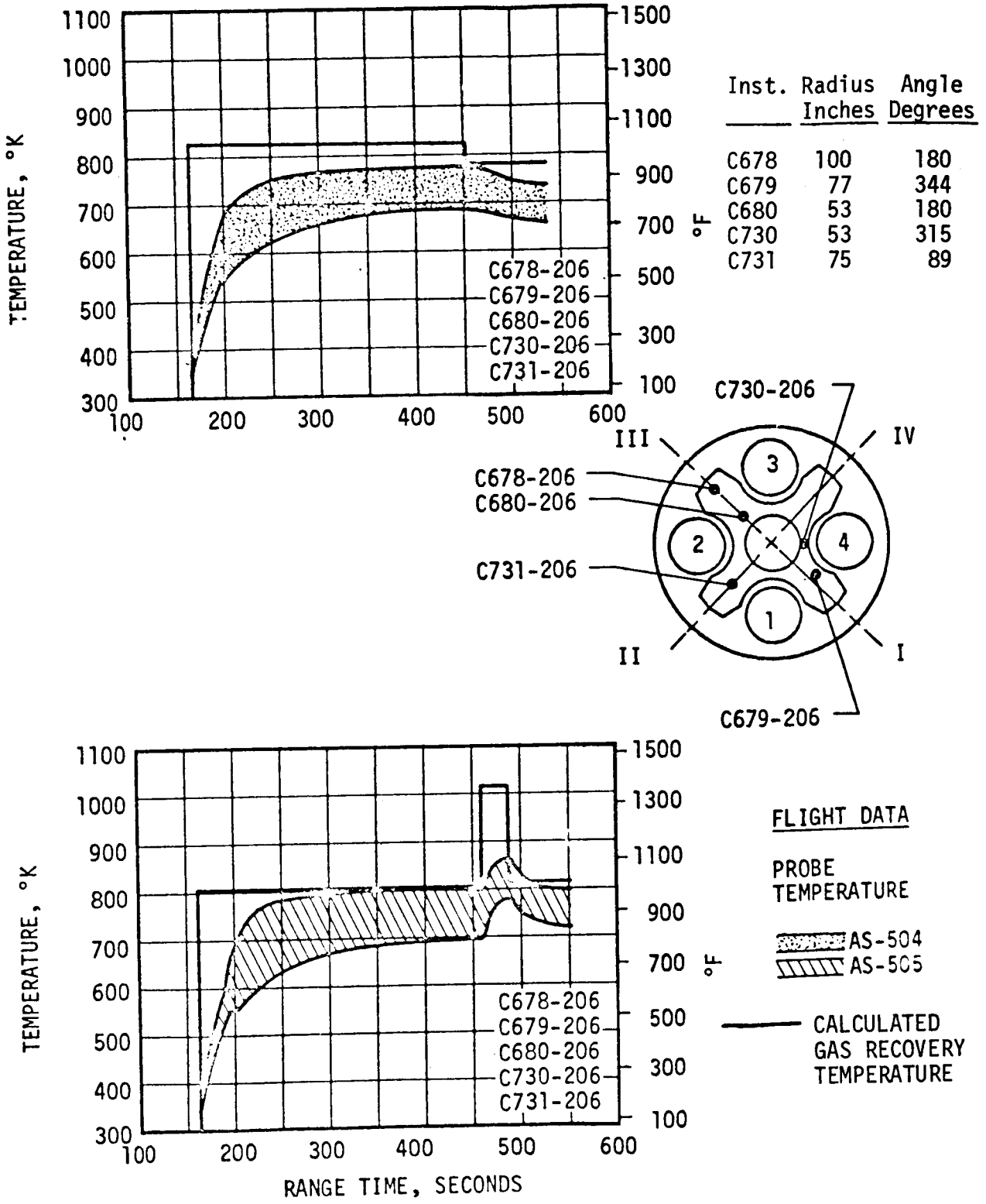

FIGURE 6.5-4 TYPICAL HEAT SHIELD GAS RECOVERY TEMPERATURES ON AS-504 and AS-505.

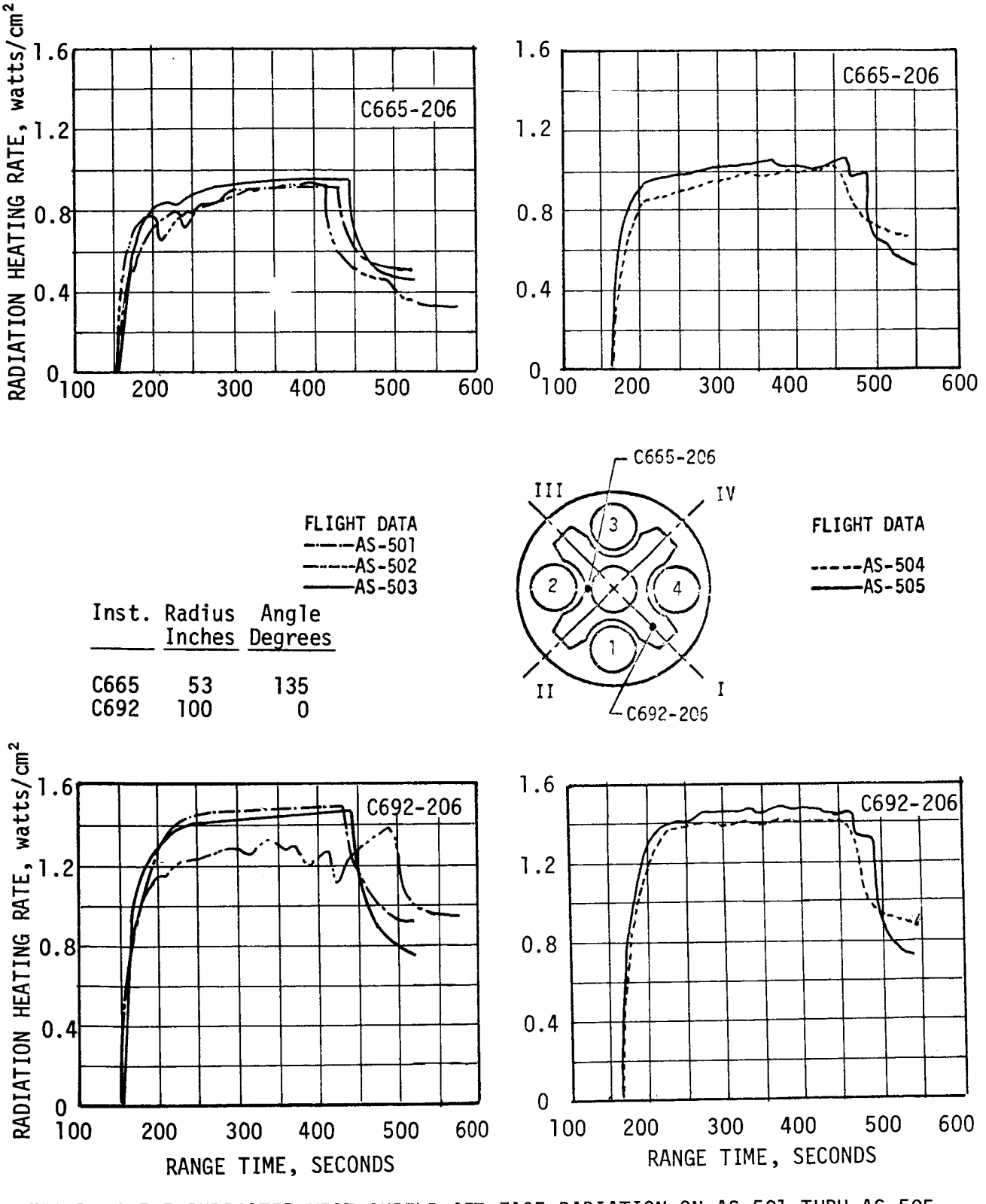

FIGURE 6.5-5 INDICATED HEAT SHIELD AFT FACE RADIATION ON AS-501 THRU AS-505.

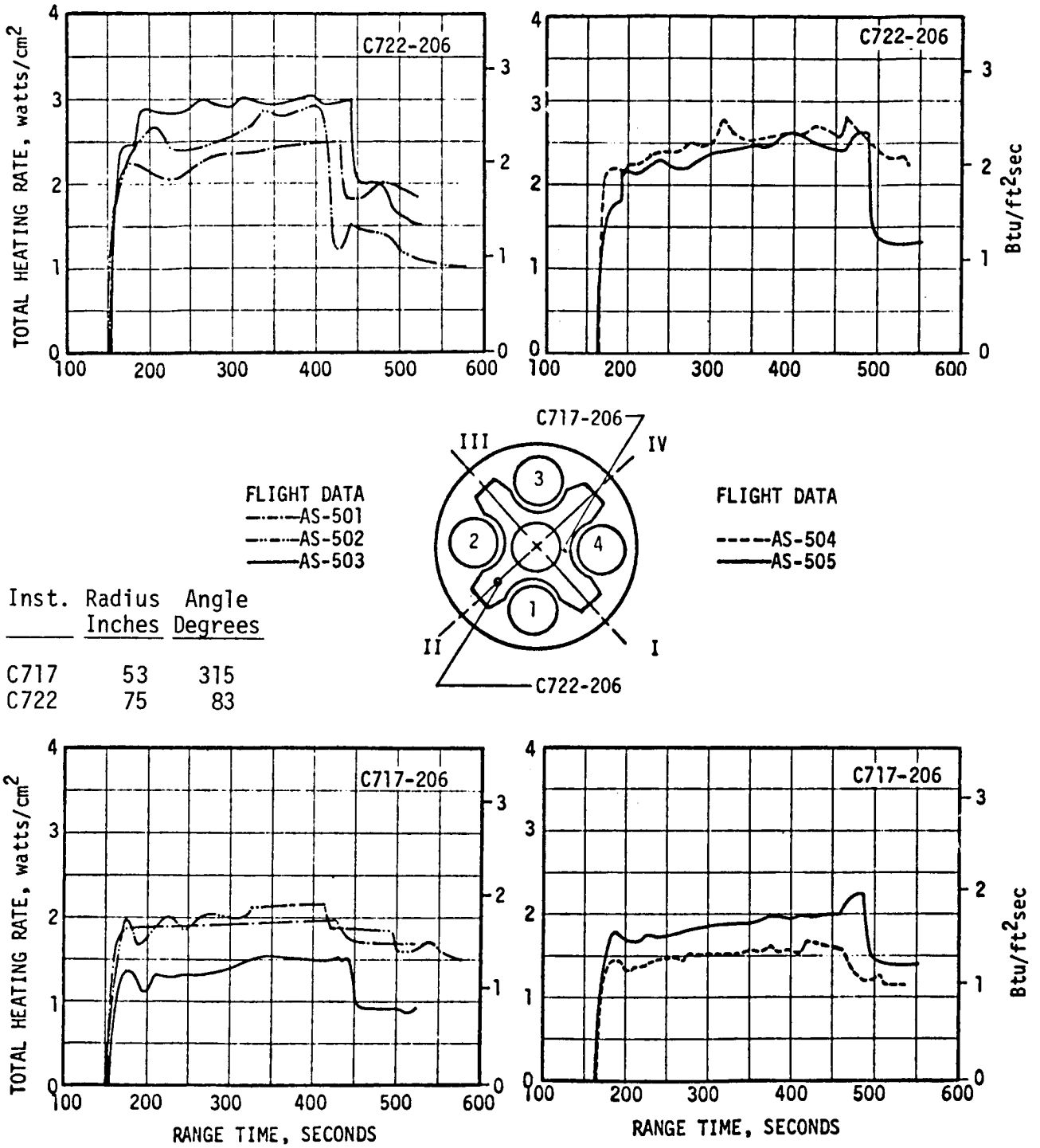

Inst.	Radius Inches	Angle Degrees
C717	53	315
C722	75	83

FIGURE 6.5-6 HEAT SHIELD AFT FACE TOTAL HEATING RATES ON AS-501 thru AS-505.

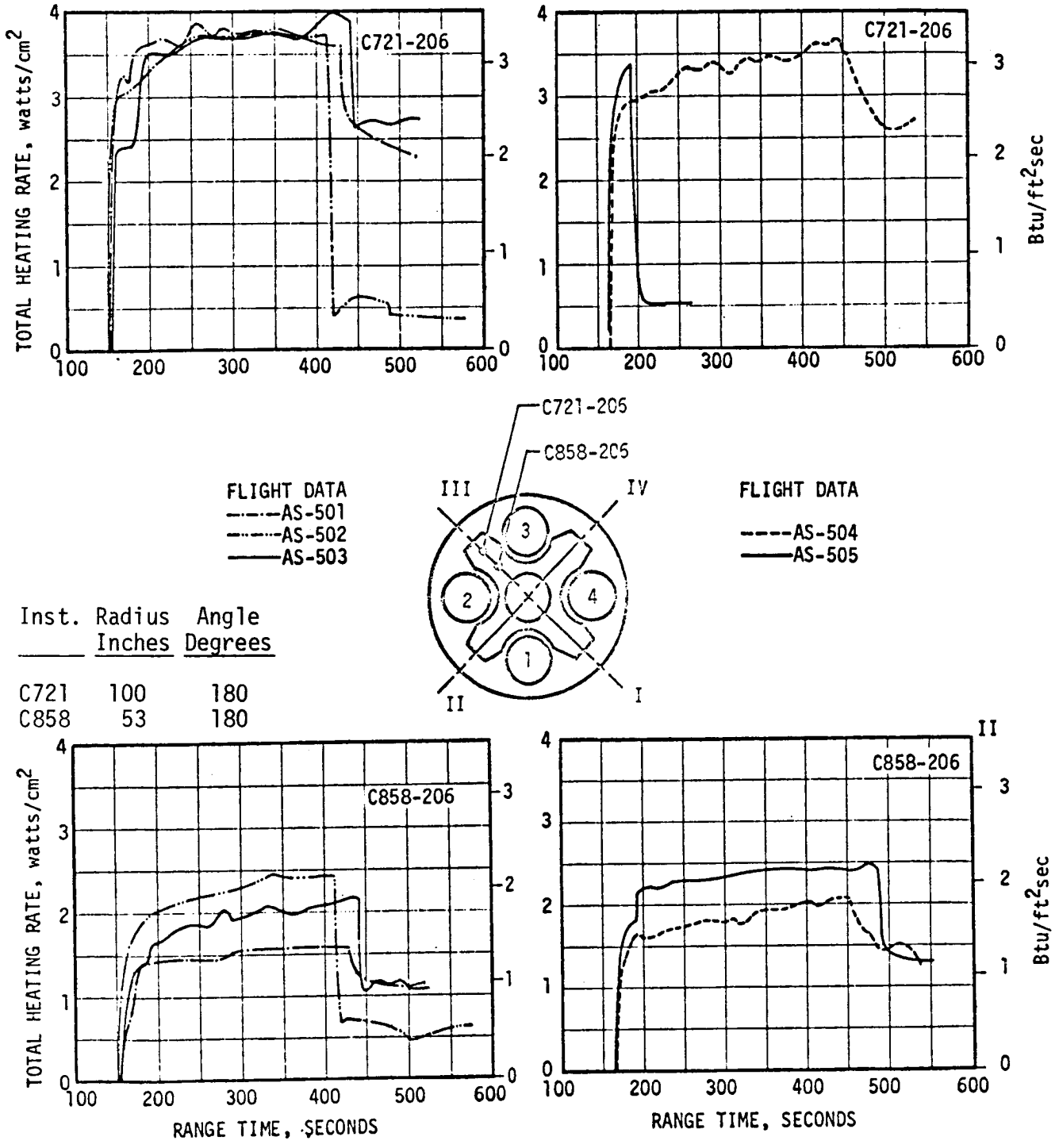

FIGURE 6.5-7 HEAT SHIELD AFT FACE TOTAL HEATING RATES ON AS-501 thru AS-505.

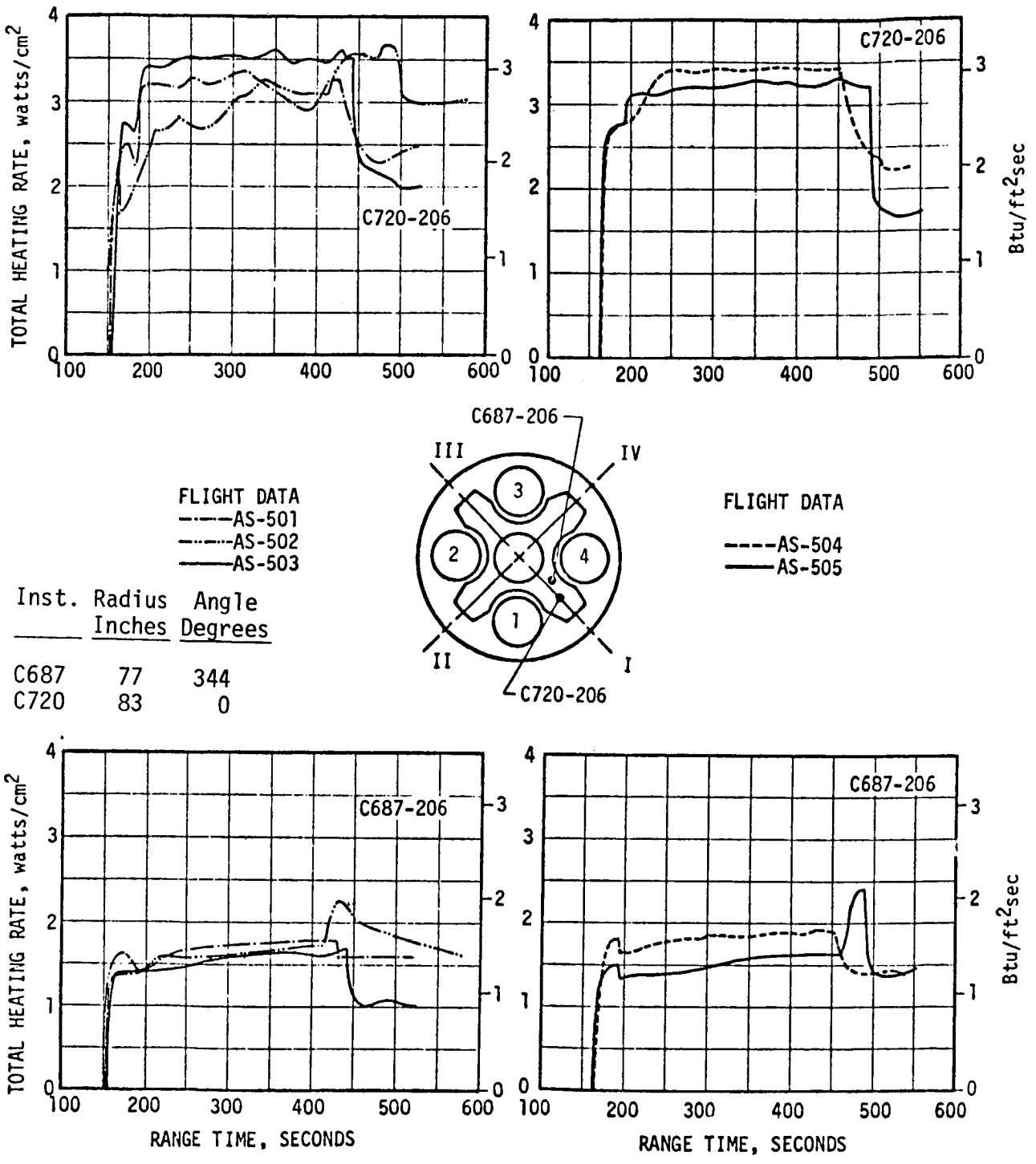

FIGURE 6.5-8 HEAT SHIELD AFT FACE TOTAL HEATING RATES ON AS-501 thru AS-505.

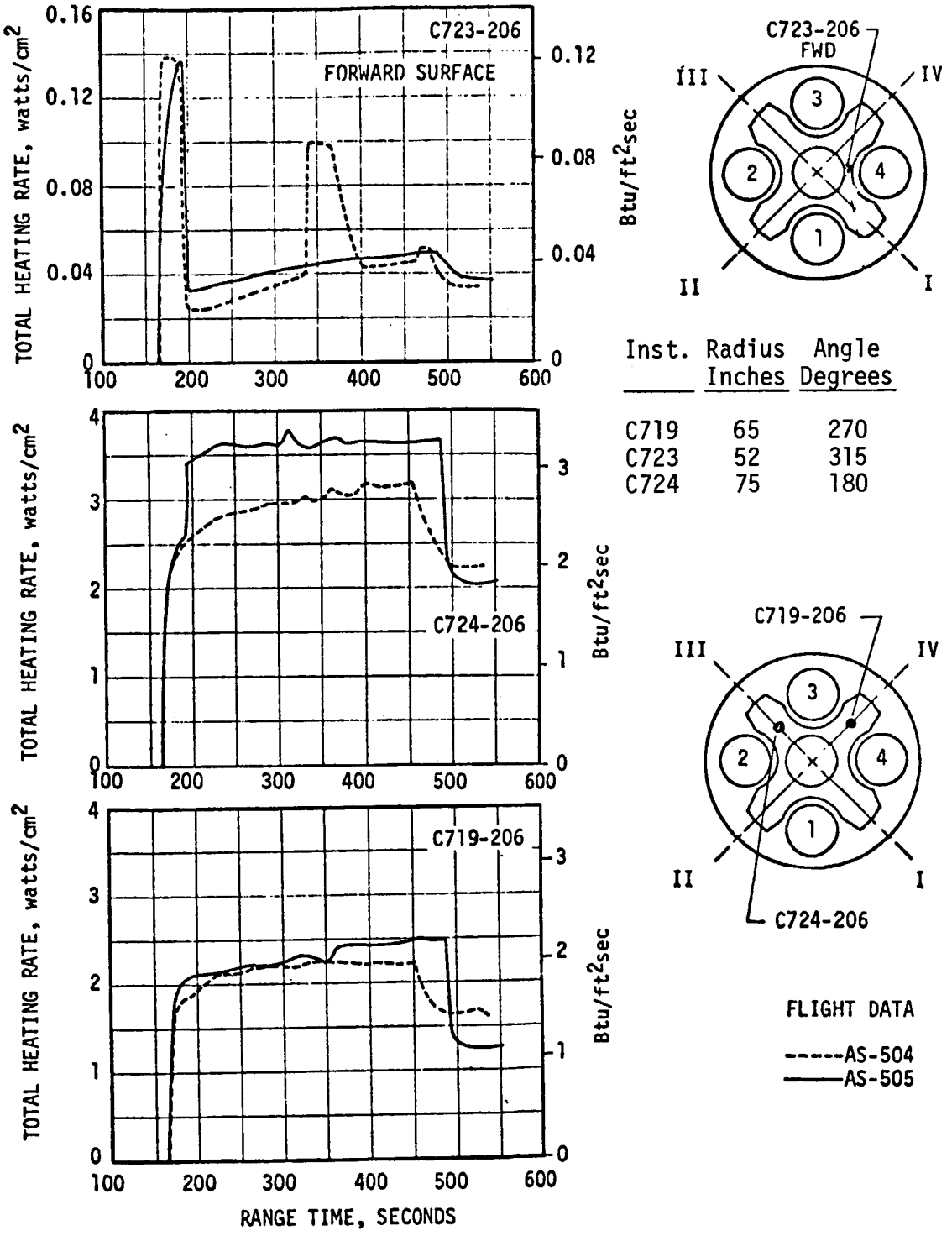

FIGURE 6.5-9 TOTAL HEATING RATES ON HEAT SHIELD FORWARD AND AFT SURFACES ON AS-504 and AS-505.

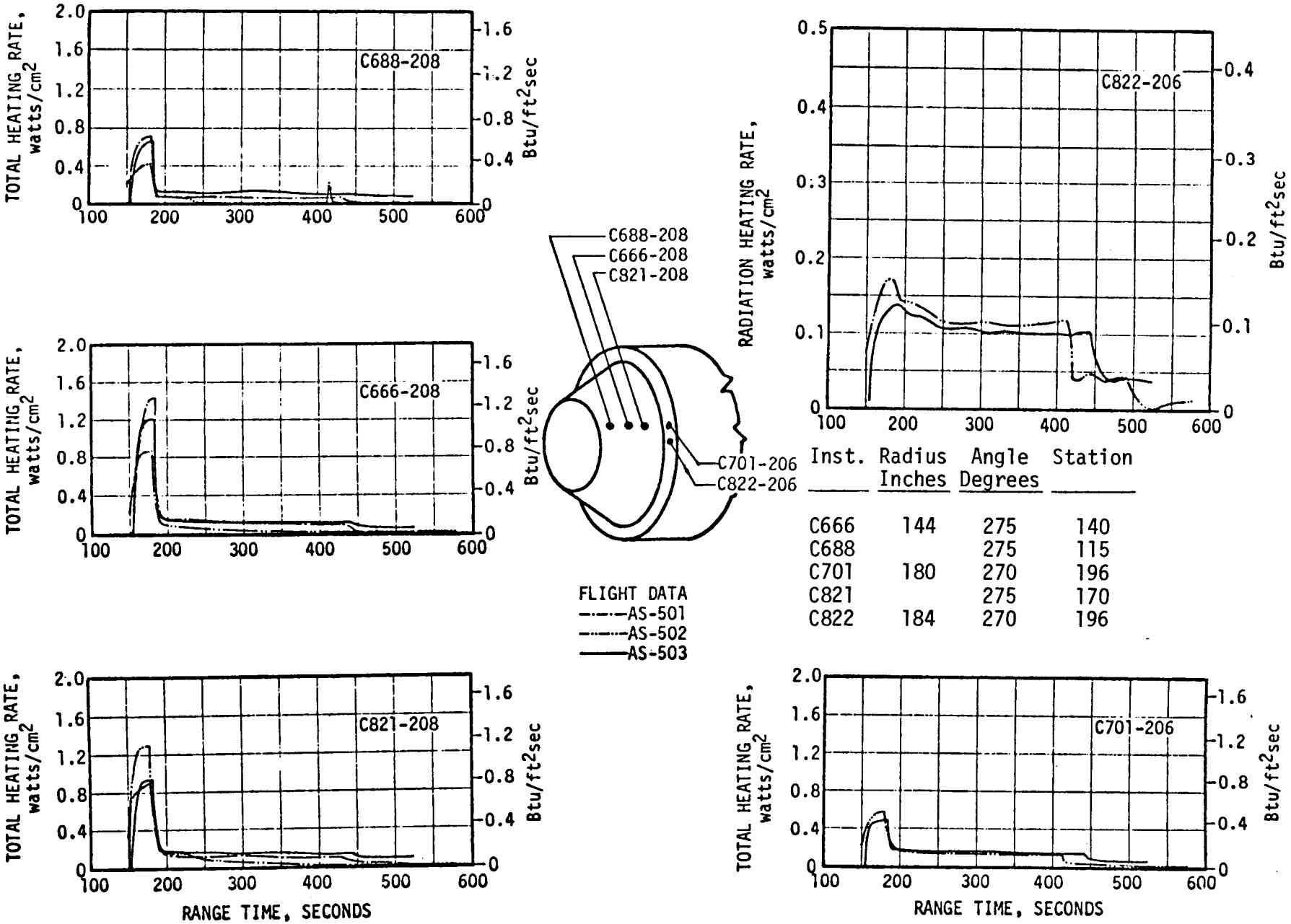

Inst.	Radius Inches	Angle Degrees	Station
C666	144	275	140
C688		275	115
C701	180	270	196
C821		275	170
C822	184	270	196

FIGURE 6.5-10 THRUST CONE TOTAL AND RADIATION HEATING RATES ON AS-501 thru AS-503.

6.6 COMPARISON OF MODEL AND FLIGHT TEST RESULTS

A precise comparison of model and flight results is almost impossible because of variations in both model and flight data which make it difficult to define a basis for comparison. During the process of model testing, a large range of configurations are tested and the data for each configuration exhibit considerable scatter. The vehicle design environment is selected from a conservative evaluation of the model results because of the large uncertainties involved in model simulation and operation. Because of this, flight deviations from the resulting design values are not necessarily representative of poor model simulation accuracy, but rather a combination of uncertainties in model simulation and in the important factors which affect the base environment. Because of these uncertainties, the model results can be evaluated based on different criteria to indicate agreement with the flight test results or large discrepancies depending upon the perspective chosen. Based on the conservative evaluation of model results which represents the design environment, the convective heating on the flight vehicle was significantly over-predicted by the model results. But evaluation of the model results based on flight experience with adjustments for the cooling effects of the turbine exhaust injection into the rocket nozzle wall can show reasonably good agreement with the measured convection heating.

The comparisons to be presented for convective heating will illustrate the range of model and flight results with comments on the effect of reduced recovery temperature. Comparisons will be made using the analytical predictions of radiation since scale effects limited the model radiation to approximately 4 percent of the values measured in flight. Before reviewing the comparison of radiative and convective heating, the base pressure results will be compared.

Pressure

Since base pressure was not a critical factor in the S-II base design, a conservative estimate of the base pressure was used for design and relatively few measurements of pressure were made during the model test program. Based on the measurements which were made, heat shield aft face pressures in the range of 0.02 to 0.035 psia would have been predicted from prototype model tests with engines near the null position. Parametric model tests with the heat shield closer to the nozzle exit (43 rather than 60 inches) indicated an average pressure of 0.045 psia at the maximum pressure location. This would increase to 0.051 psia if corrected for the increase in nozzle stagnation pressure from 632 to 715 psia for the PMR shift from 5.0 to 5.5.

Flight test results indicate good agreement with the model results on the inner portion of the heat shield while they are much higher in the outer regions. The general behavior and range of data are illustrated in Figure 6.6-1. The flight results shown illustrate pressures (averaged over the indicated flights) for three flight conditions: (1) interstage on, (2) just after second plane separation, and (3) at high altitude just before the PMR step (or CECO on AS-505). Model data should be expected to agree with the lowest flight results since external flow was not simulated in the model tests, but the flight results at the peak location are 60 to 70 percent above the model

results. This is probably due to the increase in the reversed mass flow from the turbine exhaust injection into the nozzle boundary layer. Comparative model results with and without turbine exhaust are limited, but at two comparable locations (both at a full scale radius of 83 inches) the model turbine exhaust simulation caused an increase in heat shield pressure of 30 to 56 percent.

Pressures on the thrust cone with the interstage skirt removed are so low on both model and flight tests that measurement is difficult and comparisons would be more representative of instrumentation problems than scale differences. With the interstage in place the pressure measured on the model (0.024 psia) is slightly lower than the range of 0.029 to 0.035 psia recorded in flight, but the measurements were in slightly different positions. Considering the difficulties in achieving steady flow in the interstage during a short duration test, the agreement is considered very good.

Radiation Heating

Two methods of predicting radiation described in Section 6.3 were used to define the base environment since model radiation is greatly different from full scale values. In the comparison with flight results, the radiation predictions used as the design environment (Reference 6-2) will be referred to as "design prediction," while the later analysis using a band model description of the gaseous radiation (Reference 6-10) will be referred to as "band model."

Comparison of the flight data and predicted radiation on the heat shield is shown in Figure 6.6-2. The indicated flight results are reduced by 35 percent for comparison with the design environment to compensate for calorimeter errors described previously. The size of the adjustment was taken from the sample analysis of Reference 6-9 which was for a gage at the 100 inch radius. It is expected that the correction required at the 53 inch radius would be less due to the reduced total heating at this location, but no evaluation of this effect has been made. The comparison of flight radiation measurements with preflight predictions indicate that the predictions are 25 to 75 percent too high on the heat shield, but the indicated error is questionable due to the large correction required in the flight data and the uncertainty in some of the data used in the correction.

Peak values of radiation heating indicated on the thrust cone close-out (typical data in Figure 6.5-10) are approximately equal to the predicted values, but no evaluation has been made of the possible errors in thrust cone measurements caused by the calorimeter construction. The low level of total heating on the thrust cone might reduce the error due to heating of the calorimeter window, but the relatively low spectral cut-off of the window transmission ($\approx$3.5 μm) would block a significant portion of the radiation from the plumes. The result could be that the actual incident radiation is higher than indicated. Comparisons both with and without the interstage shown in Table 6.6-1 present the range of indicated results and design predictions.

6.6 (Continued)

TABLE 6.6-1. COMPARISON OF THRUST CONE RADIATION

	HEATING RATE - WATTS/CM^2	
	INTERSTAGE ON	INTERSTAGE OFF
Flight	0.13 - 0.18	0.10 - 0.13
Design Prediction	0.29	0.15
Band Model	-	0.15

Convective Heating

Due to interest in various engine deflection arrangements, model tests with a true null engine arrangement at a mixture ratio of 5.5 were limited, and no tests were run with slight outboard deflections representative of the engine positions resulting from precant on the first five flight vehicles. However, the probable effect of the slight outboard deflection would be to reduce the heating rate by less than 20 percent which is small in comparison to the spread between flight and model data.

The comparison of flight and model convective heating on the heat shield in Figure 6.6-3 shows good agreement near the center nozzle on a line between outboard engines with the model results becoming much greater at larger radii and between center and outboard engines. The differences in the results are attributed to the higher recovery temperature on the model because of the absence of turbopump exhaust injection into the nozzle.

A possible explanation of the good agreement near the center nozzles is that heating at this location is caused by recirculation of gas from the reversed flow impingement regions farther out on the heat shield. Because of this, the model flow is cooled more than the flight vehicle by the cooler heat shield surface so the temperature difference between model and flight conditions is reduced and better data agreement results.

Adjustments for recovery temperature are difficult since the recovery temperature varies with position on the heat shield and no direct measurement of recovery temperature could be made on the model. Based on temperature measurements made on the model it is expected that the recovery to surface temperature difference is nominally about twice the flight value in regions of maximum heating and increases to almost three times the flight value for model measurements used in the design criteria. If the model heating rates could be adjusted to flight conditions based on the correct temperature difference for flight conditions with turbine exhaust injection into the nozzles, the flight and model heating would probably agree within the uncertainties in the measurements and engine misalignment effects. This would indicate that there is no large scale effect on the heat transfer coefficient.

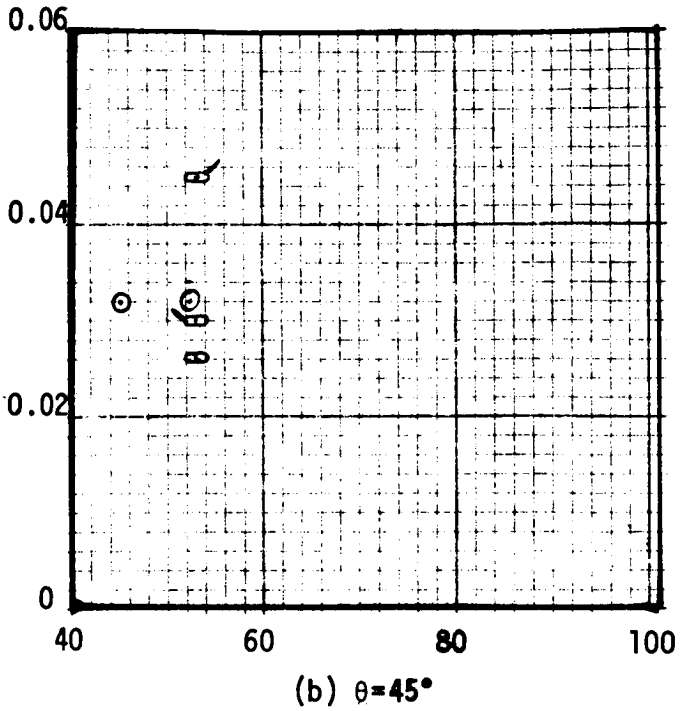

(b) θ=45°

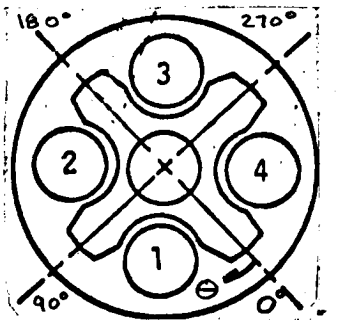

Average Flight Data

Symbol	Flights	Instrument
△	5	D162
◇	3	D94
□	3	D95
▽	2	D161
⬭	5	D157

Flags

Interstage on
Just after interstage separation
None Just before PMR step or CECO
⊙ Average Prototype Model data from MSFC tests for O/F = 5.5
0 Average Prototype Model data from CAL corrected to O/F=5.5

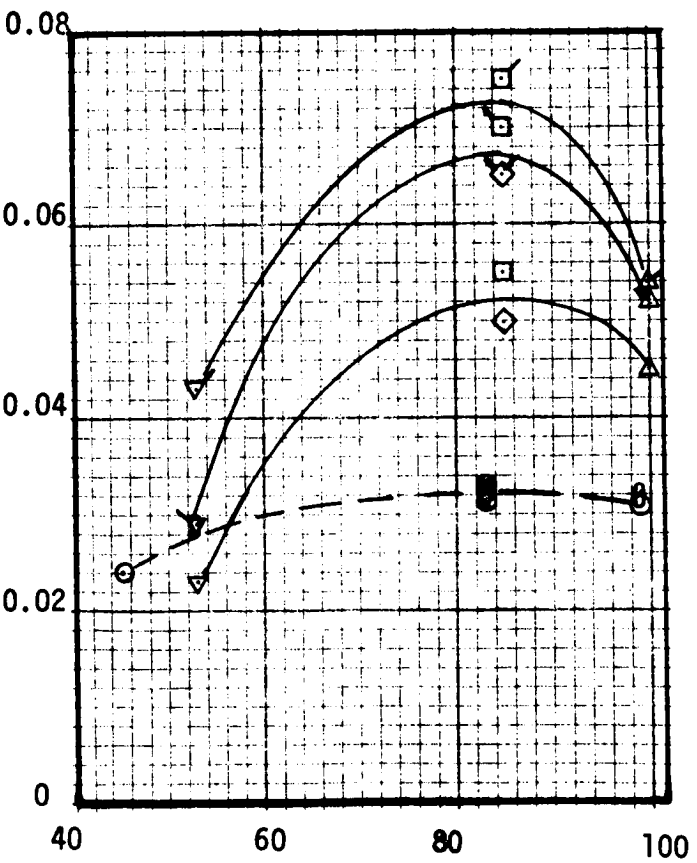

(a) θ=0°

Figure 6.6-1 Comparison of model and flight measurements of heat shield aft face pressures.

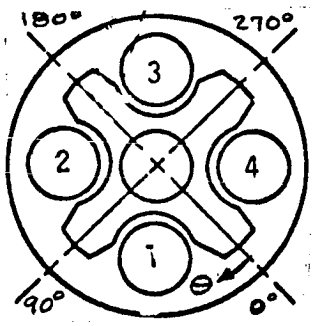

⊙ Indicated flight data averaged from peak values on AS501 thru AS505

⊡ Flight indication x 0.65

⊖ Band model prediction

—— Design prediction for all θ Distribution used to reduce total heating data to convective heating.

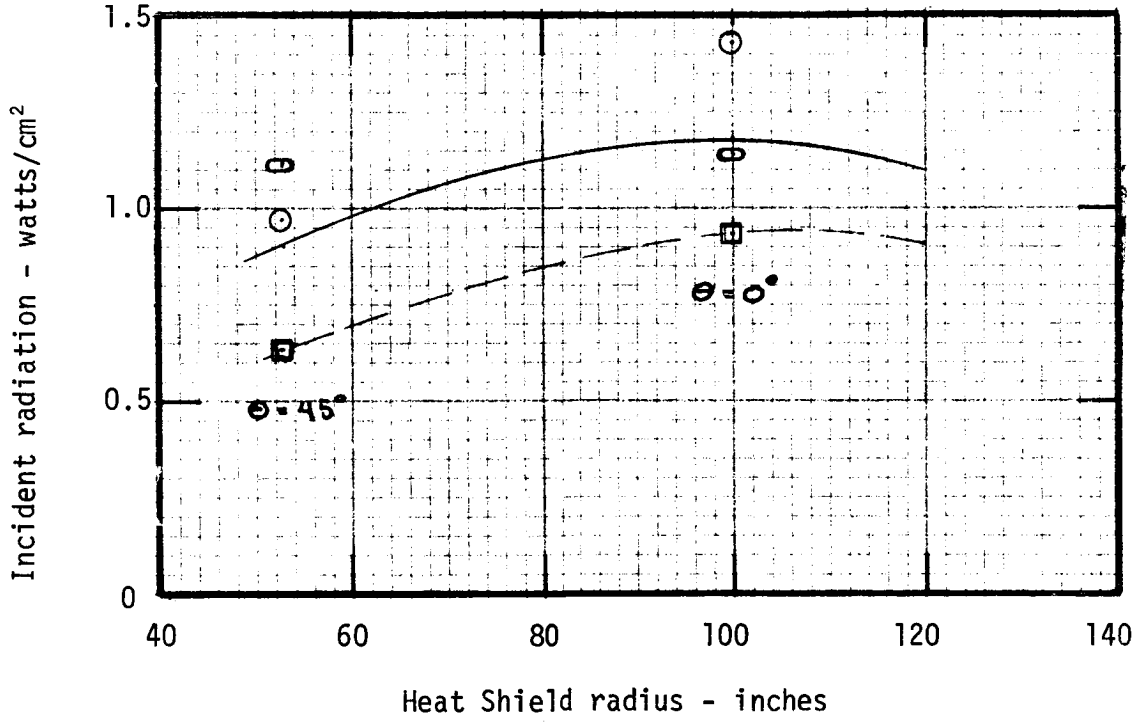

Figure 6.6-2 Comparison of heat shield radiation heating rates for 5 engine operation with PMR ≃ 5.5.

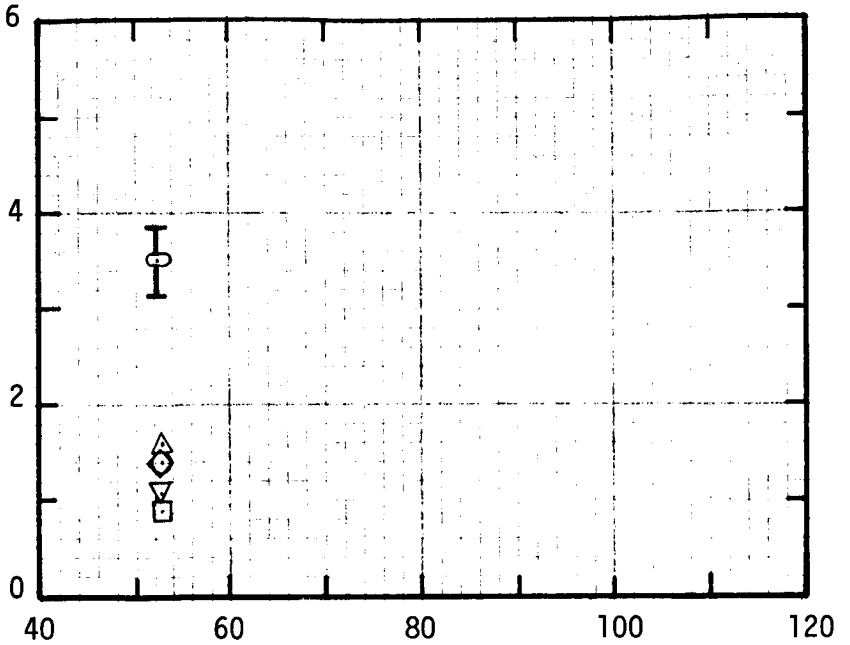

(b) θ = 45°

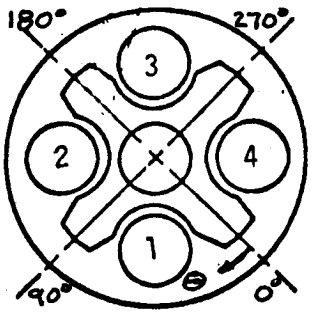

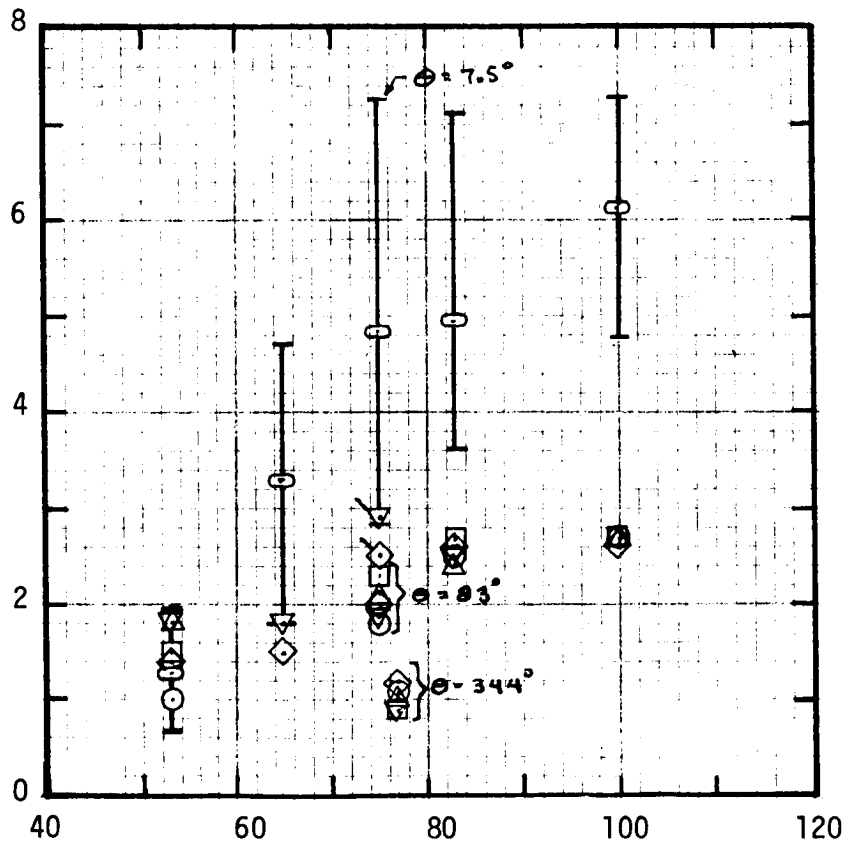

Convective heating rate - watts/cm^2

Heat shield radius - inches

(a) Radial lines between outboard engines at 0°, 180°, or 270° except, as noted.

Flight

- ○ 501
- △ 502
- □ 503
- ◇ 504
- ▽ 505
- ⬭ Average model data from MSFC tests at PMR=5.5
- I Range of model data
- \ Inst. C724 - other data at 75 in. is C722

Note: Radiation values used in reducing total heating rates are indicated in Fig. 6.6-2.

Figure 6.6-3 Comparison of model and flight convective heating.

6.7 REFERENCES

6-1. NAR Internal Letter LEVA-190-405-71/32, "J-2 Engine Exhaust Plume Impingement Heating Rates and Pressures for Skylab ICD," March 25, 1971.

6-2. NAR Internal Letter S-II/S-I 65-68 Addendum I, "Radiation Figures for Inclusion in S-II Final Design Base Region Thermal Environment," August 9, 1965.

6-3. Sergeant, R. J., "Base Heating Scaling Criteria for a Four-Engine Rocket Cluster Operating at High Altitude," AIAA Paper 65-826 presented at the Aerothermochemistry of Turbulent Flows Conference, December 1965.

6-4. Rickard, W. D., "High Altitude Investigations on the Saturn S-II Stage Using Short-Duration Techniques. Part I - Parameter Studies," Cornell Aeronautical Laboratory HM-1510-Y-17(I), April 1965.

6-5. Rickard, W. D., "High Altitude Investigations on the Saturn S-II Stage Using Short-Duration Techniques. Part II - Prototype Base Environment," Cornell Aeronautical Laboratory HM-1510-Y-17 (II), April 1965.

6-6. Boeing Document D5-15796-1, "Aerothermodynamics Flight Evaluation Summary - AS-501 through AS-503," June 19, 1969.

6-7. Boeing Document D5-15796-2, "Aerothermodynamics Flight Evaluation Summary - AS-504 through AS-505," November 14, 1969.

6-8. NAR Internal Letter S-II-190-700-69-21, "AS-503 S-II Base Region Gas Recovery Temperature Evaluation," March 7, 1969.

6-9. NAR Internal Letter LEVA-190-405-71/110, "Transient Analysis of the S-II Flight Radiometer," October 1971.

6-10. White, S. A. and Reardon, J. E., "Prediction of the Saturn S-II Base Radiation Environment," Hayes International Report 1469, August 1967.

THIS PAGE LEFT BLANK INTENTIONALLY

CONTENTS

SECTION 7.0 OTHER DATA

7.1	GENERAL DISCUSSION	7-2
7.2	REFERENCES	7-3

7.0 OTHER DATA

7.1 GENERAL DISCUSSION

This section includes a list of references which contain base heating data from previous model and flight test programs such as Polaris, Minuteman, Titan, Delta, Thor and Jupiter. These references provide the reader additional base heating data for defining effects of solid propellants, base geometry and engine operating conditions. Most of these references are classified. The following show the references pertinent to various booster vehicles.

a. Polaris (References 7-1 through 7-7)

b. Minuteman (References 7-8 through 7-13)

c. Titan (References 7-14 through 7-21)

d. Delta (Reference 7-22)

e. Thor (References 7-23 and 7-24)

f. Jupiter (Reference 7-25)

7.2 REFERENCES

7-1. Etemad, G. A., G. H. Parker, and M. L. Sheeren, "Flow Characteristics, Convective and Radiative Heating in Base Areas of the Polaris Missile," Symposium Proceedings on Simulated Altitude Testing of Rocket and Missile Components (Confidential), AF AEDC TR-60-6, 3-5-1 to 3-5-39 (1960).

7-2. Bettencourt, H. S.; and Sutphin, D. L., "Polaris A3 Base Heating Thermodynamics Analysis Report," Lockheed Missiles and Space Company LMSC-803299, October 3, 1963 (Confidential).

7-3. Antonides, G. J.; Hines, F. L., and Wong, R. C., "Thermodynamics Analysis Report on Polaris A3 Scale Model Base Environment Program (P8/P16)," Lockheed Missiles and Space Company, LMSC-802106, December 2, 1962 (Confidential).

7-4. Anon., "A3 Polaris Preliminary Base Heating Thermodynamics Analysis Report," Lockheed Missiles and Space Company, LMSC-801935, September 21, 1962 (Confidential).

7-5. Austin, R. F., and Milillo, J. R., "Polaris Missile Tests at Transonic Speeds in the AEDC 16-Foot Transonic Circuit. Phase IV: Solid Propellant Tests of 0.20-Scale Model," AEDC-TN-59-135, November 1959 (Confidential).

7-6. Barton, D. L., and Wilson, R. L., "Tests of an ABL 1/3-Scale Second Stage Polaris Rocket Motor at High Altitudes," AEDC-TN-60-151, August 1960 (Confidential).

7-7. Barkham, J. E., et al, "Establishment of Thermal Characteristics in Base Area of Polaris Missile," Lockheed Missiles and Space Division LMSD-450955, April 11, 1959 (Confidential).

7-8. Liepman, H. P., "Minuteman Base Heating Studies and Preflight Test Results," Ballistic Systems Division BSD-TN-61-9, July 1961 (Confidential).

7-9. Irvine, T. M., "Minuteman Thermal Environment During Launch as Measured in 1/20-Scale Tests," Boeing Document D2-4567, December 1960 (Confidential).

7-10. Barnes, R. H., and Homer, W. R., "Summary Report of Results of Minuteman Model Tests to Investigate Inflight Base Heating," Boeing Document D2-9719, August 1961 (Confidential).

7-11. Brunner, D. W., "Launch Thermal Environment, Summary - AMR Flight Test Program, WS-133A (Minuteman)," Boeing Document D2-14744, June 1963 (Confidential).

7-12. Barnes, R. H., "Design Heating Data, Minuteman - Inflight Base Heating," Boeing Document D2-3976-3, December 1960 (Confidential).

7.2 (Continued)

7-13. Suddarth, J. L., and Kurtovich, D. D., "Minuteman Launch Radiation Heating," Boeing Document D2-5936, February 1961 (Confidential).

7-14. Weeks, R. M., "624A (Titan IIIC). Phase III: Base Heating and Recirculation Wind Tunnel Test Post-Test Report," Space Systems Division, SSD-CR-64-15, April 1964 (Confidential).

7-15. Weeks, R. M., "624A (Titan IIIC). Phases I and II: Base Heating and Recirculation Test Post-Test Report," Space Systems Division SSD-CR-63-217, December 1963 (Confidential).

7-16. Baker, C. D., "Base Heating and Base Pressure Investigation of a 5.5-Percent-Scale Titan III Booster with Solid-Propellant Booster Motors," AEDC-TDR-63-194, October 1963 (Confidential).

7-17. Gerke, P. D., "Base Heating and Base Pressure Investigation of a 5.5-Percent-Scale Titan III, Phase III," AEDC-TDR-63-259, January 1964 (Confidential).

7-18. Olson, D., "642A (Titan IIIC). Phase IV: Base Heating and Recirculation Wind Tunnel Test, Post-Test Report," Space Systems Division SSD-CR-64-85, June 1964 (Confidential).

7-19. Harper, R. E., "Variation of Exhaust Plume Radiant Heat Flux with Altitude from 1/33-Scale Titan III Solid Propellant Rocket Motors," AEDC-TDR-63-101, June 1963 (Confidential).

7-20. Weeks, R. M., "642A (Titan IIIC). Phase III: Base Heating and Recirculation Wind Tunnel Test Pretest Report," Space Systems Division SSD-CR-63-142, July 1963 (Confidential).

7-21. Trost, J. E., "Review of Base Heating Flight Test Data Titan II Missiles N-25 and N-26," AD-828-733, May 1964 (Confidential).

7-22. Greenwald, G. F., "Base Thermal Environment of the Delta Launch Vehicle with Six Strap-on Solid Propellant Motors," presented to the AIAA 7th Propulsion Joint Specialists Conference, Salt Lake City, Utah, June 14, 1971.

7-23. Jackson, R. H., "Base Region Environmental Results Obtained from Three Thor Boosters," DAC-SM-46507, June 1965 (Confidential).

7-24. "Base Recirculation on a 10.7-Percent Scale Model of Thorad Afterbody at Trajectory Mach Number of 0.33 to 3.05," AEDC-TDR-63-136, August 1963 (Confidential).

7-25. "Jupiter Base Plate Heating," ABMA DSD-TM-25-59, October 1959 (Confidential).

☆U.S. Government Printing Office: 1972 -- 746-821/4716 Region No. 4